RECTANGULAR WAVEGUIDE MATERIAL CHARACTERIZATION: ANISOTROPIC PROPERTY EXTRACTION AND MEASUREMENT VALIDATION

By

Benjamin Reid Crowgey

A DISSERTATION

Submitted to
Michigan State University
in partial fulfillment of the requirements
for the degree of

Electrical Engineering – Doctor of Philosophy

2013

ABSTRACT

RECTANGULAR WAVEGUIDE MATERIAL CHARACTERIZATION: ANISOTROPIC PROPERTY EXTRACTION AND MEASUREMENT VALIDATION

By

Benjamin Reid Crowgey

Rectangular waveguide methods are appealing for measuring isotropic and anisotropic materials because of high signal strength due to field confinement, and the ability to control the polarization of the applied electric field. As a stepping stone to developing methods for characterizing materials with fully-populated anisotropic tensor characteristics, techniques are presented in this dissertation to characterize isotropic, biaxially anisotropic, and gyromagnetic materials. Two characterization techniques are investigated for each material, and thus six different techniques are described. Additionally, a waveguide standard is introduced which may be used to validate the measurement of the permittivity and permeability of materials at microwave frequencies.

The first characterization method examined is the Nicolson-Ross-Weir (NRW) technique for the extraction of isotropic parameters of a sample completely filling the cross-section of a rectangular waveguide. A second technique is proposed for the characterization of an isotropic conductor-backed sample filling the cross-section of a waveguide. If the sample is conductor-backed, and occupies the entire cross-section, a transmission measurement is not available, and thus a method must be found for providing two sufficiently different reflection measurements.The technique proposed here is to place a waveguide iris in front of the sample, exposing the sample to a spectrum of evanescent modes. By measuring the reflection coefficient with and without an iris, the necessary two data may be obtained to determine the material parameters. A mode-matching approach is used to determine the theoretical response of a sample placed behind the waveguide iris. This response is used in a root-searching algorithm to determine permittivity and permeability by comparing to measurements of the reflection coefficient.

For the characterization of biaxially anisotropic materials, the first method considers an extension of the NRW technique for characterization of a sample filling the cross-section of a waveguide. Due to the rectangular nature of the waveguide, typically three different samples are manufactured from the same material in order to characterize the six complex material parameters. The second technique for measuring the electromagnetic properties of a biaxially anisotropic material sample uses a reduced-aperture waveguide sample holder designed to accommodate a cubical sample. All the tensor material parameters can then be determined by measuring the reflection and transmission coefficients of a single sample placed into several orientations. The parameters are obtained using a root-searching algorithm by comparing theoretically computed and measured reflection and transmission coefficients. The theoretical coefficients are determined using a mode matching technique.

The first technique for characterizing the electromagnetic properties of gyromagnetic materials considers requires filling the cross-section of a waveguide. The material parameters are extracted from the measured reflection and transmission coefficients. Since the cross-sectional dimensions of waveguides become prohibitively large at low frequencies, and it is at these frequencies that the gyromagnetic properties are most pronounced, sufficiently large samples may not be available. Therefore, the second technique uses a reduced-aperture sample holder that does not require the sample to fill the entire cross section of the guide. The theoretical reflection and transmission coefficients for both methods are determined using a mode matching technique. A nonlinear least squares method is employed to extract the gyromagnetic material parameters.

Finally, this dissertation introduces a waveguide standard that acts as a surrogate material with both electric and magnetic properties and is useful for verifying systems designed to characterize engineered materials using the NRW technique. A genetic algorithm is used to optimize the all-metallic structure to produce a surrogate with both relative permittivity and permeability near six across S-band, and with low sensitivity to changes in geometry to reduce the effects of fabrication errors.

For the women in my life: Martha, Stacey, and Elliana.

ACKNOWLEDGMENTS

There are so many people who deserve my appreciation. I first must thank my committee members who so graciously agreed to help me with the completion of my PhD. Thank you, Dr. Leo Kempel, for all the years of advice and support. Though you have become increasingly busy over the years with administrative duties, you have always found the time to meet with me to discuss research, give opinions, or just see how I'm doing. It has really meant a lot to me, and it's amazing to think how far I've come since sitting in on your cell phone freshmen seminar. To Dr. Shanker Balasubramaniam, I have appreciated the many years of challenging coursework, humorous advice, and helpful insight on the material discussed in this dissertation. I enjoyed posting you up on the basketball court and you putting me back in my place in the classroom. Maybe one day soon I will take up running like you so frequently say I should. Another special thanks is extended to Dr. Prem Chahal, who has been available many times to answer questions in times of confusion and to give general advice from the industry perspective. Thanks to Dr. Andrew Christlieb for agreeing to participate in my graduate committee and for his recommendations on this work.

Recognition must be extended to those at AFOSR since the majority of this work was performed under Subcontract Agreement FA 9550-09-1-0182. Additionally, thank you to Dr. Tayfun Ozdemir for supporting me for a couple of semesters while I worked on the very interesting UAV project. I had a terrific time performing this research, and I hope to work with you again. Thank you to General Electric for allowing me to participate on the conductor-backed material characterization project. A special thanks to Craig Baucke and Glen Hilderbrand for their helpful insight into this project. It was great working with you.

Dr. Mike Havrilla deserves my appreciation for all the years of advice and insightful conversations. Additionally, thank you for letting us use your S-band waveguides, which still have yet to be returned to you. Thanks also to Captain Milo Hyde, IV, from AFIT for sharing measurement data with me.

Thanks to all of my Ben Crowgey associates, fellow students, office mates, and friends. Since I've been here for so many years, I've gotten to know many of you. I can say each and every one of you made this an enjoyable journey and I will forever remember the years here at MSU. Special thanks goes out to Dr. Raoul Ouedraogo for his many years of help with anything related to EM. You are a good friend and I hope to stay in contact with you for many years to come. Also thanks go to Junyan Tang for your numerous amount of hours spent in the lab measuring the different types of material this dissertation uses for characterization. I will miss your Tang-isms and helpful weight loss advice. My appreciation to Collin Meierbachtol for all your help. Anytime I had a random question you were there with the answer, you were my go-to guy. Thank you Josh Myers for helping me disengage from everyday work and enjoy the time spent in our office. To Korede Akinlabi-Oladimeji and Andrew Temme, thank you for the years of friendship and assistance with measurements, coursework, and everyday issues.

Very special thanks go to Dr. Edward Rothwell for being an exceptional and knowledgeable advisor. The amount of time you spent in your office assisting and guiding me through both school and life is time I will always cherish. Words seriously can not express how much I have appreciated everything you've done for me over the years. I am sure if I did try to express these feeling in words, I'd make you pull your hair out because of my many grammatical and logic writing errors. I know the writing of this dissertation has been a journey for both of us, but I really do appreciate all the time you've spent reviewing it. All said and done, I know I could not have asked for a better advisor. Thank you.

I am indebted to my parents John and Martha Crowgey for their love and support. You've been there from the beginning and I know I would not be where I am now if it wasn't for you. Especially to my mother, who is and was always a phone call away. You made my life during graduate school easier and I can't begin to tell you how much that has meant to me. To my sisters Sarah and Julie, thank you being there when I needed you like big sisters should. To my whole family, you have pushed and applauded me, and for all of that

I am thankful. Thank you Granddad for always knowing my potential and making sure I achieved my goals. I did it. I miss you, but I always know you are with me.

Finally I want to thank my wife, Stacey, for all of her support, motivation, encouragement, and patience while I completed my education. You spent numerous hours looking over this dissertation before I sent it to Dr. Rothwell for final review. I know he appreciates those hours as much, if not more, as me. We met while I was completing my masters here at MSU, moved in together during the second year of my doctorate, got married when I was in the middle of the program, and welcomed a little girl into the world when I was finishing my degree. Needless to say, these years with you have been eventful and memorable, and I am sure we will never forget this time in our lives when I was completing my PhD. It is now time to move on to the next phase of our lives, and I can't wait.

TABLE OF CONTENTS

LIST OF TABLES

LIST OF FIGURES

CHAPTER 1

INTRODUCTION AND BACKGROUND

1.1 Electromagnetic Material Characterization

Electromangetic material characterization has long been an interest of the research community. The goal is to determine permittivity (ϵ) and permeability (μ), also known as the constitutive parameters, as accurately as possible [1]. The constitutive parameters describe the effect externally applied electric and magnetic fields have on a material. Many disciplines rely on the knowledge of the electromagnetic material properties, including stealth and integrated circuits. In stealth technology, the constitutive parameters describe how effectively a particular materials absorbs a radar signal [2]. Integrated circuits rely on new materials, and subsequently accurate knowledge of constitutive parameters, to increase the ability to transmit higher bandwidth signals as clock speeds in electronic devices continue to increase [3].

Engineered materials, which have gained increasing importance in a variety of applications at microwave frequencies, often have anisotropic electromagnetic characteristics. The use of engineered materials in the design of radio frequency (RF) systems requires an ac-

curate knowledge of material constitutive parameters. Some recently synthesized materials include the use of graphene nanoribbons or metallic inclusions in miniaturization of electronic components [4]-[5], ferrite loaded polymers to increase EMI shielding [6], cellular materials such as honeycomb structures to decrease radar cross section [7]-[8], and anisotropic materials used to enhance antenna operation [9]-[10]. Since the properties of these materials are often hard to accurately predict (due to modeling uncertainties and variability in the manufacturing process), they are usually measured in a laboratory.

The theoretical implications of anisotropic materials are well described in the literature [11], and several techniques for the characterization of these materials have been introduced. These include free space methods [12]-[13], resonant cavity methods [14]-[17], open-ended waveguide probe methods [18]-[19], and rectangular waveguide methods [20]-[22]. Free-space methods are unattractive for many materials because the sample size must be large compared to the footprint of the interrogating beam to minimize edge diffraction, and samples are generally limited in size. Similarly, contact probe methods require sample sizes larger than the probe aperture. Cavity methods usually involve small samples but are inherently narrowband, and thus characterization of materials over a wide frequency range is difficult. This dissertation concentrates on the use of rectangular waveguide applicators for anisotropic material characterization.

1.2 Rectangular Waveguide Material Characterization

Rectangular waveguide methods are popular for measuring the electromagnetic properties of materials because of ease of sample preparation, high signal strength, and wide bandwidth. A variety of characterization techniques use rectangular waveguide applicators. In these techniques, samples can be placed inside the guide, against an open-ended flange, or even pressed against a slot cut into a waveguide wall. The most common method is to machine a sample to fill the cross-section of the waveguide and measure the transmission and reflection

coefficients. These measurements provide the two necessary data to find both material parameters of an isotropic sample. One of the most widely used extraction algorithms is the Nicolson-Ross-Weir (NRW) method [23]-[24]. The attraction of the NRW characterization method results from the availability of closed-form expressions for μ and ϵ. The NRW extraction can be used with rectangular waveguides [25], coaxial applicators [26]-[27], free-space methods [28], and stripline measurements [29]. Unfortunately, a closed form expression is not available for most types of anisotropic materials. Typically, these parameters are obtained using iterative solvers, such as Newton's method [30]-[31] or a least squares approach [32]-[33] by comparing theoretically computed and measured reflection and transmission coefficients.

Rectangular waveguide characterization techniques can be limited by sample size restrictions or poor signal-to-noise ratio (SNR) for the transmission. To maintain dominant mode excitation, the cross section of a waveguide becomes larger as the operational frequency of the guide decreases. In [34], the authors make use of a reduced-waveguide technique to characterize isotropic materials with small electrical size at low frequencies, avoiding the large waveguides ordinarily required. The reflection and transmission coefficients are measured to determine the scalar permittivity and permeability. The use of waveguide applicators may also result in extracted material parameters that are highly sensitive to error propagation from measurement uncertainties. This is especially prominent when measuring high loss or highly reflective samples where there is poor SNR for the transmission coefficient measurement. In [35] the authors present a partially-filled waveguide method that enhances transmission quality and accuracy of the material characterization. It was demonstrated that this method accurately characterizes samples with low-loss and high-loss parameters. To calculate the theoretical reflection and transmission coefficients, both of these techniques use a mode-matching technique to accommodate the high-order mode excitation resulting from the waveguide discontinuities. The extraction of material parameters was performed in [34] using a nonlinear least squares algorithm, while [35] used a Newton root search method.

Other rectangular waveguide techniques make use of only the reflection measurements because of the simplification of the measurement configuration, or because a transmission measurement is not available. Two common types of reflection-only characterization techniques are underlay and overlay methods [36]. Underlay methods make use of changing the backing of the material under test (MUT). The air/conductor backed method [37] measures a sample first with the MUT backed by a conductor and then with the MUT backed by air. In a rectangular waveguide these measurements are performed with the MUT backed by a short circuit and a match load. In the layer-shift method [38] the reflection is measured with a conductor placed at two positions behind the MUT. For a rectangular waveguide measurement system this is done using two different offset shorts.

Overlay methods are commonly used when the backing of the MUT cannot be altered. Magnetic radar-absorbing materials (MagRAM) are often applied to the conducting surfaces of air vehicles to reduce radar cross section. To ensure proper aircraft design, the electromagnetic properties of these materials must be accurately characterized. Unfortunately, the process of bonding the MagRAM to the conductor produces a chemical reaction that alters the intrinsic electromagnetic properties of the absorber in unpredictable ways, and thus it is crucial that the absorber be characterized while still attached to the conductor backing. If the sample is conductor backed, and occupies the entire cross section of a waveguide, a transmission measurement is not available, and thus a method must be found for providing two sufficiently different reflection measurements. Overlay methods are prominent in contact probe characterization techniques. In [39], the authors achieve the characterization of ϵ and μ of a conductor-backed sample using a rectangular open-ended waveguide probe applicator. Two independent reflection measurements are obtained using either two thicknesses of the same material or one measurement with one material and a second measurement with a known material as a top layer. The theoretical reflection coefficients necessary for characterization are determined using a variational method to develop expressions of the waveguide impedance. The approach using two thicknesses is useful in the lab where two samples of the

MUT are available, but it is not practical in the field where the MUT is typically affixed to a conductor backing. However, material characterization using the two-layer method in the field is possible since a known layer of material can be placed on top of a conductor-backed sample without having to remove the conductor backing.

Another contact probe method is described in [40], where the authors discuss the use of a two-iris waveguide probe technique to characterize lossy, conductor-backed materials. A open-ended rectangular waveguide is applied to the MUT, and the reflection coefficient is measured under two conditions. First, the reflection is measured when the open-ended waveguide aperture is unobstructed, and a second measurement is obtained when an iris is placed in the aperture of the guide. This provides the two necessary data to characterize the constitutive parameters. The theoretical reflection coefficients are determined using a combination of a modal expansion in the waveguide and aperture regions with a magnetic-field integral equation (MFIE). It is found that this technique is not as accurate as the two-thickness method but is better than the two-layer method. Since the two-thickness method cannot be employed in the field, the two-iris technique provides a favorable contact probe method.

A method is describe in [41] where conductor backed material samples are characterized through the use of a transverse slot cut in the bottom wall of a rectangular waveguide. The reflection and transmission coefficients of the sample pressed against the waveguide slot are measured. The theoretical coefficients were determined using a MFIE technique. A Newton's complex root search algorithm is then employed to iteratively solve for the constitutive parameters by comparing measurements to theory. This technique was partially successful using the transmission and reflection measurements for characterization. However, it was determined that using measurements of two separate thicknesses of the same material was more encouraging for characterization of ϵ and μ.

This dissertation investigates a characterization technique for determining scalar ϵ and μ of a conductor-back material when two thicknesses of a sample are not available. In the

present case, there is no need for measurements to be conducted in the field; therefore a sample can be manufactured for placement inside a rectangular waveguide for laboratory measurements. An iris approach, like that discussed in [40], is used to provide the two necessary reflection measurements for characterization.

1.3 Biaxially Anisotropic Material Characterization

The tensors for biaxial materials have six nonzero entries, corresponding to six complex material parameters, and therefore a minimum three different sets of complex reflection and transmission coefficient measurements are required. The typical inverse problem consists of first determining what measured data are sufficient for unequivocal determination of the constitutive parameters, and secondly, what experimental setup is preferred to collect the needed data. Some methods consider only characterizing the permittivity tensor, which reduces the number of unknown constitutive parameters to three. One such method uses a cavity perturbation technique to determine the permittivity parameters of a sample [17]. Here, the authors present the methodology to characterize low-loss engineered material and naturally uniaxial dielectrics. In the case of uniaxial dielectric materials there are only two unknown material parameters, because two dielectric material parameters are identical and the third is different. Multiple samples are manufactured and measured with the axes of the material tensor aligned with the geometry of the cavity. Using the multiple measurements, the cavity perturbation technique is combined with a finite element (FEM) solver to determine the permittivity tensor and loss tangents. This method proved to produce highly accurate results for characterizing the loss tangents. However, like most cavity methods, the characterization is inherently narrow-band.

Another method that considers characterizing only the dielectric material properties is discussed in [42]. The authors use a modified free-space focused beam system to measure the co- and cross-polarized transmission coefficients. Plane waves probe the material to provide

the adequate number of measurements for characterization. This approach uses a hybrid global-local optimization to obtain the material parameters by minimizing the difference between theoretically computed and measured transmission coefficients. The theoretical coefficients are determined using a computational electromagnetic (CEM) modeling tool. Using CEM modeling for calculation of the theoretical coefficients can be computationally expensive. Thus, the overall extraction of the material parameters is computationally intensive when a lengthy optimizer is used. Analytical solutions for the theoretical coefficients are more attractive since the time required for convergence of the solutions is typically serval orders of magnitude smaller than the time required for CEM modeling tools.

In [18], the authors describe a waveguide probe system for characterizing both the electric and magnetic biaxial material properties. Here the authors extended the open-ended waveguide probe method to anisotropic materials. This method makes use of higher-order modes produced at the probe aperture. These higher-order modes have fields with components in multiple directions, and thus the fields are related to all of the entries in the biaxial tensors. To determine the material parameters, multiple measurements with the probe oriented in multiple directions is required. Two coupled electric field integral equations (EFIEs) for the aperture field are solved numerically using a method of moments. The electric field is then expressed in terms of the material parameters. A Newton-Raphson method is employed to minimize the difference between theoretically computed and measured reflection coefficients. Like with most waveguide probe applicators, the size of the required sample must be larger than the probe aperture for accurate characterization.

Placement of a biaxial sample in the cross-section of a rectangular waveguide is considered in [20]. The necessary measurements required for characterization are obtained by using TE_{10} and TE_{20} mode excitations. Closed-form solutions for three out of the six material parameters are derived assuming these two different excitations. By rotating and measuring the sample again, the additional material parameters can be extracted in closed form. Here four measurements are obtained to characterize three material parameters. The additional

measurement greatly simplifies the steps needed to solve the inverse problem. A complicated measurement fixture is proposed in this paper where the two different modes are excited; however, no actual measurements of a biaxial sample were carried out. The authors do not go into detail on how to rotate the sample such that the fields interrogate all the material parameters. Since the shape of the sample must be rectangular to fill the cross section of the guide, it is assumed that a separate sample must be manufactured with the material parameters aligned differently.

This dissertation investigates two biaxial material characterization techniques. The first is an extension of the NRW method, where solutions for all six material parameters can be obtained in closed form. Much like in [20], multiple samples are required. However, a complicated waveguide applicator is not needed for characterization. To characterize a biaxial material using a single sample, the second method considers a sample holder which can accommodate a cubical sample. Here the single sample is interrogated in multiple orientations. This reduced-waveguide technique is similar to the isotropic characterization method discussed in [34]. However, the goal in [34] was to accommodate samples of small electrical size at low frequencies. Thus, sample shapes were typically not cubical, and a single sample was measured under one orientation to determine the scalar permittivity and permeability. In this dissertation the multiple measurements of the single sample provide the necessary measurements for full biaxial material characterization.

1.4 Gyromagnetic Material Characterization

Gyromagnetic materials are commonly used in microwave devices such as circulators, phase shifters, and tunable filters [43]. As a step towards full anisotropic tensor characterization, this dissertation considers the extraction of diagonal and off-diagonal tensor entries. Gyromagnetic materials have scalar permittivity and anisotropic permeability. The permeability tensor has two equivalent (μ_g) and one different (μ_0) diagonal entries, and two off-diagonal

entries. The two off-diagonal tensor entries are determined using the same parameter κ. Thus characterizing gyromagnetic materials require the extraction of three complex unknowns: ϵ, μ_g, and κ.

In [22] and [44] the authors describe a method for measuring the complex scalar permittivity and permeability tensor components of a gyromagnetic material using a partially filled waveguide technique. A sample partially fills the cross-section of the guide in the broad dimension while extending fully in the shorter dimension. The sample is placed off center about the broad dimension. A known isotropic material is inserted next to the gyromagnetic sample for support. A mode-matching technique is used to derive the theoretical reflection and transmission coefficients. With this anisotropic material off center, the waveguide system is nonreciprocal, which means $S_{11} = S_{22}$ and $S_{21} \neq S_{12}$. The nonreciprocity of the system permits the characterization of the permeability tensor and scalar permittivity from a signal set of measurements. The material parameters are extracted using an optimization method which seems to minimize the difference between theoretically computed and measured S-parameters. In this technique, the calculation of the theoretical S-parameters needs to deal with a complicated field structure in the sample regions. This complicated field structure includes finding the modal propagation constants by solving a transcendental equation. Thus the implementation of this technique is numerically complicated.

In this dissertation, two methods are investigated for the characterization of gyromagnetic materials. The first approach considers completely filling the cross-section of a rectangular waveguide while the second technique uses a reduced aperture sample holder to accommodate samples of small electrical size. The calculation of the theoretical reflection and transmission coefficients for both methods are analytically less complex than the approach described in [22] and [44]. Thus the implementation of the techniques described in this dissertation are numerically less complicated.

1.5 Overview of Research

The motivation for this dissertation is to explore the possible methods for characterization of anisotropic materials. As a stepping stone to developing methods for characterizing materials with fully-populated anisotropic tensor characteristics, techniques are presented in this dissertation to characterize isotropic, biaxially anisotropic, and gyromagnetic materials. Two characterization techniques are investigated for each of these materials, and thus six different techniques are described. Additionally, a waveguide standard is introduced which may be used to validate the measurement of the permittivity and permeability of materials at microwave frequencies.

Chapter 2 provides the mathematical background required for the modal analysis used in anisotropic material characterization techniques discussed in this dissertation. A bianisotropic medium containing sources is considered for transverse and longitudinal direction decomposition. Following this, a TE/TM decomposition is performed and the resulting differential equation is solved using a Fourier transformation method. Next the geometries of the materials considered in this dissertation considers are restricted to fit into a rectangular waveguide applicator and the appropriate wave equations arenderived. These wave equations are then solved using separation of variables in conjunction with the application of boundary conditions on the waveguide conducting walls. Finally, expressions for the modal fields for various anisotropic materials placed inside a rectangular waveguide are formulated. These can then be used in the proposed characterization techniques.

The third chapter presents two methods for characterizing isotropic materials. The first technique is the classical NRW extraction method for a sample filling the cross section of a rectangular waveguide. The second technique assumes the sample is conductor-backed and occupies the entire cross section. Here a transmission measurement is not available, and thus a method must be found for providing two sufficiently different reflection measurements. The technique proposed investigates placing a waveguide iris in front of the sample, thereby ex-

posing the sample to a spectrum of evanescent modes. By measuring the reflection coefficient with and without an iris, the necessary two data may be obtained to determine ϵ and μ. A mode-matching approach is used to determine the theoretical response of a sample placed behind a waveguide iris. This response is used in a root-searching algorithm to determine ϵ and μ using measurements of the reflection coefficient. A Monte Carlo analysis is used to characterize the sensitivity of the technique to typical measurement uncertainties, thereby providing a basis for the design of the waveguide applicator. Measured results are presented using commercially-available absorbers to establish the efficacy of both techniques.

Chapter 4 discusses two techniques for measuring the electromagnetic properties of a biaxially anisotropic material sample. The first approach uses three samples machined from the same material with the axes of the permittivity and permeability tensors aligned with the geometry of the waveguide. The six complex material parameters can be extracted from the measured reflection and transmission coefficients of these three samples using closed-form expressions. The second technique uses a reduced-aperture waveguide sample holder designed to accommodate a cubical sample. All of the tensor material parameters can then be determined by measuring the reflection and transmission coefficients of a single sample placed into several orientations. The theoretical reflection and transmission coefficients necessary to perform the material parameter extraction are obtained using a modal analysis technique. A Newton's method is used to perform the extraction by comparing theoretically computed and measured reflection and transmission coefficients. A Monte Carlo analysis is used to investigate the effects of the propagation of random error inherent to a vector network analyzer (VNA) used in measurement for both techniques. S-band material parameters are extracted for a biaxial sample placed in the reduced-aperture waveguide sample holder.

The fifth chapter describes two characterization techniques used to determine the electromagnetic properties of gyromagnetic materials. The first technique examined considers completely filling the cross-section of a waveguide. The material parameters are extracted from the measured reflection and transmission coefficients. Unfortunately, the available sample

size for gyromagnetic materials is too small to completely fill the waveguide cross section. To address this issue, the second technique describes the use of a reduced-aperture sample holder that does not require the sample to fill the entire cross section. Modal analysis is used in both methods to determine the reflection and transmission coefficients of the dominant mode. A non-linear least squares method is employed to extract the gyromagnetic material parameters. Details on the methodology for obtaining the theoretical reflection and transmission coefficients and a comparison to a full wave FEM solver are presented for both techniques. A Monte Carlo analysis is used to characterize the sensitivity of the reduced aperture approach to typical measurement uncertainties for different sized apertures.

The sixth chapter in this dissertation introduces a waveguide standard that acts as a surrogate material with both electric and magnetic properties and is useful for verifying systems designed to characterize engineered materials using the NRW technique. A genetic algorithm was used to optimize the all-metallic structure of the standard to produce a surrogate with both relative permittivity and permeability near six across S-band, and with low sensitivity to changes in geometry to reduce the effects of fabrication errors. A mode-matching approach allows the user to predict the material properties with high accuracy, and thus compensate for differences in geometry due to machining inaccuracy or limited availability of component parts. The mode-matching method also allows the user to design standards that may be used within other measurement bands. An example standard is characterized experimentally, the errors due to uncertainties in measured dimensions and the experimental repeatability are explored, and the usefulness of the standard as a verification tool is validated. The final chapter discusses any concluding remarks and suggestions for future work.

CHAPTER 2

Mathematical Background

2.1 Introduction

This chapter presents the theory required for the formulation of the waveguide modal analysis for anisotropic materials filling a rectangular waveguide. The field structures are first examined for a bianisotropic medium containing electric and magnetic sources. The sources and fields are decomposed along transverse and longitudinal directions. Next a TE/TM decomposition of the fields is performed, and the transverse fields are related to the longitudinal fields in terms of a differential equation. The differential equation is solved using a Fourier transform method. Then the specific materials of interest in this dissertation are considered for the derivation of the TE/TM wave equations. The solution to the wave equation determines the longitudinal fields. Additionally, expressions are derived that explicitly relate the transverse fields to the longitudinal fields. The wave equation is then solved using separation of variables and the application of boundary conditions at the rectangular waveguide conducting walls.

2.2 Fields in a Bianisotropic Material

The characterization of the electromagnetic properties of a material is largely dependent on the physical behavior of the material in the presence of an electromagnetic field. Maxwell's equations and the constitutive relations describe the overall relationship between the electromagnetic field and the media through which the field propagates. Consider a homogeneous bianisotropic medium containing phasor electric current sources, $\vec{J}(\vec{r})$, and magnetic current sources, $\vec{J}_m(\vec{r})$. Maxwell's equations in the frequency domain are given by

$$\nabla \times \vec{E}(\vec{r}) = -j\omega\vec{B}(\vec{r}) - \vec{J}_m(\vec{r}) \tag{2.1}$$

$$\nabla \times \vec{H}(\vec{r}) = j\omega\vec{D}(\vec{r}) + \vec{J}(\vec{r}) \tag{2.2}$$

$$\nabla \cdot \vec{D} = \rho \tag{2.3}$$

$$\nabla \cdot \vec{B} = \rho_m. \tag{2.4}$$

The constitutive relationships are expressed as

$$\vec{D}(\vec{r}) = \bar{\bar{\epsilon}} \cdot \vec{E}(\vec{r}) + \bar{\bar{\xi}} \cdot \vec{H}(\vec{r}) \tag{2.5}$$

$$\vec{B}(\vec{r}) = \bar{\bar{\zeta}} \cdot \vec{E}(\vec{r}) + \bar{\bar{\mu}} \cdot \vec{H}(\vec{r}). \tag{2.6}$$

Here $\vec{E}$ is the electric field intensity, $\vec{H}$ is the magnetic field intensity, $\vec{D}$ is the electric flux density, and $\vec{B}$ is the magnetic flux density. Additionally, $\bar{\bar{\epsilon}}$ is the permittivity dyadic and $\bar{\bar{\mu}}$ is the permeability dyadic. The quantities $\bar{\bar{\xi}}$ and $\bar{\bar{\zeta}}$ are coupling dyadics, and ρ and ρ_m are the electric and magnetic charge density, respectively. In (2.1) - (2.6) it is assumed that $\bar{\bar{\mu}}$ and $\bar{\bar{\epsilon}}$ do not depend on applied field strengths or spatial coordinates and thus the material is linear and homogeneous.

2.2.1 Decomposition of Fields and Sources into Transverse and Longitudinal Components

The first step for field decomposition is obtaining equations that relate the transverse field to the longitudinal fields. For brevity, the dependence on $\vec{r}$ in (2.1) - (2.6) will be left implicit. The sources and fields are decomposed into their respective transverse and longitudinal parts. The longitudinal component of $\vec{A}$ is defined as $\hat{u}A_u$, where $\hat{u}$ is a constant but otherwise arbitrary direction. Here

$$A_u = \hat{u} \cdot \vec{A}. \tag{2.7}$$

The transverse component in turn is defined as

$$\vec{A_\rho} = \vec{A} - \hat{u}A_u, \tag{2.8}$$

such that $\hat{u} \cdot \vec{A_\rho} = 0$. Using this notation, the longitudinal component of $\vec{B}$ is given by

$$B_u = \hat{u} \cdot \vec{B}. \tag{2.9}$$

Using the constitutive relationship for bianisotropic media, (2.6), and the distributive identity (A.2), (2.9) becomes

$$B_u = \hat{u} \cdot \left[\overline{\overline{\zeta}} \cdot \vec{E}\right] + \hat{u} \cdot \left[\overline{\overline{\mu}} \cdot \vec{H}\right]. \tag{2.10}$$

From the dyadic identity (A.2), it can be shown that

$$B_u = \vec{\zeta_u} \cdot \vec{E} + \vec{\mu}_u \cdot \vec{H}, \tag{2.11}$$

where $\vec{\zeta}_u = \hat{u} \cdot \overline{\overline{\zeta}}$ and $\vec{\mu}_u = \hat{u} \cdot \overline{\overline{\mu}}$. The electric and magnetic fields are then decomposed into their respective transverse and longitudinal components, resulting in

$$B_u = \vec{\zeta}_u \cdot \left[\vec{E}_\rho + \hat{u}E_u\right] + \vec{\mu}_u \cdot \left[\vec{H}_\rho + \hat{u}H_u\right]. \tag{2.12}$$

Using the distributive property again and defining $\zeta_{uu} = \vec{\zeta}_u \cdot \hat{u}$ and $\mu_{uu} = \vec{\mu}_u \cdot \hat{u}$, the longitudinal component of $\vec{B}$ is given as

$$B_u = \vec{\zeta}_u \cdot \vec{E}_\rho + \zeta_{uu}E_u + \vec{\mu}_u \cdot \vec{H}_\rho + \mu_{uu}H_u. \tag{2.13}$$

With the longitudinal component determined, the transverse component is expressed using (2.8), yielding

$$\vec{B}_\rho = \overline{\overline{\zeta}} \cdot \vec{E} + \overline{\overline{\mu}} \cdot \vec{H} - \hat{u}\left[\vec{\zeta}_u \cdot \vec{E}_\rho + \zeta_{uu}E_u + \vec{\mu}_u \cdot \vec{H}_\rho + \mu_{uu}H_u\right]. \tag{2.14}$$

Decomposing $\vec{E}$ and $\vec{H}$ into their transverse and longitudinal parts and rearranging (2.14) gives

$$\begin{aligned} \vec{B}_\rho &= \overline{\overline{\zeta}} \cdot \left[\vec{E}_\rho + \hat{u}E_u\right] - \hat{u}\left(\vec{\zeta}_u \cdot \vec{E}_\rho\right) - \hat{u}\left(\zeta_{uu}E_u\right) \\ &\quad + \overline{\overline{\mu}} \cdot \left[\vec{H}_\rho + \hat{u}H_u\right] - \hat{u}\left(\vec{\mu}_u \cdot \vec{H}_\rho\right) - \hat{u}\left(\mu_{uu}H_u\right). \end{aligned} \tag{2.15}$$

Using the distributive property again results in

$$\begin{aligned} \vec{B}_\rho &= \left[\overline{\overline{\zeta}} - \hat{u}\vec{\zeta}_u\right] \cdot \vec{E}_\rho + \left[\vec{\zeta}_{\bar{u}} - \hat{u}\zeta_{uu}\right] E_u \\ &\quad + \left[\overline{\overline{\mu}} - \hat{u}\vec{\mu}_u\right] \cdot \vec{H}_\rho + \left[\vec{\mu}_{\bar{u}} - \hat{u}\mu_{uu}\right] H_u, \end{aligned} \tag{2.16}$$

where $\vec{\zeta}_{\bar{u}} = \overline{\overline{\zeta}} \cdot \hat{u}$ and $\vec{\mu}_{\bar{u}} = \overline{\overline{\mu}} \cdot \hat{u}$. This is simplifed further by defining

$$\overline{\overline{\zeta}}_{\rho} = \overline{\overline{\zeta}} - \hat{u}\vec{\zeta}_{u} \tag{2.17}$$

$$\overline{\overline{\mu}}_{\rho} = \overline{\overline{\mu}} - \hat{u}\vec{\mu}_{u} \tag{2.18}$$

$$\vec{\zeta}_{\rho u} = \vec{\zeta}_{\bar{u}} - \hat{u}\zeta_{uu} \tag{2.19}$$

$$\vec{\mu}_{\rho u} = \vec{\mu}_{\bar{u}} - \hat{u}\mu_{uu}. \tag{2.20}$$

The expression in (2.16) for the transverse component of $\vec{B}$ is then reduced to

$$\vec{B}_{\rho} = \overline{\overline{\zeta}}_{\rho} \cdot \vec{E}_{\rho} + \vec{\zeta}_{\rho u} E_u + \overline{\overline{\mu}}_{\rho} \cdot \vec{H}_{\rho} + \vec{\mu}_{\rho u} H_u. \tag{2.21}$$

Following a similar procedure, the electric flux density, $\vec{D}$, can be decomposed into transverse and longitudinal components. This decomposition results in

$$D_u = \vec{\epsilon}_u \cdot \vec{E}_{\rho} + \epsilon_{uu} E_u + \vec{\xi}_u \cdot \vec{H}_{\rho} + \xi_{uu} H_u \tag{2.22}$$

$$\vec{D}_{\rho} = \overline{\overline{\epsilon}}_{\rho} \cdot \vec{E}_{\rho} + \vec{\epsilon}_{\rho u} E_u + \overline{\overline{\xi}}_{\rho} \cdot \vec{H}_{\rho} + \vec{\xi}_{\rho u} H_u, \tag{2.23}$$

where $\vec{\epsilon}_u = \hat{u} \cdot \overline{\overline{\epsilon}}$, $\vec{\xi}_u = \hat{u} \cdot \overline{\overline{\xi}}$, $\vec{\epsilon}_{\bar{u}} = \overline{\overline{\epsilon}} \cdot \hat{u}$, $\vec{\xi}_{\bar{u}} = \overline{\overline{\xi}} \cdot \hat{u}$, $\overline{\overline{\epsilon}}_{\rho} = \overline{\overline{\epsilon}} - \hat{u}\vec{\epsilon}_u$, $\overline{\overline{\xi}}_{\rho} = \overline{\overline{\xi}} - \hat{u}\vec{\xi}_u$, $\vec{\epsilon}_{\rho u} = \vec{\epsilon}_{\bar{u}} - \hat{u}\epsilon_{uu}$, and $\vec{\xi}_{\rho u} = \vec{\xi}_{\bar{u}} - \hat{u}\xi_{uu}$.

The bianisotropic medium considered here contains phasor electrical and magnetic current sources; these sources must also be decomposed into their respective transverse and longitudinal parts. The decomposition of the sources are carried out in a manner similar to the decomposition of the fields, resulting in

$$\vec{J}_m = \vec{J}_{m\rho} + \hat{u} J_{mu} \tag{2.24}$$

$$\vec{J} = \vec{J}_{\rho} + \hat{u} J_u, \tag{2.25}$$

where $J_{mu} = \hat{u} \cdot \vec{J}_m$ and $J_u = \hat{u} \cdot \vec{J}$.

2.2.2 Decomposition of Maxwell's Equations into Transverse and Longitudinal Components

Now that $\vec{B}$ and $\vec{D}$ are decomposed into transverse and longitudinal components, the next step is decomposing the operators in Maxwell's equations into transverse and longitudinal parts. First note that

$$\frac{\partial}{\partial u} \equiv \hat{u} \cdot \nabla, \tag{2.26}$$

and that the transverse del operator is defined as

$$\nabla_\rho \equiv \nabla - \hat{u}\frac{\partial}{\partial u}. \tag{2.27}$$

Using these definitions, the vector curl can be decomposed into transverse and longitudinal components. The transverse component of the vector curl is determined using the identity (A.4) as

$$\left(\nabla \times \vec{A}\right)_\rho = -\hat{u} \times \hat{u} \times \left(\nabla \times \vec{A}\right). \tag{2.28}$$

Using the identity (A.6), (2.28) becomes

$$\left(\nabla \times \vec{A}\right)_\rho = -\hat{u} \times \hat{u} \times \left(\nabla_\rho \times \vec{A}_\rho\right) - \hat{u} \times \hat{u} \times \left(\hat{u} \times \left[\frac{\partial \vec{A}_\rho}{\partial u} - \nabla_\rho A_u\right]\right). \tag{2.29}$$

Here the first term on the right side is equal to zero by property (A.7). Using the identity in (A.9) the second term on the right side can be rewritten as

$$-\hat{u}\left\{\hat{u} \cdot \left(\hat{u} \times \left[\frac{\partial \vec{A}_\rho}{\partial u} - \nabla_\rho A_u\right]\right)\right\} + (\hat{u} \cdot \hat{u})\left(\hat{u} \times \left[\frac{\partial \vec{A}_\rho}{\partial u} - \nabla_\rho A_u\right]\right). \tag{2.30}$$

The first of these terms in (2.29) is analyzed. The expression

$$\hat{u} \cdot \left(\hat{u} \times \left[\frac{\partial \vec{A}_\rho}{\partial u} - \nabla_\rho A_u \right] \right) \tag{2.31}$$

is rearranged using the property (A.10), yielding

$$\hat{u} \cdot \left(\hat{u} \times \left[\frac{\partial \vec{A}_\rho}{\partial u} - \nabla_\rho A_u \right] \right) = \left[\frac{\partial \vec{A}_\rho}{\partial u} - \nabla_\rho A_u \right] \cdot (\hat{u} \times \hat{u}) \,. \tag{2.32}$$

Here $(\hat{u} \times \hat{u}) = 0$, and thus the transverse component of the vector curl is given by

$$\left(\nabla \times \vec{A} \right)_\rho = \hat{u} \times \left[\frac{\partial \vec{A}_\rho}{\partial u} - \nabla_\rho A_u \right] . \tag{2.33}$$

Using the property (2.8), the longitudinal part is just the difference between the curl and its transverse component. Thus

$$\hat{u} \left(\hat{u} \cdot \nabla \times \vec{A} \right) = \nabla_\rho \times \vec{A}_\rho. \tag{2.34}$$

With the curl operation decomposed, Maxwell's equations can be decomposed into transverse and longitudinal parts, which results in

$$\begin{aligned}
\nabla_\rho \times \vec{E}_\rho &= -j\omega \hat{u} B_u - \hat{u} J_{mu} && (2.35)\\
\hat{u} \times \left[\frac{\partial \vec{E}_\rho}{\partial u} - \nabla_\rho E_u \right] &= -j\omega \vec{B}_\rho - \vec{J}_{m\rho} && (2.36)\\
\nabla_\rho \times \vec{H}_\rho &= j\omega \hat{u} D_u + \hat{u} J_u && (2.37)\\
\hat{u} \times \left[\frac{\partial \vec{H}_\rho}{\partial u} - \nabla_\rho H_u \right] &= j\omega \vec{D}_\rho + \vec{J}_\rho. && (2.38)
\end{aligned}$$

Now (2.21) is substituted into (2.36), giving

$$-\hat{u} \times \nabla_\rho E_u + \hat{u} \times \frac{\partial \vec{E}_\rho}{\partial u} = -j\omega \left[\overline{\overline{\zeta}}_\rho \cdot \vec{E}_\rho + \vec{\zeta}_{\rho u} E_u + \overline{\overline{\mu}}_\rho \cdot \vec{H}_\rho + \vec{\mu}_{\rho u} H_u \right] - \vec{J}_{m\rho}. \tag{2.39}$$

Then substituting the expressions for the longitudinal component of $\vec{D}$, (2.23), into (2.38), results in

$$-\hat{u}\times\nabla_\rho H_u+\hat{u}\times\frac{\partial\vec{H}_\rho}{\partial u}=j\omega\left[\bar{\bar{\epsilon}}_\rho\cdot\vec{E}_\rho+\vec{\epsilon}_{\rho u}E_u+\bar{\bar{\xi}}_\rho\cdot\vec{H}_\rho+\vec{\xi}_{\rho u}H_u\right]+\vec{J}_\rho. \tag{2.40}$$

Taking the cross product of $\hat{u}$ and the expressions in $(2.39)and(2.40)$ results in

$$\begin{aligned}-\hat{u}\times\hat{u}\times\nabla_\rho E_u+\hat{u}\times\hat{u}\times\frac{\partial\vec{E}_\rho}{\partial u}=&-j\omega\hat{u}\times\left(\bar{\bar{\zeta}}_\rho\cdot\vec{E}_\rho\right)-j\omega\hat{u}\times\left(\vec{\zeta}_{\rho u}E_u\right)\\&-j\omega\hat{u}\times\left(\bar{\bar{\mu}}_\rho\cdot\vec{H}_\rho\right)-j\omega\hat{u}\times\left(\vec{\mu}_{\rho u}H_u\right)-\hat{u}\times\vec{J}_{m\rho},\end{aligned} \tag{2.41}$$

and

$$\begin{aligned}-\hat{u}\times\hat{u}\times\nabla_\rho H_u+\hat{u}\times\hat{u}\times\frac{\partial\vec{H}_\rho}{\partial u}=&\,j\omega\hat{u}\times\left(\bar{\bar{\epsilon}}_\rho\cdot\vec{E}_\rho\right)+j\omega\hat{u}\times\left(\vec{\epsilon}_{\rho u}E_u\right)\\&+j\omega\hat{u}\times\left(\bar{\bar{\xi}}_\rho\cdot\vec{J}_\rho\right)+j\omega\hat{u}\times\left(\vec{\xi}_{\rho u}H_u\right)+\hat{u}\times\vec{J}_\rho,\end{aligned} \tag{2.42}$$

respectively.

To simplify (2.41) and (2.42), the longitudinal component of $\vec{A}$ is considered. Using the property (A.4) and (2.8), it can be shown that

$$\hat{u}\times\left[\hat{u}\times\nabla_\rho A_u\right]=-\left[\nabla_\rho A_u-\hat{u}\left(\hat{u}\cdot\nabla_\rho A_u\right)\right]. \tag{2.43}$$

Using (2.27), (2.43) may be expressed as

$$\hat{u}\times\left[\hat{u}\times\nabla_\rho A_u\right]=-\left[\nabla_\rho A_u-\hat{u}\left(\hat{u}\cdot\left\{\nabla A_u-\hat{u}\frac{\partial A_u}{\partial u}\right\}\right)\right]. \tag{2.44}$$

From (2.26), this expression reduces to

$$\hat{u}\times\left[\hat{u}\times\nabla_\rho A_u\right]=-\left[\nabla_\rho A_u-\hat{u}\left(\hat{u}\cdot\left\{\nabla A_u-\hat{u}\left(\hat{u}\cdot\nabla A_u\right)\right\}\right)\right]. \tag{2.45}$$

Using the property $(A.1)$ this expression becomes

$$\hat{u} \times \left[\hat{u} \times \nabla_\rho A_u\right] = -\left[\nabla_\rho A_u - \hat{u}\left(\hat{u} \cdot \nabla A_u - \hat{u} \cdot \nabla A_u\right)\right] \tag{2.46}$$

or

$$\hat{u} \times \left[\hat{u} \times \nabla_\rho A_u\right] = -\nabla_\rho A_u. \tag{2.47}$$

Similarly, using the property (A.4) and (2.8), it can be shown that

$$\hat{u} \times \left[\hat{u} \times \frac{\partial \vec{A}_\rho}{\partial u}\right] = -\left[\frac{\partial \vec{A}_\rho}{\partial u} - \hat{u}\left(\hat{u} \cdot \frac{\partial \vec{A}_\rho}{\partial u}\right)\right] \tag{2.48}$$

or

$$\hat{u} \times \left[\hat{u} \times \frac{\partial \vec{A}_\rho}{\partial u}\right] = -\frac{\partial}{\partial u}\left[\vec{A}_\rho - \hat{u}\left(\hat{u} \cdot \vec{A}_\rho\right)\right]. \tag{2.49}$$

Then from property (A.5), this expression becomes

$$\hat{u} \times \left[\hat{u} \times \frac{\partial \vec{A}_\rho}{\partial u}\right] = -\vec{A}_\rho. \tag{2.50}$$

Using the relationships in (2.47) and (2.50), (2.41) and (2.42) reduce to

$$\begin{aligned} \nabla_\rho E_u - \frac{\partial \vec{E}_\rho}{\partial u} = {} & -j\omega\hat{u} \times \left(\overline{\overline{\zeta}}_\rho \cdot \vec{E}_\rho\right) - j\omega\hat{u} \times \left(\vec{\zeta}_{\rho u} E_u\right) - j\omega\hat{u} \times \left(\overline{\overline{\mu}}_\rho \cdot \vec{H}_\rho\right) \\ & -j\omega\hat{u} \times \left(\vec{\mu}_{\rho u} H_u\right) - \hat{u} \times \vec{J}_{m\rho} \end{aligned} \tag{2.51}$$

$$\begin{aligned} \nabla_\rho H_u - \frac{\partial \vec{H}_\rho}{\partial u} = {} & j\omega\hat{u} \times \left(\overline{\overline{\epsilon}}_\rho \cdot \vec{H}_\rho\right) + j\omega\hat{u} \times \left(\vec{\epsilon}_{\rho u} H_u\right) + j\omega\hat{u} \times \left(\overline{\overline{\xi}}_\rho \cdot \vec{E}_\rho\right) \\ & +j\omega\hat{u} \times \left(\vec{\xi}_{\rho u} E_u\right) + \hat{u} \times \vec{J}_\rho. \end{aligned} \tag{2.52}$$

These expressions can be simplified further by considering the dyadic $\overline{\overline{P}}$, where $\overline{\overline{P}}_\rho =$

$\left(\overline{\overline{P}} - \hat{u}\vec{P}_u\right)$ and $\vec{P}_u = \hat{u} \cdot \overline{\overline{P}}$. Using the identity from (A.3) it can be shown that

$$\hat{u} \times \left(\overline{\overline{P}}_\rho \cdot \vec{A}_\rho\right) = \left(\hat{u} \times \overline{\overline{P}}_\rho\right) \cdot \vec{A}_\rho \tag{2.53}$$

or

$$\hat{u} \times \left(\overline{\overline{P}}_\rho \cdot \vec{A}_\rho\right) = \left(\hat{u} \times \left[\overline{\overline{P}} - \hat{u}\vec{P}_u\right]\right) \cdot \vec{A}_\rho. \tag{2.54}$$

Since $\hat{u} \times \hat{u} = 0$, this expression becomes

$$\hat{u} \times \left(\overline{\overline{P}}_\rho \cdot \vec{A}_\rho\right) = \left(\hat{u} \times \overline{\overline{P}}\right) \cdot \vec{A}_\rho. \tag{2.55}$$

Additionally, using the dyadic $\overline{\overline{P}}$ and the transverse component of $\vec{A}$, where $\vec{P}_{\rho u} = \left(\vec{P}_{\bar{u}} - \hat{u}P_{uu}\right)$, $\vec{P}_{\bar{u}} = \overline{\overline{P}} \cdot \hat{u}$, and $P_{uu} = \hat{u} \cdot \overline{\overline{P}} \cdot \hat{u}$, it can be shown that

$$\hat{u} \times \left(\vec{P}_{\rho u} A_u\right) = \left(\hat{u} \times \left[\vec{P}_{\bar{u}} - \hat{u}P_{uu}\right] A_u\right) \tag{2.56}$$

or

$$\hat{u} \times \left(\vec{P}_{\rho u} A_u\right) = \left(\hat{u} \times \left[\overline{\overline{P}} \cdot \hat{u}\right] A_u - \hat{u} \times \hat{u}\left[\hat{u} \cdot \overline{\overline{P}} \cdot \hat{u}\right] A_u\right). \tag{2.57}$$

Since $\hat{u} \times \hat{u} = 0$, this expression becomes

$$\hat{u} \times \left(\vec{P}_{\rho u} A_u\right) = \hat{u} \times \left[\overline{\overline{P}} \cdot \hat{u}\right] A_u. \tag{2.58}$$

Using the identity (A.3) then results in

$$\hat{u} \times \left(\vec{P}_{\rho u} A_u\right) = \left(\hat{u} \times \overline{\overline{P}}\right) \cdot \hat{u} A_u. \tag{2.59}$$

Employing the properties from (2.55) and (2.59), (2.51) and (2.52) become

$$\nabla_\rho E_u - \frac{\partial \vec{E}_\rho}{\partial u} = -j\omega\left(\hat{u}\times\overline{\overline{\zeta}}\right)\cdot\vec{E}_\rho - j\omega\left(\hat{u}\times\overline{\overline{\zeta}}\right)\cdot\hat{u}E_u - j\omega\left(\hat{u}\times\overline{\overline{\mu}}\right)\cdot\vec{H}_\rho \\ -j\omega\left(\hat{u}\times\overline{\overline{\mu}}\right)\cdot\hat{u}H_u - \hat{u}\times\vec{J}_{m\rho} \tag{2.60}$$

$$\nabla_\rho H_u - \frac{\partial \vec{H}_\rho}{\partial u} = j\omega\left(\hat{u}\times\overline{\overline{\epsilon}}\right)\cdot\vec{E}_\rho + j\omega\left(\hat{u}\times\overline{\overline{\epsilon}}\right)\cdot\hat{u}E_u + j\omega\left(\hat{u}\times\overline{\overline{\xi}}\right)\cdot\vec{H}_\rho \\ +j\omega\left(\hat{u}\times\overline{\overline{\xi}}\right)\cdot\hat{u}H_u + \hat{u}\times\vec{J}_\rho. \tag{2.61}$$

By defining $\overline{\overline{\zeta}}_{ux} = \hat{u}\times\overline{\overline{\zeta}}$, $\overline{\overline{\mu}}_{ux} = \hat{u}\times\overline{\overline{\mu}}$, $\overline{\overline{\epsilon}}_{ux} = \hat{u}\times\overline{\overline{\epsilon}}$, and $\overline{\overline{\xi}}_{ux} = \hat{u}\times\overline{\overline{\xi}}$, (2.60) and (2.61) can be expressed as

$$\nabla_\rho E_u - \frac{\partial \vec{E}_\rho}{\partial u} = -j\omega\overline{\overline{\zeta}}_{ux}\cdot\vec{E}_\rho - j\omega\overline{\overline{\zeta}}_{ux}\cdot\hat{u}E_u - j\omega\overline{\overline{\mu}}_{ux}\cdot\vec{H}_\rho \\ -j\omega\overline{\overline{\mu}}_{ux}\cdot\hat{u}H_u - \hat{u}\times\vec{J}_{m\rho} \tag{2.62}$$

$$\nabla_\rho H_u - \frac{\partial \vec{H}_\rho}{\partial u} = j\omega\overline{\overline{\epsilon}}_{ux}\cdot\vec{E}_\rho + j\omega\overline{\overline{\epsilon}}_{ux}\cdot\hat{u}E_u + j\omega\overline{\overline{\xi}}_{ux}\cdot\vec{H}_\rho \\ +j\omega\overline{\overline{\xi}}_{ux}\cdot\hat{u}H_u + \hat{u}\times\vec{J}_\rho. \tag{2.63}$$

2.2.3 $\vec{H}_\rho$ in Terms of E_u, H_u, and Sources

The $\vec{H}_\rho$ field will first be related to the $\vec{E}_u$, $\vec{H}_u$, and the sources by substituting (2.63) into (2.62). Before the substitution, (2.63) is rearranged to become

$$j\omega\overline{\overline{\epsilon}}_{ux}\cdot\vec{E}_\rho = -\frac{\partial \vec{H}_\rho}{\partial u} + \nabla_\rho H_u - j\omega\overline{\overline{\epsilon}}_{ux}\cdot\hat{u}E_u - j\omega\overline{\overline{\xi}}_{ux}\cdot\vec{H}_\rho \\ -j\omega\overline{\overline{\xi}}_{ux}\cdot\hat{u}H_u - \hat{u}\times\vec{J}_\rho. \tag{2.64}$$

Taking the dot product of $\left(\overline{\overline{\epsilon}}_{ux}\right)^{-1}$ and (2.64) and diving by $j\omega$ yields

$$\vec{E}_\rho = \left(\overline{\overline{\epsilon}}_{ux}\right)^{-1}\cdot\left\{-\frac{1}{j\omega}\frac{\partial \vec{H}_\rho}{\partial u} + \frac{1}{j\omega}\nabla_\rho H_u - \overline{\overline{\epsilon}}_{ux}\cdot\hat{u}E_u - \overline{\overline{\xi}}_{ux}\cdot\vec{H}_\rho \right. \\ \left. -\overline{\overline{\xi}}_{ux}\cdot\hat{u}H_u - \frac{1}{j\omega}\hat{u}\times\vec{J}_\rho\right\}. \tag{2.65}$$

Here $\left(\overline{\overline{\epsilon}}_{ux}\right)^{-1}\cdot\left(\overline{\overline{\epsilon}}_{ux}\right)=\overline{\overline{I}}$. This expression is now substituted into (2.62) and results in

$$\nabla\rho E_u-\left(\overline{\overline{\epsilon}}_{ux}\right)^{-1}\cdot\left\{-\frac{1}{j\omega}\frac{\partial^2\vec{H}_\rho}{\partial u^2}+\frac{1}{j\omega}\nabla\rho\frac{\partial H_u}{\partial u}-\overline{\overline{\epsilon}}_{ux}\cdot\hat{u}\frac{\partial E_u}{\partial u}-\overline{\overline{\xi}}_{ux}\cdot\frac{\partial\vec{H}_\rho}{\partial u}\right.$$
$$\left.-\overline{\overline{\xi}}_{ux}\cdot\hat{u}\frac{\partial H_u}{\partial u}-\frac{1}{j\omega}\hat{u}\times\frac{\partial\vec{J}_\rho}{\partial u}\right\}=-j\omega\overline{\overline{\zeta}}_{ux}\cdot\hat{u}E_u-j\omega\overline{\overline{\mu}}_{ux}\cdot\vec{H}_\rho-j\omega\overline{\overline{\mu}}_{ux}\cdot\hat{u}H_u$$
$$-\hat{u}\times\vec{J}_{m\rho}-j\omega\overline{\overline{\zeta}}_{ux}\cdot\left(\overline{\overline{\epsilon}}_{ux}\right)^{-1}\cdot\left\{-\frac{1}{j\omega}\frac{\partial\vec{H}_\rho}{\partial u}+\frac{1}{j\omega}\nabla\rho H_u-\overline{\overline{\epsilon}}_{ux}\cdot\hat{u}E_u-\overline{\overline{\xi}}_{ux}\cdot\vec{H}_\rho\right.$$
$$\left.-\overline{\overline{\xi}}_{ux}\cdot\hat{u}H_u-\frac{1}{j\omega}\hat{u}\times\vec{J}_\rho\right\}. \quad (2.66)$$

Taking the dot product of $\overline{\overline{\epsilon}}_{ux}$ and (2.66) yields

$$\overline{\overline{\epsilon}}_{ux}\cdot\nabla\rho E_u+\frac{1}{j\omega}\frac{\partial^2\vec{H}_\rho}{\partial u^2}-\frac{1}{j\omega}\nabla\rho\frac{\partial H_u}{\partial u}+\overline{\overline{\epsilon}}_{ux}\cdot\hat{u}\frac{\partial E_u}{\partial u}+\overline{\overline{\xi}}_{ux}\cdot\frac{\partial\vec{H}_\rho}{\partial u}$$
$$+\overline{\overline{\xi}}_{ux}\cdot\hat{u}\frac{\partial H_u}{\partial u}+\frac{1}{j\omega}\hat{u}\times\frac{\partial\vec{J}_\rho}{\partial u}=-j\omega\overline{\overline{\epsilon}}_{ux}\cdot\left(\overline{\overline{\zeta}}_{ux}\cdot\hat{u}E_u\right)-j\omega\overline{\overline{\epsilon}}_{ux}\cdot\left(\overline{\overline{\mu}}_{ux}\cdot\vec{H}_\rho\right)$$
$$-j\omega\overline{\overline{\epsilon}}_{ux}\cdot\left(\overline{\overline{\mu}}_{ux}\cdot\hat{u}H_u\right)-\overline{\overline{\epsilon}}_{ux}\cdot\left(\hat{u}\times\vec{J}_{m\rho}\right)-\overline{\overline{\gamma}}_E\cdot\left\{-\frac{1}{j\omega}\frac{\partial\vec{H}_\rho}{\partial u}\right.$$
$$\left.+\frac{1}{j\omega}\nabla\rho H_u-\overline{\overline{\epsilon}}_{ux}\cdot\hat{u}E_u-\overline{\overline{\xi}}_{ux}\cdot\vec{H}_\rho-\overline{\overline{\xi}}_{ux}\cdot\hat{u}H_u-\frac{1}{j\omega}\hat{u}\times\vec{J}_\rho\right\}, \quad (2.67)$$

where $\overline{\overline{\gamma}}_E=j\omega\left(\overline{\overline{\epsilon}}_{ux}\cdot\overline{\overline{\zeta}}_{ux}\cdot\left(\overline{\overline{\epsilon}}_{ux}\right)^{-1}\right)$. Expanding the expression associated with dot product of $\overline{\overline{\gamma}}_E$ in (2.67) gives

$$\overline{\overline{\epsilon}}_{ux}\cdot\nabla\rho E_u+\frac{1}{j\omega}\frac{\partial^2\vec{H}_\rho}{\partial u^2}-\frac{1}{j\omega}\nabla\rho\frac{\partial H_u}{\partial u}+\overline{\overline{\epsilon}}_{ux}\cdot\hat{u}\frac{\partial E_u}{\partial u}$$
$$+\overline{\overline{\xi}}_{ux}\cdot\frac{\partial\vec{H}_\rho}{\partial u}+\overline{\overline{\xi}}_{ux}\cdot\hat{u}\frac{\partial H_u}{\partial u}+\frac{1}{j\omega}\hat{u}\times\frac{\partial\vec{J}_\rho}{\partial u}=-j\omega\overline{\overline{\epsilon}}_{ux}\cdot\left(\overline{\overline{\zeta}}_{ux}\cdot\hat{u}E_u\right)$$
$$-j\omega\overline{\overline{\epsilon}}_{ux}\cdot\left(\overline{\overline{\mu}}_{ux}\cdot\vec{H}_\rho\right)-j\omega\overline{\overline{\epsilon}}_{ux}\cdot\left(\overline{\overline{\mu}}_{ux}\cdot\hat{u}H_u\right)-\overline{\overline{\epsilon}}_{ux}\cdot\left(\hat{u}\times\vec{J}_{m\rho}\right)$$
$$+\overline{\overline{\gamma}}_E\cdot\frac{1}{j\omega}\frac{\partial\vec{H}_\rho}{\partial u}-\frac{1}{j\omega}\overline{\overline{\gamma}}_E\cdot\nabla\rho H_u+j\omega\overline{\overline{\epsilon}}_{ux}\cdot\left(\overline{\overline{\zeta}}_{ux}\cdot\hat{u}E_u\right)$$
$$+\overline{\overline{\gamma}}_E\cdot\left(\overline{\overline{\xi}}_{ux}\cdot\vec{H}_\rho\right)+\overline{\overline{\gamma}}_E\cdot\left(\overline{\overline{\xi}}_{ux}\cdot\hat{u}H_u\right)+\overline{\overline{\gamma}}_E\cdot\left(\frac{1}{j\omega}\hat{u}\times\vec{J}_\rho\right). \quad (2.68)$$

The two terms of $j\omega\overline{\overline{\epsilon}}_{ux} \cdot \left(\overline{\overline{\zeta}}_{ux} \cdot \hat{u}E_u\right)$ on the right-hand side cancel out. Rearranging the expression to have the transverse components on the left-hand side and longitudinal components on the right-hand side, and multiplying through by $j\omega$ results in

$$\begin{aligned}
&\frac{\partial^2 \vec{H}_\rho}{\partial u^2} + j\omega\overline{\overline{\xi}}_{ux} \cdot \frac{\partial \vec{H}_\rho}{\partial u} - \overline{\overline{\gamma}}_E \cdot \left[\frac{\partial \vec{H}_\rho}{\partial u} + j\omega\overline{\overline{\xi}}_{ux} \cdot \vec{H}_\rho\right] - \overline{\overline{k}}_E \cdot \vec{H}_\rho \\
&= -j\omega\overline{\overline{\epsilon}}_{ux} \cdot \left(\nabla_\rho E_u + \hat{u}\frac{\partial E_u}{\partial u}\right) + \nabla_\rho \frac{\partial H_u}{\partial u} - j\omega\overline{\overline{\xi}}_{ux} \cdot \hat{u}\frac{\partial H_u}{\partial u} - \hat{u} \times \frac{\partial \vec{J}_\rho}{\partial u} \\
&+\overline{\overline{k}}_E \cdot \hat{u}H_u - j\omega\overline{\overline{\epsilon}}_{ux} \cdot \left(\hat{u} \times \vec{J}_{m\rho}\right) + \overline{\overline{\gamma}}_E \cdot \left[j\omega\overline{\overline{\xi}}_{ux} \cdot \hat{u}H_u - \nabla_\rho H_u + \hat{u} \times \vec{J}_\rho\right], \qquad (2.69)
\end{aligned}$$

where $\overline{\overline{k}}_E = \omega^2\left(\overline{\overline{\epsilon}}_{ux} \cdot \overline{\overline{\mu}}_{ux}\right)$. From (2.27), the first term of the right side reduces to $-j\omega\overline{\overline{\epsilon}}_{ux} \cdot \nabla E_u$. Finally, the transverse components of $\vec{H}$ may now be related to the longitudinal components and sources through the differential equation

$$\begin{aligned}
&\frac{\partial^2 \vec{H}_\rho}{\partial u^2} + j\omega\overline{\overline{\xi}}_{ux} \cdot \frac{\partial \vec{H}_\rho}{\partial u} - \overline{\overline{\gamma}}_E \cdot \left[\frac{\partial \vec{H}_\rho}{\partial u} + j\omega\overline{\overline{\xi}}_{ux} \cdot \vec{H}_\rho\right] - \overline{\overline{k}}_E \cdot \vec{H}_\rho \\
&= -j\omega\overline{\overline{\epsilon}}_{ux} \cdot \nabla E_u + \nabla_\rho \frac{\partial H_u}{\partial u} - j\omega\overline{\overline{\xi}}_{ux} \cdot \hat{u}\frac{\partial H_u}{\partial u} - \hat{u} \times \frac{\partial \vec{J}_\rho}{\partial u} + \overline{\overline{k}}_E \cdot \hat{u}H_u \\
&-j\omega\overline{\overline{\epsilon}}_{ux} \cdot \left(\hat{u} \times \vec{J}_{m\rho}\right) + \overline{\overline{\gamma}}_E \cdot \left[j\omega\overline{\overline{\xi}}_{ux} \cdot \hat{u}H_u - \nabla_\rho H_u + \hat{u} \times \vec{J}_\rho\right]. \qquad (2.70)
\end{aligned}$$

2.2.4 $\vec{E}_\rho$ in Terms of E_u, H_u, and Sources

In a similar set of steps the field $\vec{E}_\rho$ may be related to the fields $\vec{E}_u$, $\vec{H}_u$ and the sources through the substitution of (2.62) into (2.63). First (2.62) is rearranged as

$$\begin{aligned}
j\omega\overline{\overline{\mu}}_{ux} \cdot \vec{H}_\rho = \frac{\partial \vec{E}_\rho}{\partial u} - \nabla_\rho E_u - j\omega\overline{\overline{\zeta}}_{ux} \cdot \vec{E}_\rho - j\omega\overline{\overline{\zeta}}_{ux} \cdot \hat{u}E_u \\
-j\omega\overline{\overline{\mu}}_{ux} \cdot \hat{u}H_u - \hat{u} \times \vec{J}_{m\rho}. \qquad (2.71)
\end{aligned}$$

Taking the dot product of $\left(\overline{\overline{\mu}}_{ux}\right)^{-1}$ and (2.71) and then diving by $j\omega$ results in

$$\vec{H}_\rho = \left(\overline{\overline{\mu}}_{ux}\right)^{-1} \cdot \left\{ \frac{1}{j\omega}\frac{\partial \vec{E}_\rho}{\partial u} - \frac{1}{j\omega}\nabla_\rho E_u - \overline{\overline{\zeta}}_{ux} \cdot \vec{E}_\rho - \overline{\overline{\zeta}}_{ux} \cdot \hat{u}E_u \right.$$
$$\left. -\overline{\overline{\mu}}_{ux} \cdot \hat{u}H_u - \frac{1}{j\omega}\hat{u} \times \vec{J}_{m\rho} \right\}. \tag{2.72}$$

Here $\left(\overline{\overline{\mu}}_{ux}\right)^{-1} \cdot \overline{\overline{\mu}}_{ux} = \overline{\overline{I}}$. This expression is now substituted into (2.62) and produces

$$\nabla_\rho H_u - \left(\overline{\overline{\mu}}_{ux}\right)^{-1} \cdot \left\{ \frac{1}{j\omega}\frac{\partial^2 \vec{E}_\rho}{\partial u^2} - \frac{1}{j\omega}\nabla_\rho \frac{\partial E_u}{\partial u} - \overline{\overline{\zeta}}_{ux} \cdot \frac{\partial \vec{E}_\rho}{\partial u} - \overline{\overline{\zeta}}_{ux} \cdot \hat{u}\frac{\partial E_u}{\partial u} \right.$$
$$\left. -\overline{\overline{\mu}}_{ux} \cdot \hat{u}\frac{\partial H_u}{\partial u} - \frac{1}{j\omega}\hat{u} \times \frac{\partial \vec{J}_{m\rho}}{\partial u} \right\} = j\omega\overline{\overline{\epsilon}}_{ux} \cdot \vec{E}_\rho + j\omega\overline{\overline{\epsilon}}_{ux} \cdot \hat{u}E_u + j\omega\overline{\overline{\xi}}_{ux} \cdot \hat{u}H_u$$
$$+\hat{u} \times \vec{J}_\rho + j\omega\overline{\overline{\xi}}_{ux} \cdot \left(\overline{\overline{\mu}}_{ux}\right)^{-1} \cdot \left\{ \frac{1}{j\omega}\frac{\partial \vec{E}_\rho}{\partial u} - \frac{1}{j\omega}\nabla_\rho E_u - \overline{\overline{\zeta}}_{ux} \cdot \vec{E}_\rho - \overline{\overline{\zeta}}_{ux} \cdot \hat{u}E_u \right.$$
$$\left. -\overline{\overline{\mu}}_{ux} \cdot \hat{u}H_u - \frac{1}{j\omega}\hat{u} \times \vec{J}_{m\rho} \right\}. \tag{2.73}$$

Taking the dot product of $\overline{\overline{\mu}}_{ux}$ and (2.73) results in

$$\overline{\overline{\mu}}_{ux} \cdot \nabla_\rho H_u - \frac{1}{j\omega}\frac{\partial^2 \vec{E}_\rho}{\partial u^2} + \frac{1}{j\omega}\nabla_\rho \frac{\partial E_u}{\partial u} + \overline{\overline{\zeta}}_{ux} \cdot \frac{\partial \vec{E}_\rho}{\partial u} + \overline{\overline{\zeta}}_{ux} \cdot \hat{u}\frac{\partial E_u}{\partial u}$$
$$+\overline{\overline{\mu}}_{ux} \cdot \hat{u}\frac{\partial H_u}{\partial u} + \frac{1}{j\omega}\hat{u} \times \frac{\partial \vec{J}_{m\rho}}{\partial u} = j\omega\overline{\overline{\mu}}_{ux} \cdot \left(\overline{\overline{\epsilon}}_{ux} \cdot \vec{E}_\rho\right) + j\omega\overline{\overline{\mu}}_{ux} \cdot \left(\overline{\overline{\epsilon}}_{ux} \cdot \hat{u}E_u\right)$$
$$+j\omega\overline{\overline{\mu}}_{ux} \cdot \left(\overline{\overline{\xi}}_{ux} \cdot \hat{u}H_u\right) + \overline{\overline{\mu}}_{ux} \cdot \left(\hat{u} \times \vec{J}_\rho\right) + \overline{\overline{\gamma}}_H \cdot \left\{ \frac{1}{j\omega}\frac{\partial \vec{E}_\rho}{\partial u} \right.$$
$$\left. -\frac{1}{j\omega}\nabla_\rho E_u - \overline{\overline{\zeta}}_{ux} \cdot \vec{E}_\rho - \overline{\overline{\zeta}}_{ux} \cdot \hat{u}E_u - \overline{\overline{\mu}}_{ux} \cdot \hat{u}H_u - \frac{1}{j\omega}\hat{u} \times \vec{J}_{m\rho} \right\}, \tag{2.74}$$

where $\overline{\overline{\gamma}}_H = j\omega\left[\overline{\overline{\mu}}_{ux}\cdot\overline{\overline{\xi}}_{ux}\cdot\left(\overline{\overline{\mu}}_{ux}\right)^{-1}\right]$. Expanding the expressions associated with the dot product of $\overline{\overline{\gamma}}_H$ in (2.74) gives

$$\begin{aligned}
&\overline{\overline{\mu}}_{ux}\cdot\nabla_\rho H_u - \frac{1}{j\omega}\frac{\partial^2\vec{E}_\rho}{\partial u^2} + \frac{1}{j\omega}\nabla_\rho\frac{\partial E_u}{\partial u} + \overline{\overline{\zeta}}_{ux}\cdot\frac{\partial\vec{E}_\rho}{\partial u}\\
+\overline{\overline{\zeta}}_{ux}\cdot\hat{u}\frac{\partial E_u}{\partial u} + \overline{\overline{\mu}}_{ux}\cdot\hat{u}\frac{\partial H_u}{\partial u} + \frac{1}{j\omega}\hat{u}\times\frac{\partial\vec{J}_{m\rho}}{\partial u} &= j\omega\overline{\overline{\mu}}_{ux}\cdot\left(\overline{\overline{\epsilon}}_{ux}\cdot\vec{E}_\rho\right)\\
+j\omega\overline{\overline{\mu}}_{ux}\cdot\left(\overline{\overline{\epsilon}}_{ux}\cdot\hat{u}E_u\right) + j\omega\overline{\overline{\mu}}_{ux}\cdot\left(\overline{\overline{\xi}}_{ux}\cdot\hat{u}H_u\right) + \overline{\overline{\mu}}_{ux}\cdot\left(\hat{u}\times\vec{J}_\rho\right)&\\
+\overline{\overline{\gamma}}_H\cdot\frac{1}{j\omega}\frac{\partial\vec{E}_\rho}{\partial u} - \frac{1}{j\omega}\overline{\overline{\gamma}}_H\cdot\nabla_\rho E_u - \overline{\overline{\gamma}}_H\cdot\left(\overline{\overline{\zeta}}_{ux}\cdot\vec{E}_\rho\right)&\\
-\overline{\overline{\gamma}}_H\cdot\left(\overline{\overline{\zeta}}_{ux}\cdot\hat{u}E_u\right) - j\omega\overline{\overline{\mu}}_{ux}\cdot\left(\overline{\overline{\xi}}_{ux}\cdot\hat{u}H_u\right) - \overline{\overline{\gamma}}_H\cdot\left(\frac{1}{j\omega}\hat{u}\times\vec{J}_{m\rho}\right).&
\end{aligned}\tag{2.75}$$

The two terms of $j\omega\overline{\overline{\mu}}_{ux}\cdot\left(\overline{\overline{\xi}}_{ux}\cdot\hat{u}H_u\right)$ on the right-hand side cancel out. Rearranging the expression to have the transverse components on the left-hand side and longitudinal components on the right-hand side and multiplying through by $-j\omega$ results in

$$\begin{aligned}
&\frac{\partial^2\vec{E}_\rho}{\partial u^2} - j\omega\overline{\overline{\zeta}}_{ux}\cdot\frac{\partial\vec{E}_\rho}{\partial u} + \overline{\overline{\gamma}}_E\cdot\left[\frac{\partial\vec{E}_\rho}{\partial u} - j\omega\overline{\overline{\zeta}}_{ux}\cdot\vec{E}_\rho\right] - \overline{\overline{k}}_H\cdot\vec{E}_\rho\\
&= j\omega\overline{\overline{\mu}}_{ux}\cdot\left(\nabla_\rho H_u + \hat{u}\frac{\partial H_u}{\partial u}\right) + \nabla_\rho\frac{\partial E_u}{\partial u} + j\omega\overline{\overline{\zeta}}_{ux}\cdot\hat{u}\frac{\partial E_u}{\partial u} + \hat{u}\times\frac{\partial\vec{J}_{m\rho}}{\partial u}\\
&+\overline{\overline{k}}_H\cdot\hat{u}E_u - j\omega\overline{\overline{\mu}}_{ux}\cdot\left(\hat{u}\times\vec{J}_\rho\right) + \overline{\overline{\gamma}}_H\cdot\left[j\omega\overline{\overline{\zeta}}_{ux}\cdot\hat{u}E_u + \nabla_\rho E_u + \hat{u}\times\vec{J}_{m\rho}\right],
\end{aligned}\tag{2.76}$$

where $\overline{\overline{k}}_H = \omega^2\left(\overline{\overline{\mu}}_{ux}\cdot\overline{\overline{\epsilon}}_{ux}\right)$. From (2.27), the first term of the right side reduces to $j\omega\overline{\overline{\mu}}_{ux}\cdot\nabla H_u$. Finally, the transverse components of $\vec{E}$ may be expressed in terms of the longitudinal components and sources, through the differential equation

$$\begin{aligned}
&\frac{\partial^2\vec{E}_\rho}{\partial u^2} - j\omega\overline{\overline{\zeta}}_{ux}\cdot\frac{\partial\vec{E}_\rho}{\partial u} + \overline{\overline{\gamma}}_E\cdot\left[\frac{\partial\vec{E}_\rho}{\partial u} - j\omega\overline{\overline{\zeta}}_{ux}\cdot\vec{E}_\rho\right] - \overline{\overline{k}}_H\cdot\vec{E}_\rho\\
&= j\omega\overline{\overline{\mu}}_{ux}\cdot\nabla H_u + \nabla_\rho\frac{\partial E_u}{\partial u} + j\omega\overline{\overline{\zeta}}_{ux}\cdot\hat{u}\frac{\partial E_u}{\partial u} + \hat{u}\times\frac{\partial\vec{J}_{m\rho}}{\partial u}\\
&+\overline{\overline{k}}_H\cdot\hat{u}E_u - j\omega\overline{\overline{\mu}}_{ux}\cdot\left(\hat{u}\times\vec{J}_\rho\right) + \overline{\overline{\gamma}}_H\cdot\left[j\omega\overline{\overline{\zeta}}_{ux}\cdot\hat{u}E_u + \nabla_\rho E_u + \hat{u}\times\vec{J}_{m\rho}\right].
\end{aligned}\tag{2.77}$$

2.2.5 TE/TM Decomposition of the Fields in a Bianisotropic material

To analyze materials inside a rectangular waveguide, typically the electromagnetic fields are first decomposed into TE and TM fields. TE/TM field decomposition is the source-free special case of longitudinal/transverse decomposition. Setting $\vec{J} = 0$ and $\vec{J}_m = 0$, (2.70) and (2.77) become

$$\begin{aligned}\frac{\partial^2 \vec{H}_\rho}{\partial u^2} + j\omega\overline{\overline{\xi}}_{ux} \cdot \frac{\partial \vec{H}_\rho}{\partial u} - \overline{\overline{\gamma}}_E \cdot \left[\frac{\partial \vec{H}_\rho}{\partial u} + j\omega\overline{\overline{\xi}}_{ux} \cdot \vec{H}_\rho\right] - \overline{\overline{k}}_E \cdot \vec{H}_\rho \\ = -j\omega\overline{\overline{\epsilon}}_{ux} \cdot \nabla E_u + \nabla_\rho \frac{\partial H_u}{\partial u} - j\omega\overline{\overline{\xi}}_{ux} \cdot \hat{u}\frac{\partial H_u}{\partial u} + \overline{\overline{k}}_E \cdot \hat{u}H_u \\ + \overline{\overline{\gamma}}_E \left[j\omega\overline{\overline{\xi}}_{ux} \cdot \hat{u}H_u - \nabla_\rho H_u\right] \end{aligned} \tag{2.78}$$

and

$$\begin{aligned}\frac{\partial^2 \vec{E}_\rho}{\partial u^2} - j\omega\overline{\overline{\zeta}}_{ux} \cdot \frac{\partial \vec{E}_\rho}{\partial u} + \overline{\overline{\gamma}}_H \cdot \left[\frac{\partial \vec{E}_\rho}{\partial u} - j\omega\overline{\overline{\zeta}}_{ux} \cdot \vec{E}_\rho\right] - \overline{\overline{k}}_H \cdot \vec{E}_\rho \\ = j\omega\overline{\overline{\mu}}_{ux} \cdot \nabla H_u + \nabla_\rho \frac{\partial E_u}{\partial u} + j\omega\overline{\overline{\zeta}}_{ux} \cdot \hat{u}\frac{\partial E_u}{\partial u} + \overline{\overline{k}}_H \cdot \hat{u}E_u \\ + \overline{\overline{\gamma}}_H \cdot \left[j\omega\overline{\overline{\zeta}}_{ux} \cdot \hat{u}E_u + \nabla_\rho E_u\right], \end{aligned} \tag{2.79}$$

respectively. The electromagnetic field is now completely specified in terms of two scalar fields E_u and H_u. To solve the differential equations, it is beneficial to use superposition since the right-hand side of the equation has two forcing terms. These equations can be solved by considering only one forcing term at a time and then adding the results. If $E_u = 0$ then the field is termed TE to the $\hat{u}$ direction. When $H_u = 0$ the fields are termed TM to the $\hat{u}$ direction. The relationships between transverse and longitudinal fields in the TE case

are given as

$$\frac{\partial^2 \vec{H}_\rho}{\partial u^2} + j\omega\bar{\bar{\xi}}_{ux} \cdot \frac{\partial \vec{H}_\rho}{\partial u} - \bar{\bar{\gamma}}_E \cdot \left[\frac{\partial \vec{H}_\rho}{\partial u} + j\omega\bar{\bar{\xi}}_{ux} \cdot \vec{H}_\rho\right] - \bar{\bar{k}}_E \cdot \vec{H}_\rho$$
$$= \nabla_\rho \frac{\partial H_u}{\partial u} - j\omega\bar{\bar{\xi}}_{ux} \cdot \hat{u}\frac{\partial H_u}{\partial u} + \bar{\bar{k}}_E \cdot \hat{u}H_u + \bar{\bar{\gamma}}_E \left[j\omega\bar{\bar{\xi}}_{ux} \cdot \hat{u}H_u - \nabla_\rho H_u\right] \quad (2.80)$$

$$\frac{\partial^2 \vec{E}_\rho}{\partial u^2} - j\omega\bar{\bar{\zeta}}_{ux} \cdot \frac{\partial \vec{E}_\rho}{\partial u} + \bar{\bar{\gamma}}_H \cdot \left[\frac{\partial \vec{E}_\rho}{\partial u} - j\omega\bar{\bar{\zeta}}_{ux} \cdot \vec{E}_\rho\right] - \bar{\bar{k}}_H \cdot \vec{E}_\rho = j\omega\bar{\bar{\mu}}_{ux} \cdot \nabla H_u, \quad (2.81)$$

and in the TM case as

$$\frac{\partial^2 \vec{H}_\rho}{\partial u^2} + j\omega\bar{\bar{\xi}}_{ux} \cdot \frac{\partial \vec{H}_\rho}{\partial u} - \bar{\bar{\gamma}}_E \cdot \left[\frac{\partial \vec{H}_\rho}{\partial u} + j\omega\bar{\bar{\xi}}_{ux} \cdot \vec{H}_\rho\right] - \bar{\bar{k}}_E \cdot \vec{H}_\rho = -j\omega\bar{\bar{\epsilon}}_{ux} \cdot \nabla E_u \quad (2.82)$$

$$\frac{\partial^2 \vec{E}_\rho}{\partial u^2} - j\omega\bar{\bar{\zeta}}_{ux} \cdot \frac{\partial \vec{E}_\rho}{\partial u} + \bar{\bar{\gamma}}_E \cdot \left[\frac{\partial \vec{E}_\rho}{\partial u} - j\omega\bar{\bar{\zeta}}_{ux} \cdot \vec{E}_\rho\right] - \bar{\bar{k}}_H \cdot \vec{E}_\rho$$
$$= \nabla_\rho \frac{\partial E_u}{\partial u} + j\omega\bar{\bar{\zeta}}_{ux} \cdot \hat{u}\frac{\partial E_u}{\partial u} + \bar{\bar{k}}_H \cdot \hat{u}E_u + \bar{\bar{\gamma}}_H \cdot \left[j\omega\bar{\bar{\zeta}}_{ux} \cdot \hat{u}E_u + \nabla_\rho E_u\right]. \quad (2.83)$$

2.2.6 Explicit Expressions for the Transverse Field Components

The differential equations in (2.80) - (2.83) can be solved using the Fourier transform pairs

$$F(\vec{\rho}, \beta) = \int_{-\infty}^{\infty} f(\vec{\rho}, u)\, \mathrm{e}^{-j\beta u} du \quad (2.84)$$

$$f(\vec{\rho}, u) = \frac{1}{2\pi}\int_{-\infty}^{\infty} F(\vec{\rho}, \beta)\, \mathrm{e}^{j\beta u} d\beta, \quad (2.85)$$

to obtain explicit expressions for the transverse field components. In (2.84) and (2.85) β is the transform variable. Standard transform notation is

$$f(\vec{\rho}, u) \leftrightarrow F(\vec{\rho}, \beta), \quad (2.86)$$

where $\leftrightarrow$ designates a Fourier transform pair. The transform of the derivative of $f(\vec{\rho}, u)$ is found by differentiating (2.85) which gives

$$\frac{\partial}{\partial u} f\left(\vec{\rho}, u\right) = \frac{1}{2\pi} \int_{-\infty}^{\infty} j\beta F\left(\vec{\rho}, \beta\right) \mathrm{e}^{j\beta u} du \tag{2.87}$$

and so

$$\frac{\partial}{\partial u} f(\vec{\rho}, u) \leftrightarrow j\beta F\left(\vec{\rho}, \beta\right). \tag{2.88}$$

2.2.6.1 TE Decomposition

Performing the Fourier transform of (2.80) and (2.81) results in

$$\begin{aligned} \beta^2 \vec{H}_\rho(\vec{\rho}, \beta) + \omega\beta \overline{\overline{\xi}}_{ux} \cdot \vec{H}_\rho(\vec{\rho}, \beta) + j\overline{\overline{\gamma}}_E \cdot \left[\beta \vec{H}_\rho(\vec{\rho}, \beta) + \omega \overline{\overline{\xi}}_{ux} \cdot \vec{H}_\rho(\vec{\rho}, \beta)\right] + \overline{\overline{k}}_E \cdot \vec{H}_\rho(\vec{\rho}, \beta) \\ = -j\beta \nabla_\rho H_u(\vec{\rho}, \beta) - \omega\beta \overline{\overline{\xi}}_{ux} \cdot \hat{u} H_u(\vec{\rho}, \beta) - \overline{\overline{k}}_E \cdot \hat{u} H_u(\vec{\rho}, \beta) \\ -\overline{\overline{\gamma}}_E \cdot \left[j\omega \overline{\overline{\xi}}_{ux} \cdot \hat{u} H_u(\vec{\rho}, \beta) - \nabla_\rho H_u(\vec{\rho}, \beta)\right] \end{aligned} \tag{2.89}$$

$$\begin{aligned} \beta^2 \vec{E}_\rho(\vec{\rho}, \beta) - \omega\beta \overline{\overline{\zeta}}_{ux} \cdot \vec{E}_\rho(\vec{\rho}, \beta) - j\overline{\overline{\gamma}}_E \cdot \left[\beta \vec{E}_\rho(\vec{\rho}, \beta) - \omega \overline{\overline{\zeta}}_{ux} \cdot \vec{E}_\rho(\vec{\rho}, \beta)\right] + \overline{\overline{k}}_H \cdot \vec{E}_\rho(\vec{\rho}, \beta) \\ = -j\omega \overline{\overline{\mu}}_{ux} \cdot \left[\nabla_\rho H_u(\vec{\rho}, \beta) + j\beta \hat{u} H_u(\vec{\rho}, \beta)\right]. \end{aligned} \tag{2.90}$$

These expressions may also be written as

$$\begin{aligned} \overline{\overline{\eta}} \cdot \vec{H}_\rho(\vec{\rho}, \beta) &= -j\beta \nabla_\rho H_u(\vec{\rho}, \beta) - \omega\beta \overline{\overline{\xi}}_{ux} \cdot \hat{u} H_u(\vec{\rho}, \beta) \\ &\quad -\overline{\overline{k}}_E \cdot \hat{u} H_u(\vec{\rho}, \beta) - \overline{\overline{\gamma}}_E \cdot \left[j\omega \overline{\overline{\xi}}_{ux} \cdot \hat{u} H_u(\vec{\rho}, \beta) - \nabla_\rho H_u(\vec{\rho}, \beta)\right] \end{aligned} \tag{2.91}$$

$$\overline{\overline{\tau}} \cdot \vec{E}_\rho(\vec{\rho}, \beta) = -j\omega \overline{\overline{\mu}}_{ux} \cdot \left[\nabla_\rho H_u(\vec{\rho}, \beta) + j\beta \hat{u} H_u(\vec{\rho}, \beta)\right], \tag{2.92}$$

where

$$\overline{\overline{\eta}} = \left[\beta^2\overline{\overline{I}} + \omega\beta\overline{\overline{\xi}}_{ux} + j\beta\overline{\overline{\gamma}}_E + j\omega\overline{\overline{\gamma}}_E\overline{\overline{\xi}}_{ux} + \overline{\overline{k}}_E\right] \tag{2.93}$$

and

$$\overline{\overline{\tau}} = \left[\beta^2\overline{\overline{I}} - \omega\beta\overline{\overline{\zeta}}_{ux} - j\beta\overline{\overline{\gamma}}_H + j\omega\overline{\overline{\gamma}}_H\overline{\overline{\zeta}}_{ux} + \overline{\overline{k}}_H\right]. \tag{2.94}$$

The expressions for the transverse field components for the TE case are

$$\begin{aligned}\vec{H}_\rho(\vec{\rho},\beta) &= \overline{\overline{\eta}}^{-1}\cdot\Big\{-j\beta\nabla_\rho H_u(\vec{\rho},\beta) - \omega\beta\overline{\overline{\xi}}_{ux}\cdot\hat{u}H_u(\vec{\rho},\beta) - \overline{\overline{k}}_E\cdot\hat{u}H_u(\vec{\rho},\beta)\\ &\quad -\overline{\overline{\gamma}}_E\cdot\Big[j\omega\overline{\overline{\xi}}_{ux}\cdot\hat{u}H_u(\vec{\rho},\beta) - \nabla_\rho H_u(\vec{\rho},\beta)\Big]\Big\} \qquad (2.95)\\ \vec{E}_\rho(\vec{\rho},\beta) &= \overline{\overline{\tau}}^{-1}\cdot\left\{-j\omega\overline{\overline{\mu}}_{ux}\cdot\left[\nabla_\rho H_u(\vec{\rho},\beta) + j\beta\hat{u}H_u(\vec{\rho},\beta)\right]\right\}. \qquad (2.96)\end{aligned}$$

2.2.6.2 TM Decomposition

Performing the Fourier transform of (2.82) and (2.83) yields

$$\begin{aligned}\beta^2\vec{H}_\rho(\vec{\rho},\beta) + \omega\beta\overline{\overline{\xi}}_{ux}\cdot\vec{H}_\rho(\vec{\rho},\beta) + j\overline{\overline{\gamma}}_E\cdot\Big[\beta\vec{H}_\rho(\vec{\rho},\beta) + \omega\overline{\overline{\xi}}_{ux}\cdot\vec{H}_\rho(\vec{\rho},\beta)\Big] + \overline{\overline{k}}_E\cdot\vec{H}_\rho(\vec{\rho},\beta)\\ = j\omega\overline{\overline{\epsilon}}_{ux}\cdot\left[\nabla_\rho E_u(\vec{\rho},\beta) + j\beta\hat{u}E_u(\vec{\rho},\beta)\right] \qquad (2.97)\end{aligned}$$

$$\begin{aligned}\beta^2\vec{E}_\rho(\vec{\rho},\beta) - \omega\beta\overline{\overline{\zeta}}_{ux}\cdot\vec{E}_\rho(\vec{\rho},\beta) - j\overline{\overline{\gamma}}_E\cdot\Big[\beta\vec{E}_\rho(\vec{\rho},\beta) - \omega\overline{\overline{\zeta}}_{ux}\cdot\vec{E}_\rho(\vec{\rho},\beta)\Big] + \overline{\overline{k}}_H\cdot\vec{E}_\rho(\vec{\rho},\beta)\\ = -j\beta\nabla_\rho E_u(\vec{\rho},\beta) + \omega\beta\overline{\overline{\zeta}}_{ux}\cdot\hat{u}E_u(\vec{\rho},\beta) - \overline{\overline{k}}_H\cdot\hat{u}E_u(\vec{\rho},\beta)\\ -\overline{\overline{\gamma}}_H\cdot\Big[j\omega\overline{\overline{\zeta}}_{ux}\cdot\hat{u}E_u(\vec{\rho},\beta) + \nabla_\rho E_u(\vec{\rho},\beta)\Big]. \qquad (2.98)\end{aligned}$$

Using the definitions given in (2.93) and (2.94), (2.97) and (2.98) become

$$\overline{\overline{\eta}} \cdot \vec{H}_\rho(\vec{\rho},\beta) = j\omega\overline{\overline{\epsilon}}ux \cdot \left[\nabla\rho E_u(\vec{\rho},\beta) + j\beta\hat{u}E_u(\vec{\rho},\beta)\right] \tag{2.99}$$

$$\begin{aligned}\overline{\overline{\tau}} \cdot \vec{E}_\rho(\vec{\rho},\beta) &= -j\beta\nabla\rho E_u(\vec{\rho},\beta) + \omega\beta\overline{\overline{\zeta}}_{ux} \cdot \hat{u}E_u(\vec{\rho},\beta) - \overline{\overline{k}}_H \cdot \hat{u}E_u(\vec{\rho},\beta) \\ &\quad -\overline{\overline{\gamma}}_H \cdot \left[j\omega\overline{\overline{\zeta}}_{ux} \cdot \hat{u}E_u(\vec{\rho},\beta) + \nabla\rho E_u(\vec{\rho},\beta)\right].\end{aligned} \tag{2.100}$$

Finally, the expressions for the transverse field components for the TM case are

$$\vec{H}_\rho(\vec{\rho},\beta) = \overline{\overline{\eta}}^{-1} \cdot \left\{j\omega\overline{\overline{\epsilon}}ux \cdot \left[\nabla\rho E_u(\vec{\rho},\beta) + j\beta\hat{u}E_u(\vec{\rho},\beta)\right]\right\} \tag{2.101}$$

$$\begin{aligned}\vec{E}_\rho(\vec{\rho},\beta) &= \overline{\overline{\tau}}^{-1} \cdot \Big\{-j\beta\nabla\rho E_u(\vec{\rho},\beta) + \omega\beta\overline{\overline{\zeta}}_{ux} \cdot \hat{u}E_u(\vec{\rho},\beta) - \overline{\overline{k}}_H \cdot \hat{u}E_u(\vec{\rho},\beta) \\ &\quad -\overline{\overline{\gamma}}_H \cdot \left[j\omega\overline{\overline{\zeta}}_{ux} \cdot \hat{u}E_u(\vec{\rho},\beta) + \nabla\rho E_u(\vec{\rho},\beta)\right]\Big\}.\end{aligned} \tag{2.102}$$

2.2.7 Homogeneous Wave Equations for the Longitudinal Field Components

The homogeneous wave equations for the longitudinal field components are obtained using the expressions from the longitudinal decomposition of Maxwell's equations. Substituting (2.13) into (2.35) and setting the source to zero results in

$$\begin{aligned}\nabla\rho \times \vec{E}_\rho(\vec{\rho},\beta) = -j\omega\hat{u}\Big[&\vec{\zeta}_u \cdot \vec{E}_\rho(\vec{\rho},\beta) + \zeta_{uu}E_u(\vec{\rho},\beta) \\ &+\vec{\mu}_u \cdot \vec{H}_\rho(\vec{\rho},\beta) + \mu_{uu}H_u(\vec{\rho},\beta)\Big].\end{aligned} \tag{2.103}$$

Similarly, substituting (2.22) into (2.37) and eliminating the sources yields

$$\nabla\rho \times \vec{H}_\rho(\vec{\rho},\beta) = j\omega\hat{u}\left[\vec{\epsilon}_u \cdot \vec{E}_\rho(\vec{\rho},\beta) + \epsilon_{uu}E_u(\vec{\rho},\beta) + \vec{\xi}_u \cdot \vec{H}_\rho(\vec{\rho},\beta) + \xi_{uu}H_u(\vec{\rho},\beta)\right]. \tag{2.104}$$

2.2.7.1 TE Homogeneous Wave Equation

The decomposition of TE to the u-direction requires $E_u(\vec{\rho},\beta)=0$. Thus (2.103) becomes

$$\nabla_\rho \times \vec{E}_\rho(\vec{\rho},\beta) = -j\omega\hat{u}\vec{\zeta}_u \cdot \vec{E}_\rho(\vec{\rho},\beta) - j\omega\hat{u}\vec{\mu}_u \cdot \vec{H}_\rho(\vec{\rho},\beta) - j\omega\hat{u}\mu_{uu}H_u(\vec{\rho},\beta). \tag{2.105}$$

Now substituting (2.95) and (2.96) into (2.105) yields the homogeneous wave equation for $H_u(\vec{\rho},\beta)$

$$\begin{aligned}
&\nabla_\rho \times \left[\overline{\overline{\tau}}^{-1} \cdot \left\{-j\omega\overline{\overline{\mu}}_{ux} \cdot \left[\nabla_\rho H_u(\vec{\rho},\beta) + j\beta\hat{u}H_u(\vec{\rho},\beta)\right]\right\}\right] \\
&= -j\omega\hat{u}\vec{\zeta}_u \cdot \left[\overline{\overline{\tau}}^{-1} \cdot \left\{-j\omega\overline{\overline{\mu}}_{ux} \cdot \left[\nabla_\rho H_u(\vec{\rho},\beta) + j\beta\hat{u}H_u(\vec{\rho},\beta)\right]\right\}\right] - j\omega\hat{u}\mu_{uu}H_u(\vec{\rho},\beta) \\
&\quad -j\omega\hat{u}\vec{\mu}_u \cdot \left[\overline{\overline{\eta}}^{-1} \cdot \left\{-j\beta\nabla_\rho H_u(\vec{\rho},\beta) - \omega\beta\overline{\overline{\xi}}_{ux} \cdot \hat{u}H_u(\vec{\rho},\beta) - \overline{\overline{k}}_E \cdot \hat{u}H_u(\vec{\rho},\beta)\right.\right. \\
&\quad \left.\left. -\overline{\overline{\gamma}}_E \cdot \left(j\omega\overline{\overline{\xi}}_{ux} \cdot \hat{u}H_u(\vec{\rho},\beta) - \nabla_\rho H_u(\vec{\rho},\beta)\right)\right\}\right].
\end{aligned} \tag{2.106}$$

2.2.7.2 TM Homogeneous Wave Equation

The decomposition of TM to the u-direction requires $H_u(\vec{\rho},\beta)=0$. Thus (2.104) becomes

$$\nabla_\rho \times \vec{H}_\rho(\vec{\rho},\beta) = j\omega\hat{u}\vec{\epsilon}_u \cdot \vec{E}_\rho(\vec{\rho},\beta) + j\omega\vec{\xi}_u \cdot \vec{H}_\rho(\vec{\rho},\beta) + j\omega\xi_{uu}H_u(\vec{\rho},\beta). \tag{2.107}$$

Substituting (2.101) and (2.102) into (2.107) gives the homogenous wave equation for $E_u(\vec{\rho},\beta)$ as

$$\begin{aligned}
&\nabla_\rho \times \left[\overline{\overline{\eta}}^{-1} \cdot \left\{j\omega\overline{\overline{\epsilon}}_{ux} \cdot \left[\nabla_\rho E_u(\vec{\rho},\beta) + j\beta\hat{u}E_u(\vec{\rho},\beta)\right]\right\}\right] \\
&= j\omega\hat{u}\vec{\xi}_u \cdot \left[\overline{\overline{\eta}}^{-1} \cdot \left\{j\omega\overline{\overline{\epsilon}}_{ux} \cdot \left[\nabla_\rho E_u(\vec{\rho},\beta) + j\beta\hat{u}E_u(\vec{\rho},\beta)\right]\right\}\right] + j\omega\hat{u}\epsilon_{uu}E_u(\vec{\rho},\beta) \\
&\quad +j\omega\hat{u}\vec{\epsilon}_u \cdot \left[\overline{\overline{\tau}}^{-1} \cdot \left\{-j\beta\nabla_\rho E_u(\vec{\rho},\beta) + \omega\beta\overline{\overline{\zeta}}_{ux} \cdot \hat{u}E_u(\vec{\rho},\beta) - \overline{\overline{k}}_H \cdot \hat{u}E_u(\vec{\rho},\beta)\right.\right. \\
&\quad \left.\left. -\overline{\overline{\gamma}}_H \cdot \left(j\omega\overline{\overline{\zeta}}_{ux} \cdot \hat{u}E_u(\vec{\rho},\beta) + \nabla_\rho E_u(\vec{\rho},\beta)\right)\right\}\right].
\end{aligned} \tag{2.108}$$

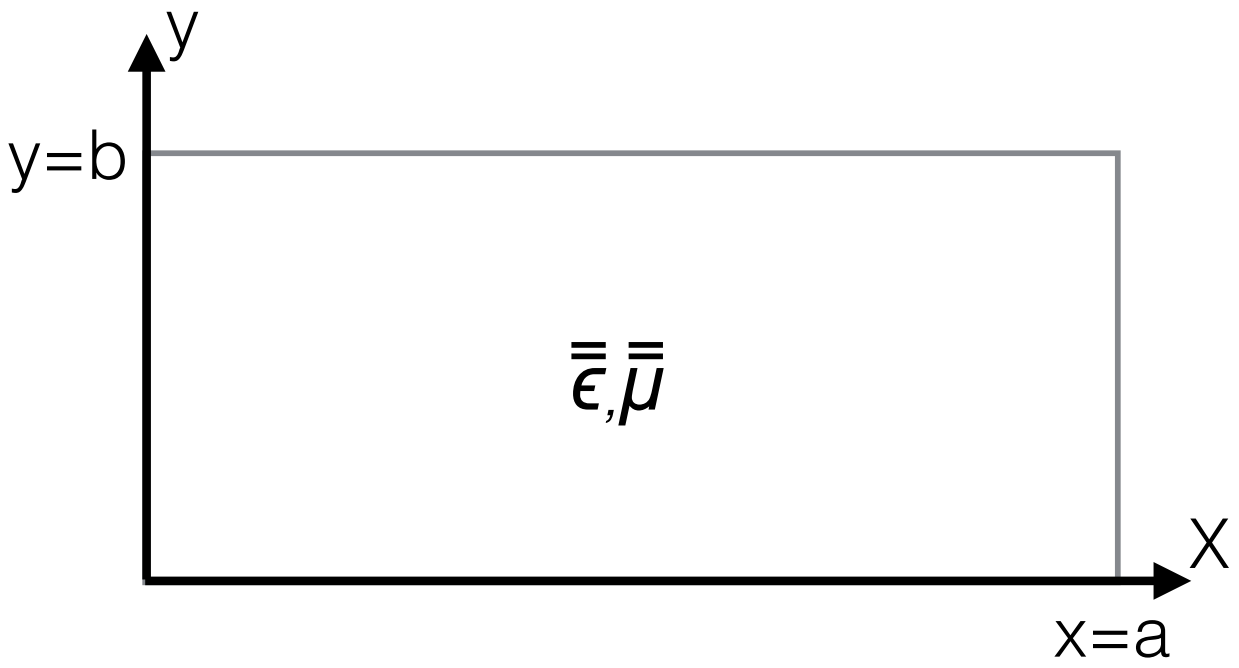

Figure 2.1: Cross-section view of a rectangular waveguide used in derivations for isotropic and gyromagnetic materials.

2.3 Specialization to Rectangular Waveguides

With expressions for the homogeneous wave equations for TE and TM fields in a bianisotropic material determined, the special cases of less complex media completely filling a rectangular waveguide are considered. The resulting homogeneous wave equations will be solved using a separation of variables technique in conjunction with the application of boundary conditions of the transverse field at the conducting surfaces of the guide. An expression for the longitudinal field may be determined and subsequently the transverse fields can be derived using (2.95) and (2.96) for fields TE to the u-direction and (2.101) and (2.102) for fields TM to the u-direction.

2.3.1 Isotropic Material Filled Guide

Isotropic material are considered first. Those materials have the tensor entries

$$\overline{\overline{\epsilon}} = \epsilon \begin{bmatrix} 1 & 0 & 0 \\ 0 & 1 & 0 \\ 0 & 0 & 1 \end{bmatrix} = \epsilon \overline{\overline{I}} \tag{2.109}$$

and

$$\overline{\overline{\mu}} = \mu \begin{bmatrix} 1 & 0 & 0 \\ 0 & 1 & 0 \\ 0 & 0 & 1 \end{bmatrix} = \mu \overline{\overline{I}}. \tag{2.110}$$

Additionally, cross coupling between the electric and magnetic fields does not exist, and so $\overline{\overline{\zeta}} = 0$ and $\overline{\overline{\xi}} = 0$. In order to derive the homogenous wave equation for isotropic material, the general bianisotropic homogenous wave equations for TE fields, (2.106), and for TM fields, (2.108), are reduced to their respective isotropic forms. These equations are given by

$$\begin{aligned} &\nabla_\rho \times \left[\overline{\overline{\tau}}^{-1} \cdot \left\{ -j\omega\mu\hat{u} \times \nabla_\rho H_u(\vec{\rho}, \beta) \right\} \right] \\ &= -j\omega\mu\hat{u} H_u(\vec{\rho}, \beta) - j\omega\mu\hat{u}\hat{u} \cdot \left[\overline{\overline{\eta}}^{-1} \cdot \left\{ -j\beta \nabla_\rho H_u(\vec{\rho}, \beta) \right\} \right] \end{aligned} \tag{2.111}$$

for TE decomposition and

$$\begin{aligned} &\nabla_\rho \times \left[\overline{\overline{\eta}}^{-1} \cdot \left\{ -j\omega\epsilon\hat{u} \times \nabla_\rho E_u(\vec{\rho}, \beta) \right\} \right] \\ &= -j\omega\epsilon\hat{u} E_u(\vec{\rho}, \beta) + j\omega\epsilon\hat{u}\hat{u} \cdot \left[\overline{\overline{\tau}}^{-1} \cdot \left\{ -j\beta \nabla_\rho E_u(\vec{\rho}, \beta) \right\} \right] \end{aligned} \tag{2.112}$$

for TM decomposition. Here

$$\overline{\overline{\tau}} = \beta^2 \overline{\overline{I}} + \omega^2 \mu\epsilon \left(\hat{u} \times \overline{\overline{I}} \right) \cdot \left(\hat{u} \times \overline{\overline{I}} \right) = \overline{\overline{\eta}}. \tag{2.113}$$

Consider the case of fields TE to z for the filled waveguide shown in Figure 2.1. The equation (2.111) can be written as

$$\begin{aligned}\left[\hat{x}\frac{\partial}{\partial x}+\hat{y}\frac{\partial}{\partial y}\right]\times\left[\overline{\overline{\tau}}^{-1}\cdot\left\{-j\omega\mu\left[\hat{y}\frac{\partial H_z(\vec{\rho},\beta)}{\partial x}-\hat{x}\frac{\partial H_z(\vec{\rho},\beta)}{\partial y}\right]\right\}\right]\\ =-\hat{z}j\omega\mu H_z(\vec{\rho},\beta)-\hat{z}\hat{z}j\omega\mu\cdot\left[\overline{\overline{\eta}}^{-1}\cdot\left\{-j\beta\left(\hat{x}\frac{\partial H_z(\vec{\rho},\beta)}{\partial x}+\hat{y}\frac{\partial H_z(\vec{\rho},\beta)}{\partial y}\right)\right\}\right],\end{aligned}\tag{2.114}$$

where

$$\overline{\overline{\tau}}^{-1}=\overline{\overline{\eta}}^{-1}=\hat{x}\hat{x}\frac{1}{\beta-\omega^2\epsilon\mu}+\hat{y}\hat{y}\frac{1}{\beta-\omega^2\epsilon\mu}+\hat{z}\hat{z}\frac{1}{\beta^2}.\tag{2.115}$$

Thus the wave equation for TE_z fields reduces to

$$\left(\frac{\partial^2}{\partial x^2}+\frac{\partial^2}{\partial y^2}+k_c^2\right)H_z(\vec{\rho},\beta)=0,\tag{2.116}$$

where the wavenumber, k_c, is

$$k_c^2=\omega^2\mu\epsilon-\beta^2.\tag{2.117}$$

Through a similar set of steps, the TM_z wave equation for isotropic materials is found to be

$$\left(\frac{\partial^2}{\partial x^2}+\frac{\partial^2}{\partial y^2}+k_c^2\right)E_z(\vec{\rho},\beta)=0,\tag{2.118}$$

where the wavenumber is described in (2.117).

2.3.1.1 Solution to the TE_z Wave Equation for Isotropic Material Filled Guide

To solve the TE_z wave equation, (2.116), a separation of variables is utilized, in conjunction with applying boundary conditions on the tangential electric field at the interfaces between the isotropic material and the perfectly conducting waveguide surfaces. Using the product

solution of $H_z(\vec{\rho},\beta) = X(x,\beta)Y(y,\beta)$, (2.116) becomes

$$Y(y,\beta)\frac{\partial^2 X(x,\beta)}{\partial x^2} + X(x,\beta)\frac{\partial^2 Y(y,\beta)}{\partial y^2} + k_c^2 X(x,\beta)Y(y,\beta) = 0. \tag{2.119}$$

Dividing through by $X(x)Y(y)$ gives

$$\frac{1}{X(x,\beta)}\frac{\partial^2 X(x,\beta)}{\partial x^2} + \frac{1}{Y(y,\beta)}\frac{\partial^2 Y(y,\beta)}{\partial y^2} + k_c^2 = 0. \tag{2.120}$$

By observing that each term in (2.120) must equal a constant, this equation can be expressed as

$$k_c^2 = k_x^2 + k_y^2, \tag{2.121}$$

where

$$k_x^2 = -\frac{1}{X(x,\beta)}\frac{\partial^2 X(x,\beta)}{\partial x^2} \tag{2.122}$$

and

$$k_y^2 = -\frac{1}{Y(y,\beta)}\frac{\partial^2 Y(y,\beta)}{\partial y^2}. \tag{2.123}$$

These are two separated ordinary differential equations,

$$\frac{\partial^2 X(x,\beta)}{\partial x^2} + k_x^2 X(x,\beta) = 0 \tag{2.124}$$

$$\frac{\partial^2 Y(y,\beta)}{\partial y^2} + k_y^2 Y(y,\beta) = 0. \tag{2.125}$$

It will be shown through the application of boundary conditions on the tangential fields that β takes the form of discrete eigenvalues. Additionally, k_x and k_y in (2.122) and (2.123) take

on discrete values. The eigenfield associated with these eigenvalues is

$$H_z(\vec{\rho},z) = \left[A_n \sin(\, k_{xn}x\,) + B_n \cos\left(k_{xn}x\right)\right]\left[C_n \sin(\, k_{yn}y\,) + D_n \cos\left(k_{yn}y\right)\right] \mathrm{e}^{\pm j\beta_n z}. \quad (2.126)$$

In the exponential, a negative sign corresponds to a wave traveling in the $+z$ direction while a positive sign corresponds to a traveling in the $-z$ direction. For the following expressions wherever a β appears a sign is included to designate the directions of the wave. For brevity, the dependence on $\vec{\rho}$ and z will be left implicit.

To determine the transverse field components for TE modes in isotropic materials, (2.96) and (2.95) first must be reduced from bianisotropic to isotropic form. These expressions are described by

$$\vec{E}_\rho = \bar{\bar{\tau}}^{-1} \cdot \left\{-j\omega\mu\left[\hat{u} \times \nabla_\rho H_u\right]\right\} \quad (2.127)$$

$$\vec{H}_\rho = \bar{\bar{\eta}}^{-1} \cdot \left\{\mp j\beta_n \nabla_\rho H_u\right\}. \quad (2.128)$$

Referring to the geometry in Figure 2.1 and assuming TE_z modes, (2.127) and (2.128) are expressed as

$$\vec{E}_\rho = \hat{x}\frac{j\omega\mu}{\beta_n^2 - \omega^2\mu\epsilon}\frac{\partial H_z}{\partial y} - \hat{y}\frac{j\omega\mu}{\beta_n^2 - \omega^2\mu\epsilon}\frac{\partial H_z}{\partial x} \quad (2.129)$$

$$\vec{H}_\rho = \mp\hat{x}\frac{j\beta_n}{\beta_n^2 - \omega^2\mu\epsilon}\frac{\partial H_z}{\partial x} \mp \hat{y}\frac{j\beta_n}{\beta_n^2 - \omega^2\mu\epsilon}\frac{\partial H_z}{\partial y}. \quad (2.130)$$

Now with general expressions for the transverse fields, the solution to the wave equation, (2.126), can be substituted into (2.130) and (2.129) which results in the transverse electric

field components expressed as

$$E_x = -\frac{j\omega\mu}{\omega^2\mu\epsilon - \beta_n^2}\left[A_n \sin(\, k_{xn}x\,) + B_n \cos\left(k_{xn}x\right)\right] \times \left[C_n k_{yn} \cos\left(k_{yn}y\right) - D_n k_{yn} \sin\left(k_{yn}y\right)\right] \mathrm{e}^{\pm j\beta_n z} \tag{2.131}$$

$$E_y = \frac{j\omega\mu}{\omega^2\mu\epsilon - \beta_n^2}\left[A_x k_{xn} \cos(\, k_{xn}x\,) - B_x k_{xn} \sin\left(k_{xn}x\right)\right] \times \left[A_y \sin\left(k_{yn}y\right) + B_y \cos\left(k_{yn}y\right)\right] \mathrm{e}^{\pm j\beta_n z}, \tag{2.132}$$

and the transverse magnetic field components expressed as

$$H_x = \pm\frac{j\beta_n}{\omega^2\mu\epsilon - \beta_n^2}\left[A_n k_{xn} \cos(\, k_{xn}x\,) - B_n k_{xn} \sin\left(k_{xn}x\right)\right] \times \left[C_n \sin\left(k_{yn}y\right) + D_n \cos\left(k_{yn}y\right)\right] \mathrm{e}^{\pm j\beta_n z} \tag{2.133}$$

$$H_y = \pm\frac{j\beta_n}{\omega^2\mu\epsilon - \beta_n^2}\left[A_n \sin(\, k_{xn}x\,) + B_n \cos\left(k_{xn}x\right)\right] \times \left[C_n k_y \cos\left(k_{yn}y\right) - D_n k_y \sin\left(k_{yn}y\right)\right] \mathrm{e}^{\pm j\beta_n z}. \tag{2.134}$$

The next step is applying the boundary condition on the tangential components of the electric field at the perfectly conducting surfaces of the rectangular waveguide walls. At the interface $y = 0$, the tangental electric field boundary condition requires

$$\frac{j\omega\mu k_{yn}}{\omega^2\mu\epsilon - \beta_n^2}\left[A_n \sin\left(k_{xn}x\right) + B_n \cos\left(k_{xn}x\right)\right] C_n \mathrm{e}^{\pm j\beta_n z} = 0. \tag{2.135}$$

The tangential electric field boundary condition at $x = 0$ requires

$$\frac{j\omega\mu k_{xn}}{\omega^2\mu\epsilon - \beta_n^2}\left[C_n \sin(\, k_{yn}y\,) + D_n \cos\left(k_{yn}y\right)\right] A_n \mathrm{e}^{\pm j\beta_n z} = 0. \tag{2.136}$$

Therefore, the coefficients A_n and C_n equal zero. Defining $B_n D_n = F_n$, then

$$H_z = F_n \cos\left(k_{xn}x\right) \cos\left(k_{yn}y\right) \mathrm{e}^{\pm j\beta_n z}. \tag{2.137}$$

At $x = a$ the tangential electric field boundary condition for E_y requires

$$-\frac{j\omega\mu k_{xn}}{\omega^2\mu\epsilon - \beta_n^2} F_n \sin(k_{xn}a) \cos\left(k_{yn}y\right) \mathrm{e}^{\pm j\beta_n z} = 0. \tag{2.138}$$

This means $k_{xn}a$ must be an integer multiple of π and therefore $k_{xn} = \frac{u_n\pi}{a}$ where u_n is an integer. Similarly, applying the tangential electric field boundary conditions for E_x at $y = b$ requires

$$\frac{j\omega\mu k_{yn}}{\omega^2\mu\epsilon - \beta_n^2} F_n \cos(k_{xn}x) \sin\left(k_{yn}b\right) \mathrm{e}^{\pm j\beta_n z} = 0, \tag{2.139}$$

which leads to $k_{yn} = \frac{v_n\pi}{b}$ where v_n is an integer. Since the modal analysis in this dissertation for isotropic materials use both TE and TM modes the variables u_n and v_n are introduced to distinguish between the different types of modes. Here the variables u_n and v_n correspond to the indices (u, v) for a TE_{uv} wave (if the n^{th} mode is TE_z) or a TM_{uv} wave (if the n^{th} mode is TM_z). As was mentioned previously, β takes on discrete values and the propagation constant for mode n is given by

$$\beta_n = \sqrt{\omega^2\mu\epsilon - k_{cn}^2}. \tag{2.140}$$

Here k_{cn} is the cutoff wave number of the n^{th} mode and is given by

$$k_{cn} = \sqrt{k_{xn}^2 + k_{yn}^2}. \tag{2.141}$$

The electric field components then reduce to

$$E_x = \frac{j\omega\mu k_{yn}}{k_{cn}^2} F_n \cos(k_{xn}x) \sin\left(k_{yn}y\right) \mathrm{e}^{\pm j\beta_n z} \tag{2.142}$$

$$E_y = -\frac{j\omega\mu k_{xn}}{k_{cn}^2} F_n \sin(k_{xn}x) \cos\left(k_{yn}y\right) \mathrm{e}^{\pm j\beta_n z}, \tag{2.143}$$

and the magnetic field components become

$$H_x = \mp \frac{j\beta_n k_{xn}}{k_{cn}^2} F_n \sin\left(k_{xn}x\right) \cos\left(k_{yn}y\right) \mathrm{e}^{\pm j\beta_n z} \tag{2.144}$$

$$H_y = \mp \frac{j\beta_n k_{yn}}{k_{cn}^2} F_n \cos\left(k_{xn}x\right) \sin\left(k_{yn}y\right) \mathrm{e}^{\pm j\beta_n z}, \tag{2.145}$$

where F_n is the modal amplitude coefficient. By defining the variable

$$K_n = \frac{j\omega\mu}{k_{cn}^2}, \tag{2.146}$$

(2.142) - (2.145) reduce to

$$E_x = F_n K_n k_{yn} \cos\left(k_{xn}x\right) \sin\left(k_{yn}y\right) \mathrm{e}^{\pm j\beta_n z} \tag{2.147}$$

$$E_y = -F_n K_n k_{xn} \sin\left(k_{xn}x\right) \cos\left(k_{yn}y\right) \mathrm{e}^{\pm j\beta_n z} \tag{2.148}$$

$$H_x = \mp F_n \frac{K_n}{Z_n} k_{xn} \sin\left(k_{xn}x\right) \cos\left(k_{yn}y\right) \mathrm{e}^{\pm j\beta_n z} \tag{2.149}$$

$$H_y = \mp F_n \frac{K_n}{Z_n} k_{yn} \cos\left(k_{xn}x\right) \sin\left(k_{yn}y\right) \mathrm{e}^{\pm j\beta_n z}, \tag{2.150}$$

where $Z_n = \omega\mu/\beta_n$ is the TE modal wave impedance. Since (2.147) - (2.150) all share the common variable K_n, a new variable can be defined as $C_n = F_n K_n$ which results in the electric and magnetic transverse field equations for TE_z modes reducing to

$$\vec{E}_\rho\left(\vec{r}\right) = C_n \vec{e}_n\left(\vec{\rho}\right) \mathrm{e}^{\pm j\beta_n z} \tag{2.151}$$

$$\vec{H}_\rho\left(\vec{r}\right) = \mp C_n \vec{h}_n\left(\vec{\rho}\right) \mathrm{e}^{\pm j\beta_n z}. \tag{2.152}$$

Here $\vec{e}_n\left(\vec{\rho}\right)$ and $\vec{h}_n\left(\vec{\rho}\right)$ are the transverse electric and magnetic modal fields, respectively,

and are given by

$$\vec{e}_n(\vec{\rho}) = \hat{x}k_{yn}\cos(k_{xn}x)\sin\left(k_{yn}y\right) - \hat{y}k_{xn}\sin(k_{xn}x)\cos\left(k_{yn}y\right), \tag{2.153}$$

$$\vec{h}_n(\vec{\rho}) = \frac{\hat{z}\times\vec{e}_n(\vec{\rho})}{Z_n} =$$

$$\frac{1}{Z_n}\left[\hat{x}k_{xn}\sin(k_{xn}x)\cos\left(k_{yn}y\right) + \hat{y}k_{yn}\cos(k_{xn}x)\sin\left(k_{yn}y\right)\right]. \tag{2.154}$$

Note that the definitions of $\vec{e}_n(\vec{\rho})$ and $\vec{h}_n(\vec{\rho})$ in (2.153) and (2.154) are different than those given in [45] and [46].

2.3.1.2 Solution to the TM$_z$ Wave Equation for Isotropic Filled Guide

To solve the TM$_z$ wave equation, (2.118), a separation of variables is utilized in conjunction with applying the boundary conditions on the tangential electric field at the perfectly conducting waveguide walls. Using the product solution of $E_z(\vec{\rho},\beta) = X(x,\beta)Y(y,\beta)$ and following the similar steps outlined for the TE$_z$ case, results in

$$\frac{\partial^2 X(x,\beta)}{\partial x^2} + k_x^2 X(x,\beta) = 0 \tag{2.155}$$

$$\frac{\partial^2 Y(y,\beta)}{\partial y^2} + k_y^2 Y(y,\beta) = 0. \tag{2.156}$$

As it was shown for the TE$_z$ case, with the application of boundary conditions, β, k_x, and k_y take the form of discrete eigenvalues. The eigenfield associated with on these eigenvalues is

$$E_z = \left[A_n\sin(\,k_{xn}x\,) + B_n\cos(k_{xn}x)\right]\left[C_n\sin(\,k_{yn}y\,) + D_n\cos\left(k_{yn}y\right)\right]\mathrm{e}^{\pm j\beta_n z}. \tag{2.157}$$

The transverse field components for the TM modes in the isotropic material are reduced from the general expressions for bianisotropic material, (2.101) and (2.102), thus resulting

in

$$\vec{H}_\rho = \overline{\overline{\eta}} \cdot \left\{ j\omega\epsilon \left[\hat{u} \times \nabla_\rho E_u \right] \right\} \tag{2.158}$$

$$\vec{E}_\rho = \overline{\overline{\eta}}^{-1} \cdot \left\{ \mp j\beta_n \nabla_\rho E_u \right\}. \tag{2.159}$$

Referring to the geometry in Figure 2.1 and assuming TM_z modes, (2.158) and (2.159) become

$$\vec{E}_\rho = \mp \hat{x} \frac{j\beta_n}{\beta_n^2 - \omega^2\mu\epsilon} \frac{\partial E_z}{\partial x} \mp \hat{y} \frac{j\beta_n}{\beta_n^2 - \omega^2\mu\epsilon} \frac{\partial E_z}{\partial y} \tag{2.160}$$

$$\vec{H}_\rho = \hat{x} \frac{j\omega\epsilon}{\beta_n^2 - \omega^2\mu\epsilon} \frac{\partial E_z}{\partial y} - \hat{y} \frac{j\omega\epsilon}{\beta_n^2 - \omega^2\mu\epsilon} \frac{\partial E_z}{\partial x}. \tag{2.161}$$

Now with general expressions for the transverse fields, the solution to the wave equation, (2.157), can be substituted into (2.160) and (2.161). The transverse electric field components are thus given by

$$E_x = \pm \frac{j\beta_n}{k_{cn}^2} \left[A_n k_{xn} \cos(\, k_{xn} x\,) - B_n k_{xn} \sin\left(k_{xn} x\right) \right] \times \left[C_n \sin\left(k_{yn} y\right) + D_n \cos\left(k_{yn} y\right) \right] \mathrm{e}^{\pm j\beta_n z} \tag{2.162}$$

$$E_y = \pm \frac{j\beta_n}{k_{cn}^2} \left[A_n \sin(\, k_{xn} x\,) + B_n \cos\left(k_{xn} x\right) \right] \times \left[C_n k_{yn} \cos\left(k_{yn} y\right) - D_n k_{yn} \sin\left(k_{yn} y\right) \right] \mathrm{e}^{\pm j\beta_n z}, \tag{2.163}$$

and the transverse magnetic field components are

$$H_x = \frac{j\omega\epsilon}{k_{cn}^2} \left[A_n \sin(\, k_{xn} x\,) + B_n \cos\left(k_{xn} x\right) \right] \times \left[C_n k_{yn} \cos\left(k_{yn} y\right) - D_n k_{yn} \sin\left(k_{yn} y\right) \right] \mathrm{e}^{\pm j\beta_n z} \tag{2.164}$$

$$H_y = \frac{j\omega\epsilon}{k_{cn}^2} \left[A_n k_{xn} \cos(\, k_{xn} x\,) - B_n k_{xn} \sin\left(k_{xn} x\right) \right] \times \left[C_n \sin\left(k_{yn} y\right) + D_n \cos\left(k_{yn} y\right) \right] \mathrm{e}^{\pm j\beta_n z}. \tag{2.165}$$

Following the procedure outlined in the TE case, the boundary conditions on the tangential field components are applied at the perfectly conducting walls. Through these steps, the longitudinal electric field component reduces to

$$E_z = F_n \sin\left(k_{xn}x\right) \sin\left(k_{yn}y\right) \mathrm{e}^{\pm j\beta_n z}. \tag{2.166}$$

The transverse electric field components are given by

$$E_x = \pm \frac{j\beta_n k_{xn}}{k_{cn}^2} F_n \cos\left(k_{xn}x\right) \sin\left(k_{yn}y\right) \mathrm{e}^{\pm j\beta_n z} \tag{2.167}$$

$$E_y = \pm \frac{j\beta_n k_{yn}}{k_{cn}^2} F_n \sin\left(k_{xn}x\right) \cos\left(k_{yn}y\right) \mathrm{e}^{\pm j\beta_n z}, \tag{2.168}$$

and the transverse magnetic field components are

$$H_x = \frac{j\omega\epsilon k_{yn}}{k_{cn}^2} F_n \sin\left(k_{xn}x\right) \cos\left(k_{yn}y\right) \mathrm{e}^{\pm j\beta_n z} \tag{2.169}$$

$$H_y = -\frac{j\omega\epsilon k_{xn}}{k_{cn}^2} F_n \cos\left(k_{xn}x\right) \sin\left(k_{yn}y\right) \mathrm{e}^{\pm j\beta_n z}, \tag{2.170}$$

where F_n is the modal amplitude coefficient. By defining the quantity

$$L_n = \frac{j\beta_n}{k_{cn}^2}, \tag{2.171}$$

(2.167) - (2.170) reduces to

$$E_x = \pm F_n L_n k_{xn} \cos\left(k_{xn}x\right) \sin\left(k_{yn}y\right) \mathrm{e}^{\pm j\beta_n z} \tag{2.172}$$

$$E_y = \pm F_n L_n k_{yn} \sin\left(k_{xn}x\right) \cos\left(k_{yn}y\right) \mathrm{e}^{\pm j\beta_n z} \tag{2.173}$$

$$H_x = F_n \frac{L_n}{Z_n} k_{yn} \sin\left(k_{xn}x\right) \cos\left(k_{yn}y\right) \mathrm{e}^{\pm j\beta_n z} \tag{2.174}$$

$$H_y = -F_n \frac{L_n}{Z_n} k_{xn} \cos\left(k_{xn}x\right) \sin\left(k_{yn}y\right) \mathrm{e}^{\pm j\beta_n z}, \tag{2.175}$$

where $Z_n = \frac{\beta_n}{\omega\epsilon}$ is the TM modal wave impedance. Since the transverse field equations all share the variable L_n, a new variable $D_n = F_n L_n$ is defined which results in a simplified form of the electric and magnetic transverse field equations for TM_z modes:

$$\vec{E}_\rho(\vec{r}) = \mp D_n \vec{e}_n(\vec{\rho})\, \mathrm{e}^{\pm j\beta_n z} \tag{2.176}$$

$$\vec{H}_\rho(\vec{r}) = D_n \vec{h}_n(\vec{\rho})\, \mathrm{e}^{\pm j\beta_n z}. \tag{2.177}$$

Here $\vec{e}_n(\vec{\rho})$ and $\vec{h}_n(\vec{\rho})$ are the transverse electric and magnetic modal fields, respectively, and are given by

$$\vec{e}_n(\vec{\rho}) = -\hat{x} k_{xn} \cos(k_{xn}x) \sin\left(k_{yn}y\right) - \hat{y} k_{yn} \sin(k_{xn}x) \cos\left(k_{yn}y\right), \tag{2.178}$$

$$\vec{h}_n(\vec{\rho}) = \frac{\hat{z} \times \vec{e}_n(\vec{\rho})}{Z_n^{TM}} =$$

$$\frac{1}{Z_n^{TM}} \left[\hat{x} k_{yn} \sin(k_{xn}x) \cos\left(k_{yn}y\right) - k_{xn} \cos(k_{xn}x) \sin\left(k_{yn}y\right)\right]. \tag{2.179}$$

To help with subsequent modal analysis, it is beneficial for the TE and TM field expressions to have the same form. By substituting $D_n = \mp C_n$, (2.176) and (2.177) becomes

$$\vec{E}_\rho(\vec{r}) = C_n \vec{e}_n(\vec{\rho})\, \mathrm{e}^{\pm j\beta_n z} \tag{2.180}$$

$$\vec{H}_\rho(\vec{r}) = \mp C_n \vec{h}_n(\vec{\rho})\, \mathrm{e}^{\pm j\beta_n z}. \tag{2.181}$$

Since this substitution only affects the modal amplitude constants, as long as this change is implemented in both equations, the results are the same. Consequently, the general expressions for the isotropic transverse fields for TE and TM modes are of the same form, but with different transverse electric and magnetic modal fields.

2.3.2 Biaxial Material Filled Guide

The next type of material to be considered is a biaxially anisotropic material. Biaxial materials are anisotropic and have six non-zero complex permittivity and permeability tensor entries,

$$\overline{\overline{\epsilon}} = \begin{bmatrix} \epsilon_x & 0 & 0 \\ 0 & \epsilon_y & 0 \\ 0 & 0 & \epsilon_z \end{bmatrix} \tag{2.182}$$

and

$$\overline{\overline{\mu}} = \begin{bmatrix} \mu_x & 0 & 0 \\ 0 & \mu_y & 0 \\ 0 & 0 & \mu_z \end{bmatrix}. \tag{2.183}$$

In order to derive the homogenous wave equation for biaxial material, the general bianisotropic homogenous wave equations for TE waves, (2.106), and for TM waves, (2.108), are reduced to their respective anisotropic form. The TE decomposition is given by

$$\begin{aligned} &\nabla_\rho \times \left[\overline{\overline{\tau}}^{-1} \cdot \left\{-j\omega\overline{\overline{\mu}}_{ux} \cdot \left[\nabla_\rho H_u(\beta) + j\beta\hat{u}H_u(\beta)\right]\right\}\right] \\ &= -j\omega\hat{u}\mu_{uu}H_u(\beta) - j\omega\hat{u}\vec{\mu}_u \cdot \left[\overline{\overline{\eta}}^{-1} \cdot \left\{-j\beta\nabla_\rho H_u(\beta) - \overline{\overline{k}}_E \cdot \hat{u}H_u(\beta)\right\}\right], \end{aligned} \tag{2.184}$$

and the TM decompositions is expressed as

$$\begin{aligned} &\nabla_\rho \times \left[\overline{\overline{\eta}}^{-1} \cdot \left\{j\omega\overline{\overline{\epsilon}}_{ux} \cdot \left[\nabla_\rho E_u(\beta) + j\beta\hat{u}E_u(\beta)\right]\right\}\right] \\ &= j\omega\hat{u}\epsilon_{uu}E_u(\beta) + j\omega\hat{u}\vec{\epsilon}_u \cdot \left[\overline{\overline{\tau}}^{-1} \cdot \left\{-j\beta\nabla_\rho E_u(\beta) - \overline{\overline{k}}_H \cdot \hat{u}E_u(\beta)\right\}\right]. \end{aligned} \tag{2.185}$$

Measurements of a biaxial sample with finite thickness typically uses empty waveguide extensions connected to a sample holder. A vector network analyzer (VNA) measures the reflection and transmission coefficients of a biaxial sample completely filling the cross-section of the sample holder. In the waveguide extension, the first mode that propagates is TE_{10}.

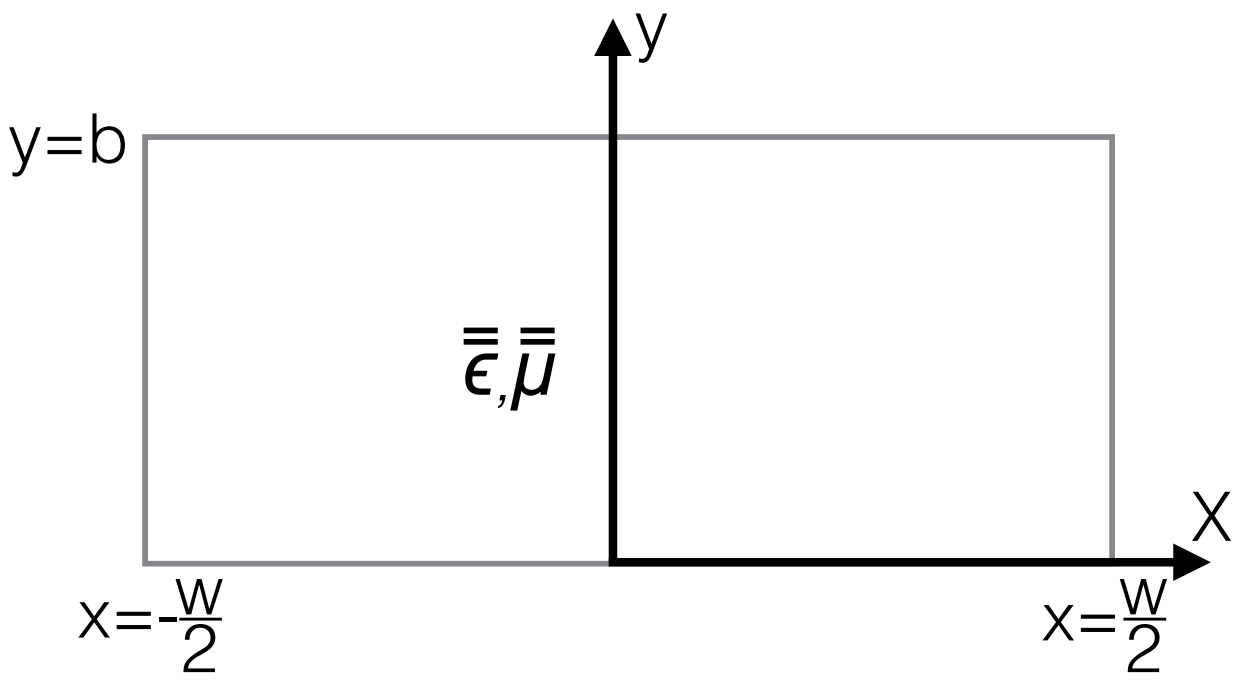

Figure 2.2: Cross-section view of rectangular waveguide used in derivations for biaxially anisotropic materials.

It will be shown further on in this dissertation that when this mode is incident on a biaxial material there is no coupling between orthogonal field components and therefore no excitation of higher order modes. All of the characterization techniques for biaxial materials completely filling the cross-section described in this dissertation assume the presence of only TE modes.

Consider a waveguide completely filled with a biaxial material, as shown in Figure 2.2 . For TE_z modes, the expressions in (2.184) become

$$\begin{aligned}
&\left[\hat{x}\frac{\partial}{\partial x}+\hat{y}\frac{\partial}{\partial y}\right] \\
&\times\left[\bar{\bar{\tau}}^{-1}\cdot\left\{-j\omega\left(\mu_x\hat{y}\hat{x}-\mu_y\hat{x}\hat{y}\right)\cdot\left[\hat{x}\frac{\partial H_z}{\partial x}+\hat{y}\frac{\partial H_z}{\partial y}+j\beta\hat{z}H_z\right]\right\}\right] \\
&=-j\omega\hat{z}\mu_z H_z-j\omega\hat{z}\left(\hat{z}\mu_z\right)\cdot\left[\bar{\bar{\eta}}^{-1}\cdot\left\{-j\beta\left(\hat{x}\frac{\partial H_z}{\partial x}-\hat{y}\frac{\partial H_z}{\partial y}\right)\right.\right. \\
&\qquad\left.\left.-\omega^2\left(-\hat{y}\hat{y}\epsilon_x\mu_y-\hat{x}\hat{x}\epsilon_y\mu_x\right)\cdot\hat{z}H_z\right\}\right]. \qquad (2.186)
\end{aligned}$$

Here

$$\overline{\overline{\tau}}^{-1} = \hat{x}\hat{x}\frac{1}{\beta - \omega^2\epsilon_y\mu_x} + \hat{y}\hat{y}\frac{1}{\beta - \omega^2\epsilon_x\mu_y} + \hat{z}\hat{z}\frac{1}{\beta^2} \tag{2.187}$$

and

$$\overline{\overline{\eta}}^{-1} = \hat{x}\hat{x}\frac{1}{\beta - \omega^2\epsilon_x\mu_y} + \hat{y}\hat{y}\frac{1}{\beta - \omega^2\epsilon_y\mu_x} + \hat{z}\hat{z}\frac{1}{\beta^2}. \tag{2.188}$$

The TE_z wave equation for H_z simplifies to

$$\left[\frac{\partial^2}{\partial x^2} + \frac{\mu_y\left(\beta^2 - \omega^2\mu_x\epsilon_y\right)}{\mu_x\left(\beta^2 - \omega^2\mu_y\epsilon_x\right)}\frac{\partial^2}{\partial y^2} - \frac{\mu_z}{\mu_x}\left(\beta^2 - \mu_x\epsilon_y\right)\right] H_z = 0. \tag{2.189}$$

2.3.2.1 Solution to the TE_z Wave Equation for Biaxial Material Filled Guide

In addition to describing a characterization technique for biaxial material completely filling the cross-section of a guide, this dissertation considers a reduced-aperture waveguide approach for single-sample characterization purposes. The reduction of the of the waveguide is symmetric about the width. Therefore, although a single TE_{10} mode is incident from an empty waveguide region onto the sample region, because of mode conversion at the discontinuity with the reduced aperture, an infinite number of waveguide modes are reflected back into the empty guide. Also, there are an infinite number of modes present in the reduced-aperture material region and the rectangular waveguide receiving extension. However, because the aperture is symmetric about the width of the guide, only rectangular waveguide modes of structure TE_{n0} $(n = 1, 2, 3, \ldots)$ are supported in the waveguide extensions and in the sample region. For TE_{n0} modes in a rectangular waveguide there is no y-dependence of the fields and the wave equation reduces to

$$\left(\frac{\partial^2}{\partial x^2} + k_c^2\right) H_z(\vec{\rho}, \beta) = 0 \tag{2.190}$$

where

$$k_c^2 = \frac{\mu_z}{\mu_x}\left(\omega^2\mu_x\epsilon_y - \beta^2\right) \tag{2.191}$$

is the cutoff wavenumber.

To solve (2.190) a separation of variables technique is used in conjunction with the application of boundary conditions on the tangential electric field at the perfectly conducting waveguide walls. As was shown when considering isotropic materials, with the application of boundary conditions β and k_{cn} take the form of discrete eigenvalues. The eigenfield associated with these eigenvalues is

$$H_z(x,z) = \left[A_n \sin\left(k_{cn}x\right)) + B_n \cos\left(k_{cn}x\right)\right] \mathrm{e}^{\pm j\beta_n z}. \tag{2.192}$$

To determine the transverse field components for TE modes in a biaxial material, (2.95) and (2.96) first must be simplified to anisotropic form. This gives

$$\vec{H}_\rho = \overline{\overline{\eta}}^{-1} \cdot \left\{\mp j\beta_n \nabla_\rho H_u - \overline{\overline{k}}_E \cdot \hat{u} H_u\right\} \tag{2.193}$$

$$\vec{E}_\rho = \overline{\overline{\tau}} \cdot \left\{-j\omega\overline{\overline{\mu}}_{ux} \cdot \left[\nabla_\rho H_u + j\beta\hat{u}H_u\right]\right\}. \tag{2.194}$$

Then using the tensors described in (2.182) and (2.183) and assuming TE_z modes, (2.193) and (2.194) become

$$\vec{E}_\rho(x,z) = \hat{x}\frac{j\omega\mu_y}{\beta_n^2 - \mu_y\epsilon_x}\frac{\partial H_z}{\partial y} - \hat{y}\frac{j\omega\mu_x}{\beta_n^2 - \mu_x\epsilon_y}\frac{\partial H_z}{\partial x} \tag{2.195}$$

$$\vec{H}_\rho(x,z) = \mp\hat{x}\frac{j\beta_n}{\beta_n^2 - \mu_x\epsilon_y}\frac{\partial H_z}{\partial x} \mp \hat{y}\frac{j\beta}{\beta_n^2 - \mu_y\epsilon_x}\frac{\partial H_z}{\partial y}. \tag{2.196}$$

Since only TE_{n0} modes are of interest, the transverse field equations reduce to

$$E_y(x,z) = -\frac{j\omega\mu_x}{\beta_n^2 - \omega^2\mu_x\epsilon_y}\frac{\partial H_z}{\partial x} \tag{2.197}$$

$$H_x(x,z) = \mp\frac{j\beta_n}{\beta_n^2 - \omega^2\mu_x\epsilon_y}\frac{\partial H_z}{\partial x}. \tag{2.198}$$

The axial field, (2.192), can now be substituted into (2.197) and (2.198) giving

$$E_y = -\frac{j\omega\mu_x k_{cn}}{\omega^2\mu_x\epsilon_y - \beta_n^2}\left[A_n\cos\left(k_{cn}x\right) - B_n\sin\left(k_{cn}x\right)\right]\mathrm{e}^{\pm j\beta_n z} \tag{2.199}$$

$$H_x = \mp\frac{j\beta_n k_{cn}}{\omega^2\mu_x\epsilon_y - \beta_n^2}\left[A_n\cos\left(k_{cn}x\right) - B_n\sin\left(k_{cn}x\right)\right]\mathrm{e}^{\pm j\beta_n z}. \tag{2.200}$$

The next step is applying the boundary condition on the tangential component of the electric field at the perfectly conducting waveguide walls. At the interfaces $x = \pm\frac{w}{2}$, the tangental electric field boundary condition requires

$$-\frac{j\omega\mu_x k_{cn}}{\omega^2\mu_x\epsilon_y - \beta_n^2}\left[A_n\cos\left(\frac{wk_{cn}}{2}\right) - B_n\sin\left(\frac{wk_{cn}}{2}\right)\right]\mathrm{e}^{\pm j\beta_n z} = 0. \tag{2.201}$$

and

$$-\frac{j\omega\mu_x k_{cn}}{\omega^2\mu_x\epsilon_y - \beta_n^2}\left[A_n\cos\left(-\frac{wk_{cn}}{2}\right) - B_n\sin\left(-\frac{wk_{cn}}{2}\right)\right]\mathrm{e}^{\pm j\beta_n z} = 0. \tag{2.202}$$

These can be expressed in matrix form as

$$\begin{bmatrix} \cos\left(\frac{k_{cn}w}{2}\right) & -\sin\left(\frac{k_{cn}w}{2}\right) \\ -\cos\left(\frac{k_{cn}w}{2}\right) & \sin\left(\frac{k_{cn}w}{2}\right) \end{bmatrix}\begin{bmatrix} A \\ B \end{bmatrix} = \begin{bmatrix} 0 \\ 0 \end{bmatrix}. \tag{2.203}$$

This system of homogeneous linear equations has a non-trivial solution, if its determinant is zero [47]. Therefore, the matrix in (2.203) has an infinite number of solutions if its

determinant is equal to zero. The determinant is given by

$$\cos\left(\frac{wk_{cn}}{2}\right)\sin\left(\frac{wk_{cn}}{2}\right)+\cos\left(\frac{wk_{cn}}{2}\right)\sin\left(\frac{wk_{cn}}{2}\right)=0, \tag{2.204}$$

or

$$2\cos\left(\frac{wk_{cn}}{2}\right)\sin\left(\frac{wk_{cn}}{2}\right)=0. \tag{2.205}$$

From (2.205) it is determined that $k_{cn}=\frac{n\pi}{w}$. The variable k_{cn} is the cutoff wavenumber for the n^{th} TE_{n0} mode in the sample region. As was stated previously, β takes on discrete values and thus the propagation constant for mode n is given by

$$\beta_n=\sqrt{\omega^2\mu_x\epsilon y-\frac{\mu_x}{\mu_z}k_{cn}^2}. \tag{2.206}$$

The equations for the tangential electric field boundary condition, (2.201) and (2.202), also gives the expression

$$A_n=\frac{B_n\sin\left(\frac{k_{cn}w}{2}\right)}{\cos\left(\frac{k_{cn}w}{2}\right)}. \tag{2.207}$$

Substituting (2.207) into the general expression for the longitudinal magnetic field component, (2.192), results in

$$H_z(x,z)=B_n'\cos\left[k_{cn}\left(x-\frac{w}{2}\right)\right]\mathrm{e}^{\pm j\beta_n z}, \tag{2.208}$$

where

$$B_n'=\frac{B_n}{\cos\left(\frac{k_{cn}w}{2}\right)}. \tag{2.209}$$

This new expression for the longitudinal magnetic field component also ends up altering the expressions for the transverse field components, which are now given by

$$E_y(x,z) = B_n' \frac{j\omega\mu_x k_{cn}}{\omega^2\mu_x\epsilon_y - \beta_n^2} \sin\left[k_{cn}\left(x - \frac{w}{2}\right)\right] \mathrm{e}^{\pm j\beta_n z} \tag{2.210}$$

$$H_x(x,z) = \pm B_n' \frac{j\beta_n k_{cn}}{\omega^2\mu_x\epsilon_y - \beta_n^2} \sin\left[k_{cn}\left(x - \frac{w}{2}\right)\right] \mathrm{e}^{\pm j\beta_n z}. \tag{2.211}$$

These equations can be simplified using (2.206), which results in

$$E_y(x,z) = -B_n' \frac{j\omega\mu_z k_{cn}}{k_{cn}^2} \sin\left[k_{cn}\left(x - \frac{w}{2}\right)\right] \mathrm{e}^{\pm j\beta_n z} \tag{2.212}$$

$$H_x(x,z) = \mp B_n' \frac{j\beta_n k_{cn}}{\mu_x k_{cn}^2} \sin\left[k_{cn}\left(x - \frac{w}{2}\right)\right] \mathrm{e}^{\pm j\beta_n z} \tag{2.213}$$

or

$$E_y(x,z) = -B_n' K_n \sin\left[k_{cn}\left(x - \frac{w}{2}\right)\right] \mathrm{e}^{\pm j\beta_n z} \tag{2.214}$$

$$H_x(x,z) = \mp B_n' \frac{K_n}{Z_n} \sin\left[k_{cn}\left(x - \frac{w}{2}\right)\right] \mathrm{e}^{\pm j\beta_n z}. \tag{2.215}$$

Here $K_n = j\omega\mu_z/k_{cn}^2$ and $Z_n = \omega\mu_x/\beta_n$ is the modal wave impedance. By defining the variable $C_n = B_n' K_n$, the transverse field equations reduce to

$$E_y(x,z) = C_n e_{yn}(x) \mathrm{e}^{\pm j\beta_n z} \tag{2.216}$$

$$H_x(x,z) = \mp C_n h_{xn}(x) \mathrm{e}^{\pm j\beta_n z}, \tag{2.217}$$

where the modal transverse field equations are given by

$$e_{yn}(x) = -k_{cn} \sin\left[k_{cn}\left(x - \frac{w}{2}\right)\right] \tag{2.218}$$

$$h_{xn}(x) = \frac{\hat{z} \times e_{yn}(x)}{Z_n} = \frac{k_{cn}}{Z_n} \sin\left[k_{cn}\left(x - \frac{w}{2}\right)\right]. \tag{2.219}$$

2.3.3 Gyromagnetic Material Filled Guide

The final type of material considered is a gyromagnetic material magnetized along the y-axis of Figure 2.1. The permittivity dyadic is given by

$$\overline{\overline{\epsilon}} = \epsilon \overline{\overline{I}}, \tag{2.220}$$

and the permeability dyadic is expressed as

$$\overline{\overline{\mu}} = \begin{bmatrix} \mu_g & 0 & -j\kappa \\ 0 & \mu_y & 0 \\ j\kappa & 0 & \mu_g \end{bmatrix}. \tag{2.221}$$

Using the constitutive parameter tensor and the general bianisotropic wave equations for TE fields, (2.106), and for TM fields, (2.108), the homogenous equation for anisotropic material is given by

$$\begin{aligned} &\nabla_\rho \times \left[\overline{\overline{\tau}}^{-1} \cdot \left\{ -j\omega \overline{\overline{\mu}}_{ux} \cdot \left[\nabla_\rho H_u + j\beta \hat{u} H_u \right] \right\} \right] \\ &= -j\omega \hat{u} \mu_{uu} H_u - j\omega \hat{u} \vec{\mu}_u \cdot \left[\overline{\overline{\eta}}^{-1} \cdot \left\{ -j\beta \nabla_\rho H_u - \overline{\overline{k}}_E \cdot \hat{u} H_u \right\} \right], \end{aligned} \tag{2.222}$$

and

$$\begin{aligned} &\nabla_\rho \times \left[\overline{\overline{\eta}}^{-1} \cdot \left\{ j\omega \overline{\overline{\epsilon}}_{ux} \cdot \left[\nabla_\rho E_u + j\beta \hat{u} E_u \right] \right\} \right] \\ &= j\omega \hat{u} \epsilon_{uu} E_u + j\omega \hat{u} \vec{\epsilon}_u \cdot \left[\overline{\overline{\tau}}^{-1} \cdot \left\{ -j\beta \nabla_\rho E_u - \overline{\overline{k}}_H \cdot \hat{u} E_u \right\} \right], \end{aligned} \tag{2.223}$$

respectively.

Consider a sample of gyromagnetic material filling the cross-section of the rectangular waveguide shown in Figure 2.1, with finite thickness, and magnetized along the y-axis. When the TE_{10} propagates inside an empty waveguide extension and this mode is incident on the

sample, a coupling exists between orthogonal field components in the sample. This coupling results in an excitation of higher-order modes. It will be shown in this dissertation that when a TE_{10} is incident on this sample, and the sample is magnetized along the y-axis, only TE_{n0} modes are supported. The homogeneous wave equation for TE_z fields is given by

$$\begin{aligned}
&\left[\hat{x}\frac{\partial}{\partial x}+\hat{y}\frac{\partial}{\partial y}\right] \\
&\times\left[\overline{\overline{\tau}}^{-1}\cdot\left\{-j\omega\left(\mu_g\hat{y}\hat{x}-j\delta\hat{y}\hat{z}-\mu_y\hat{x}\hat{y}\right)\cdot\left[\hat{x}\frac{\partial H_z}{\partial x}+\hat{y}\frac{\partial H_z}{\partial y}+j\beta\hat{z}H_z\right]\right\}\right] \\
&=-j\omega\hat{z}\mu_g H_z+\left(\omega\kappa\hat{z}\hat{x}-j\omega\hat{z}\hat{z}\mu_g\right)\cdot\left[\overline{\overline{\eta}}^{-1}\cdot\left\{-j\beta\left(\hat{x}\frac{\partial H_z}{\partial x}+\hat{y}\frac{\partial H_z}{\partial y}\right)\right.\right. \\
&\qquad\left.\left.-\omega^2\left(-\hat{y}\hat{y}\epsilon\mu_y-\hat{x}\hat{x}\epsilon\mu_g+j\hat{x}\hat{z}\delta\epsilon\right)\cdot\hat{z}H_z\right\}\right], \qquad (2.224)
\end{aligned}$$

where

$$\begin{aligned}
\overline{\overline{\eta}}^{-1}=&\left(\frac{1}{\beta^2-\omega^2\mu_g\epsilon}\right)\hat{x}\hat{x}+\left(\frac{1}{\beta^2-\omega^2\mu_y\epsilon}\right)\hat{y}\hat{y}+\frac{1}{\beta^2}\hat{z}\hat{z} \\
&-\left(\frac{j\omega\kappa\epsilon}{\beta^2\left(\beta^2-\omega^2\mu_g\epsilon\right)}\right)\hat{x}\hat{z}, \qquad (2.225)
\end{aligned}$$

and

$$\overline{\overline{\tau}}^{-1}=\left(\frac{1}{\beta^2-\omega^2\mu_y\epsilon}\right)\hat{x}\hat{x}+\left(\frac{1}{\beta^2-\omega^2\mu_g\epsilon}\right)\hat{y}\hat{y}+\frac{1}{\beta^2}\hat{z}\hat{z}. \qquad (2.226)$$

The wave equation simplifies to

$$\left(\frac{\partial^2}{\partial x^2}+\frac{\mu_y}{\mu_g}\frac{\beta^2-\mu_g\epsilon\omega^2}{\beta^2-\mu_y\epsilon\omega^2}\frac{\partial^2}{\partial y^2}+k_c^2\right)H_z=0, \qquad (2.227)$$

where the cutoff wavenumber is given by

$$k_c^2=\omega^2\mu_g\epsilon\left(1-\frac{\kappa^2}{\mu_g^2}\right)-\beta^2. \qquad (2.228)$$

2.3.3.1 Solution to the TE$_z$ Wave Equation for Gyromagnetic Material Filled Guide

For TE$_{n0}$ modes in a rectangular waveguide there is no y-dependence of the fields, and the wave equation in (2.227) reduces to

$$\left(\frac{\partial^2}{\partial x^2} + k_c^2\right) H_z(x) = 0. \tag{2.229}$$

As was shown for the isotropic and biaxial material filled guides, through the application of boundary conditions, β and k_{cn} will take the form of discrete eigenvalues. The eigenfield associated with these eigenvalues is

$$H_z(x,z) = \left[A_n \sin\left(k_{cn}x\right) + B_n \cos\left(k_{cn}x\right)\right] e^{\pm j\beta_n z}. \tag{2.230}$$

To determine the transverse field components for TE modes in a gyromagnetic material, (2.95) and (2.96) are reduce to anisotropic form, which results in

$$\vec{H}_\rho = \overline{\overline{\eta}}^{-1} \cdot \left\{\mp j\beta_n \nabla_\rho H_u - \overline{\overline{k}}_E \cdot \hat{u} H_u\right\} \tag{2.231}$$

$$\vec{E}_\rho = \overline{\overline{\tau}} \cdot \left\{-j\omega\overline{\overline{\mu}}_{ux} \cdot \left[\nabla_\rho H_u + j\beta\hat{u}H_u\right]\right\}. \tag{2.232}$$

Considering the waveguide geometry shown in Figure 2.1 and the material tensors in (2.182) and (2.183), the expressions in (2.231) and (2.232) become

$$\vec{H}_\rho(x,z) = \hat{x}\left[\mp\frac{j\beta_n}{\beta_n^2 - \mu_g\epsilon\omega^2}\frac{\partial H_z}{\partial x} + \frac{j\omega^2\kappa\epsilon}{\beta_n^2 - \mu_g\epsilon\omega^2}H_z\right] \mp \hat{y}\frac{j\beta_n}{\beta_n^2 - \mu_y\epsilon\omega^2}\frac{\partial H_z}{\partial y} \tag{2.233}$$

$$\vec{E}_\rho(x,z) = \hat{x}\frac{j\omega\mu_y}{\beta_n^2 - \mu_y\epsilon\omega^2}\frac{\partial H_z}{\partial y} - \hat{y}\left[\frac{j\omega\mu_g}{\beta_n^2 - \mu_g\epsilon\omega^2}\frac{\partial H_z}{\partial x} + \frac{j\omega\kappa\beta_n}{\beta_n^2 - \mu_g\epsilon\omega^2}H_z\right]. \tag{2.234}$$

Since in this dissertation only higher order TE$_{n0}$ modes are analyzed, the transverse fields

are

$$\vec{H}_x(x,z) = \hat{x}\left[\mp\frac{j\beta_n}{\beta_n^2 - \mu_g\epsilon\omega^2}\frac{\partial H_z}{\partial x} + \frac{j\omega^2\kappa\epsilon}{\beta_n^2 - \mu_g\epsilon\omega^2}H_z\right] \tag{2.235}$$

$$\vec{E}_y(x,z) = -\hat{y}\left[\frac{j\omega\mu_g}{\beta_n^2 - \mu_g\epsilon\omega^2}\frac{\partial H_z}{\partial x} \pm \frac{j\omega\kappa\beta_n}{\beta_n^2 - \mu_g\epsilon\omega^2}H_z\right]. \tag{2.236}$$

The axial magnetic field (2.230), can be substituted into (2.236), resulting in

$$\vec{E}_y(x,z) = -\frac{j\omega}{\beta_n^2 - \mu_g\epsilon\omega^2}\left[\mu_g k_{cn}A_n\cos(k_{cn}x) - \beta_n\mu_g k_{cn}B_n\sin(k_{cn}x)\pm\right.$$
$$\left.\kappa\beta_n A_n\sin(k_{cn}x) \pm \kappa\beta_n B_n\cos(k_{cn}x)\right]e^{\pm j\beta_n z}. \tag{2.237}$$

The unknown eigenvalues may be determined by applying the boundary conditions on E_y at the interfaces between the material and the conduction waveguide walls. At $x = 0$, the boundary condition on the tangential electric field requires

$$-\frac{j\omega}{\beta_n^2 - \mu_g\epsilon\omega^2}\left[\mu_g k_{cn}A_n \pm \kappa\beta_n B_n\right]e^{\pm j\beta_n z} = 0 \tag{2.238}$$

or

$$A_n = \mp\frac{\kappa B_n\beta_n}{\mu_g k_{cn}}. \tag{2.239}$$

Substituting the expression for A_n into (2.237) yields,

$$E_y(x,z) = \frac{j\omega}{\beta_n^2 - \mu_g\epsilon\omega^2}B_n\frac{\kappa^2}{\mu_g k_{cn}}\left[\frac{\mu^2 k_{cn}^2}{\kappa^2} + \beta_n^2\right]\sin(k_{cn}x)e^{\pm j\beta_n z}. \tag{2.240}$$

Next, inserting the expression for A_n into (2.230) gives

$$H_z(x,z) = B_n\left[\cos(k_{cn}s) \mp \frac{\kappa\beta_n}{\mu_g k_{cn}}\sin(k_{cn}x).\right]e^{\pm j\beta_n z} \tag{2.241}$$

This expression for the solution to the wave equation is substituted into (2.236) and simplified, giving

$$H_x(x,z) = \mp\frac{j\beta_n B}{\omega^2\mu_g\epsilon - \beta_n^2}\left[\sin(k_{cn}x) \mp \frac{\kappa k_{cn}}{\mu_g\beta_n}\cos(k_{cn}x)\right]e^{\pm j\beta_n z}. \tag{2.242}$$

At $z = a$, the boundary condition on the tangential electric field requires

$$\frac{-j\omega B\mu_g}{\omega^2\mu_g\epsilon - \beta_n^2}\left(1 - \frac{\kappa^2}{\mu_g^2}\right)\sin(k_{cn}z)e^{\pm j\beta_n z} = 0 \tag{2.243}$$

or

$$\sin(k_{cn}a) = 0. \tag{2.244}$$

From (2.244) it is determined that $k_{cn} = n\pi/a$. Here k_{cn} is the cutoff waveguide for the n^{th} TE_{n0} mode in the sample region. The propagation constant for mode n is found from (2.228)

$$\beta_n = \sqrt{\omega^2\mu_g\epsilon\left(1 - \frac{\kappa^2}{\mu^2}\right) - k_{cn}^2}. \tag{2.245}$$

Next, using (2.245) the transverse fields in (2.240) and (2.242) become

$$E_y(x,z) = \frac{-j\omega B_n\mu_g}{k_{cn}}\left(1 - \frac{\kappa^2}{\mu_g^2}\right)\sin(k_{cn}x)e^{\pm j\beta_n z} \tag{2.246}$$

$$H_x(x,z) = \mp\frac{j\beta_n B}{k_{cn}}\left[\sin(k_{cn}x) \mp \frac{\kappa k_{cn}}{\mu_g\beta_n}\cos(k_{cn}x)\right]e^{\pm j\beta_n z}. \tag{2.247}$$

By defining

$$K_n = j\omega\mu_g/k_{cn}^2, \tag{2.248}$$

(2.246) and (2.247) reduce to

$$E_y(x,z) = -B_n K_n k_{cn} \left(1 - \frac{\kappa^2}{\mu_g^2}\right) \sin\left(k_{cn}x\right) e^{\pm j\beta_n z} \tag{2.249}$$

$$H_x(x,z) = \mp B_n \frac{K_n k_{cn}}{Z_n} \left[\sin\left(k_{cn}x\right) \mp \frac{\kappa k_{cn}}{\mu_g \beta_n} \cos\left(k_{cn}x\right)\right] e^{\pm j\beta_n z}, \tag{2.250}$$

where and $Z_n = \omega\mu_g/\beta_n$ is the modal wave impedance. By defining $C_n = B_n K_n$, the transverse field equations reduce to

$$E_y(x,z) = -C_n k_{cn} \left(1 - \frac{\kappa^2}{\mu_g^2}\right) \sin\left(k_{cn}x\right) e^{\pm j\beta_n z} \tag{2.251}$$

$$H_x(x,z) = \mp \frac{C_n k_{cn}}{Z_n} \left[\sin\left(k_{cn}x\right) \mp \frac{\kappa k_{cn}}{\mu_g \beta_n} \cos\left(k_{cn}x\right)\right] e^{\pm j\beta_n z}. \tag{2.252}$$

CHAPTER 3

ISOTROPIC MATERIAL CHARACTERIZATION

3.1 Introduction

This chapter presents two methods for characterizing isotropic materials using rectangular waveguides. The first technique described is the classical "Nicolson-Ross-Weir" (NRW) extraction applied to an isotropic material completing filling the cross-section of a rectangular waveguide [23]-[24]. This method extracts the material parameters using closed form expressions from the measurement of reflection and transmission coefficients. The convenience of the NRW method, and its insensitivity to propagation of measurement uncertainties, commonly makes it a first choice for characterization of isotropic materials. It is for these reasons that this dissertation makes use of the NRW extraction method and extends the technique to biaxially anisotropic materials (Section 4.2). In addition, the developed waveguide verification standard described in this dissertation (Chapter 6) assumes the use of this classical extraction algorithm.

The second technique is a reflection-only method for conductor-backed absorbing materials using rectangular waveguides. If the sample is conductor backed, and occupies the

entire cross-section of the guide, then a transmission measurement is not available, and thus a method must be found for providing two sufficiently different reflection measurements. The technique proposed here is to place a waveguide iris in front of the sample, exposing the sample to a spectrum of evanescent modes. By measuring the reflection coefficient both with and without an iris the necessary two measurements may be obtained to determine ϵ and μ.

3.2 NRW Characterization for Isotropic Materials

The classic NRW extraction algorithm employs the measured reflection and transmission coefficients for a waveguide section completely filled by the material. The attraction of the NRW characterization method results from the availability of closed-form expressions for μ and ϵ. This contrasts with methods requiring an iterative solver such as Newton's method [30]-[31] or a least squares approach [32]-[33]. The closed-form expressions are well-conditioned for most of the material parameters of interest, except when the material thickness approaches multiples of a half wavelength. The NRW extraction can be used with rectangular waveguides [25], coaxial applicators [26]-[27], free-space methods [28], and stripline measurements [29]. This section presents the method for isotropic material characterization using this classical technique with rectangular waveguides.

3.2.1 NRW Derivation

Assume the sample placed in the cross-sectional plane of the waveguide is linear and homogeneous as well as isotropic. The permittivity and permeability are represented by the constitutive material tensors

$$\bar{\bar{\epsilon}} = \epsilon_0 \begin{bmatrix} \epsilon_r & 0 & 0 \\ 0 & \epsilon_r & 0 \\ 0 & 0 & \epsilon_r \end{bmatrix} \tag{3.1}$$

and

$$\overline{\overline{\mu}} = \mu_0 \begin{bmatrix} \mu_r & 0 & 0 \\ 0 & \mu_r & 0 \\ 0 & 0 & \mu_r \end{bmatrix}, \tag{3.2}$$

where tensor entries are complex quantities: $\epsilon_r = \epsilon_r' + j\epsilon_r'', \mu_r = \mu_r' + j\mu_r''$.

Figure 3.1 shows the experimental configuration used in the NRW method. A sample with unknown properties is placed into a sample holder occupying the region $0 \leq z \leq d$ in a rectangular waveguide system. Waveguide extensions are then attached to guarantee only the dominant mode is present at the measurement ports. The S-parameters S_{11} and S_{21} are measured and used to determine the sample propagation constant and the interfacial reflection coefficient which then can be used to extract ϵ_r and μ_r.

3.2.1.1 Field Structure in a Waveguide Filled with Isotropic Material

Assume a TE_{10} mode is incident from the transmitting empty waveguide ($z < 0$). This field will couple into the TE_{10} material filled waveguide mode since the field structure in both regions is identical. In the empty and sample waveguide region, it can be shown from Section 2.3.1.1 that the TE_{10} mode is the dominant mode ($n = 1$), which means $u_1 = 1$ and $v_1 = 0$. Therefore, $k_{x1}^{e,s} = \pi/a$, $k_{y1}^{e,s} = 0$, and thus $k_{c1}^{e,s} = \pi/a$ is the cutoff wavenumber for the first order mode. Now, using (2.140) the propagation constant in the empty guide is given by

$$\beta_1^e = \sqrt{k_0^2 - \left(k_{c1}^e\right)^2}, \tag{3.3}$$

and the propagation constant in the sample region results in

$$\beta_1^s = \sqrt{k_0^2 \epsilon_r \mu_r - \left(k_{c1}^s\right)^2}, \tag{3.4}$$

where $k_0 = \omega\sqrt{\mu_0\epsilon_0}$. The transverse fields from (2.151) - (2.152) for both regions are given by

$$E_y^{e,s}(x,z) = C_1 e_{y1}^{e,s}(x)\, \mathrm{e}^{\pm j\beta_1^{e,s} z} \tag{3.5}$$

$$H_x^{e,s}(x,z) = \mp C_1 h_{x1}^{e,s}(x)\, \mathrm{e}^{\pm j\beta_1^{e,s} z}. \tag{3.6}$$

Here $e_{y1}^{e,s}$ and $h_{x1}^{e,s}$ are the transverse electric and magnetic modal fields in the empty guide and sample regions, and are expressed as

$$e_{y1}^{e,s} = -k_{x1}^{e,s} \sin\left(k_{x1}^{e,s} x\right), \tag{3.7}$$

$$h_{x1}^{e,s} = \frac{k_{x1}^{e,s}}{Z_1^{e,s}} \sin\left(k_{x1}^{e,s} x\right), \tag{3.8}$$

where the modal wave impedance in the empty guide and sample region is given by $Z_1^e = \omega\mu_0/\beta_1^e$ and $Z_1^s = \omega\mu_0\mu_r/\beta_1^e$, respectively.

3.2.1.2 Solution for Reflection and Transmission Coefficients

The transverse fields in the sample region and in the waveguide extensions can be represented using the modal fields, with the modal amplitudes determined through the application of boundary conditions. The dominant-mode transverse fields for the transmitting extensions, $z < 0$, may thus be written as

$$E_y(x,z) = -A^i k_{x1}^e \sin\left(k_{x1}^e x\right) \mathrm{e}^{-j\beta_1^e z} - A^r k_{x1}^e \sin\left(k_{x1}^e x\right) \mathrm{e}^{j\beta_1^e z} \tag{3.9}$$

$$H_x(x,z) = A^i \frac{k_{x1}^e}{Z_1^e} \sin\left(k_{x1}^e x\right) \mathrm{e}^{-j\beta_1^e z} - A^r \frac{k_{x1}^e}{Z_1^e} \sin\left(k_{x1}^e x\right) \mathrm{e}^{j\beta_1^e z}. \tag{3.10}$$

Similarly, the dominant-mode transverse fields in the sample region $0 < z < d$ may be written as

$$E_y(x,z) = -B^+ k_{x1}^s \sin\left(k_{x1}^s x\right) \mathrm{e}^{-j\beta_1^s z} - B^- k_{x1}^s \sin\left(k_{x1}^s x\right) \mathrm{e}^{j\beta_1^s z} \tag{3.11}$$

$$H_x(x,z) = \frac{B^+}{Z_1^s} k_{x1}^s \sin\left(k_{x1}^s x\right) \mathrm{e}^{-j\beta_1^s z} - \frac{B^-}{Z_1^s} k_{x1}^s \sin\left(k_{x1}^s x\right) \mathrm{e}^{j\beta_1^s z}, \tag{3.12}$$

while those in the receiving waveguide extension, $z > d$, may be expressed as

$$E_y(x,z) = -C^t k_{x1}^e \sin\left(k_{x1}^e x\right) \mathrm{e}^{-j\beta_1^e (z-d)} \tag{3.13}$$

$$H_x(x,z) = C^t \frac{k_{x1}^e}{Z_1^e} \sin\left(k_{x1}^e x\right) \mathrm{e}^{-j\beta_1^e (z-d)}. \tag{3.14}$$

Here, A^i is the amplitude of the incident TE_{10} wave.

The modal amplitudes A^r, B^+, B^-, and C^t may be determined by applying the boundary conditions on E_y and H_x at the interfaces between the isotropic sample and the empty guides. At the interface $z = 0$, the tangential electric field boundary condition requires

$$\left[A^i + A^r\right] k_{x1}^e \sin\left(k_{x1}^e x\right) = \left[B^+ + B^-\right] k_{x1}^s \sin\left(k_{x1}^s x\right), \tag{3.15}$$

and thus since $k_{x1}^s = k_{x1}^e$,

$$\left[A^i + A^r\right] = \left[B^+ + B^-\right]. \tag{3.16}$$

The tangential magnetic field boundary condition at $z = 0$ requires

$$\left[A^i - A^r\right] \frac{k_{x1}^e}{Z_1^e} \sin\left(k_{x1}^e x\right) = \left[B^+ - B^-\right] \frac{k_{x1}^s}{Z_1^s} \sin\left(k_{x1}^s x\right), \tag{3.17}$$

or

$$\left[A^i - A^r\right] \frac{Z_1^s}{Z_1^e} = \left[B^+ - B^-\right]. \tag{3.18}$$

At $z = d$, the boundary condition on the tangential electric field requires

$$\left[B^+ \mathrm{e}^{-j\beta_1^s d} + B^- \mathrm{e}^{j\beta_1^s d}\right] k_{x1}^s \sin\left(k_{x1}^s x\right) = C^t k_{x1}^e \sin\left(k_{x1}^e x\right), \tag{3.19}$$

or

$$\left[B^+ \mathrm{e}^{-j\beta_1^s d} + B^- \mathrm{e}^{j\beta_1^s d}\right] = C^t, \tag{3.20}$$

while the boundary condition on the tangential magnetic field at $z = d$ results in

$$\left[B^+ \mathrm{e}^{-j\beta_1^s d} - B^- \mathrm{e}^{j\beta_1^s d}\right] \frac{k_{x1}^s}{Z_1^s} \sin\left(k_{x1}^s x\right) = C^t \frac{k_{x1}^e}{Z_1^e} \sin\left(k_{x1}^e x\right), \tag{3.21}$$

or

$$\left[B^+ \mathrm{e}^{-j\beta_1^s d} - B^- \mathrm{e}^{j\beta_1^s d}\right] \frac{1}{Z_1^s} = C^t \frac{1}{Z_1^e}. \tag{3.22}$$

The reflection coefficient, $R = A^r/A^i$, is determined by first adding (3.16) to (3.18), yielding,

$$2B^+ = A^i \left(\frac{Z_1^s}{Z_1^e} + 1\right) - A^r \left(\frac{Z_1^s}{Z_1^e} - 1\right), \tag{3.23}$$

and then subtracting (3.16) from (3.18), producing

$$2B^- = -A^i \left(\frac{Z_1^s}{Z_1^e} - 1\right) + A^r \left(\frac{Z_1^s}{Z_1^e} + 1\right). \tag{3.24}$$

Adding (3.20) and (3.22) results in

$$2B^{+} = C^{t}\left[\frac{Z_1^s}{Z_1^e} + 1\right] \mathrm{e}^{j\beta_1^s d}, \tag{3.25}$$

while subtracting (3.20) from (3.22) gives

$$2B^{-} = -C^{t}\left[\frac{Z_1^s}{Z_1^e} - 1\right] \mathrm{e}^{-j\beta_1^s d}. \tag{3.26}$$

Then dividing (3.26) by (3.25) produces

$$\frac{B^{-}}{B^{+}} = -\left[\frac{Z_1^s - Z_1^e}{Z_1^s + Z_1^e}\right] \mathrm{e}^{-j2\beta_1^s d}, \tag{3.27}$$

which can also be written as

$$\frac{B^{-}}{B^{+}} = -\Gamma P^2. \tag{3.28}$$

Here the interfacial reflection coefficient is established as

$$\Gamma = \frac{Z_1^s - Z_1^e}{Z_1^s + Z_1^e}, \tag{3.29}$$

and the propagation factor is defined as

$$P = \mathrm{e}^{-j\beta_1^s d}. \tag{3.30}$$

Next, dividing (3.24) by (3.25) gives

$$\frac{B^{-}}{B^{+}} = -\frac{A^i\left(\frac{Z_1^s - Z_1^e}{Z_1^e}\right) - A^r\left(\frac{Z_1^s + Z_1^e}{Z_1^e}\right)}{A^i\left(\frac{Z_1^s + Z_1^e}{Z_1^e}\right) - A^r\left(\frac{Z_1^s - Z_1^e}{Z_1^e}\right)}. \tag{3.31}$$

Multiplying the numerator and denominator by Z_1^e/A^i yields

$$\frac{B^-}{B^+} = -\frac{\left(Z_1^s - Z_1^e\right) - \frac{A^r}{A^i}\left(Z_1^s + Z_1^e\right)}{\left(Z_1^s + Z_1^e\right) - \frac{A^r}{A^i}\left(Z_1^s - Z_1^e\right)}, \tag{3.32}$$

and dividing this expression by $(Z_1^s + Z_1^e)$ produces

$$\frac{B^-}{B^+} = -\frac{\Gamma - R}{1 - R\Gamma}. \tag{3.33}$$

The reflection coefficient is now determined by setting (3.28) equal to (3.33), which results in

$$\Gamma P^2 = \frac{\Gamma - R}{1 - R\Gamma}. \tag{3.34}$$

Solving for R then gives

$$R = \frac{\Gamma\left(1 - P^2\right)}{1 - \Gamma^2 P^2}. \tag{3.35}$$

Next, the transmission coefficient, $T = C^t/A^i$, can be derived by first rearranging (3.20):

$$B^+ \mathrm{e}^{-j\beta_1^s d}\left[1 + \frac{B^-}{B^+}\mathrm{e}^{j2\beta_1^s d}\right] = C^t \tag{3.36}$$

Substituting (3.28), this expression becomes

$$B^+ \mathrm{e}^{-j\beta_1^s d}\left[1 + \Gamma\right] = C^t. \tag{3.37}$$

Then (3.23) can be substituted, yielding

$$\frac{1}{2}\left[A^i\left(\frac{Z_1^s + Z_1^e}{Z_1^e}\right) - A^r\left(\frac{Z_1^s - Z_1^e}{Z_1^e}\right)\right]\left[1 - \Gamma\right]\mathrm{e}^{-j\beta_1^s d} = C^t. \tag{3.38}$$

Factoring A^i/Z_1^e and rearranging the equation produces

$$\frac{C^t}{A^i}\mathrm{e}^{j\beta_1^s d} = \frac{1}{2Z_1^e}\left[\left(Z_1^s + Z_1^e\right) - \frac{A^r}{A^i}\left(Z_1^s - Z_1^e\right)\right][1-\Gamma], \tag{3.39}$$

or

$$T\mathrm{e}^{j\beta_1^s d} = \frac{1}{2Z_1^e}\left[\left(Z_1^s + Z_1^e\right) - R\left(Z_1^s - Z_1^e\right)\right][1-\Gamma]. \tag{3.40}$$

Factoring out $Z_1^s - Z_1^e$ gives

$$T\mathrm{e}^{j\beta_1^s d} = \frac{1}{2Z_1^e}\left(Z_1^s + Z_1^e\right)\left[1 - R\frac{Z_1^s - Z_1^e}{Z_1^s + Z_1^e}\right][1-\Gamma], \tag{3.41}$$

which can also be written as

$$T\mathrm{e}^{j\beta_1^s d} = \frac{1}{2Z_1^e}\left(Z_1^s + Z_1^e\right)[1 - R\Gamma][1-\Gamma]. \tag{3.42}$$

Substituting (3.29) then yields

$$T\mathrm{e}^{j\beta_1^s d} = \frac{1}{2Z_1^e}\left(Z_1^s + Z_1^e\right)\frac{2Z_1^e}{Z_1^s + Z_1^e}[1 - R\Gamma], \tag{3.43}$$

and through addition algebraic manipulation, the transmission coefficient becomes

$$T = (1 - R\Gamma)\,P. \tag{3.44}$$

Finally, using the equation for the reflection coefficient, (3.35), the transmission coefficient is expressed as

$$T = \frac{P\left(1 - \Gamma^2\right)}{1 - \Gamma^2 P^2}. \tag{3.45}$$

Note that S_{11} and S_{21} are typically measured at the ports of the waveguide extensions. With properly applied phase shift, these may be transformed to the faces of the material sample at $z = 0$ and $z = d$. In that case $S_{11} = R$ and $S_{21} = T$. This process is called de-embedding and is described in detail in Appendix B.

3.2.2 Validation of Theoretical Analysis

It is useful to validate the theoretical reflection and transmission coefficients derived in the previous section. The theoretical model is validated against the computational finite element (FEM) solver HFSS with an Eccossorb FGM125 test sample. FGM125 has approximate material parameters of $\epsilon_r = 7.3197 - j0.0464$ and $\mu_r = 0.5756 - j0.4842$ at 10.09 GHz. These values were obtained using the waveguide NRW method and were provided by Captain Milo Hyde IV of the Air Force Institute of Technology; they are tabulated in [46]. Though the material properties for FGM125 vary with frequency, for this validation the material parameters are assumed to be frequency independent. This provides a general validation of the theory.

The derived theoretical expressions were used to compute the reflection and transmission coefficients for the FGM125 material paced in the cross-section of an X-band waveguide system. The dimensions of the X-band system are $a = 22.86$ mm, $b = 10.16$ mm, and $d = 3.175$ mm. Figure 3.2 shows S_{11} and S_{21} at the faces of the sample computed using (3.35) and (3.45). Also shown are the values of the reflection and transmission coefficient computed using HFSS. The waveguide extensions were explicitly modeled in the EM solver and were of significant length to ensure that only the fundamental TE_{10} mode propagates; these lengths were chosen to be 50 mm. The convergence in HFSS was specified to a maximum delta S of 0.01, which is defined as the absolute difference between all S-parameters from two succeeding iterations computed at a chosen "solution frequency" of 12.4 GHz (this is HFSS terminology and does not imply that the problem is only solved at one frequency). The S-parameters were computed at 31 frequency points over the X-band range of $8.2 - 12.4$ GHz

using an HFSS discrete frequency sweep. Choosing a "solution frequency" of 12.4 GHz ensures convergence using a fine mesh since this is the highest frequency analyzed. Excellent agreement is obtained between the theoretical equations and HFSS, thus validating the computation of the theoretical reflection and transmission coefficients.

3.2.3 Extraction Process

The S-parameters are measured using a vector network analyzer (VNA) attached at the end of the waveguide extensions shown in Figure 3.1. The S-parameters are then mathematically transformed to obtain the S-parameters at the sample planes, S_{11} and S_{21}, as is discussed in Appendix B. In this case $S_{11} = R$ and $S_{21} =$. These sample-plane S-parameters are used to determine the sample propagation constant β_1^s and the interfacial reflection coefficient Γ, which may in turn be used to find ϵ_r and μ_r.

Define

$$V_1 = S_{21} + S_{11} \tag{3.46}$$

$$V_2 = S_{21} - S_{11}. \tag{3.47}$$

Substituting (3.35) and (3.45), these variables then become

$$V_1 = \frac{P - \Gamma}{1 + \Gamma P} \tag{3.48}$$

$$V_2 = \frac{P - \Gamma}{1 - \Gamma P}. \tag{3.49}$$

From (3.48), the propagation factor is given by

$$P = \frac{V_1 - \Gamma}{1 - \Gamma V_1}. \tag{3.50}$$

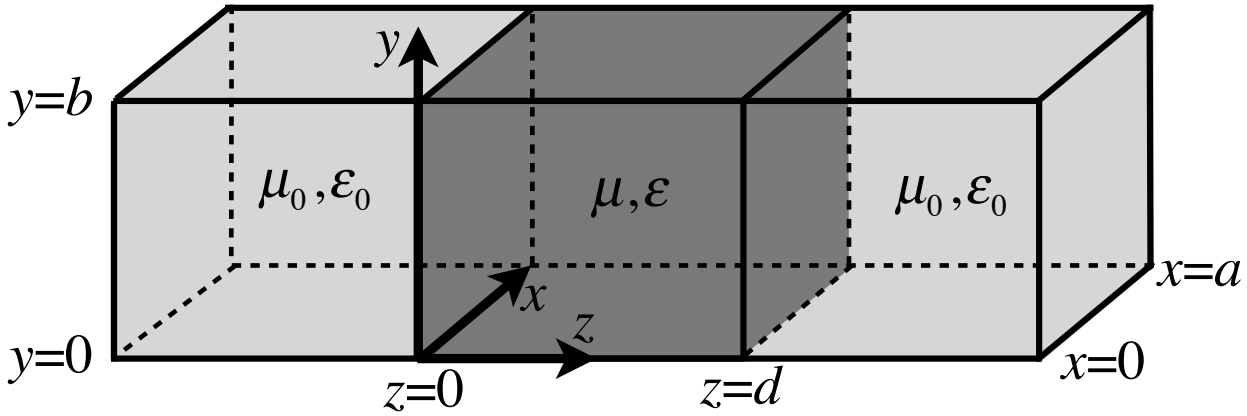

Figure 3.1: Rectangular waveguide with isotropic sample placed in cross-sectional region with waveguide extensions attached.

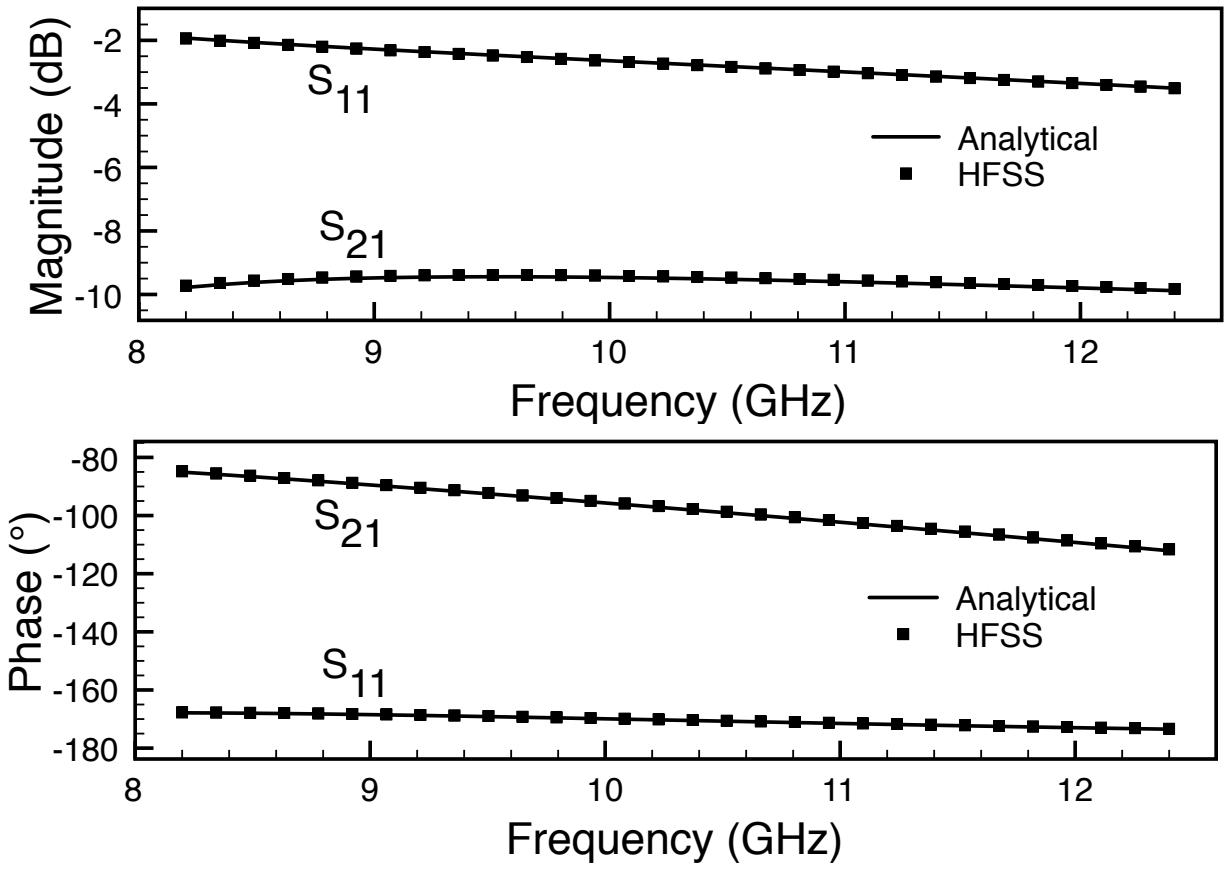

Figure 3.2: S-parameters computed for a FGM125 test material.

Next, (3.49) is multiplied by $1 - \Gamma P$ yielding

$$V_2 (1 - \Gamma P) = P - \Gamma. \tag{3.51}$$

Then inserting (3.50) into (3.51) gives

$$V_2 - V_2\Gamma \left[\frac{V_1 - \Gamma}{1 - \Gamma V_1} \right] = \frac{V_1 - \Gamma}{1 - \Gamma V_1} - \Gamma. \tag{3.52}$$

Multiplying through by $1 - PV_1$ and simplifying the expression results in

$$\Gamma^2 - 2\Gamma X + 1 = 0, \tag{3.53}$$

where

$$X = \frac{1 - V_1 V_2}{V_1 - V_2}. \tag{3.54}$$

The solution to (3.53) is

$$\Gamma = X \pm \sqrt{X^2 - 1}. \tag{3.55}$$

Here the appropriate sign is chosen such that $|\Gamma| \leq 1$.

The propagation constant is then determined from (3.30) as

$$\beta_1^s = -\frac{\ln(P) \pm j2n\pi}{jd}, \tag{3.56}$$

where n depends on the thickness of the sample in terms of a wavelength. Proper choice of n is discussed in Section 3.2.4. Next, rearranging (3.29) gives

$$\frac{Z_1^s}{Z_1^e} = \frac{1 + \Gamma}{1 - \Gamma}, \tag{3.57}$$

and the expressions for the modal impedances can then be substituted yielding

$$\frac{Z_1^s}{Z_1^e} = \frac{\beta_1^e}{\beta_1^s}\mu_r. \tag{3.58}$$

Combining (3.57) and (3.58) gives

$$\mu_r = \frac{1+\Gamma}{1-\Gamma}\frac{\beta_1^s}{\beta_1^e}, \tag{3.59}$$

thus providing a closed-form expression for the permeability of the isotropic sample. Using (3.4), an expression for ϵ can also be derived. First, k_0 is brought outside the square root yielding

$$\beta_1^s = k_0\sqrt{\epsilon_r\mu_r - \left(\frac{k_{x1}^s}{k_0}\right)^2} \tag{3.60}$$

or

$$\left(\frac{\beta_1^s}{k_0}\right)^2 = \epsilon_r\mu_r - \left(\frac{k_{x1}^s}{k_0}\right)^2. \tag{3.61}$$

Next, inserting (3.59) and simplifying gives

$$\epsilon_r = \left[\left(\frac{\beta_1^s}{k_0}\right)^2 + \left(\frac{k_{x1}^s}{k_0}\right)^2\right]\frac{\beta_1^e}{\beta_1^s}\frac{1-\Gamma}{1+\Gamma}. \tag{3.62}$$

Thus, by measuring S_{11} and S_{21} for an isotropic sample filling the cross-section of a rectangular waveguide, two equations, (3.59) and (3.62), can be used to extract the two material parameters μ_r and ϵ_r.

It is important to validate the inversion method before proceeding with the characterization of unknown materials. Therefore, the FGM125 material parameters outlined in Section 3.2.2 are used in HFSS to generate S-parameters with the sample completely filling the

cross-section of an X-band waveguide, and the NRW extraction method is performed. The HFSS simulation uses the same model as was used to generate the data for Figure 3.2. The results of the characterization are shown in Figure 3.3. As expected, the characterized material parameters are in accordance with the parameters used in the HFSS simulation. This extraction gives confidence in the characterization technique before moving forward with measurements.

3.2.4 Phase Ambiguity

An ambiguity exists when the electrical length of the material reaches a half wavelength and every subsequent full wavelength, where the value n in (3.56) must be incremented. The correct value of n must be determined for accurate characterization. This ambiguity results from the VNA measuring the phase of the S-parameters from -180° to $+180^\circ$. The phase shift through the material is determined from the propagation factor, which is computed using the measured S-parameters via (3.50). Since the VNA measures the phase of the S-parameters from -180° to $+180^\circ$, the computed phase shift will wrap around when these measurement boundaries are met. Thus when measuring a sample of material, the phase shift can actually wrap around multiple times and this needs to accounted for in (3.56). This is done by incrementing n every time the phase shift wraps around.

The 1-way propagation factor for a wave traveling through the sample region is given by

$$P = \mathrm{e}^{-jd\left(\beta_{1r}^{s} + j\beta_{1i}^{s}\right)} \tag{3.63}$$

where the propagation constant in the material is split into its real and imaginary components. This expression can also be written as

$$P = \mathrm{e}^{\left(\beta_{1i}^{s} d\right)} \mathrm{e}^{(j\phi)}, \tag{3.64}$$

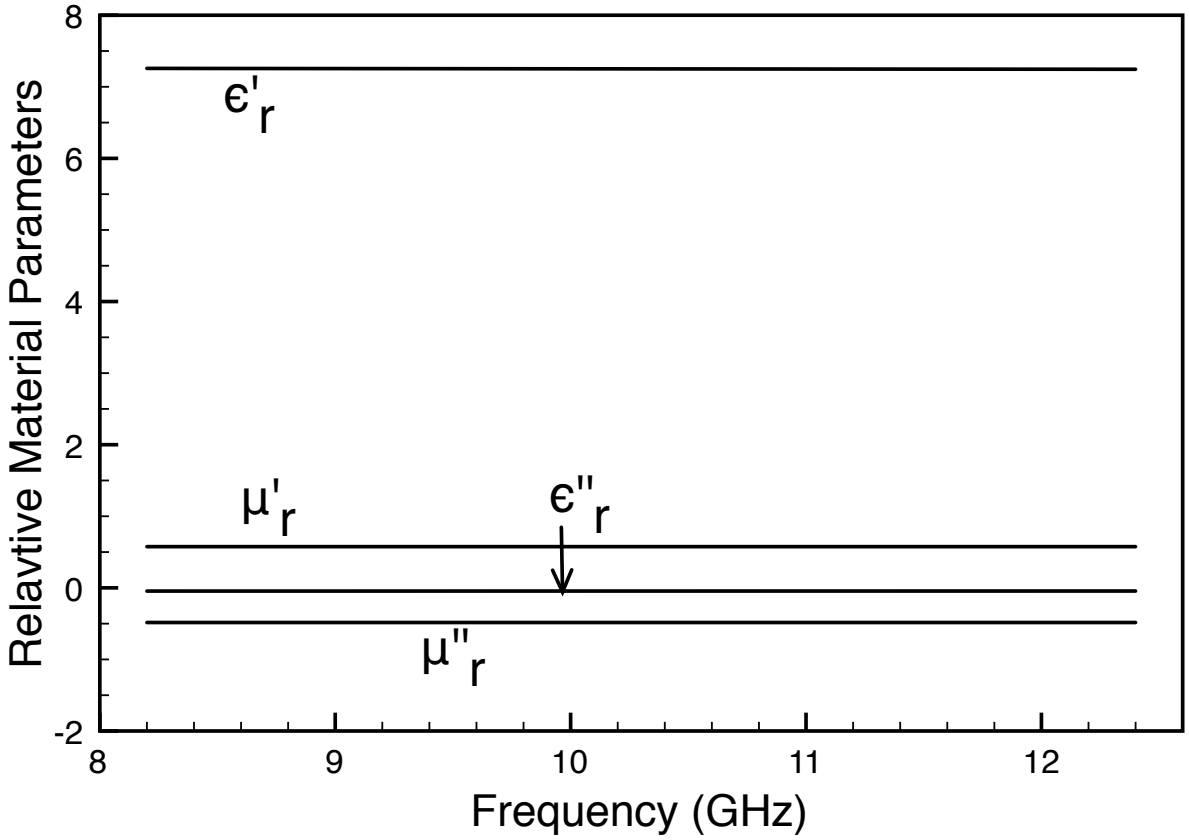

Figure 3.3: Extracted permittivity using HFSS generated S-parameters.

where $\phi = -\beta_{1r}^{s} d$ is the phase shift through the material. The wavelength in the material is given by

$$\lambda^{s} = \frac{2\pi}{\beta_{1r}^{s}}. \tag{3.65}$$

Thus phase shift through the material is given by

$$\phi = -\frac{2\pi}{\lambda^{s}} d. \tag{3.66}$$

The first wrap around occurs when $\phi = -180^{\circ}$ or $\phi = -\pi$, where

$$\phi = -\pi = -\frac{2\pi}{\lambda^{s}} d. \tag{3.67}$$

Thus the first phase wrap happens when the thickness of the sample is a half-wavelength, or $d = \lambda^{s}/2$. An example of phase wrap can be seen in Figure 3.4. Here an FGM125 sample was simulated using (3.66) where β_{1}^{s} was determined using (3.4). The phase shift was determined with the FGM125 sample placed inside an X-band waveguide and simulated from 8.2 GHz to 12.4 GHz. The thickness of the FGM125 sample was chosen to be6.35 mm. From Figure 3.4, it can be seen that n should be zero from 8.2 GHz to approximately 11.1 GHz. Around 11.1 GHz, or when $\phi = -\pi$ radians, the phase wraps around and n should change to one. The next phase wrap doesn't occurs until $\phi = -3\pi$ radians. Using (3.66) it is found that, $n = 1$ for $\lambda^{s}/2 < d < 3\lambda^{s}/2$. Figure 3.4 also shows the typical sort of error that results when using the NRW method to extract the permittivity when the wrong value of n is used over certain portions of the frequency band. Though not shown, the permeability follows a similar trend.

The ambiguity causes problems when measuring an unknown sample, since the values of ϵ_r and μ_r are yet to be determined, and so λ^{s} is not known *a priori*. Thus the number of times the phase shift wraps around is unknown. A typical solution is to fabricate samples that

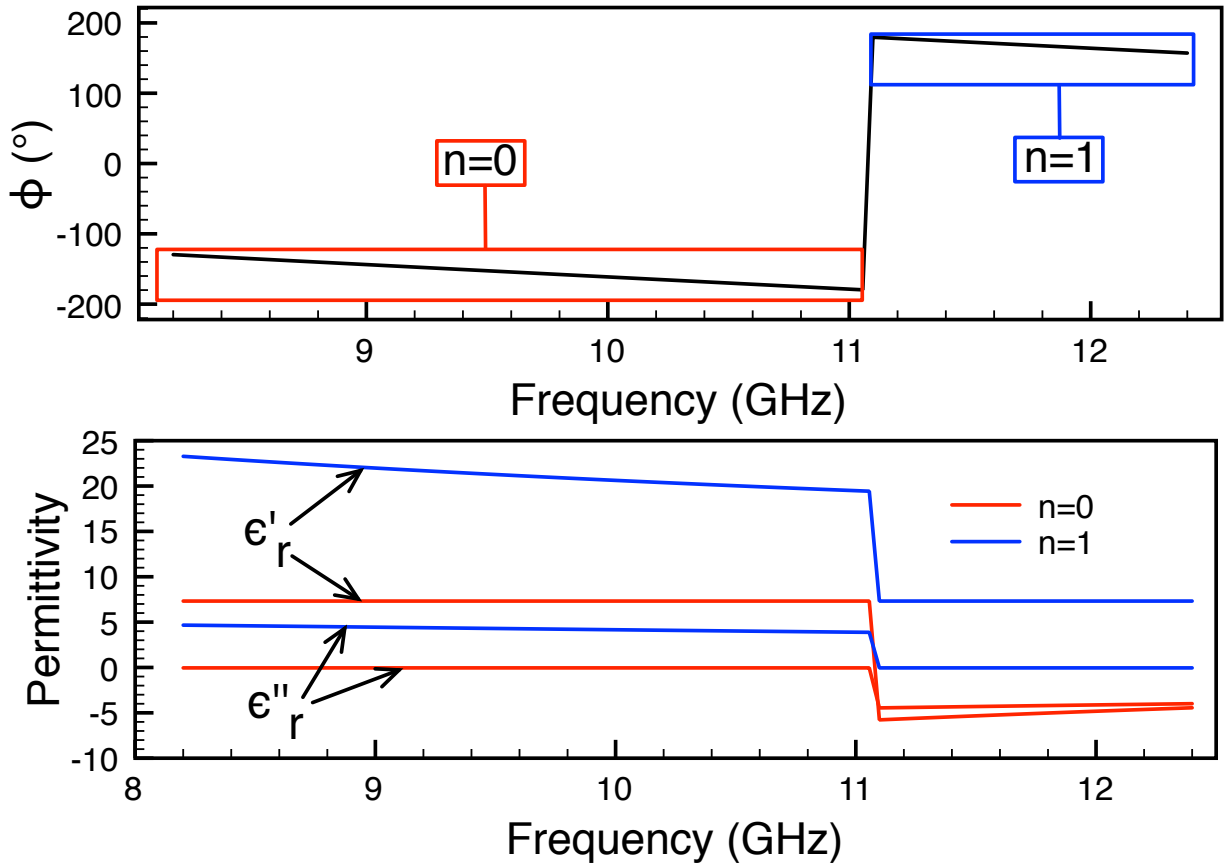

Figure 3.4: Upper plot shows phase shift through material while lower plot shows extraction of permittivity from S-parameters using NRW method where $n = 0$ and $n = 1$. For interpretation of the references to color in this and all other figures, the reader is referred to the electronic version of this dissertation.

are thin and assume the half-wavelength boundary does not occur within the measurement band.

3.2.5 Experimental Results

To experimentally validate the NRW technique at X-band, the S-parameters from a sample of Eccosorb FGM125 were measured and the material parameters extracted. The measurement system consisted of two 152 mm long section of WR-90 commercial X-band waveguide, which acted as extensions, with coaxial transitions attached at the ends. Since a sample holder was not manufactured to the specific thickness to the FGM125 sample, as an alternative, the sample was placed inside the waveguide extension connected to Port 1. The S-parameters were then mathematically de-embedded to the faces of the sample. This type of sample insertion is the second case discussed in Appendix B, where the mathematical equations used for the de-embedding are given.

Measurements of the S-parameters of the FGM125 sample placed into the waveguide extensions were made using an Aglient E5071C VNA. The VNA was calibrated using an X7005M Maury Microwave X-Band calibration kit, consisting of two offset shorts and a load. The measurements were made with VNA settings of -5 dBm source power, 64 averages, and an IF bandwidth of 5 kHz. Finally, the material parameters were extracted using the measured values of S_{11} and S_{21}.

The measurement repeatability error was assessed by measuring the FGM125 sample 5 separate times, with the VNA calibrated at the start of each set of measurements. The permittivity parameters extracted from the 5 measurements are shown in Figure 3.5, while the permeability parameters are shown in Figure 3.6. The center solid line in these figures represents the mean of the extracted values while the upper and lower solid lines define the 95% confidence levels, or $\pm$ two standard deviations. The dotted lines in Figure 3.5 and Figure 3.6 show the material parameters of a different sample of FGM125 extracted from S-parameter measurements performed at AFIT using the NRW method. These material

parameters are tabulated in [46]. A strong agreement exists between the characterization of the two different FGM125 samples; however, the extraction of the permeability parameters are slightly different. This is mostly due to material parameters of FGM125 varying among stock. Though the comparison of the results from the two extractions vary slightly, it still gives confidence the NRW characterization method is outlined properly in this dissertation.

3.2.6 Summary

The NRW method for the characterization of isotropic materials using rectangular waveguides is described. Closed-form expression are given to characterize the two complex material parameters. A discussion is presented on the ambiguity that exists when the electrical length of the material reaches a half wavelength and subsequent full wavelengths. Validation of the technique was performed using S-parameters generated using HFSS for an FGM125 sample filling the cross-section of an X-band waveguide. Additionally, measurements of the S-parameters for a sample of FGM125 were used for further validation of the technique.

3.3 Measurement of the Electromagnetic Properties of a Conductor-backed Material Using a Waveguide-Iris Technique

Magnetic radar-absorbing materials (MagRAM) are often applied to the conducting surfaces of air vehicles to reduce radar cross-section. To ensure proper aircraft design, the electromagnetic properties of these materials must be accurately characterized. Unfortunately, the process of bonding the MagRAM to the conductor produces a chemical reaction that alters the intrinsic electromagnetic properties of the absorber in unpredictable ways, and thus it is crucial that the absorber be characterized while still attached to the conductor backing.

As outlined in Section 3.2, a sample is typically placed into the cross-section of a wave-

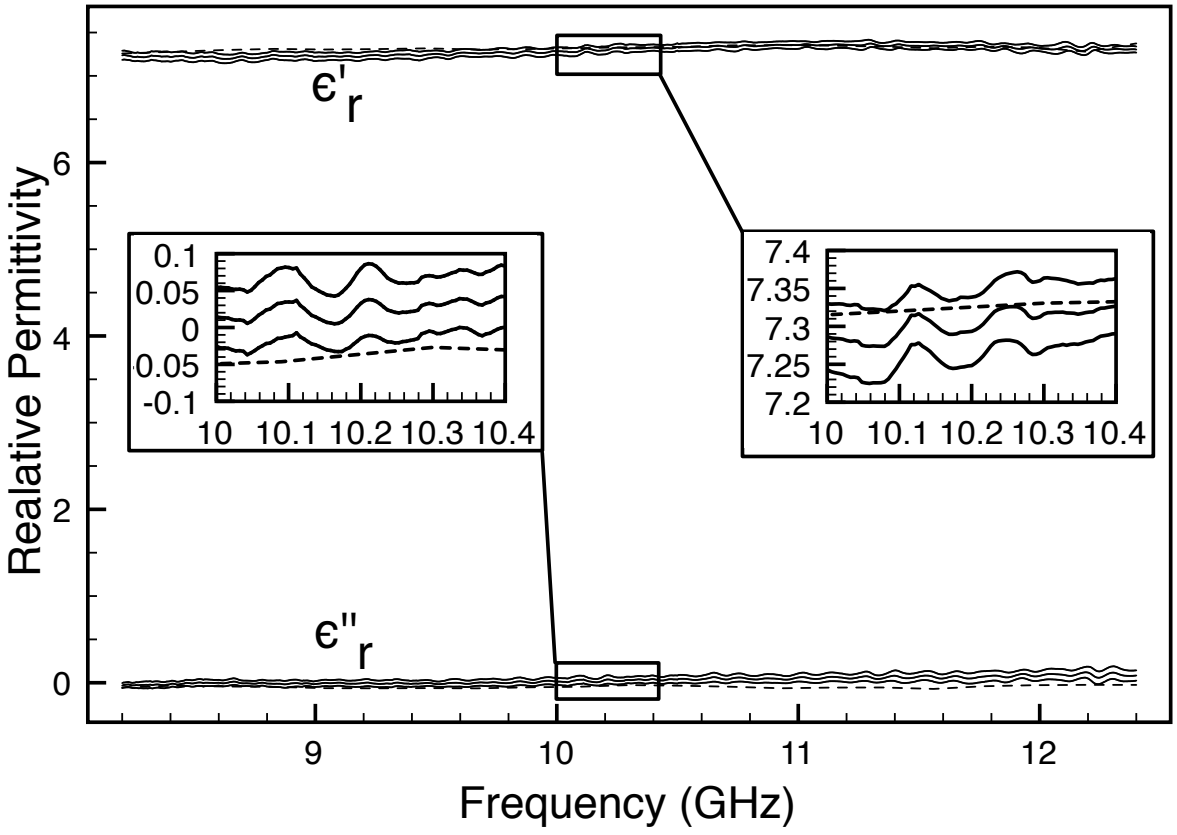

Figure 3.5: Real parts of relative permittivity extracted from 5 sets of measurements. Center solid line is the average of the measurements. Upper and lower lines show the 95% confidence intervals. Dotted line shows permittivity extracted from the S-parameter measurements performed at AFIT with a different sample than the one used at MSU.

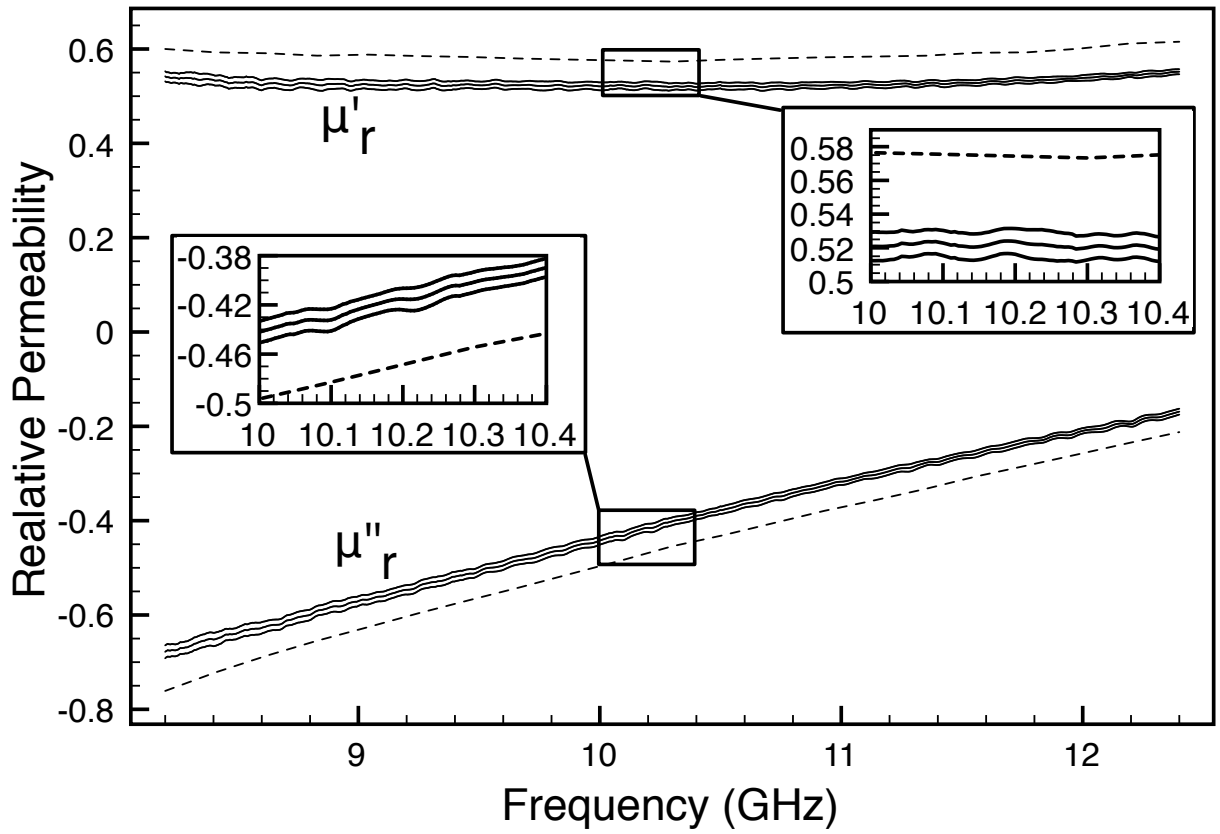

Figure 3.6: Real parts of relative permeability extracted from 5 sets of measurements. Center solid line is the average of the measurements. Upper and lower lines show the 95% confidence intervals. Dotted line shows permeability extracted from the S-parameter measurements performed at AFIT with a different sample than the one used at MSU.

guide and the transmission and reflection coefficients are measured, providing the two necessary data to find both the permittivity and permeability of the sample. If the sample is conductor-backed, and occupies the entire cross-section, a transmission measurement is not available, and thus a method must be found for providing two sufficiently different reflection measurements. The technique proposed here is to place a waveguide iris in front of the sample, exposing the sample to a spectrum of evanescent modes. By measuring the reflection coefficient with and without an iris, the two necessary data may be obtained to determine ϵ and μ. A mode-matching approach is used to determine the theoretical response of a sample placed behind a waveguide iris. This response may be used in a root-searching algorithm to determine ϵ and μ using measurements of the reflection coefficient.

3.3.1 Theoretical Reflection and Transmission Coefficients

The conductor-backed material under test is assumed to be linear and homogeneous, with tensor constitutive parameters

$$\overline{\overline{\epsilon}} = \epsilon_0 \begin{bmatrix} \epsilon_S & 0 & 0 \\ 0 & \epsilon_S & 0 \\ 0 & 0 & \epsilon_S \end{bmatrix} \tag{3.68}$$

and

$$\overline{\overline{\mu}} = \mu_0 \begin{bmatrix} \mu_S & 0 & 0 \\ 0 & \mu_S & 0 \\ 0 & 0 & \mu_S \end{bmatrix}, \tag{3.69}$$

where tensor entries are complex quantities: $\epsilon_S = \epsilon_S' + j\epsilon_S'', \mu_S = \mu_S' + j\mu_S''$.

The reflection coefficient is measured under two conditions: with and without an iris placed in front of the conductor-backed material. Thus, the theoretical reflection coefficients must accurately be determined under these two conditions.

3.3.1.1 Reflection Coefficient with Iris

For the calculation of the theoretical reflection coefficient with the iris, consider Figure 3.7. The conductor-backed material with thickness δ is placed a distance d away from an iris of thickness Δ and a window opening width of w_2. The iris itself consists of two waveguide junctions: a reduced step and an expanded step. The iris is centered about the width of the guide. If a single TE_{10} mode is assumed to be incident on the iris boundary from the transmitting region, then because of mode conversion at the discontinuity with the iris an infinite number of waveguide modes are reflected back into the transmitting region. Additionally, an infinite number of waveguide modes are transmitted into the iris region, which are then incident on the discontinuity at the expanded-step boundary, and thus a spectrum of modes are also reflected back into the iris region and transmitted into the guide region containing the material under test. Since the electric field of the incident TE_{10} mode is even about the width of the transmitting guide, and because the iris is also symmetric about the width of the guide, only modes with electric fields even about the width of the guide will be excited. Thus, only TE_{n0} modes with odd values of n are needed to describe the fields in each of the waveguide regions.

To simplify the mode matching technique, each of the iris junctions are analyzed separately. Consider a general reduced-step junction shown in Figure 3.8, where $w_B < w_A$. The isotropic transverse field equations from (2.151) and (2.152) can be used in each of these regions where the waveguide is centered about the y-axis, as long as the sinusoidal functions are offset by either $w_A/2$ or $w_B/2$. Since only TE_{n0} modes are excited, $v = 0$ for all excited modes. This leads to $k_{yn} = 0$, reducing the transverse field equations to

$$E_y^{A,B}(x,z) = C_n e_{yn}^{A,B}(x)\, \mathrm{e}^{\pm j\beta_n^{A,B} z} \tag{3.70}$$

$$H_x^{A,B}(x,z) = \mp C_n h_{xn}^{A,B}(x)\, \mathrm{e}^{\pm j\beta_n^{A,B} z}. \tag{3.71}$$

Here $e_{yn}^{A,B}$ and $h_{xn}^{A,B}$ are the transverse electric and magnetic modal fields, respectively, and

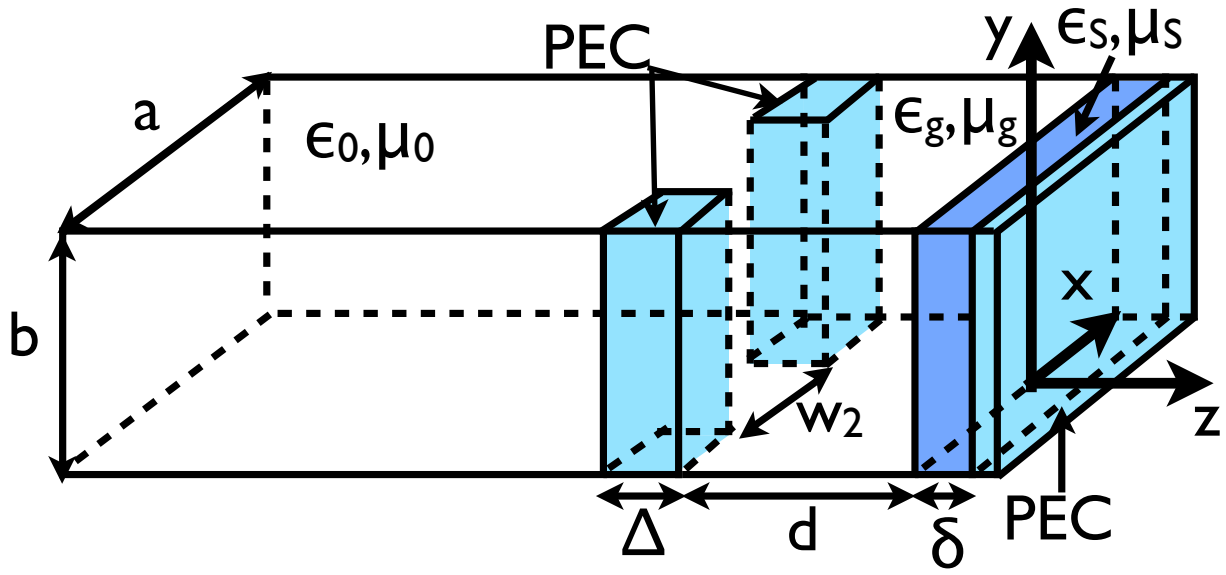

Figure 3.7: Conductor-backed material with iris and waveguide extension attached.

are found from (2.153) and (2.154) to be

$$e_{yn}^{A,B}(x) = -k_{xn}^{A,B} \sin\left[k_{xn}^{A,B}\left(x - \frac{w_{A,B}}{2}\right)\right], \tag{3.72}$$

$$h_{xn}^{A,B}(x) = -\frac{e_{yn}^{A,B}(x)}{Z_n^{A,B}}, \tag{3.73}$$

where $k_{xn}^{A,B} = n\pi/a$ and $Z_n^{A,B} = \omega\mu_0\mu_{A,B}/\beta_n^{A,B}$. Here $\beta_n^{A,B}$ is determined from (2.140) as

$$\beta_n^{A,B} = \sqrt{(k^{A,B})^2 - (k_{xn}^{A,B})^2}, \tag{3.74}$$

where $k^{A,B} = k_0\sqrt{\mu_{A,B}\epsilon_{A,B}}$.

Using only odd values of n to describe the fields can be confusing when programing the mode matching technique. Therefore, a change to the indexing of n can be implemented, where n will now order the odd modes instead of all the modes. This is done by first

examining the sinusoidal functions in the expressions for $e_n^{A,B}$ and $h_n^{A,B}$:

$$\sin\left[k_{c,n}^{A,B}\left(x-\frac{w_{A,B}}{2}\right)\right]=\sin\left[\frac{n\pi}{w_{A,B}}\left(x-\frac{w_{A,B}}{2}\right)\right]\qquad n=1,3,5\ldots. \tag{3.75}$$

$$\tag{3.76}$$

This can also be expressed as

$$\sin\left[k_{c,n}^{A,B}\left(x-\frac{w_{A,B}}{2}\right)\right]=\sin\left[\frac{2n-1}{w_{A,B}}\pi\left(x-\frac{w_{A,B}}{2}\right)\right]\qquad n=1,2,3\ldots. \tag{3.77}$$

$$\tag{3.78}$$

Expanding the product and using a trigonometric identity results in

$$\sin\left[k_{c,n}^{A,B}\left(x-\frac{w_{A,B}}{2}\right)\right]=-\cos\left[\frac{2n-1}{w_{A,B}}\pi x\right]\sin\left[\frac{2n-1}{2}\pi\right]\qquad n=1,2,3\ldots, \tag{3.79}$$

or

$$\sin\left[k_{c,n}^{A,B}\left(x-\frac{w_{A,B}}{2}\right)\right]=(-1)^n\cos\left[\frac{2n-1}{w_{A,B}}\pi x\right]\qquad n=1,2,3\ldots. \tag{3.80}$$

Hence (4.80) and (4.81) become

$$e_{yn}^{A,B}(x)=-k_{c,n}^{A,B}(-1)^n\cos\left[k_{c,n}^{A,B}\pi x\right], \tag{3.81}$$

$$h_{xn}^{A,B}(x)=-\frac{e_{yn}^{A,B}(x)}{Z_n^e}, \tag{3.82}$$

where $k_{c,n}^{A,B}=\frac{2n-1}{w_{A,B}}$.

The transverse fields in regions A and B can be expanded in an infinite sum of modal fields, with modal amplitudes to be determined through the application of appropriate

boundary conditions. The transverse fields in region A, $z < 0$, are given by

$$E_y(x,z) = \sum_{n=1}^{N} a_n^A e_n^A(x) e^{-j\beta_n^A z} + \sum_{n=1}^{N} b_n^A e_n^A(x) e^{j\beta_n^A z} \tag{3.83}$$

$$H_y(x,z) = \sum_{n=1}^{N} a_n^A h_n^A(x) e^{-j\beta_n^A z} - \sum_{n=1}^{N} b_n^A h_n^A(x) e^{j\beta_n^A z}, \tag{3.84}$$

and the transverse fields in region B, $z > 0$, are described as

$$E_y(x,z) = \sum_{n=1}^{N} a_n^B e_n^B(x) e^{-j\beta_n^B z} + \sum_{n=1}^{N} b_n^B e_n^B(x) e^{j\beta_n^B z} \tag{3.85}$$

$$H_y(x,z) = \sum_{n=1}^{N} a_n^B h_n^B(x) e^{-j\beta_n^B z} - \sum_{n=1}^{N} b_n^B h_n^B(x) e^{j\beta_n^B z}. \tag{3.86}$$

The unknown modal amplitude coefficients a_n^A, a_n^B, b_n^A, and b_n^B may be determined by applying the boundary conditions on E_y and H_x at the interfaces between regions A and B. At $z = 0$, the boundary condition on tangential electric field requires

$$\sum_{n=1}^{N} a_n^A e_n^A(x) + \sum_{n=1}^{N} b_n^A e_n^A(x) = \begin{cases} \sum_{n=1}^{N} a_n^B e_n^B(x) + \sum_{n=1}^{N} b_n^B e_n^B(x), & |x| < \dfrac{w_B}{2} \\ 0, & |x| > \dfrac{w_B}{2}, \end{cases} \tag{3.87}$$

while the boundary condition on tangential magnetic field requires

$$\sum_{n=1}^{N} a_n^A h_n^A(x) - \sum_{n=1}^{N} b_n^A h_n^A(x) = \sum_{n=1}^{N} a_n^B h_n^B(x) - \sum_{n=1}^{N} b_n^B h_n^B(x). \tag{3.88}$$

The system of functional equations (3.87)-(3.88) may be transformed into a system of linear equations by applying appropriate testing operators. First, the equation resulting from the tangential electric field boundary condition, (3.87), is multiplied by $e_m^A(x)$ and integrated over $-w_A/2 \le x \le w_A/2$. Then, the equation resulting from the tangential magnetic field boundary condition, (3.88), is multiplied by $h_m^B(x)$ and integrated over $-w_B/2 \le x \le w_B/2$.

Here $1 \leq m \leq N$. This results in

$$\sum_{n=1}^{N} a_n^A \int_{-\frac{w_A}{2}}^{\frac{w_A}{2}} e_n^A(x) e_m^A(x) dx + \sum_{n=1}^{N} b_n^A \int_{-\frac{w_A}{2}}^{\frac{w_A}{2}} e_n^A(x) e_m^A(x) dx =$$
$$\sum_{n=1}^{N} a_n^B \int_{-\frac{w_B}{2}}^{\frac{w_B}{2}} e_n^B(x) e_m^A(x) dx + \sum_{n=1}^{N} b_n^B \int_{-\frac{w_B}{2}}^{\frac{w_B}{2}} e_n^B(x) e_m^A(x) dx \tag{3.89}$$

$$\sum_{n=1}^{N} a_n^A \int_{-\frac{w_B}{2}}^{\frac{w_B}{2}} h_n^A(x) h_m^A(x) dx - \sum_{n=1}^{N} b_n^A \int_{-\frac{w_B}{2}}^{\frac{w_B}{2}} h_n^A(x) h_m^A(x) dx =$$
$$\sum_{n=1}^{N} a_n^B \int_{-\frac{w_B}{2}}^{\frac{w_B}{2}} h_n^B(x) h_m^A(x) dx - \sum_{n=1}^{N} b_n^B \int_{-\frac{w_B}{2}}^{\frac{w_B}{2}} h_n^B(x) h_m^A(x) dx. \tag{3.90}$$

By defining new quantities, these expressions results in

$$\sum_{n=1}^{N} a_n^A C_{mn} + \sum_{n=1}^{N} b_n^A C_{mn} = \sum_{n=1}^{N} a_n^B D_{mn} + \sum_{n=1}^{N} b_n^B D_{mn} \tag{3.91}$$
$$\sum_{n=1}^{N} a_n^A E_{mn} - \sum_{n=1}^{N} b_n^A E_{mn} = \sum_{n=1}^{N} a_n^B F_{mn} - \sum_{n=1}^{N} b_n^B F_{mn}, \tag{3.92}$$

where

$$C_{mn} = \int_{-\frac{w_A}{2}}^{\frac{w_A}{2}} e_m^A(x) e_n^A(x) dx, \qquad D_{mn} = \int_{-\frac{w_B}{2}}^{\frac{w_B}{2}} e_m^A(x) e_n^B(x) dx, \tag{3.93}$$

$$E_{mn} = \int_{-\frac{w_B}{2}}^{\frac{w_B}{2}} \frac{e_m^B(x) e_n^A(x)}{Z_n^A} dx, \qquad F_{mn} = \int_{-\frac{w_B}{2}}^{\frac{w_B}{2}} \frac{e_m^B(x) e_n^B(x)}{Z_n^B} dx. \tag{3.94}$$

This yields the $2N \times 2N$ matrix equation

$$\left[\begin{array}{c|c} D & D \\ \hline F & -F \end{array}\right] \left[\begin{array}{c} a^B \\ \hline b^B \end{array}\right] = \left[\begin{array}{c|c} C & C \\ \hline E & -E \end{array}\right] \left[\begin{array}{c} a^A \\ \hline b^A \end{array}\right], \tag{3.95}$$

where each block of the matrix comprises $N \times N$ submatrices. These submatrix entries are specified in Appendix B.1.

Next, the expanded step junction, as shown in Figure 3.9, where $w_A < w_B$, is analyzed. The transverse field equations (3.83) - (3.86) are the same as with the reduced step junction, while the expressions resulting from the implementation of the boundary conditions change. At $z = 0$, the tangential electric field boundary condition requires

$$\sum_{n=1}^{N} a_n^B e_n^B(x) + \sum_{n=1}^{N} b_n^B e_n^B(x) = \begin{cases} \sum_{n=1}^{N} a_n^A e_n^A(x) + \sum_{n=1}^{N} b_n^A e_n^A(x), & |x| < \dfrac{w_A}{2} \\ 0, & |x| > \dfrac{w_A}{2}, \end{cases} \tag{3.96}$$

while the tangential magnetic field boundary condition requires

$$\sum_{n=1}^{N} a_n^A h_n^A(x) - \sum_{n=1}^{N} b_n^A h_n^A(x) = \sum_{n=1}^{N} a_n^B h_n^B(x) - \sum_{n=1}^{N} b_n^B h_n^B(x). \tag{3.97}$$

As was done for the reduced step junction, the system of functional equations (3.96)-(3.97) may be transformed into a system of linear equations by applying the appropriate testing

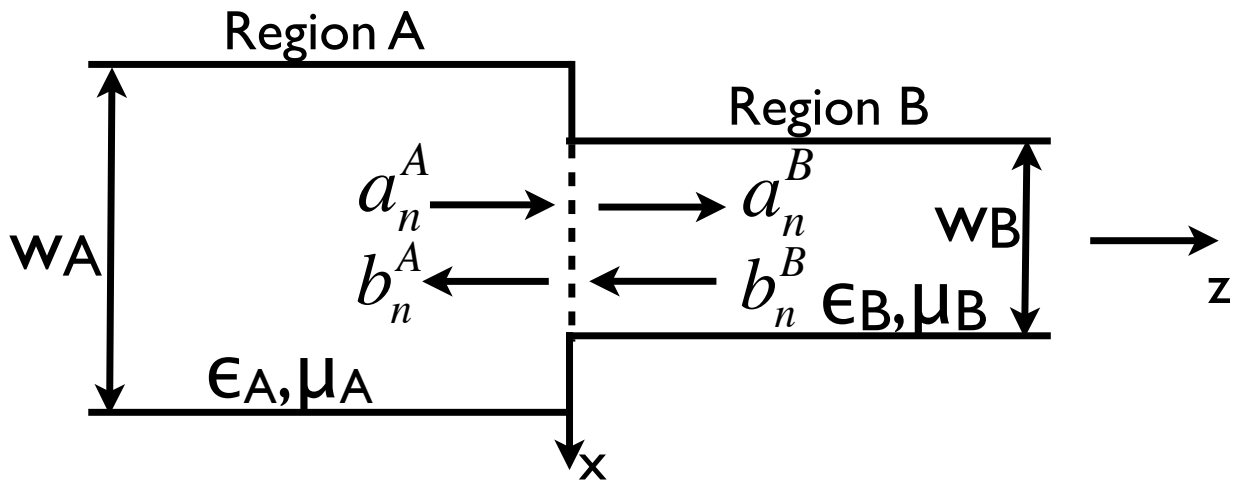

Figure 3.8: Top view of reduced step junction.

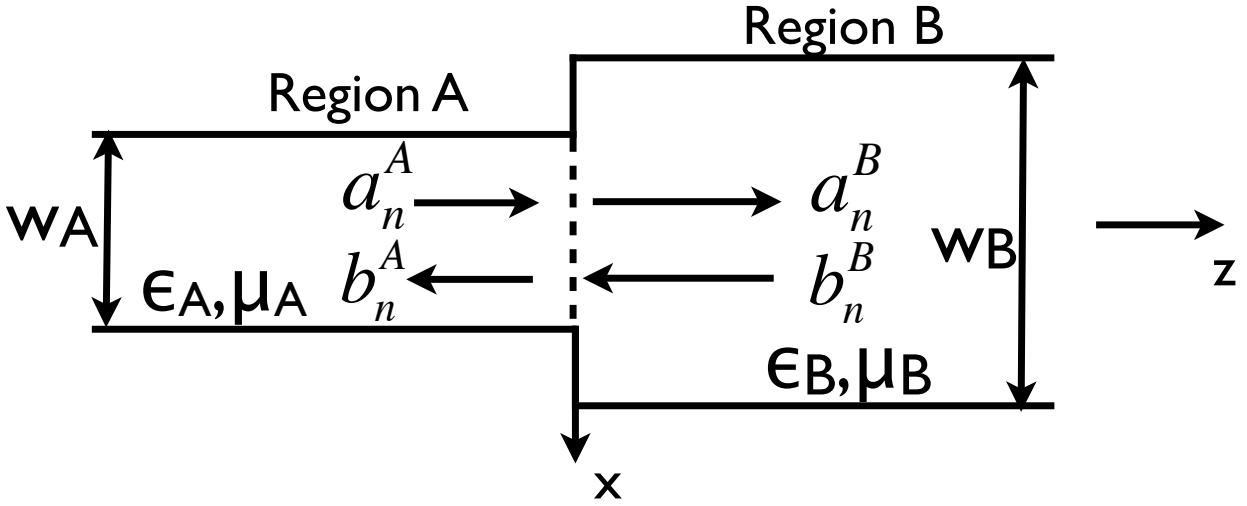

Figure 3.9: Top view of expanded step junction.

operators. The equation resulting from the tangential electric field boundary condition, (3.96), is multiplied by $e_m^A(x)$ and integrated over $-w_B/2 \leq x \leq w_B/2$. Then the equation resulting from the tangential magnetic field boundary condition, (3.97), is multiplied by $h_m^B(x)$ and integrated over $-w_A/2 \leq x \leq w_A/2$. Once again $1 \leq m \leq N$. This results in

$$\begin{aligned}
&\sum_{n=1}^{N} a_n^B \int_{-\frac{w_B}{2}}^{\frac{w_B}{2}} e_n^B(x) e_m^B(x) dx + \sum_{n=1}^{N} b_n^B \int_{-\frac{w_B}{2}}^{\frac{w_B}{2}} e_n^B(x) e_m^B(x) dx = \\
&\quad \sum_{n=1}^{N} a_n^A \int_{-\frac{w_A}{2}}^{\frac{w_A}{2}} e_n^A(x) e_m^B(x) dx + \sum_{n=1}^{N} b_n^A \int_{-\frac{w_A}{2}}^{\frac{w_A}{2}} e_n^A(x) e_m^B(x) dx \qquad (3.98) \\
&\sum_{n=1}^{N} a_n^A \int_{-\frac{w_A}{2}}^{\frac{w_A}{2}} h_n^A(x) h_m^A(x) dx - \sum_{n=1}^{N} b_n^A \int_{-\frac{w_A}{2}}^{\frac{w_A}{2}} h_n^A(x) h_m^A(x) dx = \\
&\quad \sum_{n=1}^{N} a_n^B \int_{-\frac{w_A}{2}}^{\frac{w_A}{2}} h_n^B(x) h_m^A(x) dx - \sum_{n=1}^{N} b_n^B \int_{-\frac{w_A}{2}}^{\frac{w_A}{2}} h_n^B(x) h_m^A(x) dx. \qquad (3.99)
\end{aligned}$$

By defining new quantities, these expressions become

$$\sum_{n=1}^{N} a_n^A L_{mn} + \sum_{n=1}^{N} b_n^A L_{mn} = \sum_{n=1}^{N} a_n^B M_{mn} + \sum_{n=1}^{N} b_n^B M_{mn} \qquad (3.100)$$

$$\sum_{n=1}^{N} a_n^A O_{mn} - \sum_{n=1}^{N} b_n^A O_{mn} = \sum_{n=1}^{N} a_n^B W_{mn} - \sum_{n=1}^{N} b_n^B W_{mn}, \qquad (3.101)$$

where

$$L_{mn} = \int_{-\frac{w_B}{2}}^{\frac{w_B}{2}} e_m^B(x) e_n^B(x) dx, \qquad M_{mn} = \int_{-\frac{w_A}{2}}^{\frac{w_A}{2}} e_m^A(x) e_n^B(x) dx, \tag{3.102}$$

$$O_{mn} = \int_{-\frac{w_A}{2}}^{\frac{w_A}{2}} \frac{e_m^A(x) e_n^B(x)}{Z_n^B} dx, \qquad W_{mn} = \int_{-\frac{w_A}{2}}^{\frac{w_A}{2}} \frac{e_n^A(x) e_m^A(x)}{Z_n^A} dx. \tag{3.103}$$

This yields the $2N \times 2N$ matrix equation

$$\left[\begin{array}{c|c} L & L \\ \hline O & -O \end{array}\right] \left[\begin{array}{c} a^B \\ \hline b^B \end{array}\right] = \left[\begin{array}{c|c} M & M \\ \hline W & -W \end{array}\right] \left[\begin{array}{c} a^A \\ \hline b^A \end{array}\right], \tag{3.104}$$

where L, W, M, and O are $N \times N$ submatrices with entries specified in Appendix B.1.

With general expressions for the two different step junctions determined, a pinched-down iris is analyzed. Consider the waveguide setup shown in Figure 3.10. The first junction is a reduced step. Thus using (3.95), it can be shown that

$$\left[\begin{array}{c|c} C & C \\ \hline E & -E \end{array}\right] \left[\begin{array}{c} a^A \\ \hline b^A \end{array}\right] = \left[\begin{array}{c|c} D & D \\ \hline F & -F \end{array}\right] \left[\begin{array}{c} a^B \\ \hline b^B \end{array}\right], \tag{3.105}$$

where $w_A = w_1$, $w_B = w_2$, $\epsilon_A = \epsilon_0$, $\epsilon_B = \epsilon_i$, $\mu_A = \mu_0$, and $\mu_B = \mu_i$. Next, the expanded step junction can be analyzed using (3.104) such that

$$\left[\begin{array}{c|c} L & L \\ \hline O & -O \end{array}\right] \left[\begin{array}{c} a^C \\ \hline b^C \end{array}\right] = \left[\begin{array}{c|c} M & M \\ \hline W & -W \end{array}\right] \left[\begin{array}{c} a^D \\ \hline b^D \end{array}\right]. \tag{3.106}$$

Here $w_A = w_2$, $w_B = w_1$, $\epsilon_A = \epsilon_i$, $\epsilon_B = \epsilon_0$, $\mu_A = \mu_i$, and $\mu_B = \mu_0$. In (3.106), since the width of the guides on either side of the iris are equivalent, the submatrices reduce to

$L = C$, $M = D$, $O = E$, and $W = F$, and thus

$$\left[\begin{array}{c|c} D & D \\ \hline F & -F \end{array}\right] \left[\begin{array}{c} a^C \\ \hline b^C \end{array}\right] = \left[\begin{array}{c|c} C & C \\ \hline E & -E \end{array}\right] \left[\begin{array}{c} a^D \\ \hline b^D \end{array}\right]. \tag{3.107}$$

Now, the modal amplitude coefficients at Port A are shifted to Port D using

$$\left[\begin{array}{c} a^C \\ \hline b^C \end{array}\right] = \left[\begin{array}{c|c} P^- & 0 \\ \hline 0 & P^+ \end{array}\right] \left[\begin{array}{c} a^B \\ \hline b^B \end{array}\right], \tag{3.108}$$

where

$$P^{\pm}_{mn} = \delta_{mn} \mathrm{e}^{\pm j\beta^i_n \Delta}. \tag{3.109}$$

Here δ_{mn} is Kronecker delta and β^i_n is the propagation constant in the iris region. Now, (3.108) can also be expressed as

$$\left[\begin{array}{c} a^C \\ \hline b^C \end{array}\right] = \left[P\right] \left[\begin{array}{c} a^B \\ \hline b^B \end{array}\right], \tag{3.110}$$

or

$$a^C = P a^B \tag{3.111}$$

$$b^B = P b^C. \tag{3.112}$$

Next, substituting (3.111) into (3.105) and (3.112) into and (3.107), results in

$$C a^A + C b^A \;\; = \;\; D a^B + D P b^C \tag{3.113}$$

$$Ea^A - Eb^A = Fa^B - FPb^C \tag{3.114}$$

$$DPa^B + Db^C = Ca^D + Cb^D \tag{3.115}$$

$$FPa^B - Fb^C = Ea^D - Eb^D. \tag{3.116}$$

Multiplying (3.113) and (3.115) by C^{-1}, and (3.114) and (3.116) by F^{-1} yields

$$a^A + b^A = Ua^B + UPb^C \tag{3.117}$$

$$Va^A - Vb^A = a^B - Pb^C \tag{3.118}$$

$$UPa^B + Ub^C = a^D + b^D \tag{3.119}$$

$$Pa^B - b^C = -Va^D - Vb^D, \tag{3.120}$$

where $U = C^{-1}D$ and $V = F^{-1}E$. Now, rearranging (3.118) produces

$$a^B = Pb^C + Va^A - Vb^A, \tag{3.121}$$

which can then be substituted into (3.117), (3.119), and (3.120), resulting in

$$a^A + b^A = UPb^C + UVa^A - UVb^A + UPb^C \tag{3.122}$$

$$UPPb^C + UPVa^A - UPVb^A + Ub^C = a^D + b^D \tag{3.123}$$

$$PPb^C + PVa^A - PVb^A - b^C = Va^D - Vb^D. \tag{3.124}$$

Rearranging (3.124) and factoring b^C gives

$$[I - PP]\, b^C = PVa^A - PVb^A - Va^D + Vb^D, \tag{3.125}$$

or

$$b^C = [I - PP]^{-1} PVa^A - [I - PP]^{-1} PVb^A$$
$$- [I - PP]^{-1} Va^D + [I - PP]^{-1} Vb^D. \tag{3.126}$$

Here I is the identity matrix. Substituting (3.126) into (3.122) yields

$$a^A + b^A = 2UP [I - PP]^{-1} PVa^A - 2UP [I - PP]^{-1} PVb^A$$
$$-2UP [I - PP]^{-1} Va^D + 2UP [I - PP]^{-1} Vb^D + UVa^A - UVb^A. \tag{3.127}$$

This is then rearranged, resulting in

$$\left\{I - UV - 2UP [I - PP]^{-1} PV\right\} a^A + \left\{I + UV + 2UP [I - PP]^{-1} PV\right\} b^A =$$
$$\left\{-2UP [I - PP]^{-1} V\right\} a^D + \left\{2UP [I - PP]^{-1} V\right\} b^D. \tag{3.128}$$

The expression

$$UV + 2UP [I - PP]^{-1} PV, \tag{3.129}$$

which appears multiple times in (3.128), can be reduced by factoring U and V and simplifying, resulting in

$$UV + 2UP [I - PP]^{-1} PV = USV, \tag{3.130}$$

where

$$S_{mn} = \frac{1 + P_{mn}^2}{1 - P_{mn}^2}. \tag{3.131}$$

Note that since P is diagonal, the resulting S matrix is also diagonal. Thus inserting (3.130)

into (3.128) gives

$$[I - USV]\, a^A + [I + USV]\, b^A = \left\{-2UP\,[I - PP]^{-1}\, V\right\} a^D + \left\{2UP\,[I - PP]^{-1}\, V\right\} b^D. \tag{3.132}$$

Through similar simplification, the expressions on the right-hand side of (3.132) reduces to

$$[I - USV]\, a^A + [I + USV]\, b^A = [-UTV]\, a^D + [UTV]\, b^D, \tag{3.133}$$

where

$$T_{mn} = \frac{2P_{mn}}{1 - P_{mn}^2}. \tag{3.134}$$

The matrix T is also diagonal. Next, substituting (3.126) into (3.123) and simplifying results in

$$[UTV]\, a^A + [-UTV]\, b^A = [I + USV]\, a^D + [I - USV]\, b^D. \tag{3.135}$$

These two equations, (3.133) and (3.135), can now be written in matrix form as

$$\left[\begin{array}{c|c} K & \bar{K} \\ \hline J & -J \end{array}\right] \left[\begin{array}{c} a^A \\ \hline b^A \end{array}\right] = \left[\begin{array}{c|c} -J & J \\ \hline \bar{K} & K \end{array}\right] \left[\begin{array}{c} a^D \\ \hline b^D \end{array}\right], \tag{3.136}$$

where $K = I - USV$, $\bar{K} = I + USV$, and $J = UTV$. This reduces the system of equations from four equations with $4N$ unknowns, (3.113) - (3.114), to a system of two equations with $2N$ unknowns, (3.136).

Now assuming a^A is known, the remaining modal amplitude coefficients, a^D, b^A and

b^D, can be determined by first defining

$$b^D = Ra^D, \tag{3.137}$$

where R is called the reflection matrix. This reflection matrix depends on what type of load is being attached to Port D. A myriad of loads can be attached to the iris region and the subsequent reflection matrix derived. In this dissertation, the expressions for the theoretical reflection coefficient for an iris placed in front of a conductor-backed material sample are derived. Substituting (3.137) into (3.133) and (3.135) results in

$$Ka^A + \bar{K}b^A = -Ja^D + JRa^D \tag{3.138}$$

$$Ja^A - Jb^A = \bar{K}a^D + KRa^D \tag{3.139}$$

or

$$Ka^A + \bar{K}b^A = J\left(R - I\right)a^D \tag{3.140}$$

$$Ja^A - Jb^A = \left(\bar{K} + KR\right)a^D. \tag{3.141}$$

This can be written as a matrix equation

$$\left[\begin{array}{c|c} J\left(R-I\right) & -\bar{K} \\ \hline \bar{K}+KR & J \end{array}\right]\left[\begin{array}{c} a^D \\ \hline b^A \end{array}\right] = \left[\begin{array}{c} Ka^A \\ \hline Ja^A \end{array}\right], \tag{3.142}$$

which, upon solution, gives the desired reflection coefficient for a terminated iris.

The reflection matrix for a material-loaded guide is required in (3.142) to find the desired reflection coefficient. This may be determined as follows. Considering Figure 3.11, the

transverse fields for the region $-d < z < 0$, are written as

$$E_y(x,z) = \sum_{n=1}^{N} a_n^g e_n^g(x) \mathrm{e}^{-j\beta_n^g z} + \sum_{n=1}^{N} b_n^g e_n^g(x) \mathrm{e}^{j\beta_n^g z} \tag{3.143}$$

$$H_x(x,z) = \sum_{n=1}^{N} a_n^g h_n^g(x) \mathrm{e}^{-j\beta_n^g z} - \sum_{n=1}^{N} b_n^g h_n^g(x) \mathrm{e}^{j\beta_n^g z}, \tag{3.144}$$

while those in the sample region, $0 < z < \delta$, are

$$E_y(x,z) = \sum_{n=1}^{N} a_n^s e_n^s(x) \mathrm{e}^{-j\beta_n^s z} + \sum_{n=1}^{N} b_n^s e_n^s(x) \mathrm{e}^{j\beta_n^s z} \tag{3.145}$$

$$H_x(x,z) = \sum_{n=1}^{N} a_n^s h_n^s(x) \mathrm{e}^{-j\beta_n^s z} - \sum_{n=1}^{N} b_n^s h_n^s(x) \mathrm{e}^{j\beta_n^s z}. \tag{3.146}$$

Here, $e_n(x)$ and $h_n(x)$ are the transverse electric and magnetic modal fields, respectively, and as shown in (4.80) and (4.81) are given by

$$e_n^{g,s}(x) = -k_{xn}^{g,s} \, (-1)^n \cos\left[k_{xn}^{g,s} x\right] \tag{3.147}$$

$$h_n^{g,s}(x) = \frac{e_n^{g,s}(x)}{Z_n^{g,s}}, \tag{3.148}$$

where $k_{xn}^{g,s} = (2n-1)\pi/w_1$ and $Z_n^{g,s} = \omega\mu_0\mu_{g,s}/\beta_n^{g,s}$. The propagation constant $\beta_n^{g,s}$ determined from (2.140) as

$$\beta_n^{g,s} = \sqrt{(k^{g,s})^2 - \left(k_{xn}^{g,s}\right)^2}, \tag{3.149}$$

where $k^{g,s} = k_0\sqrt{\mu_{g,s}\epsilon_{g,s}}$.

Expressions for the unknown modal amplitude coefficients a_n^g, b_n^g, a_n^s, and b_n^s may be determined by applying the boundary conditions on transverse electric and magnetic fields at the interfaces between the guide and sample region and between the sample region and conducting surface. At the interface $z = 0$ the tangential electric field boundary condition

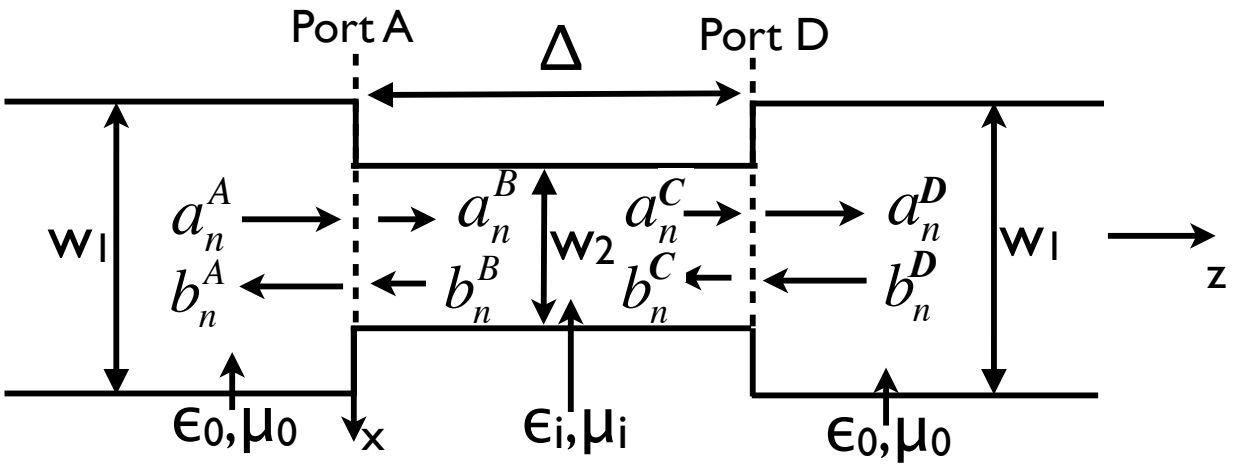

Figure 3.10: Top view of pinched-down iris.

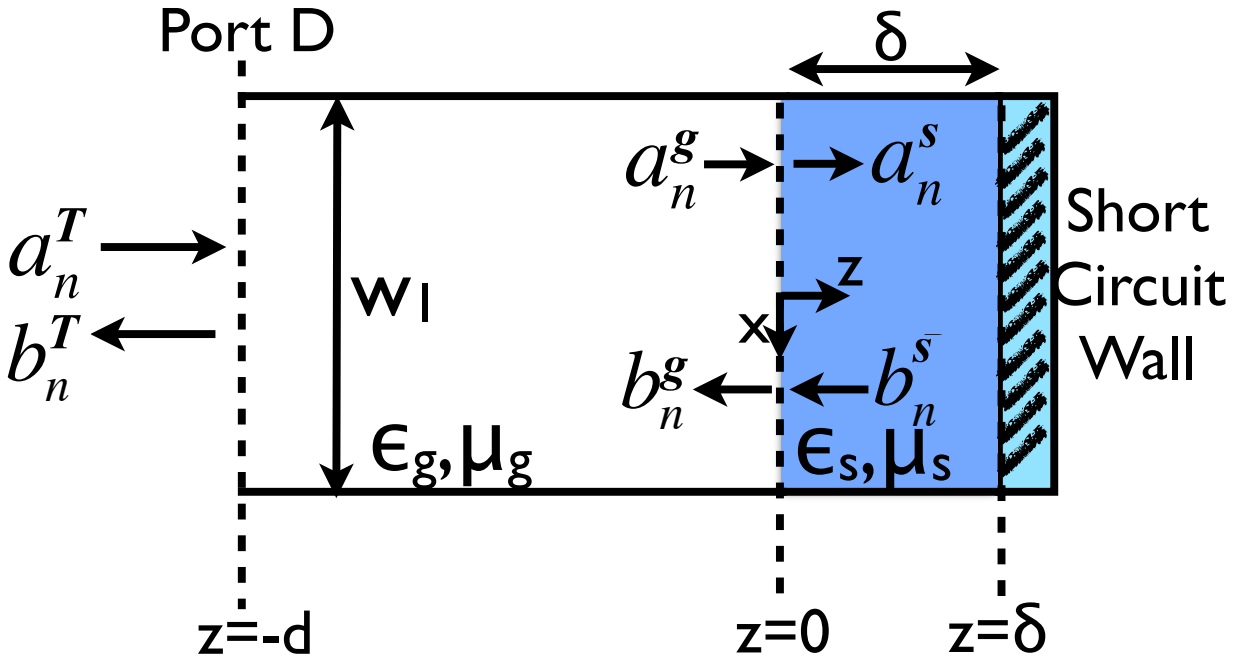

Figure 3.11: Top view of material-loaded guide.

requires

$$\sum_{n=1}^{N} a_n^g e_n^g(x) + \sum_{n=1}^{N} b_n^g e_n^g(x) = \sum_{n=1}^{N} a_n^s e_n^s(x) + \sum_{n=1}^{N} b_n^s e_n^s(x), \tag{3.150}$$

or, since $e_n^g(x) = e_n^s(x)$,

$$a_n^g + b_n^g = a_n^s + b_n^s. \tag{3.151}$$

The tangential magnetic field boundary condition requires

$$\sum_{n=1}^{N} a_n^g e_n^g(x) - \sum_{n=1}^{N} b_n^g h_n^g(x) = \sum_{n=1}^{N} a_n^s h_n^s(x) - \sum_{n=1}^{N} b_n^s h_n^s(x) \tag{3.152}$$

or

$$\frac{a_n^g}{Z_n^g} - \frac{b_n^g}{Z_n^g} = \frac{a_n^s}{Z_n^s} - \frac{b_n^s}{Z_n^s}. \tag{3.153}$$

At $z = \delta$ the boundary condition on the tangential electric field requires

$$\sum_{n=1}^{N} a_n^s e_n^s(x) \mathrm{e}^{-j\beta_n^s \delta} + \sum_{n=1}^{N} b_n^s e_n^s(x) \mathrm{e}^{j\beta_n^s \delta} = 0 \tag{3.154}$$

or

$$a_n^s \mathrm{e}^{-j\beta_n^s \delta} + b_n^s \mathrm{e}^{j\beta_n^s \delta} = 0. \tag{3.155}$$

Rearranging (3.155) and substituting into (3.151) and (3.153) gives

$$a_n^g + b_n^g = a_n^s \left[1 - e_n^2\right] \tag{3.156}$$

$$-a_n^g + g_n^g = \frac{Z_n^g}{Z_n^s} a_n^s \left[1 + e_n^2\right], \tag{3.157}$$

where $e_n = \mathrm{e}^{-j\beta_n^s \delta}$. Dividing (3.156) by (3.157) results in

$$\frac{a_n^g + b_n^g}{-a_n^g + b_n^g} = \frac{Z_n^s}{Z_n^g} Q_n, \tag{3.158}$$

where

$$Q_n = \frac{1 - e_n^2}{1 + e_n^2}. \tag{3.159}$$

This expression is recognized as a tangent function, and can be written as

$$Q_n = j \tan\left(\beta_n^s \delta\right). \tag{3.160}$$

Now, multiplying (3.158) by $Z_n^g \left(-a_n^g + b_n^g\right)$ yields

$$Z_n^g a_n^g + Z_n^g b_n^g = Z_n^g Q_n a_n^g - Z_n^g Q_n b_n^g. \tag{3.161}$$

This expression is rearranged to give

$$\frac{b_n^g}{a_n^g} = \frac{Z_n^s Q_n - Z_n^g}{Z_n^s Q_n + Z_n^g}. \tag{3.162}$$

Now, as is shown in Appendix B, the modal field coefficients can be shifted from one interface to another. Thus the expressions to shift the modal field coefficients from the interface at $z = 0$ to $z = -d$ are

$$a_n^g = a_n^T \mathrm{e}^{-j\beta_n^g d} \tag{3.163}$$

$$b_n^T = b_n^g \mathrm{e}^{-j\beta_d^g d}. \tag{3.164}$$

These expressions can then be inserted into (3.162). Thus the reflection vector, $r_n = b_n^T / a_n^T$,

is determined to be

$$r_n = \mathrm{e}^{-j\beta_n^g 2d} \frac{Z_n^s Q_n - Z_n^g}{Z_n^s Q_n + Z_n^g}. \tag{3.165}$$

This in turn means the reflection matrix, $[R]$ from (3.138), is a diagonal matrix with entries $R_{mn} = \delta_{mn} r_n$. Once the modal coefficient b^A is found by solving the matrix equation from (3.142), the reflection coefficient at Port A is given by

$$S_{11}^I = \frac{b_1^A}{a_1^A}. \tag{3.166}$$

3.3.1.2 Reflection Coefficient with No Iris

The characterization of ϵ_s and μ_s is also dependent on the measurement of the reflection coefficient from the conductor-backed sample with no iris present. The theoretical reflection coefficient for no-iris case is determined in this section. Because the no-iris setup is the same as shown in Figure 3.11, (3.165) can be used directly. The reflection coefficient at the measurement plane $z = -d$ is given by

$$S_{11}^N = \frac{b_1^T}{a_1^T} = r_1. \tag{3.167}$$

With no iris present, only the TE_{10} mode is implicated, thus

$$S_{11}^N = \mathrm{e}^{-j\beta_1^g 2d} \frac{Z_1^s Q_1 - Z_1^g}{Z_1^s Q_1 + Z_1^g}. \tag{3.168}$$

3.3.2 Validation of Theoretical Analysis

Once again, the theoretical analysis is validated before using it for parameter extraction. As was done for the NRW method in Section 3.2.2, the theoretical model is validated against

HFSS with an FGM125 test sample. Using the FGM125 material parameters given in Section 3.2.2, the theoretical analysis was used to compute the reflection coefficient from the sample placed in an X-band waveguide with dimensions $a = 22.86$ mm and $b = 10.16$ mm. The iris waveguide dimensions are $d = 1$ mm, $\Delta = 1$ mm, and $w_2 = 7.62$ mm. The results of this theoretical analysis are shown in Figure 3.12. Absolute tolerances of 0.1 dB for $|S_{11}^I|$ and 0.01° for $\angle S_{11}^I$ were chosen so that the accuracy of the computed modal analysis is better than the expected measurement accuracy of the HP 8510C vector network analyzer. These tolerances were obtained using the *HP 8510 Specifications & Performance Verification Program*. For the FGM 125 material considered, the S-parameters typically converge to the specified tolerance with $N = 140$ terms.

Also shown in Figure 3.12 is S_{11}^I computed using HFSS. The waveguide port was once again model with a length of 50 mm. The convergence tolerance in HFSS was specified as a maximum delta S of 0.01 at the solution frequency 12.4 GHz. Excellent agreement is obtained between the modal analysis and HFSS, thus validating the modal computation.

Figure 3.13 shows the reflection coefficient for the no-iris case computed using the theoretical analysis and HFSS. The theoretical analysis was used to determine the reflection coefficient from a sample of FGM125 sample with conductor-backing. The HFSS results were obtained with similar port dimensions and convergence criteria used for the HFSS iris simulation. Once again excellent agreement is achieved, which provides confidence before implementation of the forward problem in the extraction routine.

3.3.3 Extraction Process

With the measurements of the reflection coefficients with no iris, S_{11}^N, and with an iris, S_{11}^I, the permittivity and permeability can be extracted. A complex root solver such as a Newton's method can be used to solve for two complex unknowns from two independent measurements. Experience has shown that with typical values of experimental error it can sometimes be difficult to find solutions to this system of equations. This is why closed-

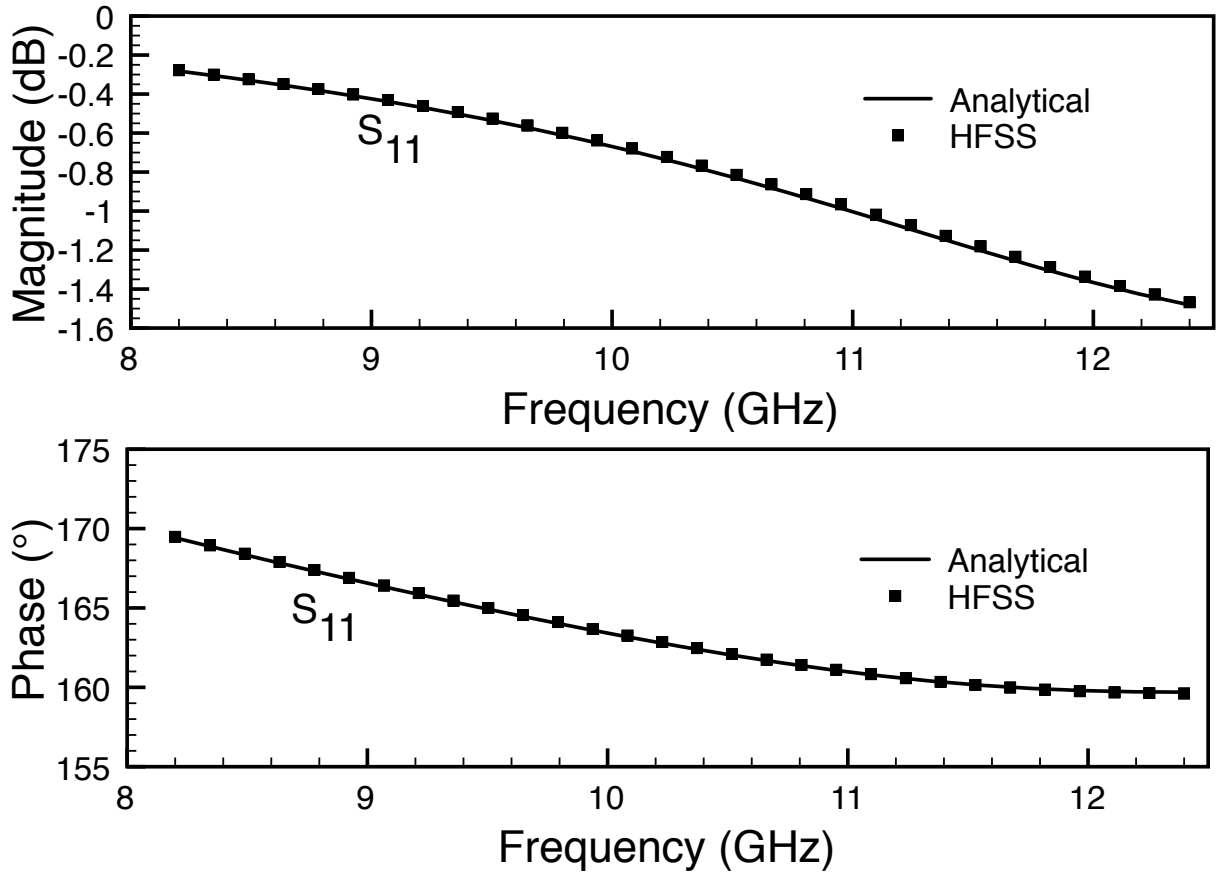

Figure 3.12: S-parameters computed for a conductor-backed FGM125 test material placed behind an iris.

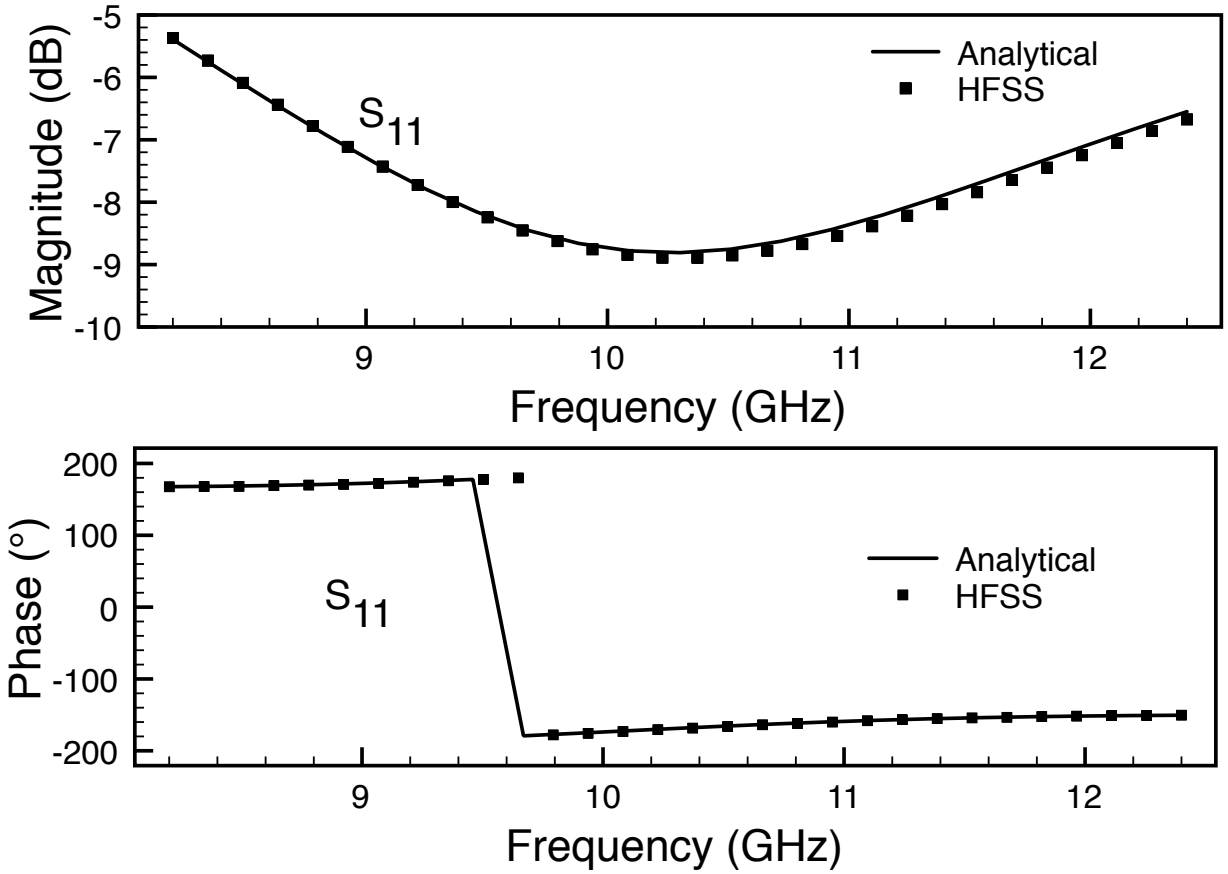

Figure 3.13: S-parameters computed for a conductor-backed FGM125 test material.

form equations such as those in the NRW method or the Air-backed/Conductor-backed [37] method are preferred. An alternative approach allows a complex root-solver to determine k^s from one measurement and then closed-form expressions can be used to compute μ_s and ϵ_s. First, Z_1^s is solved for in (3.168) resulting in

$$Z_1^s Q_1 = Z_1^g \frac{1+\tilde{S}_{11}^N}{1-\tilde{S}_{11}^N} = \alpha, \tag{3.169}$$

where

$$\tilde{S}_{11}^N = S_{11}^N \mathrm{e}^{j\beta_1^g 2d}. \tag{3.170}$$

This α value is a known quantity since S_{11}^N is measured and the impedance of the guide depends on known values of μ_g and ϵ_g. Now, (3.169) can also be expressed as

$$\frac{\omega\mu_s}{\beta_1^s} Q_1 = \alpha, \tag{3.171}$$

and solving for μ_s results in

$$\mu_s = \frac{\beta_1^s}{Q_1}\frac{\alpha}{\omega}. \tag{3.172}$$

The only unknown values in (3.172) are Q_1 and β_1^s. From (3.160) it is seen that Q_1 only depends on β_1^s and the known value of δ. Therefore, the only unknown value is β_1^s, which depends on $k^s = k_0\sqrt{\mu_s\epsilon_s}$. A secant method can then be used to extract k^s from the measurement of S_{11}^I. Knowing k^s, β_1^s can be computed, which in turn can be used to compute Q_1. With β_1^s and Q_1 determined μ_s is found using (3.172). Finally using μ_s and k^s, ϵ_s can be determined.

Once again the extraction process is validated with the characterization of a known material. The FGM125 material parameters are extracted from the HFSS generated S-

parameters shown in Figure 3.12 and Figure 3.13. Here the distance between the iris and the material is $d = 1$ mm. Figure 3.14 shows the results of the characterization. Also shown in Figure 3.14 are the material parameters extracted from S-parameters generate in HFSS with $d = 1$ mm in the model. Note that the material parameters used to generate the S-parameters in HFSS assume frequency independent values of $\epsilon_S = 7.3197 - j0.0464$ and $\mu_S = 0.5756 - j0.4842$. The extracted constitutive parameters shown in Figure 3.14 are frequency dependent and not consistent with the values used in HFSS. The material parameter ϵ_S'' is especially inconsistent since the values become positive. This is a result of the S-parameter error propagating through to the extraction. Notice that the constitutive parameters are more consistent with the values used in HFSS when the distance between the material and iris is decreased. The effects of the propagation of S-parameter uncertainty on the characterization of the material parameters is explored in greater detail in Section 3.3.4.

3.3.4 Iris Design

This characterization method for conductor-back materials can be customized for a particular material by optimizing the iris-measurement system so that it has minimal sensitivity to S-parameter uncertainty. To determine the optimal iris geometry a Monte Carlo technique was used to study effects of the propagation of the random error inherent to the VNA used in the measurements. Depending on the material under test, the geometrical parameters of the iris measurement (Δ, d, and w_2 in Figure 3.7) are optimized to have low sensitivity to uncertainties of the measured S-parameters. A single parameter sweep was used to perform an exhaustive search of each geometrical parameter assuming the remaining two parameters were fixed. The fixed parameters in each of the parameter sweeps were determined through initial observations of random configurations of the iris-measurement system. The Monte Carlo analysis of the propagation of VNA uncertainty was used for each of the individual configurations in the parameter sweep and the amount of propagated error was calculated.

The uncertainties of the measured S-parameters used in the Monte Carlo error analysis

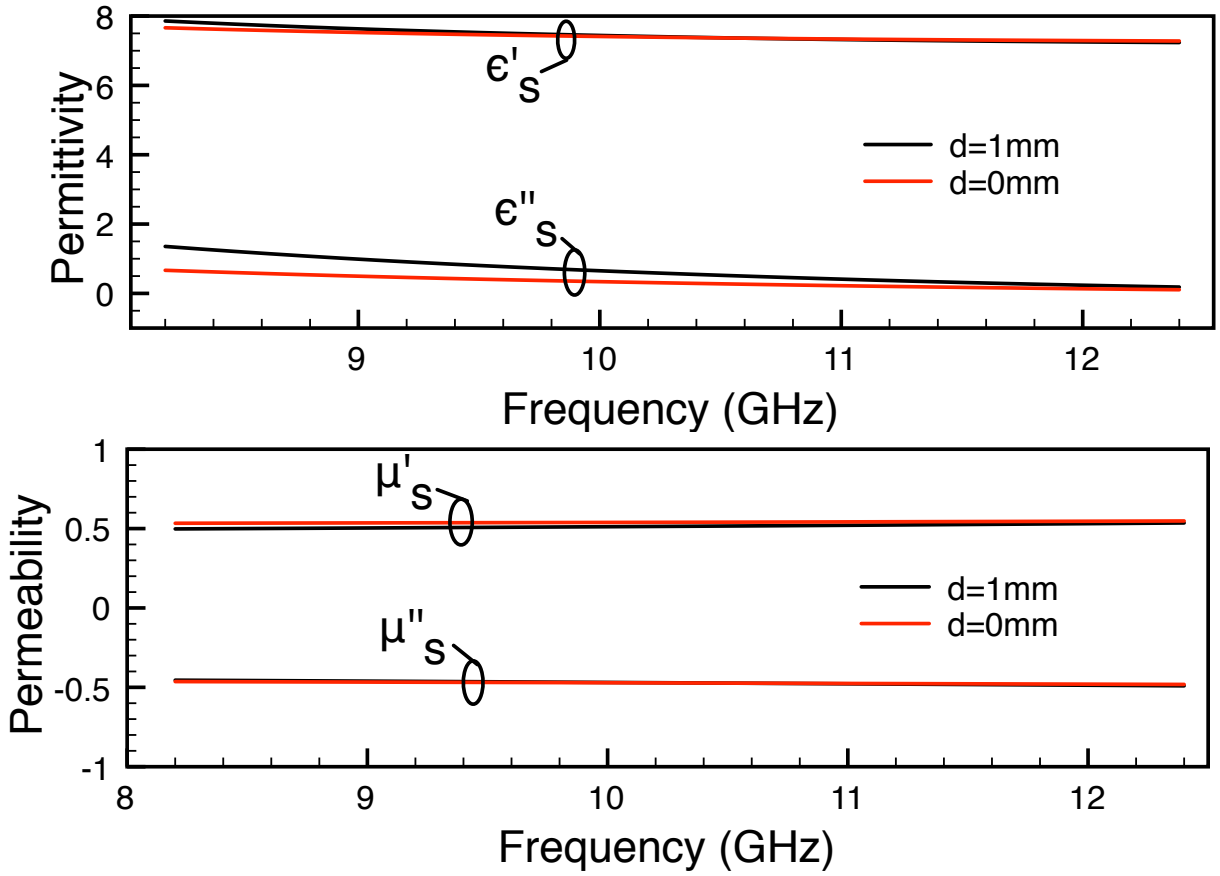

Figure 3.14: Extraction of permittivity and permeability from S-parameter generated using HFSS with $d = 0$ mm and $d = 1$ mm in the model.

were chosen to be smaller than those for an HP8510C network analyzer system, due to the strong sensitivity of this technique to S-parameter uncertainty. The uncertainties for the HP8510C network analyzer were determined using the software package *HP 8510 Specifications & Performance Verification Program* provided by Hewlett Packard. Although the VNA measurement uncertainty is dependent on S-parameter amplitudes, for the range of amplitudes encountered in this dissertation the VNA measurement uncertainty can be assumed to be amplitude and frequency independent. Using the software package, the statistical variance of S_{11} is specified linearly in amplitude and phase as values of $\sigma_{A_{11}} = 0.004$ and $\sigma_{\phi_{11}} = 0.8^{\circ}$, respectively, for the HP8510C network analyzer. It should be noted that this is not the analyzer used in subsequent measurements; however, these values give a worse case set of uncertainties to gauge in the iris-measurement design optimization. Unfortunately, these uncertainty values prove to be too high for the iris characterization technique and the resulting extracted parameters are very inaccurate. Therefore, the statistical variance on phase is reduced to $\sigma_{\phi_{11}} = 0.1^{\circ}$.

The materials under test originally planned for experimental validation were Eccosorb FGM125 and FGM40. The geometry of the FGM125 sample is $w_1 = 22.86$ mm, $b = 10.16$ mm, and $\delta = 3.175$ mm. The geometry of the FGM40 sample is $w_1 = 22.86$ mm, $b = 10.16$ mm, and $\delta = 1.016$ mm. The forward problem was solved at 8.2 GHz, 10.09 GHz, and 12.4 GHz using the geometrical parameters determined from the parameter sweep. The material parameters of FGM125 and FGM40 at these frequencies are shown Table 3.1 and Table 3.2, respectively. White Gaussian noise was then added to each of the S-parameter sets, and the noisy data was used to extract the material parameters. Five hundred trials were used in the Monte Carlo analysis in each of the parameter sweeps, and the average values of the material parameters and the standard deviations were calculated.

The first material used in the iris-measurement design is FGM125. The effects of changing the thickness of the iris (Δ) were studied first. In these simulations the iris opening was set to half the width of the X-band waveguide, $w_2 = 11.43$ mm (0.45 inches), and the distance

Table 3.1: Nominal material parameters for FGM125. These data were obtained using the waveguide NRW method. Data provided by Captain Milo Hyde IV form the Air Force Institute of Technology , Wright-Patterson AFB, Dayton, OH [46]

Frequency (GHz)	Relative Permittivity	RelativePermeability
8.2	$7.258 - j0.056$	$0.600 - j0.761$
10.9	$7.320 - j0.046$	$0.576 - j0.484$
12.4	$7.374 - j0.025$	$0.615 - j0.212$

Table 3.2: Nominal material parameters for FGM40. These data were obtained using the waveguide NRW method. Data provided by Captain Milo Hyde IV form the Air Force Institute of Technology , Wright-Patterson AFB, Dayton, OH [46]

Frequency (GHz)	Relative Permittivity	RelativePermeability
8.2	$21.864 - j0.390$	$2.088 - j2.537$
10.9	$22.036 - j0.332$	$1.668 - j2.354$
12.4	$22.244 - j0.166$	$1.245 - j2.110$

between the iris and the material was set to $d = 0$ mm. The forward problem was solved at 21 iris thicknesses evenly distributed from 0.1 mm to 4 mm at the three frequencies. To better gauge the effectiveness of this characterization technique, the results of the Monte Carlo error analysis are compared against the two-thickness method, which is another reflection-only measurement technique with relatively low sensitivity to propagation of measured S-parameter error [27]. The second measurement in the two-thickness technique assumes a thickness of 2δ. Instead of plotting the average values and 2σ error bars, as will be done in subsequent Monte Carlo error analyses in this dissertation, the values obtained by dividing the error of the iris technique (σ_{iris}) by the error from the two-thickness technique ($\sigma_{\text{2-Thick}}$) are plotted. This gives a sense of how many times worse the iris technique is compared to the two-thickness approach. Figures 3.15 - 3.17 show the results of the Δ parameter sweep for the FGM125 sample. It is seen that the thinner the iris is, the less sensitive the extracted material parameters are to the propagation of measured S-parameter uncertainty.

With the knowledge that a thin iris is best, the distance between the iris and the sample

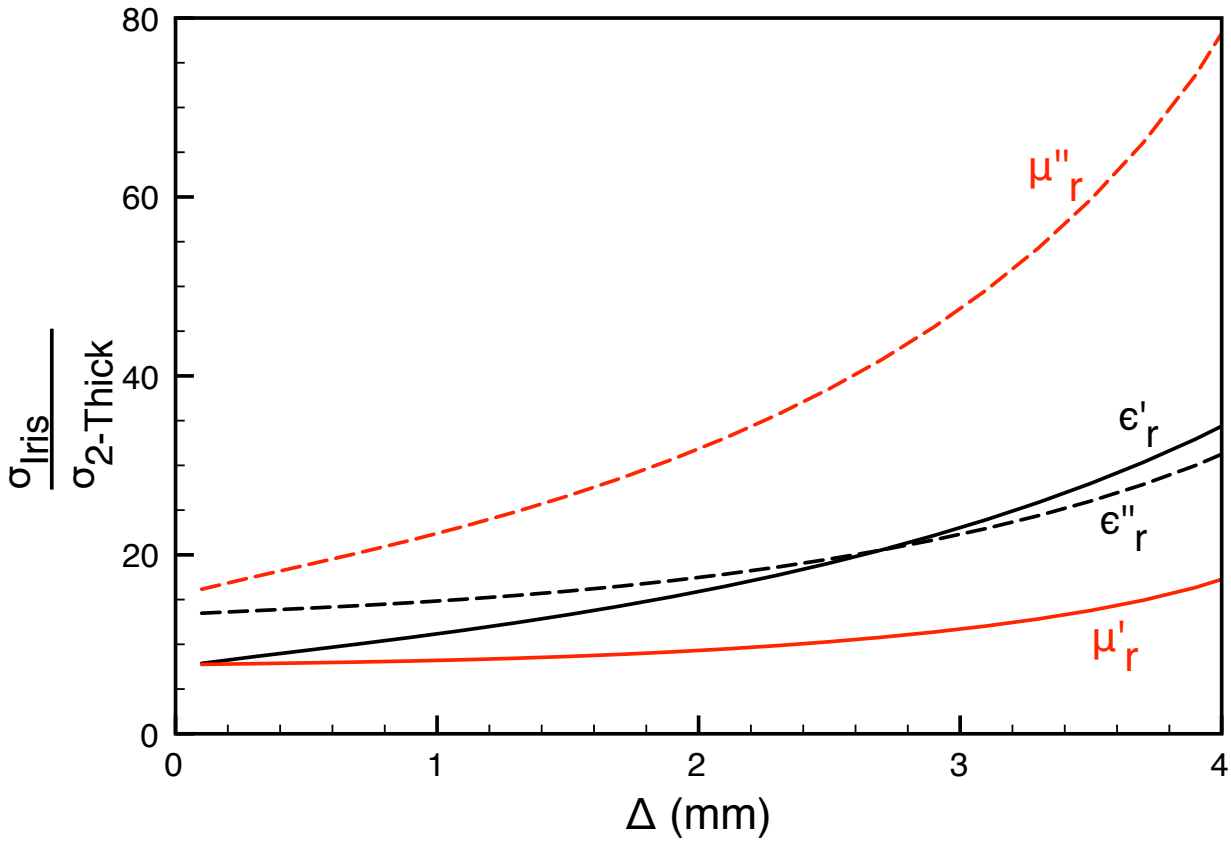

Figure 3.15: Comparison of the error in the constitutive parameters of FGM125 sample due to S-parameter error using the iris technique and two thickness method. This shows the results of the Δ parameter sweep assuming $w_2 = 11.43$ mm and $d = 0$ mm at 8.2 GHz.

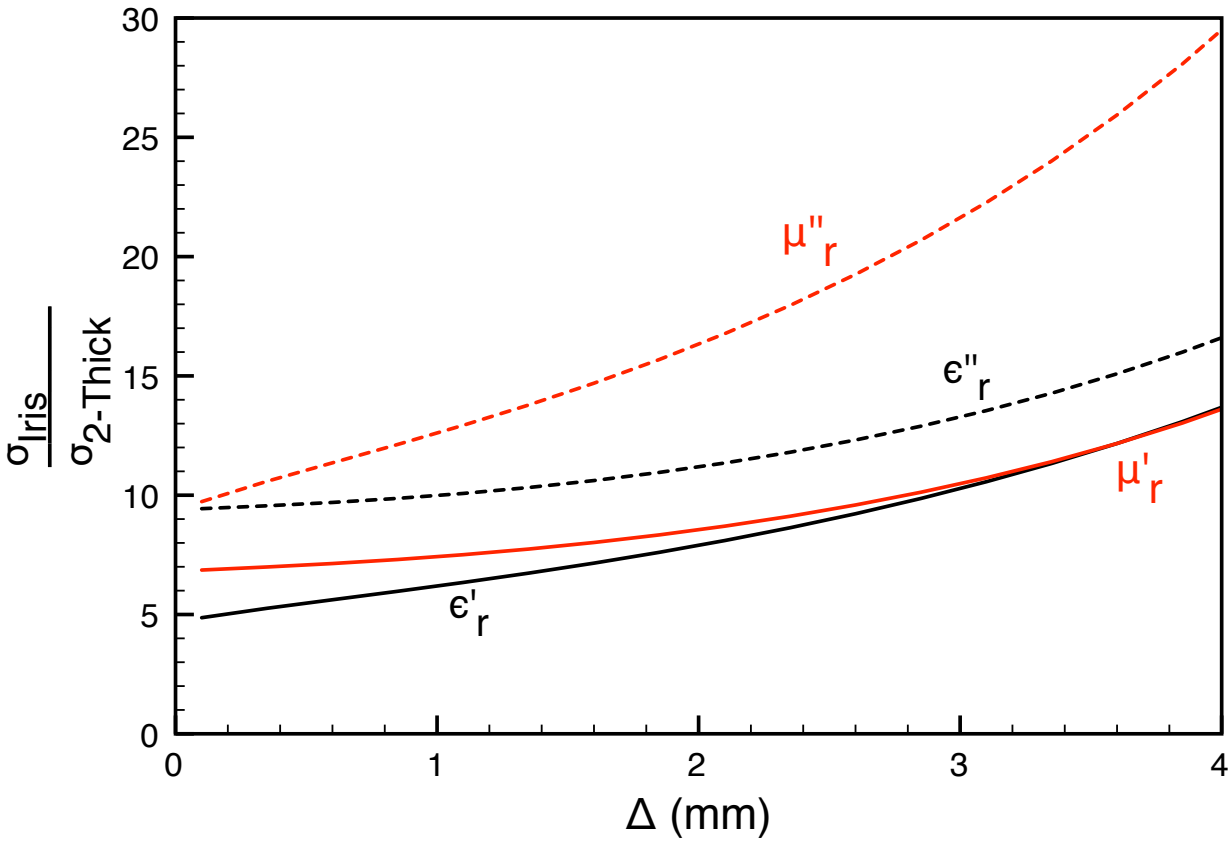

Figure 3.16: Comparison of the error in the constitutive parameters of FGM125 sample due to S-parameter error using the iris technique and two thickness method. This shows the results of the Δ parameter sweep assuming $w_2 = 11.43$ mm and $d = 0$ mm at 10.09 GHz.

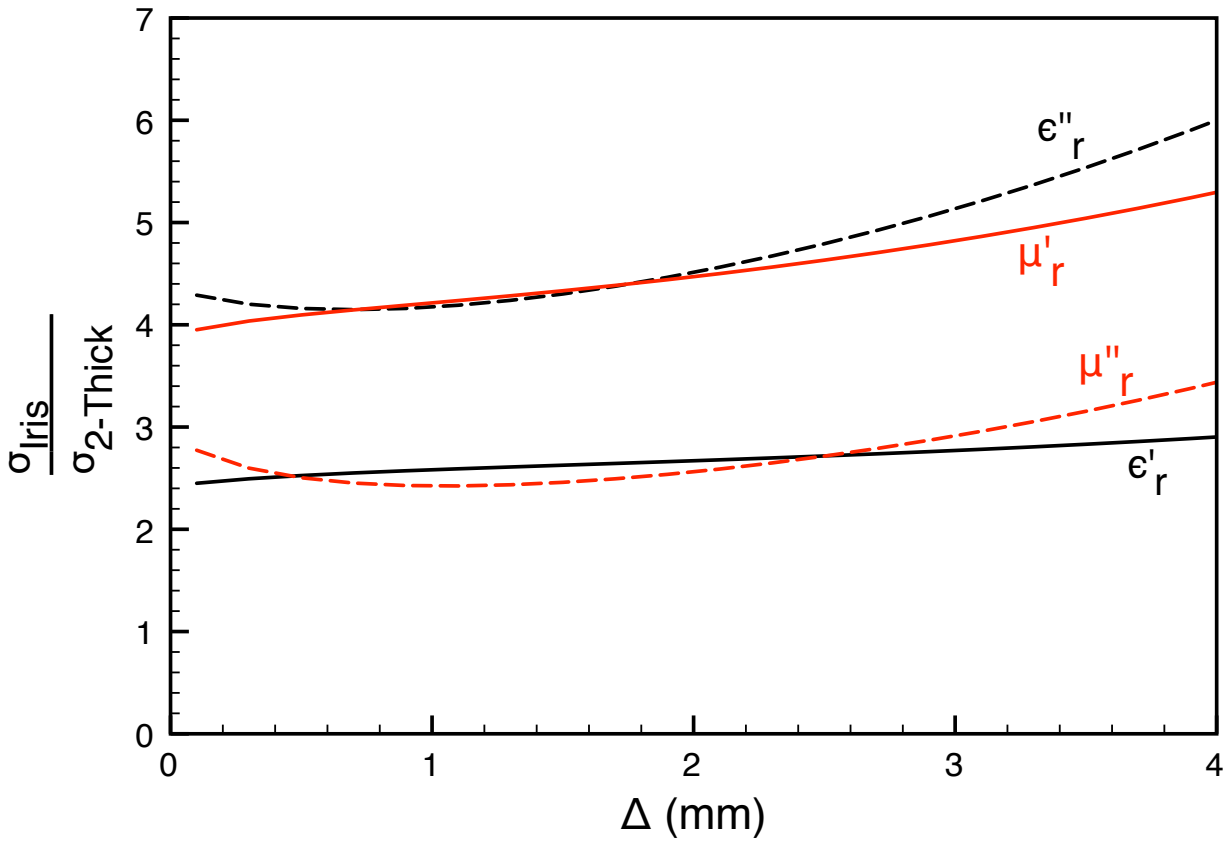

Figure 3.17: Comparison of the error in the constitutive parameters of FGM125 sample due to S-parameter error using the iris technique and two thickness method. This shows the results of the Δ parameter sweep assuming $w_2 = 11.43$ mm and $d = 0$ mm at 12.4 GHz.

was analyzed. Here d is swept from 0 mm to 2 mm at 0.1 mm steps. In these simulations the iris opening was once again set to $w_2 = 11.43$ mm (0.45 inches) and as determined from the previous parameter sweep, a narrow iris thickness was used, specifically, the thickness was set to $\Delta = 0.1$ mm. The results of this parameter sweep are shown in Figures 3.18 through 3.20. From these figures it is determined that the least error occurs when the FGM125 material sample is placed against the iris.

Finally, the last parameter sweep analyzes the effects of changing the width of the iris opening while keeping $d = 0$ mm and $\Delta = 0.1$ mm fixed. The iris width, w_2, is swept from 5.08 mm (0.2 inches) to 16.51 mm (0.65 inches) at 21 evenly spaced steps. Figures 3.21 through 3.23 show the results of the parameter sweep. It was determined that the optimal iris opening width is 7.62 inches (0.3 inches) for measurements of an FGM125 sample.

A similar iris measurement design was implemented for measurements of FGM40. Figures 3.24 through 3.26 show the results of the Δ parameter sweep from 0.1 mm to 4 mm with $w_2 = 11.43$ mm and $d = 0$ mm fixed. The results of the d parameter sweep from 0 mm to 2 mm are shown in Figures 3.27 through 3.29. Here the parameters Δ and w_2 are fixed to be 0.1 mm and $w_2 = 11.43$ mm, respectively. Finally, Figures 3.30 through 3.32 show the results of the w_2 parameter sweep from 2.55 mm (0.1 inches) to 15.24 mm (0.6 inches) with $\Delta = 0.1$ mm and $d = 0$ mm. Similar to the FGM125 analysis, the optimal thickness of the iris is to be as thin as possible and the optimal position of the sample is at $d = 0$ mm. It was also determined that the best iris opening width is 5.08 mm (0.2 inches) for the measurement of FGM40.

3.3.5 Experimental Results

To experimentally validate the proposed technique at X-band, an iris waveguide insert was machined from 360 brass. The iris was made for the characterization of FGM125. The specified inner dimensions of the iris are $w_2 = 0.3$ inches by $b = 0.9$ inches, and measurement of the constructed iris using precision calipers showed that the iris was constructed with a

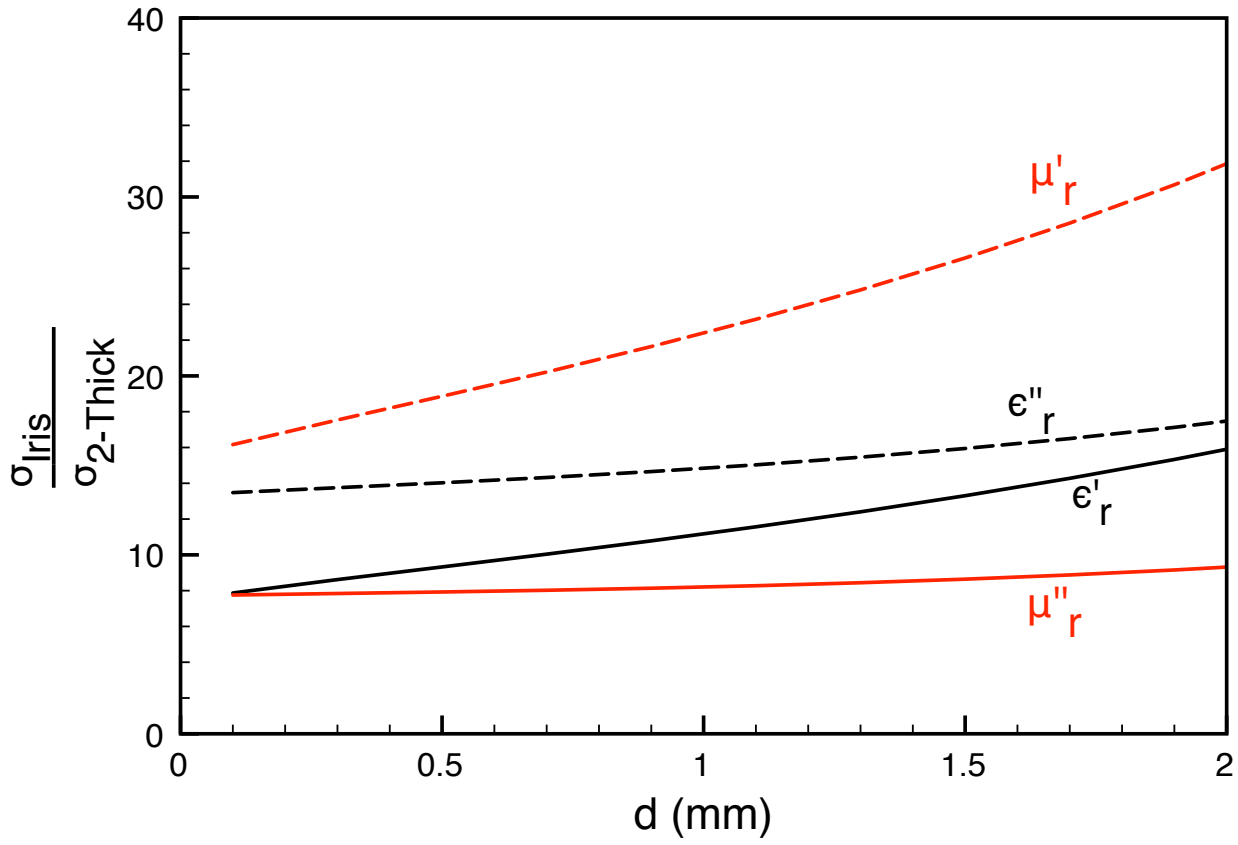

Figure 3.18: Comparison of the error in the constitutive parameters of FGM125 sample due to S-parameter error using the iris technique and two thickness method. This shows the results of the d parameter sweep assuming $w_2 = 11.43$ mm and $\Delta = 0.1$ mm at 8.2 GHz.

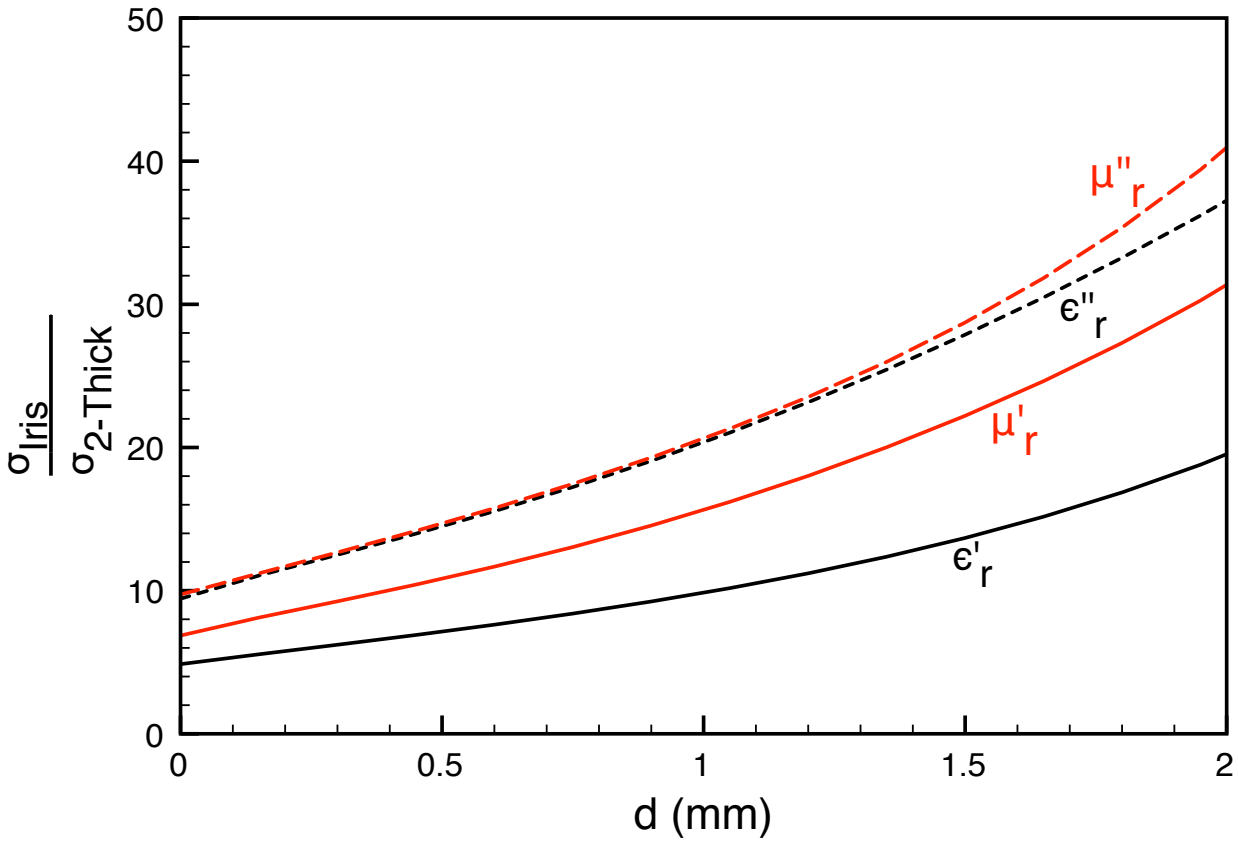

Figure 3.19: Comparison of the error in the constitutive parameters of FGM125 sample due to S-parameter error using the iris technique and two thickness method. This shows the results of the d parameter sweep assuming $w_2 = 11.43$ mm and $\Delta = 0.1$ mm at 10.09 GHz.

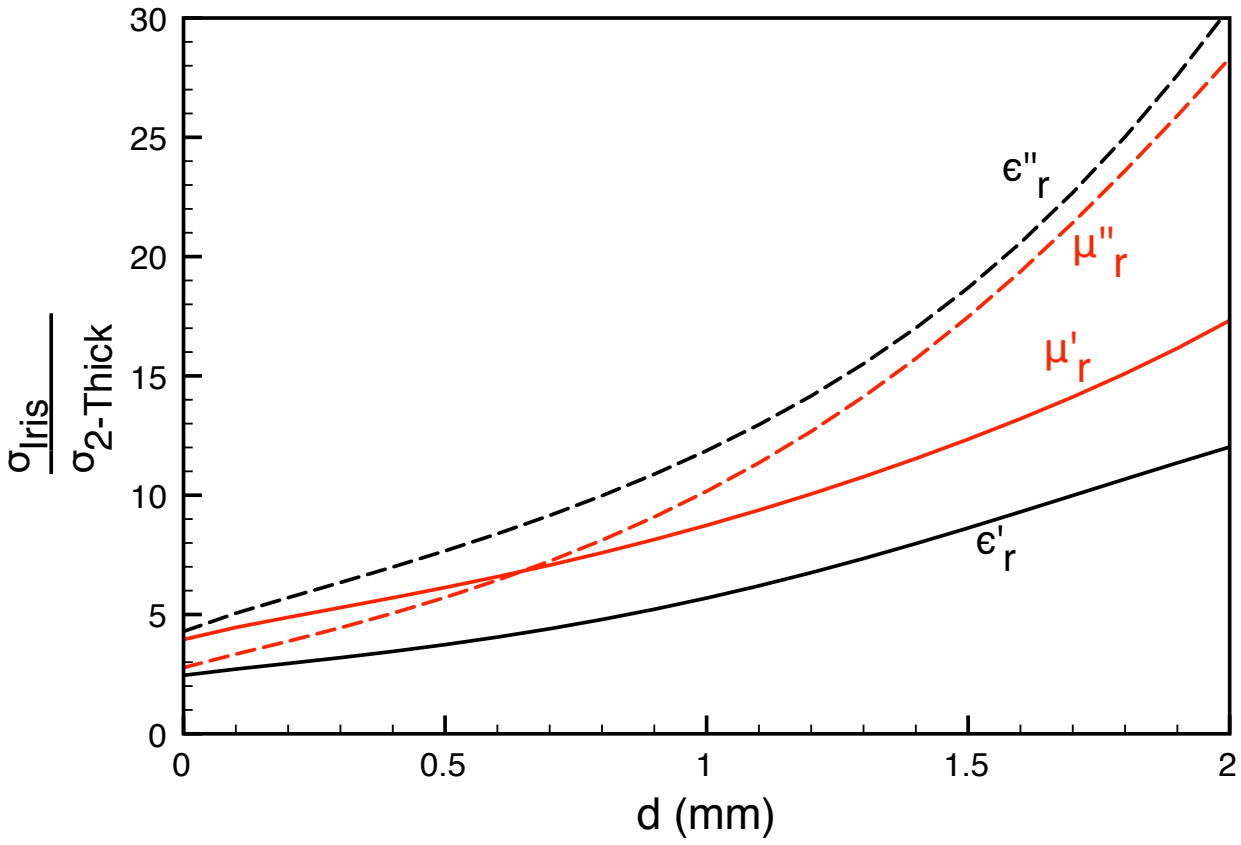

Figure 3.20: Comparison of the error in the constitutive parameters of FGM125 sample due to S-parameter error using the iris technique and two thickness method. This shows the results of the d parameter sweep assuming $w_2 = 11.43$ mm and $\Delta = 0.1$ mm at 12.4 GHz.

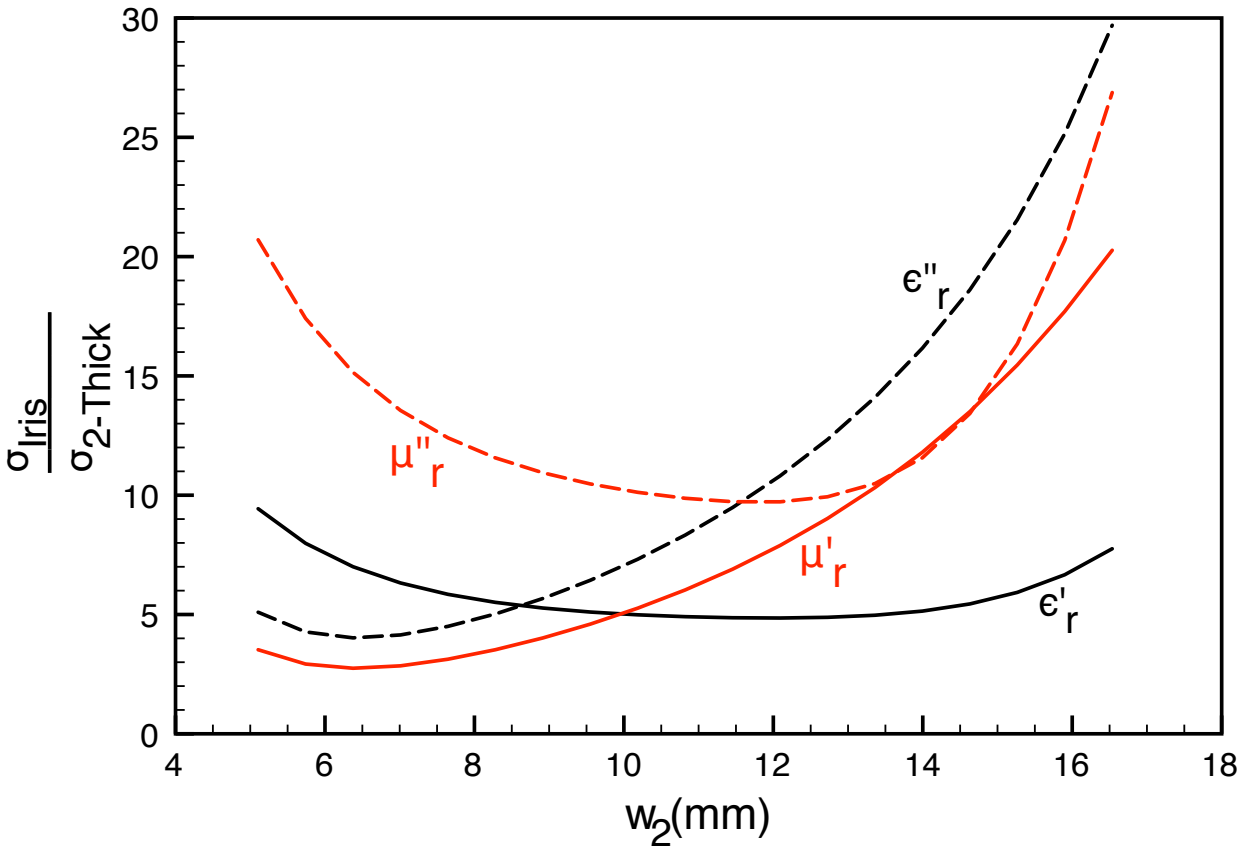

Figure 3.21: Comparison of the error in the constitutive parameters of FGM125 sample due to S-parameter error using the iris technique and two thickness method. This shows the results of the w_2 parameter sweep assuming $d = 0$ mm and $\Delta = 0.1$ mm at 8.2 GHz.

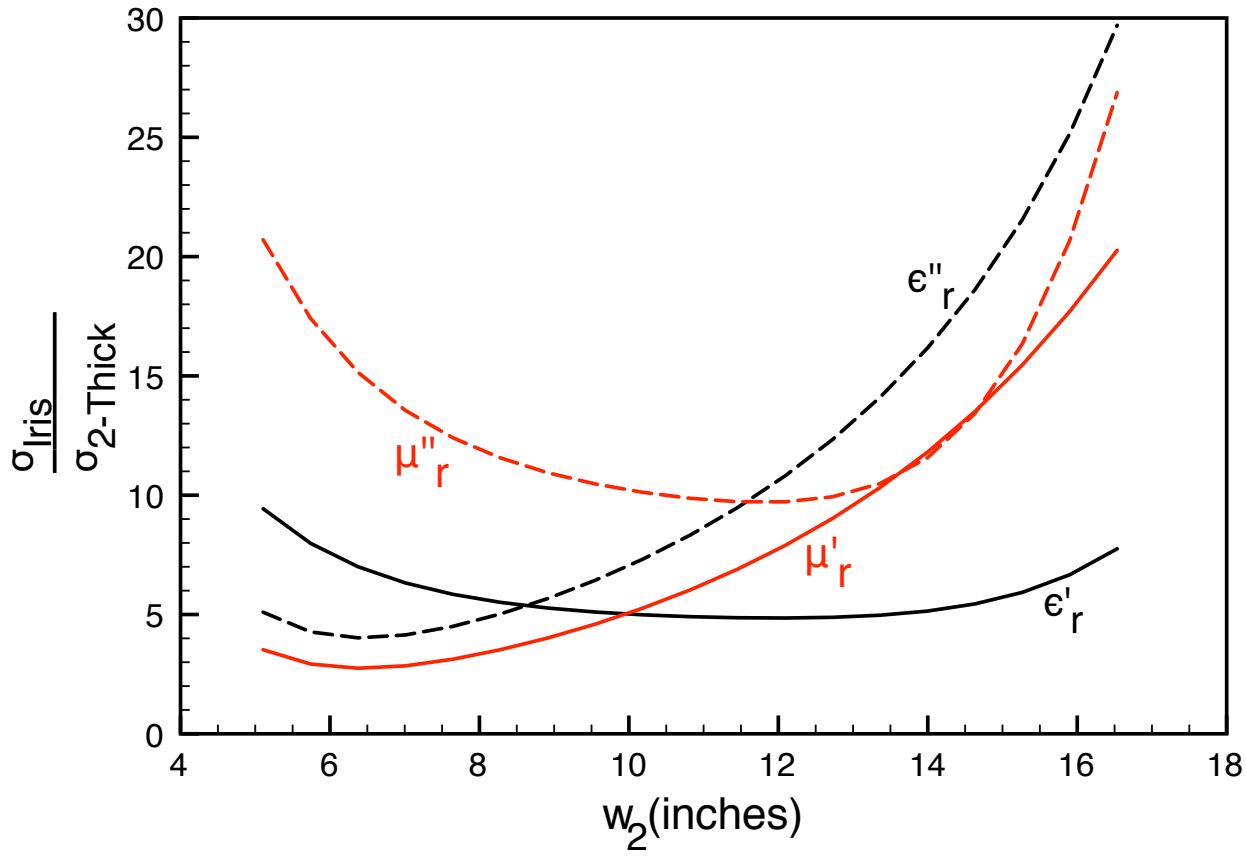

Figure 3.22: Comparison of the error in the constitutive parameters of FGM125 sample due to S-parameter error using the iris technique and two thickness method. This shows the results of the w_2 parameter sweep assuming $d = 0$ mm and $\Delta = 0.1$ mm at 10.09 GHz.

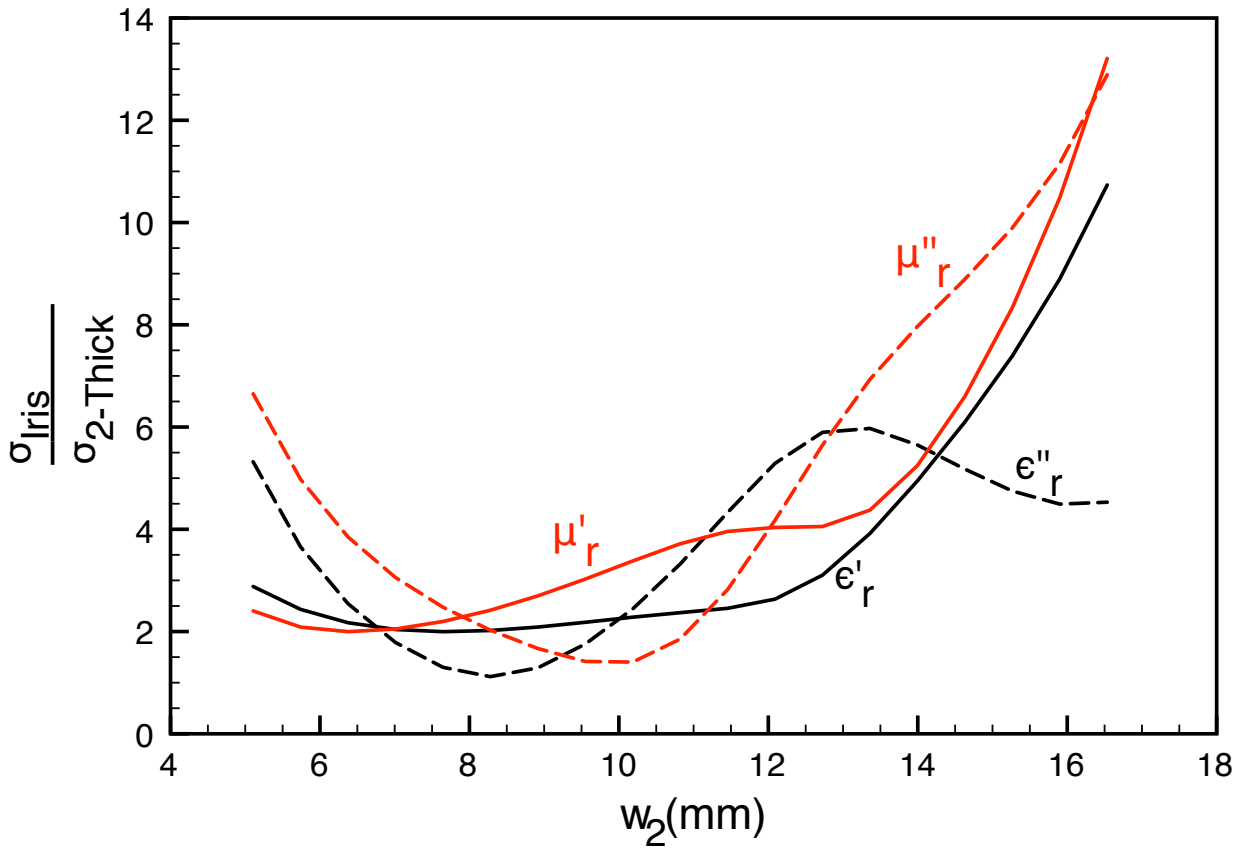

Figure 3.23: Comparison of the error in the constitutive parameters of FGM125 sample due to S-parameter error using the iris technique and two thickness method. This shows the results of the w_2 parameter sweep assuming $d = 0$ mm and $\Delta = 0.1$ mm at 12.4 GHz.

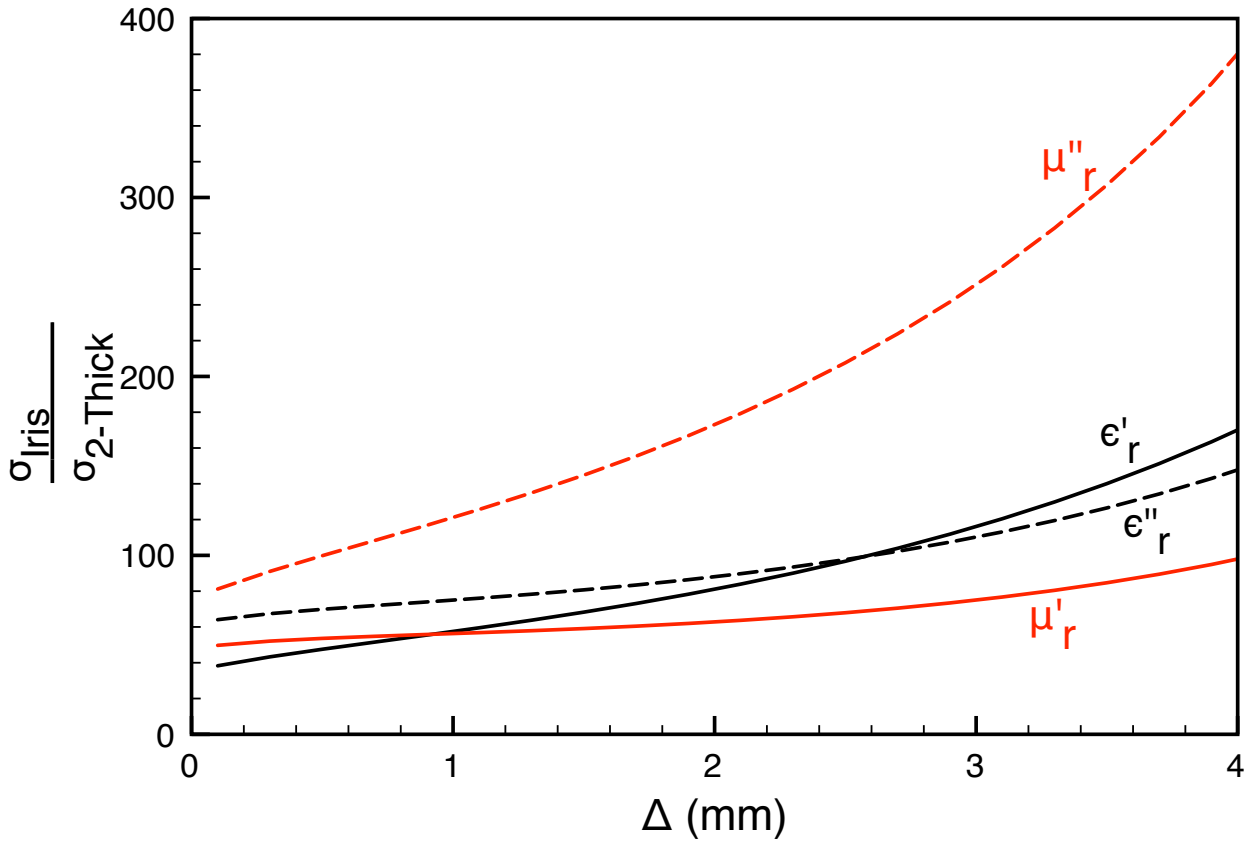

Figure 3.24: Comparison of the error propagated to constitutive parameters of FGM40 sample from S-parameter error using the iris technique and two thickness method. This shows the results of the Δ parameter sweep assuming $w_2 = 11.43$ mm and $d = 0$ mm at 8.2 GHz.

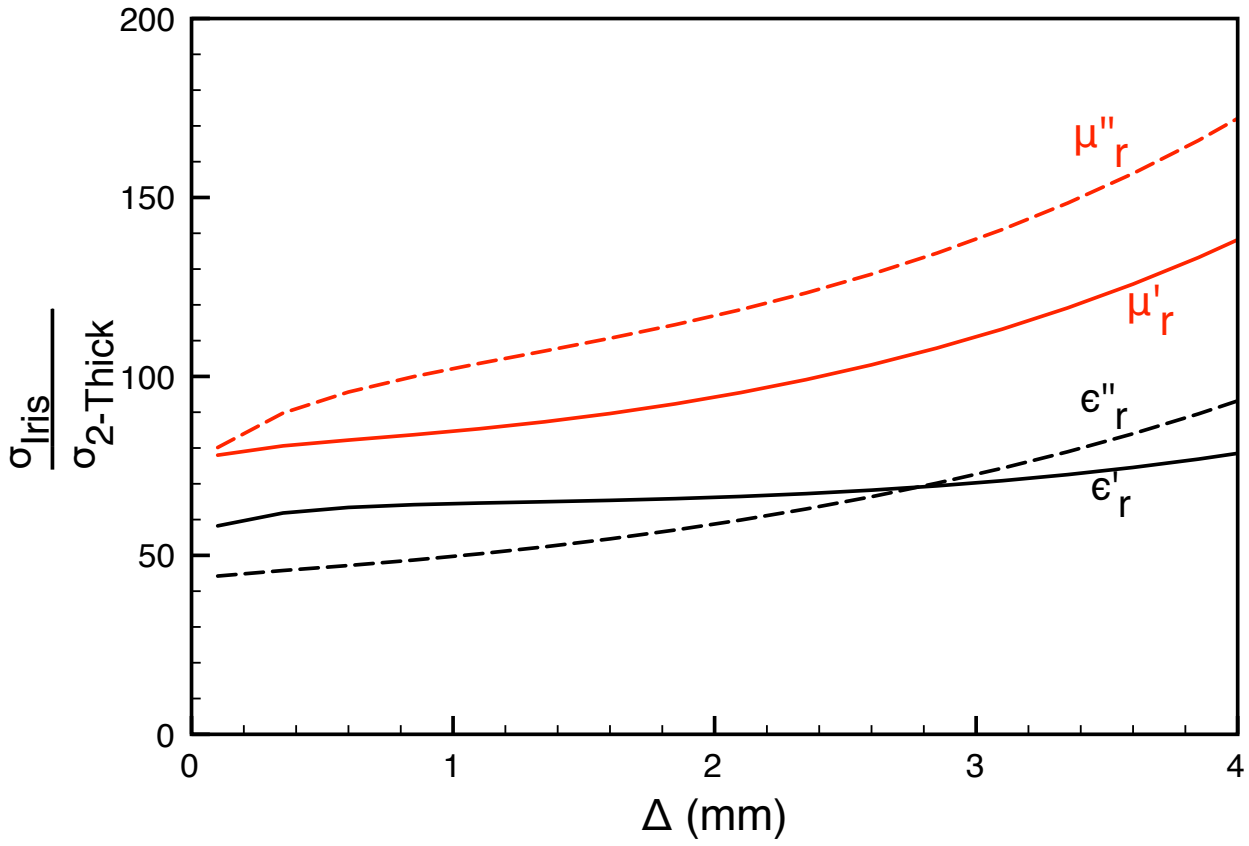

Figure 3.25: Comparison of the error propagated to the constitutive parameters of FGM40 sample from S-parameter error using the iris technique and two thickness method. This shows the results of the Δ parameter sweep assuming $w_2 = 11.43$ mm and $d = 0$ mm at 10.09 GHz.

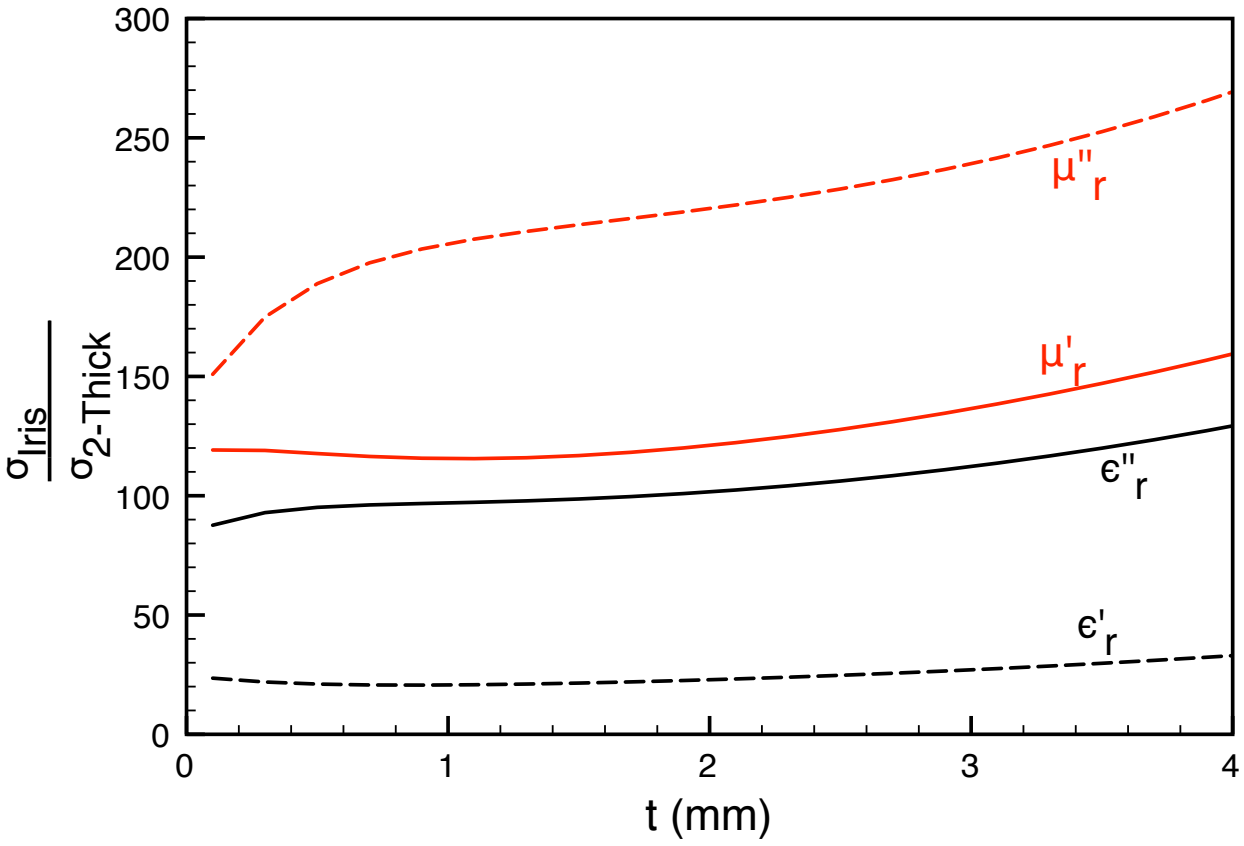

Figure 3.26: Comparison of the error propagated to the constitutive parameters of FGM40 sample from S-parameter error using the iris technique and two thickness method. This shows the results of the Δ parameter sweep assuming $w_2 = 11.43$ mm and $d = 0$ mm at 12.4 GHz.

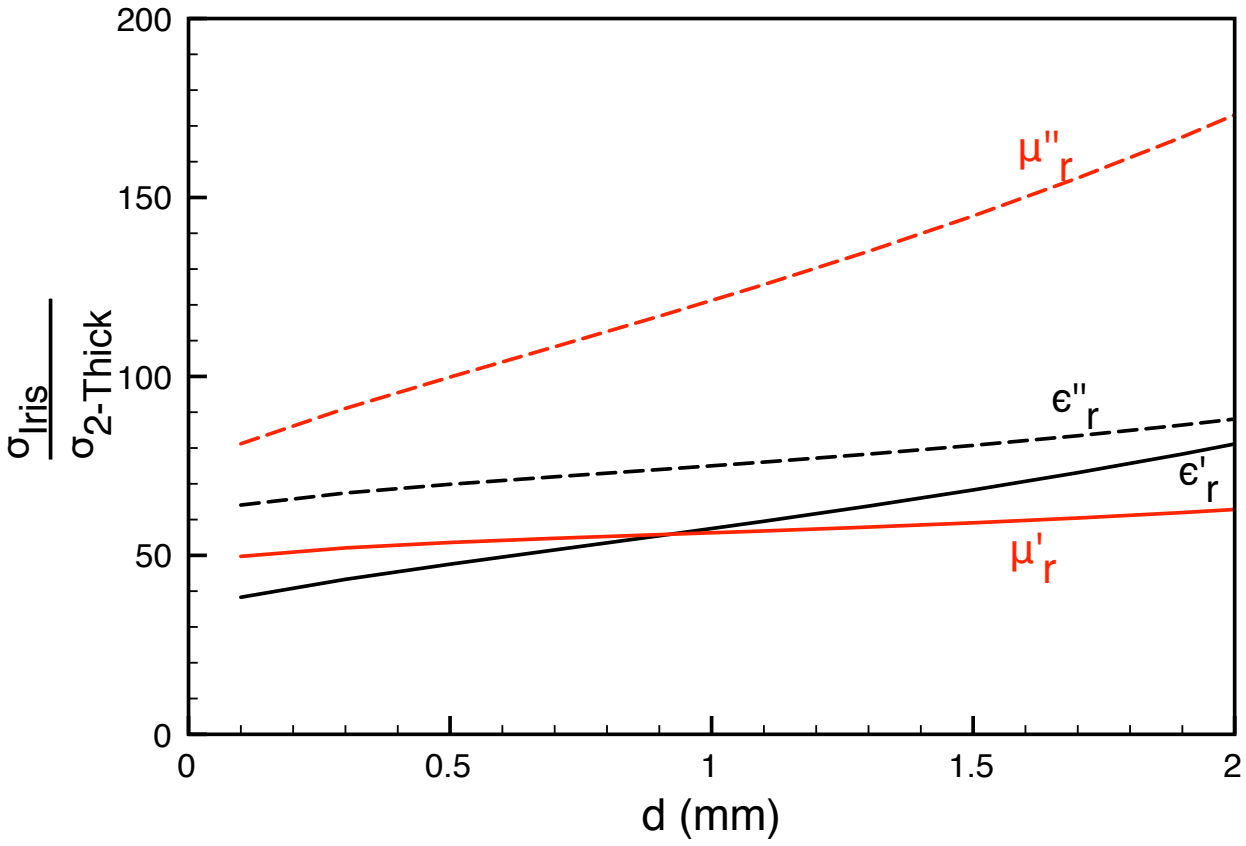

Figure 3.27: Comparison of the error propagated to constitutive parameters of FGM40 sample from S-parameter error using the iris technique and two thickness method. This shows the results of the d parameter sweep assuming $w_2 = 11.43$ mm and $\Delta = 0.1$ mm at 8.2 GHz.

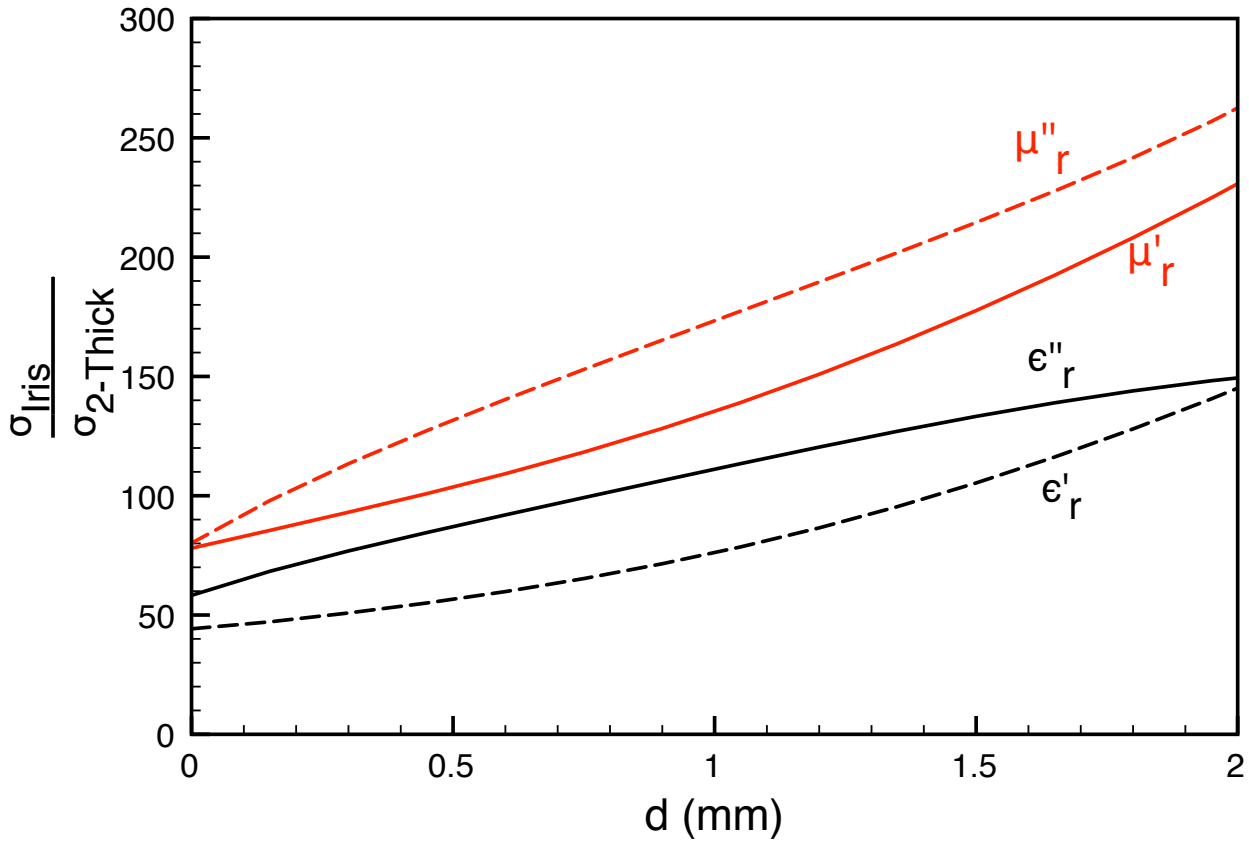

Figure 3.28: Comparison of the error propagated to constitutive parameters of FGM40 sample from S-parameter error using the iris technique and two thickness method. This shows the results of the d parameter sweep assuming $w_2 = 11.43$ mm and $\Delta = 0.1$ mm at 10.09 GHz.

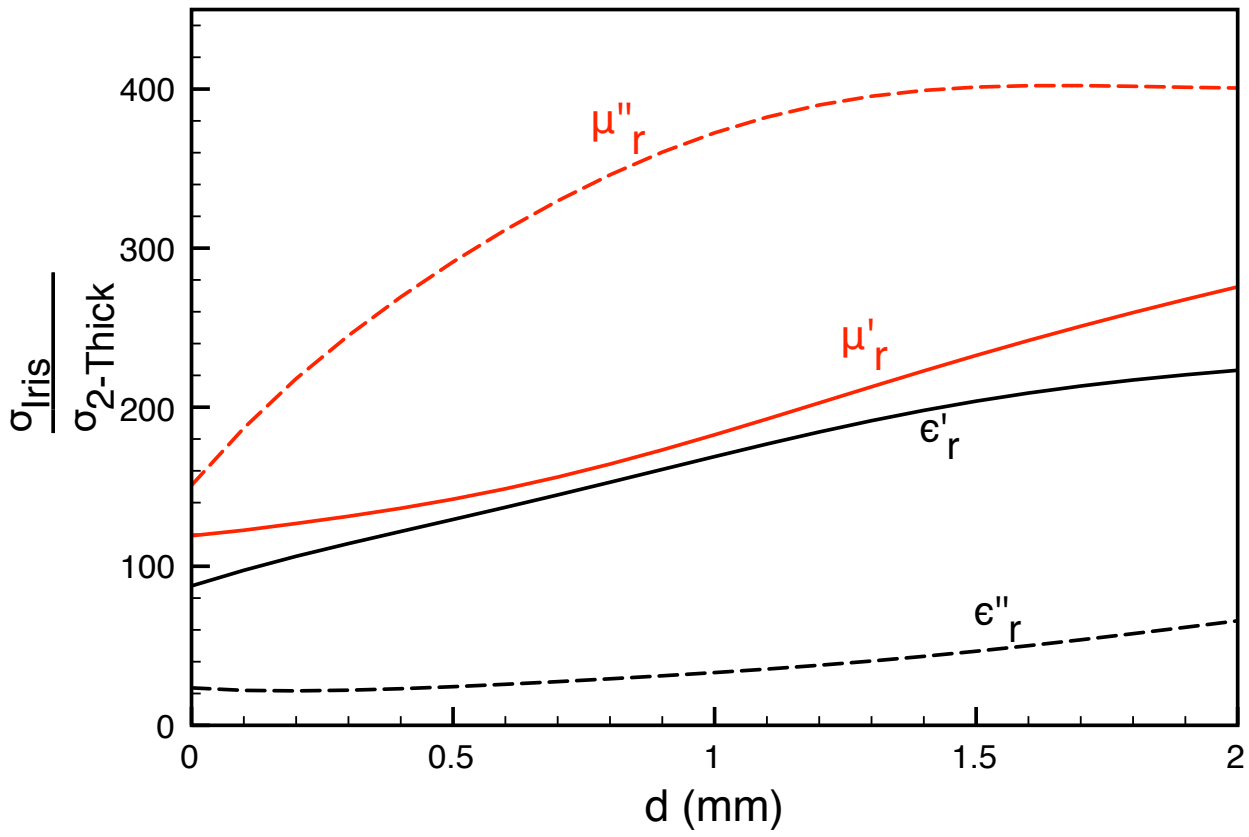

Figure 3.29: Comparison of the error propagated to constitutive parameters of FGM40 sample from S-parameter error using the iris technique and two thickness method. This shows the results of the d parameter sweep assuming $w_2 = 11.43$ mm and $\Delta = 0.1$ mm at 12.4 GHz.

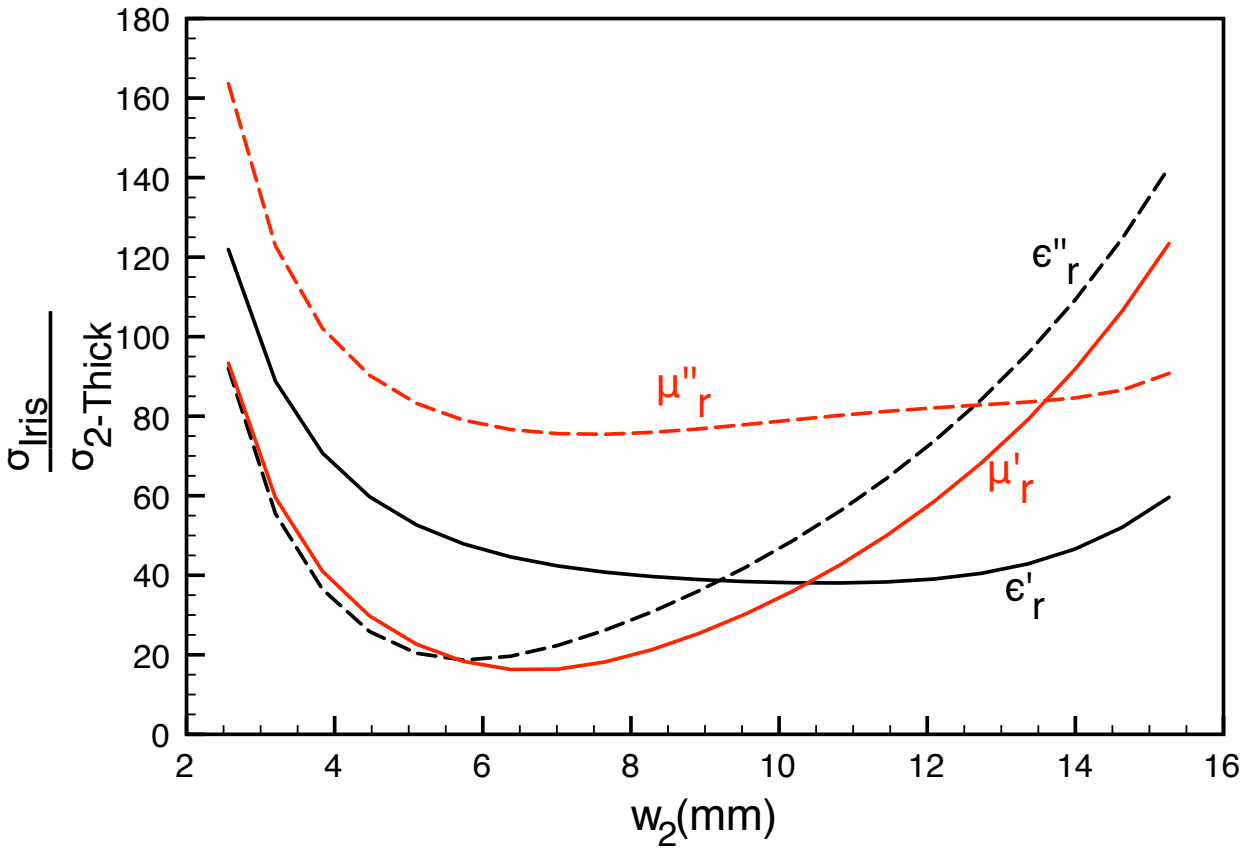

Figure 3.30: Comparison of the error propagated to constitutive parameters of FGM40 sample from S-parameter error using the iris technique and two thickness method. This shows the results of the w_2 parameter sweep assuming $d = 0$ mm and $\Delta = 0.1$ mm at 8.2 GHz.

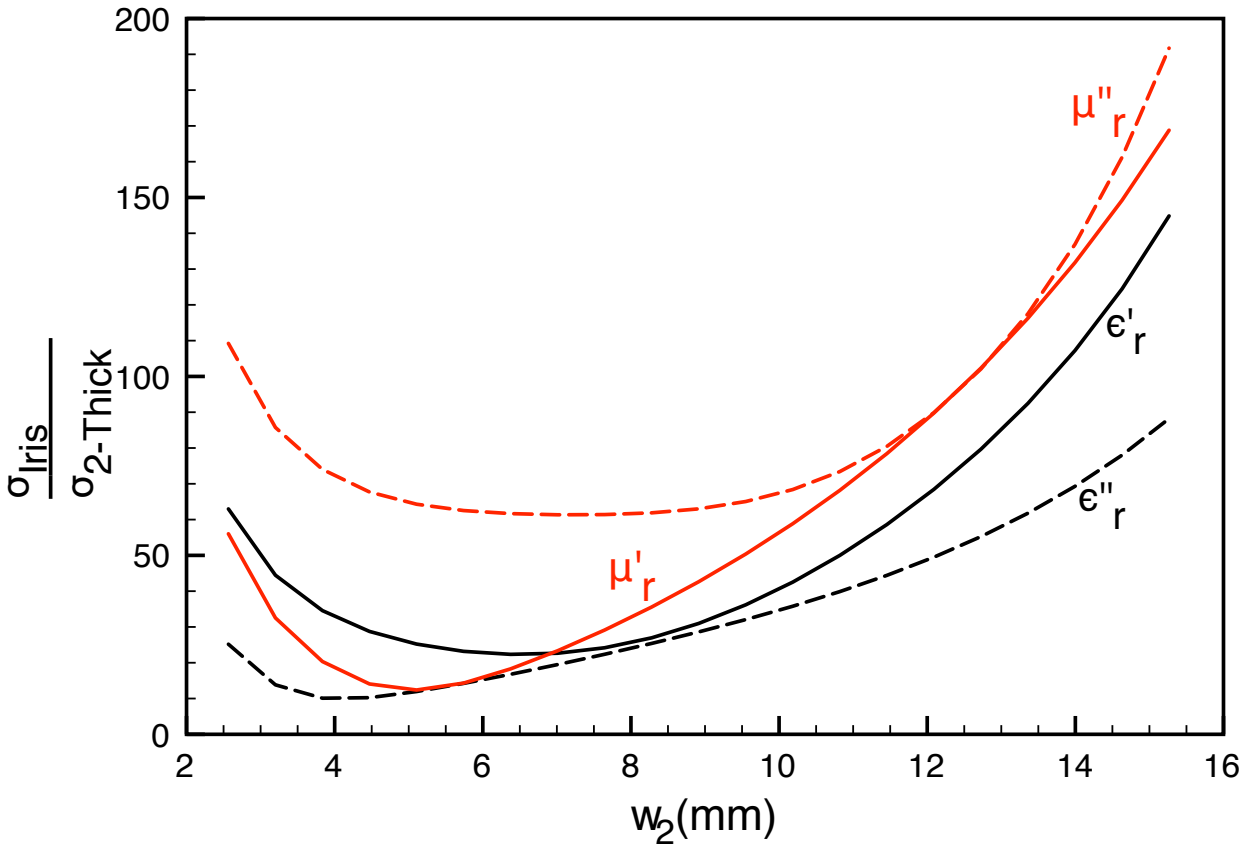

Figure 3.31: Comparison of the error propagated to constitutive parameters of FGM40 sample from S-parameter error using the iris technique and two thickness method. This shows the results of the w_2 parameter sweep assuming $d = 0$ mm and $\Delta = 0.1$ mm at 10.09 GHz.

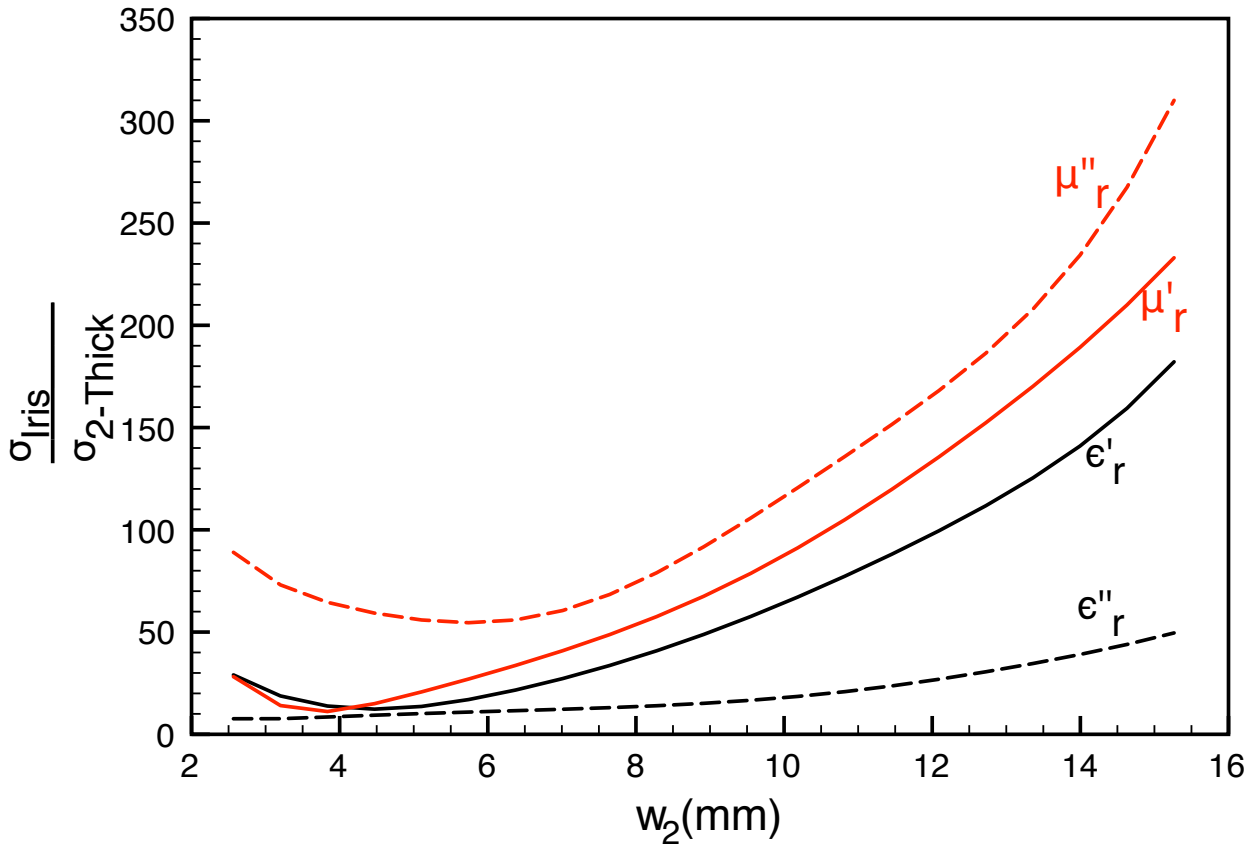

Figure 3.32: Comparison of the error propagated to constitutive parameters of FGM40 sample from S-parameter error using the iris technique and two thickness method. This shows the results of the w_2 parameter sweep assuming $d = 0$ mm and $\Delta = 0.1$ mm at 12.4 GHz.

manufacturing error of less than 5 mils. The iris was inserted between two 6 inch long commercial X-band waveguide extensions of cross-section 0.4 inch by 0.9 inch. A sliding short with a cross-section of 0.4 inch by 0.9 inch was used as a sample holder to provide the conductor backing of the FGM125 sample.

A sample of FGM125 was cut from a sheet of Eccosorb FGM125. Figure 3.33 shows a picture of the iris, FGM125 sample, waveguide extension, and sliding short sample holder. The sample was cut approximately 0.01 mm larger than the inner dimensions of the sliding short so that when inserted it would compress slightly and eliminate air gaps between the FGM125 sample and the sliding short walls. The thickness of the sample is 2.96 mm.

Measurements of the S-parameters of the FGM125 sample with and without the iris were made using an Agilent E5071C VNA. The VNA was calibrated using a Maury Microwave X7005M X-band calibration kit, consisting of two offset shorts and a load. The measurements were made with VNA settings of -5 dBm source power, 64 averages, and an IF bandwidth of 5 kHz. Finally, the material parameters were extracted using the measured values of S_{11}^{I} and S_{11}^{N}. The results of the characterization are shown in Figure 3.34. Also shown is the characterization of the same sample using the air-backed/conductor-backed method. There exists good agreement between the two methods for the extraction of the permeability. However, the characterization of the permittivity is poor using the iris technique.

The error in the extraction of the permittivity is a direct result of the propagation of error from the S-parameter measurements. Figure 3.35 and Figure 3.36 show the comparison of the measured S_{11}^{I} and S_{11}^{N}, respectively, to the computed values of S_{11}^{I} and S_{11}^{N} generated using the material parameters extracted with the air-back/conductor-backed method. The deviation of the measurement from theory, and the strong oscillations in the measured values, cause a dramatic effect on the permittivity characterization. The most notable deviation is the extraction of ϵ_r'', where the values are positive across the frequency band. Thus, it can be concluded that while this technique can be used to accurately characterize permeability, the characterization of permittivity is not reliable.

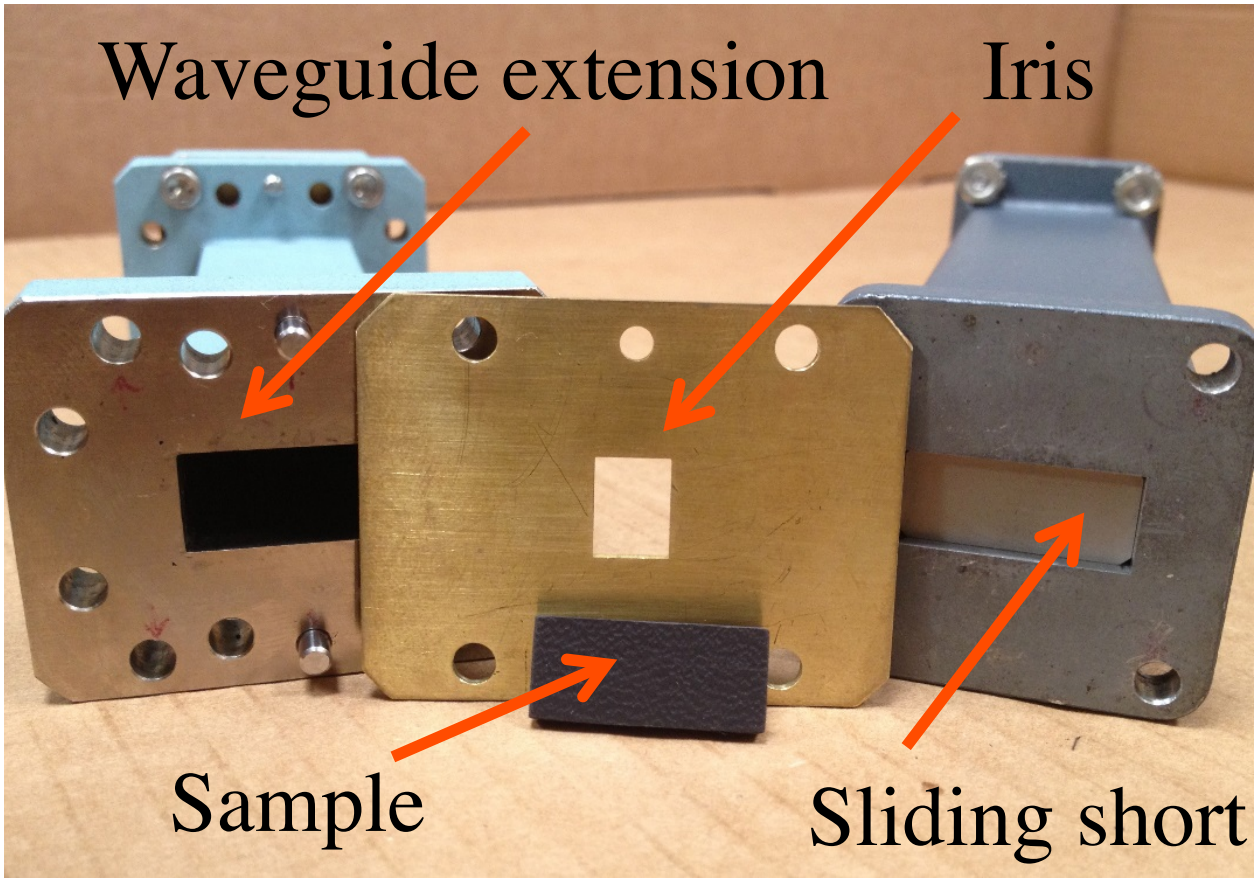

Figure 3.33: Manufactured iris with waveguide extension, sliding short sample holder, and FGM125 sample.

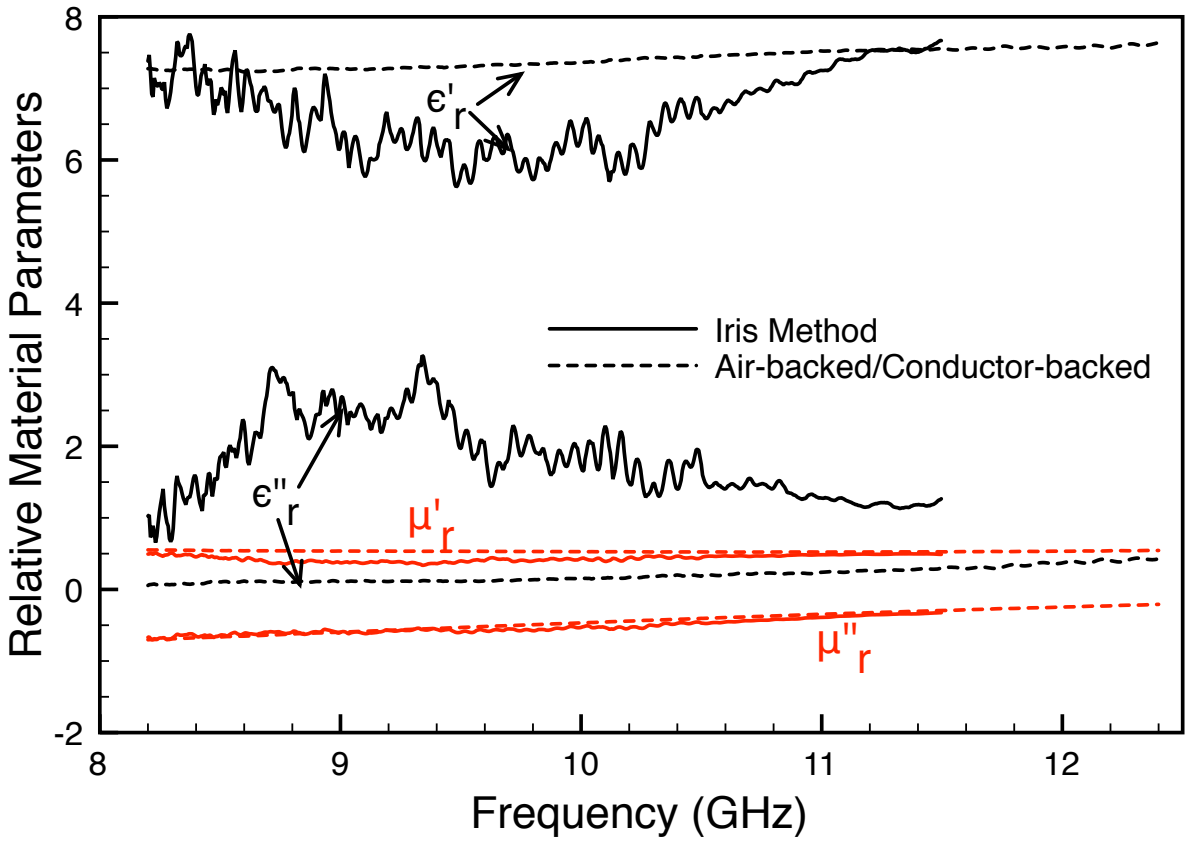

Figure 3.34: Relative permittivity and permeability extracted using the iris technique and the air-backed/conductor-backed method.

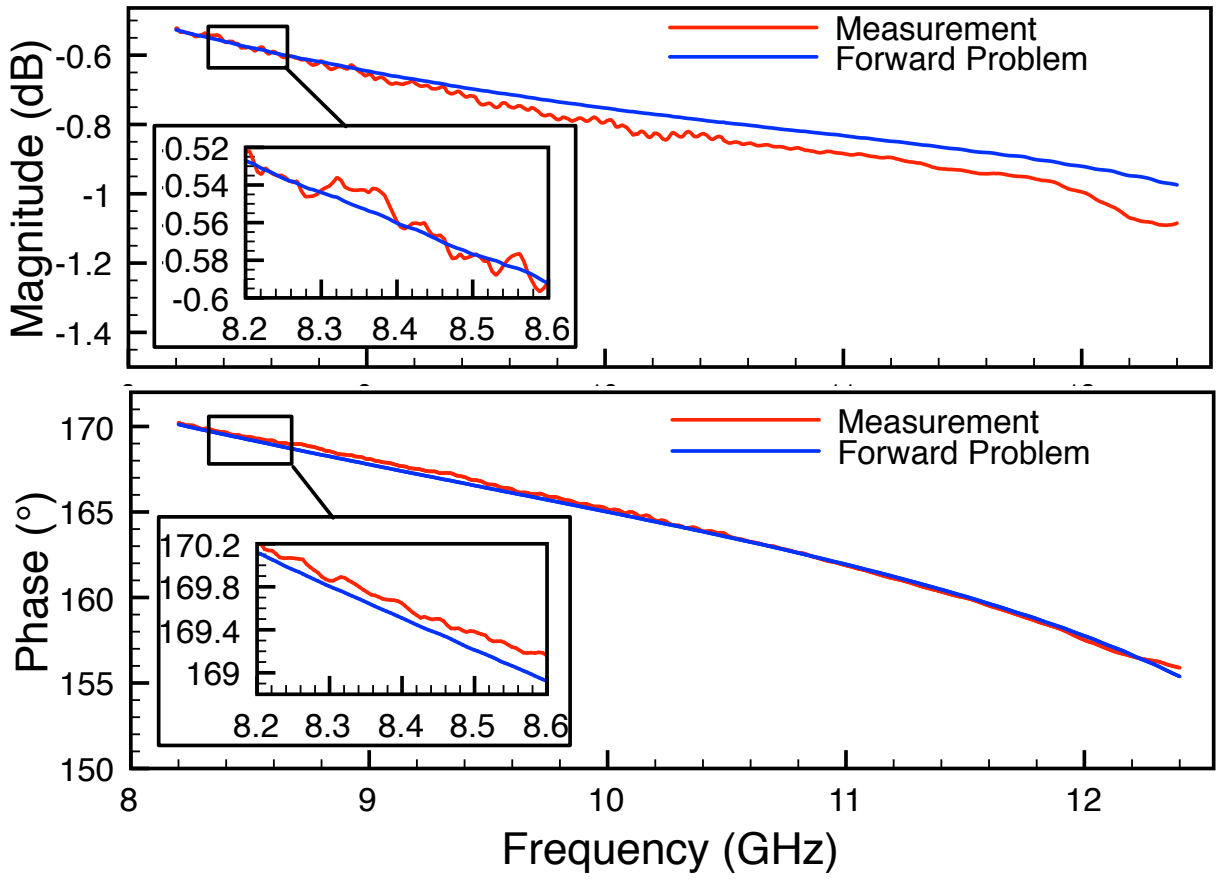

Figure 3.35: Comparison of measured and forward problem generated S_{11}^{I}.

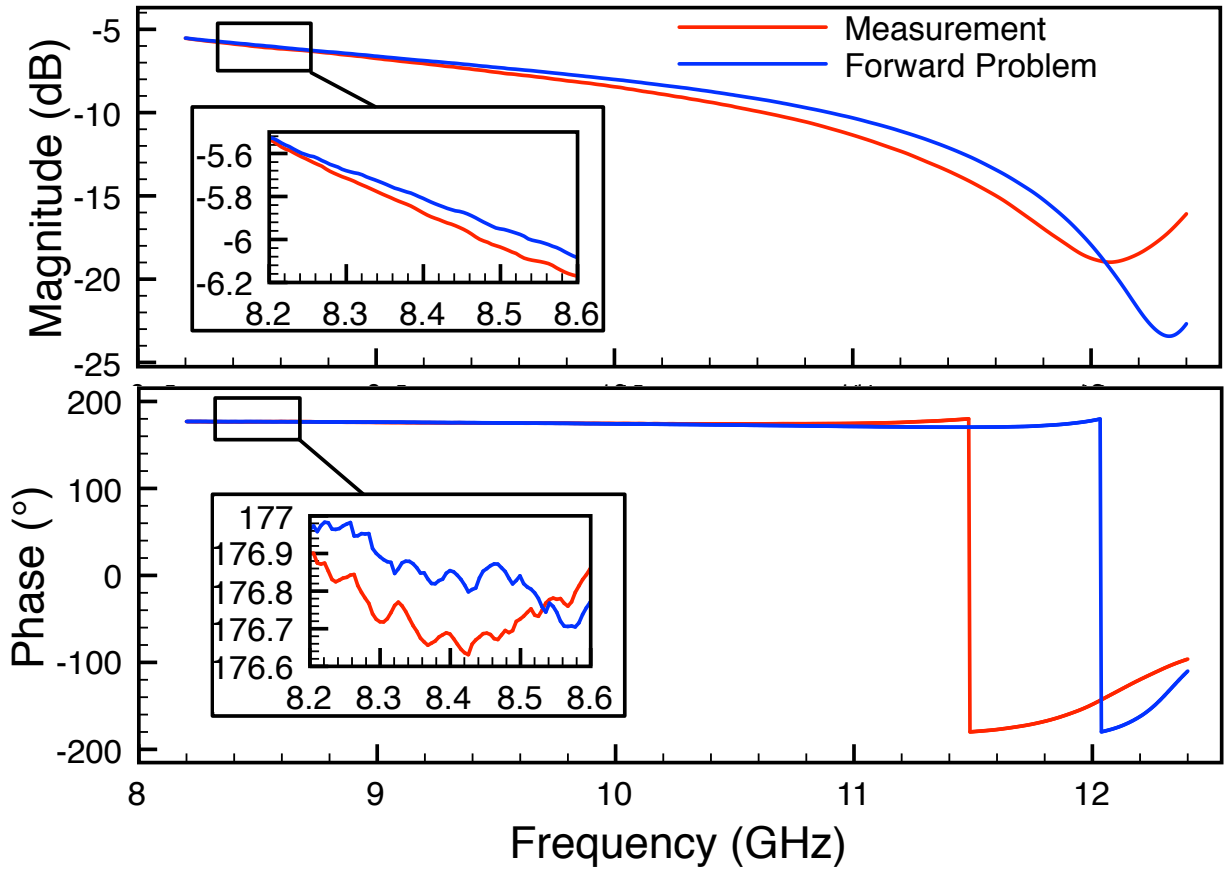

Figure 3.36: Comparison of measured and forward problem generated S_{11}^N.

3.3.6 Summary

A reflection-only measurement technique is outlined for characterizing conductor-backed materials. The measurements of the reflection coefficients for a conductor-backed material with and without the presence of an iris are used to characterize the permeability and permittivity. A mode-matching technique is outlined for computing the theoretical reflection coefficient from an iris in front of a conductor-backed sample. The dimensions of the iris measurement system were optimized to reduce the amount of S-parameter error propagated through to the characterization. Using these dimensions, an iris was fabricated and the technique was validated using laboratory measurements of a FGM125 sample. It was found that the technique is very sensitivity to S-parameter error, especially for the characterization of ϵ_r''. The technique performs very well for the characterization of the permeability.

CHAPTER 4

BIAXIAL MATERIAL CHARACTERIZATION

4.1 Introduction

This chapter presents two methods for characterizing biaxially anisotropic materials using rectangular waveguides. The first technique uses an extension of the NRW method (Section 3.2) applied to biaxial materials. These materials react differently depending on the incident wave polarization, but do not establish coupling between orthogonal field components. The tensors for biaxial materials have a total of six nonzero entries, corresponding to complex material parameters, and therefore three different sets of reflection and transmission measurements are required. This technique yields closed form solutions for all six material parameters. Due to the rectangular nature of the waveguide, typically three separate samples are manufactured from the material for placement in the cross-sectional plane of the waveguide. These samples are manufactured so the axes of the permittivity and permeability tensors align with the geometry of the waveguide.

The second technique uses a reduced-aperture, square-waveguide sample holder, such that a cubical sample can be used to characterize. This provides the minimum three reflection and

transmission measurements required for characterization and allows all material parameters to be determined from one sample. The sample holder is positioned between two empty sections rectangular waveguides to guarantee only the dominant mode is present at the sample holder, and the S-parameters are measured. Mode matching is used to determine the theoretical reflection and transmission coefficients of the dominant mode. Measurements of the reflection and transmission coefficients for various orientations of the same sample within the sample holder produce multiple transcendental equations. The inverse problem is then solved using a Newton's method to find the material parameters.

4.2 NRW Material Characterization Extended to Biaxially Anisotropic Materials

Of the techniques proposed for measuring properties of isotropic materials, the most accurate are those that expose a sample of the material to an electromagnetic wave and use measurements of the reflection and transmission of the wave to determine the permittivity and permeability. Confinement of the wave produces good signal strength, so an appealing approach is to put a layer of the material into a rectangular waveguide and use a network analyzer to measure the reflection and transmission coefficients as a function of frequency. Using simple guided wave theory, closed-form inverse expressions for permittivity and permeability may be obtained (see Section 3.2). These expressions are well-conditioned for most of the material parameters of interest, except, as was discussed previously, when the material thickness approaches multiples of a half wavelength. This section presents an extension of the classical waveguide technique for biaxial anisotropic materials and will describe the waveguide technique along with exploring parameter sensitivity by performing a Monte Carlo error analysis.

4.2.1 Theoretical Reflection and Transmission Coefficients

The sample placed in the cross-sectional plane of the waveguide is assumed to be linear and homogeneous. The permittivity and permeability has the constitutive material tensors

$$\overline{\overline{\epsilon}} = \epsilon_0 \begin{bmatrix} \epsilon_x & 0 & 0 \\ 0 & \epsilon_y & 0 \\ 0 & 0 & \epsilon_z \end{bmatrix} \tag{4.1}$$

and

$$\overline{\overline{\mu}} = \mu_0 \begin{bmatrix} \mu_x & 0 & 0 \\ 0 & \mu_y & 0 \\ 0 & 0 & \mu_z \end{bmatrix}, \tag{4.2}$$

where tensor entries are relative complex quantities: $\epsilon_x = \epsilon_x' + j\epsilon_x'', \mu_x = \mu_x' + j\mu_x''$ and so on.

The waveguide system, shown in Figure 4.1, consist of empty waveguide sections attached to the sample region. It is assumed that the empty waveguide sections are of adequate length such that a single TE_{10} rectangular waveguide mode is incident on the sample from the transmitting section ($z < 0$) and that single mode is obtained at the receiving extension ($z > d$).

4.2.1.1 Field Structure in a Waveguide Filled with Biaxial Material

The TE_{10} mode incident from the transmitting empty waveguide couples into the TE_{10} biaxial filled waveguide mode since the field structure in both regions is identical. This means the fields of the TE_{10} mode do not couple into orthogonal field components and therefore higher order modes are not excited. This can be seen by first specializing the field equations for the isotropic material filled guide (Section 2.3.1.1) and the biaxial filled guide (Section 2.3.2.1) to the waveguide setup shown in Figure 4.1. The field equations for the

isotopic material can be used to represent the propagating TE_{10} mode in the transmitting region, and the field equations for the biaxial material can be used to determine the TE_{10} mode in the sample region.

In the empty waveguide region, it can be shown from Section 2.3.1.1 that the TE_{10} mode is the dominant mode ($n = 1$), which means $u_1 = 1$ and $v_1 = 0$. Therefore, $k^e_{x1} = \pi/a$, $k^e_{y1} = 0$, and $k^e_{c1} = \pi/a$ is the cutoff wavenumber for the first order mode. Now, using (2.140) the propagation constant is given by

$$\beta^e_1 = \sqrt{k_0^2 - \left(k^e_{c1}\right)^2} \tag{4.3}$$

where $k_0 = \omega\sqrt{\mu_0\epsilon_0}$. The transverse field equations from (2.151) - (2.152) then results in

$$E^e_y(x,z) = C_1 e^e_{y1}(x)\, \mathrm{e}^{\pm j\beta^e_1 z} \tag{4.4}$$

$$H^e_x(x,z) = \mp C_1 h^e_{x1}(x)\, \mathrm{e}^{\pm j\beta^e_1 z}. \tag{4.5}$$

Here e^e_{y1} and h^e_{x1} are the transverse electric and magnetic modal fields in the empty guide, respectively, and are expressed as

$$e^e_{y1} = -k^e_{x1} \sin\left(k^e_{x1} x\right), \tag{4.6}$$

$$h^e_{x1} = \frac{k^e_{x1}}{Z^e_n} \sin\left(k^e_{x1} x\right), \tag{4.7}$$

where the modal wave impedance in the empty guide is given by $Z^e_1 = \omega\mu_0/\beta^e_1$.

From Section (2.3.2.1) a TE_{10} mode in the biaxial material filled sample region implies that $n = 1$, and so $k^s_{c1} = \pi/a$ is the cutoff wavenumber for the first order mode. Thus the propagation constant from (2.206) is given by

$$\beta^s_1 = \sqrt{k_0^2 \mu_x \epsilon y - \frac{\mu_x}{\mu_y} k^2_{c1}}. \tag{4.8}$$

The transverse field equations from (2.216)-(2.217) become

$$E_y^s(x,z) = C_1 e_{y1}^s(x)\, \mathrm{e}^{\pm j\beta_1^s z} \tag{4.9}$$

$$H_x^s(x,z) = \mp C_1 h_{y1}^s(x)\, \mathrm{e}^{\pm j\beta_1^s z}, \tag{4.10}$$

where the modal fields are given by

$$e_{y1}^s(x) = -k_{c1}^s \sin\left(k_{c1}^s\right) \tag{4.11}$$

$$h_{x1}^s(x) = \frac{k_{c1}^s}{Z_1^s} \sin\left(k_{c1}^s\right). \tag{4.12}$$

Here the modal wave impedance in the empty guide is given by $Z_1^s = \omega\mu_0\mu_x/\beta_1^s$.

It is clearly seen from the transverse field equations that the field structures in the empty guide and in the sample region are identical; this results in direct coupling of the first order mode from the empty region to the biaxially filled sample region. Thus a mode matching analysis does not need to be used to calculate the reflection and transmission coefficients.

4.2.1.2 Solution for Reflection and Transmission Coefficients

The transverse fields in the sample region and in the waveguide extensions can be represented using the modal fields, with the modal amplitudes determined through the application of boundary conditions. For the empty waveguide region $z < 0$ the fields are

$$Ey(x,z) = -H^i k_{x1}^e \sin\left(k_{x1}^e x\right) \mathrm{e}^{-j\beta_1^e z} - H^r k_{x1}^e \sin\left(k_{x1}^e x\right) \mathrm{e}^{j\beta_1^e z} \tag{4.13}$$

$$Hx(x,z) = H^i \frac{k_{x1}^e}{Z_1^e} \sin\left(k_{x1}^e x\right) \mathrm{e}^{-j\beta_1^e z} - H^r \frac{k_{x1}^e}{Z_1^e} \sin\left(k_{x1}^e x\right) \mathrm{e}^{j\beta_1^e z}. \tag{4.14}$$

Here, H^i is the amplitude of the incident TE_{10} wave, and is assumed to be known during analysis. In the sample region, $0 < z < d$, the transverse fields are given by

$$E_y(x,z) = -H^+ k^s_{c1} \sin\left(k^s_{c1}x\right) \mathrm{e}^{-j\beta^s_1 z} - H^- k^s_{c1} \sin\left(k^s_{c1}x\right) \mathrm{e}^{j\beta^s_1 z} \tag{4.15}$$

$$H_x(x,z) = H^+ \frac{k^s_{c1}}{Z^s_1} \sin\left(k^s_{c1}x\right) \mathrm{e}^{-j\beta^s_1 z} - H^- \frac{k^s_{c1}}{Z^s_1} \sin\left(k^s_{c1}x\right) \mathrm{e}^{j\beta^s_1 z}. \tag{4.16}$$

In the receiving waveguide extension, $z > d$, the fields are

$$E_y(x,z) = -H^t k^e_{x1} \sin\left(k^e_{x1}x\right) \mathrm{e}^{-j\beta^e_1 (z-d)} \tag{4.17}$$

$$H_x(x,z) = H^t \frac{k^e_{x1}}{Z^e_1} \sin\left(k^e_{x1}x\right) \mathrm{e}^{-j\beta^e_1 (z-d)}. \tag{4.18}$$

The modal amplitudes H^r, H^+, H^-, and H^t may be determined by applying the boundary conditions on E_y and H_x at the interfaces between the biaxial sample and empty guide. Applying the boundary condition on the tangential electric field at $z = 0$ results in

$$\left[H^i + H^r\right] k^e_{x1} \sin\left(k^e_{x1}x\right) = \left[H^+ + H^-\right] k^s_{c1} \sin\left(k^s_{c1}x\right), \tag{4.19}$$

and since $k^s_{c1} = k^e_{x1}$, then

$$\left[H^i + H^r\right] = \left[H^+ + H^-\right]. \tag{4.20}$$

The tangential magnetic field boundary condition at $z = 0$ requires

$$\left[H^i - H^r\right] k^e_{x1} \frac{k^e_{x1}}{Z^e_1} \sin\left(k^e_{x1}x\right) = \left[H^+ - H^-\right] k^s_{c1} \frac{k^s_{c1}}{Z^s_1} \sin\left(k^s_{c1}x\right), \tag{4.21}$$

or

$$\left[H^i - H^r\right] \frac{Z^s_1}{Z^e_1} = \left[H^+ - H^-\right]. \tag{4.22}$$

At $z = d$, the boundary condition on the tangential electric field requires

$$\left[H^{+}\mathrm{e}^{-j\beta_1^s d} + H^{-}\mathrm{e}^{j\beta_1^s d}\right] k_{c1}^s \sin\left(k_{c1}^s x\right) = H^t k_{x1}^e \sin\left(k_{x1}^e x\right), \tag{4.23}$$

or

$$\left[H^{+}\mathrm{e}^{-j\beta_1^s d} + H^{-}\mathrm{e}^{j\beta_1^s d}\right] = H^t, \tag{4.24}$$

while the boundary condition on the tangential magnetic field at $z = d$ results in

$$\left[H^{+}\mathrm{e}^{-j\beta_1^s d} - H^{-}\mathrm{e}^{j\beta_1^s d}\right] \frac{k_{c1}^s}{Z_1^s} \sin\left(k_{c1}^s x\right) = H^t \frac{k_{x1}^e}{Z_1^e} \sin\left(k_{x1}^e x\right), \tag{4.25}$$

or

$$\left[H^{+}\mathrm{e}^{-j\beta_1^s d} - H^{-}\mathrm{e}^{j\beta_1^s d}\right] \frac{1}{Z_1^s} = H^t \frac{1}{Z_1^e}. \tag{4.26}$$

Now, to determine the reflection coefficient, $R = H^r/H^i$, (4.20) is added to (4.22) yielding

$$2H^{+} = H^i \left(\frac{Z_1^s}{Z_1^e} + 1\right) - H^r \left(\frac{Z_1^s}{Z_1^e} - 1\right), \tag{4.27}$$

while subtracting (4.20) from (4.22) produces

$$2H^{-} = -H^i \left(\frac{Z_1^s}{Z_1^e} - 1\right) + H^r \left(\frac{Z_1^s}{Z_1^e} + 1\right). \tag{4.28}$$

Similarly, adding (4.24) and (4.26) together results in

$$2H^{+} = H^t \left[\frac{Z_1^s}{Z_1^e} + 1\right] \mathrm{e}^{j\beta_1^s d}, \tag{4.29}$$

and subtracting (4.24) from (4.26) gives

$$2H^- = -H^t \left[\frac{Z_1^s}{Z_1^e} - 1 \right] \mathrm{e}^{-j\beta_1^s d}. \tag{4.30}$$

The next step is to divide (4.30) by (4.29) producing

$$\frac{H^-}{H^+} = - \left[\frac{Z_1^s - Z_1^e}{Z_1^s + Z_1^e} \right] \mathrm{e}^{-j2\beta_1^s d}, \tag{4.31}$$

which can also be written as

$$\frac{H^-}{H^+} = -\Gamma P^2. \tag{4.32}$$

Here the interfacial reflection coefficient is established as

$$\Gamma = \frac{Z_1^s - Z_1^e}{Z_1^s + Z_1^e}, \tag{4.33}$$

and the propagation factor is defined as

$$P = \mathrm{e}^{-j\beta_1^s d}. \tag{4.34}$$

Next (4.28) is divided by (4.29) giving

$$\frac{H^-}{H^+} = -\frac{H^i \left(\frac{Z_1^s - Z_1^e}{Z_1^e} \right) - H^r \left(\frac{Z_1^s + Z_1^e}{Z_1^e} \right)}{H^i \left(\frac{Z_1^s + Z_1^e}{Z_1^e} \right) - H^r \left(\frac{Z_1^s - Z_1^e}{Z_1^e} \right)}. \tag{4.35}$$

Multiplying the numerator and denominator by Z_1^e / H^i yields

$$\frac{H^-}{H^+} = -\frac{\left(Z_1^s - Z_1^e \right) - \frac{H^r}{H^i} \left(Z_1^s + Z_1^e \right)}{\left(Z_1^s + Z_1^e \right) - \frac{H^r}{H^i} \left(Z_1^s - Z_1^e \right)}, \tag{4.36}$$

and dividing through by $(Z_1^s + Z_1^e)$ produces

$$\frac{H^-}{H^+} = -\frac{\Gamma - R}{1 - R\Gamma}. \tag{4.37}$$

Now setting (4.32) equal to (4.37) results in

$$\Gamma P^2 = \frac{\Gamma - R}{1 - R\Gamma}, \tag{4.38}$$

and through algebraic manipulation the reflection coefficient is determined to be

$$R = \frac{\Gamma\left(1 - P^2\right)}{1 - \Gamma^2 P^2}. \tag{4.39}$$

Next, the transmission coefficient, $T = H^t/H^i$, can be derived by first rearranging (4.24):

$$H^+ \mathrm{e}^{-j\beta_1^s d}\left[1 + \frac{H^-}{H^+}\mathrm{e}^{j2\beta_1^s d}\right] = H^t. \tag{4.40}$$

Using (4.32), this equation becomes

$$H^+ \mathrm{e}^{-j\beta_1^s d}\left[1 + \Gamma\right] = H^t. \tag{4.41}$$

Then (4.27) can be substituted, yielding

$$\frac{1}{2}\left[H^i\left(\frac{Z_1^s + Z_1^e}{Z_1^e}\right) - H^r\left(\frac{Z_1^s - Z_1^e}{Z_1^e}\right)\right]\left[1 - \Gamma\right]\mathrm{e}^{-j\beta_1^s d} = H^t. \tag{4.42}$$

Factoring H^i/Z_1^e and rearranging the equation produces

$$\frac{H^t}{H^i}\mathrm{e}^{j\beta_1^s d} = \frac{1}{2Z_1^e}\left[\left(Z_1^s + Z_1^e\right) - \frac{H^r}{H^i}\left(Z_1^s - Z_1^e\right)\right]\left[1 - \Gamma\right], \tag{4.43}$$

or

$$T\mathrm{e}^{j\beta_1^s d} = \frac{1}{2Z_1^e}\left[\left(Z_1^s + Z_1^e\right) - R\left(Z_1^s - Z_1^e\right)\right]\left[1-\Gamma\right]. \tag{4.44}$$

Simplifying further gives

$$T\mathrm{e}^{j\beta_1^s d} = \frac{1}{2Z_1^e}\left(Z_1^s + Z_1^e\right)\left[1 - R\frac{Z_1^s - Z_1^e}{Z_1^s + Z_1^e}\right]\left[1-\Gamma\right], \tag{4.45}$$

also which can be written as

$$T\mathrm{e}^{j\beta_1^s d} = \frac{1}{2Z_1^e}\left(Z_1^s + Z_1^e\right)\left[1 - R\Gamma\right]\left[1-\Gamma\right]. \tag{4.46}$$

Then (4.33) can be substituted, yielding

$$T\mathrm{e}^{j\beta_1^s d} = \frac{1}{2Z_1^e}\left(Z_1^s + Z_1^e\right)\frac{2Z_1^e}{Z_1^s + Z_1^e}\left[1 - R\Gamma\right], \tag{4.47}$$

and through addition alalgebraic manipulation, the transmission coefficient becomes

$$T = \left(1 - R\Gamma\right)P. \tag{4.48}$$

Now, using the equation for the reflection coefficient, (4.39), the transmission coefficient is expressed as

$$T = \frac{P\left(1-\Gamma^2\right)}{1-\Gamma^2 P^2}. \tag{4.49}$$

4.2.2 Validation of Theoretical Analysis

Before parameter extraction is performed, it is very important to validate the theoretical reflection and transmission coefficients of a biaxial sample completely filling the cross-section

of a waveguide. Table 4.1 shows a fictitious biaxial test sample which is used to validate the theoretical model against the computational FEM solver HFSS. Because a fictitious material is being considered, each of the material parameters can be chosen such that none of the diagonal tensor entries are the same. This provides a general validation of the theory.

Table 4.1: Material parameters for a fictitious biaxial material.

Parameter	Value
ϵ_x	2.0
ϵ_y	2.35
ϵ_z	3.50
μ_x	2.75
μ_y	2.25
μ_z	5

Theoretical analysis was used to compute the reflection and transmission coefficient for the fictitious material paced in the cross-section of an S-band waveguide system. The dimensions of the S-band system are $a = 72.136$ mm, $b = 34.036$ mm, and $d = 10$ mm. Figure 4.2 shows R and T computed using Figure 4.39 and Figure 4.49, respectively, with the orientation of the sample axes aligned with the geometry of the waveguide. Also shown in Figure 4.2 are the values of the reflection and transmission coefficient computed using HFSS. The waveguide extensions were explicitly modeled in the EM solver and were of significant length to ensure that only the fundamental TE_{10} mode propagates; these lengths were chosen to be 100 mm. The convergence in HFSS was specified to a maximum delta S of 0.001, which is defined as the absolute difference between all S-parameters from two succeeding iterations at the solution frequency of 3.95 GHz. Excellent agreement is obtained between the theoretical equations and HFSS, thus validating the computation of the theoretical reflection and transmission coefficients.

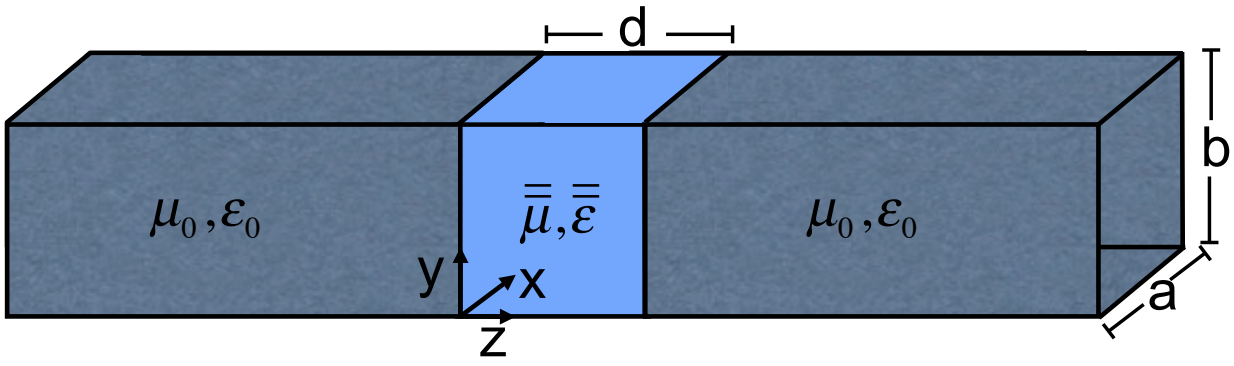

Figure 4.1: Rectangular waveguide with biaxial sample placed in cross-sectional region with waveguide extensions attached.

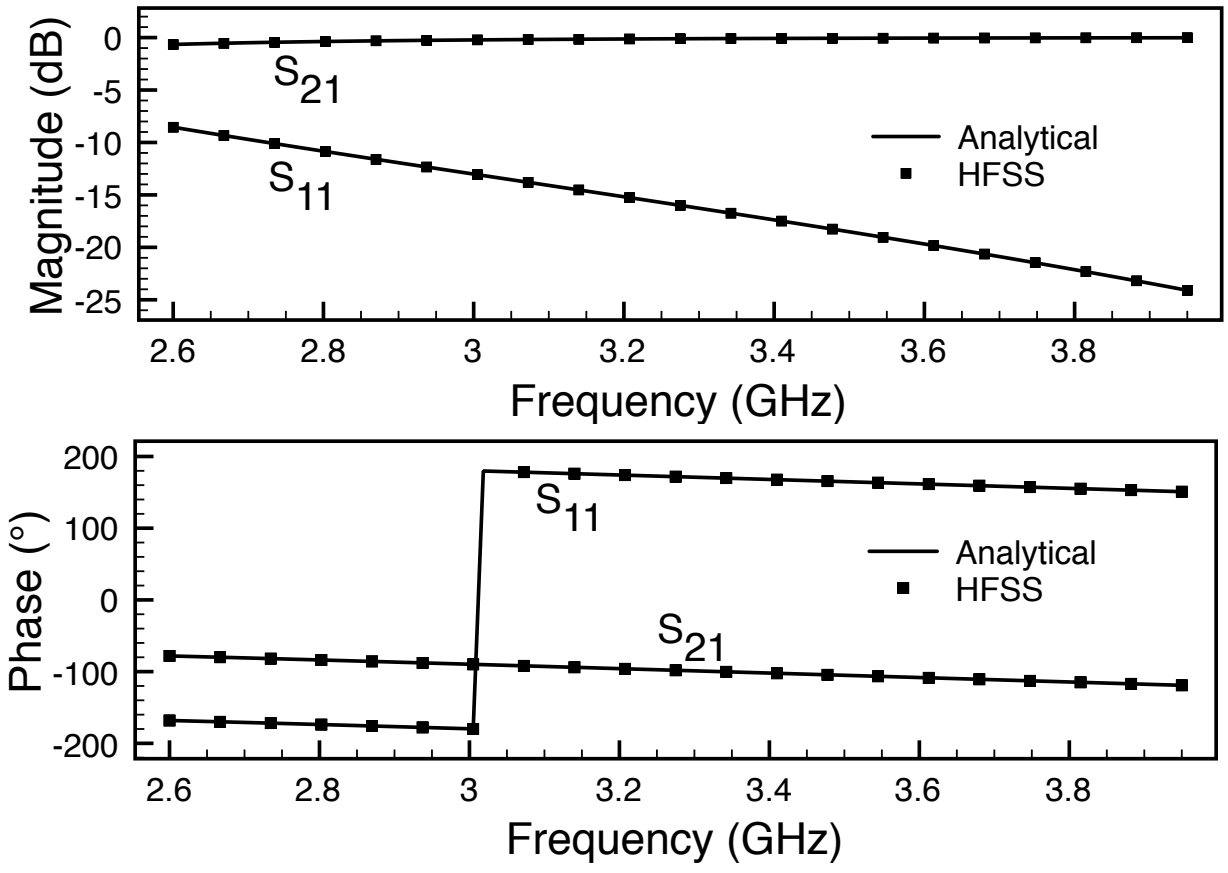

Figure 4.2: S-parameters computed for a biaxial test material.

4.2.3 Extraction Process

The interfacial reflection coefficient, Γ, and the propagation factor can be extracted form the measurements of R and T using an NRW method [23] - [24]. It is known that the measured S-parameters, S_{11}^m and S_{21}^m, are equal to the reflection and transmission coefficients, respectively. These S-parameters are used to determine the sample propagation constant β_1^s and the interfacial reflection coefficient Γ, which may in turn be used to find permittivities and permeabilities. Thus, as was done in Section 3.2.1, the S-parameters are combined into two auxiliary variables,

$$V_1 = S_{21}^m + S_{11}^m \tag{4.50}$$

$$V_2 = S_{21}^m - S_{11}^m. \tag{4.51}$$

Now using (4.39) and (4.49) these variable become

$$V_1 = \frac{P - \Gamma}{1 + \Gamma P} \tag{4.52}$$

$$V_2 = \frac{P - \Gamma}{1 - \Gamma P}. \tag{4.53}$$

Rearranging (4.52) to determine the propagation factor yields

$$P = \frac{V_1 - \Gamma}{1 - \Gamma V_1}. \tag{4.54}$$

Similarly rearranging (4.53) and then inserting (4.54) gives

$$V_2 - V_2\Gamma \left[\frac{V_1 - \Gamma}{1 - \Gamma V_1}\right] = \frac{V_1 - \Gamma}{1 - \Gamma V_1} - \Gamma. \tag{4.55}$$

Multiplying through by $1 - PV_1$ and simplifying the expression results in

$$\Gamma^2 - 2\Gamma X + 1 = 0, \tag{4.56}$$

where

$$X = \frac{1 - V_1 V_2}{V_1 - V_2}. \tag{4.57}$$

Using the quadratic equation, the solution to (4.56) is

$$\Gamma = X \pm \sqrt{X^2 - 1}, \tag{4.58}$$

where the appropriate sign is chosen such that $|\Gamma| \leq 1$.

Next, the propagation constant is determined using (4.34), such that

$$\beta_1^s = -\frac{\ln(P) \pm j2n\pi}{jd}, \tag{4.59}$$

where n depends on the thickness of the sample in terms of wavelengths. This n value is the same n value discussed in Section 3.2.4. Next (4.33) can be rearranged such that

$$\frac{Z_1^s}{Z_1^e} = \frac{1 + \Gamma}{1 - \Gamma}. \tag{4.60}$$

Using the expressions for the modal impedances, it can be shown that

$$\frac{Z_1^s}{Z_1^e} = \frac{\beta_1^e}{\beta_1^s}\mu_x. \tag{4.61}$$

Combining (4.60) and (4.61) gives

$$\mu_x = \frac{1 + \Gamma}{1 - \Gamma}\frac{\beta_1^s}{\beta_1^e}, \tag{4.62}$$

which is the first material parameter extracted from the measurements. Now using (4.8) an

expression for the next material parameter can be derived. First, factoring $k_0\sqrt{\mu_x}$ yields

$$\beta_1^s = k_0\sqrt{\mu_x}\sqrt{\epsilon_y - \frac{1}{\mu_z}\left(\frac{k_{c1}^s}{k_0}\right)^2} \tag{4.63}$$

or

$$\left(\frac{\beta_1^s}{k_0}\right)^2 = \mu_x\left[\epsilon_y - \frac{1}{\mu_z}\left(\frac{k_{c1}^s}{k_0}\right)^2\right]. \tag{4.64}$$

Next, inserting (4.62) and simplifying gives

$$\epsilon_y = \frac{\beta_1^s\beta_1^e}{k_0^2}\frac{1-\Gamma}{1+\Gamma} + \frac{1}{\mu_z}\left(\frac{k_{c1}^s}{k_0}\right)^2. \tag{4.65}$$

Thus, by measuring S_{11}^m and S_{21}^m from a biaxial sample filling the cross-section of a rectangular waveguide, two equations, (4.62) and (4.65), can be used to extract the two material parameters μ_x and ϵ_y. To determine the other four unknown material parameters, additional measurements are needed. A measurement procedure to determine all six parameters is discussed in the following section.

4.2.4 Measurement Procedure

Due to the rectangular shape of the waveguide, enough measurements for full tensor characterization can not be determined from one sample using the method discussed above. Multiple samples are required to obtain the additional measurements needed for characterization. At a minimum, three samples with the material tensor rotated in orthogonal orientations is required. To simplify the measurement procedure, consider the material tensors expressed

as

$$\overline{\overline{\epsilon}} = \epsilon_0 \begin{bmatrix} \epsilon_A & 0 & 0 \\ 0 & \epsilon_B & 0 \\ 0 & 0 & \epsilon_C \end{bmatrix} \tag{4.66}$$

and

$$\overline{\overline{\mu}} = \mu_0 \begin{bmatrix} \mu_A & 0 & 0 \\ 0 & \mu_B & 0 \\ 0 & 0 & \mu_C \end{bmatrix}. \tag{4.67}$$

The determination of the six relative biaxial material parameters $(\epsilon_A, \epsilon_B, \epsilon_C, \mu_A, \mu_B, \mu_C)$ requires a minimum of six independent measurements. The parameters can be determined by measuring S_{11} and S_{21} with each of the axes (A, B, C) individually aligned along the y-direction. The most straightforward approach is to measure the transmission and reflection coefficients for the samples placed with the A, B, C, axes under the following three orientations,

$$(A, B, C) \rightarrow (x, y, z) \Rightarrow \text{Sample } 1, \tag{4.68}$$

$$(A, B, C) \rightarrow (z, x, y) \Rightarrow \text{Sample } 2, \tag{4.69}$$

$$(A, B, C) \rightarrow (y, z, x) \Rightarrow \text{Sample } 3. \tag{4.70}$$

Using (4.62), the material parameters μ_A, μ_B, and μ_C can be extracted from the S-parameter measurements for Sample 1, Sample 2 and Sample 3, respectively. With all the permeabilities characterized, the permittivities, ϵ_A, ϵ_B, and ϵ_C, can be determined using (4.65), from the S-parameter measurements for Sample 3, Sample 1, and Sample 2, respectively.

The extraction process is validated using the fictitious material parameters listed in Table 4.1. These parameters are used in HFSS to generate S-parameters for the multiple samples with their material axes aligned in the three orientations previously described. The HFSS

analysis uses the same waveguide model as was used to simulate the data in Figure 4.2. Figure 4.3 and Figure 4.4 show the results of the permittivity characterization, while Figure 4.5 and Figure 4.6 show the permeability extraction. The results are in accordance with the values listed in Table 4.1 and give reassurance of the characterization technique before proceeding with the error and sensitivity analysis.

4.2.5 Error and Sensitivity Analysis

The error in the extracted material parameters may be placed into two categories. The first results from inaccuracies in the theoretical reflection and transmission coefficients, either because an imperfect mathematical model of the experimental apparatus is used, or because of errors in the numerical solution to the theoretical problem. The present analysis uses closed-form expressions for the reflection and transmission coefficients and therefore this type of error is not an issue.

The second source of error is due to measurement inaccuracies and can be divided into systematic error and random error. Systematic error mostly arises from the imperfect construction of the sample holder and fabricated sample. Construction inaccuracies can produce gaps between the sample and waveguide walls and cause uncertainty in geometric parameters such as sample length. Random error includes sample alignment (which may change from experiment to experiment) and measurement uncertainty inherent in the VNA. It is difficult to model the errors produced by uncertainty in the geometrical parameters, due to the analysis assumption that the sample completely fills the cross-section of the guide, and does not provide an accessible means for including air gaps or oversized samples. When measurements are carried out, attempts must be made to reduce this error to the greatest extent possible by using the smallest available manufacturing tolerances and ensuring that the sample fits tightly within the holder. It is expected that these errors should be similar to those encountered with other waveguide methods [27]-[48]. In comparison, propagation of the random error inherent to the VNA may be easily studied using Monte Carlo techniques,

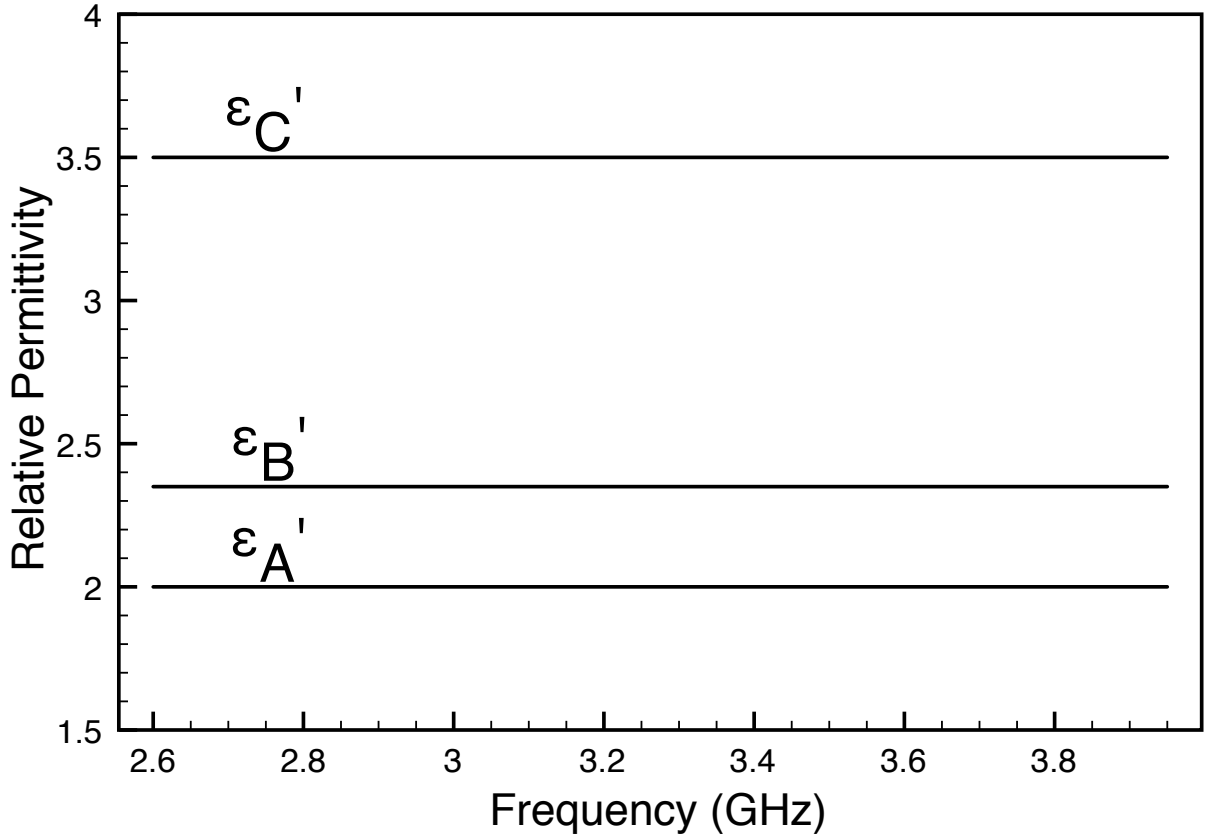

Figure 4.3: Permittivity extraction using HFSS generated S-parameters.

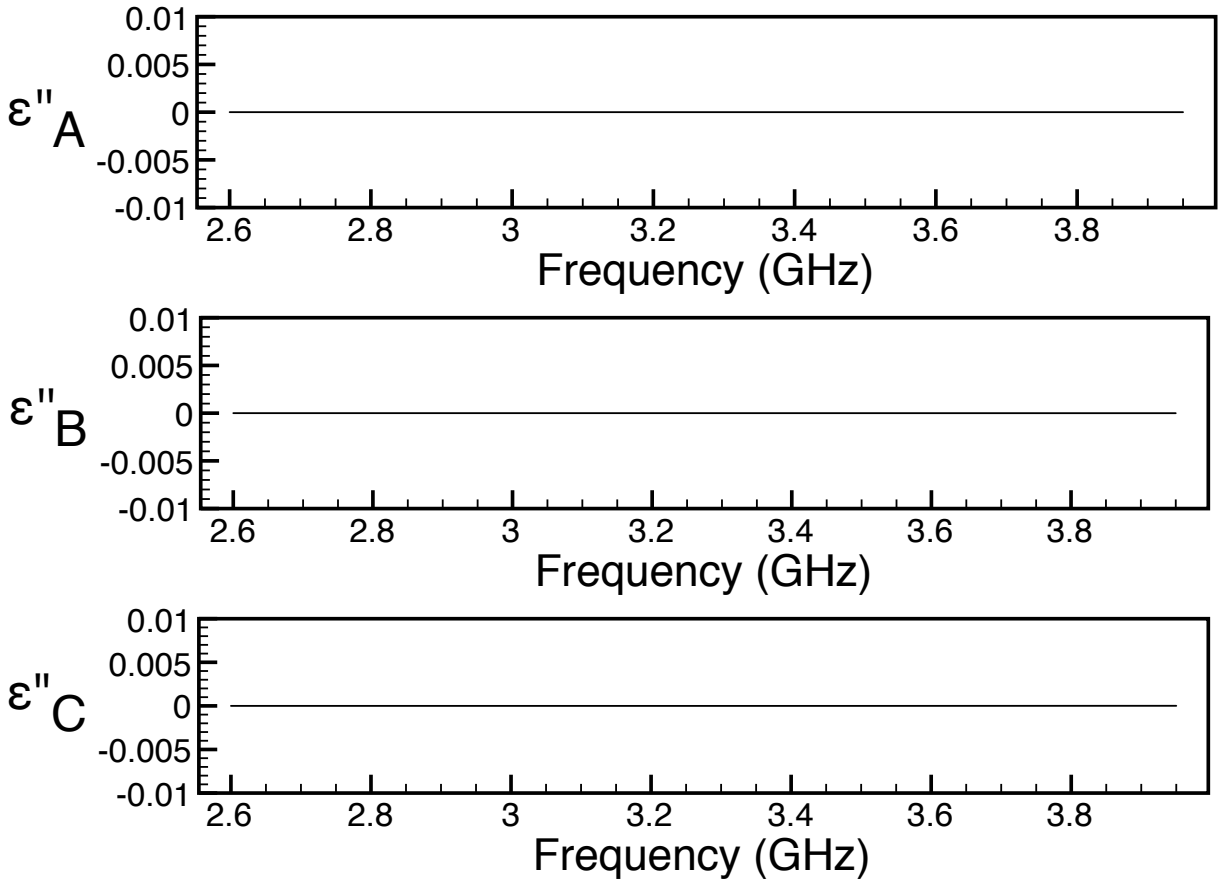

Figure 4.4: Permittivity extraction using HFSS generated S-parameters.

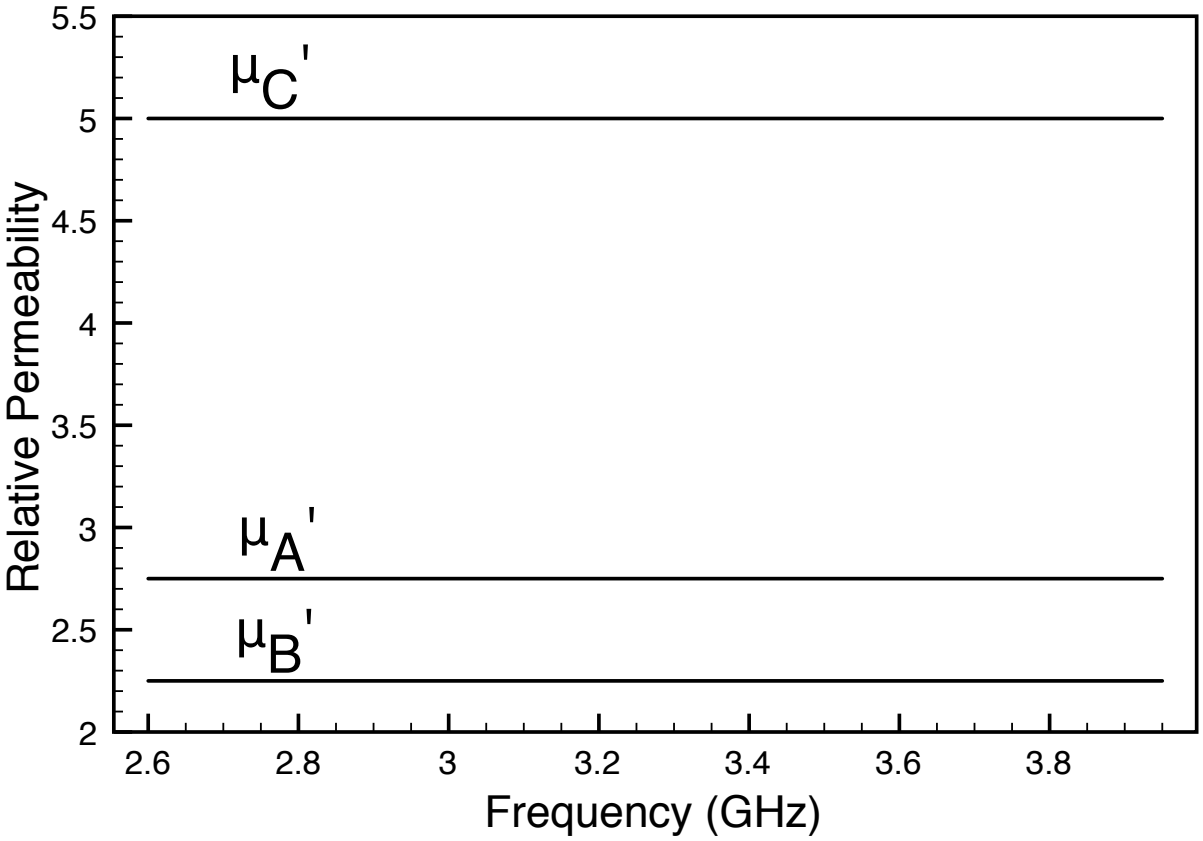

Figure 4.5: Permeability extraction using HFSS generated S-parameters.

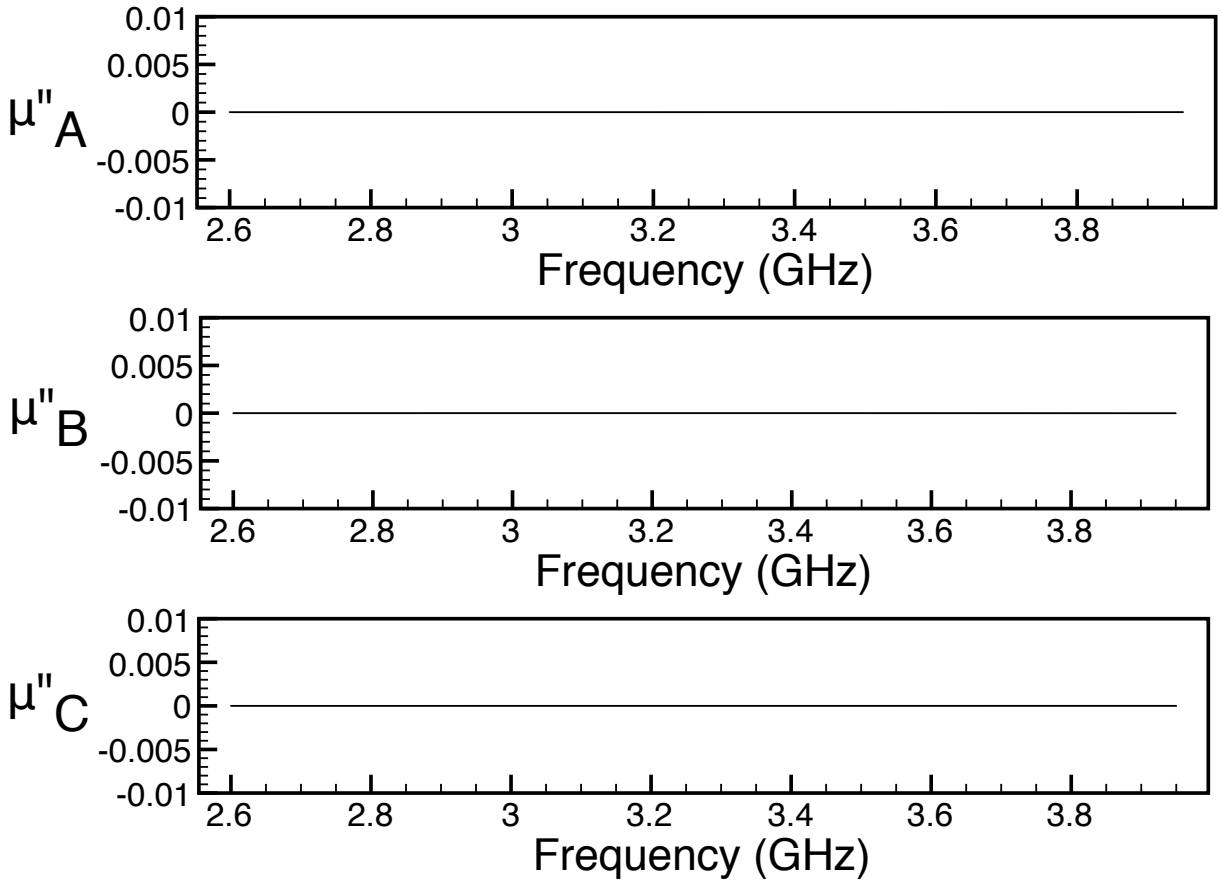

Figure 4.6: Permeability extraction using HFSS generated S-parameters.

and simple error bounds established.

The uncertainties of the measured S-parameters were determined for an HP8510C network analyzer system using the software package *HP 8510 Specifications & Performance Verification Program* provided by Hewlett Packard. Although VNA measurement uncertainty is dependent on S-parameter amplitudes, for the range of amplitudes encountered in this work the VNA measurement uncertainty can be assumed independent of amplitude and frequency. Statistical variance of S_{11} is specified linearly in amplitude and phase, and for the equipment used in the experiment, values of $\sigma_{A_{11}} = 0.004$ and $\sigma_{\phi_{11}} = 0.8^\circ$ were indicated. Variance of S_{21} is specified logarithmically in amplitude and linearly in phase, and values of $\sigma_{A_{21}} = 0.04$ dB and $\sigma_{\phi_{21}} = 2.0^\circ$ were found to be appropriate.

The fictitious test material describe in Table 4.1 was used in the the Monte Carlo analysis of the propagation of VNA uncertainty. The geometry of the sample is $a = 72.136$ mm, $b = 34.036$ mm, and $d = 10$ mm. The forward problem was solved at 31 frequency points over the portion of S-band from 2.6 to 3.95 GHz with the axes of the material tensor aligned in the three orientation outlined in Section Figure 4.2.4. White gaussian noise was then added to each of the S-parameter sets, and the noisy data was used to extract the material parameters. The standard deviations used to generate the additive noise are those indicated by the *HP 8510 Specifications & Performance Verification Program*. This Monte Carlo analysis used $100,000$ trials, and the average values of the material parameters were calculated, along with the standard deviations. Figure 4.7 - 4.10 show the results of the Monte Carlo error analysis. In these figures, the center of each triplet of lines is the average value of the $100,00$ trials, while the two surrounding lines indicate the 95% confidence interval of ± 2 standard deviations. The error in the extracted material parameters due to S-parameter noise is small when comparing to other material characterization techniques in this dissertation. This is to be expected since this technique is an extension of the NRW method, which is often used due to its insensitivity to measurement error.

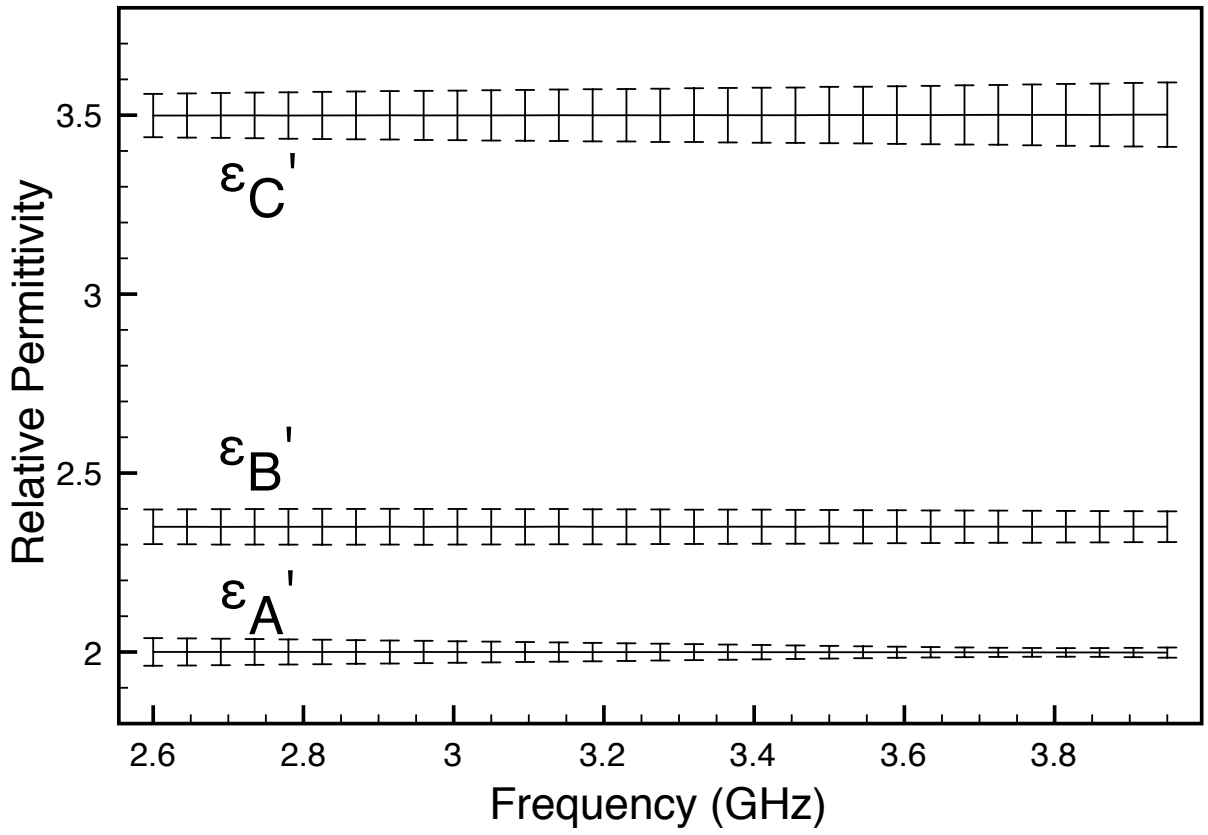

Figure 4.7: Real relative permittivities for a fictitious material extracted using 100,000 random trials. Center line is the average of the trials. Upper and lower bars show the 95% confidence interval.

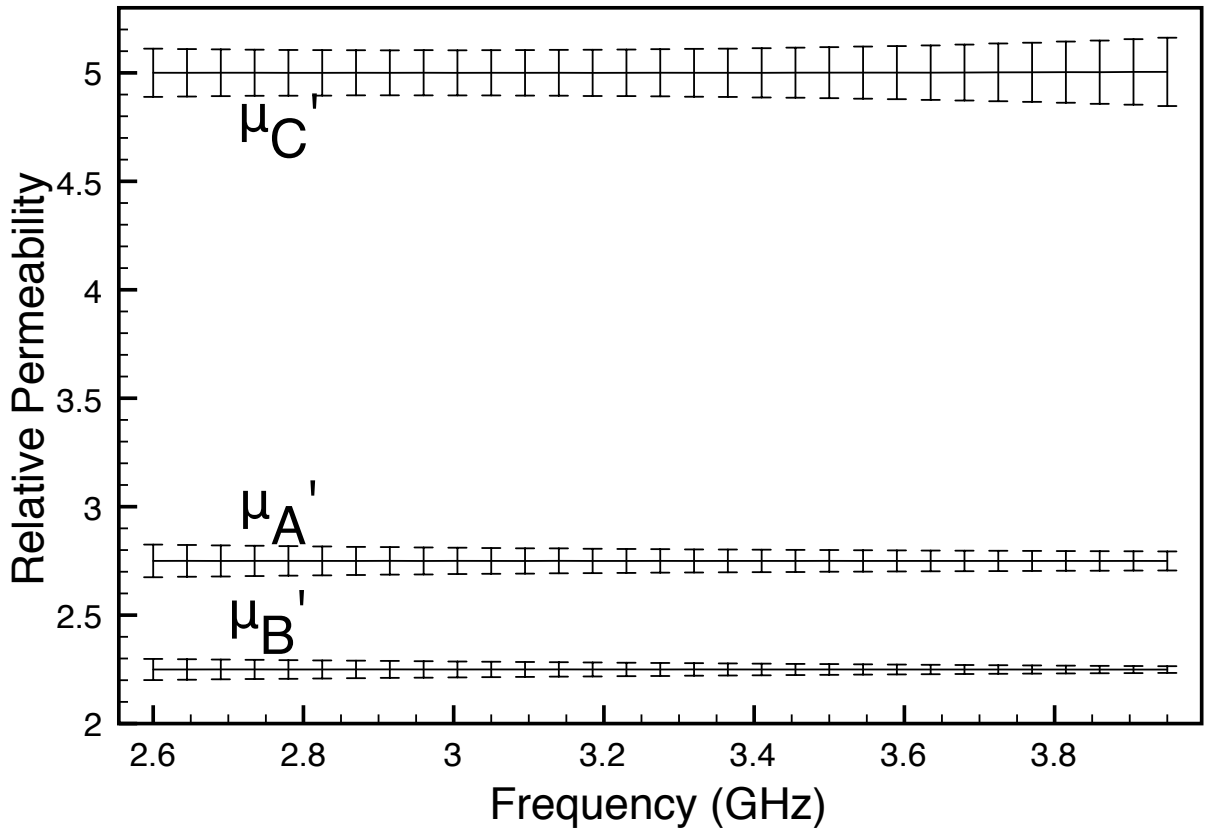

Figure 4.8: Real relative permeabilities for a fictitious material extracted using 100,000 random trials. Center line is the average of the trials. Upper and lower bars show the 95% confidence interval.

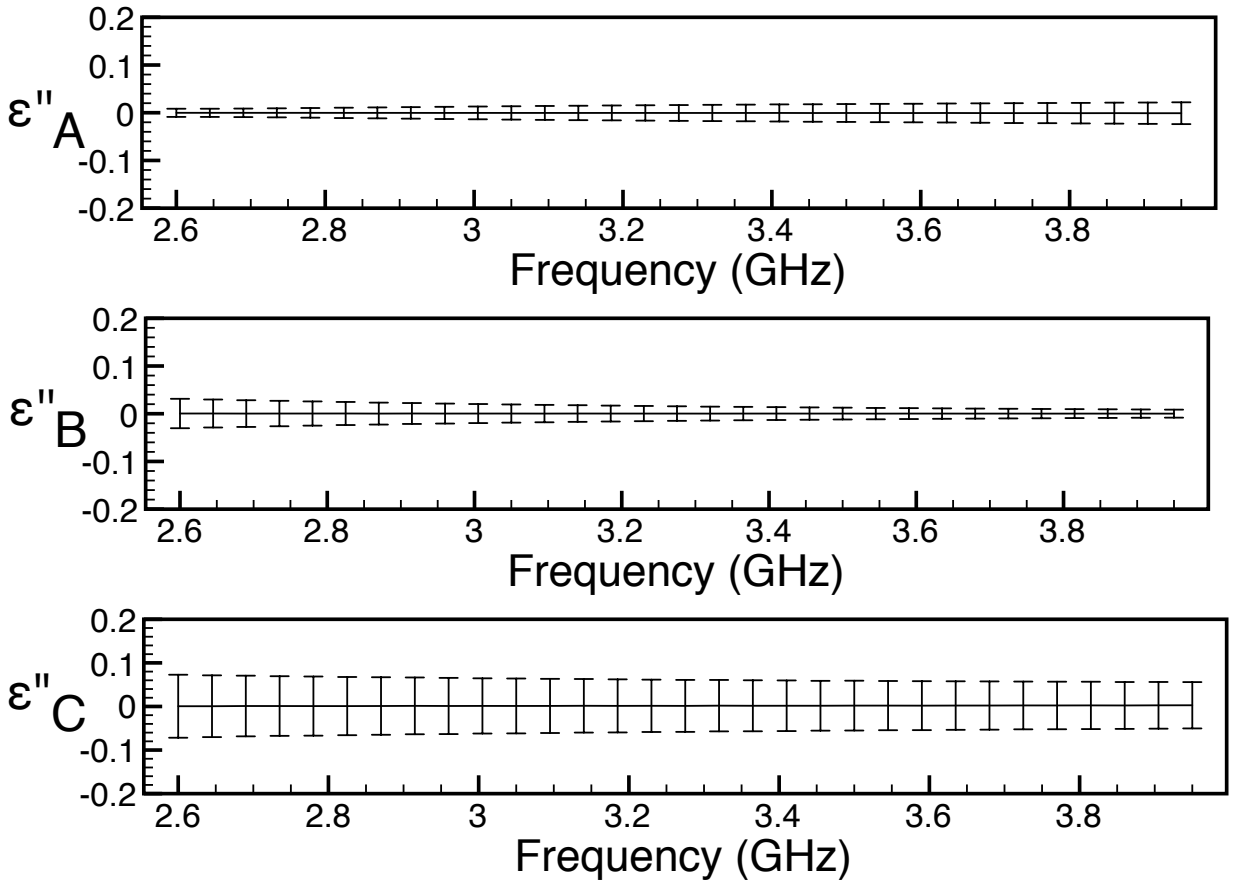

Figure 4.9: Imaginary relative permittivities for a fictitious material extracted using 100,000 random trials. Center line is the average of the trials. Upper and lower bars show the 95% confidence interval.

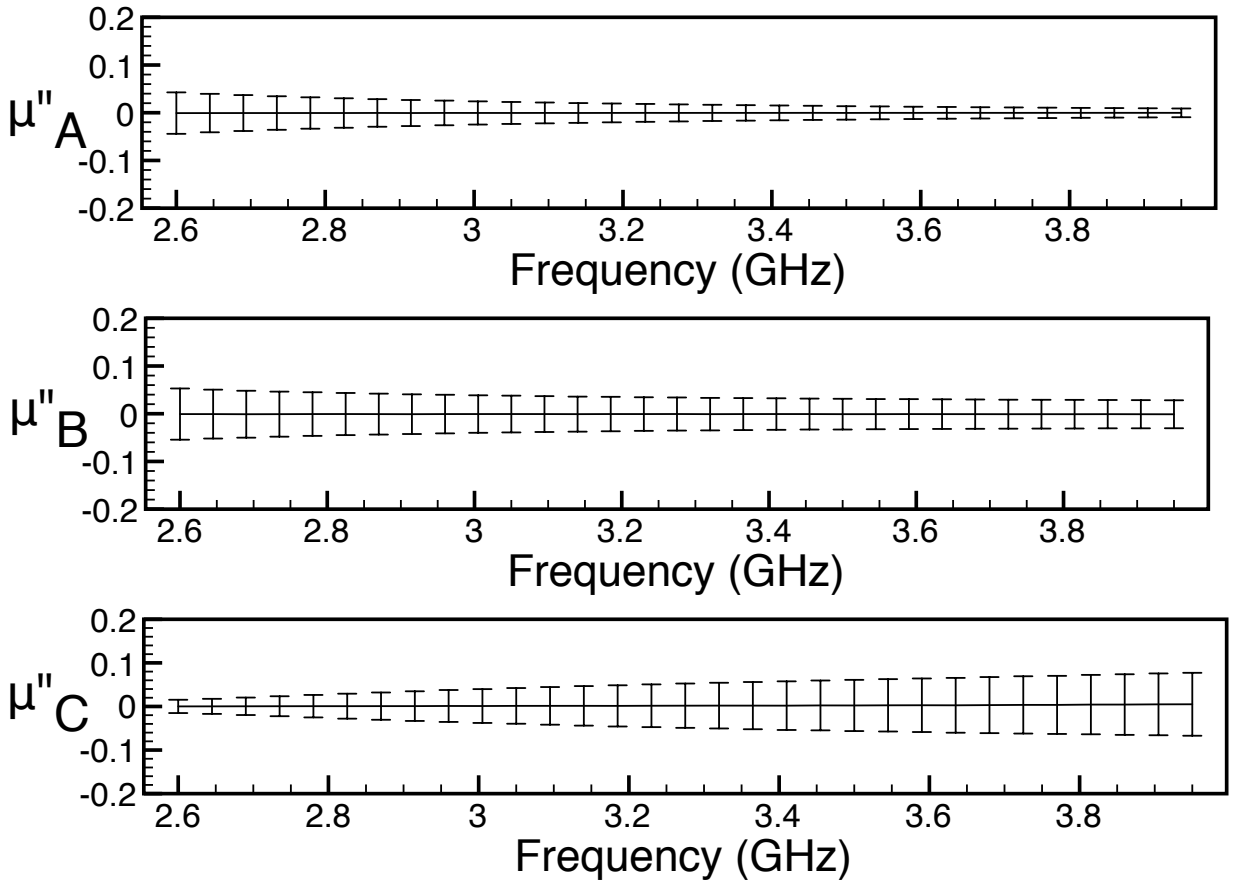

Figure 4.10: Imaginary relative permeabilities for a fictitious material extracted using 100,000 random trials. Center line is the average of the trials. Upper and lower bars show the 95% confidence interval.

4.2.6 Summary

An extension of the NRW method to biaxially anisotropic materials was introduced. Closed-form expressions were given to characterize the six complex material parameters. A step toward validation was gained using the HFSS generated S-parameters for characterization of the fictitious test sample. The performance of the technique was established using a Monte Carlo error analysis based on network analyzer error. Total validation of the technique was not completed since no measurements of biaxial material were conducted. The major flaw of this approach is requiring three distinct samples completely filling the cross-section of the waveguide. To eliminate this issue, the following section describes a technique in which biaxial material can be characterized using a single sample.

4.3 Material Characterization of Biaxial Material Using a Reduced Aperture Waveguide

This section presents a convenient waveguide method that allows full biaxial tensor characterization using a single sample, in comparison to the multiple samples needed in the method described in the previous section. The theory and results described here are also published in [49]. A sample manufactured in the shape of a cube is placed into a reduced-aperture square-waveguide sample holder, and the transmission and reflection coefficients are measured with the cube in several orientations. Inversion is accomplished by minimizing the difference between the theoretical reflection and transmission coefficients and the measured S-parameters. Ideally, only three orientations are required, but it has been found that by measuring the S-parameters at a fourth orientation the numerical complexity of parameter extraction is reduced significantly. Because a carefully computed forward problem is needed for accurate characterization, a mode-matching approach is used to obtain the theoretical reflection and transmission coefficients. This allows the error in the forward problem to be

easily controlled by specifying an appropriate number of modes.

4.3.1 Theoretical Transmission and Reflection Coefficients Using Mode-Matching Analysis

The material under test (MUT) is assumed to be linear and homogeneous, with a permittivity and a permeability that are biaxial along the orthogonal axes A, B, and C. The MUT thus has the tensor constitutive parameters

$$\overline{\overline{\epsilon}} = \epsilon_0 \begin{bmatrix} \epsilon_A & 0 & 0 \\ 0 & \epsilon_B & 0 \\ 0 & 0 & \epsilon_C \end{bmatrix} \tag{4.71}$$

and

$$\overline{\overline{\mu}} = \mu_0 \begin{bmatrix} \mu_A & 0 & 0 \\ 0 & \mu_B & 0 \\ 0 & 0 & \mu_C \end{bmatrix}, \tag{4.72}$$

where the values ϵ_A, μ_A, etc., are relative parameters, and are complex quantities: $\epsilon_A = \epsilon'_A + j\epsilon''_A$, $\mu_A = \mu'_A + j\mu''_A$, etc.

The reduced aperture waveguide dimensions, shown in 4.11, consists of empty waveguide extensions connected to a sample holder that is completely filled by the MUT. A cross-section view of the reduced-aperture guide is shown in 4.12. The MUT and associated sample holder are cubical, allowing the same sample to be inserted in 24 different orientations. The width and length of the sample holder are chosen to be identical to the height of the waveguide extensions. It is assumed that the lengths of the extensions are such that a single TE_{10} rectangular waveguide mode is incident on the sample holder from the sending ($z < 0$) extension, and that a single mode appears at the end of the receiving ($z > d$) extension.

Since the constitutive material parameters are determined by minimizing the difference between the measured and the theoretically computed reflection and transmission coeffi-

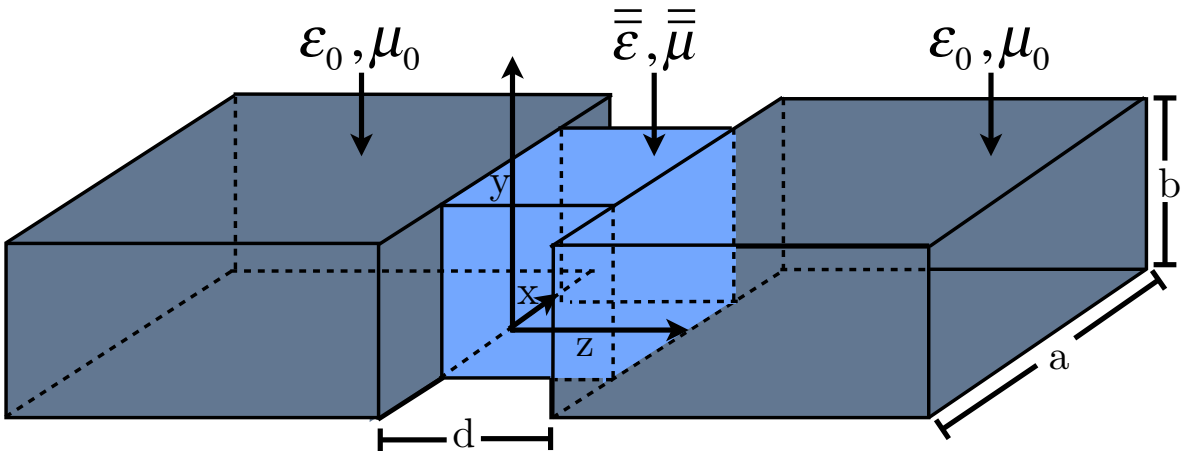

Figure 4.11: Waveguide cubical sample holder with waveguide extensions attached.

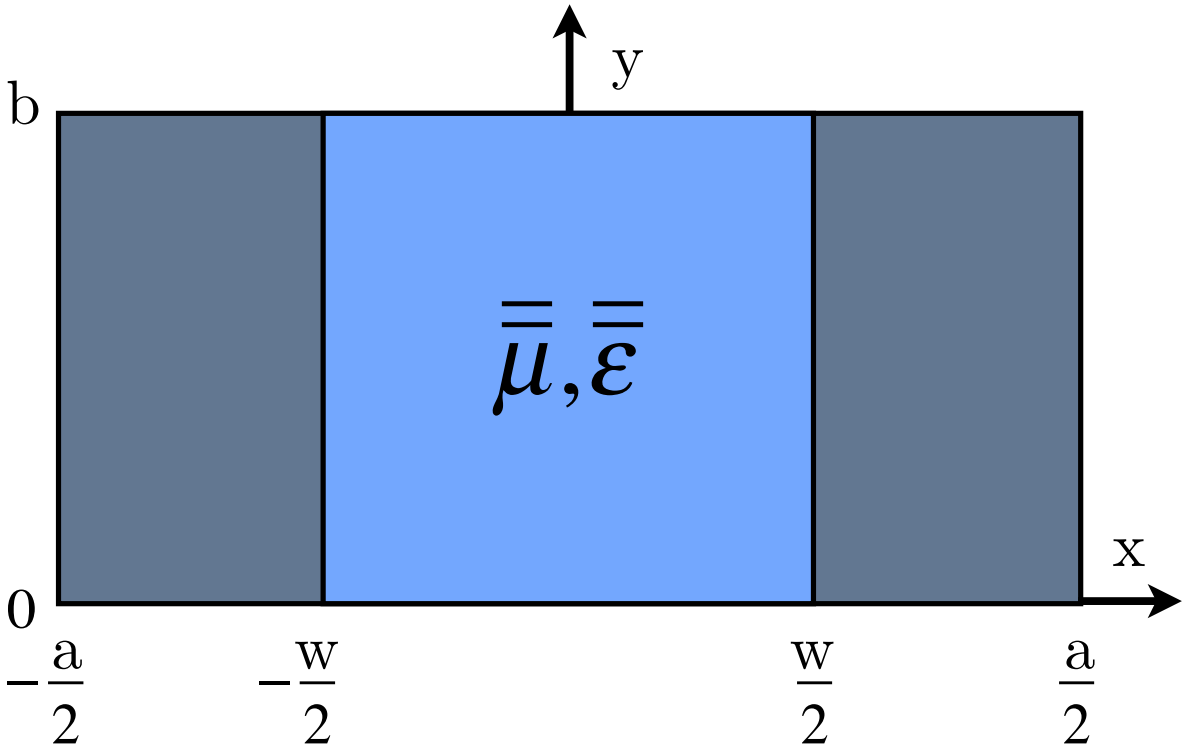

Figure 4.12: Cross-sectional view of reduced-aperture waveguide.

cients, accurate material characterization depends on careful modeling of the measurement apparatus. This is accomplished by computing the S-parameters of the reduced-aperture waveguide system using a mode-matching technique, which accommodates the higher order modes excited at the interface between the empty waveguide extensions and the sample holder. In this manner, the modeling error can be controlled in a predictable fashion.

Although a single TE_{10} rectangular waveguide mode is incident on the sample holder, as shown in 4.13, because of mode conversion at the discontinuity with the reduced aperture an infinite number of waveguide modes are reflected into the transmitting extension, while an infinite number of waveguide modes are transmitted into the sample region $0 < z < d$. The transmitted modal fields are incident on the discontinuity at $z = d$, and thus a spectrum of modes is also reflected back into the sample region, and transmitted into the rectangular waveguide receiving extension. However, because the electric field of the incident TE_{10} mode is even about $x = 0$, and because the aperture is symmetric about $x = 0$, only modes with electric fields even about $x = 0$ will be excited. Thus, only TE_{n0} modes with odd values of n are needed to describe the fields in each of the waveguide regions. Note that since the fields in the waveguide section filled with biaxial material are of similar structure to those in the empty waveguide extensions, modes in all sections can be numbered identically.

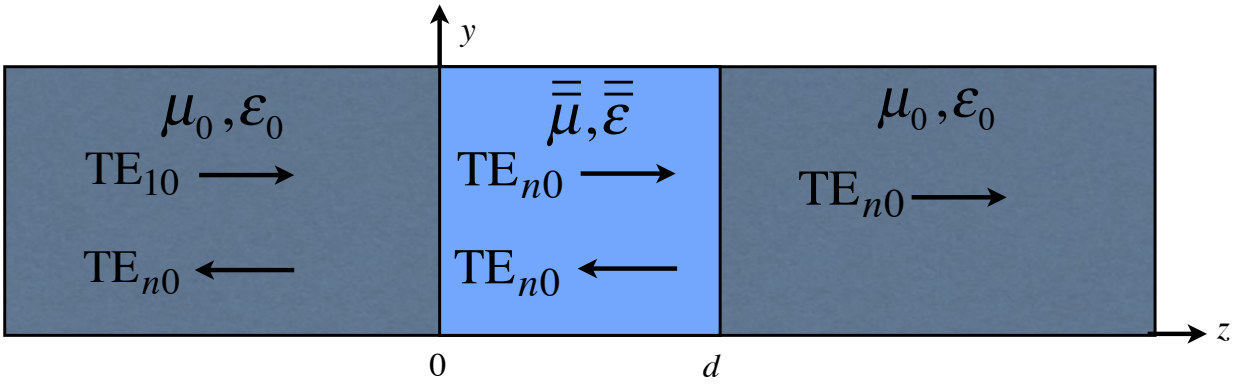

Figure 4.13: Side view of reduced aperture waveguide.

4.3.1.1 Field Structure in a Waveguide Filled with Biaxial Material

The material sample can be placed into the cubical sample holder in a number of orientations. Assume that an orientation has been chosen such that the material is biaxial along the directions x, y and z of 4.11. The wave equation for $H_z(x,y)$ for TE_z fields in the sample region is given by (2.189) where μ_x, ϵ_x, etc., are relative parameters, and $k_0 = \omega\sqrt{\mu_0\epsilon_0}$ is the free-space wavenumber. For TE_{n0} modes in a rectangular waveguide there is no $y-$dependence of the fields and the wave equation reduces to (2.190). This wave equation is written again in this section to reiterate what material parameters are used in the calculation of the forward problem:

$$\left[\frac{\partial^2}{\partial x^2} + \left(k_{cn}^s\right)^2\right] H_z^s(x) = 0 \tag{4.73}$$

where

$$\left(k_{cn}^s\right)^2 = \frac{\mu_z}{\mu_x}\left[k_0^2\mu_x\epsilon_y - \left(\beta_n^s\right)^2\right] \tag{4.74}$$

is the cutoff wavenumber. This equation is solved using separation of variables and applying the boundary conditions on the tangential electric field at the perfectly conducting waveguide walls in Section 2.3.2.1. This leads to the following expressions for the transverse fields

$$E_y^s(x,z) = C_n e_{yn}^s(x)\,\mathrm{e}^{j\beta_n^s z} \tag{4.75}$$

$$H_x^s(x,z) = \mp C_n h_{yn}^s(x)\,\mathrm{e}^{\pm j\beta_n^s z}, \tag{4.76}$$

where the transverse modal fields are

$$e_{yn}^s(x) = -k_{cn}^s \sin\left[k_{cn}^s\left(x - \frac{w}{2}\right)\right], \quad h_{xn}^s(x) = -\frac{e_{yn}^s(x)}{Z_n^s}. \tag{4.77}$$

Here $w = b$ is the width of the guide, $k_{cn}^s = n\pi/w$ is the cutoff wavenumber for the n^{th} TE_{n0} mode ($n = 1, 2, \ldots$), and $Z_n^s = \eta_0\mu_x(k_0/\beta_n^s)$ is the modal wave impedance with $\eta_0 = \sqrt{\mu_0/\epsilon_0}$ the free-space intrinsic impedance. Note that β_n^s is determined from k_{cn}^s

using (4.74).

The isotropic transverse field equations from (2.151) and (2.152) can be used in this empty guide region for the present technique where the width of the waveguide is centered about the y-axis, as long as sinusoidal functions will be offset by $a/2$. Also, since only TE_{n0} modes are excited, $v = 0$ for all excited modes. This leads to $k_{yn} = 0$, reducing the transverse field equations to

$$E_y^e(x,z) = C_n e_{yn}^e(x)\, \mathrm{e}^{\pm j\beta_n^e z} \tag{4.78}$$

$$H_x^e(x,z) = \mp C_n h_{xn}^e(x)\, \mathrm{e}^{\pm j\beta_n^e z}. \tag{4.79}$$

Here e_{yn}^e and h_{xn}^e are the transverse electric and magnetic modal fields in the empty guide, respectively, and are shown from (2.153) and (2.154) to be

$$e_{yn}^e(x) = -k_{xn}^e \sin\left[k_{xn}^e\left(x - \frac{a}{2}\right)\right], \tag{4.80}$$

$$h_{xn}^e(x) = -\frac{e_{yn}^e(x)}{Z_n^e}, \tag{4.81}$$

where $k_{xn}^e = n\pi/a$ and $Z_n^e = \eta_0(k_0/\beta_n^e)$, with β_n^e determined from k_{cn}^e through

$$\beta_n^e = \sqrt{k_0^2 - (k_{cn}^e)^2}. \tag{4.82}$$

4.3.1.2 Solution for S-Parameters Using Modal Expansions

The transverse fields in the sample holder and in the waveguide extensions can be expanded in an infinite sum of modal fields, with modal amplitudes to be determined through application

of appropriate boundary conditions. For the empty waveguide extension region $z < 0$,

$$E_y(x,z) = A_1^+ e_{y1}^e(x) \mathrm{e}^{-j\beta_1^e z} + \sum_{\substack{n=1 \\ \text{odd}}}^{\infty} A_n^- e_{yn}^e(x) \mathrm{e}^{j\beta_n^e z} \tag{4.83}$$

$$H_x(x,z) = A_1^+ h_{y1}^e(x) \mathrm{e}^{-j\beta_1^e z} - \sum_{\substack{n=1 \\ \text{odd}}}^{\infty} A_n^- h_{yn}^e(x) \mathrm{e}^{j\beta_n^e z}. \tag{4.84}$$

Here A_1^+ is the amplitude of the incident TE_{10} wave, which is taken to be known during analysis. In the sample holder, $0 < z < d$, the transverse fields are

$$E_y(x,z) = \sum_{\substack{n=1 \\ \text{odd}}}^{\infty} \left[B_n^+ \mathrm{e}^{-j\beta_n^s z} + B_n^- \mathrm{e}^{j\beta_n^s z} \right] e_{yn}^s(x) \tag{4.85}$$

$$H_x(x,z) = \sum_{\substack{n=1 \\ \text{odd}}}^{\infty} \left[B_n^+ \mathrm{e}^{-j\beta_n^s z} - B_n^- \mathrm{e}^{j\beta_n^s z} \right] h_{yn}^s(x). \tag{4.86}$$

Finally, in the waveguide extension $z > d$ the fields are

$$E_y(x,z) = \sum_{\substack{n=1 \\ \text{odd}}}^{\infty} C_n^+ e_{yn}^e(x) \mathrm{e}^{-j\beta_n^e (z-d)} \tag{4.87}$$

$$H_x(x,z) = \sum_{\substack{n=1 \\ \text{odd}}}^{\infty} C_n^+ h_{yn}^e(x) \mathrm{e}^{-j\beta_n^e (z-d)}. \tag{4.88}$$

The modal amplitudes A_n^-, B_n^+, B_n^- and C_n^+ may be determined by applying the boundary conditions on E_y and H_x at the interfaces between the two waveguide extensions and

the sample holder. At $z = 0$ the boundary condition on tangential electric field requires

$$A_1^+ e_{y1}^e(x) + \sum_{\substack{n=1 \\ \text{odd}}}^{\infty} A_n^- e_{yn}^e(x)$$

$$= \begin{cases} \sum_{\substack{n=1 \\ \text{odd}}}^{\infty} \left[B_n^+ + B_n^- \right] e_{yn}^s(x), & 0 < |x| < \frac{w}{2} \\ 0, & \frac{w}{2} < |x| < \frac{a}{2} \end{cases} \tag{4.89}$$

while the boundary condition on tangential magnetic field requires

$$A_1^+ h_{y1}^e(x) - \sum_{\substack{n=1 \\ \text{odd}}}^{\infty} A_n^- h_{yn}^e(x) =$$

$$\sum_{\substack{n=1 \\ \text{odd}}}^{\infty} \left[B_n^+ - B_n^- \right] h_{yn}^s(x), \qquad 0 < |x| < \frac{w}{2}. \tag{4.90}$$

At $z = d$ the boundary condition on tangential electric field requires

$$\sum_{\substack{n=1 \\ \text{odd}}}^{\infty} C_n^+ e_{yn}^e(x) =$$

$$\begin{cases} \sum_{\substack{n=1 \\ \text{odd}}}^{\infty} \left[B_n^+ \mathrm{e}^{-j\beta_n^s d} + B_n^- \mathrm{e}^{j\beta_n^s d} \right] e_{yn}^s(x), & 0 < |x| < \frac{w}{2} \\ 0, & \frac{w}{2} < |x| < \frac{a}{2} \end{cases} \tag{4.91}$$

while the boundary condition on tangential magnetic field requires

$$\sum_{\substack{n=1 \\ \text{odd}}}^{\infty} C_n^+ h_{yn}^e(x) =$$

$$\sum_{\substack{n=1 \\ \text{odd}}}^{\infty} \left[B_n^+ \mathrm{e}^{-j\beta_n^s d} - B_n^- \mathrm{e}^{j\beta_n^s d} \right] h_{yn}^s(x), \quad 0 < |x| < \frac{w}{2}. \tag{4.92}$$

To convert the system of functional equations (4.89)-(4.92) to a system of linear equations, the infinite summations are each truncated at N terms and the following testing operations are applied. First, (4.89) is multiplied by $e^e_{ym}(x)$ and integrated over $-a/2 < x < a/2$. Second, (4.90) is multiplied by $Z^s_m h^s_{xm}(x)$ and integrated over $-w/2 < x < w/2$. Third, (4.91) is multiplied by $e^e_{ym}(x)$ and integrated over $-a/2 < x < a/2$. Lastly, (4.92) is multiplied by $Z^s_m h^s_{xm}(x)$ and integrated over $-w/2 < x < w/2$. Here $1 \leq m \leq N$. This yields the $4N \times 4N$ matrix equation

$$\left[\begin{array}{c|c|c|c} -D_{mn} & F_{mn} & 0 & F_{mn}e_n \\ \hline P_{mn} & Q_{mn} & 0 & -Q_{mn}e_n \\ \hline 0 & F_{mn}e_n & -D_{mn} & F_{mn} \\ \hline 0 & -Q_{mn}e_n & P_{mn} & Q_{mn} \end{array}\right] \left[\begin{array}{c} A^-_n \\ \hline B^+_n \\ \hline C^+_n \\ \hline b^-_n \end{array}\right] = A^+_1 \left[\begin{array}{c} D_{m1} \\ \hline P_{m1} \\ \hline 0 \\ \hline 0 \end{array}\right]. \tag{4.93}$$

Here the indices m and n are unique to each submatrix, $e_n = \exp\{-j\beta^s_n d\}$, and $b^-_n = B^-_n / e_n$. Note that b^-_n is introduced to avoid overflow during computation. In (4.93), D_{mn}, Q_{mn}, P_{mn} and F_{mn} are $N \times N$ sub-matrices with entries specified in Appendix B.2. Once the modal coefficients are found, the S-parameters of the system are given by

$$S_{11} = \frac{A^-_1}{A^+_1}, \quad S_{21} = \frac{C^+_1}{A^+_1}. \tag{4.94}$$

4.3.2 Specification of Computational Accuracy

To assess the performance of the extraction procedure, it is important to have a clear measure of the accuracy of the computed theoretical S-parameters. With the mode-matching approach this is easily done by terminating the modal series at N terms and properly choosing N. Rather than merely truncating the modal series when a specified accuracy has been achieved, the extrapolation technique described in [50] is used. It is found that the S-parameters may be extrapolated to the limit as $1/N \to 0$, with N the number of modes used

in both the sample region and in the waveguide extensions. To show how the S-parameters converge as a function of $1/N$ a sample of teflon placed inside an S-band reduced aperture sample holder is considered. The teflon sample is taken to be a lossless dielectric with real relative permittivity of 2.1. The dimensions for the S-band system are $a = 72.136$ mm and $b = w = d = 34.036$ mm. Figure 4.14 shows the reflection and transmission coefficients at 2.6 GHz. It is desirable to estimate the effect of using an infinite number of modes without the use of a large number of modes. By examining the magnitude and phase of the S-parameters vs. $1/N$, a trend may exist in which the value for the magnitude and phase can be extrapolated to estimate their values when $1/N = 0$, which corresponds to $N = \infty$; this produces an improved estimate of the reflection and transmission coefficients.

Several different extrapolation methods exist, including linear extrapolation, polynomial extrapolation, and least squares. Examining Figure 4.14 shows there is a linear trend to the data. This linear trend suggests that a simple linear extrapolation can be used to estimate modal series as N approaches ∞. A similar trend is seen when examining the other frequencies across the band. The linear trend may also be seen for coefficients computed in the middle of the frequency band of interest, 3.275 GHz, in 4.15, and may also be seen for the upper end, 3.95 GHz, in Figure 4.16.

The series is terminated when the extrapolated values of the magnitude and phase of the S-parameters have reached specified tolerances for M contiguous values of N. Experience shows that a value of $M = 5$ is sufficient to guarantee convergence to desired accuracy in the method presented here. It is found that by using this extrapolation technique, the S-Parameters may be efficiently computed to high tolerance with many fewer terms in the modal series compared to truncation based on using the value of the series.

4.3.3 Validation of Theoretical Analysis

It is important to validate the theoretical model before employing it in parameter extraction. To do this, a fictitious biaxial test material is considered, with material parameters shown

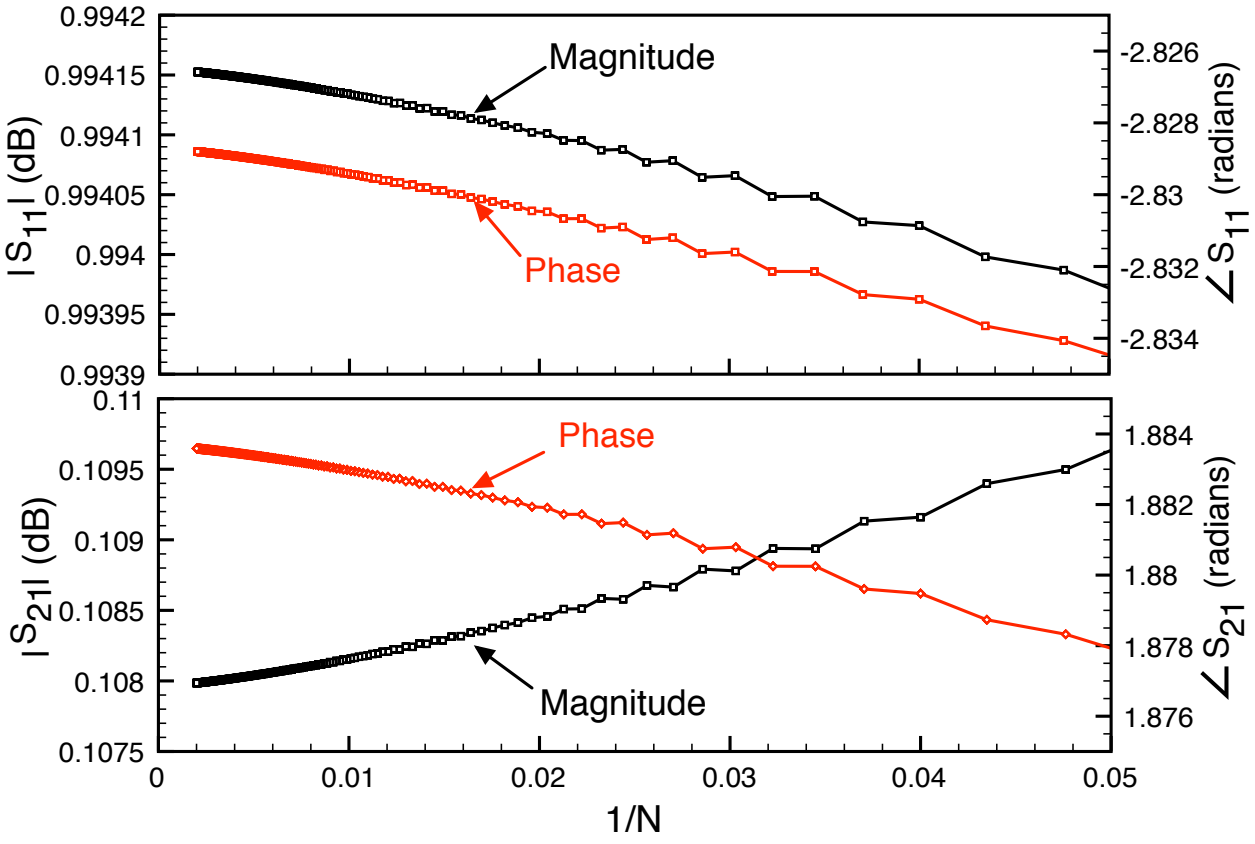

Figure 4.14: Magnitude and phase of reflection and transmission coefficients for teflon sample completely filling reduced-aperture waveguide sample regions at 2.6 GHz. These coefficients are plotted vs. $1/N$.

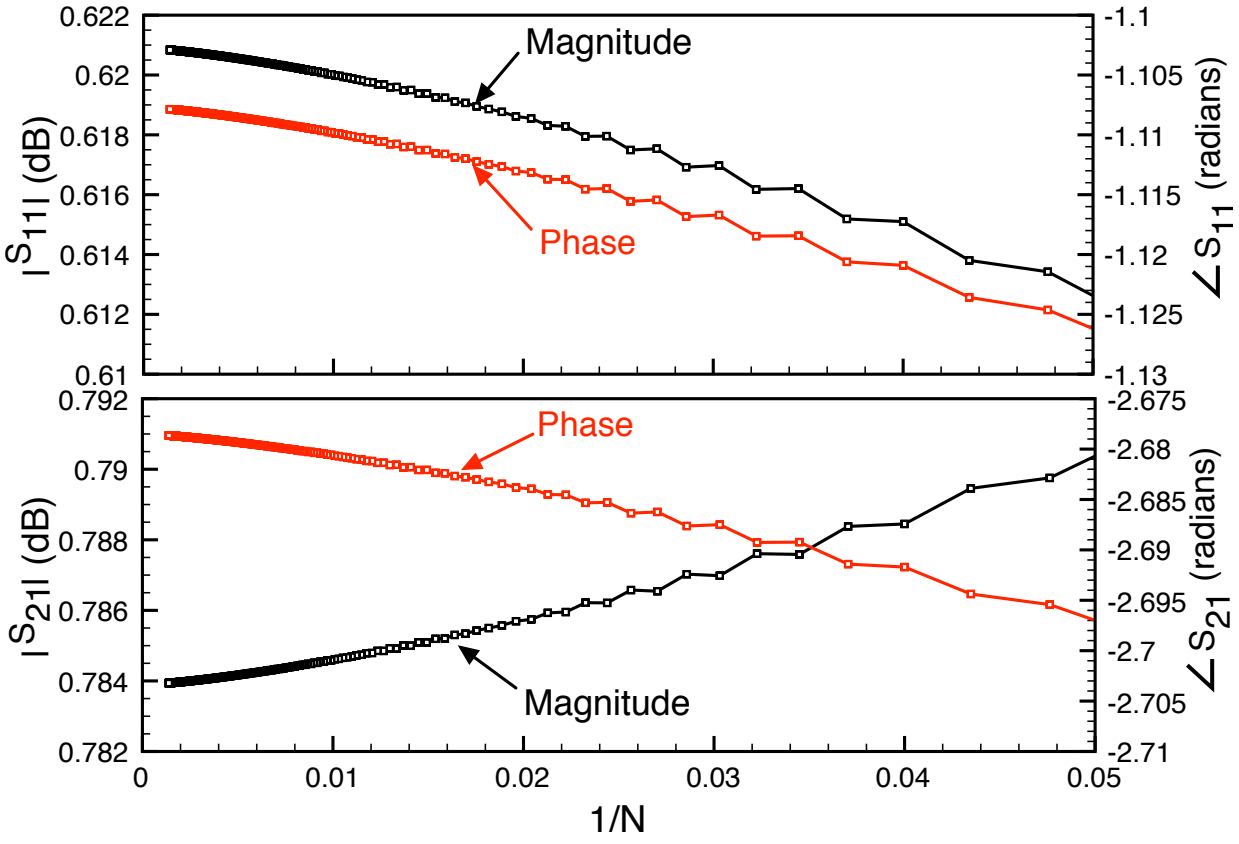

Figure 4.15: Magnitude and phase of reflection and transmission coefficients for teflon sample completely filling reduced-aperture waveguide sample regions at 3.275 GHz. These coefficients are plotted vs. $1/N$.

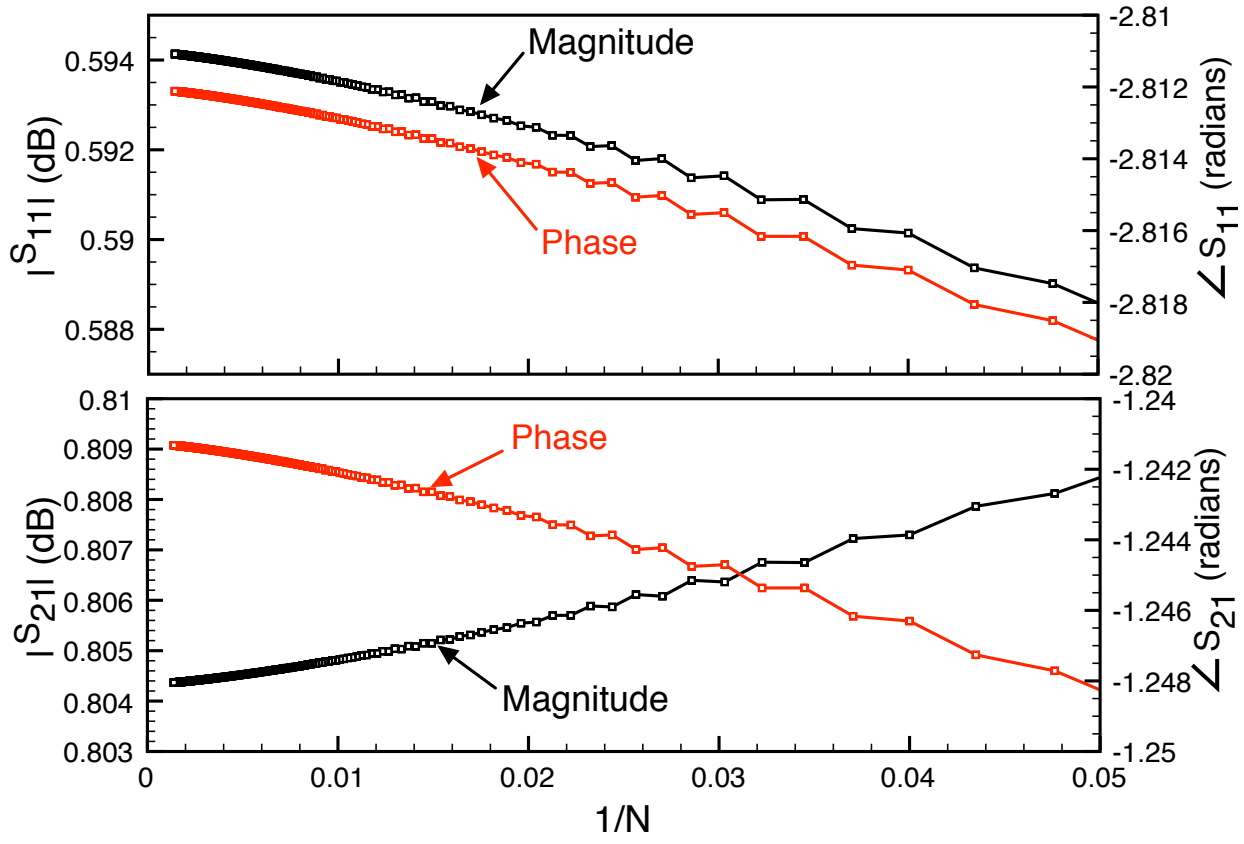

Figure 4.16: Magnitude and phase of reflection and transmission coefficients for teflon sample completely filling reduced-aperture waveguide sample regions at 3.95 GHz. These coefficients are plotted vs. $1/N$.

in Figure 4.2. By using a fictitious material, each of the parameters can be chosen to have different values, allowing for the most general validation of the theory.

Table 4.2: Material parameters for a fictitious biaxial material.

Parameter	Value
ϵ_A	2-j0.1
ϵ_B	4-j0.5
ϵ_C	3-j0
μ_A	1-j0.2
μ_B	2.5-j0
μ_C	2-j1

The mode matching technique was used to compute the S-parameters for the fictitious material placed into a cubical sample holder in an S-band waveguide system. Figure 4.17 shows S_{11} and S_{21} computed using the modal series with the orientation $(A, B, C) \rightarrow (x, y, z)$, meaning that the A-axis of the sample is aligned with the x-axis of the waveguide, etc. Absolute tolerances of 0.1 dB for $|S|$ and 0.01° for $\angle S$ were chosen so that the accuracy of the computed series is significantly better than the expected measurement accuracy of the HP 8510C vector network analyzer (VNA) used in subsequent experiments. For the material considered, the S-parameters typically converge to the specified tolerances within $N = 81$ terms.

Also shown in Figure 4.17 are the values of the S-parameters computed using the commercial EM solver HFSS. The waveguide extensions must be explicitly modeled in HFSS, and must be sufficiently long to ensure that only the fundamental TE_{10} mode propagates at the waveguide ports. Here the extensions were chosen to be 82.98 mm in length. The convergence tolerance in HFSS was specified as a maximum delta S of 0.001, which is the absolute difference between S-parameters from two iterations at the solution frequency of 3.95 GHz. It is seen that excellent agreement is obtained between the modal analysis and HFSS, validating the modal computation of the theoretical S-parameters. Note that computational time is significantly shorter using the modal analysis compared to the HFSS finite

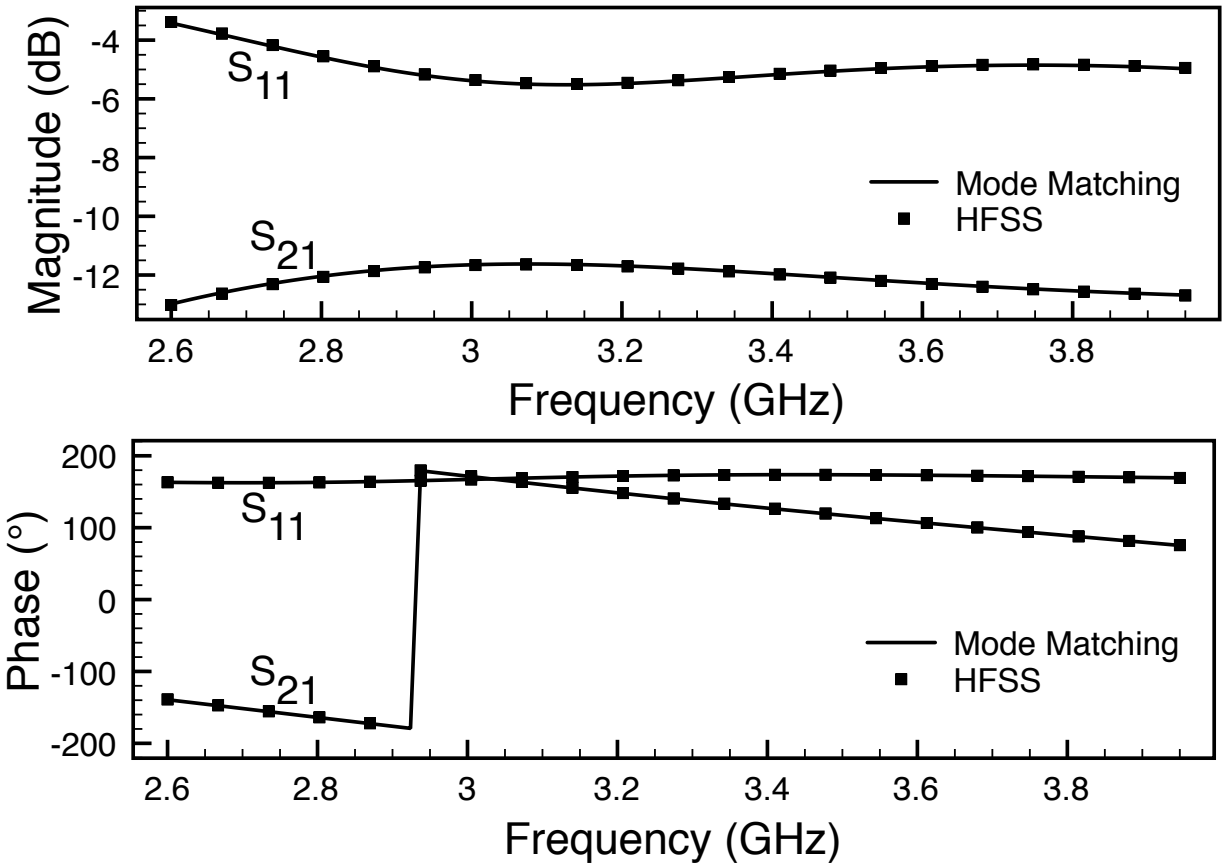

Figure 4.17: S-parameters computed for a biaxial test material.

element method solver. For a typical set of parameters, the modal analysis programmed in Fortran is several orders of magnitude faster than FEM, and thus provides a good basis for performing parameter extraction.

4.3.4 Extraction Process

Determination of the the six biaxial material parameters $(\epsilon_A, \epsilon_B, \epsilon_C, \mu_A, \mu_B, \mu_C)$ requires a minimum of six independent measurements. However, if it is known *a priori* that the material is nonmagnetic (i.e., $\mu_A = \mu_B = \mu_C = 1$), then the extraction process is simplified greatly. The parameters ϵ_A, ϵ_B, and ϵ_C can be determined independently by measuring S_{21} with each of the axes (A, B, C) individually aligned along the y-direction, since only ϵy is implicated in (4.74). For instance, if the A direction is chosen to coincide with y, then ϵ_A may be found as the solution to the equation

$$S_{21}^{\text{thy}}(\epsilon_A) - S_{21}^{\text{meas}} = 0, \tag{4.95}$$

which is easily determined using Newton's method.

For the generally biaxial case the most straightforward approach is to measure the transmission and reflection coefficients for the sample placed with its A, B, and C axes under three orientations, as follows:

$$(A, B, C) \rightarrow (x, y, z) \quad \Rightarrow \left[S_{11,1}^{\text{meas}}, S_{21,1}^{\text{meas}}\right], \tag{4.96}$$

$$(A, B, C) \rightarrow (z, x, y) \quad \Rightarrow \left[S_{11,2}^{\text{meas}}, S_{21,2}^{\text{meas}}\right], \tag{4.97}$$

$$(A, B, C) \rightarrow (y, z, x) \quad \Rightarrow \left[S_{11,3}^{\text{meas}}, S_{21,3}^{\text{meas}}\right]. \tag{4.98}$$

The material parameters are then found by solving the following system of six nonlinear

complex equations in the six complex unknown material parameters:

$$S_{11,n}^{\text{thy}}(\epsilon_A, \epsilon_B, \epsilon_C, \mu_A, \mu_B, \mu_C) - S_{11,n}^{\text{meas}} = 0,\ n = 1, 2, 3, \tag{4.99}$$

$$S_{21,n}^{\text{thy}}(\epsilon_A, \epsilon_B, \epsilon_C, \mu_A, \mu_B, \mu_C) - S_{21,n}^{\text{meas}} = 0,\ n = 1, 2, 3. \tag{4.100}$$

Experience shows that with typical values of experimental error it can be difficult to find solutions to the system of equations (4.99)-(4.100), even with good initial guesses. An alternative approach allows a subset of the six material parameters to be first determined, and these parameters to be subsequently used in the computation of the remaining parameters. This approach is based on the observation from (4.74) that only three of the six material parameters are implicated in a measurement under any one orientation. That is, only ϵ_y, μ_x, and μ_z appear in (4.74).

Refer to Figure 4.11. First, measurements are made with these orientations:

$$(A, B, C) \rightarrow (x, y, z) \quad \Rightarrow \left[S_{11,1}^{\text{meas}}, S_{21,1}^{\text{meas}}\right], \tag{4.101}$$

$$(A, B, C) \rightarrow (-z, y, x) \quad \Rightarrow \left[S_{11,2}^{\text{meas}}, S_{21,2}^{\text{meas}}\right]. \tag{4.102}$$

These measurements only implicate the parameters ϵ_B, μ_A, and μ_C. Using three out of the four complex measurements yields the following system of equations with three unknowns:

$$S_{11,n}^{\text{thy}}(\epsilon_B, \mu_A, \mu_C) - S_{11,n}^{\text{meas}} = 0,\ n = 1, \tag{4.103}$$

$$S_{21,n}^{\text{thy}}(\epsilon_B, \mu_A, \mu_C) - S_{21,n}^{\text{meas}} = 0,\ n = 1, 2, \tag{4.104}$$

which can be solved using a Newton's method. Note that the different between $S_{11,2}^{\text{thy}}$ and $S_{11,2}^{\text{meas}}$ could be used in place of one of the transmission coefficient equations, however, experience has shown more efficient characterization using (4.103) and (4.104). Additionally, a least squares approach could be used in place of a Newton's method and use all four measurements instead of eliminating the use of $S_{11,2}^{\text{meas}}$. Next, a measurement is made under

the orientation

$$(A, B, C) \rightarrow (y, -x, z) \quad \Rightarrow \left[S_{11,3}^{\text{meas}}, S_{21,3}^{\text{meas}}\right]. \tag{4.105}$$

This measurement implicates ϵ_A, μ_B, and μ_C. However, μ_C is known from solving (4.103)-(4.104), and thus the system of equations

$$S_{11,3}^{\text{thy}}(\epsilon_A, \mu_B) - S_{11,3}^{\text{meas}} = 0, \tag{4.106}$$

$$S_{21,3}^{\text{thy}}(\epsilon_A, \mu_B) - S_{21,3}^{\text{meas}} = 0, \tag{4.107}$$

can be solved for ϵ_A and μ_B. Finally, a last measurement is made under the orientation

$$(A, B, C) \rightarrow (z, x, y) \quad \Rightarrow \left[S_{11,4}^{\text{meas}}, S_{21,4}^{\text{meas}}\right]. \tag{4.108}$$

This measurement implicates ϵ_C, μ_A, and μ_B. However, at this point only ϵ_C is unknown, and thus the single complex equation

$$S_{21,4}^{\text{thy}}(\epsilon_C) - S_{21,4}^{\text{meas}} = 0 \tag{4.109}$$

is solved using a Newton's method.

The drawback to this approach is that an additional measurement is required. However, experience shows that reducing the number of unknowns improves the extraction process to the extent where the extra experimental effort is advantageous.

It is important to validate the inversion method before proceeding with the characterization of unknown materials. Therefore, the fictitious material parameters from Table 4.2 are used in HFSS to generated S-parameters with the cube in four orientations, and the four-orientation extraction method is performed. The HFSS simulation uses the same model as was used to generate the data for Figure 4.17. The results of the characterization are shown in Figure 4.18 and Figure 4.19. As expected, the characterized material parameters are in accordance with the parameters shown in Table 4.2. This extraction gives confidence in the

characterization technique before moving forward with error analysis and measurements.

4.3.5 Error and Sensitivity Analysis

As done with previous characterization techniques, and described in Section 4.2.5, a Monte Carlo technique was used to study effects on the propagation of the random error inherent to the VNA used in the measurements. Once again, the uncertainties of the measured S-parameters were determined for an HP8510C network analyzer system using the software package *HP 8510 Specifications & Performance Verification Program* provided by Hewlett Packard and the values used for the statistical variance of S_{11} and S_{21} as outlined in Section 4.2.5.

A Monte Carlo analysis of the propagation of VNA uncertainty was undertaken using the fictitious test material with the parameters given in Table 4.2. The geometry of the sample is $a = 72.136$ mm and $b = w = d = 34.036$ mm. The forward problem was solved at 101 frequency points over the portion of S-band from 2.6 to 3.95 GHz under the four orientations described in Section 4.3.4. White gaussian noise was then added to each of the S-parameter sets and the noisy data used to extract the material parameters according to the four-measurement process of Section 4.3.4. The standard deviations used to generate the additive noise are those indicated by the *HP 8510 Specifications & Performance Verification Program*. The process was repeated 500 times, and the average values of the material parameters were calculated, along with the standard deviations. Results are shown in Figure 4.20 and Figure 4.21. In these figures, the center of each triplet of lines is the average value of the 500 trials, while the two surrounding lines indicate the 95% confidence interval of ± 2 standard deviations. These results for VNA uncertainty will be compounded by any systematic errors present in the experiment, and have values typical of those encountered with other material extraction methods, such as [51] and [40]. Note that for low loss materials with small ϵ'' and μ'', the relative error in the measured imaginary parts can be quite severe, even though the absolute error may be less than those for ϵ' and μ'.

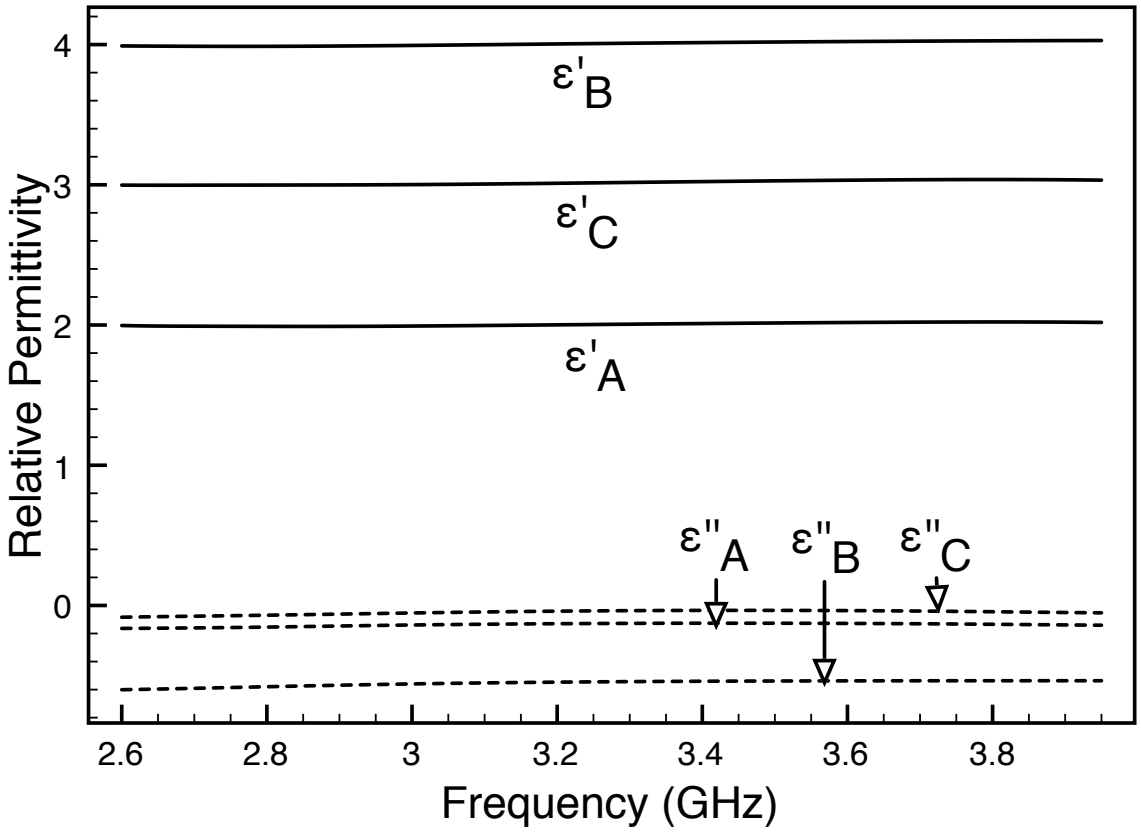

Figure 4.18: Extracted permittivity using HFSS generated S-parameters.

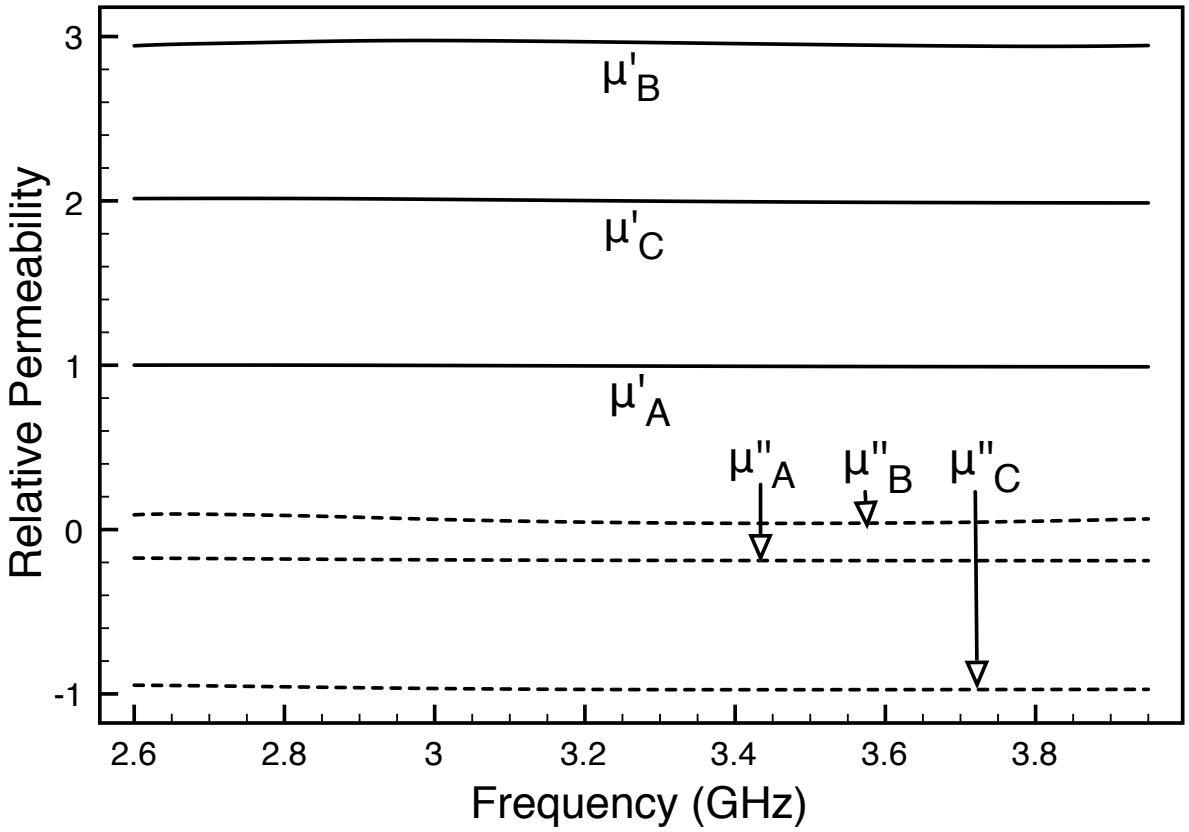

Figure 4.19: Extracted permeability using HFSS generated S-parameters.

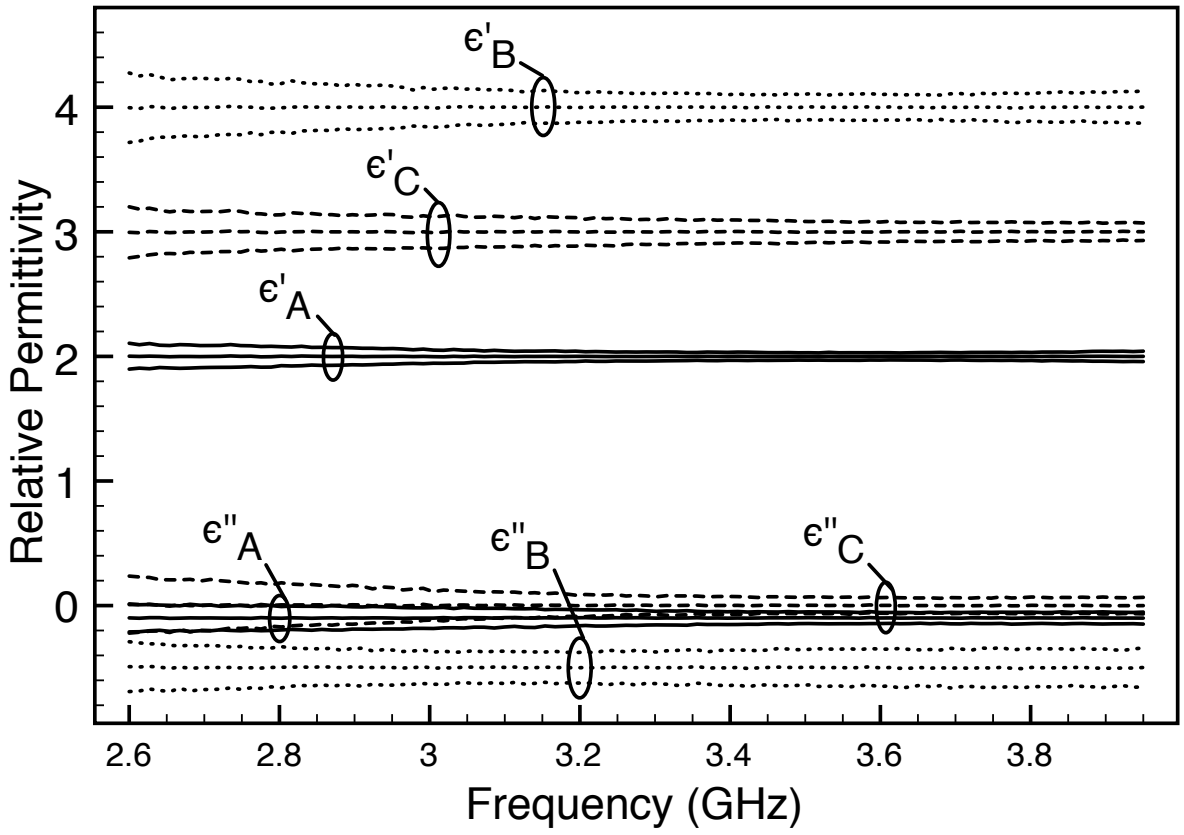

Figure 4.20: Relative permittivities for a fictitious material extracted using 500 random trials. Center line is the average of the trials. Upper and lower lines show the 95% confidence interval.

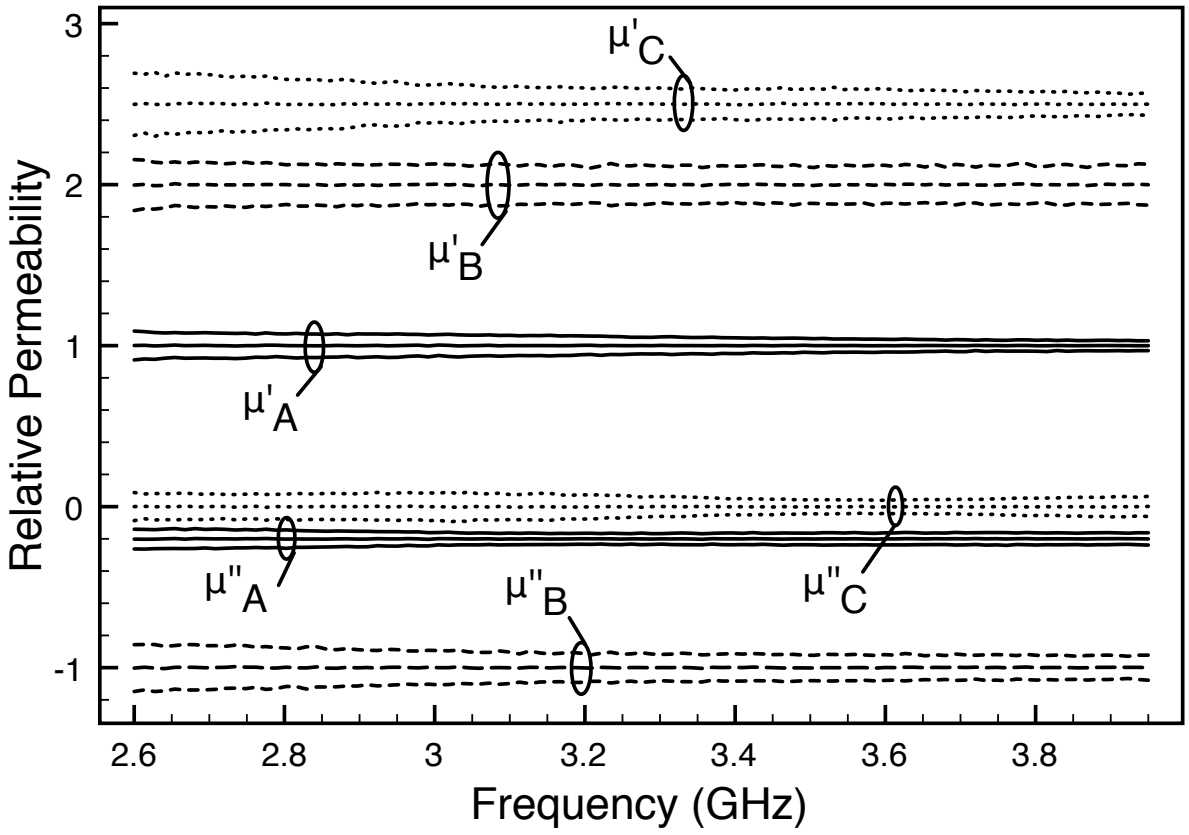

Figure 4.21: Relative permeabilities for a fictitious material extracted using 500 random trials. Center line is the average of the trials. Upper and lower lines show the 95% confidence interval.

4.3.6 Experimental Results

To experimentally validate the proposed technique at S-band, a reduced-aperture waveguide was machined from 360 brass. The specified inner dimensions of the cubical sample holder are $b = w = d = 34.036$ mm, and measurement of the constructed sample using precision calipers showed that the holder was constructed with tolerances of less than 0.04 mm. The holder was aligned with two 152.4 mm-long commercial S-band waveguide extensions of cross-section dimension 34.036 mm by 72.136 mm and holes for precision alignment pins were drilled in the sample holder to guarantee high repeatability of the alignment of the holder and the extensions. This is necessary since the extensions must be removed to calibrate the system and to insert and remove the sample.

Two samples were constructed to test the system. The first is a simple isotropic teflon cube. The properties of teflon are well-established, and since the material is isotropic, it can be used to characterize the repeatability of measurements as the sample is rotated into the required four orientations. Figure 4.22 shows a picture of the sample holder and the teflon sample. The sample was constructed approximately 0.01 mm larger than the inner dimensions of the sample holder so that when inserted it would compress slightly and eliminate air gaps between the MUT and the sample holder walls.

Measurements of the S-parameters of the teflon sample placed into the four required orientations were made using an HP 8510C VNA. The VNA was calibrated using the Thru-Reflect-Line (TRL) algorithm internal to the 8510C, with an aluminum plate used as the reflection standard, and a 33.53 mm-long section of commercial waveguide used as the line standard. As with the sample holder, precision alignment pins were used to ensure repeatability of the alignment of the guides. All measurements were made with a 10 dBm source power, 32 averages, and a 25 ms dwell time.

Teflon is a low-loss dielectric with a real relative permittivity of approximately 2.1. To assess repeatability error, the teflon sample was measured 10 separate times, with the system

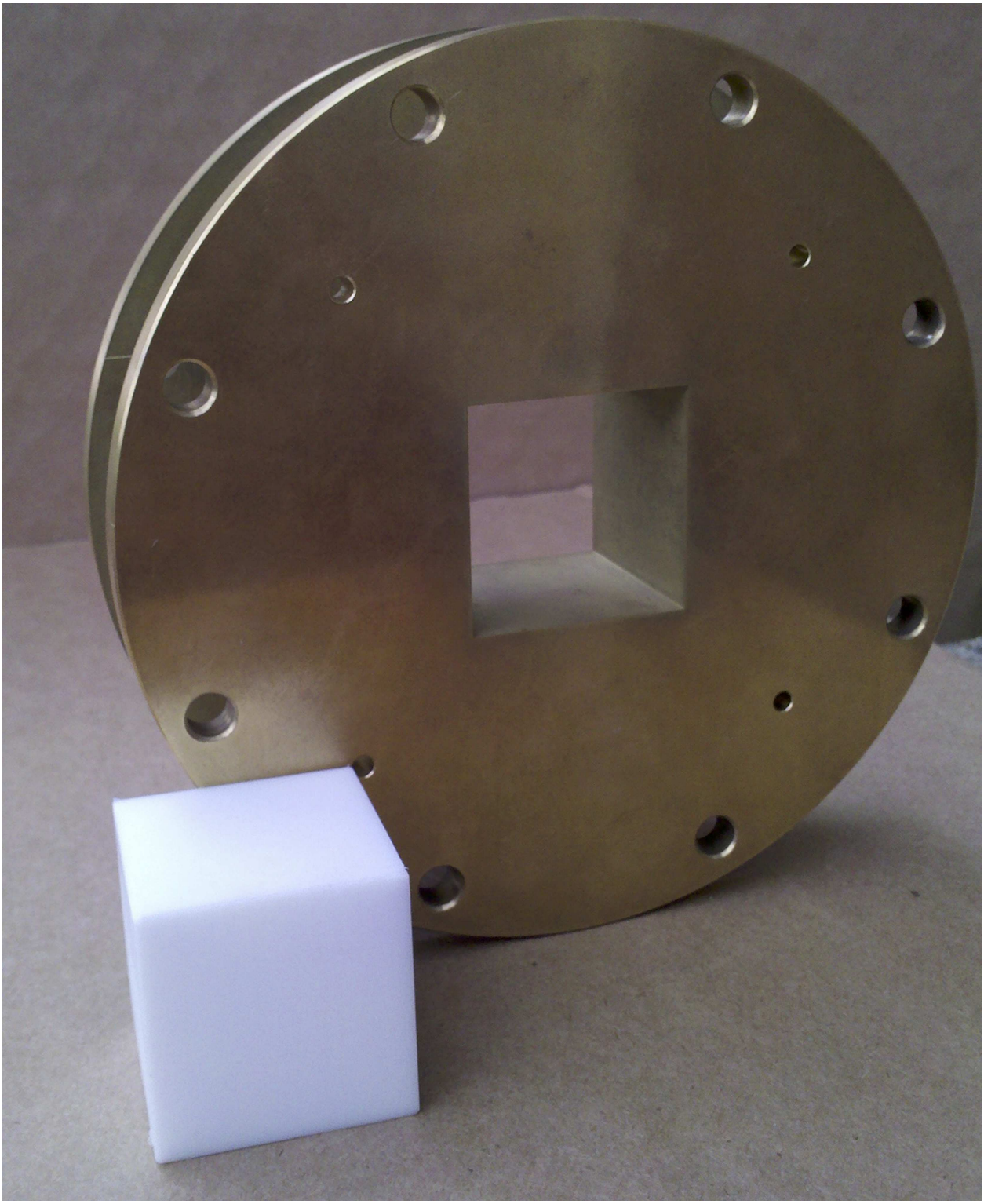

Figure 4.22: Cubical sample holder and teflon sample.

recalibrated between sample measurements. The results of the characterization are shown in Figure 4.23 and Figure 4.24, where the center solid lines represent the mean extracted values of the 10 measurement sets and the upper and lower circles show the 95% confidence interval ($\pm$ two standard deviations). Although teflon is isotropic, the measurements were conducted assuming a biaxial material sample, and so six material parameters were computed for each measurement set. The mean extracted values for each of the three permittivities and each of the three permeabilities overlap closely in Figure 4.23 and Figure 4.24, as expected for an isotropic material. Note that to avoid clutter, only the confidence intervals for ϵ_A and μ_A are shown in Figure 4.23 and Figure 4.24. The confidence intervals for the remaining material parameters are very similar. The extracted mean values show excellent agreement to the expected material parameters of teflon and the confidence intervals closely resemble the error bars shown in Figure 4.20 and Figure 4.21, suggesting that the dominant repeatability error is due to S-parameter measurement uncertainty.

To test the characterization procedure using an anisotropic material, a cube was constructed by using layers of alternating dielectrics as shown in Figure 4.25. This produces a material with anisotropic (uniaxial) dielectric properties, but isotropic magnetic properties. Since commercial, off-the-shelf anisotropic dielectric and anisotropic magnetic material is not readily available, a uniaxial cube was constructed by gluing together Rogers RO3010 circuit board (the light layers in Figure 4.25) and Rogers RT/duroid 5870 circuit board (dark layers). The 3010 board has a thickness of $t_1 = 1.27$mm, a dielectric constant of $\epsilon'_{r1} = 10.2$ and a loss tangent of $\tan\delta_1 = 0.0022$. The 5870 board has a thickness of $t_2 = 3.4$mm, a dielectric constant of $\epsilon'_{r2} = 2.33$ and a loss tangent of $\tan\delta_2 = 0.0012$. If the B direction is chosen to be aligned perpendicular to the layer interfaces, then it is expected that ϵ_A and ϵ_C should be identical, but different from ϵ_B. The advantage to using this structure is that simple formulas exist for estimating ϵ_A, ϵ_B, and ϵ_C.

Note that at the highest frequency considered in the measurements, the free-space electrical length of the stack period is $k_0(t_1 + t_2) = 0.387$. Since $k_0\sqrt{\epsilon'_{r1}}(t_1 + t_2) \ll 2\pi$, the

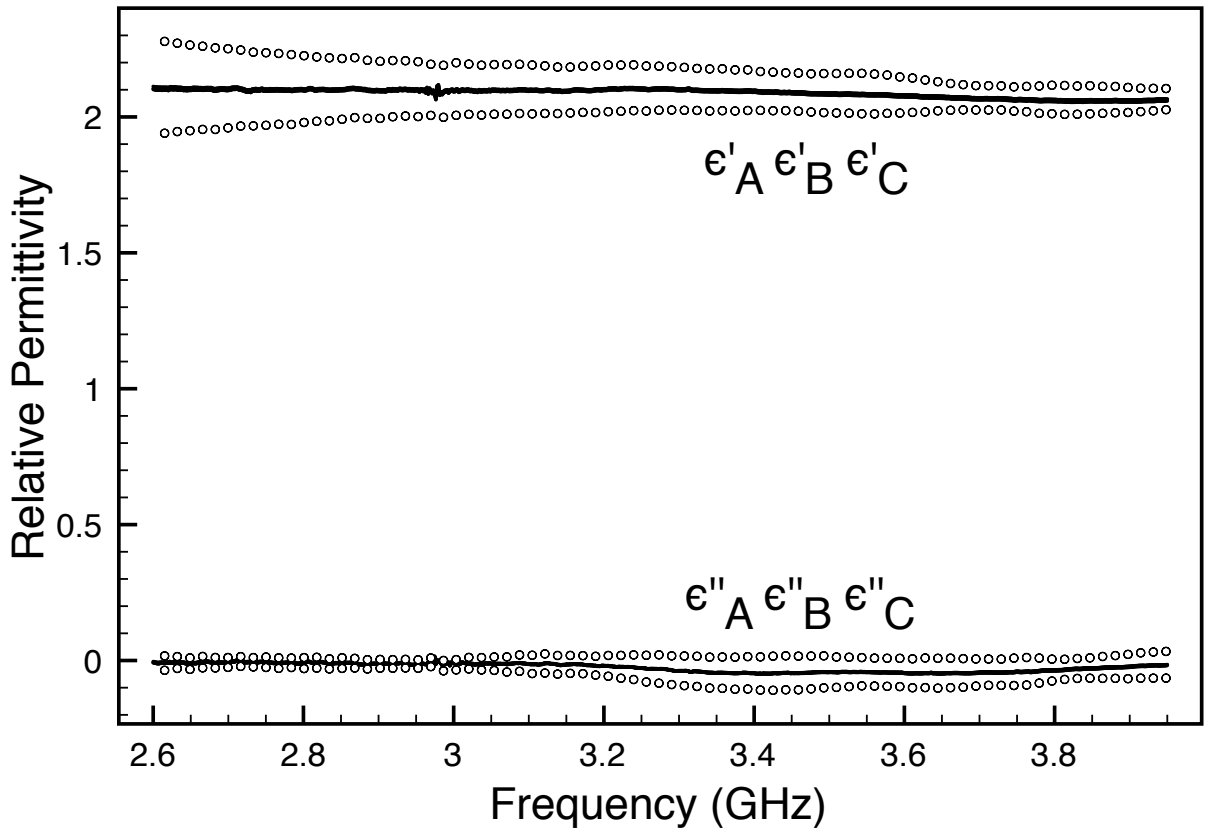

Figure 4.23: Relative permittivities extracted from 10 sets of teflon measurements. Center line is the average of the measurements. Upper and lower circles show the 95% confidence interval for ϵ_A.

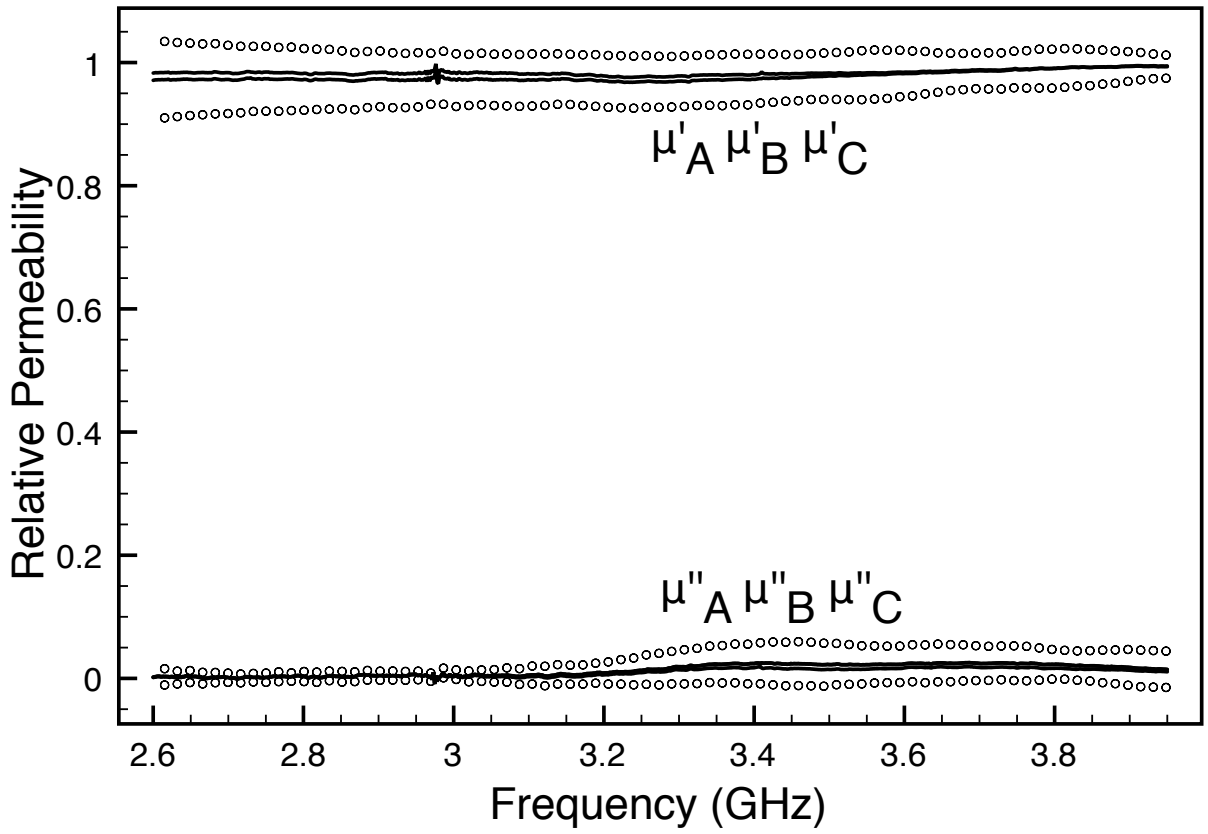

Figure 4.24: Relative permeabilities extracted from 10 sets of teflon measurements. Center line is the average of the measurements. Upper and lower circles show the 95% confidence interval for μ_A.

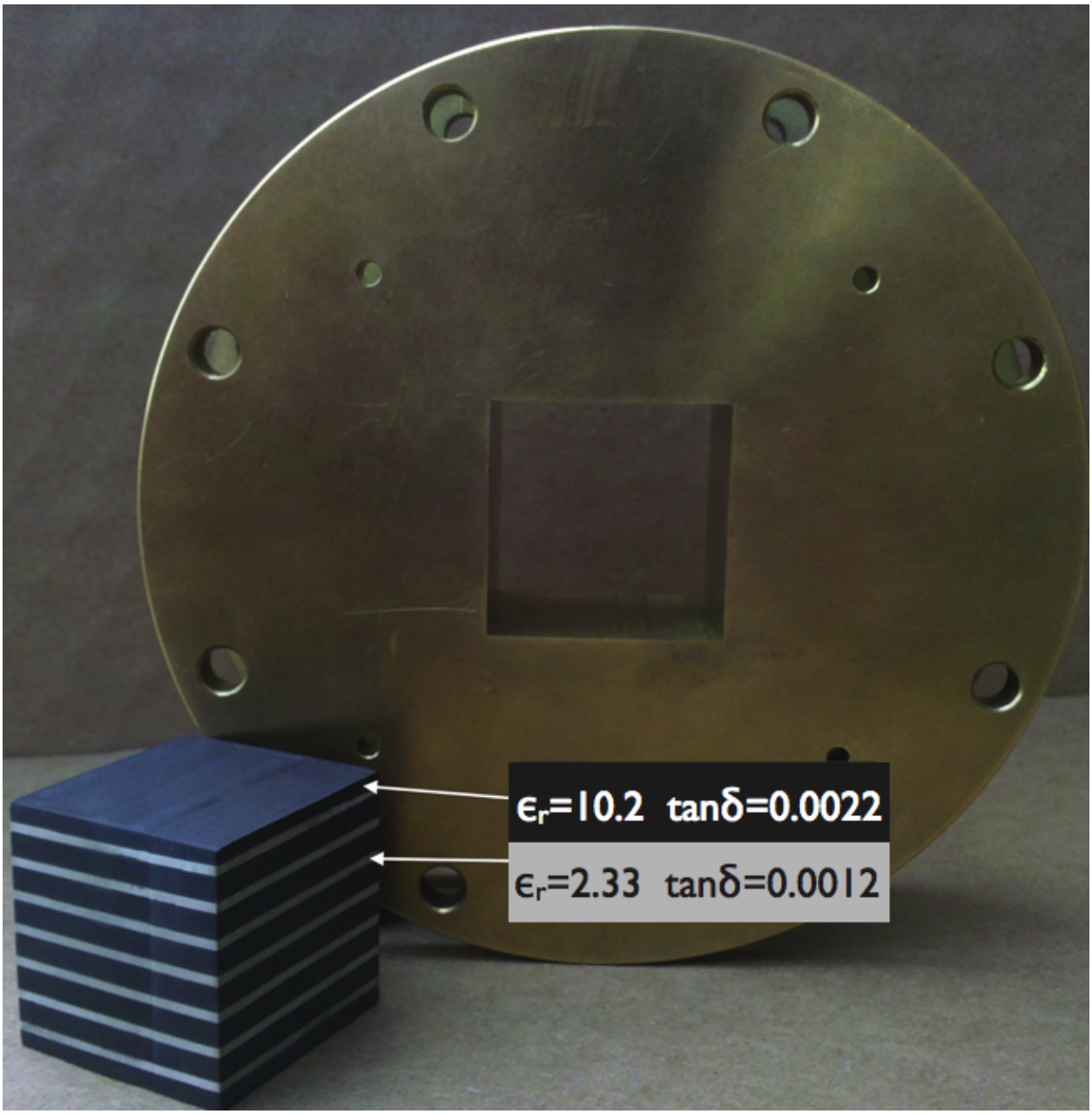

Figure 4.25: Cubical sample holder and alternating-layer dielectric sample.

following approximate formulas may be used to determine the biaxial material constants [59],

$$\epsilon_B = \left[\frac{1}{\epsilon_{r2}} - \frac{\epsilon_{r1} - \epsilon_{r2}}{\epsilon_{r1}\epsilon_{r2}} \frac{t_1}{t_1 + t_2}\right]^{-1}, \tag{4.110}$$

$$\epsilon_A = \epsilon_C = \epsilon_{2r} + (\epsilon_{1r} - \epsilon_{2r}) \frac{t_1}{t_1 + t_2}, \tag{4.111}$$

where $\epsilon_{r1} = \epsilon'_{r1}(1 - j \tan\delta_1)$ and $\epsilon_{r2} = \epsilon'_{r2}(1 - j \tan\delta_2)$. Substituting the board parameters gives $\epsilon_B = 2.95 - j0.0038$ and $\epsilon_A = \epsilon_C = 4.47 - j0.0081$. It is expected that the formula for ϵ_A and ϵ_C will be less accurate than the formula for ϵ_B, since the presence of internal reflections within the layers is most significant when the cube is oriented such that the interfaces lie normal to the wave propagation. Results given in [53] for a layered sample in a non-reduced rectangular guide suggest that a deviation of as much as 10-20 percent may be expected unless the number of layers is significantly large. Although these results cannot be directly used with the reduced-aperture guide, they suggest that a deviation of 10 percent would not be unexpected. Also note that the circuit boards themselves are slightly anisotropic due to the alignment of the glass fibers used in their construction, and thus it is expected that ϵ_A and ϵ_C should be slightly different [54]. However, no attempt is made to quantify this difference theoretically.

Similar to the measurements of the teflon cube, the layered cube was measured 10 separate times. The results of the extraction are shown in Figure 4.26 through Figure 4.31, where the solid lines represent the averaged extracted material parameter and the upper and lower circles show the 95% confidence intervals for the 10 measurement sets. In each of these figures, gaps are seen in the extracted parameters over certain ranges of frequency. This is due to the well-known difficulty of extracting material parameters near frequencies where the sample thickness approaches one half of a guided wavelength. This problem is inherent to all guided-wave techniques in which both permittivity and permeability are determined (including the Nicolson-Ross-Wier closed-form method for isotropic materials [23]-[24]), and

is due to the propagation of measurement uncertainties. It can be seen in Figure 4.26 that as the frequency nears 3.7 GHz, the uncertainties begin to grow dramatically. within the indicated gap, the uncertainties become so large that extraction is completely unreliable. This is a drawback of using a cubical sample holder, since the thickness of the material cannot be reduced to avoid these half-wavelength gaps when the material parameters are sufficiently large. Experience has shown that the a frequency range within approximately $\pm 5\%$ of the half-wavelength frequency should be avoided, and data within that range is not displayed in the figures. Across other portions of the frequency band, the averaged extracted values are reasonably close to those predicted from (4.110)-(4.111), and the confidence intervals are consistent with the error due to S-parameter uncertainty described in Section 4.3.5. As discussed above, it is not surprising to find that there is a deviation of about 10% in ϵ_A and ϵ_C from the result predicted using the simple formula (4.111).

The process of extracting the various material parameters in stages, with ϵ_B, μ_A, and μ_C determined first, produces an unfortunate cascading of half-wavelength gaps in the extracted data. Figure 4.27, Figure 4.29 and Figure 4.31 only show gaps near 3.7 GHz since the orientations used to determine these parameters produce just a single half-wavelength point in the measurement band. Similarly, the orientations used to determine ϵ_A, ϵ_C, and μ_B produce only a single half-wavelength point near 2.8 GHz, and thus gaps at this frequency can be seen in Figure 4.26, Figure 4.28 and Figure 4.30. However, since the previously extracted values of ϵ_B, μ_A, and μ_C are used to find ϵ_A, ϵ_C, and μ_B, the gaps at 3.7 GHz in those data are also present in Figure 4.26, Figure 4.28 and Figure 4.30.

Because the material parameters do not vary strongly with frequency, their values within the gap regions may be approximated through interpolation. A simple approach is to fit a polynomial function to the mean data, and evaluate the polynomial in the gap. For the materials considered here, it is found that a fifth order polynomial fits the data well over the entire measurement band. Figure 4.32 and Figure 4.33 show the interpolating polynomials evaluated across the measurement band. These interpolated results show good agreement

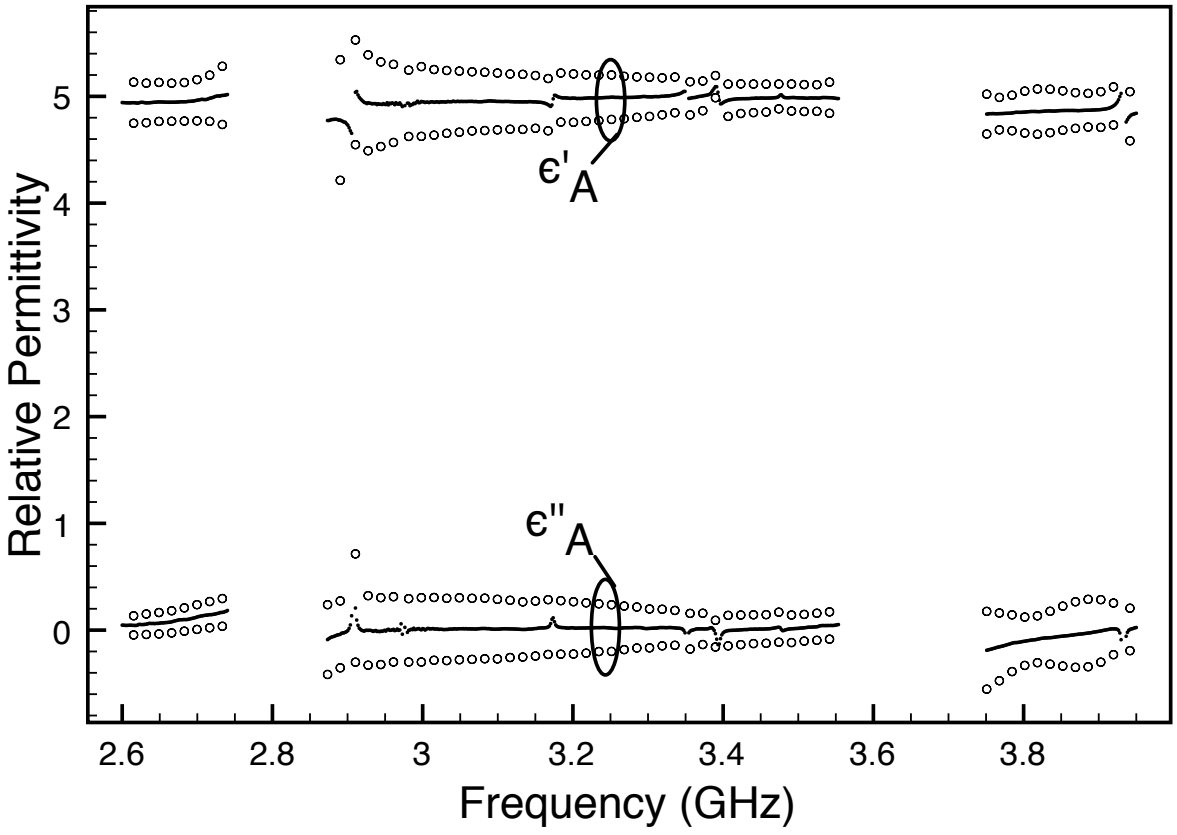

Figure 4.26: Relative permittivity ϵ_A extracted from 10 sets of measurements. Center line is the average of the measurements. Upper and lower circles show the 95% confidence interval.

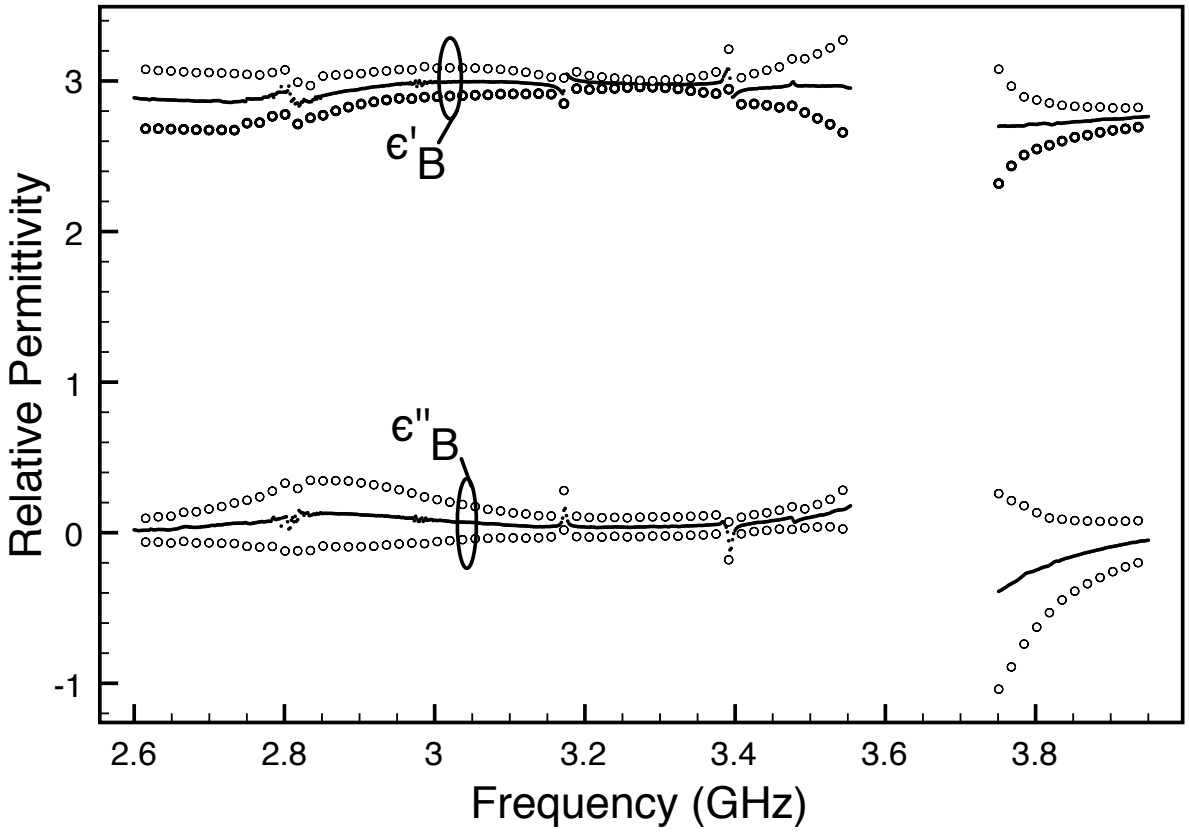

Figure 4.27: Relative permittivity ϵ_B extracted from 10 sets of measurements. Center line is the average of the measurements. Upper and lower circles show the 95% confidence interval.

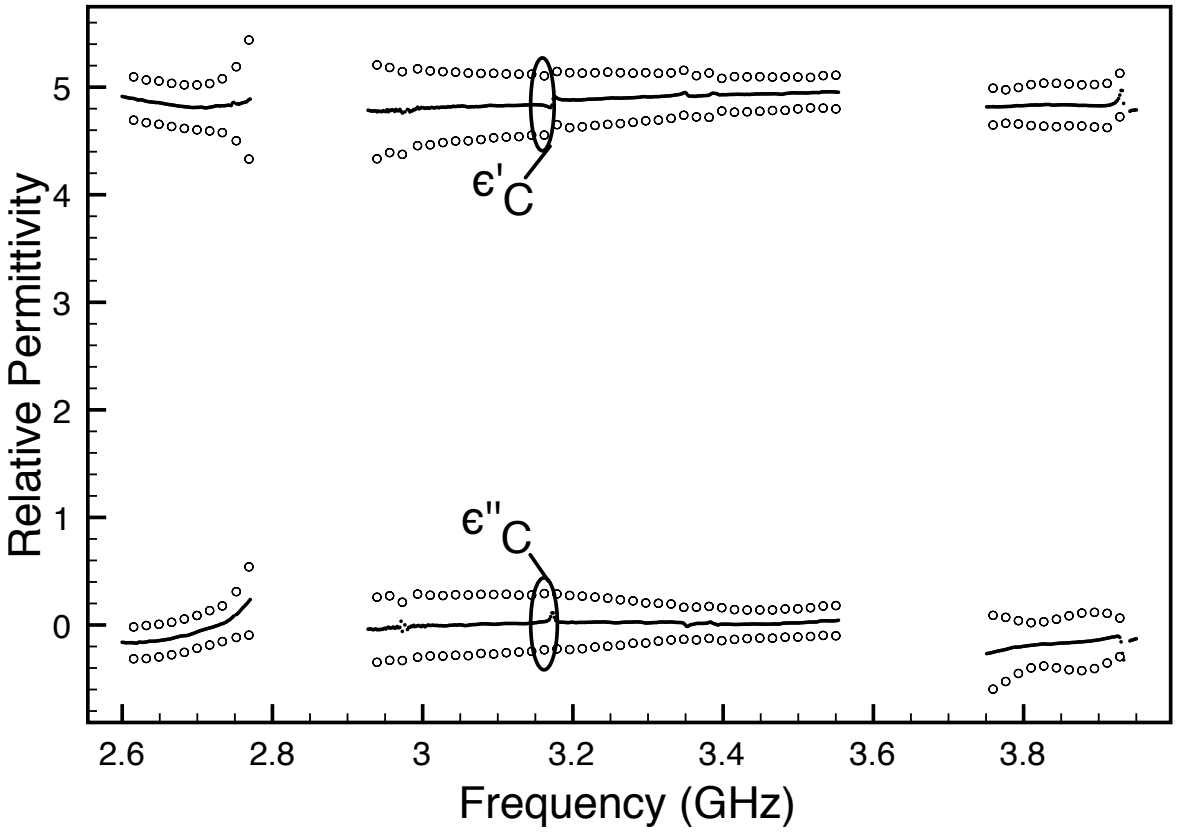

Figure 4.28: Relative permittivity ϵ_C extracted from 10 sets of measurements. Center line is the average of the measurements. Upper and lower circles show the 95% confidence interval.

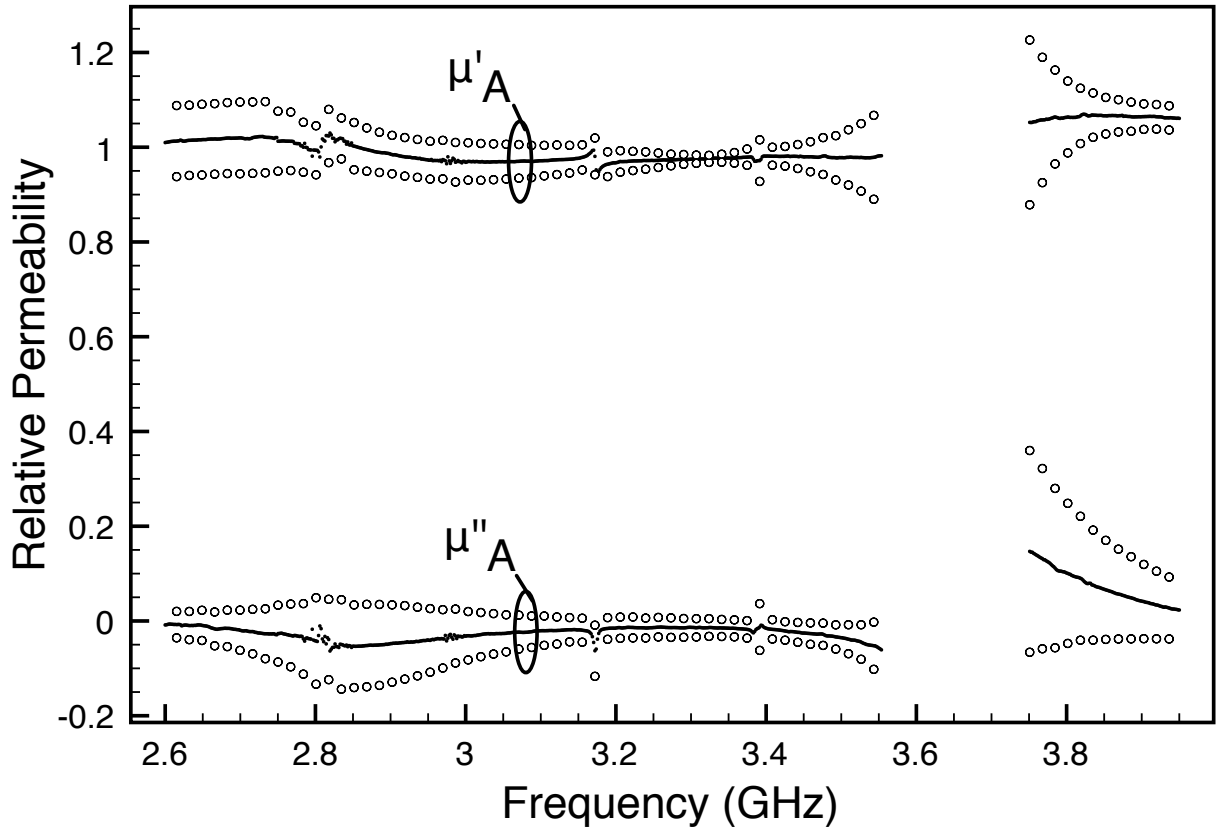

Figure 4.29: Relative permeability μ_A extracted from 10 sets of measurements. Center line is the average of the measurements. Upper and lower circles show the 95% confidence interval.

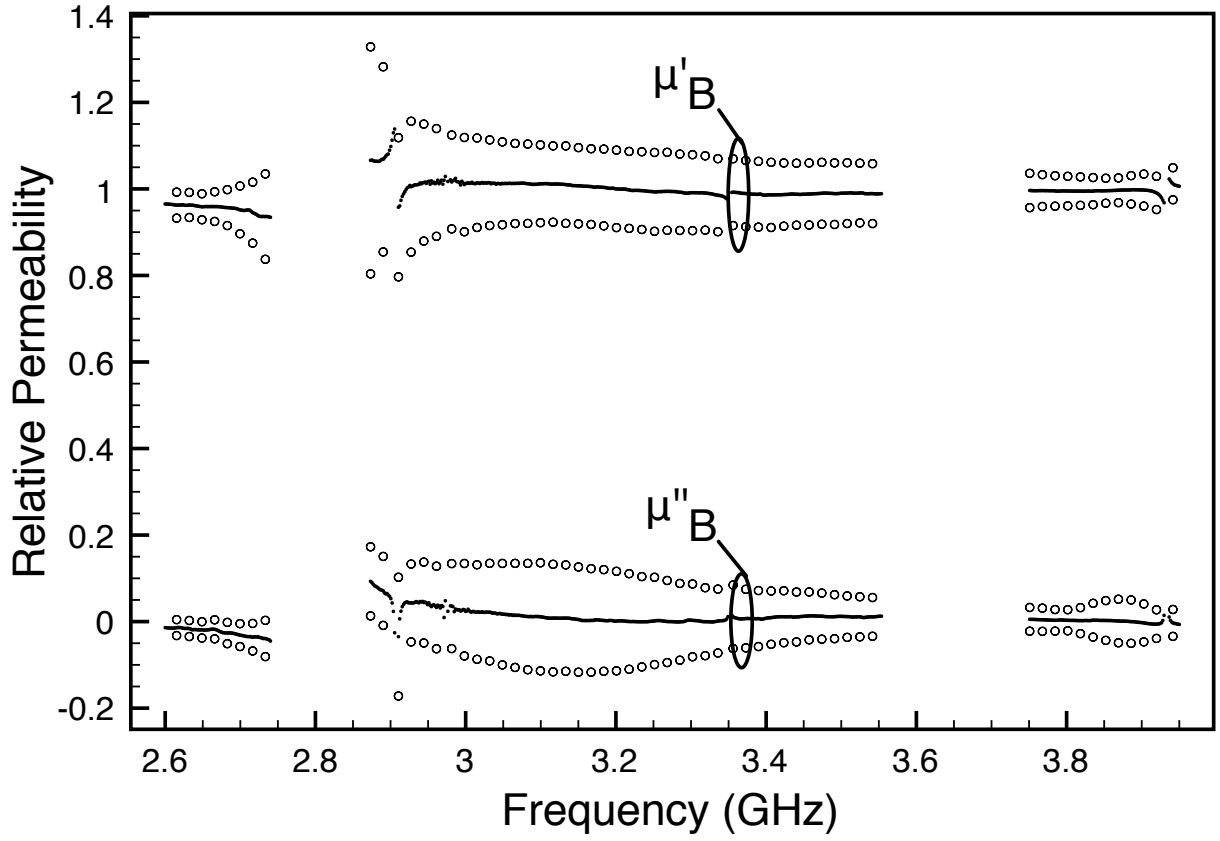

Figure 4.30: Relative permeability μ_B extracted from 10 sets of measurements. Center line is the average of the measurements. Upper and lower circles show the 95% confidence interval.

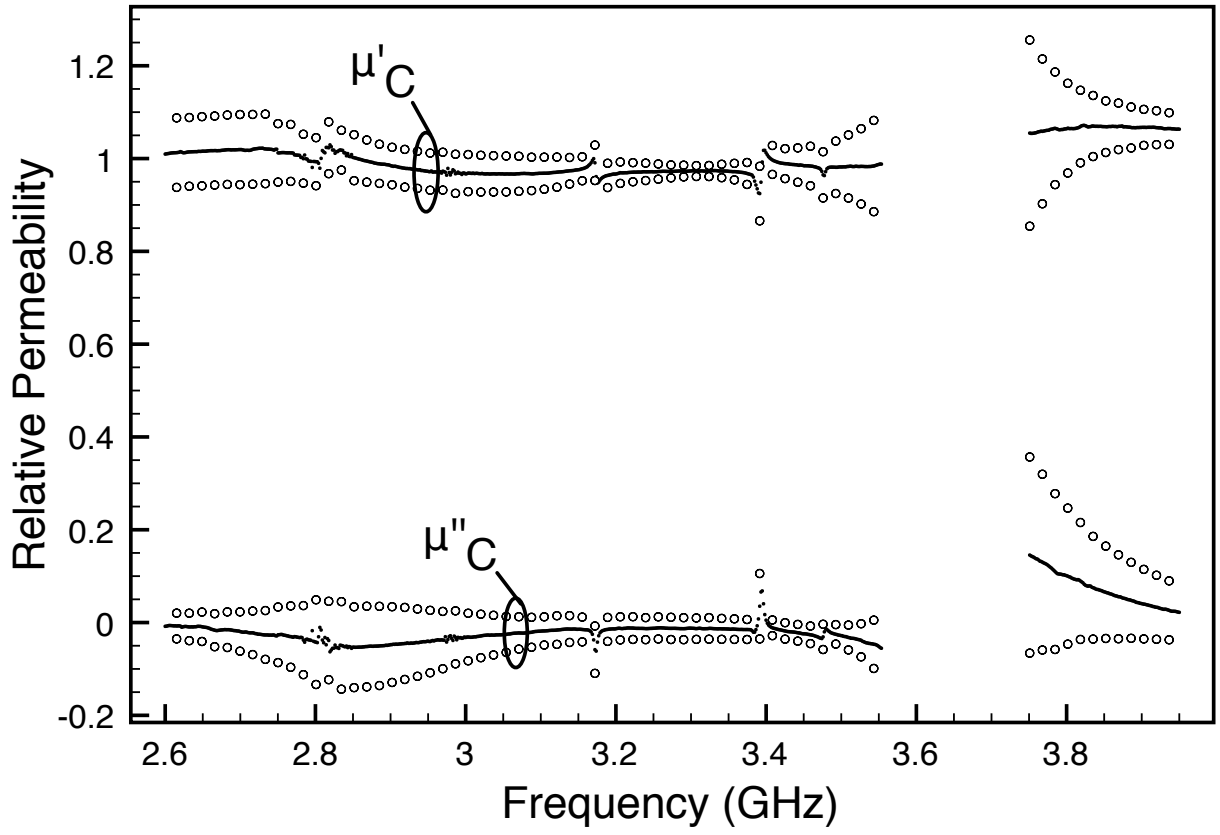

Figure 4.31: Relative permeability μ_C extracted from 10 sets of measurements. Center line is the average of the measurements. Upper and lower circles show the 95% confidence interval.

with the expected values from the simple formula outlined previously. Note that there is a small amount of unphysical oscillation in the permeabilities, due to the variations in these parameters near the edges of the gap regions. This oscillation can be reduced by using a lower order polynomial, or by taking slightly wider gaps.

Because it is known *a priori* that the layered cube is nonmagnetic, the permittivity parameters ϵ_A, ϵ_B, and ϵ_C can be determined independently from three measurements of S_{21} using (4.95). Figure 4.34 shows the extracted values using the same 10 measurements used to generate Figure 4.28-4.31. It is clearly seen that the difficulties at half-wavelength frequencies do not occur in this case, and thus there are no gaps in the data. This is because only transmission coefficients are used in the extraction, and the extracted material parameters are less sensitive to uncertainty in S_{21} than in S_{11}. The results are very close to those of Figure 4.32 found using the extrapolating polynomial.

Although the use of a non-magnetic uniaxial material does not fully explore the ability of the proposed technique to extract all the parameters of a biaxial sample, the agreement between ϵ_A and ϵ_C gives good evidence that the technique is viable.

4.3.7 Summary

A reduced aperture waveguide method is introduced for measuring the permittivity and permeability of biaxially anisotropic materials. Only a single cubical sample is required to completely characterize the material under test. This contrasts with the three distinct samples required when using the standard waveguide technique in which a sample completely fills the rectangular waveguide cross section. The performance of the technique is established using an error analysis based on network analyzer uncertainty, and validation is provided by laboratory measurements of a teflon and a stacked dielectric layered sample. It is found that the technique performs very well for regions of the frequency band where the electrical length of the sample does not approach a half wavelength, and that an interpolating polynomial may be used to supply the data near the half-wavelength points

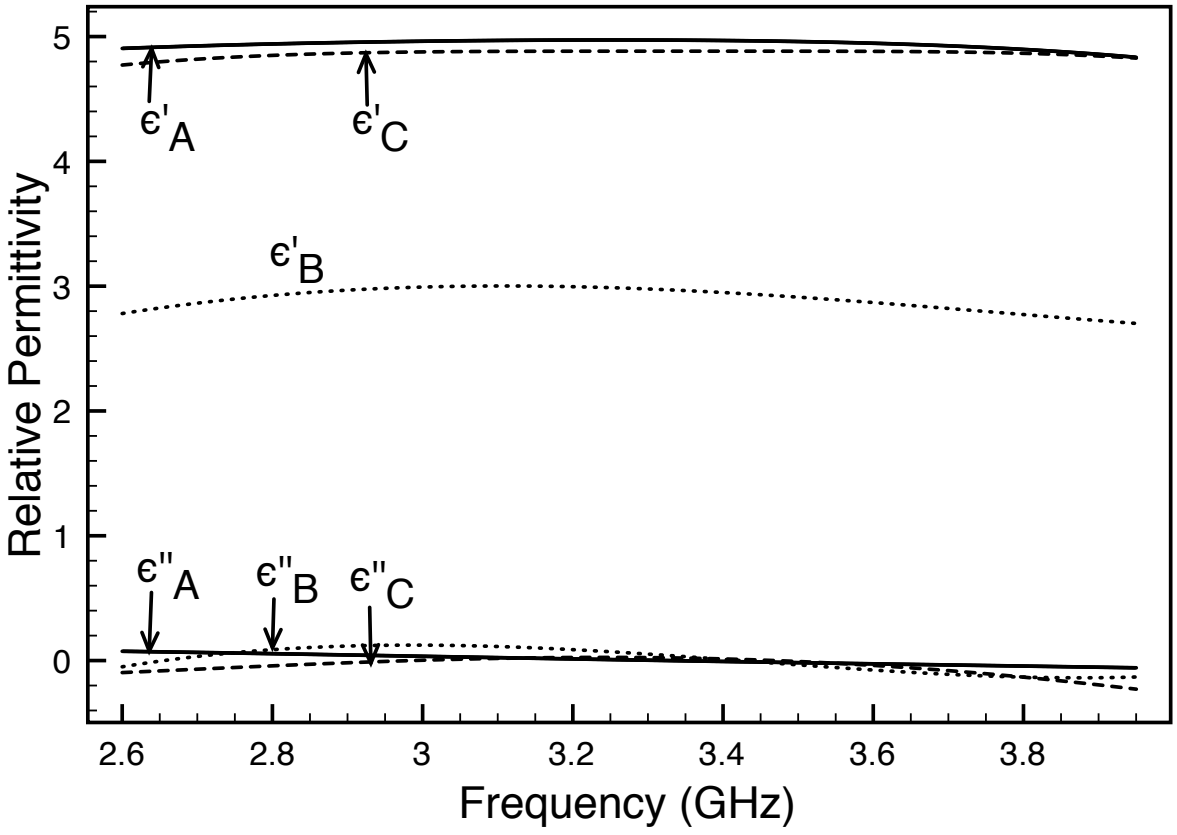

Figure 4.32: Average permittivity from 10 sets of measurements extrapolated using a fifth order polynomial.

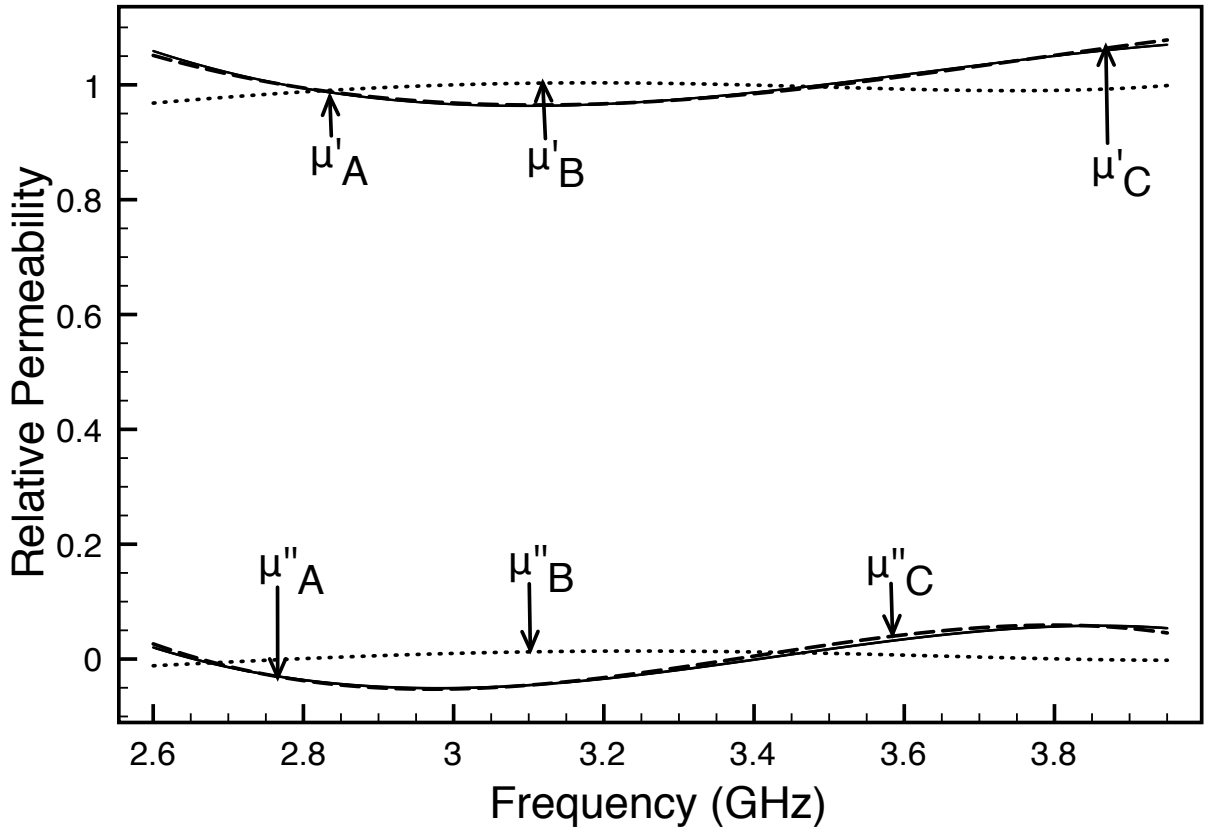

Figure 4.33: Average permeability from 10 sets of measurements extrapolated using a fifth order polynomial.

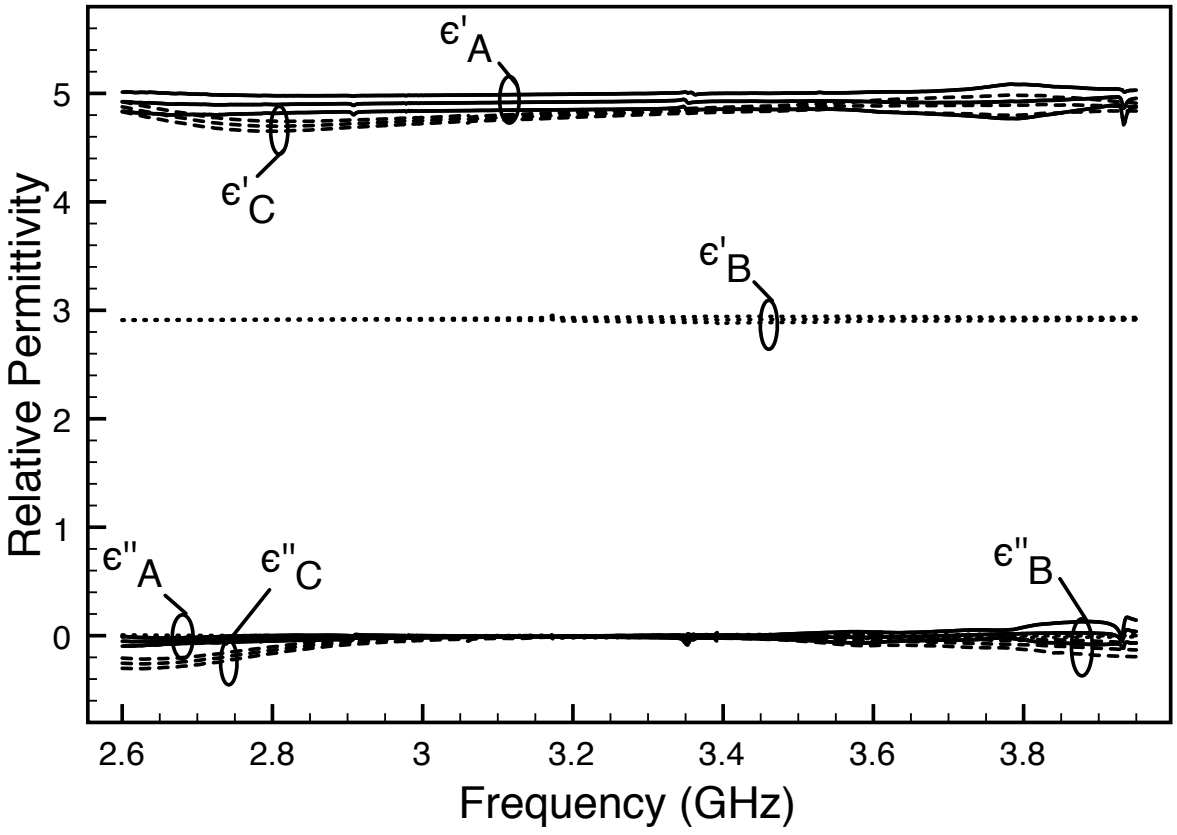

Figure 4.34: Relative permittivity extracted from 10 sets of measurements assuming the sample is nonmagnetic. Center line is the average of the measurements. Upper and lower lines show the 95% confidence interval.

CHAPTER 5

GYROMAGNETIC MATERIAL CHARACTERIZATION

5.1 Introduction

This chapter presents two methods for characterizing gyromagnetic materials using rectangular waveguides where the sample is magnetized perpendicular to the broad dimension of the guide. The first technique considers a gyromagnetic material completely filling the cross-section of a waveguide. Gyromagnetic materials react differently depending on the incident wave polarization and the wave couples into orthogonal field components. A mode-matching technique is used determine the theoretical reflection and transmission coefficients needed for material parameter characterization. The parameters are obtained using a nonlinear least squares method that seeks to minimize the difference between theoretically computed and measured reflection and transmission coefficients.

The second characterization technique uses a reduced-aperture sample holder such that the gyromagnetic sample can be machined to have a smaller width than the cross-section of the guide. The sample holder is positioned between two empty sections of rectangular waveguides to guarantee only the dominant mode is present at the sample holder. The S-

parameters are then measured. Mode matching is used to determine the theoretical reflection and transmission coefficients of the dominant mode. The inverse problem is then solved using a non-linear least squares method to determine the material parameters.

5.2 Characterization of Gyromagnetic Material Filling the Cross-Section of a Rectangular Waveguide

This section concentrates on the extraction of the effective permittivity and permeability of a sample of gyromagnetic material completely filling the cross-section of a rectangular waveguide. It is customary for optimizers or root solvers (such as the Newton's method used in Section 4.3.4) to be used to determine the constitutive parameters of materials in rectangular waveguides. In these methods, the reflection and transmission coefficients from a material placed in the cross-sectional plane of a waveguide are measured and compared to theoretical S-parameters. It is essential to have accurate formulations of the theoretical S-parameters for valid characterization of materials. A modal matching method is used to determine the reflection and transmission coefficients of the dominant mode from a sample of gyromagnetic material filling the cross section of a rectangular guide. Details on the methodology for obtaining the reflection and transmission coefficients are presented along with a comparison to a finite element full wave solver. Additionally, the characterization method is tested by extracting the material parameters from the FEM generate S-parameters.

5.2.1 Theoretical Transmission and Reflection Coefficients Using Mode-Matching Analysis

The material under test (MUT) is assumed to be linear and homogeneous with isotropic permittivity and a permeability that is uniaxial along the orthogonal axes and has off diagonal

parameters. The MUT has the tensor constitutive parameters

$$\overline{\overline{\epsilon}} = \epsilon_0 \begin{bmatrix} \epsilon_r & 0 & 0 \\ 0 & \epsilon_r & 0 \\ 0 & 0 & \epsilon_r \end{bmatrix} \tag{5.1}$$

and

$$\overline{\overline{\mu}} = \mu_0 \begin{bmatrix} \mu_g & 0 & -j\kappa \\ 0 & 1 & 0 \\ j\kappa & 0 & \mu_g \end{bmatrix}, \tag{5.2}$$

where the values ϵ_r, κ, and μ_g are relative complex quantities: $\epsilon_r = \epsilon_r' + j\epsilon_r''$, $\kappa = \kappa' + j\kappa''$ and $\mu_g = \mu_g' + j\mu_g'$. This permeability tensor is for a material biased in the y-direction, or the along the height of the waveguide. Here the off-diagonal parameter κ is given by

$$\kappa = \frac{\omega\omega_m}{\omega_0^2 - \omega^2}, \tag{5.3}$$

and the diagonal element μ_g is described as

$$\mu_g = \left(1 + \frac{\omega_0\omega_m}{\omega_0^2 - \omega^2}\right). \tag{5.4}$$

In (5.3) and (5.4), $\omega = 2\pi f$ is the operating frequency, $\omega_0 = \mu_0\gamma H_0$ is the Larmor frequency, and $\omega_m = \mu_0\gamma M_s$. Here H_0 is the strength of the internal static biasing magnetic field in oersteds and M_s the saturation magnetization typically expressed as $4\pi M_s$ gauss. The ratio of spin magnetic moment to the spin angular momentum for an electron is called the gyromagnetic ratio and is given by $\gamma = 1.759 \times 10^{11}$ C/kg. The Lamor frequency can be expressed as $f_0 = \omega_0/2\pi$ = (2.8 MHz/oersted)(H_0 oersted), and $f_m = \omega_m/2\pi$ = (2.8 MHz/oersted)($4\pi M_s$ gauss) [55]. Additionally, in order to

account for magnetic losses inherent in the magnetic materials, the linewidth ΔH is included in the calculation of the Larmor frequency. Thus, $\omega_0 = \mu_0 \gamma H_0 + j\mu_0 \gamma \Delta H/2$, or $f_0 = (2.8 \text{ MHz/oersted})(H_0 \text{ oersted} + j\Delta H/2 \text{ oersted})$. During measurements the applied biasing magnetic field will be applied external to the sample using permanent magnets and it is therefore important to understand the relationship between the external and internal biasing fields. When the applied field is parallel to the broad face of the gyromagnetic sample, which is the case considered in this dissertation, the continuity of the magnetic field at the surface of the sample results in the external field being equal to the internal field.

The waveguide system, shown in Figure 5.1, consists of empty waveguide extensions connected to a sample holder with the same cross-section as the empty guide. This sample holder is completely filled by the MUT. It is assumed that the lengths of the extensions are such that a single TE_{10} rectangular waveguide mode is incident on the sample holder from the transmitting section ($z < 0$) and that a single mode is present at the receiving extension ($z > d$).

The material parameters are obtained using optimization methods that seek to minimize the difference between theoretically computed and measured reflection and transmission coefficients. As a result, accurate formulation of the theoretical scattering parameters is critical for valid characterization of gyromagnetic materials. This is accomplished by computing the S-parameters of the gyromagnetic material filled sample holder using a mode-matching technique, which accommodate the higher order modes excited from the coupling between orthogonal field components inside the sample region.

A single TE_{10} rectangular waveguide mode is incident on the sample, as shown in Figure 5.2, and, because of mode conversion at the interface been the empty guide and sample an infinite number of waveguide modes are reflected into the transmitting extensions, while an infinite number of waveguide modes are transmitted into the sample region, $0 < z < d$. The transmitted modal fields are incident on the next interface at $z = d$, and thus a spectrum of modes is reflected into the sample region and transmitted into the empty waveguide

extensions. Since the TE_{10} mode is invariant in the y-direction and even about $x = a/2$ and the gyromagnetic material is magnetized along the y-axis, then all excited higher order modes are also y-invariant and even about $x = a/2$. Thus, only TE_{n0} modes are needed to describe the fields in each of the waveguide regions.

5.2.1.1 Field Structure in a Waveguide Filled with Gyromagnetic Material

The wave equation for $H_z(x, y)$ for TE_z fields in the sample regions is given by (2.227). For TE_{n0} modes in a rectangular waveguide there is no y-dependence of the fields and the wave equation reduces to (2.229) and is expressed as

$$\left[\frac{\partial^2}{\partial x^2} + \left(k_c^s\right)^2\right] H_z(x) = 0, \tag{5.5}$$

where

$$\left(k_c^s\right)^2 = k_0^2 \mu_g \epsilon_r \left(1 - \frac{\kappa^2}{\mu_g^2}\right) - \beta^2 \tag{5.6}$$

is the cutoff wavenumber and $k_0 = \omega^2 \mu_0 \epsilon_0$ is the free-space wavenumber. The transverse fields are given by (2.251) and (2.252) and are shown to be

$$E_y^s(x) = -C_n k_{cn}^s \left(1 - \frac{\kappa^2}{\mu_g^2}\right) \sin\left(k_{cn}^s x\right) e^{\pm j\beta_n^s z} \tag{5.7}$$

$$H_x^s(x) = \mp \frac{C_n k_{cn}^s}{Z_n^s} \left[\sin\left(k_{cn}^s x\right) \mp \frac{\kappa k_{cn}^s}{\mu_g \beta_n^s} \cos\left(k_{cn}^s x\right)\right] e^{\pm j\beta_n^s z}. \tag{5.8}$$

Here $k_{cn}^s = n\pi/a$ is the cutoff wavenumber for the n^{th} TE_{n0} modes ($n = 1, 2, 3\ldots$) and $Z_n^s = \omega\mu_0\mu_g/\beta_n^s$ is the modal wave impedance. Note that β_n^s is determined from k_{cn}^s using (5.6).

The isotropic transverse field equations from (2.151) and (2.152) are used to represent the fields in the empty guide region for the present technique. Here only TE_{n0} modes are

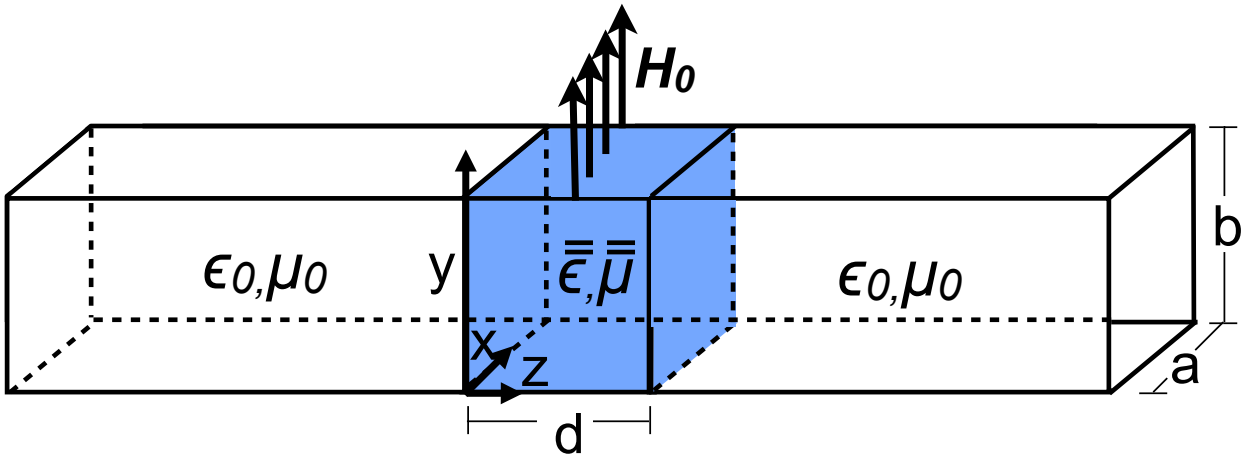

Figure 5.1: Rectangular waveguide with gyromagnetic sample placed in cross-sectional region with waveguide extensions attached.

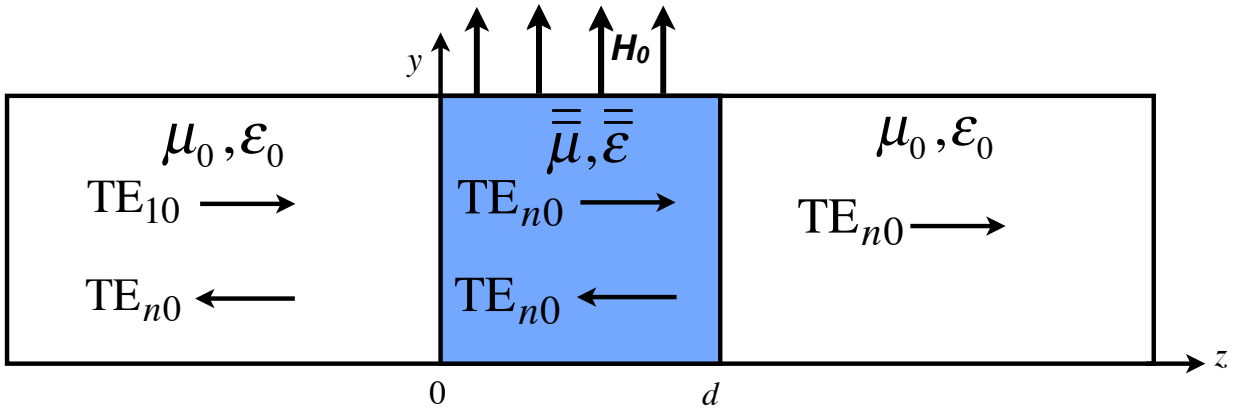

Figure 5.2: Side view of gyromagnetic material filled waveguide.

excited,. This means $v = 0$ for all excited modes. This leads to $k_{yn} = 0$, which reduces the field equations to

$$E_y^e(x,z) = -C_n k_{xn}^e \sin\left(k_{xn}^e x\right) \mathrm{e}^{\pm j\beta_n^e z} \tag{5.9}$$

$$H_x^e(x,z) = \mp C_n \frac{k_{xn}^e}{Z_n^e} \sin\left(k_{xn}^e x\right) \mathrm{e}^{\pm j\beta_n^e z}. \tag{5.10}$$

Here $k_{cn}^s = n\pi/w$ is the cutoff wavenumber, and $Z_n^e = \omega\mu_0/\beta_n^e$ is the modal wave impedance. Note that β_n^e is determined using (2.140).

5.2.1.2 Solutions for S-Parameters Using Modal Expansions

The transverse fields in the sample region and in the empty waveguide extensions can be expanded in an infinite sum of modal fields where the modal amplitude coefficients are determined through the enforcement of boundary conditions. In the empty waveguide extensions, $z < 0$ and $z > d$, the transverse fields are expressed as

$$Ey(x,z) = -a_1^+ k_{x1}^e \sin\left(k_{x1}^e x\right) \mathrm{e}^{-j\beta_1^e z} - \sum_{n=1}^{\infty} a_n^- k_{xn}^e \sin\left(k_{xn}^e x\right) \mathrm{e}^{j\beta_n^e z} \tag{5.11}$$

$$Hx(x,z) = a_1^+ \frac{k_{x1}^e}{Z_1^e} \sin\left(k_{x1}^e x\right) \mathrm{e}^{-j\beta_1^e z} - \sum_{n=1}^{\infty} a_n^- \frac{k_{xn}^e}{Z_n^e} \sin\left(k_{xn}^e x\right) \mathrm{e}^{j\beta_n^e z}, \tag{5.12}$$

and

$$Ey(x,z) = -\sum_{n=1}^{\infty} c_n^+ k_{xn}^e \sin\left(k_{xn}^e x\right) \mathrm{e}^{-j\beta_n^e (z-d)} \tag{5.13}$$

$$Hx(x,z) = \sum_{n=}^{\infty} c_n^+ \frac{k_{xn}^e}{Z_n^e} \sin\left(k_{xn}^e x\right) \mathrm{e}^{-j\beta_n^e (z-d)}, \tag{5.14}$$

respectively. In the sample region, $0 < z < d$, the transverse fields are given by

$$E_y(x,z) = -\sum_{n=1}^{\infty} k_{cn}^s \left[b_n^+ \mathrm{e}^{-j\beta_n^s z} + b_n^- \mathrm{e}^{j\beta_n^s z}\right] \left(1 - \frac{\kappa^2}{\mu_g^2}\right) \sin\left(k_{cn}^s x\right) \tag{5.15}$$

$$\begin{aligned} H_x(x,z) = &\sum_{n=}^{\infty} \frac{k_{cn}^s}{Z_n^s} b_n^+ \left[\sin\left(k_{cn}^s x\right) + \frac{\kappa k_{cn}^s}{\mu_g \beta_n^s} \cos\left(k_{cn}^s x\right)\right] \mathrm{e}^{-j\beta_n^s z} \\ &- \sum_{n=}^{\infty} \frac{k_{cn}^s}{Z_n^s} b_n^- \left[\sin\left(k_{cn}^s x\right) - \frac{\kappa k_{cn}^s}{\mu_g \beta_n^s} \cos\left(k_{cn}^s x\right)\right] \mathrm{e}^{j\beta_n^s z}. \end{aligned} \tag{5.16}$$

In (5.11) and (5.12), a_1^+ is the amplitude of the incident TE_{10} wave, which is assumed to be known during analysis. The remaining modal amplitude coefficients a_n^-, b_n^+, b_n^-, and c_n^+ may be determined by applying boundary conditions on E_y and H_x at the interfaces between the empty waveguide and sample regions. At $z = 0$ the boundary condition on the tangential electric field requires

$$\begin{aligned} &a_1^+ k_{xn}^e \sin\left(k_{x1}^e x\right) + \sum_{n=1}^{\infty} a_n^- k_{xn}^e \sin\left(k_{xn}^e x\right) = \\ &\sum_{n=1}^{\infty} k_{cn}^s \left[b_n^+ + b_n^-\right] \left(1 - \frac{\kappa^2}{\mu_g^2}\right) \sin\left(k_{cn}^s x\right), \end{aligned} \tag{5.17}$$

while the boundary condition on the tangential magnetic field requires

$$\begin{aligned} &a_1^+ \frac{k_{xn}^e}{Z_1^e} \sin\left(k_{x1}^e x\right) - \sum_{n=1}^{\infty} a_n^- \frac{k_{xn}^e}{Z_n^e} \sin\left(k_{xn}^e x\right) = \\ &\sum_{n=1}^{\infty} \frac{k_{cn}^s}{Z_n^s} b_n^+ \left[\sin\left(k_{cn}^s x\right) + \frac{\kappa k_{cn}^s}{\mu_g \beta_n^s} \cos\left(k_{cn}^s x\right)\right] - \\ &\sum_{n=1}^{\infty} \frac{k_{cn}^s}{Z_n^s} b_n^- \left[\sin\left(k_{cn}^s x\right) - \frac{\kappa k_{cn}^s}{\mu_g \beta_n^s} \cos\left(k_{cn}^s x\right)\right]. \end{aligned} \tag{5.18}$$

Similarly, imposing the tangential boundary conditions on the electric and magnetic fields at $z = d$ gives

$$\sum_{n=1}^{\infty} c_n^+ k_{xn}^e \sin\left(k_{xn}^e x\right) = \sum_{n=1}^{\infty} k_{cn}^s \left[b_n^+ \mathrm{e}^{-j\beta_n^s d} + b_n^- \mathrm{e}^{j\beta_n^s d}\right] \left(1 - \frac{\kappa^2}{\mu_g^2}\right) \sin\left(k_{cn}^s x\right), \quad (5.19)$$

and

$$\sum_{n=1}^{\infty} c_n^+ \frac{k_{xn}^e}{Z_n^e} \sin\left(k_{xn}^e x\right) = \sum_{n=1}^{\infty} \frac{k_{cn}^s}{Z_n^s} b_n^+ \left[\sin\left(k_{cn}^s x\right) + \frac{\kappa k_{cn}^s}{\mu_g \beta_n^s} \cos\left(k_{cn}^s x\right)\right] \mathrm{e}^{-j\beta_n^s d} - \sum_{n=1}^{\infty} \frac{k_{cn}^s}{Z_n^s} b_n^- \left[\sin\left(k_{cn}^s x\right) - \frac{\kappa k_{cn}^s}{\mu_g \beta_n^s} \cos\left(k_{cn}^s x\right)\right] \mathrm{e}^{j\beta_n^s d}, \quad (5.20)$$

respectively.

To convert the system of functional equations (5.17)-(5.20) to a system of linear equations, the infinite summations are each truncated at N terms and the following testing operations are applied. First, (5.17) is multiplied by $\sin\left(k_{xm}^e x\right)$ and integrated over $0 < x < a$. This results in

$$a_1^+ k_{x1}^e \frac{a}{2} \delta_{m1} + \sum_{n=1}^{N} a_n^- k_{xn}^e \frac{a}{2} \delta_{mn} = \sum_{n=1}^{N} k_{cn}^s \left[b_n^+ + b_n^-\right] \left(1 - \frac{\kappa^2}{\mu_g^2}\right) \frac{a}{2} \delta_{mn} \quad m = 1, 2, 3 \ldots N, \quad (5.21)$$

or

$$-a_m^- + b_m^+ \left(1 - \frac{\kappa^2}{\mu_g^2}\right) + b_m^- \left(1 - \frac{\kappa^2}{\mu_g^2}\right) = a_1^+ \delta_{m1} \quad m = 1, 2, 3 \ldots N. \quad (5.22)$$

Then, (5.18) is multiplied by $\sin(k^s_{cm}x)$ and integrated over $0 < x < a$. This produces

$$a_1^+ \frac{k^e_{x1}}{Z^e_m}\frac{a}{2}\delta_{m1} - \sum_{n=1}^{N} a_n^- \frac{k^e_{xn}}{Z^e_n}\frac{a}{2}\delta_{mn} = \sum_{n=1}^{N} \frac{k^s_{cn}}{Z^s_n} b_n^+ \left[\frac{a}{2}\delta_{mn} + \frac{\kappa k^s_{cn}}{\mu_g \beta^s_n}\frac{a}{2}\Delta_{mn}\right] - \sum_{n=1}^{N} \frac{k^s_{cn}}{Z^s_n} b_n^- \left[\frac{a}{2}\delta_{mn} - \frac{\kappa k^s_{cn}}{\mu_g \beta^s_n}\frac{a}{2}\Delta_{mn}\right] \qquad m = 1, 2, 3 \ldots N, \tag{5.23}$$

or

$$a_m^- \frac{k^e_{xm}}{Z^e_m} + \sum_{n=1}^{N} \frac{k^s_{cn}}{Z^s_n} b_n^+ \left[\delta_{mn} + \frac{\kappa k^s_{cn}}{\mu_g \beta^s_n}\Delta_{mn}\right] - \sum_{n=1}^{N} \frac{k^s_{xn}}{Z^s_n} b_n^- \left[\delta_{mn} - \frac{\kappa k^s_{cn}}{\mu_g \beta^s_n}\Delta_{mn}\right] = a_1^+ \frac{k^e_{x1}}{Z^e_m}\delta_{m1} \qquad m = 1, 2, 3 \ldots N. \tag{5.24}$$

Next, (5.19) is multiplied by $\sin(k^e_{xm}x)$ and integrated over $0 < x < a$. This results in

$$\sum_{n=1}^{N} c_n^+ k^e_{xn}\frac{a}{2}\delta_{mn} = \sum_{n=1}^{N} b_n^+ k^s_{cn}\left(1 - \frac{\kappa^2}{\mu_g^2}\right)\frac{a}{2}\delta_{mn}\mathrm{e}^{-j\beta^s_n d} + \sum_{n=1}^{N} b_n^- k^s_{cn}\left(1 - \frac{\kappa^2}{\mu_g^2}\right)\frac{a}{2}\delta_{mn}\mathrm{e}^{j\beta^s_n d} \qquad m = 1, 2, 3 \ldots N, \tag{5.25}$$

or

$$c_m^+ = b_m^+\left(1 - \frac{\kappa^2}{\mu_g^2}\right)\mathrm{e}^{-j\beta^s_m d} + b_m^-\left(1 - \frac{\kappa^2}{\mu_g^2}\right)\mathrm{e}^{j\beta^s_m d} \qquad m = 1, 2, 3 \ldots N. \tag{5.26}$$

Finally, (5.20) is multiplied by $\sin(k^s_{cm}x)$ and integrated over $0 < x < a$. This produces

$$\sum_{n=1}^{N} c_n^+ \frac{k^e_{xn}}{Z^e_n}\frac{a}{2}\delta_{mn} = \sum_{n=1}^{N} \frac{k^s_{cn}}{Z^s_n} b_n^+ \left[\frac{a}{2}\delta_{mn} + \frac{\kappa k^s_{cn}}{\mu_g \beta^s_n}\frac{a}{2}\Delta_{mn}\right]\mathrm{e}^{-j\beta^s_n d} - \sum_{n=1}^{N} \frac{k^s_{cn}}{Z^s_n} b_n^- \left[\frac{a}{2}\delta_{mn} - \frac{\kappa k^s_{cn}}{\mu_g \beta^s_n}\frac{a}{2}\Delta_{mn}\right]\mathrm{e}^{j\beta^s_n d} \qquad m = 1, 2, 3 \ldots N, \tag{5.27}$$

or

$$c_m^+ \frac{k_{xm}^e}{Z_m^e} = \sum_{n=1}^{N} \frac{k_{cn}^s}{Z_n^s} b_n^+ \left[\delta_{mn} + \frac{\kappa k_{cn}^s}{\mu_g \beta_n^s} \Delta_{mn}\right] \mathrm{e}^{-j\beta_n^s d}$$

$$- \sum_{n=1}^{N} \frac{k_{cn}^s}{Z_n^s} b_n^- \left[\delta_{mn} - \frac{\kappa k_{cn}^s}{\mu_g \beta_n^s} \Delta_{mn}\right] \mathrm{e}^{j\beta_n^s d} \qquad m = 1, 2, 3 \ldots N. \tag{5.28}$$

In (5.21) - (5.28),

$$\Delta_{mn} = \begin{cases} 0, & m-n \text{ even} \\ \frac{4}{\pi} \frac{m}{m^2 - n^2}, & m-n \text{ odd.} \end{cases} \tag{5.29}$$

Note that these integrals are derived in Appendix B.4. These equations can be simplified by defining $L_n = -\kappa k_{cn}^s / (\mu_g \beta_n^s)$, $C = (1 - \kappa^2/\mu_g^2)$, and $P_n^{\pm} = \mathrm{e}^{\mp j\beta_n^s d}$, which results in

$$-a_m^- + C b_m^+ + C b_m^- = \delta_{m1} a_1^+ \tag{5.30}$$

$$\frac{k_{xm}^e}{Z_m^e} a_m^- + \sum_{n=1}^{N} \frac{k_{cn}^s}{Z_n^s} b_n^+ \left[\delta_{mn} - L_n \Delta_{mn}\right] - \sum_{n=1}^{N} \frac{k_{cn}^s}{Z_n^s} b_n^- \left[\delta_{mn} + L_n \Delta_{mn}\right]$$

$$= \frac{k_{xm}^e}{Z_m^e} \delta_{m1} a_1^+ \tag{5.31}$$

$$C b_m^+ P_m^+ + C b_m^- P_m^- = c_m^+ \tag{5.32}$$

$$\sum_{n=1}^{N} \frac{k_{cn}^s}{Z_n^s} b_n^+ \left[\delta_{mn} - L_n \Delta_{mn}\right] P_n^+ - \sum_{n=1}^{N} \frac{k_{cn}^s}{Z_n^s} b_n^- \left[\delta_{mn} + L_n \Delta_{mn}\right] P_n^- = \frac{k_{xm}^e}{Z_m^e} c_m^+. \tag{5.33}$$

Next, rearranging (5.30) and substituting into (5.31) yields

$$\frac{k_{xn}^e}{Z_m^e} \left(C b_m^+ + C b_m^- - \delta_{m1} a_1^+\right) + \sum_{n=1}^{N} \frac{k_{cn}^s}{Z_n^s} b_n^+ \left[\delta_{mn} - L_n \Delta_{mn}\right]$$

$$- \sum_{n=1}^{N} \frac{k_{cn}^s}{Z_n^s} b_n^- \left[\delta_{mn} + L_n \Delta_{mn}\right] = \frac{k_{xm}^e}{Z_m^e} \delta_{m1} a_1^+. \tag{5.34}$$

The modal amplitude coefficients, b_n^+ and b_n^-, resulting from the substitution can be brought

into the summations by multiplying the coefficients by δ_{mn}. This results in

$$\sum_{n=1}^{N} b_n^+ \left\{ \delta_{mn} \left[C\frac{k_{xn}^e}{Z_n^e} + \frac{k_{cn}^s}{Z_n^s} \right] - \frac{k_{cn}^s}{Z_n^s} L_n \Delta_{mn} \right\}$$
$$+ \sum_{n=1}^{N} b_n^- \left\{ \delta_{mn} \left[C\frac{k_{xn}^e}{Z_n^e} - \frac{k_{cn}^s}{Z_n^s} \right] - \frac{k_{cn}^s}{Z_n^s} L_n \Delta_{mn} \right\} = \frac{2k_{xm}^e}{Z_m^e} \delta_{m1} a_1^+. \tag{5.35}$$

Similarly, substituting (5.32) into (5.33) results in

$$\sum_{n=1}^{N} b_n^+ \left\{ \delta_{mn} \left[C\frac{k_{xn}^e}{Z_n^e} - \frac{k_{cn}^s}{Z_n^s} \right] + \frac{k_{cn}^s}{Z_n^s} L_n \Delta_{mn} \right\} P_n^+$$
$$+ \sum_{n=1}^{N} b_n^- \left\{ \delta_{mn} \left[C\frac{k_{xn}^e}{Z_n^e} + \frac{k_{cn}^s}{Z_n^s} \right] + \frac{k_{cn}^s}{Z_n^s} L_n \Delta_{mn} \right\} P_n^- = 0. \tag{5.36}$$

Now, (5.35) and (5.36) can be represented in a $2N \times 2N$ matrix equation

$$\left[\begin{array}{c|c} D & F \\ \hline H & J \end{array}\right] \left[\begin{array}{c} b^+ \\ \hline b^- \end{array}\right] = \left[\begin{array}{c} K \\ \hline 0 \end{array}\right], \tag{5.37}$$

where D, F, H, and J are $N \times N$ sub-matrices and K is a vector with N terms.

Once the modal coefficients, b_n^+ and b_n^-, are found by solving the matrix equation, the remaining unknown modal coefficients a_n^- and c_n^+ may be determined using (5.30) and (5.32), respectively. The sample-plane S-parameters are then given by

$$S_{11} = \frac{a_1^-}{a_1^+} \tag{5.38}$$

$$S_{21} = \frac{c_1^+}{a_1^+}. \tag{5.39}$$

The modal series is terminated when the magnitude and phase of the S-parameters reach specified tolerances for M contiguous values of N. As was the case in Section 4.3.2, a value

of $M = 5$ is sufficient to guarantee convergence to desired accuracy in the method presented here.

5.2.2 Validation of the Mode-Matching Analysis

The mode-matching technique is validated by considering the gyromagnetic material G1010 made by Trans-Tech, Inc. A sample of the material with 5 mm thickness is simulated inside the cross-sectional plane of WR-650 L-band waveguide with dimensions $a = 6.50$ inches by $b = 3.25$ inches. The physical material parameters have a saturation magnetization of $4\pi M_S = 1000$ gauss, $\Delta H = 25$ oersteds, and an applied static magnetic field $H_0 = 1000$ oersteds. In this simulation a value of $\Delta H = 0$ oersteds is considered. The value of H_0 was chosen because the resulting Ferromagnetic resonance (FMR) frequency of 2.8 GHz is above the operating band of the L-band waveguide. FMR is also known as gyromagnetic resonance and occurs when the permeability parameters, (5.3) and (5.4), become infinite or when the operational frequency equals the Larmor frequency. An example of FMR is shown in Figure 5.3, where, using these physical parameters, κ and μ_g are determined from (5.3) and (5.4), respectively. FMR just above the measurement band is beneficial because the extracted μ_g and κ have interesting values, i.e. $\mu_g > 1$ and $\kappa \neq 0$. This is demonstrated in the inset of Figure 5.3, where the permeability parameters are shown over the L-band frequency range. When FMR occurs within the measurement band, the number of modes, N, needed for convergence of the S-parameters becomes exceedingly high and the computational time required for the mode matching analysis becomes prohibitively large. Thus, when FMR occurs outside the measurement band, the mode matching approach is faster, making lengthy optimizations far more feasible. When FMR is below the frequency range of interest, either $\kappa \approx 0$ and $\mu_g \approx 1$, or $\kappa < 0$ and $\mu_g < 0$. These conditions are not of interest for the characterization technique discussed in this dissertation.

The mode matching technique was simulated with absolute tolerances of 0.1 dB for $|S|$ and 0.01° for $\angle S$. These values were chosen so that the accuracy of the computed series

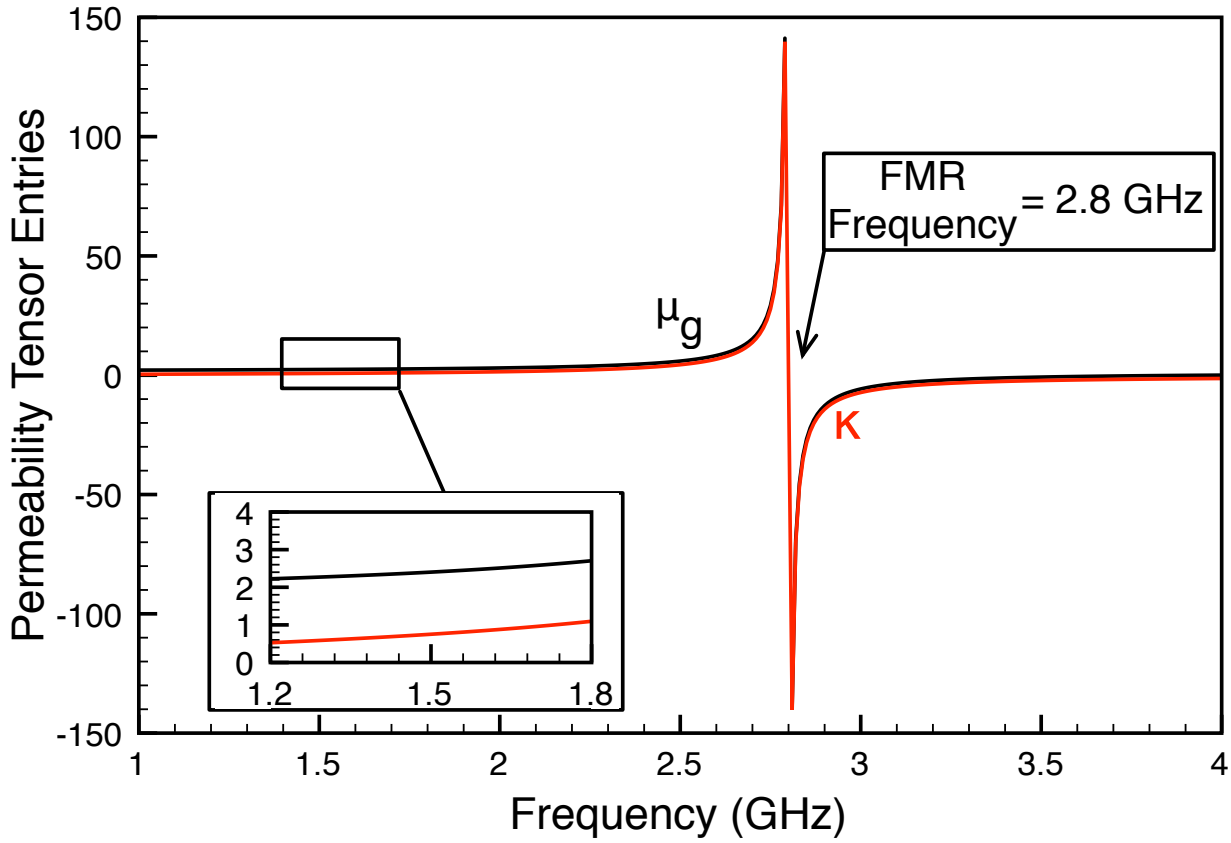

Figure 5.3: Permeability tensor entries determined using (5.3) and (5.4).

is significantly better than the expected measurement accuracy of the HP 8510C VNA. The accuracy of the S-parameters computed by the mode matching analysis was tested by comparing the simulated data to those obtained using a full-wave FEM solver developed at Michigan State University. As seen in Figure 5.4, the FEM simulated S-parameter match the results of the mode matching analysis very well across the L-band frequency range, thus validating the modal computation of the theoretical S-parameters.

5.2.3 Extraction Process

To characterize a gyromagnetic sample with one set of measurements at discrete frequencies requires extracting three complex unknown parameters (μg, κ, and ϵ_r) from two complex measurements (S_{11} and S_{21}). This results in an underdetermined system. Therefore, a non-linear least squares inversion method [56] is utilized to extract the frequency-independent parameters, M_s and H_0, along with permittivity $\epsilon_r = \epsilon_r' - j\epsilon_r''$ which is assumed to be frequency independent, although it is not. For the types of gyromagnetic materials that are of interest, the permittivity changes very little over the measurement band, and therefore the assumption of a frequency-independent permittivity is sufficient for accurate characterization. This method uses the transmission and reflection coefficients measured (or simulated) at a number of frequencies in the desired band, and employs a least squares method to solve the over-determined problem. The squared error between the measured and theoretical S-parameters is defined as

$$\upsilon = \sqrt{\sum_{j=1}^{N_f} \left[\left| S_{11,r}^{meas}(f_j) - S_{11,r}^{thy}(f_j) \right|^2 + \left| S_{11,i}^{meas}(f_j) - S_{11,i}(f_j)^{thy} \right|^2 \right]} + \sqrt{\sum_{j=1}^{N_f} \left[\left| S_{21,r}^{meas}(f_j) - S_{21,r}^{thy}(f_j) \right|^2 + \left| S_{21,i}^{meas}(f_j) - S_{21,i}^{thy}(f_j) \right|^2 \right]}, \quad (5.40)$$

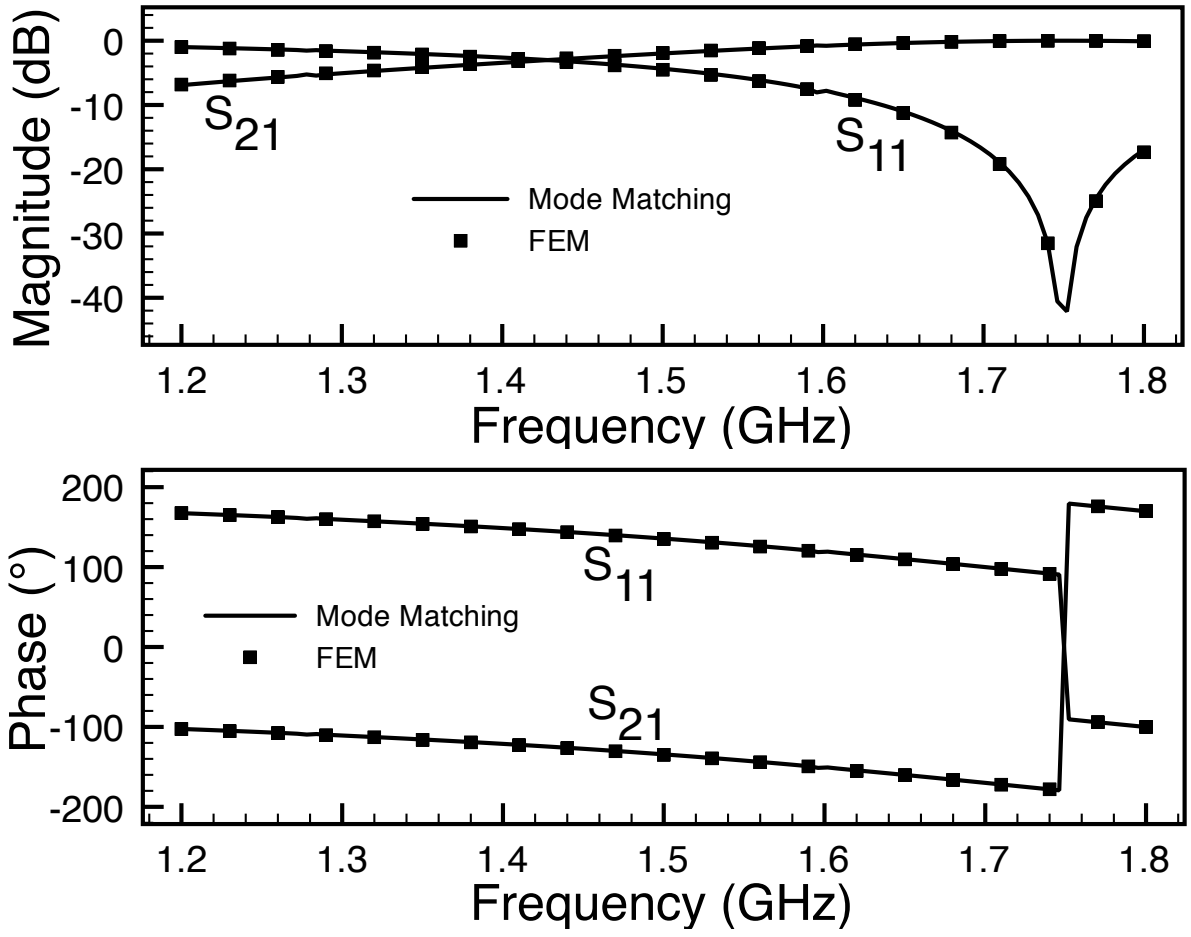

Figure 5.4: S-parameters computed for a gyromagnetic test material.

where f_j is the j^{th} frequency point, and r and i denote the real and imaginary parts of the S-parameters, respectively. Here, S^{thy} are the theoretical S-parameters calculated using modal analysis, and S^{meas} are the measured (or simulated) values.

To test the extraction method, simulated S-parameters are used as a substitute for measured S-parameters. This current technique does not characterize ΔH, since initial implementation assumed lossless permeability. Although characterization of ΔH was originally planned, obtaining large gyromagnetic samples to fill the cross-section of an L-Band or S-Band waveguide was not possible. Therefore, the second technique in this chapter discusses use of a reduce-aperture sample holder for characterizing smaller samples and subsequently ΔH is included in the analysis. To validate the current extraction technique, the FEM simulated S-parameters shown in Figure 5.4 are used, and the characterization technique is tested by extracting the material parameters from the simulated data. Figure 5.5 shows the extracted and theoretical material parameters, and it is apparent that the developed extraction routine is capable of accurately characterizing G1010 material. Note that the theoretical material parameters are determined using (5.3) and (5.4) with the physical parameter outlined in Section 5.2.2.

5.2.4 Summary

A technique for characterizing gyromagnetic materials has been developed and described in this section. The technique uses the least-squares method to find the material parameters from measured or simulated S-parameters. The technique has been tested using simulated S-parameters obtained using an in-house FEM code that includes a full tensor model of permeability. It was shown that the method is capable of accurately extracting the material parameters of the gyromagnetic material G-1010. This method has limitations since the sample size required for characterizing gyromagnetic samples with the use L-band or S-band waveguides is not feasible due to sample size restrictions.

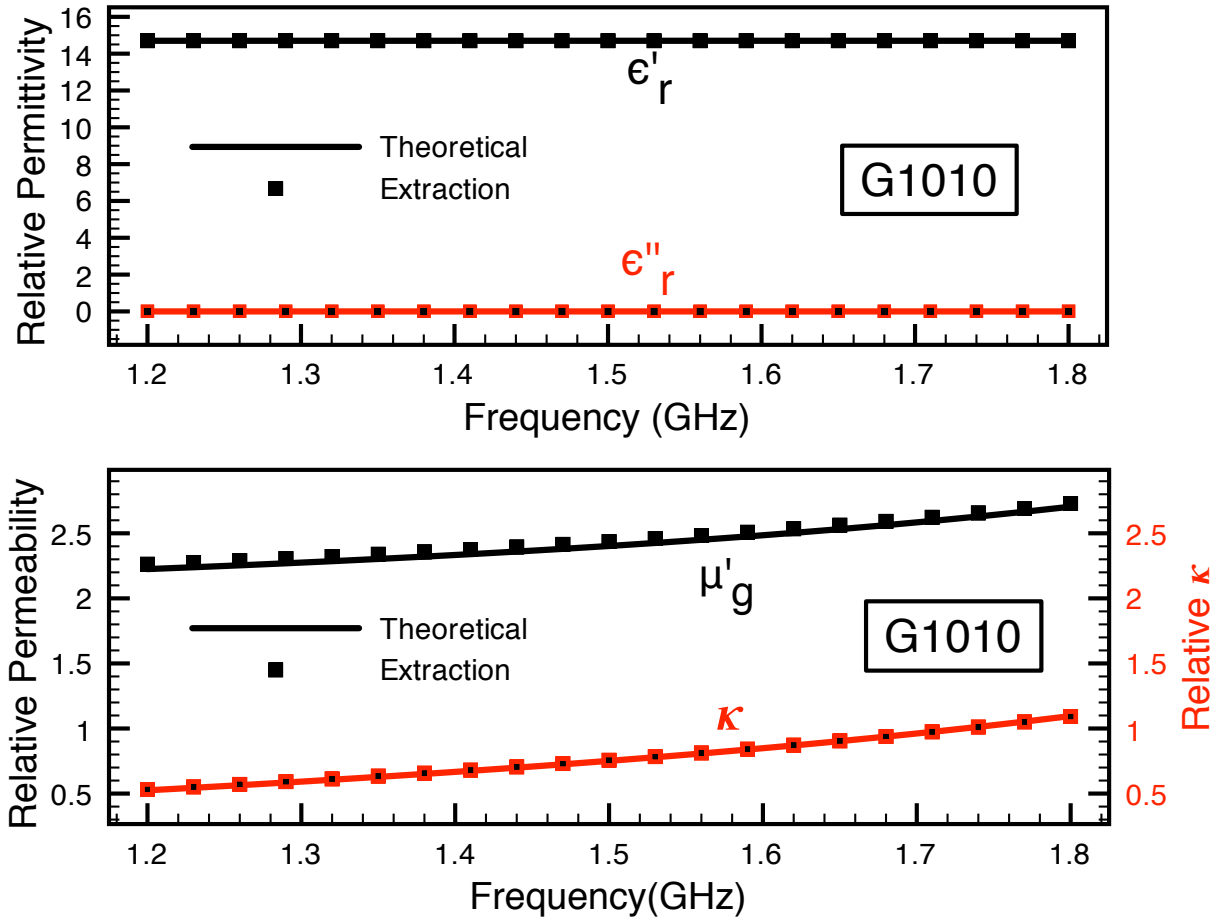

Figure 5.5: Material parameters characterized using FEM generated S-parameters.

5.3 Material Characterization of Gyromagnetic Material Using a Reduced Aperture Waveguide

The focus of this section is the extraction of the permeability tensor and isotropic permittivity of a gyromagnetic material using a reduced aperture sample holder. The cross-sectional dimensions of waveguides become prohibitively large at low frequencies, and it is at these frequencies that the gyromagnetic properties are most pronounced. However, sufficiently large samples may not be available. Therefore, the use of a reduced aperture sample holder is proposed which does not require the sample to fill the entire cross section of the guide. Modal analysis is used to determine the reflection and transmission coefficients of the dominant mode. A non-linear least squares method is employed to extract the gyromagnetic material parameters

5.3.1 Theoretical Transmission and Reflection Coefficients Using Mode-Matching Analysis

The MUT is assumed to be linear, homogeneous, and biased perpendicular to the broad dimension of the waveguide which results in the permittivity and permeability tensor given in (5.1) and (5.2). The waveguide system, shown in Figure 5.6, consists of empty waveguide extensions connected to a reduced aperture sample holder completely filled by the MUT. A cross-section view of the reduced aperture is shown in Figure 5.7. It is assumed that the lengths of the extensions are such that a single TE_{10} mode rectangular waveguide mode is incident on the sample holder from the transmitting extension ($z < 0$), and a single mode is obtained at the end of the receiving extension ($z > d$).

As with every characterization technique discussed in this dissertation, accurate formulation of the theoretical S-parameters is essential for reliable characterization of the MUT. The constitutive material parameters are determined by minimizing the difference between mea-

sured and theoretically computed reflection and transmission coefficients. The theoretical S-parameters of the reduced-aperture waveguide system are determined using a mode-matching technique which accommodates the higher order modes excited from the discontinuity with the reduced aperture and the coupling between orthogonal field components. The single TE_{10} mode incident on the sample holder results in an infinite number of waveguide modes reflected back into the transmitting extension. Additionally, an infinite number of waveguide modes are transmitted into the sample region and incident on the discontinuity at $z = d$. Thus a spectrum of modes is also reflected back into the sample region and transmitted into the waveguide extension.

Since the electric field of the TE_{10} mode incident on the sample holder, as shown in Figure 5.8, is even about $x = 0$, and because the aperture is even about $x = 0$ and the gyromagnetic material is biased along the y-axis, only modes with electric field even about $x = 0$ will be excited. Thus, only TE_{n0} modes are needed to describe the fields in each of the waveguide regions.

5.3.1.1 Field Structure in a Waveguide Filled with Gyromagnetic Material

Assume the gyromagnetic material is magnetized along the y-axis, such that the material parameters are described in (5.1) and (5.2). For TE_{n0} modes in a gyromagnetic filled rectangular waveguide region the wave equation from (2.227) reduces to (5.5), where the cutoff wavenumber is expressed in (5.6). As was shown previously in Section 2.3.3.1, the wave equation is solved using a separation of variables and enforcing the boundary conditions on the tangential electric field at the perfectly conducting waveguide walls. Since the reduced-aperture sample region is centered about $x = 0$ as seen Figure 5.6, the sinusoidal function in the transverse electric and magnetic field equations from (2.251) and (2.252) are offset by

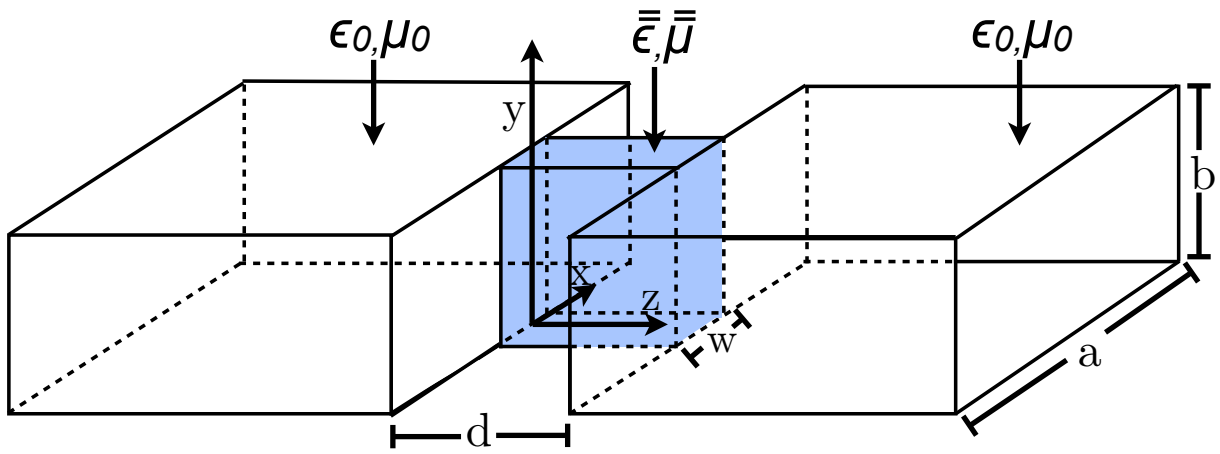

Figure 5.6: Reduced-aperture waveguide sample holder with waveguide extensions attached.

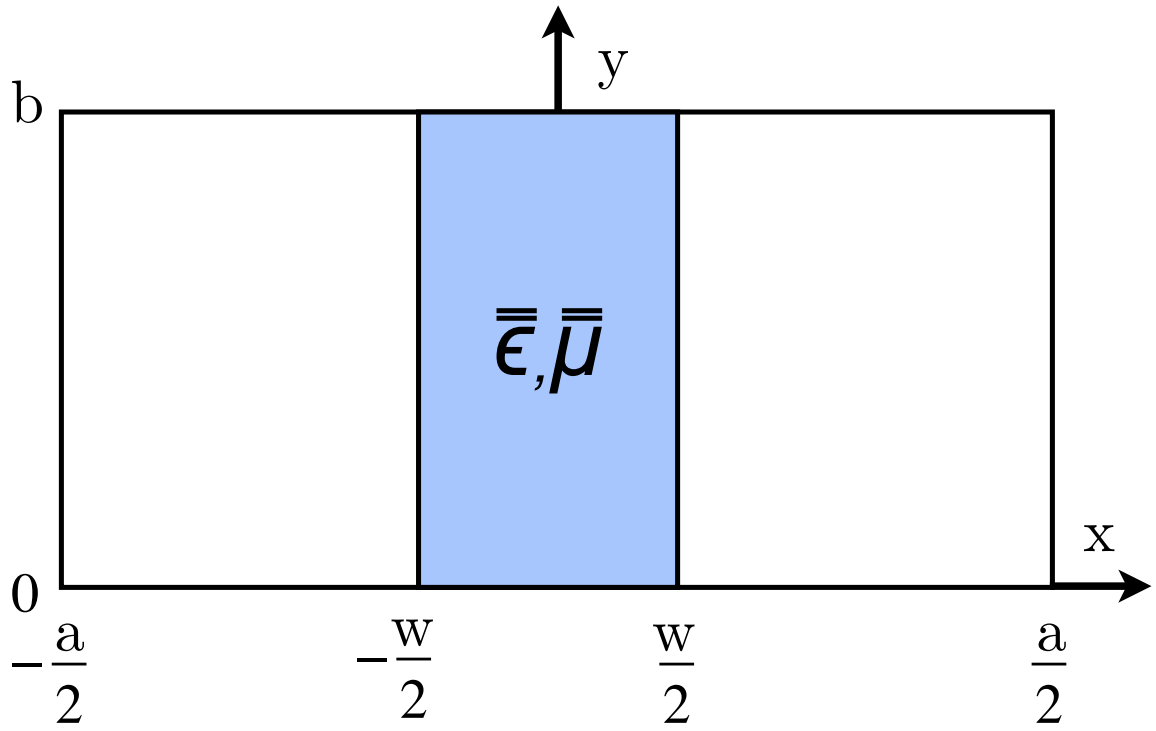

Figure 5.7: Cross-sectional view of reduced-aperture waveguide.

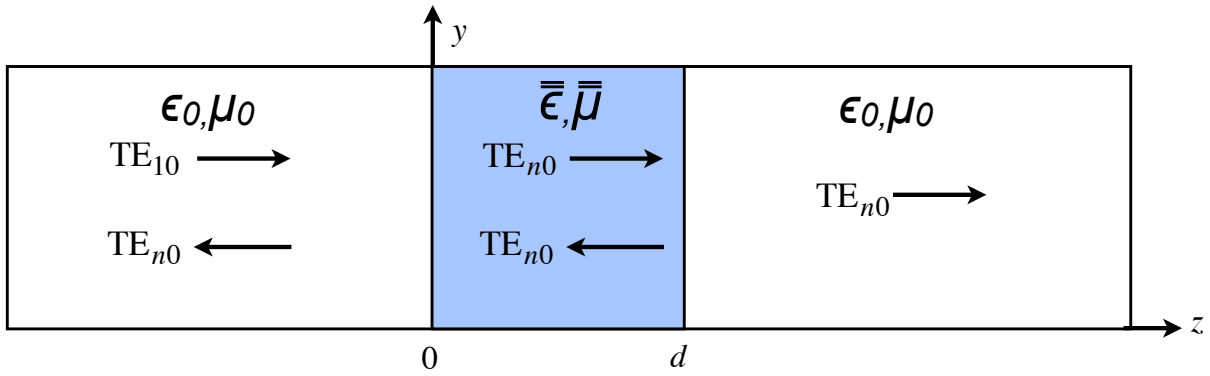

Figure 5.8: Side view of reduced aperture waveguide.

$w/2$. This results in the following transverse field equations:

$$E_y^s(x,z) = -C_n k_{cn}^s \left(1 - \frac{\kappa^2}{\mu_g^2}\right) \sin\left[k_{cn}^s\left(x - \frac{w}{2}\right)\right] e^{\pm j\beta_n^s z} \tag{5.41}$$

$$H_x^s(x,z) = \mp \frac{C_n k_{cn}^s}{Z_n^s} \left\{\sin\left[k_{cn}^s\left(x - \frac{w}{2}\right)\right] \mp \frac{\kappa k_{cn}^s}{\mu_g \beta_n^s} \cos\left[k_{cn}^s\left(x - \frac{w}{2}\right)\right]\right\} e^{\pm j\beta_n^s z}. \tag{5.42}$$

Here $k_{cn}^s = n\pi/w$ is the cutoff wavenumber for the n^{th} TE_{n0} mode, $Z_n^s = \omega\mu_0\mu_g/\beta_n^s$, and β_n^s is determined from (5.6).

The transverse field equations for the empty waveguide extensions may be determined using (5.9) and (5.10), as long as, once again, the sinusoidal functions are offset. For the empty regions, the sinusoidal functions are offset by $a/2$. This yields the following transverse field equations:

$$E_y^e(x,z) = -D_n k_{xn}^e \sin\left[k_{xn}^e\left(x - \frac{a}{2}\right)\right] \mathrm{e}^{\pm j\beta_n^e z} \tag{5.43}$$

$$H_x^e(x,z) = \mp D_n \frac{k_{xn}^e}{Z_n^e} \sin\left[k_{xn}^e\left(x - \frac{a}{2}\right)\right] \mathrm{e}^{\pm j\beta_n^e z}. \tag{5.44}$$

Here $k_{cn}^s = n\pi/w$ is the cutoff wavenumber, and $Z_n^e = \omega\mu_0/\beta_n^e$ is the modal wave impedance. Note that β_n^e is determined using (2.140).

5.3.1.2 Solution for S-Parameters Using Modal Expansions

Mode-matching analysis is utilized to first expand the transverse field in the sample holder and in the waveguide extensions in an infinite sum of modal fields. Then with the application of boundary conditions, the modal amplitudes can be determined. First, in the empty waveguide extension region, $z < 0$, the transverse fields are

$$\begin{aligned} E_y(x,z) = &-A_1^+ k_{x1}^e \sin\left[k_{x1}^e\left(x-\frac{a}{2}\right)\right] \mathrm{e}^{-j\beta_1^e z} \\ &- \sum_{n=1}^{\infty} A_n^- k_{xn}^e \sin\left[k_{xn}^e\left(x-\frac{a}{2}\right)\right] \mathrm{e}^{j\beta_n^e z} \end{aligned} \tag{5.45}$$

$$\begin{aligned} H_x(x,z) = &\frac{A_1 k_{x1}^e}{Z_1^e} \sin\left[k_{x1}^e\left(x-\frac{a}{2}\right)\right] \mathrm{e}^{-j\beta_1^e z} \\ &- \sum_{n=1}^{\infty} \frac{A_n^- k_{xn}^e}{Z_n^e} \sin\left[k_{xn}^e\left(x-\frac{a}{2}\right)\right] \mathrm{e}^{j\beta_n^e z}. \end{aligned} \tag{5.46}$$

Here A_1^+ is the amplitude of the incident TE_{10} wave and is assumed known during analysis. Next, in the sample holder region, $0 < z < d$, the transverse fields are

$$\begin{aligned} E_y(x,z) = &-\sum_{n=1}^{\infty} B_n^+ k_{cn}^s \left(1-\frac{\kappa^2}{\mu_g^2}\right) \sin\left[k_{cn}^s\left(x-\frac{w}{2}\right)\right] e^{-j\beta_n^s z} \\ &- \sum_{n=1}^{\infty} B_n^- k_{cn}^s \left(1-\frac{\kappa^2}{\mu_g^2}\right) \sin\left[k_{cn}^s\left(x-\frac{w}{2}\right)\right] e^{j\beta_n^s z} \end{aligned} \tag{5.47}$$

$$\begin{aligned} H_x(x,z) = &\sum_{n=1}^{\infty} \frac{B_n^+ k_{cn}^s}{Z_n^s} \left\{\sin\left[k_{cn}^s\left(x-\frac{w}{2}\right)\right] + \frac{\kappa k_{cn}^s}{\mu_g \beta_n^s} \cos\left[k_{cn}^s\left(x-\frac{w}{2}\right)\right]\right\} e^{-j\beta_n^s z} \\ &- \sum_{n=1}^{\infty} \frac{B_n^- k_{cn}^s}{Z_n^s} \left\{\sin\left[k_{cn}^s\left(x-\frac{w}{2}\right)\right] - \frac{\kappa k_{cn}^s}{\mu_g \beta_n^s} \cos\left[k_{cn}^s\left(x-\frac{w}{2}\right)\right]\right\} e^{j\beta_n^s z}. \end{aligned} \tag{5.48}$$

Finally, in the waveguide extension $z > d$ the fields are given by

$$E_y(x,z) = -\sum_{n=1}^{\infty} C_n^+ k_{xn}^e \sin\left[k_{xn}^e\left(x-\frac{a}{2}\right)\right] \mathrm{e}^{-j\beta_n^e(z-d)} \tag{5.49}$$

$$H_x(x,z) = \sum_{n=1}^{\infty} \frac{C_n^+ k_{xn}^e}{Z_n^e} \sin\left[k_{xn}^e\left(x-\frac{a}{2}\right)\right] \mathrm{e}^{-j\beta_n^e(z-d)}. \tag{5.50}$$

By applying the boundary conditions on Ey and H_x at the interfaces between the two waveguide extensions and the sample holder, the modal amplitude coefficients A_n^-, B_n^+, B_n^-, and C_n^+ may be determined. The boundary condition on the tangential electric field at $z = 0$ requires

$$A_1^+ k_{x1}^e \sin\left[k_{x1}^e\left(x-\frac{a}{2}\right)\right] + \sum_{n=1}^{\infty} A_n^- k_{xn}^e \sin\left[k_{xn}^e\left(x-\frac{a}{2}\right)\right] =$$

$$\begin{cases} \displaystyle\sum_{n=1}^{\infty} B_n^+ k_{cn}^s \left(1-\frac{\kappa^2}{\mu_g^2}\right) \sin\left[k_{cn}^s\left(x-\frac{w}{2}\right)\right] & \\ \quad + \sum_{n=1}^{\infty} B_n^- k_{cn}^s \left(1-\frac{\kappa^2}{\mu_g^2}\right) \sin\left[k_{cn}^s\left(x-\frac{w}{2}\right)\right], & 0 < |x| < \frac{w}{2} \\ 0, & \frac{w}{2} < |x| < \frac{a}{2}, \end{cases} \tag{5.51}$$

and the boundary condition on the tangential magnetic field requires

$$\frac{A_1 k_{x1}^e}{Z_1^e} \sin\left[k_{x1}^e\left(x-\frac{a}{2}\right)\right] - \sum_{n=1}^{\infty} \frac{A_n^- k_{xn}^e}{Z_n^e} \sin\left[k_{xn}^e\left(x-\frac{a}{2}\right)\right] =$$

$$\sum_{n=1}^{\infty} \frac{B_n^+ k_{cn}^s}{Z_n^s} \left\{\sin\left[k_{cn}^s\left(x-\frac{w}{2}\right)\right] + \frac{\kappa k_{cn}^s}{\mu_g \beta_n^s} \cos\left[k_{cn}^s\left(x-\frac{w}{2}\right)\right]\right\}$$

$$-\sum_{n=1}^{\infty} \frac{B_n^- k_{cn}^s}{Z_n^s} \left\{\sin\left[k_{cn}^s\left(x-\frac{w}{2}\right)\right] - \frac{\kappa k_{cn}^s}{\mu_g \beta_n^s} \cos\left[k_{cn}^s\left(x-\frac{w}{2}\right)\right]\right\}. \tag{5.52}$$

Additionally, the boundary condition on the tangential electric field at $z = d$ requires

$$\sum_{n=1}^{\infty} C_n^+ k_{xn}^e \sin\left[k_{xn}^e\left(x-\frac{a}{2}\right)\right] =$$

$$\begin{cases} \sum_{n=1}^{\infty} B_n^+ k_{cn}^s \left(1-\frac{\kappa^2}{\mu_g^2}\right) \sin\left[k_{cn}^s\left(x-\frac{w}{2}\right)\right] e^{-j\beta_n^s d} \\ \quad + \sum_{n=1}^{\infty} B_n^- k_{cn}^s \left(1-\frac{\kappa^2}{\mu_g^2}\right) \sin\left[k_{cn}^s\left(x-\frac{w}{2}\right)\right] e^{j\beta_n^s d}, \qquad 0<|x|<\frac{w}{2} \\ 0, \qquad \frac{w}{2}<|x|<\frac{a}{2}, \end{cases} \tag{5.53}$$

while the boundary condition on the tangential magnetic field requires

$$\sum_{n=1}^{\infty} \frac{C_n^+ k_{xn}^e}{Z_n^e} \sin\left[k_{xn}^e\left(x-\frac{a}{2}\right)\right] =$$

$$\sum_{n=1}^{\infty} \frac{B_n^+ k_{cn}^s}{Z_n^s} \left\{\sin\left[k_{cn}^s\left(x-\frac{w}{2}\right)\right] + \frac{\kappa k_{cn}^s}{\mu_g \beta_n^s} \cos\left[k_{cn}^s\left(x-\frac{w}{2}\right)\right]\right\} e^{-j\beta_n^s d}$$

$$-\sum_{n=1}^{\infty} \frac{B_n^- k_{cn}^s}{Z_n^s} \left\{\sin\left[k_{cn}^s\left(x-\frac{w}{2}\right)\right] - \frac{\kappa k_{cn}^s}{\mu_g \beta_n^s} \cos\left[k_{cn}^s\left(x-\frac{w}{2}\right)\right]\right\} e^{j\beta_n^s d}. \tag{5.54}$$

The system of functional equations (5.51) - (5.54) are converted to a system of linear equations by first truncating the infinite summations to N terms and then applying the following testing operations. The equations resulting from applying the tangential electric field boundary conditions, (5.51) and (5.54), are multiplied by $\sin\left[k_{xm}^e\left(x-a/2\right)\right]$ and integrated over $-a/2 \le x \le a/2$. Then, (5.52) and (5.54), which result from applying the tangential magnetic field boundary conditions, are multiplied by $\sin\left[k_{cm}^s\left(x-w/2\right)\right]$ and integrated over $-w/2 \le x \le w/2$. Here $1 \le m \le N$. This yields the $4N \times 4N$ matrix equation

$$\left[\begin{array}{c|c|c|c} -G & J & JP & 0 \\ \hline K & L^+ & -L^-P & 0 \\ \hline 0 & JP & J & -G \\ \hline 0 & L^+P & -L^- & -K \end{array}\right] \left[\begin{array}{c} A^- \\ \hline B^+ \\ \hline b^- \\ \hline C^+ \end{array}\right] = A_1^+ \left[\begin{array}{c} g \\ \hline k \\ \hline 0 \\ \hline 0 \end{array}\right], \tag{5.55}$$

where G, J, K, and $L^{\pm}$ are $N \times N$ submatrices, and g and k are vectors of length N. These entries specified in Appendix B.4. Here P is a diagonal matrix with entries $P_{mn} = \delta_{mn} \mathrm{e}^{-j\beta_n^s d}$, with δ_{mn} the Kronecker delta. Note that b_n^- is introduced to avoid overflow during computation.

The modal coefficients are found by solving the matrix equation in (5.55). The S-parameters of the system are given by

$$S_{11} = \frac{A_1^-}{A_1^+} \tag{5.56}$$

$$S_{21} = \frac{C_1^+}{A_1^+}. \tag{5.57}$$

Similar to the first technique discussed in this Chapter, the modal series is terminated when the magnitude and phase of the S-parameters reach specified tolerances at M contiguous values of N. Here $M = 5$ is sufficient to guarantee convergence to desired accuracy.

5.3.2 Validation of Theoretical Analysis

The mode matching technique was used to compute the S-parameters for a sample of G1010 placed into a reduced aperture sample holder in an L-band waveguide system. The dimensions of the L-band system are $a = 6.50$ inches and $b = 3.25$ inches. The sample thickness was chosen to be 0.50 inches, while the width of the aperture was set to 1.75 inches. Figure 5.9 and Figure 5.10 show S_{11} and S_{21} computed by using the modal series with the applied biasing magnetic field oriented along the y-axis of the waveguide. This biasing field value was set to 900 oersteds and the line width, ΔH, to zero. The resulting FMR occurs at 2.52 GHz. Absolute tolerances of 0.1 dB for $|S|$ and 0.01° for $\angle S$ were chosen so that the accuracy of the computed series is similar to the other techniques discussed in this dissertation. For the material and H_0 considered here, the S-parameters typically converge to the specified tolerances within $N = 136$ terms.

Also shown in Figure 5.9 and Figure 5.10 are the values of the S-parameters computed using the full-wave FEM solver developed at Michigan State University. The FEM simulation used approximately 100000 unknowns with a specified mesh size. Excellent agreement was obtained between the modal analysis and FEM for certain portions of the frequency band. However, near resonances there is a discrepancy between the two techniques. Initial thoughts were to implement higher-order basis functions in the FEM code. However, by the completion of this dissertation, the higher-order FEM code had not been tested for this problem. Therefore, to give confidence that this mode matching technique is providing accurate results, the mesh size in the FEM simulation was increased; which resulted in the FEM simulation having 400000 unknowns. There was a dramatic increase in FEM computational time for this many unknowns. Figure 5.11 and Figure 5.12 show the comparison of the mode matching technique and the FEM simulation using $400,000$ unknowns. It is seen that FEM results are trending closer to the mode matching S-parameters. This gives confidence that the theoretical S-parameters are computed properly.

5.3.3 Extraction Process

The same non-linear least squares method was used to determine the frequency independent physical parameters H_0, $4\pi M_S$, ϵ_r', ϵ_r'', and ΔH as was described in Section 5.2.3. The squared error between the measure and theoretical S-parameters is defined in (5.40). The extraction method was tested by using simulated S-parameters in lieu of measured S-parameters. The FEM generated S-parameters shown in Figure 5.11 and Figure 5.12 are used and the extraction process carried out. Figure 5.13 and Figure 5.14 show the extracted parameters of the G1010 material filling the cross-section of the reduced aperture guide. It is apparent that the significant amount of error present in the FEM simulations propagates to the characterized material parameters, causing inaccurate results. Note that the theoretical material parameters are determined using (5.3) and (5.4) with the physical parameter outline in Section 5.2.2.

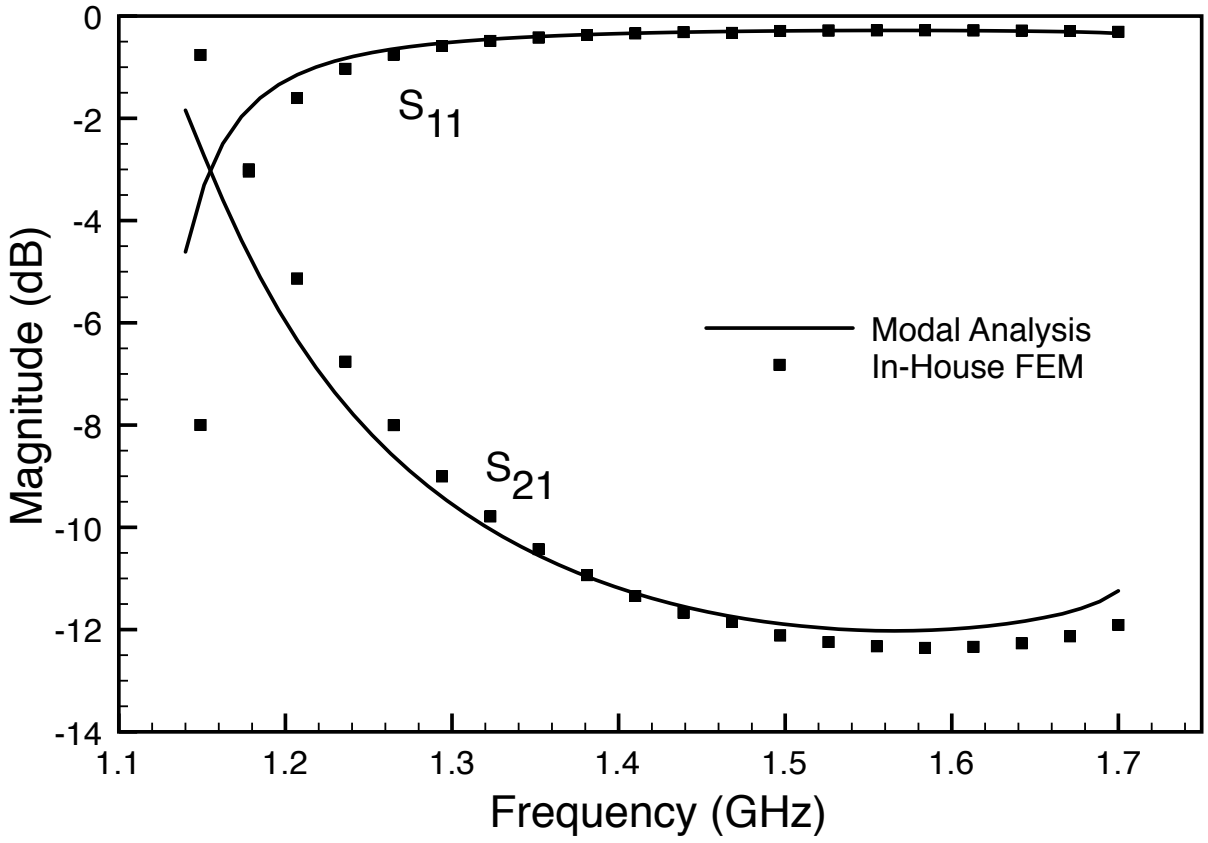

Figure 5.9: Magnitude of S-parameters computed for a gyromagnetic test material. FEM simulation uses 100000 unknowns.

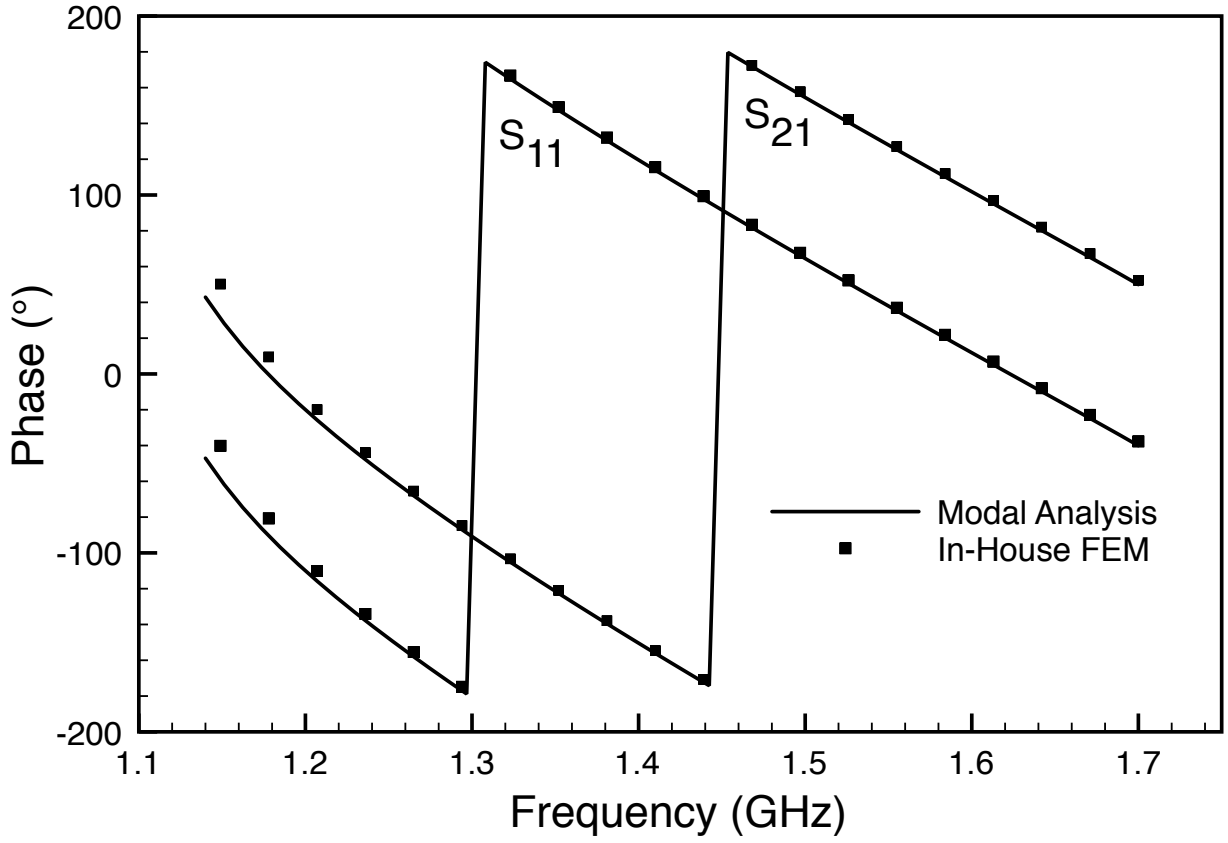

Figure 5.10: Phase of S-parameters computed for a gyromagnetic test material. FEM simulation uses 100000 unknowns.

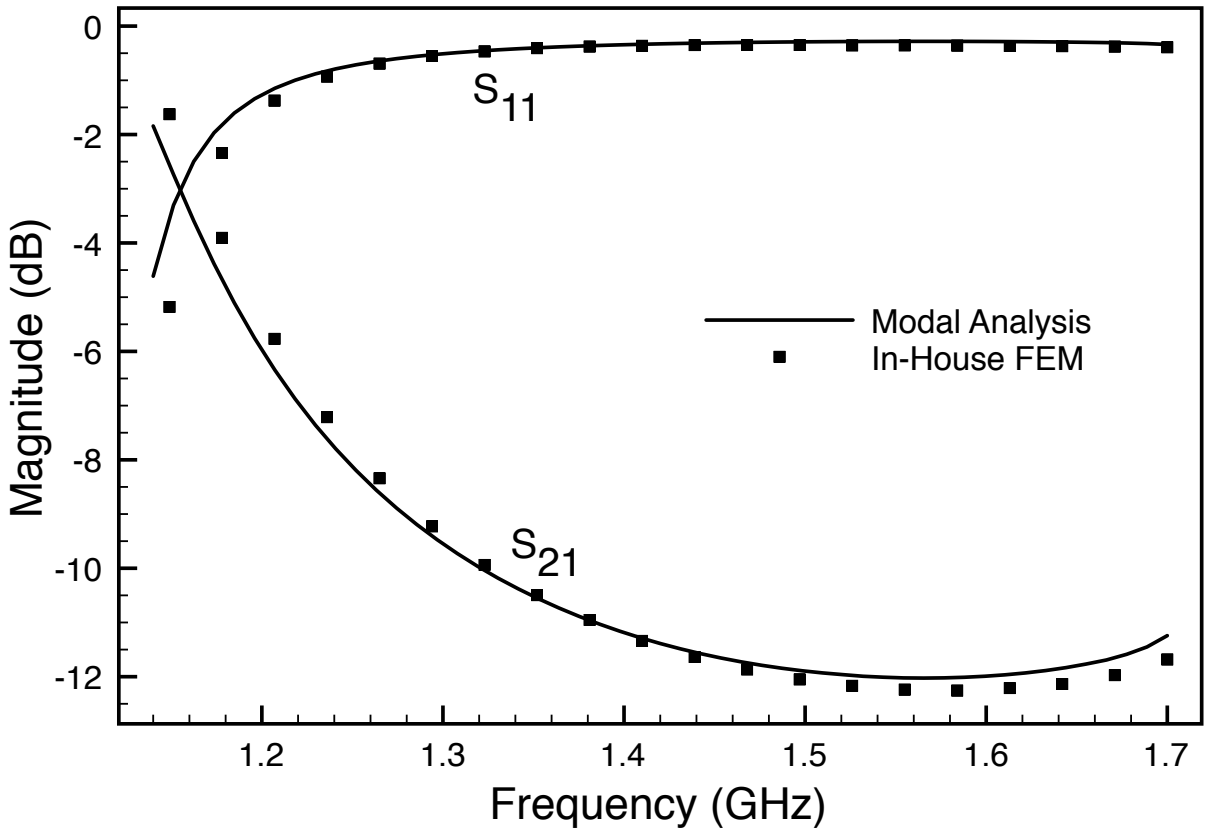

Figure 5.11: Magnitude of S-parameters computed for a gyromagnetic test material. FEM simulation uses 400000 unknowns.

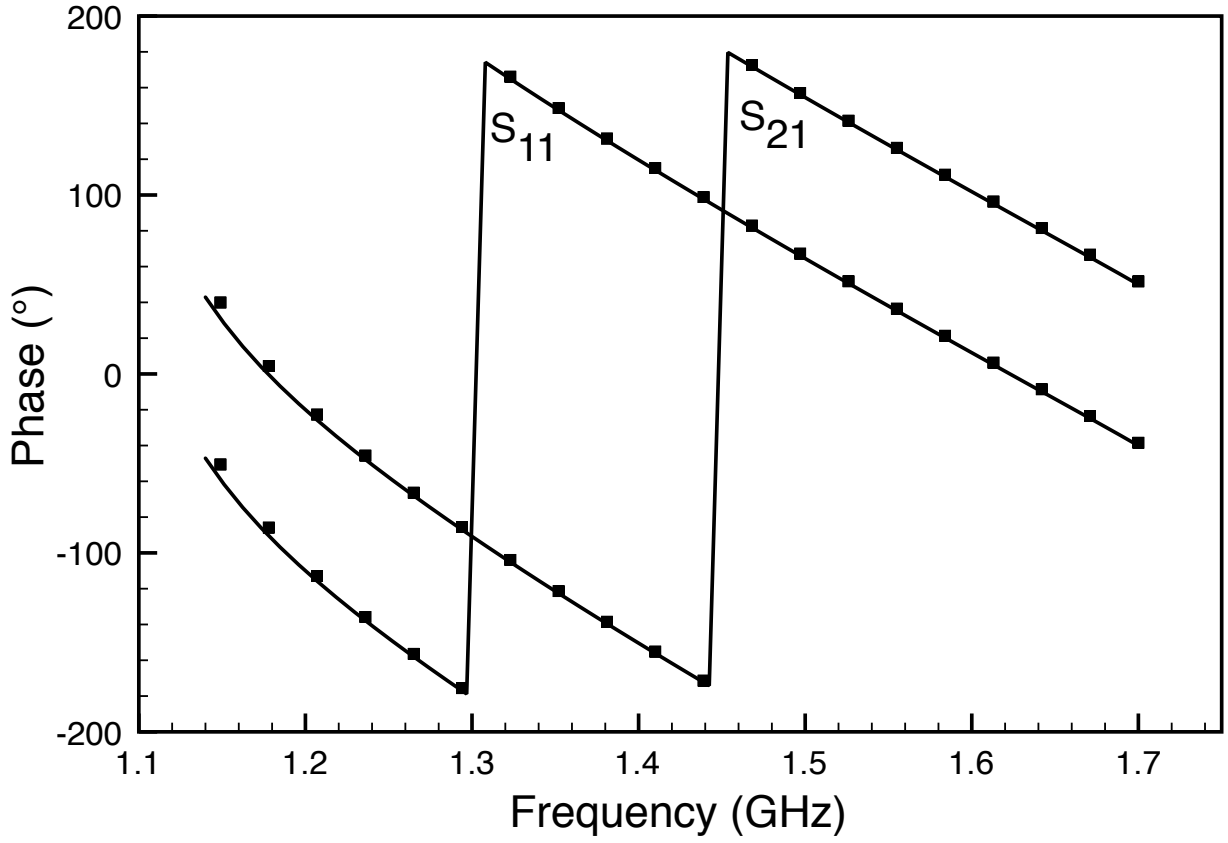

Figure 5.12: Phase of S-parameters computed for a gyromagnetic test material. FEM simulation uses 400000 unknowns.

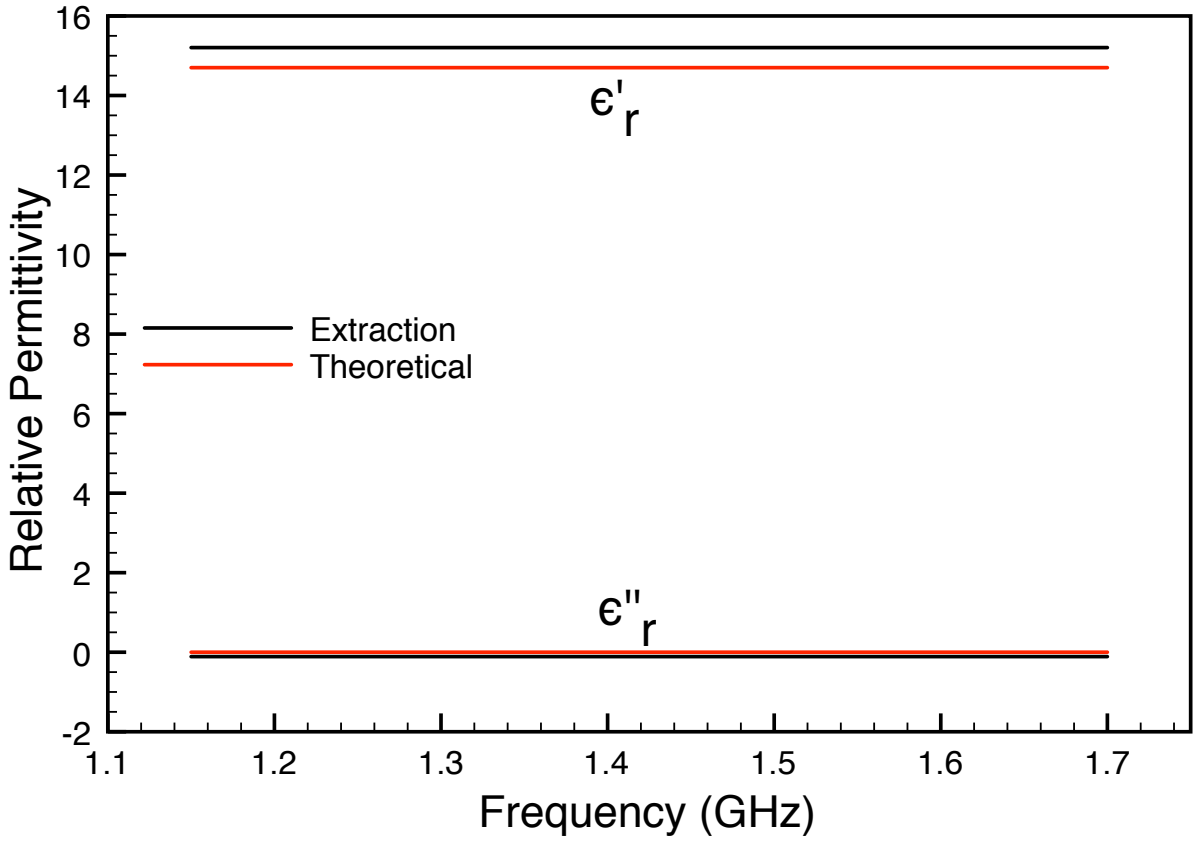

Figure 5.13: Relative permittivity parameters characterized using FEM generated S-parameters.

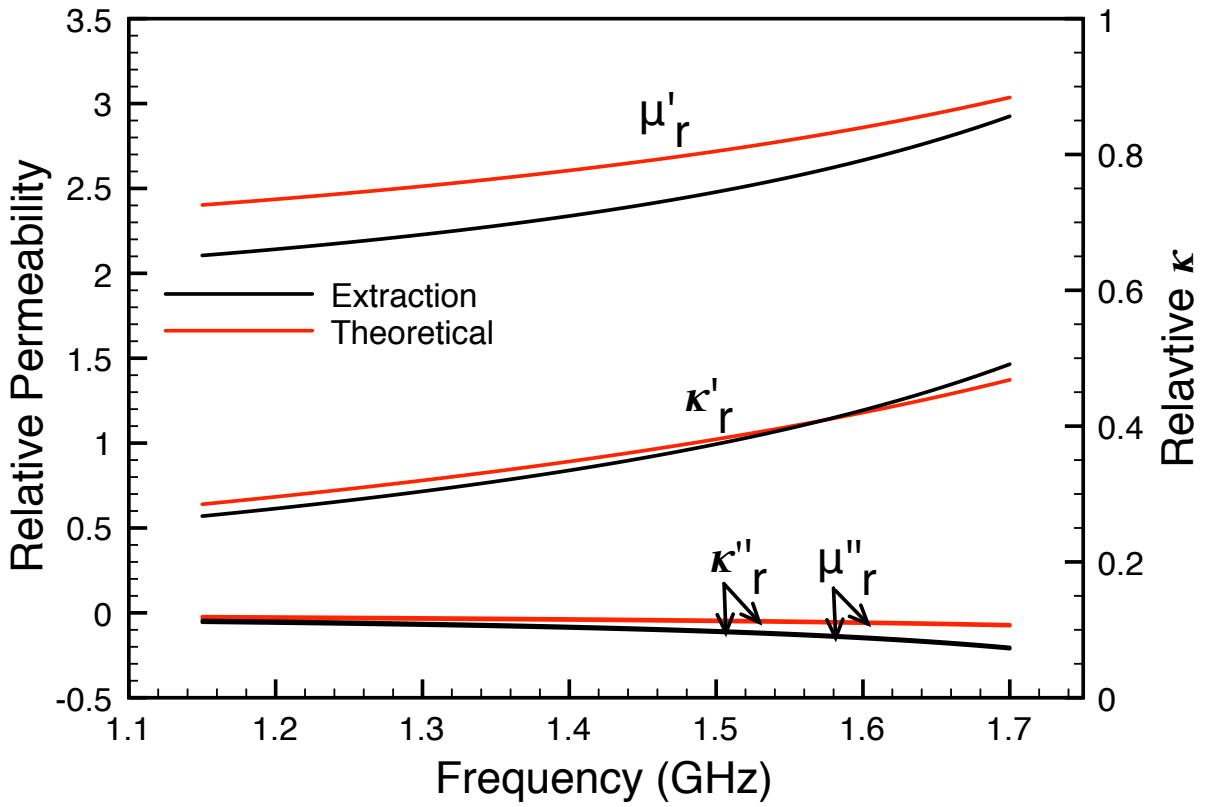

Figure 5.14: Relative permeability parameters characterized using FEM generated S-parameters.

5.3.4 Error and Sensitivity Analysis

A sensitivity analysis can be used to determine the effects of aperture size on error propagation from S-parameter uncertainties. To determine the sensitivity, a Monte Carlo technique was used to study the effects of propagation of random error inherent to the VNA. Depending on the material under test, the width of the aperture (w in Figure 5.6) can have a dramatic effect on the sensitivity to uncertainties of the measured S-parameters. Five different aperture widths were analyzed: w = 12.02 mm, 24.04 mm, 36.06 mm, 48.08 mm, and 60.10 mm.

The uncertainties of the measured S-parameters used in the Monte Carlo analysis are the same as were employed in the similar analysis done for the iris technique in Section 3.3.4. Once again, the VNA measurement uncertainty is assumed to be independent of amplitude and frequency. Statistical variance of S_{11} is specified linearly in amplitude and phase with values of $\sigma_{A_{11}} = 0.004$ and $\sigma_{\phi_{11}} = 0.8^{\circ}$. Variance of S_{21} is specified logarithmically in amplitude and linearly in phase with values $\sigma_{A_{21}} = 0.04$ dB and $\sigma_{\phi_{21}} = 2.0^{\circ}$.

The G1010 test sample described in Section 5.2.2 was used in the Monte Carlo analysis of the propagation of VNA uncertainty. The geometry of the sample holder is a = 72.136 mm, b = 34.036 mm, and d = 5 mm. The biasing magnetic field is H_0 = 2000 oersteds, while the line width is ΔH = 25 oersteds. This H_0 results in a FMR occurring at 5.60 GHz. This ΔH is the approximate value specified by Trans Tech, Inc. The forward problem was solved at 51 frequency points over the portion of S-band from 2.6 GHz to 3.95 GHz. White Gaussian noise was then added to the S-parameters, and the noisy data was used to extract the material parameters. One hundred trials were used in the Monte Carlo analysis, and the average values of the material parameters and the standard deviations were calculated for each aperture width examined. Figures 5.15 - 5.19 show the effects on the permittivity characterization with different apertures widths. Figures 5.20 - 5.24 similarly show the effects on the permeability characterization for the five different aperture widths. Note that

the red lines in these figures are the theoretical values of G1010 used to generate the S-parameters employed in the Monte Carlo analysis. It is seen that the wider the aperture is, the less sensitive the extracted material parameters are to the propagation of measured S-parameter uncertainty. Additionally, the results of the sensitivity analysis have values typical of those encountered with other material extraction methods, such as [51] and [40]. This is encouraging for characterization of measured data, which by the completion of this dissertation has not been carried out and is left for future work.

5.3.5 Summary

A reduced aperture waveguide method is introduced for measuring the permittivity and permeability of gyromagnetic materials. The technique is capable of characterizing sample sizes less than the cross-section of a rectangular waveguide. The performance of the technique is established using a sensitivity analysis based on network analyzer uncertainties. It is found that the technique performs well using simulated data, however, further validation is needed using laboratory measurements.

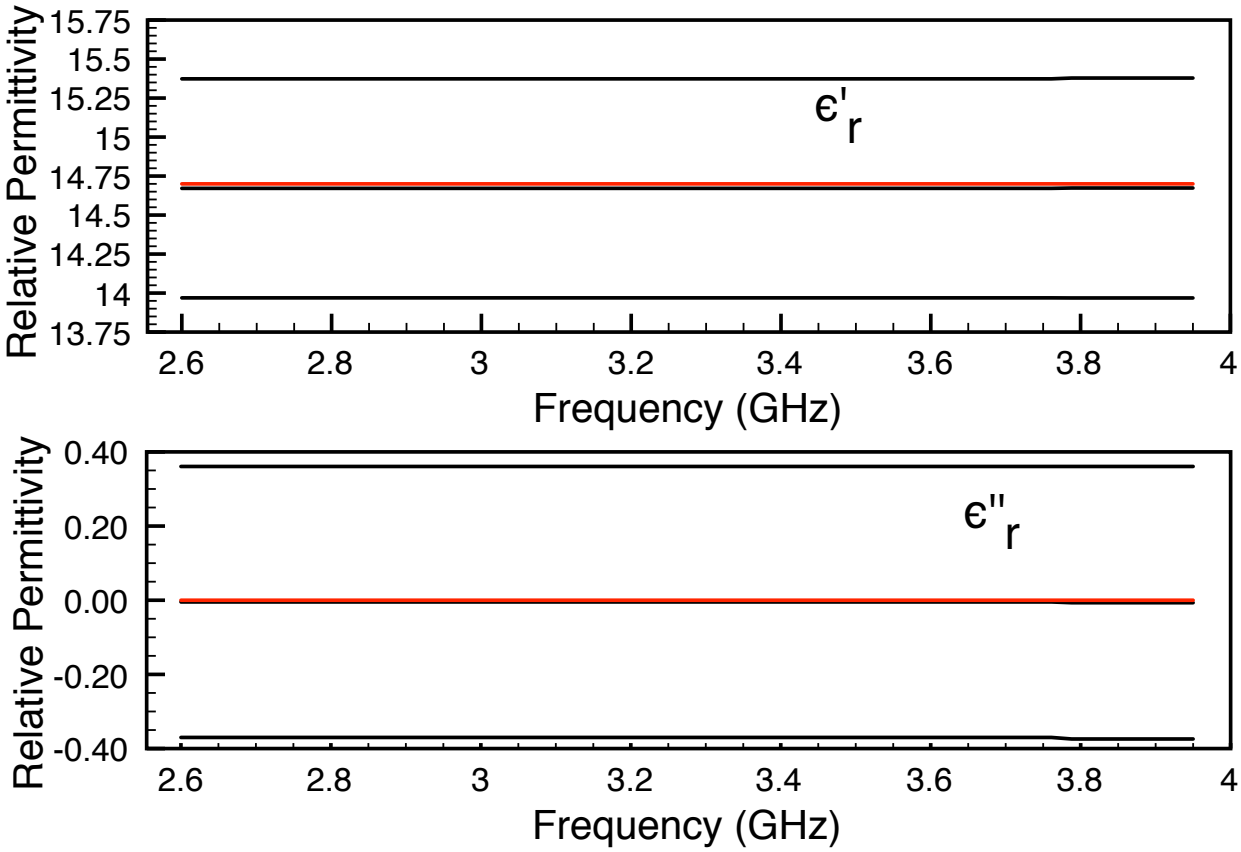

Figure 5.15: Relative permittivity extracted from 100 random trials of simulated S-parameters for a G1010 sample filling a reduced aperture of width 12.02 mm. Center black line is the average of the trials. Upper and lower black lines show the 95% confidence interval. Red lines are the theoretical permittivity values used to generate the S-parameters employed in the Monte Carlo simulation.

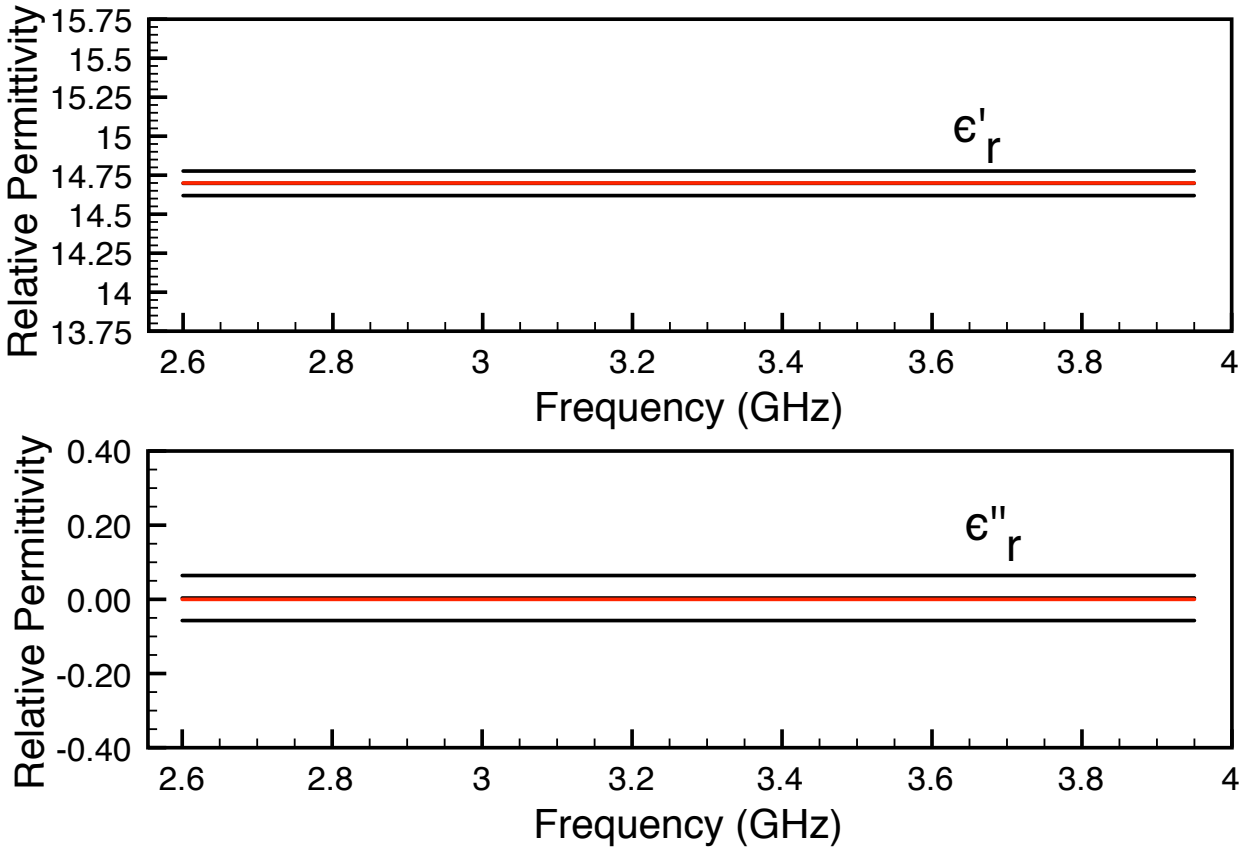

Figure 5.16: RRelative permittivity extracted from 100 random trials of simulated S-parameters for a G1010 sample filling a reduced aperture of width 24.04 mm. Center black line is the average of the trials. Upper and lower black lines show the 95% confidence interval. Red lines are the theoretical permittivity values used to generate the S-parameters employed in the Monte Carlo simulation.

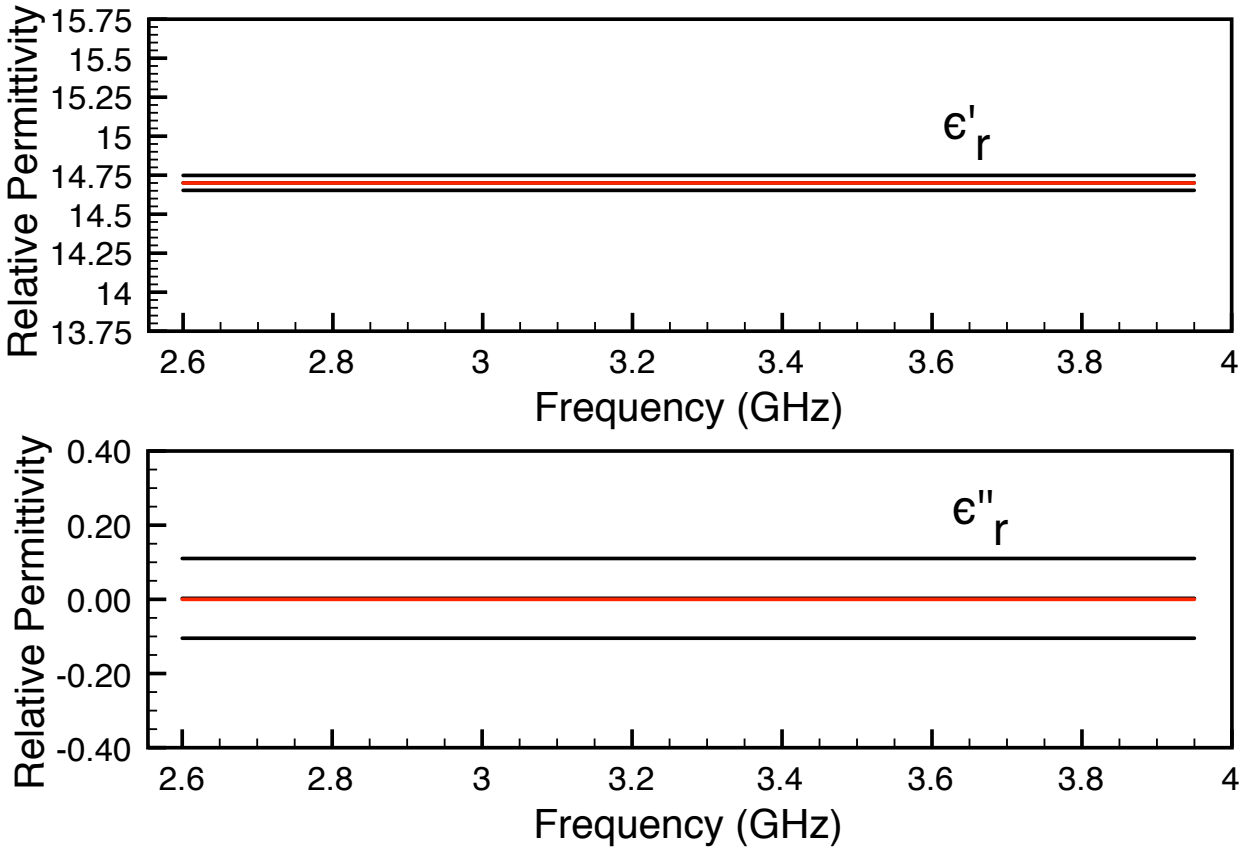

Figure 5.17: Relative permittivity extracted from 100 random trials of simulated S-parameters for a G1010 sample filling a reduced aperture of width 36.06 mm. Center black line is the average of the trials. Upper and lower black lines show the 95% confidence interval. Red lines are the theoretical permittivity values used to generate the S-parameters employed in the Monte Carlo simulation.

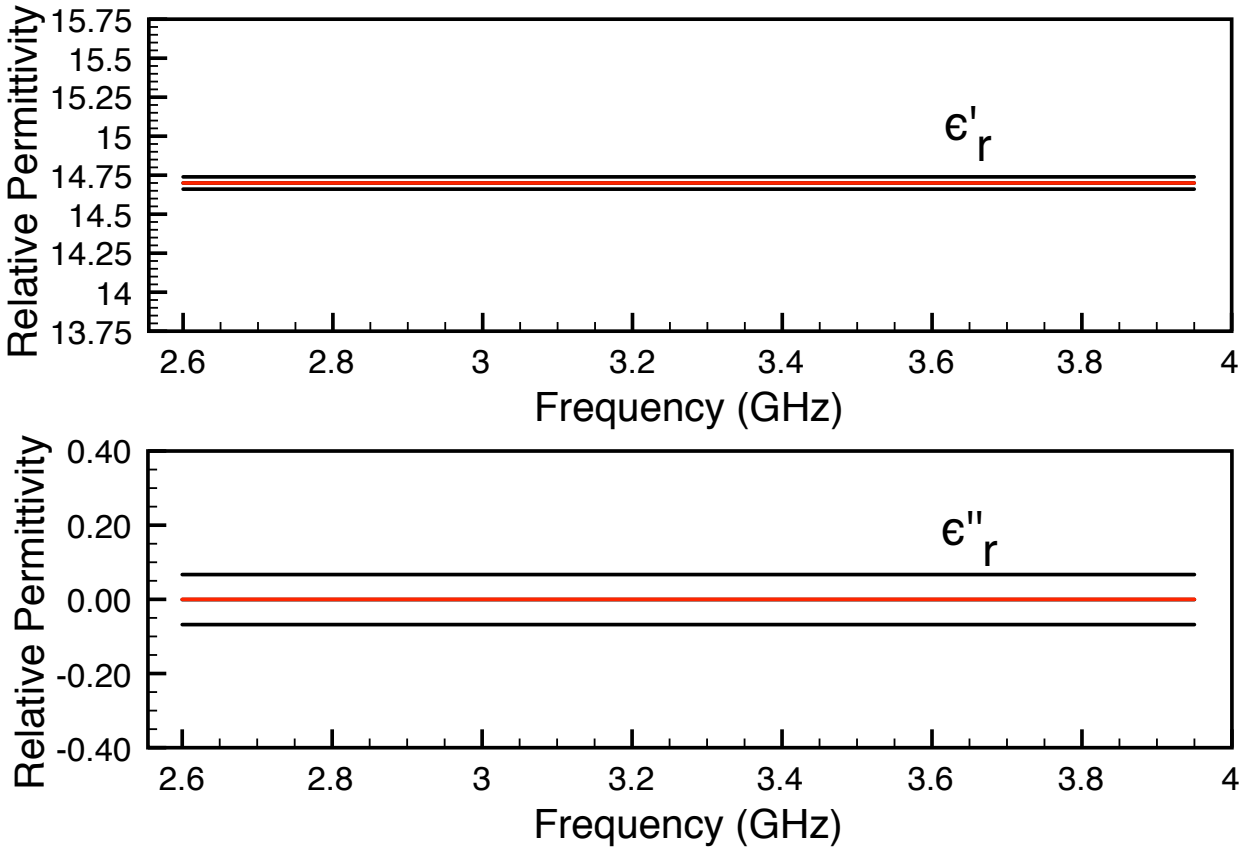

Figure 5.18: Relative permittivity extracted from 100 random trials of simulated S-parameters for a G1010 sample filling a reduced aperture of width 48.08 mm. Center black line is the average of the trials. Upper and lower black lines show the 95% confidence interval. Red lines are the theoretical permittivity values used to generate the S-parameters employed in the Monte Carlo simulation.

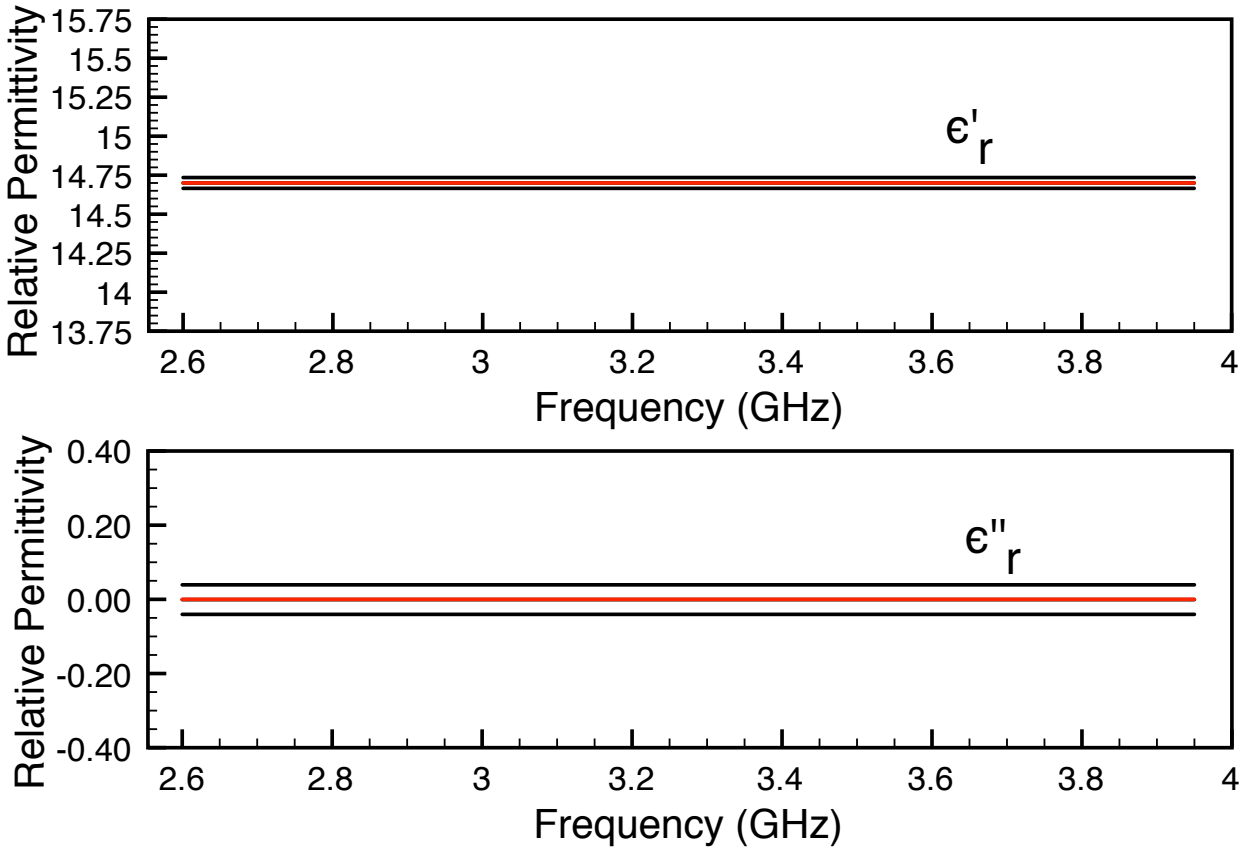

Figure 5.19: Relative permittivity extracted from 100 random trials of simulated S-parameters for a G1010 sample filling a reduced aperture of width 60.10 mm. Center black line is the average of the trials. Upper and lower black lines show the 95% confidence interval. Red lines are the theoretical permittivity values used to generate the S-parameters employed in the Monte Carlo simulation.

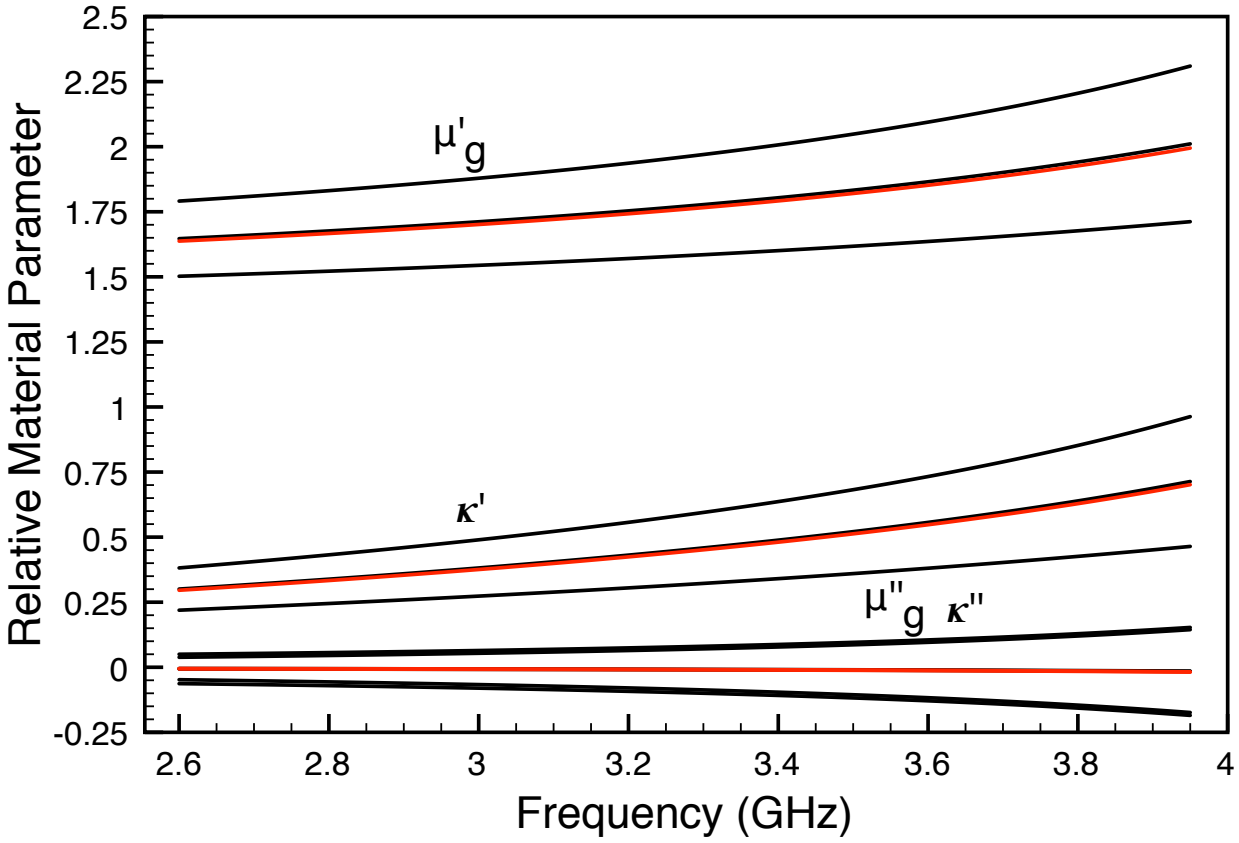

Figure 5.20: Relative permeability values extracted from 100 random trials of simulated S-parameters for a G1010 sample filling a reduced aperture of width 12.02 mm. Center black line is the average of the trials. Upper and lower black lines show the 95% confidence interval. Red lines are the theoretical permeability values determined using (5.3) and (5.4).

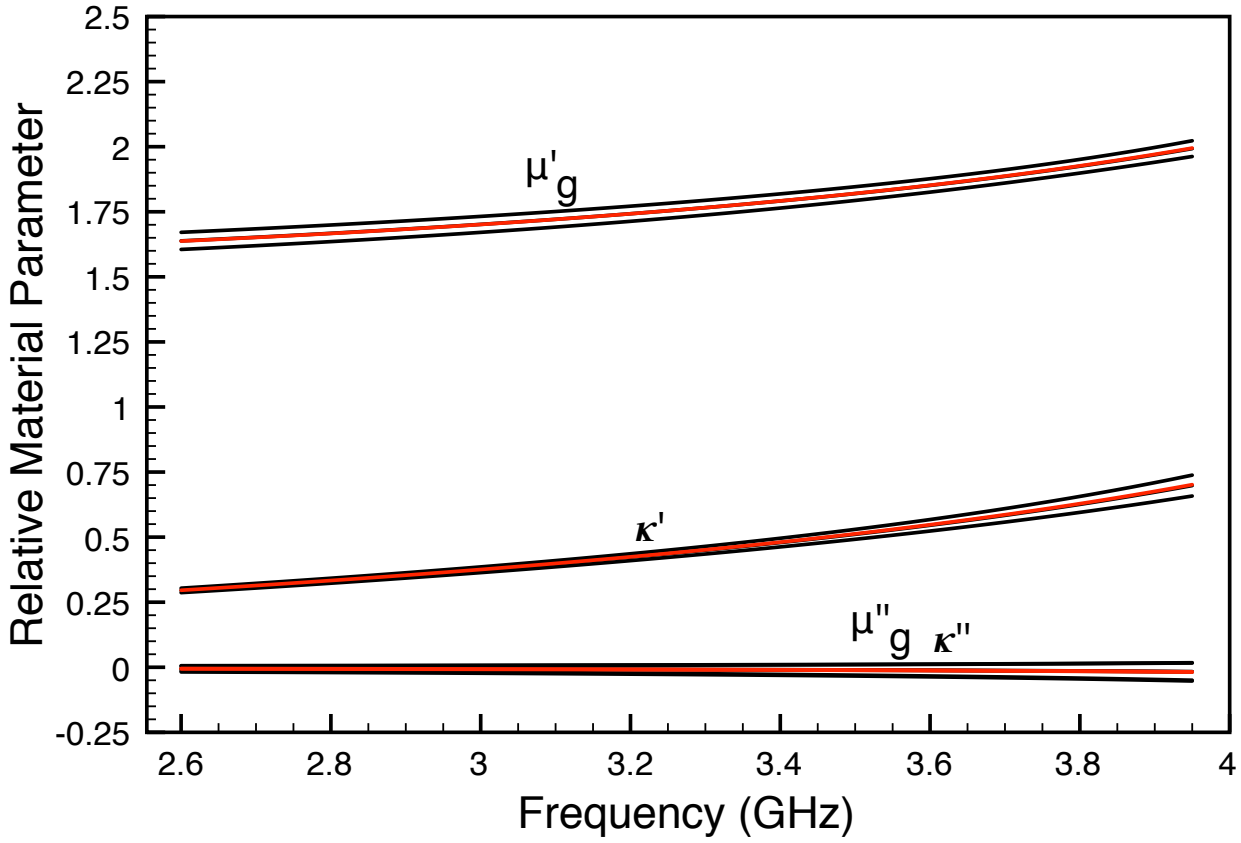

Figure 5.21: Relative permeability values extracted from 100 random trials of simulated S-parameters for a G1010 sample filling a reduced aperture of width 24.04 mm. Center black line is the average of the trials. Upper and lower black lines show the 95% confidence interval. Red lines are the theoretical permeability values determined using (5.3) and (5.4).

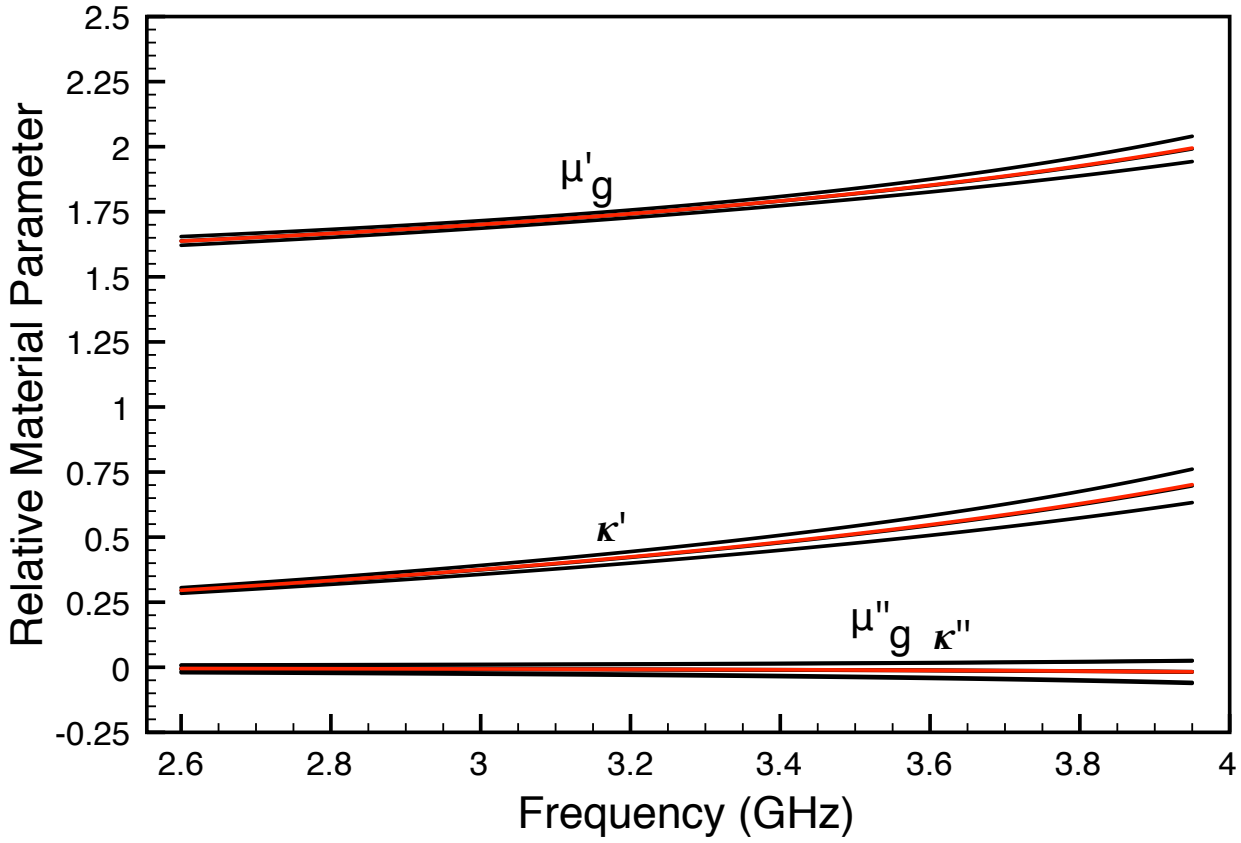

Figure 5.22: Relative permeability values extracted from 100 random trials of simulated S-parameters for a G1010 sample filling a reduced aperture of width 36.06 mm. Center black line is the average of the trials. Upper and lower black lines show the 95% confidence interval. Red lines are the theoretical permeability values determined using (5.3) and (5.4).

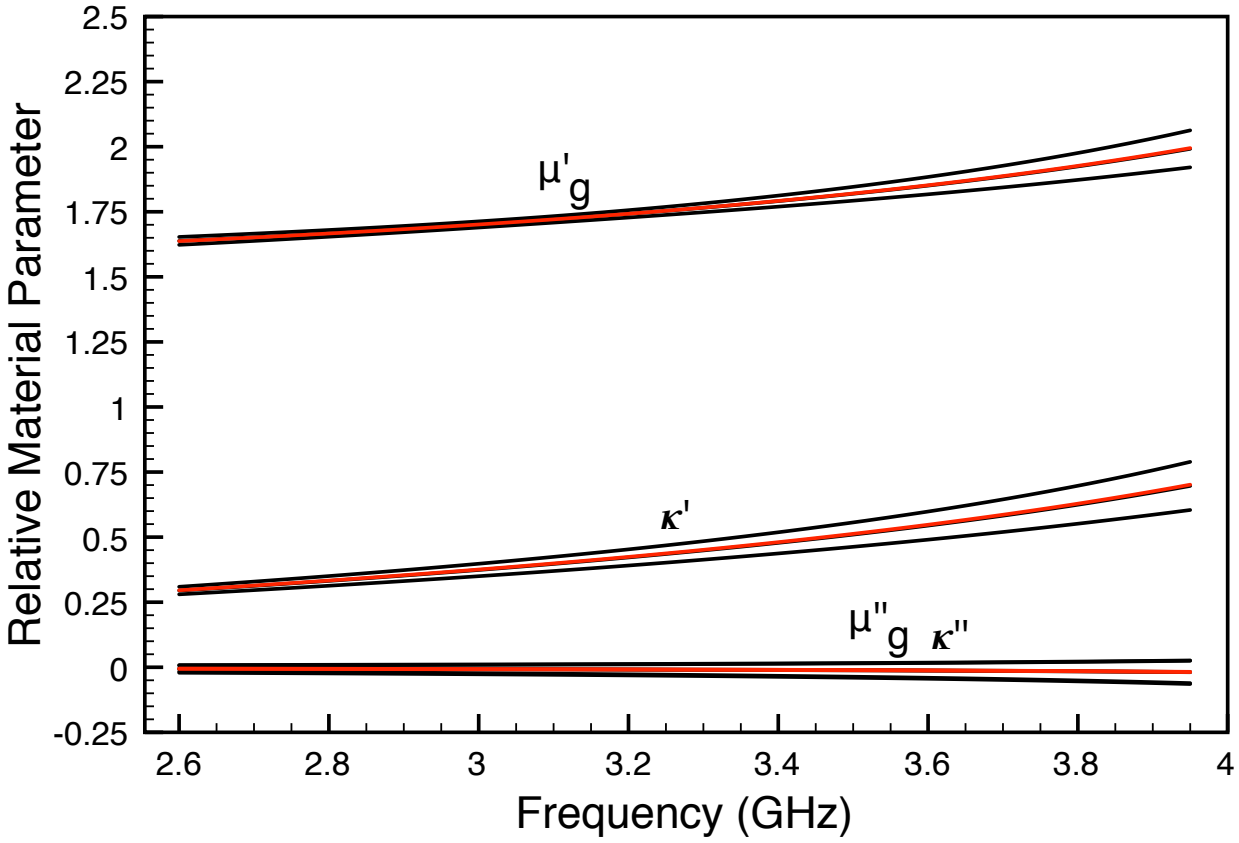

Figure 5.23: Relative permeability values extracted from 100 random trials of simulated S-parameters for a G1010 sample filling a reduced aperture of width 48.08 mm. Center black line is the average of the trials. Upper and lower black lines show the 95% confidence interval. Red lines are the theoretical permeability values determined using (5.3) and (5.4).

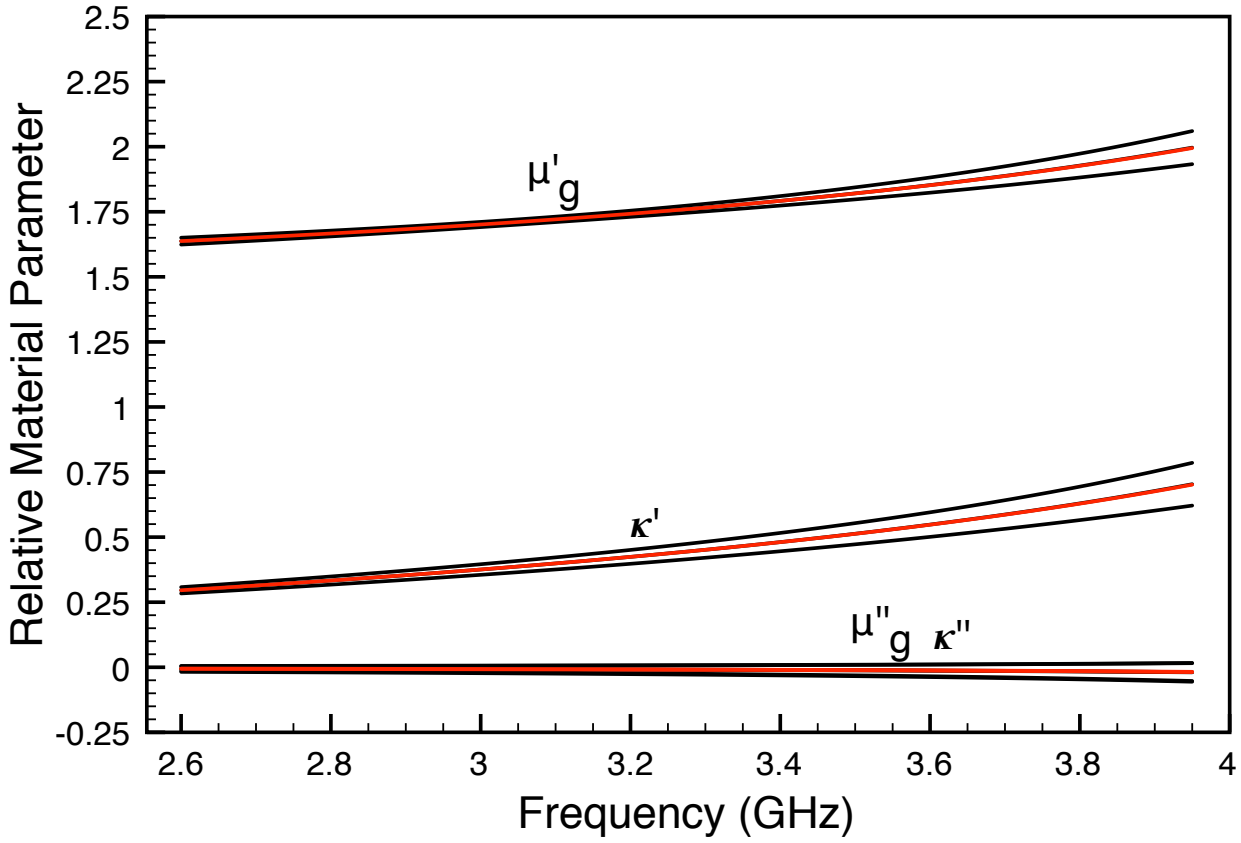

Figure 5.24: Relative permeability values extracted from 100 random trials of simulated S-parameters for a G1010 sample filling a reduced aperture of width 60.10 mm. Center black line is the average of the trials. Upper and lower black lines show the 95% confidence interval. Red lines are the theoretical permeability values determined using (5.3) and (5.4).

CHAPTER 6

VERIFICATION STANDARDS FOR MATERIAL CHARACTERIZATION

6.1 Introduction

The use of engineered materials in the design of radio frequency (RF) systems requires an accurate knowledge of material constitutive parameters. Some recently synthesized materials include graphene nanoribbons or metallic inclusions for use in miniaturization of electronic components [4]-[5], ferrite loaded polymers to increase EMI shielding [6], cellular materials such as honey comb structures to decrease radar cross-section [7]-[8], and anisotropic materials used to enhance antenna operation [9]-[10]. Since the properties of these materials are often hard to accurately predict (due to modeling uncertainties and variability in the manufacturing process), they are usually measured in a laboratory.

As seen in this dissertation, rectangular waveguide applicators are commonly used to extract the electromagnetic properties of materials. Benefits over alternative methods, such as free-space systems, include the availability of analytical expressions to describe sample interrogation, high signal strength, and the simplicity of manufacturing rectangular samples [20]-[22]. The S-parameters measured with a material sample placed in the cross-sectional

plane of a waveguide may be used to determine the complex values of the permittivity, $\epsilon = \epsilon_0(\epsilon_r' + j\epsilon_r'')$, and the permeability, $\mu = \mu_0(\mu_r' + j\mu_r'')$, from closed-form expressions described in Section 3.2.

The accuracy of a material characterization system is often established by measuring a standard material with known properties. A desirable standard material is easy to machine, is stable thermally and chemically, is readily available, and has values of constitutive parameters numerically close to those of samples of interest with only minor variations within the measurement band. If the permittivity of materials is of primary interest, a dielectric sample such as Rexolite® may be used to provide highly-predictable parameters in the microwave spectrum with a value characteristic of many plastics [35] and [57]. The recent introduction of engineered materials with magnetic as well as dielectric properties has made it more difficult to find standard test materials whose constitutive parameters are known with great accuracy and have appropriate values within the microwave spectrum. Fortunately, it is possible to create a surrogate material sample that can act as the standard test material in the sense that its use in a material measurement system will produce extracted constitutive parameters with predictable, highly-accurate, and appropriate values. The surrogate need not resemble an actual material, and in fact can be inhomogeneous and non-magnetic. The only requirement is that when inserted in place of a test material, the surrogate provides proper S-parameters that may be used in the extraction process. Although some previous work has been done to create waveguide standards using circuits, obstacles, or components [58], these fabricated structures are only meant to validate the reflection and transmission coefficients, not the extracted material parameters.

It is crucial that a material standard produce highly accurate, stable, and repeatable values of extracted permittivity and permeability across the measurement band. It must be reproducible for the majority of users, and thus should be of simple design and made from readily available materials. The values of the extracted constitutive parameters should not be overly sensitive to the geometrical dimensions of the standard, so that errors in fabrication

or changes in the operating environment (temperature, humidity, etc.) do not cause unpredictable or unacceptable results. Additionally, the values of permittivity and permeability must be predictable to high accuracy using standard, reproducible analytic techniques. For these reasons, the design adopted for the surrogate described here uses two simple metallic waveguide windows, or apertures, separated by a spacer. Given just four geometrical parameters, mode-matching techniques can be used to accurately compute the S-parameters of the surrogate material, and from these the extracted constitutive parameters may be determined. A description of the design process used to obtain an optimized geometry and a typical design for S-band using standard WR-284 dimensions are given below. Details of the theoretical analysis are also given, so that any user may design an appropriate surrogate. The measured results for an example verification standard constructed from materials on hand are shown and discussed.

6.2 Material Characterization Procedure

A verification standard provides confidence in the operation of an experimental system by producing known results under appropriate operating conditions. In the case of material characterization, the verification standard is placed into the system and known values of μ and ϵ are extracted using a specific algorithm. The standard described in this dissertation assumes the use of the classic "Nicolson-Ross-Weir" (NRW) extraction algorithm, outlined in Section 3.2, that employs the measured reflection and transmission coefficients for a waveguide section completely filled by the material [23]-[24]. Other algorithms are available that use, for instance, only reflection measurements [36]; these would require a different standard. The attraction of the NRW characterization method results from the availability of closed-form expressions for μ and ϵ. This contrasts with methods requiring an iterative solver such as Newton's method [30]-[31] or a least squares approach [32]-[33]. The convenience of the NRW method, and its insensitivity to propagation of measurement uncertainties, commonly

makes it a first choice for material characterization. Since NRW extraction can be used with rectangular waveguides [25], coaxial applicators [26]-[27], free-space methods [28], and stripline measurements [29], the concept of the waveguide surrogate described here has wide applicability, although the details of the structural design vary from system to system.

Figure 6.1 shows the experimental configuration used in the NRW method. A sample with unknown properties is placed into a sample holder occupying the region $0 \leq z \leq d$ in a rectangular waveguide system. Waveguide extensions are usually employed to guarantee only the dominant mode is present at the measurement ports. The S-parameters S_{11} and S_{21} are measured using a vector network analyzer (VNA) attached at these ports, and the S-parameters are then mathematically transformed to obtain the S-parameters at the sample planes. These sample-plane S-parameters are used to determine the sample propagation constant β and the interfacial reflection coefficient Γ, which may in turn be used to find ϵ and μ.

The waveguide standard is placed into the measurement system in a manner identical to an actual unknown material; see Figure 6.1. The length of the surrogate sample is $z_3 = d$ and thus the S-parameter planes are taken at $z = 0$ and $z = d$ as in the case of an actual sample. The NRW method assumes that the material sample is isotropic and homogeneous, and thus the measured S-parameters obey $S_{11} = S_{22}$ and $S_{12} = S_{21}$. Although it is not necessary that the waveguide standard be homogeneous, it is helpful if the S-parameters of the surrogate obey the same relationships as do those of an actual material. Thus, the waveguide standard should be symmetric in the longitudinal (z) direction. This allows the standard to be interrogated from either direction with identical results, and if the standard is constructed from lossless (or perfectly conducting) materials, it also allows the permittivity and permeability of the surrogate extracted using the NRW method to be purely real (corresponding to a lossless material). The condition under which this occurs is identified in Appendix C. Interestingly, if the waveguide standard is made from lossless materials but is not symmetric along z, the NRW method may return complex values for μ and ϵ with

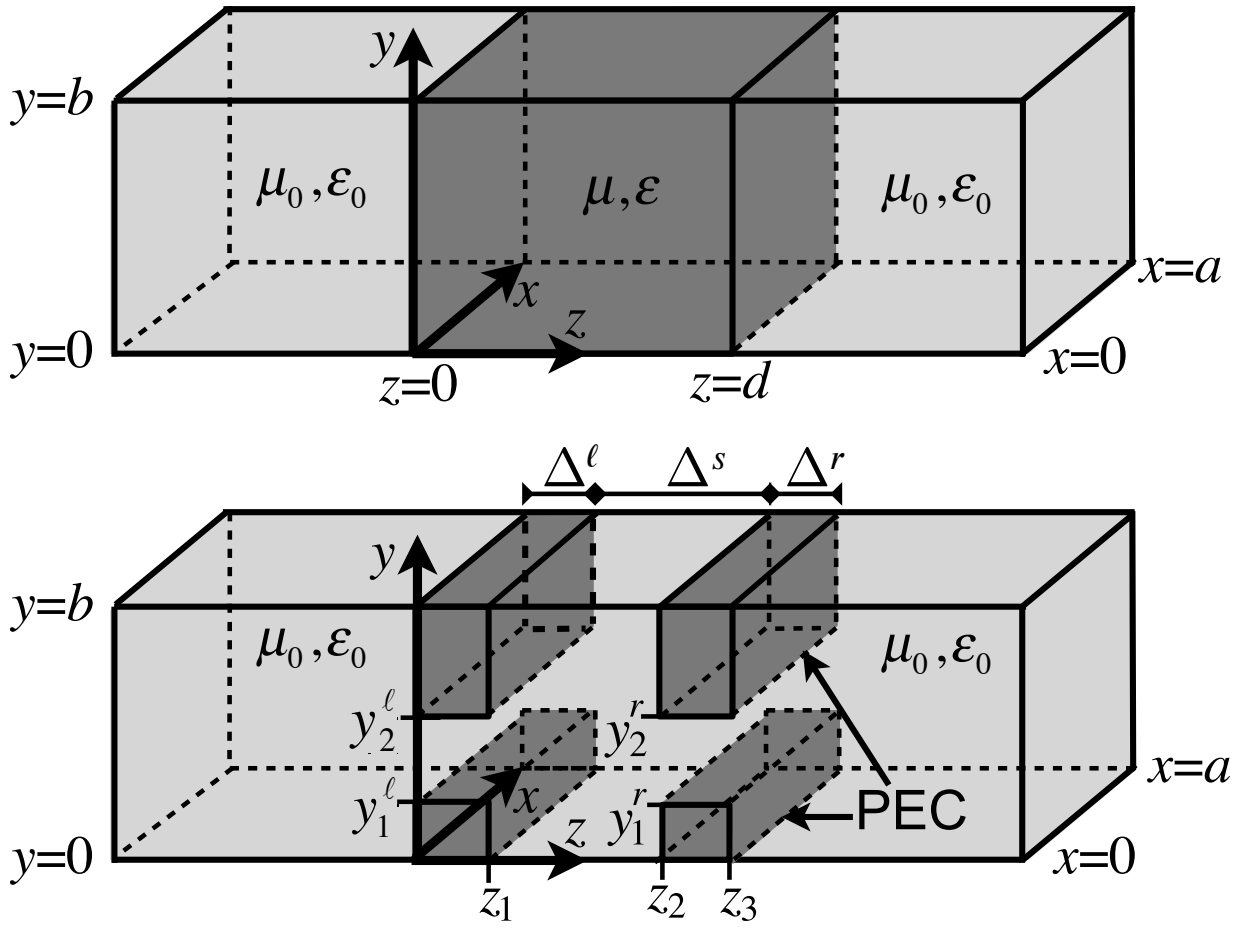

Figure 6.1: Waveguide material measurement system showing presence of material sample (top), and waveguide verification standard surrogate material (bottom). Adopted surrogate has $\Delta^\ell = \Delta^r$, $y_1^\ell = y_1^r$, and $y_2^\ell = y_2^r$.

positive imaginary parts, indicating gain, which is not a property of a useful surrogate. To demonstrate this, consider two surrogate materials, each constructed from alternating layers of perfect (lossless) dielectrics, as shown in Figure 6.2. The sample plane S-parameters of each system may be easily computed using cascaded matrices [59], and the permittivity and permeability of the surrogate extracted using the NRW method; see Figure 6.2. When the properties of the symmetric material (Sample A) are extracted, the permittivity is found to be purely real (characteristic of a lossless material). However, when the properties of the asymmetric material (Sample B) are extracted, the imaginary part of the permittivity is found to be nonzero and positive (characteristic of an active material). The extracted permeability of the asymmetric material is found to have a small negative imaginary part and a real part less than unity. This contrasts the extraction of the symmetric sample where the imaginary permeability is found to be zero. Note that in both cases, the real parts of the extracted permittivity and permeability are frequency dependent, even though the dielectric constants of the material layers are independent of frequency. This frequency dependence is expected of any inhomogeneous surrogate, and leads to the drawback that the material parameters do not obey the Kronig-Kramers relations [60]. However, an inhomogeneous surrogate is still valuable as a verification standard since its material parameters can be tailored to a desired range and, if lossless, provide a quick check of the credibility of the measurements.

6.3 Waveguide Verification Standard Design

It is important to develop a waveguide standard that is easily fabricated using materials readily available to most users. For this reason the surrogate was chosen to be constructed from purely metallic parts, and in the following analysis is assumed to be perfectly conducting. Assemblies of structures such as loops, posts, and both circular and rectangular apertures were considered, with the goal to produce a surrogate material with both a permittivity and

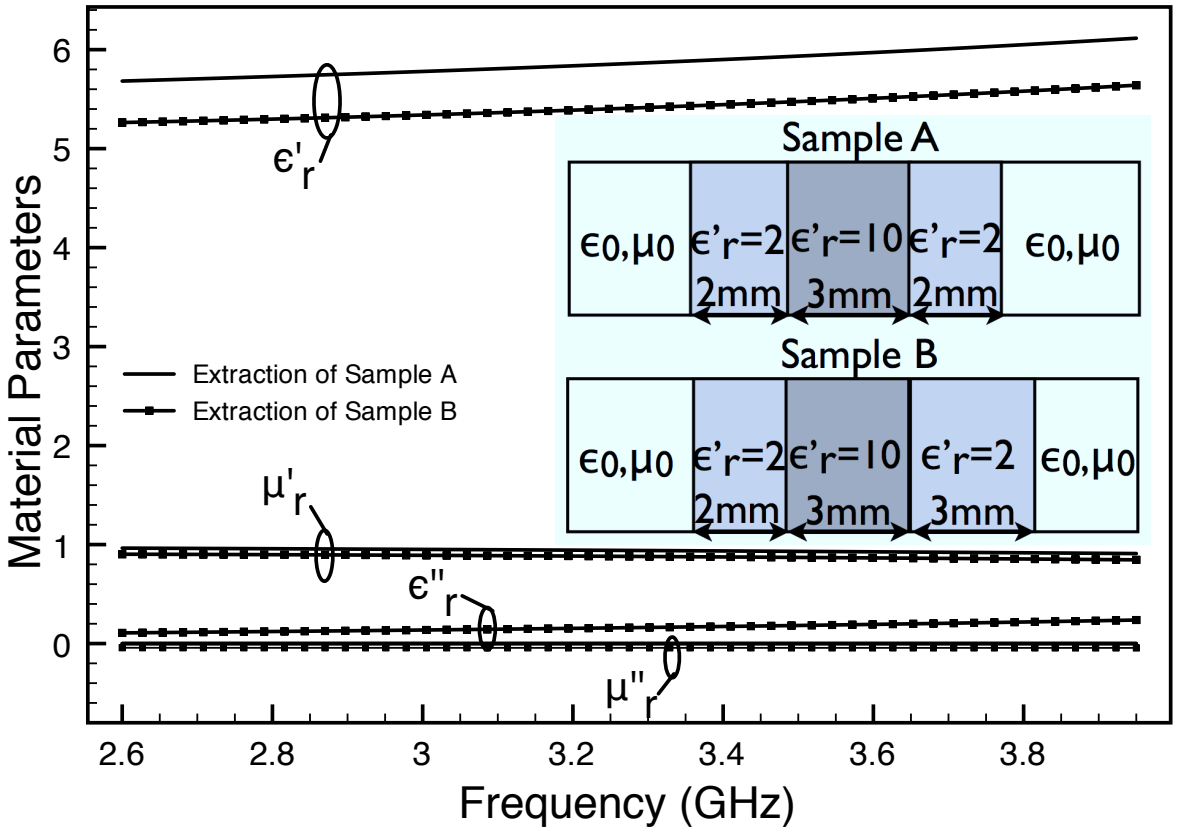

Figure 6.2: Effective material parameters extracted from symmetric and asymmetric layered dielectric surrogate materials.

a permeability as near to six as possible across S-band. (Note that materials with large but equal values of permittivity and permeability are useful in the construction of microwave antennas with enhanced radiation properties; values near 6 are a good goal.) As discussed in the previous section, by making the structure longitudinally symmetric, the extracted material parameters may be purely real and correspond to a lossless material. However, as also discussed, the parameters are frequency dependent, and thus a genetic algorithm (GA) was employed to find a structure with slowly varying parameters as near to a target value of six as possible. It is also important that the extracted material parameters be relatively insensitive to small changes in the geometry of the structure, so that tight manufacturing tolerances are not required.

To find structures that satisfy the design requirements, a combination of a GA and a Monte Carlo error analysis routine was employed. For each candidate structure, the commercial solver HFSS was used to determine the S-parameters, and the NRW method was used to find ϵ_r and μ_r. A Matlab to HFSS interface was implemented, where all exported data from HFSS was stored in Matlab and analyzed during post processing and GA execution. Figure 6.3 shows a flow chart of the Matlab to HFSS interface. An initial design of the waveguide surrogate (loops, posts, apertures, etc.) is programmed into Matlab, which in turn generates application programming interface (API) functions that are used to talk between Matlab and HFSS. The Matlab program then creates and executes an HFSS script. Using this script, HFSS draws and analyzes the structure and then exports the specified solution data back to Matlab. Then Matlab generates a new set of API functions using the next randomly determined geometrical modification (such as post radius, aperture size, sample thickness) to the surrogate design. Using the stored results from HFSS it is possible to take a small population of possible designs, analyze the permittivity and permeability, and determine if with fine tuning this type of surrogate is viable for a waveguide standard. Figure 6.4 shows a surrogate design of brass posts that was analyzed for a possible waveguide standard candidate. In this simulation, the number of posts was fixed, but the GA was used

to determine the individual radius of each post, whether the posts came from the bottom or top of the guide, and the length of each post. It was found that this type of surrogate would not meet the objectives for a waveguide standard. Typical results from the GA analysis of the brass-post surrogate design are shown in Figure 6.5. The surrogate design has highly varying ϵ_r' and μ_r', and thus is not a usable waveguide standard design. Additionally, the ϵ_r and μ_r become complex of certain portions of the frequency band. Since the surrogate design is symmetric in the longitudinal dimension and made from lossless materials, the portions of the frequency band in which the material parameters are complex result from Case 2 in Appendix C, where $X^2 \leq 1$ with $X = S_{11r}/|S_{11}|^2$. This can be seen in Figure 6.6, where the inset shows an expanded vertical region of a plot of X^2. Comparing Figure 6.5 with Figure 6.6, it can be seen that the frequencies where ϵ_r and μ_r are complex correspond with frequencies where $X^2 \leq 1$. Thus, avoiding regions where Case 2 is in effect results in an acceptable surrogate design for use as a verification standard.

Once a possible surrogate design was determined, the geometry of each candidate structure was perturbed randomly multiple times and the error that propagated to the extracted material properties was computed. After many lengthy searches, several structures were found with acceptable properties, some exhibiting highly complex geometries. One structure in particular was found to be quite promising due to its simple geometry, and was adopted as the waveguide standard analyzed and presented in this dissertation. It consists of two identical rectangular apertures of thickness $\Delta^\ell = \Delta^r$ separated by a spacer of thickness Δ^s, as shown in Figure 6.1.

The simple geometry of the adopted waveguide standard has several important advantages over more complex structures. First, it may be easily machined from simple metal sheets. Second, an easily implemented mode-matching technique may be used to analyze the structure quickly and with great accuracy, and thus commercial solvers are not required to determine the material properties of the surrogate. By controlling the accuracy of the analysis, the errors propagated to the extracted material parameters from the uncertain-

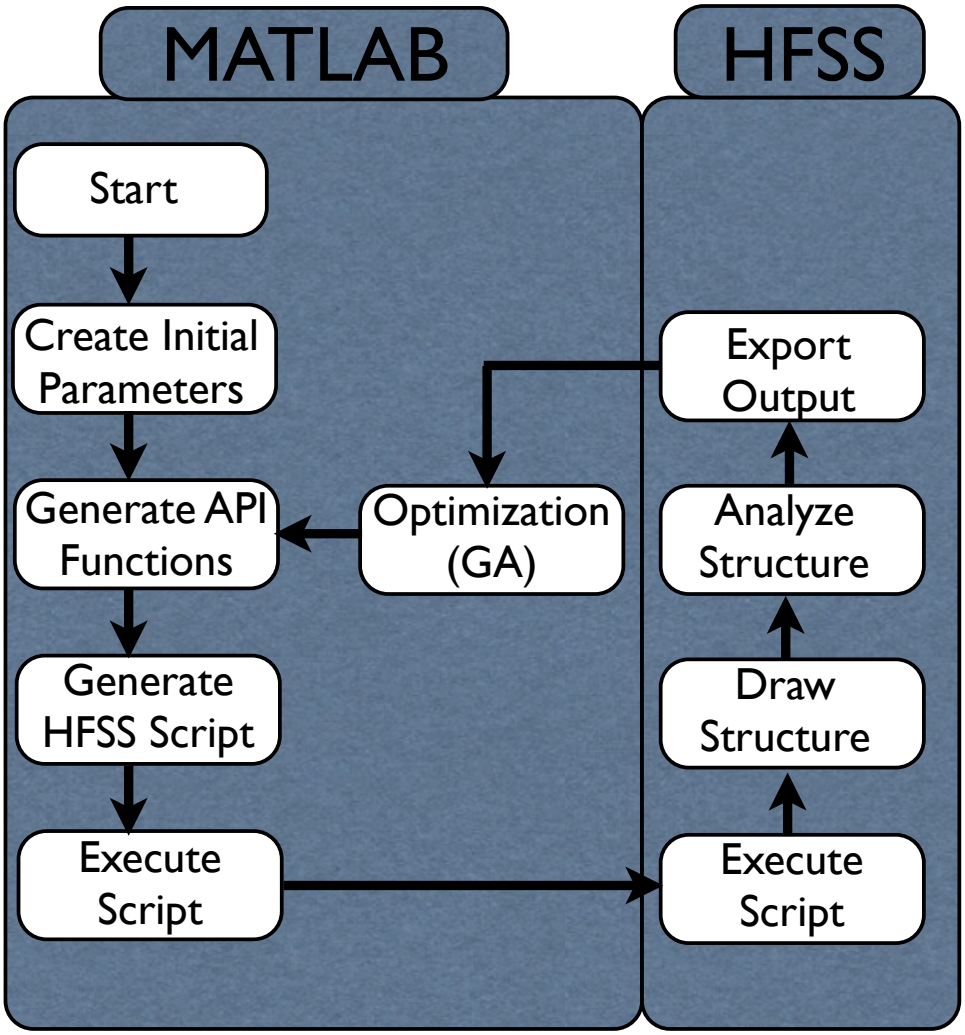

Figure 6.3: Matlab to HFSS flow chart.

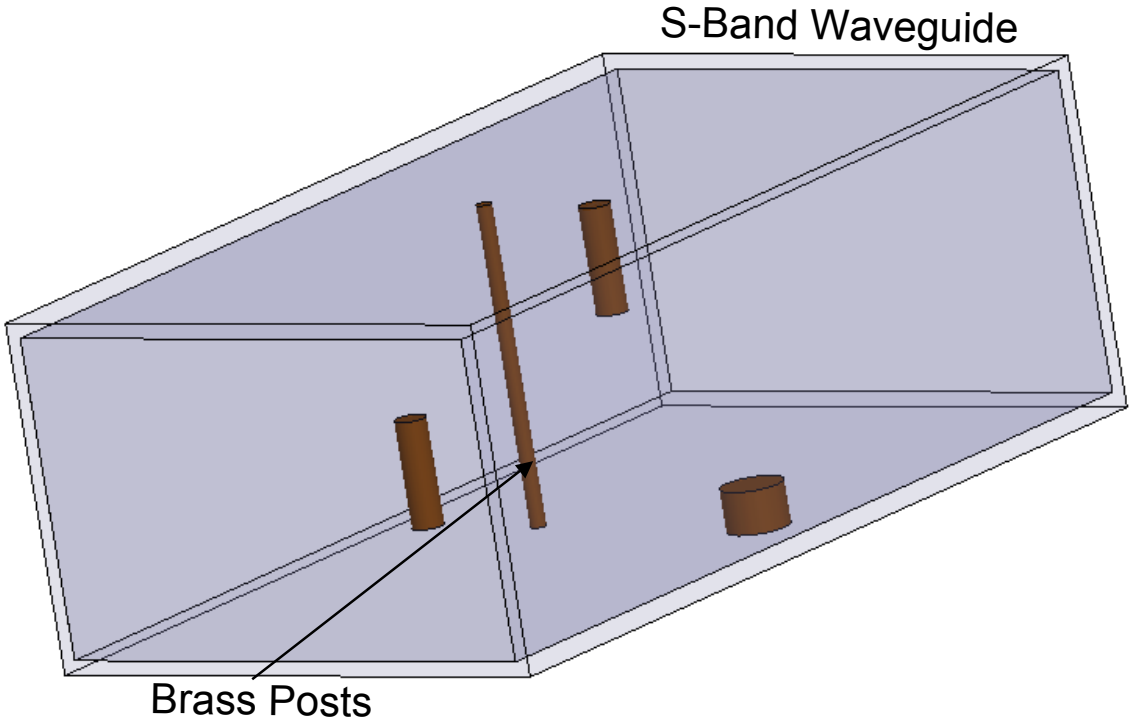

Figure 6.4: Example of brass-post surrogate design.

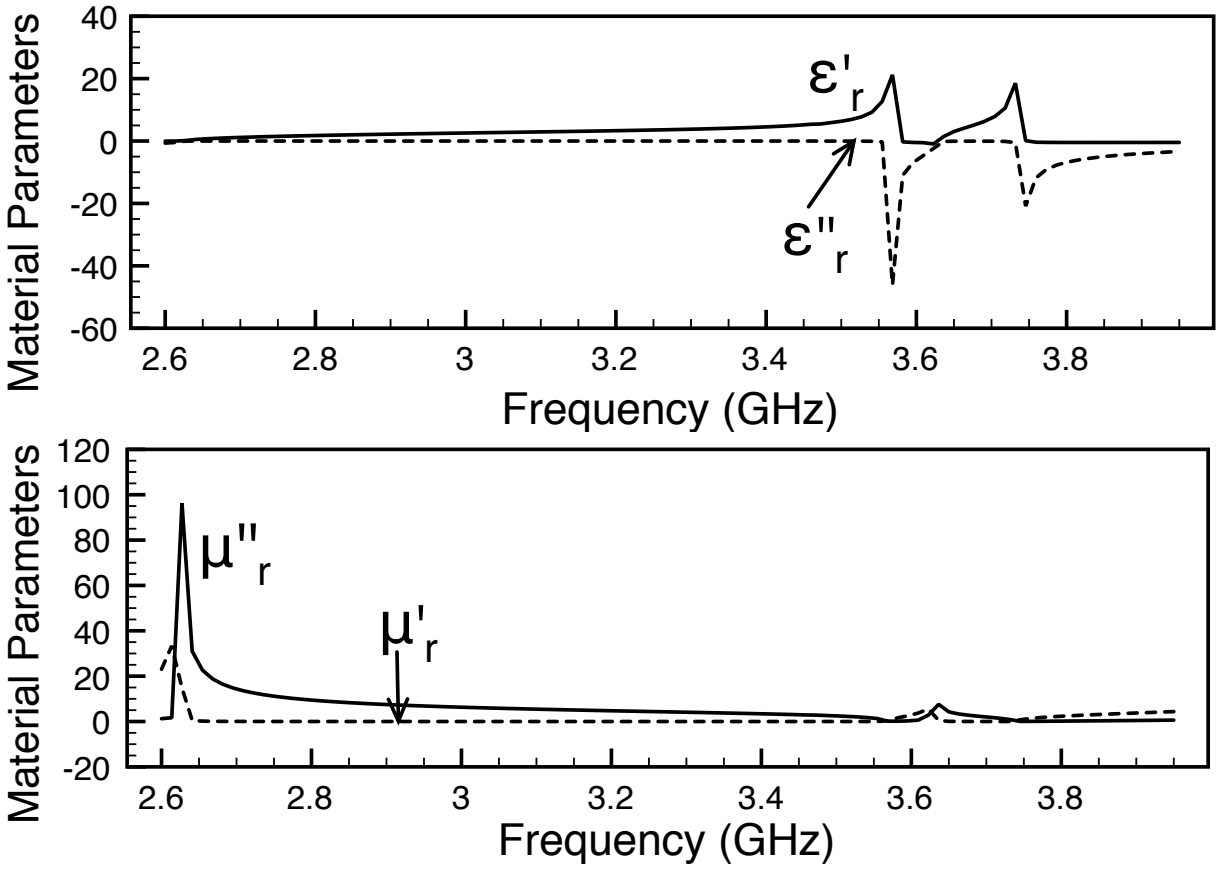

Figure 6.5: Characterization results from a GA analysis of a brass-post surrogate design.

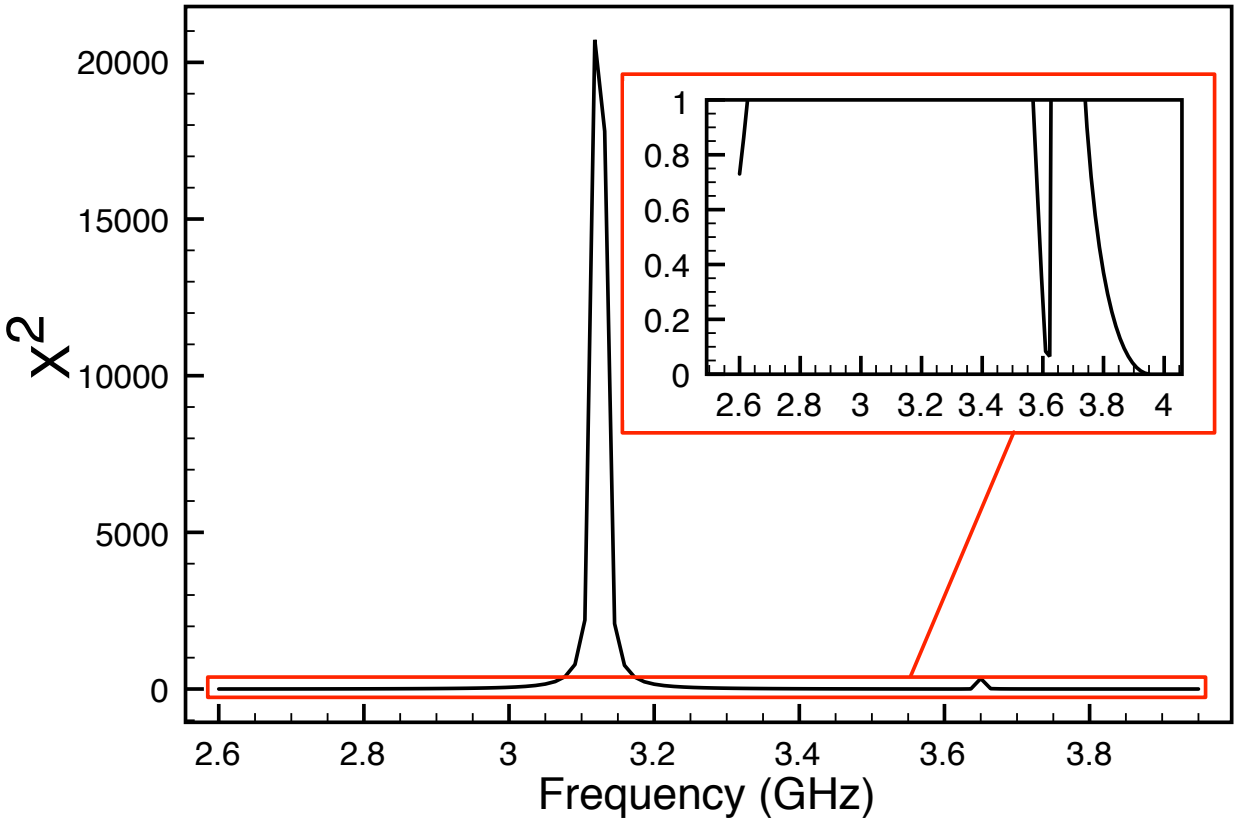

Figure 6.6: $X = \frac{S_{11r}}{|S_{11}|^2}$ for optimized brass-post surrogate. Extracted material parameters become complex over regions where $X^2 \leq 1$.

ties in the dimensions of the fabricated parts and from the uncertainties of the measured S-parameters may be appropriately calculated. Third, if the standard is manufactured using materials of thicknesses different than those described in the optimized design, or if the manufactured apertures are somewhat offset from those of the optimized design, mode matching may be used to determine the theoretical properties of the manufactured standard, and the standard may still be used to verify the accuracy of a material measurement system.

The adopted design was further tuned using an additional GA. This GA varied the vertical window positions (positions $y_1^\ell = y_1^r$ and $y_2^\ell = y_2^r$ in Figure 6.1), horizontal window positions, and the thickness of the apertures and waveguide spacer. The thicknesses of each aperture and spacer were limited to the values of United States standard brass stock (multiples of 1/16 inch, or 1.5875 mm), to simplify the fabrication process. To produce a symmetric verification standard, the apertures were assigned identical openings. The final optimized design consists of apertures with widths identical to the waveguide width and with vertical positions $y_1^\ell = y_1^r = 5.064$mm, $y_2^\ell = y_2^r = 23.86$mm. The thicknesses of the optimized design are the standard stock thicknesses $\Delta^\ell = \Delta^r = 1/8$ inch (3.175mm), and $\Delta_s = 1/2$ inch (12.7mm). The material parameters extracted from the S-parameters of the optimized design are shown in Figure 6.7. As expected, the imaginary part of the extracted parameters are zero (to computational accuracy) and the real parts are dependent on frequency. Note that the optimizer has produced a trade off between frequency variation, and values near to six. In contrast with the brass-post surrogate design, Figure 6.8 shows that $X^2 > 1$ for the entire frequency band and thus the material parameters are real.

Precise values for the material parameters produced by the optimized waveguide standard may be found by applying the mode-matching technique (see Section 6.4 for details of the mode-matching theory.) A sufficient number of modes was used ($N = 500$) to guarantee a minimum of five digits of precision in the material parameters extracted using the NRW method. The resulting values are listed in Table 6.1. Note that only the real parts of ϵ_r and μ_r are shown, since the imaginary parts are less than 10^{-5}. These values can be used to

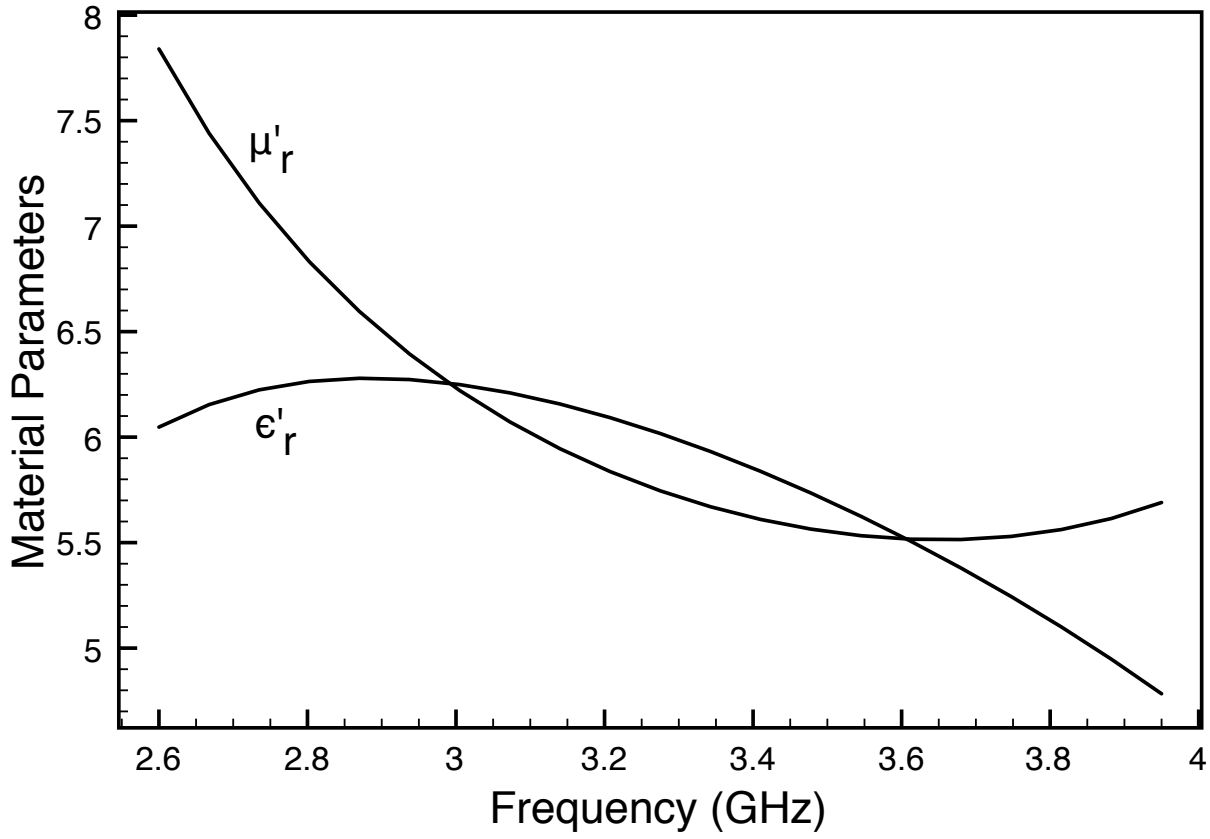

Figure 6.7: Real parts of material parameters extracted from HFSS simulation of optimized verification standard.

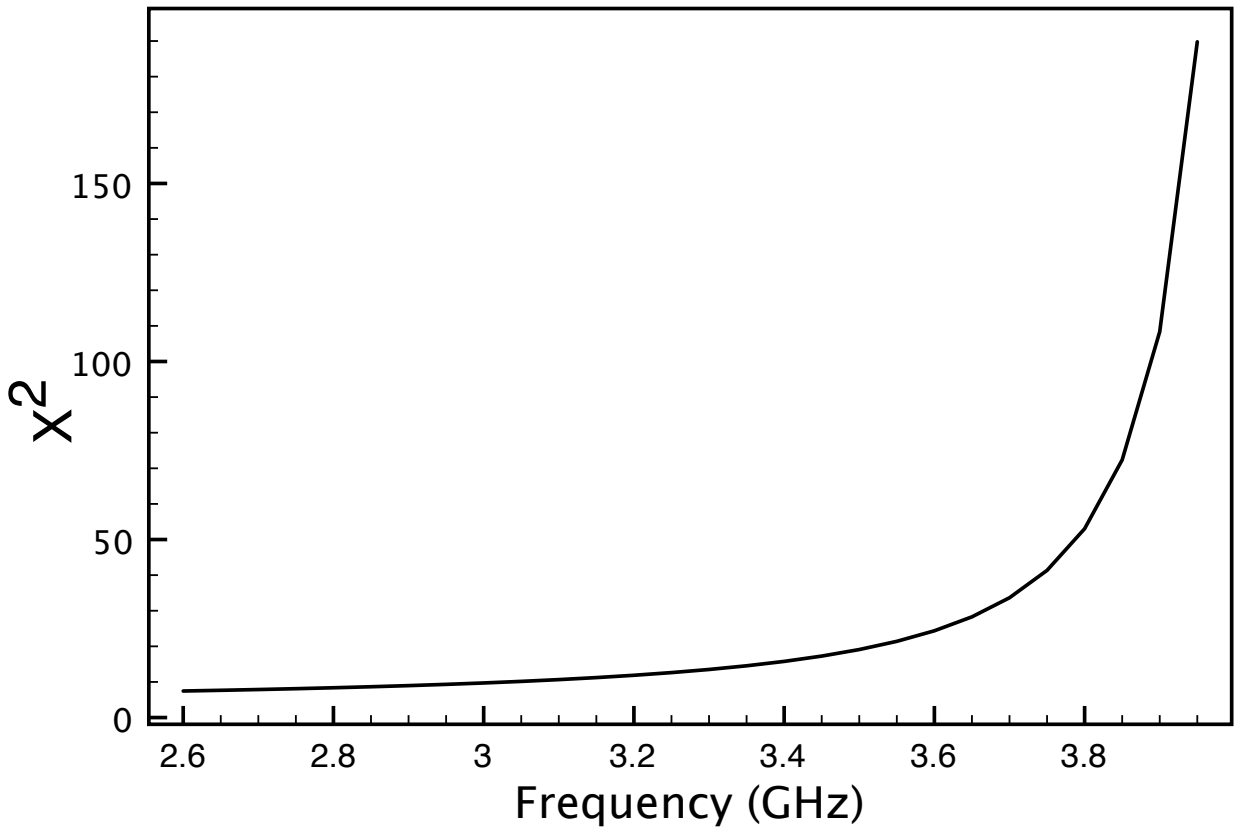

Figure 6.8: $X = \frac{S_{11r}}{|S_{11}|^2}$ of optimized verification standard. Extracted material parameters are real over regions where $X^2 > 1$.

verify the operational accuracy of waveguide material parameters measurement systems in S-band. Similar standards may be devised for other waveguide bands using the mode-matching method.

6.4 Computation of S-Parameters of adopted Waveguide Standard using Mode Matching

Useful implementation of the waveguide standard requires that the user has access to an accurate method for computing the S-parameters. For this reason, a detailed description of the mode-matching method applied to the adopted standard is presented here.

Consider the geometry of the adopted waveguide standard shown in Figure 6.1. Perfectly conducting apertures are positioned at $z = 0$ and $z = z_2$ with thickness Δ^ℓ and Δ^r, respectively. Although the adopted standard is longitudinally symmetric, the thicknesses of the apertures are allowed to be different so that the effects of manufacturing errors may be evaluated. The width of the apertures are the same as the width of the empty waveguide, a, while the vertical openings are describe by the height positions y_1^ℓ and y_2^ℓ for the left aperture, and y_1^r and y_2^r for the right aperture. The waveguide extensions are assumed to be of sufficient length such that, even though a full spectrum of higher order modes is produced at the apertures, only a TE_{10} mode is received at the measurement ports. The waveguide used is standard S-band WR-284 with dimensions $a = 2.84$ inch by $b = 1.34$ inch (72.136×34.036 mm) and a designated operational band of 2.6 to 3.95 GHz.

6.4.1 Mode Matching Analysis for the Waveguide Standard

Assume a TE_{10} mode is incident from the transmitting extension $z < 0$. Interaction of this field with the aperture at $z = 0$ generates an infinite spectrum of modes in each of the waveguide sections. However, because of the symmetry of the incident field, only the $\mathrm{TE}_{1,v}$ and $\mathrm{TM}_{1,v}$ modes are excited with nonzero amplitude [61]. The transverse fields for the

Table 6.1: Real parts of relative material parameters for the waveguide verification standard optimized for S-band using WR-284 waveguides found using mode matching. Dimensions of the standard are: $y_1^\ell = y_1^r = 5.064$ mm, $y_2^\ell = y_2^r = 23.86$ mm, $\Delta^\ell = \Delta^r = 1/8$ inch (3.175 mm), and $\Delta_s = 1/2$ inch (12.7 mm).

Frequency (GHz)	ϵ_r	μ_r
2.60	6.0356	7.8526
2.65	6.1182	7.5486
2.70	6.1797	7.2848
2.75	6.2232	7.0541
2.80	6.2509	6.8508
2.85	6.2650	6.6707
2.90	6.2670	6.5105
2.95	6.2584	6.3676
3.00	6.2403	6.2399
3.05	6.2137	6.1258
3.10	6.1795	6.0238
3.15	6.1383	5.9330
3.20	6.0908	5.8523
3.25	6.0374	5.7811
3.30	5.9785	5.7188
3.35	5.9145	5.6650
3.40	5.8457	5.6194
3.45	5.7723	5.5817
3.50	5.6944	5.5518
3.55	5.6120	5.5298
3.60	5.5254	5.5157
3.65	5.4343	5.5098
3.70	5.3389	5.5123
3.75	5.2389	5.5238
3.80	5.1342	5.5449
3.85	5.0245	5.5764
3.90	4.9096	5.6194
3.95	4.7889	5.6754

transmitting extension, $z < 0$, may thus be written as the modal series

$$\vec{E}_t(\vec{r}) = a_1^+ \vec{e}_1^f(\vec{\rho}) \mathrm{e}^{-j\beta_1^f z} + \sum_{n=1}^{N} a_n^- \vec{e}_n^f(\vec{\rho}) \mathrm{e}^{j\beta_n^f z}, \tag{6.1}$$

$$\vec{H}_t(\vec{r}) = a_1^+ \vec{h}_1^f(\vec{\rho}) \mathrm{e}^{-j\beta_1^f z} - \sum_{n=1}^{N} a_n^- \vec{h}_n^f(\vec{\rho}) \mathrm{e}^{j\beta_n^f z}, \tag{6.2}$$

where the series has been truncated at N modes for computational expediency. Similarly, the transverse fields in the region $z_1 < z < z_2$ may be written as

$$\vec{E}_t(\vec{r}) = \sum_{n=1}^{N} \left[c_n^+ \mathrm{e}^{-j\beta_n^f (z - z_1)} + c_n^- \mathrm{e}^{-j\beta_n^f (z_2 - z)} \right] \vec{e}_n^f(\vec{\rho}), \tag{6.3}$$

$$\vec{H}_t(\vec{r}) = \sum_{n=1}^{N} \left[c_n^+ \mathrm{e}^{-j\beta_n^f (z - z_1)} - c_n^- \mathrm{e}^{-j\beta_n^f (z_2 - z)} \right] \vec{h}_n^f(\vec{\rho}), \tag{6.4}$$

while those in the receiving extension, $z > z_3$, may be expressed as

$$\vec{E}_t(\vec{r}) = \sum_{n=1}^{N} f_n^+ \vec{e}_n^f(\vec{\rho}) \mathrm{e}^{-j\beta_n^f (z - z_3)}, \tag{6.5}$$

$$\vec{H}_t(\vec{r}) = \sum_{n=1}^{N} f_n^+ \vec{h}_n^f(\vec{\rho}) \mathrm{e}^{-j\beta_n^f (z - z_3)}. \tag{6.6}$$

Here a_1^+ is the known amplitude of the incident TE_{10} mode, and the $\mathrm{e}^{j\omega t}$ time convention is assumed. From (2.140) the propagation constant for mode n is given by

$$\beta_n^f = \sqrt{k_0^2 - (k_{cn}^f)^2}, \tag{6.7}$$

where k_{cn} is the cutoff wave number for the n^{th} mode expressed as

$$k_{cn}^f = \sqrt{(\pi/a)^2 + (k_{yn}^f)^2}, \tag{6.8}$$

with $k_{yn}^{f} = v_n\pi/b$. The index n orders the modes according to cutoff frequency. If the n^{th} mode is TE_z the variable v_n corresponds to a TE_{1,v_n} wave; if the n^{th} mode is TM_z this variable corresponds to a TM_{1,v_n} wave.

The fields in the aperture regions are expanded similarly as

$$\vec{E}_t(\vec{r}) = \sum_{n=1}^{N} \left[b_n^{+} \mathrm{e}^{-j\beta_n^{\ell} z} + b_n^{-} \mathrm{e}^{-j\beta_n^{\ell}(z_1 - z)} \right] \vec{e}_n^{\ell}(\vec{\rho}), \tag{6.9}$$

$$\vec{H}_t(\vec{r}) = \sum_{n=1}^{N} \left[b_n^{+} \mathrm{e}^{-j\beta_n^{\ell} z} - b_n^{-} \mathrm{e}^{-j\beta_n^{\ell}(z_1 - z)} \right] \vec{h}_n^{\ell}(\vec{\rho}), \tag{6.10}$$

in the left aperture region, $0 < z < z_1$, and

$$\vec{E}_t(\vec{r}) = \sum_{n=1}^{N} \left[d_n^{+} \mathrm{e}^{-j\beta_n^{r}(z - z_2)} + d_n^{-} \mathrm{e}^{-j\beta_n^{r}(z_3 - z)} \right] \vec{e}_n^{r}(\vec{\rho}), \tag{6.11}$$

$$\vec{H}_t(\vec{r}) = \sum_{n=1}^{N} \left[d_n^{+} \mathrm{e}^{-j\beta_n^{r}(z - z_2)} - d_n^{-} \mathrm{e}^{-j\beta_n^{r}(z_3 - z)} \right] \vec{h}_n^{r}(\vec{\rho}), \tag{6.12}$$

in the right aperture region, $z_2 < z < z_3$. Note that the propagation constants in the apertures may be different, depending on the aperture sizes, and are thus written as

$$\beta_n^{\ell,r} = \sqrt{k_0^2 - (k_{cn}^{\ell,r})^2}. \tag{6.13}$$

Here

$$k_{cn}^{\ell,r} = \sqrt{(\pi/a)^2 + (k_{yn}^{\ell,r})^2}, \tag{6.14}$$

with $k_{yn}^{\ell} = v_n\pi/w^{\ell}$ and $k_{yn}^{r} = v_n\pi/w^{r}$, where $w^{\ell} = y_2^{\ell} - y_1^{\ell}$, and $w^{r} = y_2^{r} - y_1^{r}$. As in the other waveguide sections, the modes in the apertures are ordered according to cutoff frequency.

In the above expressions, $\vec{e}_n(\vec{\rho})$ and $\vec{h}_n(\vec{\rho})$ are the transverse electric and magnetic modal

fields, respectively, and as shown in (2.153) and (2.154) are given by

$$\vec{e}_n^{f,\ell,r} = \hat{x} k_{yn}^{f,\ell,r} \cos\left(\frac{\pi x}{a}\right) \sin\left[k_{yn}^{f,\ell,r}\left(y - \delta^{f,\ell,r}\right)\right] - \hat{y}\frac{\pi}{a} \sin\left(\frac{\pi x}{a}\right) \cos\left[k_{yn}^{f,\ell,r}\left(y - \delta^{f,\ell,r}\right)\right], \tag{6.15}$$

$$\vec{h}_n^{f,\ell,r} = \frac{\hat{z} \times \vec{e}_n^{f,\ell,r}}{Z_n^{f,\ell,r}}, \tag{6.16}$$

for the TE_{1,v_n} modes and from (2.180) and (2.181) are expressed as

$$\vec{e}_n^{f,\ell,r} = -\hat{x}\frac{\pi}{a} \cos\left(\frac{\pi x}{a}\right) \sin\left[k_{yn}^{f,\ell,r}\left(y - \delta^{f,\ell,r}\right)\right] - \hat{y} k_{yn}^{f,\ell,r} \sin\left(\frac{\pi x}{a}\right) \cos\left[k_{yn}^{f,\ell,r}\left(y - \delta^{f,\ell,r}\right)\right], \tag{6.17}$$

$$\vec{h}_n^{f,\ell,r} = \frac{\hat{z} \times \vec{e}_n^{f,\ell,r}}{Z_n^{f,\ell,r}}, \tag{6.18}$$

for the TM_{1,v_n} modes. Here $\delta^f = 0$, $\delta^\ell = y_1^\ell$, $\delta^r = y_1^r$, $Z_n^{f,\ell,r} = \omega\mu_0/\beta_n^{f,\ell,r}$ is the TE wave impedance, and $Z_n^{f,\ell,r} = \beta_n^{f,\ell,r}/(\epsilon_0\omega)$ is the TM wave impedance.

The unknown modal amplitudes a_n^-, b_n^+, b_n^-, c_n^+, c_n^-, d_n^+, d_n^-, and f_n^+ may be determined by applying the boundary conditions on $\vec{E}_t$ and $\vec{H}_t$ at the interfaces between the full waveguide and the aperture regions. At the interface $z = 0$, the tangential electric field boundary condition requires

$$a_1^+ \vec{e}_1^f(\vec{\rho}) + \sum_{n=1}^{N} a_n^- \vec{e}_n^f(\vec{\rho}) = \begin{cases} \sum_{n=1}^{N}\left[b_n^+ + b_n^- \mathrm{e}^{-j\beta_n^\ell \Delta^\ell}\right] \vec{e}_n^\ell(\vec{\rho}), & \vec{\rho} \in \Omega_1 \\ 0, & \vec{\rho} \in \Delta\Omega_1 \end{cases}, \tag{6.19}$$

while the tangential magnetic field boundary condition requires

$$a_1^+ \vec{h}_1^f(\vec{\rho}) - \sum_{n=1}^{N} a_n^- \vec{h}_n^f(\vec{\rho}) =$$
$$\sum_{n=1}^{N} \left[b_n^+ - b_n^- \mathrm{e}^{-j\beta_n^\ell \Delta^\ell} \right] \vec{h}_n^\ell(\vec{\rho}), \qquad \vec{\rho} \in \Omega_1. \tag{6.20}$$

Here Ω_1 designates the aperture extending from $y = y_1^\ell$ to $y = y_2^\ell$, while $\Delta\Omega_1$ designates the remaining conducting surfaces occupying $0 < y < y_1^\ell$ and $y_2^\ell < y < b$. At $z = z_1$ the boundary condition on the tangential electric field requires

$$\sum_{n=1}^{N} \left[c_n^+ + c_n^- \mathrm{e}^{-j\beta_n^f \Delta^s} \right] \vec{e}_n^f(\vec{\rho}) =$$
$$\begin{cases} \sum_{n=1}^{N} \left[b_n^+ \mathrm{e}^{-j\beta_n^\ell \Delta^\ell} + b_n^- \right] \vec{e}_n^\ell(\vec{\rho}), & \vec{\rho} \in \Omega_1 \\ 0, & \vec{\rho} \in \Delta\Omega_1 \end{cases}, \tag{6.21}$$

while the boundary condition on the tangential magnetic field requires

$$\sum_{n=1}^{N} \left[c_n^+ - c_n^- \mathrm{e}^{-j\beta_n^f \Delta^s} \right] \vec{h}_n^f(\vec{\rho}) =$$
$$\sum_{n=1}^{N} \left[b_n^+ \mathrm{e}^{-j\beta_n^\ell \Delta^\ell} - b_n^- \right] \vec{h}_n^\ell(\vec{\rho}), \qquad \vec{\rho} \in \Omega_1. \tag{6.22}$$

Similarly imposing the tangential boundary conditions on the electric and magnetic fields at $z = z_2$ gives

$$\sum_{n=1}^{N} \left[c_n^+ \mathrm{e}^{-j\beta_n^f \Delta^s} + c_n^- \right] \vec{e}_n^f(\vec{\rho}) =$$
$$\begin{cases} \sum_{n=1}^{N} \left[d_n^+ + d_n^- \mathrm{e}^{-j\beta_n^r \Delta^r} \right] \vec{e}_n^r(\vec{\rho}), & \vec{\rho} \in \Omega_2 \\ 0, & \vec{\rho} \in \Delta\Omega_2 \end{cases}, \tag{6.23}$$

and

$$\sum_{n=1}^{N}\left[c_n^+ \mathrm{e}^{-j\beta_n^f \Delta^s} - c_n^-\right]\vec{h}_n^f(\vec{\rho}) =$$
$$\sum_{n=1}^{N}\left[d_n^+ - d_n^- \mathrm{e}^{-j\beta_n^r \Delta^r}\right]\vec{h}_n^r(\vec{\rho}), \qquad \vec{\rho}\in\Omega_2, \tag{6.24}$$

respectively. Here Ω_2 designates the aperture region between $y = y_1^r$ and $y = y_2^r$, while $\Delta\Omega_2$ designates the conducting surfaces occupying $0 < y < y_1^r$ and $y_2^r < y < b$. Finally, at $z = z_3$ the boundary conditions on the tangential electric and magnetic fields require

$$\sum_{n=1}^{N} f_n^+ \vec{e}_n^f(\vec{\rho}) =$$
$$\begin{cases} \sum_{n=1}^{N}\left[d_n^+ \mathrm{e}^{-j\beta_n^r \Delta^r} + d_n^-\right]\vec{e}_n^r(\vec{\rho}), & \vec{\rho}\in\Omega_2 \\ 0, & \vec{\rho}\in\Delta\Omega_2 \end{cases}, \tag{6.25}$$

and

$$\sum_{n=1}^{N}\left[d_n^+ \mathrm{e}^{-j\beta_n^r \Delta^r} - d_n^-\right]\vec{h}_n^r(\vec{\rho}) = \sum_{n=1}^{N} f_n^+ \vec{h}_n^f(\vec{\rho}), \ \vec{\rho}\in\Omega_2, \tag{6.26}$$

respectively.

The system of functional equations (6.19)-(6.26) may be transformed into a system of linear equations by applying appropriate testing operators as follows. First, the equations resulting from applying a tangential electric field boundary condition, (6.19), (6.21), (6.23) and (6.25), are multiplied by $\vec{e}_m^f(\vec{\rho})$ and integrated over the cross-section of the waveguide designated by $0 \le x \le a$, $0 \le y \le b$. Then, (6.20) and (6.22), which result from applying the tangential magnetic field boundary conditions on the left aperture, are multiplied by $\vec{h}_m^\ell(\vec{\rho})$ and integrated over Ω_1. Similarly for the right aperture, (6.24) and (6.26) are multiplied by $\vec{h}_m^r(\vec{\rho})$ and integrated over Ω_2. The result is a system of linear equations that may be

written in terms of an $8N \times 8N$ partitioned matrix. Note that all of the integrals may be computed in closed form, and that many matrix entries are repeated or zero. This allows the matrix to be filled rapidly and leads to the overall efficiency of the mode-matching approach compared to more generic numerical electromagnetic techniques such as finite elements. The matrix equation may be written in block form as

$$\left[\begin{array}{c|c} A^{\ell} & B^{\ell} \\ \hline B^{r} & A^{r} \end{array}\right] \left[c\right] = a_1^{+} \left[d\right]. \tag{6.27}$$

Here A^{ℓ}, B^{ℓ}, B^{r}, are A^{r} are partitioned into the $4N \times 4N$ sub-matrices

$$A^{\ell,r} = \left[\begin{array}{c|c|c|c} -G & J^{\ell,r} & J^{\ell,r}P^{\ell,r} & 0 \\ \hline K^{\ell,r} & L^{\ell,r} & -L^{\ell,r}P^{\ell,r} & 0 \\ \hline 0 & J^{\ell,r}P^{\ell,r} & J^{\ell,r} & -G \\ \hline 0 & L^{\ell,r}P^{\ell,r} & -L^{\ell,r} & -K^{\ell,r} \end{array}\right] \tag{6.28}$$

and

$$B^{\ell,r} = \left[\begin{array}{c|c|c|c} 0 & 0 & 0 & 0 \\ \hline 0 & 0 & 0 & 0 \\ \hline 0 & 0 & 0 & -GQ \\ \hline 0 & 0 & 0 & -K^{\ell,r}Q \end{array}\right], \tag{6.29}$$

where G, $J^{\ell,r}$, $K^{\ell,r}$, and $L^{\ell,r}$ are $N \times N$ sub-matrices with entries specified in Appendix B.5. Here P and Q are diagonal matrices with entries $P_{mn}^{\ell,r} = \delta_{mn}\mathrm{e}^{-j\beta_n^{\ell,r}\Delta^{\ell,r}}$ and $Q_{mn} = \delta_{mn}\mathrm{e}^{-j\beta_n^{f}\Delta^{s}}$, with δ_{mn} the Kronecker delta. The unknown vector is partitioned into eight subvectors each of length N, and is given by $c^T = \left[a_n^-, b_n^+, b_n^-, c_n^+, f_n^+, d_n^-, d_n^+, c_n^-\right]$, while the right hand side is similarly partitioned as $d^T = [G_{m1}, K_{m1}, 0, 0, 0, 0, 0, 0]$.

Once the modal coefficients are found by solving the matrix equation, the sample-plane

S-parameters of the verification standard are given by

$$S_{11} = \frac{a_1^-}{a_1^+} \tag{6.30}$$

$$S_{21} = \frac{f_1^+}{a_1^+}. \tag{6.31}$$

6.4.2 Validation of the Mode-Matching Analysis

It is important to validate the mode-matching technique before using it to compute the S-parameters of a standard design, or to establish the errors introduced by measurement or fabrication uncertainties. This is accomplished by comparing to results from the commercial EM solver HFSS. Figure 6.9 shows the values of S_{11} and S_{21} computed for the waveguide standard used to generate Table 6.1. To obtain the HFSS-computed S-parameters shown in Figure 6.9 the waveguide extensions were explicitly modeled with a length sufficient to ensure that only the fundamental TE_{10} mode is important at the waveguide ports. Here the extensions were chosen to be 55.475 mm long. This is an arbitrary value of sufficient length. The convergence in HFSS was set to a maximum ΔS of 0.0005, which is the absolute difference between the magnitudes of the S-parameters at successive iterations computed at the solution frequency 3.95 GHz. This very tight convergence criterion, which requires significant computer resources, is needed to achieve good agreement with the mode-matching S-parameters at the higher frequencies. Excellent agreement between the S-parameters obtained by the two methods is seen, giving confidence to the mode matching results. Additional validation is provided by comparing the permittivity and permeability extracted from each set of S-parameters; these results are shown in Figure 6.10.

Note that the computational time required for HFSS is approximately 60 times larger than the time required for mode matching with equivalent accuracy on a 3.5 GHz Intel quad core processor with 24 GB of RAM. Thus, the faster mode-matching approach makes lengthy optimizations far more feasible, and is used in the computationally-intensive Monte Carlo

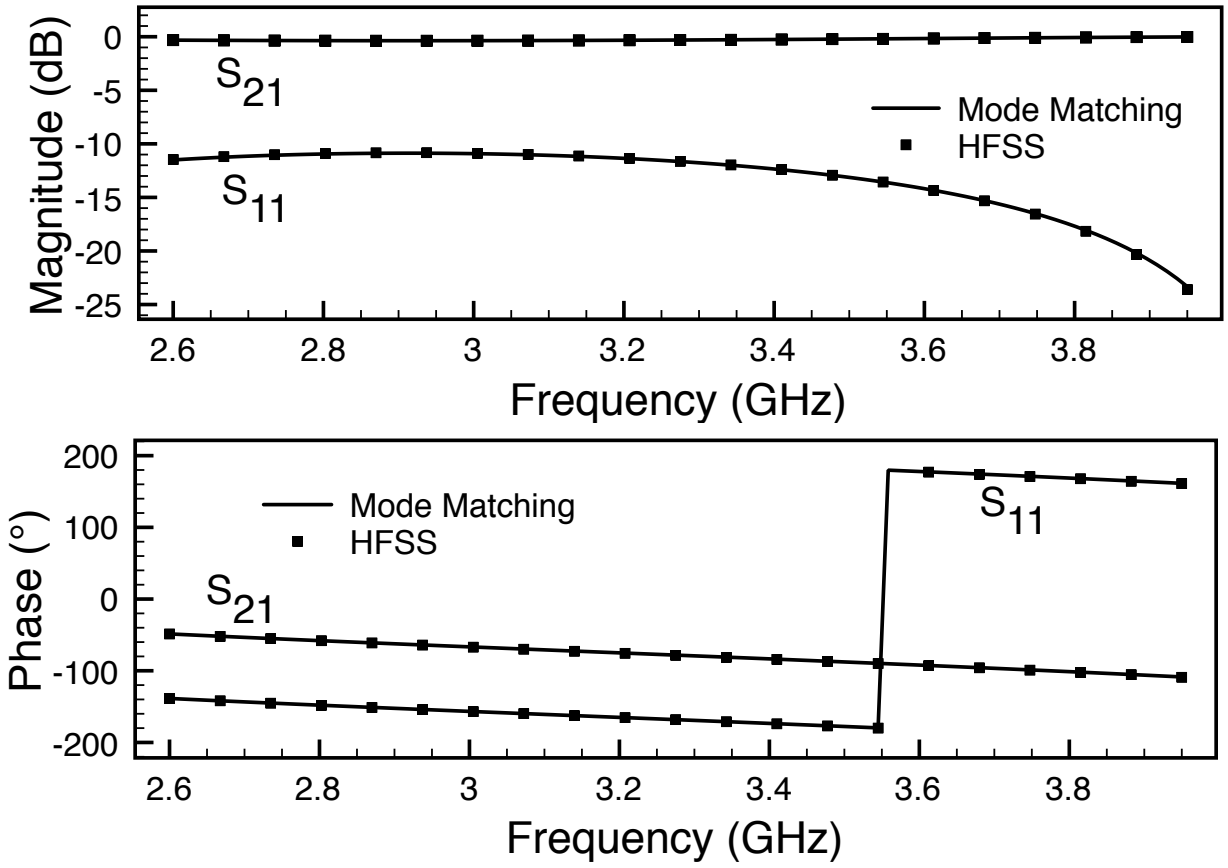

Figure 6.9: Computed S-parameters of the verification standard.

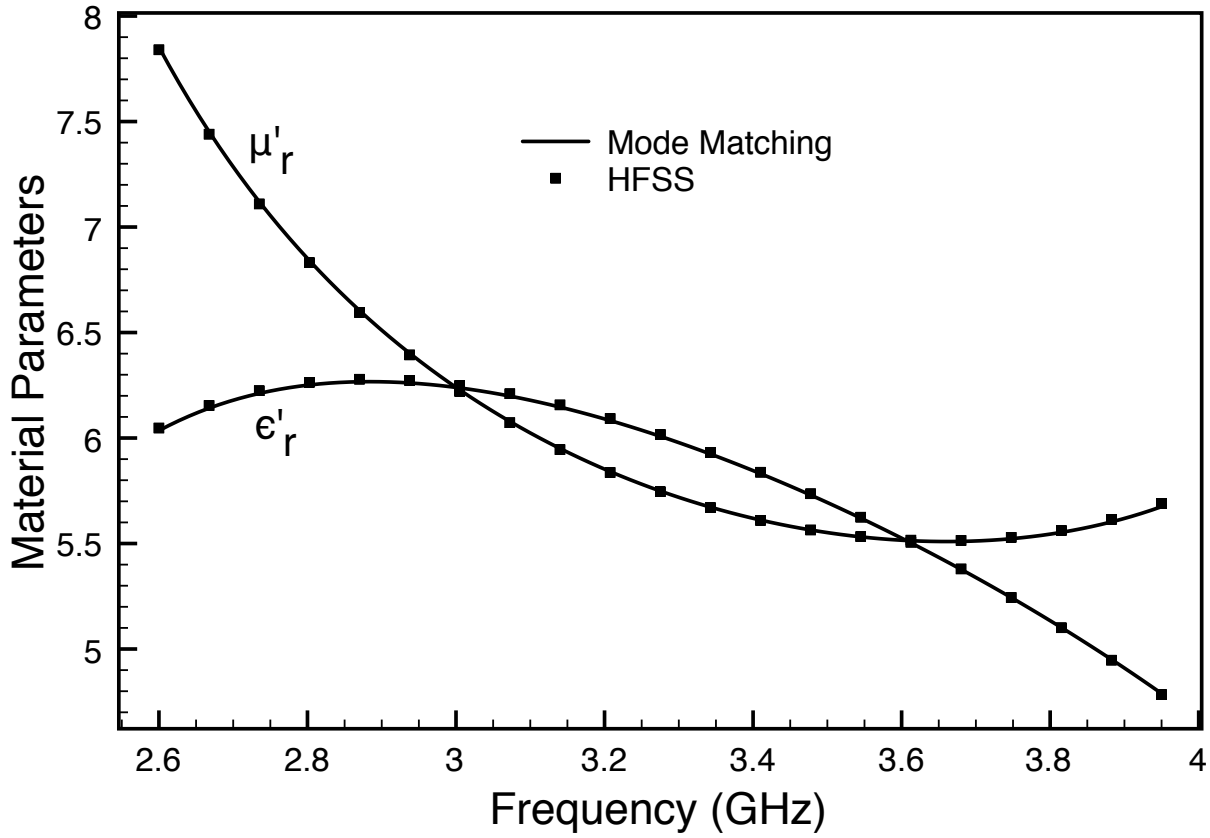

Figure 6.10: Comparison of material parameters extracted from mode matching and HFSS simulated S-parameters.

error analysis presented in the next section.

6.5 Error and Sensitivity Analysis

One of the objectives for the waveguide verification standard is to have an easily manufactured design that can be accurately characterized. Therefore, the sensitivity of the standard needs to be minor when small changes to the design geometry occur. These geometry changes can result from inaccuracies in the manufacturing process. To access this sensitivity error, a Monte Carlo error analysis was used to explore the dependence of the extracted material parameters on small changes to the geometry.

These manufacturing inaccuracies are systematic errors, which include the uncertainties in the thickness of the apertures and spacer (Δ^{ℓ}, Δ^{s}, and Δ^{r}), the vertical window positions for both apertures (y_1^{ℓ}, y_2^{ℓ}, y_1^{r}, and y_2^{r}), the uniformity of the thicknesses, and uniformity of the widow width and height. Another possible type of error is random error, which can result from the alignment of the verification standards (this may change from experiment to experiment) and measurement uncertainty inherent in the VNA. It is difficult to model all the different types of error produced by uncertainties in the geometrical parameters, since the mode-matching technique assumes uniform thicknesses and vertical window positions. However, the other systematic errors may be easily studied using Mote Carlo techniques, since the mode-matching technique is capable of analyzing different thicknesses and vertical window positions. This allows for error bounds to be established due to small inaccuracies in the manufacturing processes.

A Monte Carlo analysis on the propagation of uncertainties in the geometrical parameters was undertaken using the designed parameters outlined in Section 6.3. The forward problem was solved at 28 frequency points over the portion of S-band from 2.6 to 3.95 GHz. Dimensions were generated randomly using a Gaussian distribution with a mean value set equal to designed parameters, and a standard deviation equal to the manufacturing accuracy outlined

by the Department of Physics and Astronomy Machine Shop at Michigan State University: 5 mils for uncertainty in thickness and 2 mils for uncertainty in the aperture heights. The mode matching technique analyzed these dimensions and the erroneous S-parameter data was used to extract the material parameters. This process was repeated 500 times, and the average values and the standard deviations of the extracted material parameters were calculated. Figure 6.11 shows results of the Monte Carlo error analysis on varying the thicknesses Δ^{ℓ}, Δ^{s}, and Δ^{r}. Figure 6.12 shows results from varying the vertical window positions y_1^{ℓ}, y_2^{ℓ}, y_1^{r}, and y_2^{r}. Finally, Figure 6.13 shows the combination of uncertainties in thicknesses and vertical window positions. In these figures, the center of each triplet of lines is the average value of the 500 trials, while the two surrounding lines indicate the 95% confidence intervals of ± 2 standard deviations. For the imaginary values the mean of the 500 trials is near zero, therefore only the error is shown. Note that complex material parameters result from the asymmetric trials being analyzed in the Monte Carlo analysis. These results for geometrical uncertainties exhibit low sensitivity to possible manufacturing error, leading to the decision to fabricate and further test this surrogate design.

6.5.1 Theoretical Material Parameters for the Fabricated Standard

The thicknesses and aperture positions of the constructed inserts were measured using precision calipers with a manufacturer-specified accuracy of ± 0.02 mm. Measurements were made at 15 positions on the inserts and the mean and standard deviation computed. The mean is taken to be the estimated dimension, while the standard deviation is taken to be the uncertainty in that dimension. The results are shown in Table 6.2, along with the specified values for the optimized standard. Note that since the fabricated standard is not perfectly symmetric along z it is anticipated that measured values of μ and ϵ will have small imaginary parts.

Although the dimensions of the fabricated standard differ somewhat from those of the

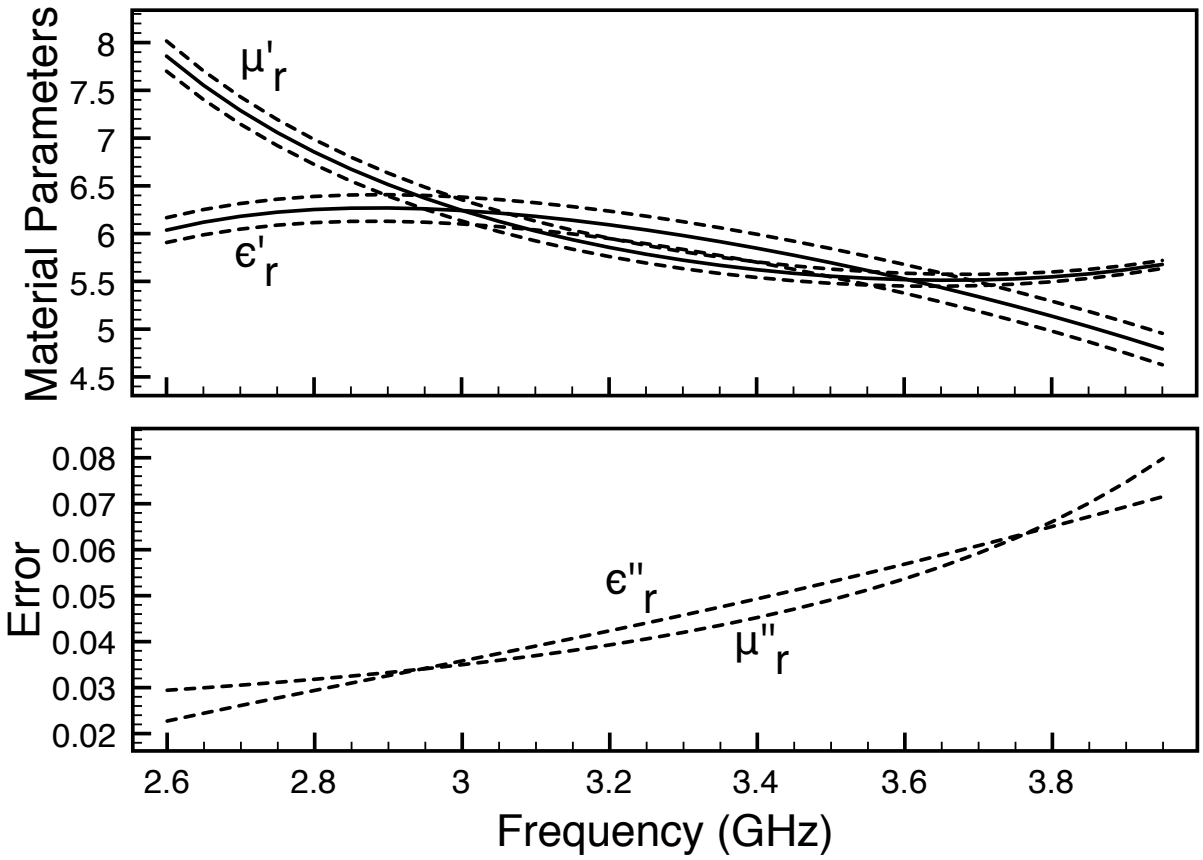

Figure 6.11: Relative constitutive parameters found when randomly varying Δ^{ℓ}, Δ^{s}, and Δ^{r} extracted using 500 trials. Center line in the upper plot is the average of real relative parameters of the trials, while the upper and lower dashed-lines show the 95% confidence intervals. The average of the imaginary relative parameters is near zero, while the lower plot shows $+2\sigma$ values.

Table 6.2: Measured dimensions of fabricated waveguide standard.

Dimension	Optimized Value (mm)	Fabricated Value (mm)
Δ^{ℓ}	3.175	3.622 ± 0.028
Δ^{r}	3.175	3.571 ± 0.038
Δ^{s}	12.7	12.347 ± 0.071
y_1^{ℓ}	5.064	5.183 ± 0.057
y_2^{ℓ}	23.86	23.907 ± 0.111
y_1^{r}	5.064	5.276 ± 0.071
y_2^{r}	23.86	23.494 ± 0.105

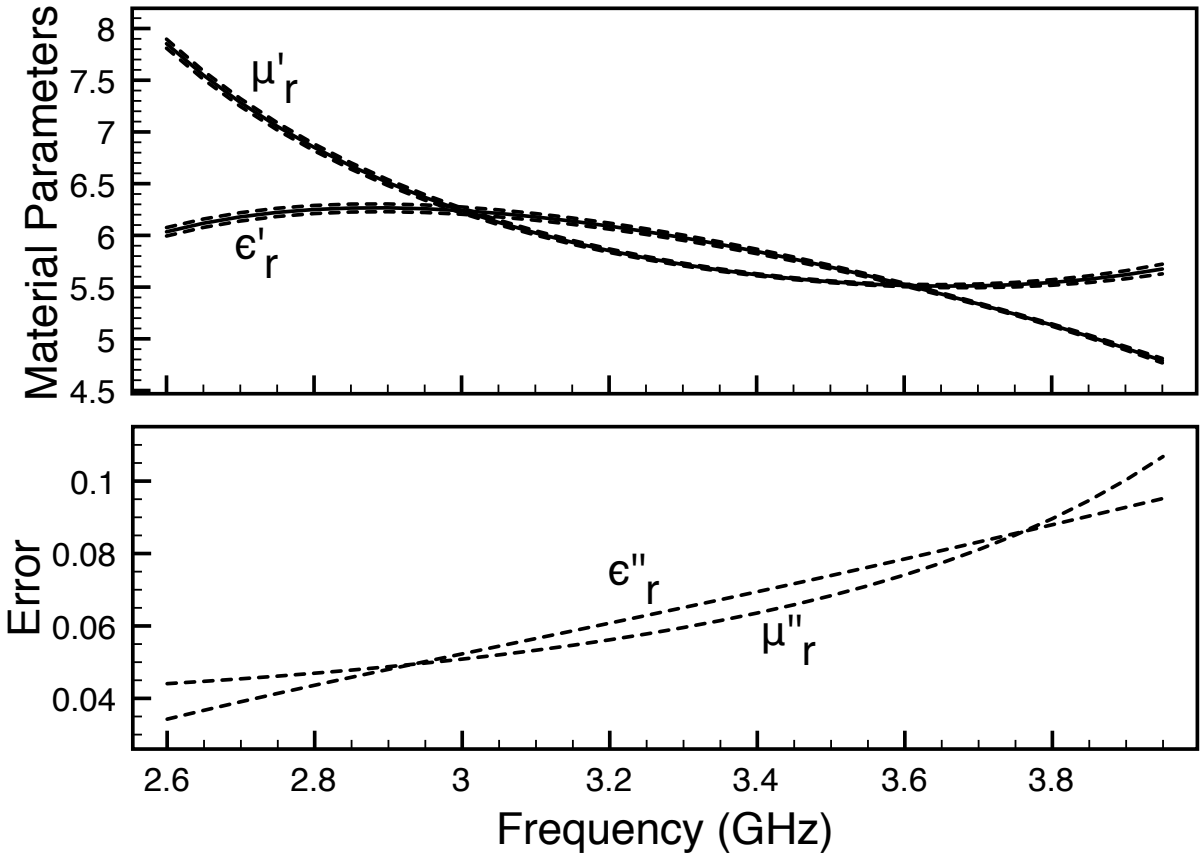

Figure 6.12: Relative constitutive parameters found when randomly varying y_1^ℓ, y_2^ℓ, y_1^r, and y_2^r extracted using 500 trials. Center line in the upper plot is the average of real relative parameters of the trials, while the upper and lower dashed-lines show the 95% confidence intervals. The average of the imaginary relative parameters is near zero, while the lower plot shows $+2\sigma$ values.

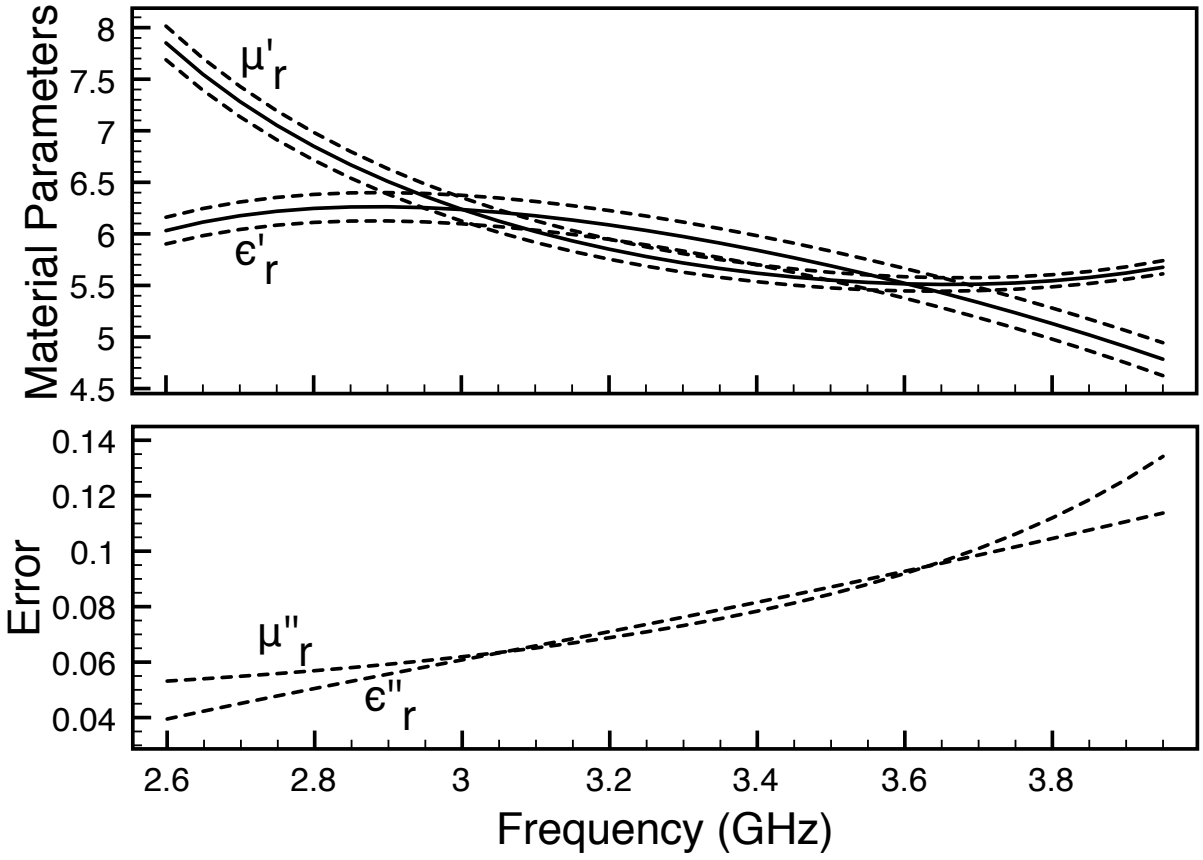

Figure 6.13: Relative constitutive parameters found when randomly varying Δ^{ℓ}, Δ^{s}, Δ^{r}, y_1^{ℓ}, y_2^{ℓ}, y_1^{r}, and y_2^{r} extracted using 500 trials. Center line in the upper plot is the average of real relative parameters of the trials, while the upper and lower dashed-lines show the 95% confidence intervals. The average of the imaginary relative parameters is near zero, while the lower plot shows $+2\sigma$ values.

optimized standard used to establish Table 6.1, the fabricated standard is still useful for its intended purpose. Because the optimization process included minimizing the sensitivity of extracted μ and ϵ to small changes in the geometrical parameters, the resulting values of μ and ϵ extracted from measurements of the fabricated standard are only slightly different than those for the optimized standard. Also, due to the availability of the mode-matching method, the dimensions of the fabricated standard may be used to establish the expected values of μ and ϵ, and these parameters used for verification of the measurement system.

The mode matching method was used to compute the theoretical S-parameters for the fabricated geometry with the mean dimensions shown in Table 6.2. These S-parameters were then used to compute the values of μ and ϵ associated with the fabricated standard. Figure 6.15 compares the real parts of these parameters with those found using the optimized design, while the imaginary parts are compared in Figure 6.16. (Recall that the optimized design is longitudinally symmetric and thus produces zero imaginary parts.) While the difference in geometry does produce a shift in the material parameters, this shift is not excessive and the values still retain their desired properties of being near 6 while varying slowly across the measurement band.

6.5.2 Measured Material Parameters for the Fabricated Standard

Measurements of the S-parameters of the verification standard were made using an Agilent E5071C VNA. The verification standard was sandwiched between two 6 inch (152.4 mm) long sections of WR-284 commercial S-band waveguide, to act as extensions, with coaxial transitions attached at the ends. The VNA was calibrated at the ends of the waveguide extensions using the Through-Reflect-Line (TRL) method. Alignment pins were used for the different assemblies to ensure high repeatability of the measurements. All measurements were made with VNA settings of -5 dBm source power, 64 averages, and an IF bandwidth of 70 kHz. Finally, the material parameters were extracted using the measured values of S_{11} and S_{21}, assuming the average values of the insert dimensions shown in Table 6.2.

Figure 6.14: Brass aperture plates forming the fabricated waveguide verification standard.

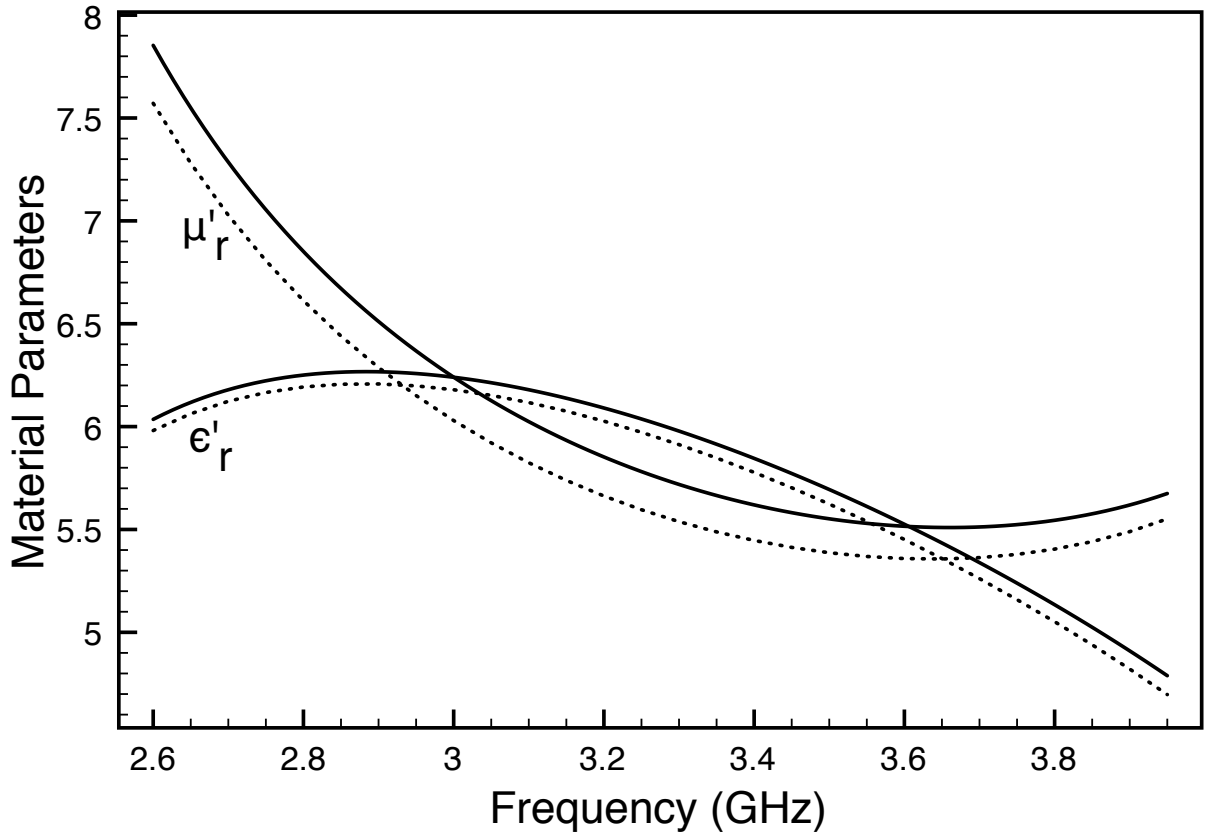

Figure 6.15: Real parts of relative permittivity and permeability for optimized geometry (solid line) and fabricated geometry (dotted line).

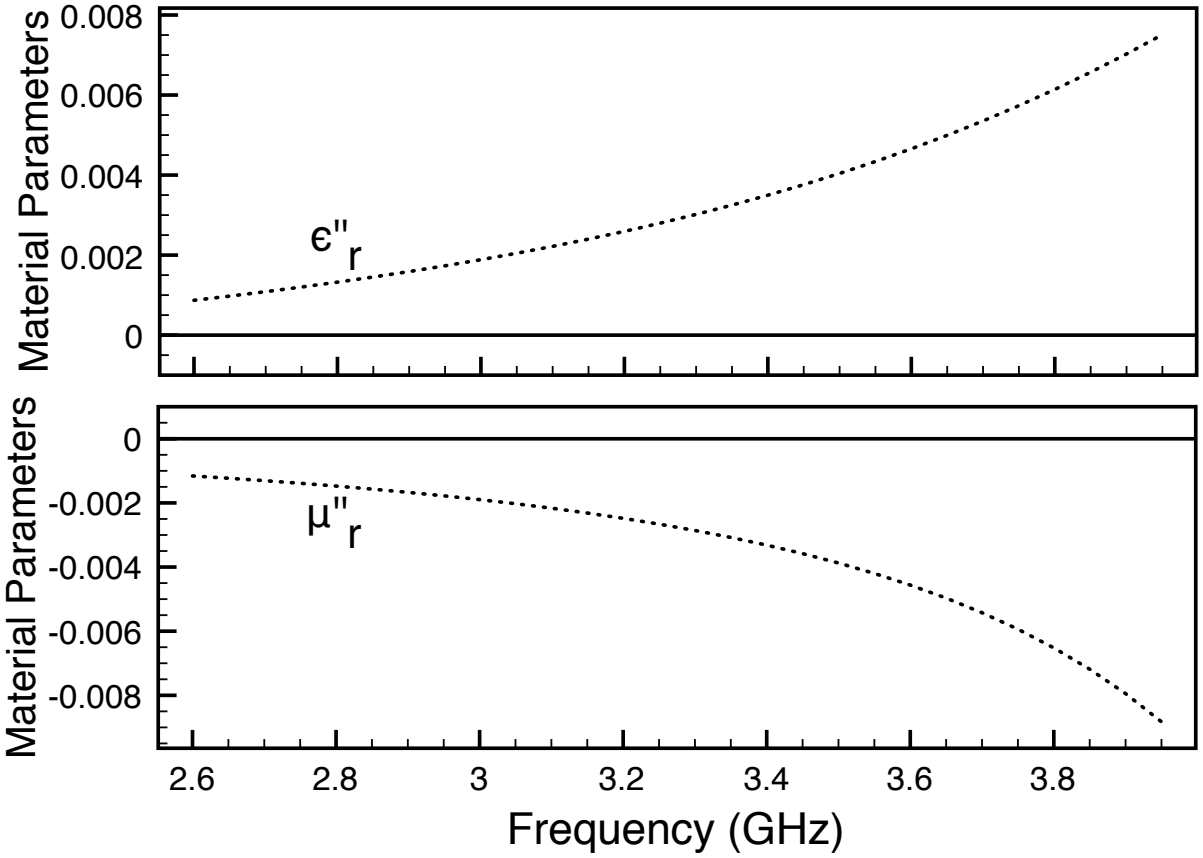

Figure 6.16: Imaginary parts of relative permittivity and permeability for optimized geometry (solid line) and fabricated geometry (dotted line).

The measurement repeatability error was assessed by measuring the verification standard 10 separate times, with the VNA calibrated at the start of each set of measurements. The real parts of the material parameters extracted from the 10 measurements are shown in Figure 6.17, while the imaginary parts are shown in Figure 6.18. The center solid line in these figures represents the mean of the extracted values while the upper and lower solid lines define the 95% confidence intervals ($\pm$ two standard deviations). The dotted lines show the theoretical material parameters from Figure 6.15 and Figure 6.16, found using the measured dimensions of the waveguide standard. Although the theoretical values for the imaginary parts lie within the 95% confidence intervals, the real parts lie just slightly outside these intervals, at least at some frequencies. This is shown more clearly in the insets, which zoom in on a chosen narrow region of the measurement band. There are several possible reasons for this, including calibration error, misalignment of the waveguide sections, imperfect electrical connections, variability in the thickness of the inserts, errors in the machining of the apertures, etc. One error that can be modeled is produced by the uncertainty in the measured values of several of the geometric parameters. These include the thicknesses of the aperture plates and spacer, and the sizes and vertical positions of the aperture openings. Unfortunately, the mode-matching approach does not allow the modeling of possible rotation of the apertures or spatial variations in thickness or opening size.

A Monte Carlo analysis was undertaken to determine the effects of geometry uncertainty on the extracted material parameters. Dimensions were generated randomly using a Gaussian distribution with a mean value set equal to the average of the measured values shown in Table 6.2, and a standard deviation equal to the standard deviation of the measured values shown in the table. The material parameters were extracted and the process repeated 500 times. The average values and the standard deviations of the extracted material parameters were calculated and are shown in Figure 6.19 and Figure 6.20. In these figures the measured data and their 95% confidence interval (solid triplet of lines) is shown along with the average Monte Carlo data and their 95% confidence interval (dashed triplet of lines). Clearly the

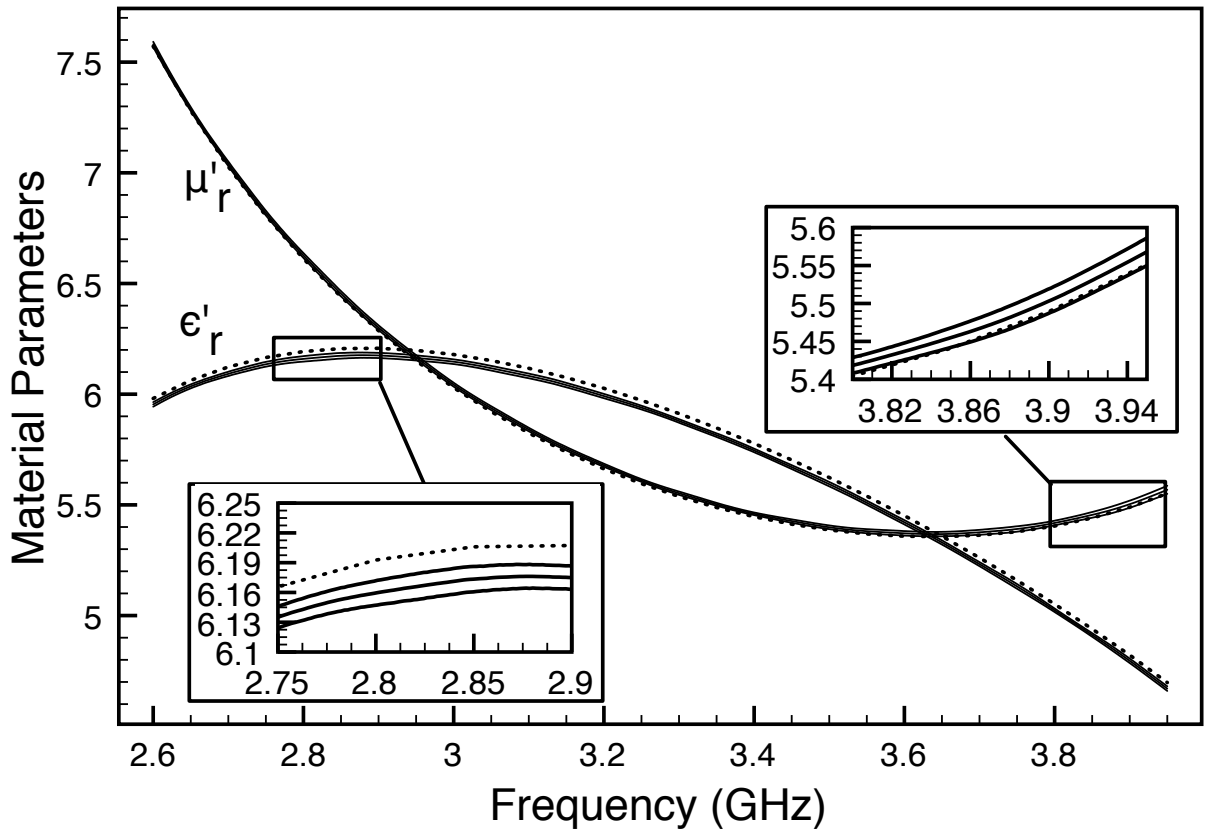

Figure 6.17: Real parts of relative permittivity and permeability extracted from 10 sets of measurements. Center solid line is the average of the measurements. Upper and lower lines show the 95% confidence intervals. Dotted line shows the material parameters extracted from the mode-matching S-parameters generated using the measured geometry.

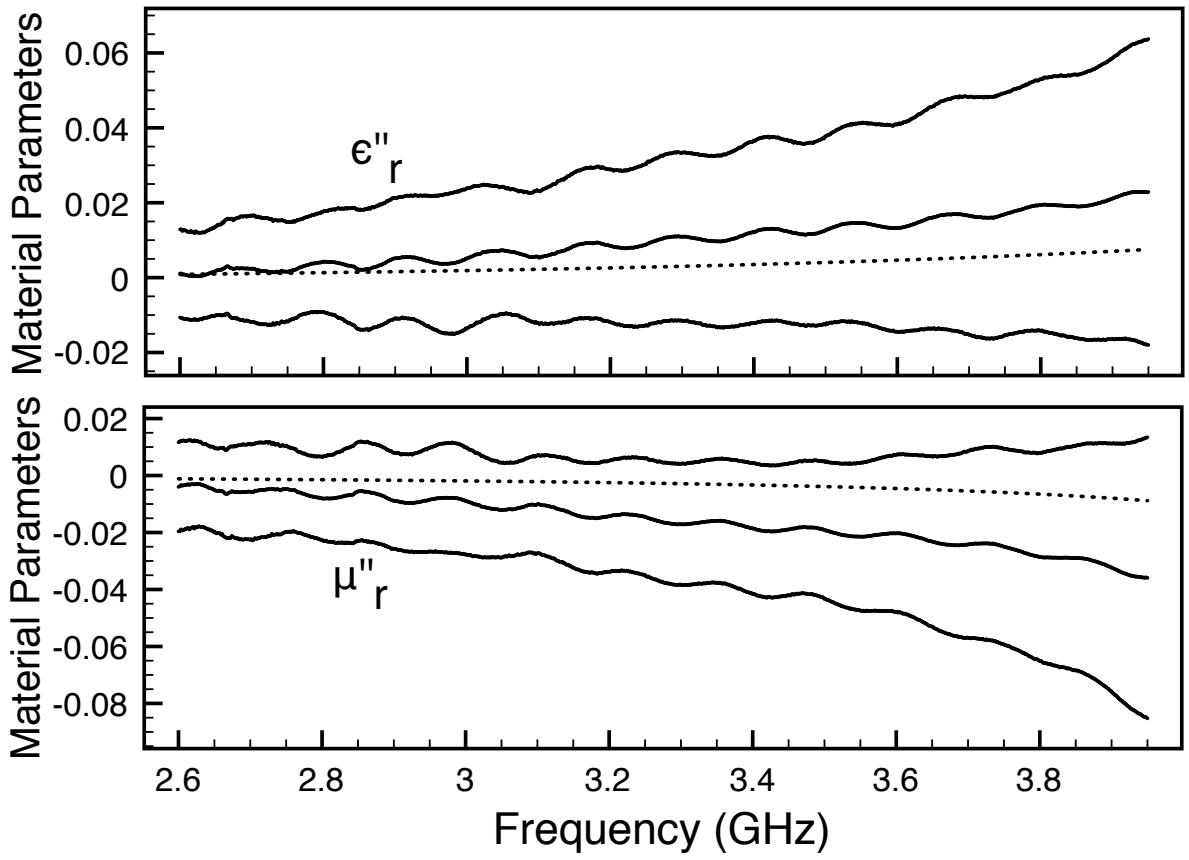

Figure 6.18: Imaginary parts of relative permittivity and permeability extracted from 10 sets of measurements. Center solid line is the average of the measurements. Upper and lower lines show the 95% confidence intervals. Dotted line shows the material parameters extracted from the mode-matching S-parameters generated using the measured geometry.

measured data (including the 95% confidence interval) lie within the uncertainty interval of the Monte Carlo data for both real and imaginary parts of μ and ϵ, and the usefulness of the standard to predict the operability of the measurement system is demonstrated.

6.6 Summary

A waveguide standard is introduced to provide a surrogate material useful for verifying material characterization systems in the microwave spectrum. A surrogate is needed since no convenient materials are available that have slowly-varying, predictable and accurately reproducible magnetic characteristics at microwave frequencies. The standard is constructed from all metal parts, allowing for easy fabrication, and is straightforward to design using a mode-matching method for analysis. Specific dimensions are provided for an S-band standard to give relative permittivity and permeability near six when using the Nicolson-Ross-Weir method. The example standard is optimized using a genetic algorithm such that the extracted material properties are not highly sensitive to changes in the geometrical parameters, and thereby reduce the need for tight manufacturing tolerances.

An example standard is measured and the errors introduced by uncertainty in the dimensions of the machined parts is characterized. By showing that the measurement precision defined by the repeatability of the experiments is consistent with the error due to propagation of geometrical uncertainties, the usefulness of the standard for verifying the proper operation of a waveguide material measurement system is demonstrated.

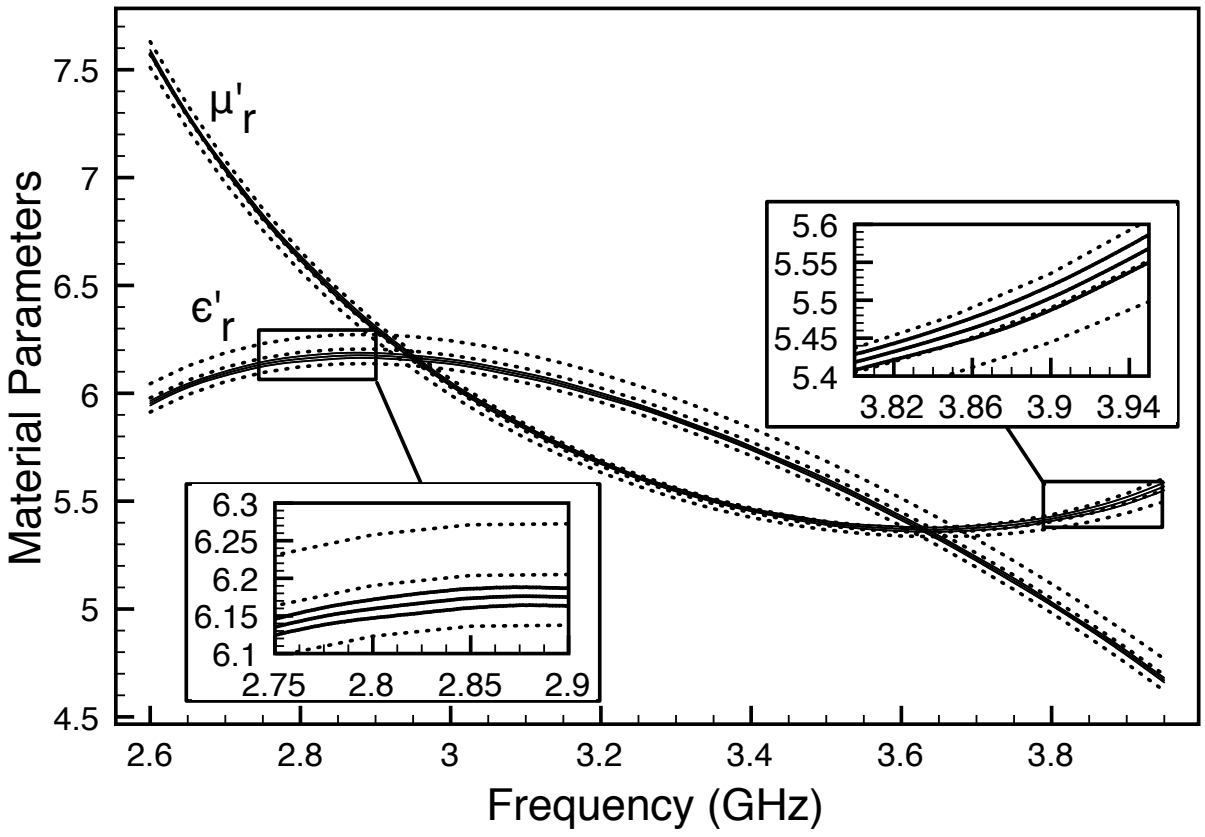

Figure 6.19: Real parts of the relative permittivity and permeability extracted from 10 sets of measurements (solid lines). Center solid line is the average of the measurements. Upper and lower solid lines show the 95% confidence intervals. Dotted lines show mode-matching results for 500 random trials. Center dotted line is the average and upper and lower dotted lines show the 95% confidence intervals.

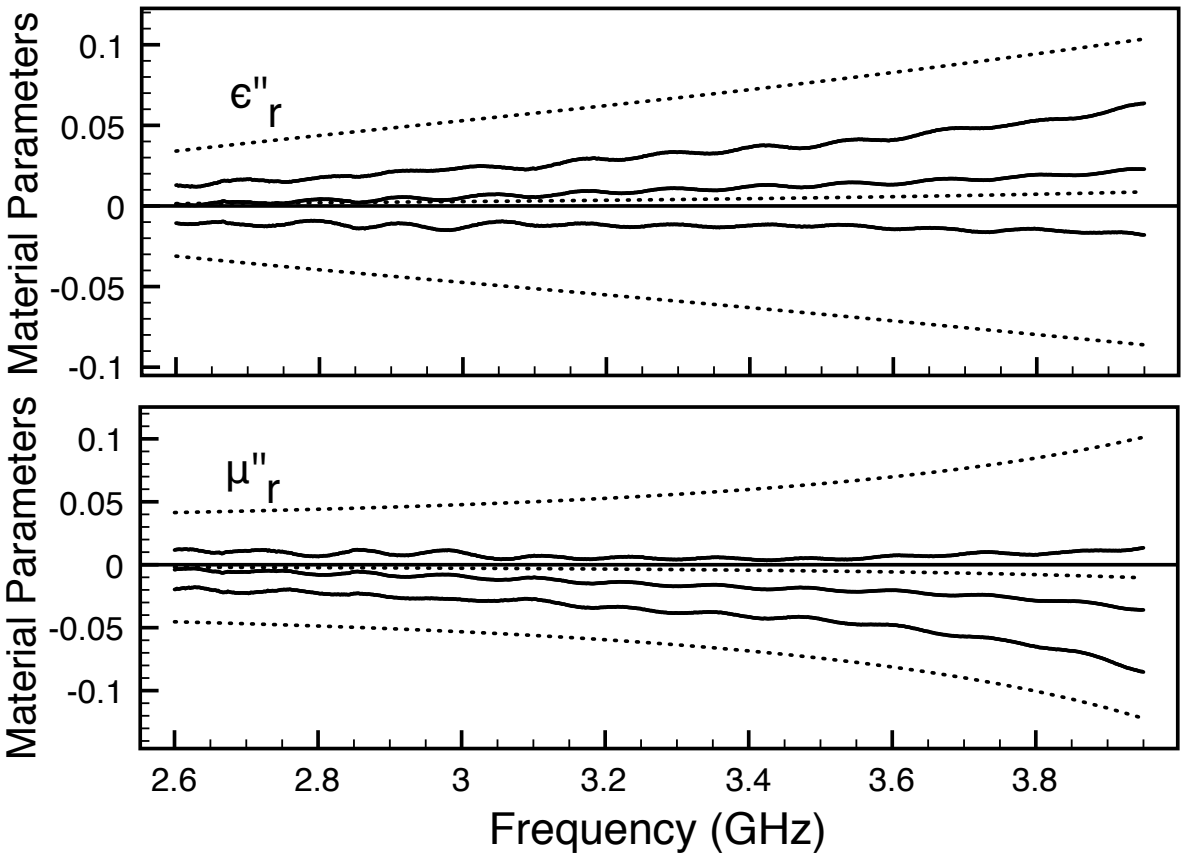

Figure 6.20: Imaginary parts of the relative permittivity and permeability extracted from 10 sets of measurements (solid lines). Center solid line is the average of the measurements. Upper and lower solid lines show the 95% confidence intervals. Dotted lines show mode-matching results for 500 random trials. Center dotted line is the average and upper and lower dotted lines show the 95% confidence intervals.

CHAPTER 7

CONCLUSIONS AND FUTURE STUDIES

Major contributions to the research community discussed in this dissertation are the new methods for the characterization of anisotropic materials. Additionally, the waveguide standard is introduced which may be used as a surrogate material useful for verifying material characterization systems in the microwave spectrum.

A general description of the NRW method is outlined for isotropic material characterization using a rectangular waveguide. An iris technique is investigated for the characterization of conductor-backed isotropic materials. A mode-matching method is used to calculate the theoretical reflection and transmission coefficients. These theoretical coefficients are used in the extraction of isotropic material parameters using a secant method. This technique was shown to be very sensitive to measurement uncertainties, especially for the characterization of ϵ''. By the completion of this dissertation accurate characterization of a conductor-backed material using this technique has not been accomplished. Possible future work includes manufacturing a sample holder for the FGM125 sample such that a shorting plate can be connected to the back of the sample. Here the use of sliding short is not necessary. Use of the shorting plate might decrease the amount of error in the measured S-parameters.

Previous work was not found on the characterization of biaxial material using closed form solutions. This dissertation described the use of the NRW method for biaxial materials without the use of an iterative solver. This technique produced accurate results using simulated S-parameter data in lieu of measurements. Future work might include the verification of this technique using measurements of biaxial or uniaxial materials.

If three samples are not available for characterization of a biaxial material, then this dissertation introduced a reduced aperture waveguide method for measuring the permittivity and permeability of biaxially anisotropic materials. Only a single cubical sample is required to completely characterize the material under test. This contrasts with the three distinct samples required when using the NRW extension technique. A mode-matching technique is used to accommodate the higher-order mode excitation resulting from the waveguide discontinuity. Then a Newton's method is employed to extract the six complex material parameters. The reduced aperture waveguide technique was used to characterize isotropic and uniaxial properties of two samples. However, as with many characterization techniques, there are limits on the accuracy of the extraction when the electrical length of the sample approaches a half wavelength. Possible future work includes exploring the use of additional measurements to ameliorate this issue. Also it is possible to construct an electrically-biaxial sample by using layers of alternating strips, as suggested in [59]. This could be accomplished by slicing a layered cube, rotating the slices by ninety degrees, and gluing the slices together. Additionally, a magnetic uniaxial sample could be constructed from alternating layers of dielectric and FGM125 or FGM40. The usefulness of using such a sample as a biaxial or magnetic uniaxial surrogate is left for future exploration.

As a next step towards full anisotropic material tensor characterization, gyromagnetic materials were considered. Previous work the characterization of gyromagnetic materials using rectangular waveguides was limited. This dissertation described two characterization methods using a completely filled cross section or reduced aperture sample holder. Here the reduced aperture sample holder is used to characterize samples with electrical size smaller

than the cross-section of a waveguide. Details on the mode matching technique used for obtaining the theoretical reflection and transmission coefficients and a comparison to a full wave FEM solver are presented for these two characterization techniques. The extraction method using a nonlinear least squares algorithm was tested by using simulated S-parameters in lieu of measurements. The sensitivity analysis for measurement uncertainties performed for the reduced-aperture technique demonstrates promise for characterization using measurements. The measurement uncertainties used in the Monte Carlo technique represent a worst case error. Since the results of the sensitivity analysis in Section 5.3.4 demonstrate that the extraction techniques is not highly sensitive to measurement uncertainties, it is hopeful that accurate characterization will result from measurements. Extraction of gyromagnetic material parameters from experimental results is left for future study.

The usefulness of the waveguide standard for verifying the proper operation of a waveguide material measurement system is demonstrated in this dissertation. Additionally a mode-matching approach is described which allows the user to predict the material properties with higher accuracy, and thus compensates for manufacturing inaccuracies. Surrogate materials of similar geometries should be useful for verifying the performance of other types of material measurements systems that employ the NRW method, such as coaxial and stripline applicators. Design of these standards is left for future study.

APPENDICES

Appendix A: Useful Identities

$$\vec{A} \cdot \left(\vec{B} + \vec{C} \right) = \vec{A} \cdot \vec{B} + \vec{A} \cdot \vec{C} \tag{A.1}$$

$$\left(\vec{A} \cdot \overline{\overline{P}} \right) \cdot \vec{B} = \vec{A} \cdot \left(\overline{\overline{P}} \cdot \vec{B} \right) = \vec{A} \cdot \overline{\overline{P}} \cdot \vec{B} \tag{A.2}$$

$$\left(\vec{A} \times \overline{\overline{P}} \right) \cdot \vec{B} = \vec{A} \cdot \left(\overline{\overline{P}} \times \vec{B} \right) \tag{A.3}$$

$$\hat{u} \times \left(\hat{u} \times \vec{A} \right) = -\vec{A}_\rho \tag{A.4}$$

$$\hat{u} \cdot \vec{A}_\rho = 0 \tag{A.5}$$

$$\nabla \times \vec{A} = \nabla_\rho \times \vec{A}_\rho + \hat{u} \times \left[\frac{\partial \vec{A}_\rho}{\partial u} - \nabla_\rho A_u \right] \tag{A.6}$$

$$\hat{u} \times \left(\nabla_\rho \times \vec{A}_\rho \right) = 0 \tag{A.7}$$

$$\hat{u} \cdot \left(\hat{u} \times \vec{A} \right) = 0 \tag{A.8}$$

$$\vec{A} \times \left(\vec{B} \times \vec{C} \right) = \vec{B} \left(\vec{A} \cdot \vec{C} \right) - \vec{C} \left(\vec{A} \cdot \vec{B} \right) \tag{A.9}$$

$$\vec{A} \cdot \left(\vec{B} \times \vec{C} \right) = \vec{C} \cdot \left(\vec{A} \times \vec{B} \right) \tag{A.10}$$

$$\overline{\overline{P}} = \overline{\overline{P}} \cdot \overline{\overline{P}}^{n-1} \tag{A.11}$$

$$\overline{\overline{P}}^{0} = \overline{\overline{I}} \tag{A.12}$$

Appendix B: De-embedding S-parameters

S-parameters of a waveguide system are measured by a VNA using waveguide to coaxial line adaptors and waveguide extensions. The extensions are used to guarantee that only the dominant waveguide mode is present at the measurement ports. A calibration is performed at the ends of the waveguide extensions and calibration planes are established there. When characterizing a material sample, the S-parameters are measured with the sample positioned somewhere in the waveguide system. Typically, the sample is placed inside a sample holder, and the holder is positioned in between the two calibration planes, as shown in Figure $B.1$. Another common sample placement is to insert the sample inside the waveguide extension as is shown in Figure $B.2$.

The characterization techniques described in this dissertation make use of sample plane S-parameters. Sample plane S-parameters are defined at the faces of the material sample while the calibration plane S-parameters are measured by the VNA at the calibration planes. The sample plane S-parameters can be obtain by properly applying corrections to the S-parameters measured by the VNA. This process is called de-embedding. De-embedding procedures for the two different sample insertion cases are described in this appendix.

In Figure $B.1$ and Figure $B.2$, the modal amplitude coefficients are shown at both the calibration and sample planes. The modal coefficients can be shifted from one plane to the other by multiplying by $\mathrm{e}^{-j\beta D}$ in the direction of the wave propagation. Here, D is the

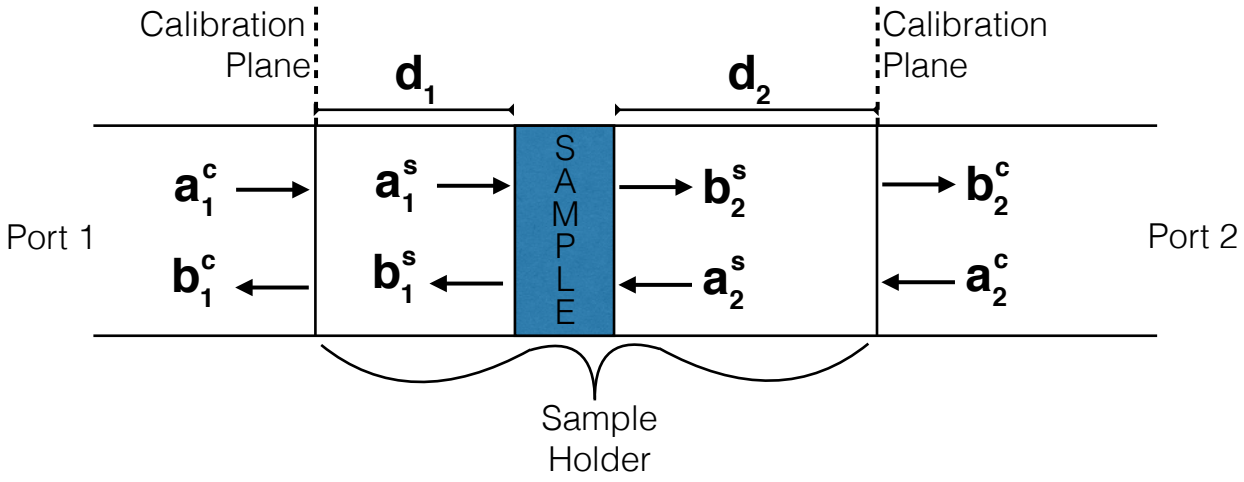

Figure B.1: Measurement and sample plane modal coefficients for a sample holder.

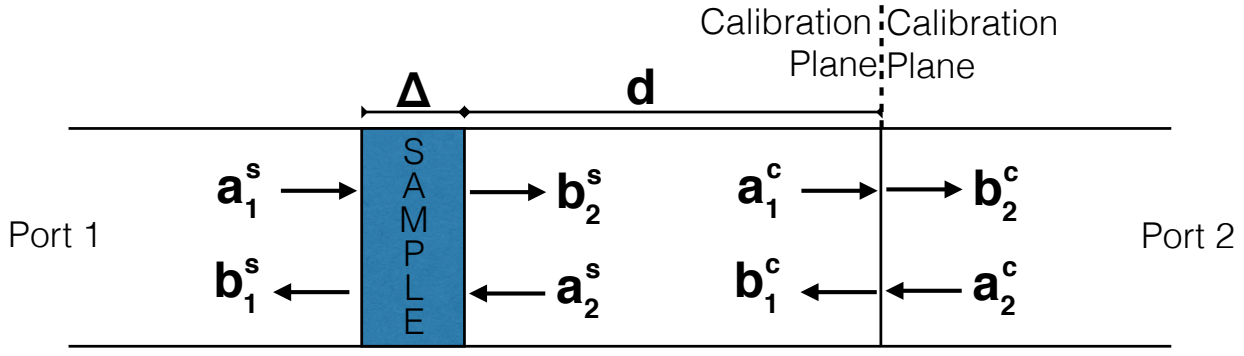

Figure B.2: Measurement and sample plane modal coefficients with sample inserted into the waveguide extension attached to port 1.

distance of the shift, and β is the propagation constant of the empty waveguide extension which can be found using (3.3). The calibration plane S-parameters are defined as

$$S_{11}^c = \frac{b_1^c}{a_1^c} \tag{B.1}$$

$$S_{21}^c = \frac{b_2^c}{a_1^c} \tag{B.2}$$

$$S_{12}^c = \frac{b_1^c}{a_2^c} \tag{B.3}$$

$$S_{22}^c = \frac{b_2^c}{a_2^c}, \tag{B.4}$$

while the sample plane S-parameters are defined as

$$S_{11}^s = \frac{b_1^s}{a_1^s} \tag{B.5}$$

$$S_{21}^s = \frac{b_2^s}{a_1^s} \tag{B.6}$$

$$S_{12}^s = \frac{b_1^s}{a_2^s} \tag{B.7}$$

$$S_{22}^s = \frac{b_2^s}{a_2^s}. \tag{B.8}$$

Consider the case shown in Figure $B.1$. The calibration and sample plane modal coefficients are related as follows:

$$a_1^s = a_1^c \mathrm{e}^{-j\beta d_1} \tag{B.9}$$

$$b_1^c = b_1^s \mathrm{e}^{-j\beta d_1} \tag{B.10}$$

$$a_2^s = a_2^c \mathrm{e}^{-j\beta d_2} \tag{B.11}$$

$$b_2^c = b_2^s \mathrm{e}^{-j\beta d_2}. \tag{B.12}$$

Here d_1 and d_2 are the distances between the sample and the ends of the waveguide ex-

tensions attached to port 1 and port 2, respectively. To express the sample plane modal coefficients in terms of calibration plane modal coefficients, $(B.10)$ is divided by $\mathrm{e}^{-j\beta d1}$ and $(B.12)$ is divided by $\mathrm{e}^{-j\beta d2}$, yielding

$$b_1^s = b_1^c \mathrm{e}^{j\beta d1} \tag{B.13}$$

$$b_2^s = b_2^c \mathrm{e}^{j\beta d2}. \tag{B.14}$$

Now, S_{11}^s can be expressed using the measured S_{11}^c, by first substituting $(B.9)$ and $(B.13)$ into $(B.5)$, which results in

$$S_{11}^s = \frac{b_1^c \mathrm{e}^{j\beta d1}}{a_1^c \mathrm{e}^{-j\beta d1}}. \tag{B.15}$$

Using $(B.1)$ and simplifying, this becomes

$$S_{11}^s = S_{11}^c \mathrm{e}^{j2\beta d1}. \tag{B.16}$$

The remaining sample plane S-parameters can be derived by a similar set of steps producing

$$S_{21}^s = S_{21}^c \mathrm{e}^{j\beta(d1+d2)} \tag{B.17}$$

$$S_{12}^s = S_{12}^c \mathrm{e}^{j\beta(d1+d2)} \tag{B.18}$$

$$S_{22}^s = S_{22}^c \mathrm{e}^{j2\beta d2}. \tag{B.19}$$

The next case involves inserting the sample inside the waveguide extension as shown in

Figure $B.2$. In this setup the calibration and sample plane modal coefficients are related by

$$a_1^c = a_1^s \mathrm{e}^{-j\beta(d+\Delta)} \tag{B.20}$$

$$b_1^s = b_1^c \mathrm{e}^{-j\beta(d+\Delta)} \tag{B.21}$$

$$a_2^s = a_2^c \mathrm{e}^{-j\beta d} \tag{B.22}$$

$$b_2^c = b_2^s \mathrm{e}^{-j\beta d}. \tag{B.23}$$

Here d is the distance between the sample and the calibration plane and Δ is the thickness of the sample. The sample plane modal coefficients are expressed in terms of calibration plane modal coefficients by dividing $(B.20)$ by $\mathrm{e}^{-j\beta(d+\Delta)}$ and $(B.23)$ by $\mathrm{e}^{-j\beta d}$. This gives

$$a_1^s = a_1^c \mathrm{e}^{j\beta(d+\Delta)} \tag{B.24}$$

$$b_2^s = b_2^c \mathrm{e}^{j\beta d}. \tag{B.25}$$

The expressions for the sample plane modal coefficients are substituted into definitions for the sample plane S-parameters, $(B.5)$ - $(B.8)$, which yields the following:

$$S_{11}^s = S_{11}^c \mathrm{e}^{-j2\beta(d+\Delta)} \tag{B.26}$$

$$S_{21}^s = S_{21}^c \mathrm{e}^{-j\beta\Delta} \tag{B.27}$$

$$S_{12}^s = S_{12}^c \mathrm{e}^{-j\beta\Delta} \tag{B.28}$$

$$S_{22}^s = S_{22}^c \mathrm{e}^{-j2\beta d}. \tag{B.29}$$

In both cases of de-embedding, since the sample plane S-parameters result from a reciprocal and symmetric system, it is known that

$$S_{21}^s = S_{12}^s \tag{B.30}$$

$$S_{11}^s = S_{22}^s. \tag{B.31}$$

However, the calibration plane S-parameters, or the S-parameters measured by the VNA, have the following relationships:

$$S_{21}^{\mathcal{C}} = S_{12}^{\mathcal{C}} \tag{B.32}$$

$$S_{11}^{\mathcal{C}} \neq S_{22}^{\mathcal{C}}. \tag{B.33}$$

This can be deduced from (B.16) and (B.19) for the first case, and from (B.26) and (B.29) for the second case. Here, since (B.31) holds true, in general $S_{11}^{\mathcal{C}} \neq S_{22}^{\mathcal{C}}$. This means the VNA measurements of the reflection coefficient at port 1 will in general be different than the reflection coefficient at port 2. However, a special case does exist when $S_{11}^{\mathcal{C}} = S_{22}^{\mathcal{C}}$. This occurs in the first case when the sample is centered in the sample holder ($d_1 = d_2$).

Appendix C: Calculation of Waveguide Transverse Mode Integrals

C.1: Iris Integrals

The derivation of the transverse mode integrals for the mode matching technique used in the calculation of the reflection coefficient from an iris in front of a conductor-backed material is outlined here. The integrals for the reduced-aperture junction, $w_B < w_A$, are

$$C_{mn} = \int_{-\frac{w_A}{2}}^{\frac{w_A}{2}} e_m^A(x) e_n^A(x) dx, \tag{C.1}$$

$$D_{mn} = \int_{-\frac{w_B}{2}}^{\frac{w_B}{2}} e_m^A(x) e_n^B(x) dx, \tag{C.2}$$

$$E_{mn} = \int_{-\frac{w_B}{2}}^{\frac{w_B}{2}} \frac{e_m^B(x) e_n^A(x)}{Z_n^A} dx, \tag{C.3}$$

$$F_{mn} = \int_{-\frac{w_B}{2}}^{\frac{w_B}{2}} \frac{e_m^B(x) e_n^B(x)}{Z_n^B} dx, \tag{C.4}$$

while the integrals for the expanded-aperture, $w_A < w_B$ are

$$L_{mn} = \int_{-\frac{w_B}{2}}^{\frac{w_B}{2}} e_m^B(x) e_n^B(x) dx, \tag{C.5}$$

$$M_{mn} = \int_{-\frac{w_A}{2}}^{\frac{w_A}{2}} e_m^A(x) e_n^B(x) dx, \tag{C.6}$$

$$O_{mn} = \int_{-\frac{w_A}{2}}^{\frac{w_A}{2}} \frac{e_m^A(x) e_n^B(x)}{Z_n^B} dx, \tag{C.7}$$

$$W_{mn} = \int_{-\frac{w_A}{2}}^{\frac{w_A}{2}} \frac{e_n^A(x) e_m^A(x)}{Z_n^A} dx. \tag{C.8}$$

First the integrals for the reduced step are evaluated. C_{mn} is expressed as

$$C_{mn} = k_{xn}^A k_{xm}^A (-1)^{n+m} \int_{\frac{-w_A}{2}}^{\frac{w_A}{2}} \cos\left(\frac{2n-1}{w_A}\pi x\right) \cos\left(\frac{2m-1}{w_A}\pi x\right) dx. \tag{C.9}$$

Using the integral identity

$$\int \cos(ax)\cos(Bx)\,dx = \frac{1}{2}\frac{\sin[(a-b)x]}{a-b} + \frac{1}{2}\frac{\sin[(a+b)x]}{a+b}, \tag{C.10}$$

C_{mn} becomes

$$C_{mn} = k_{xn}^{A} k_{xm}^{A} (-1)^{n+m} \left\{ \frac{\sin\left[\frac{\pi x}{w_A}(2n-2m)\right]}{\frac{\pi}{w_A}(2n-2m)} + \frac{\sin\left[\frac{\pi x}{w_A}(2n+2m-2)\right]}{\frac{\pi}{w_A}(2n+2m-2)} \right\}_{\frac{-w_A}{2}}^{\frac{w_A}{2}} \tag{C.11}$$

When $m \neq n$,

$$C_{mn} = 0. \tag{C.12}$$

When $m = n$, $(C.9)$ becomes

$$C_{mn} = \left(k_{xn}^{A}\right)^2 \int_{\frac{-w_A}{2}}^{\frac{w_A}{2}} \cos^2\left[\frac{2n-1}{w_A}\pi x\right] dx. \tag{C.13}$$

Through the use of integral integral identity,

$$\int \cos^2(ax)\,dx = \frac{2ax + \sin(2ax)}{4a}, \tag{C.14}$$

$(C.13)$ becomes

$$C_{mn} = \left(k_{xn}^{A}\right)^2 \frac{w_A}{2}. \tag{C.15}$$

Therefore,

$$C_{mn} = \begin{cases} \left(k_{xn}^{A}\right)^{2} \frac{w_A}{2}, & m = n \\ 0, & m \neq n \end{cases} \tag{C.16}$$

or

$$C_{mn} = \left(k_{xn}^{A}\right)^{2} \frac{w_A}{2} \delta_{mn}. \tag{C.17}$$

The integral for F_{mn} can be evaluated in a similar set of steps and is given by

$$F_{mn} = \left(k_{xn}^{B}\right)^{2} \frac{w_B}{2Z_n^B} \delta_{mn}. \tag{C.18}$$

Next, the integral for D_{mn} is expressed as

$$D_{mn} = k_{xn}^{B} k_{xm}^{A} (-1)^{n+m} \int_{\frac{-w_B}{2}}^{\frac{w_B}{2}} \cos\left[\frac{2n-1}{w_B}\pi x\right] \cos\left[\frac{2m-1}{w_A}\pi x\right] dx. \tag{C.19}$$

Using the integral identity $(C.10)$, D_{mn} becomes

$$D_{mn} = k_{xn}^{B} k_{xm}^{A} (-1)^{n+m} \left\{ \frac{\sin\left[\pi x \left(\frac{2n-1}{w_B} - \frac{2m-1}{w_A}\right)\right]}{2\pi \left(\frac{2n-1}{w_B} - \frac{2m-1}{w_A}\right)} + \frac{\sin\left[\pi x \left(\frac{2n-1}{w_B} + \frac{2m-1}{w_A}\right)\right]}{2\pi \left(\frac{2n-1}{w_B} + \frac{2m-1}{w_A}\right)} \right\} \Bigg|_{\frac{-w_B}{2}}^{\frac{w_B}{2}}, \tag{C.20}$$

or

$$D_{mn} = k_{xn}^{B} k_{xm}^{A} (-1)^{n+m} \left[\frac{\sin\left[\frac{2n-1}{2}\pi - \frac{2m-1}{2}\pi\frac{w_B}{w_A}\right]}{\pi\left(\frac{2n-1}{w_B} - \frac{2m-1}{w_A}\right)} + \frac{\sin\left[\frac{2n-1}{2}\pi + \frac{2m-1}{2}\pi\frac{w_B}{w_A}\right]}{\pi\left(\frac{2n-1}{w_B} + \frac{2m-1}{w_A}\right)} \right]. \tag{C.21}$$

Using a trigonometric identity, it can be shown that

$$\sin\left[\frac{2n-1}{2}\pi \pm \frac{2m-1}{2}\pi\frac{w_B}{w_A}\right] = \sin\left[\frac{2n-1}{2}\pi\right]\cos\left[\frac{2m-1}{2}\pi\frac{w_B}{w_A}\right], \tag{C.22}$$

or

$$\sin\left[\frac{2n-1}{2}\pi \pm \frac{2m-1}{2}\pi\frac{w_B}{w_A}\right] = -(-1)^{n}\cos\left[\frac{2m-1}{2}\pi\frac{w_B}{w_A}\right]. \tag{C.23}$$

Substituting $(C.23)$ into $(C.21)$ yields

$$D_{mn} = -k_{xn}^{B} k_{xm}^{A} (-1)^{n+m} (-1)^{n} \cos\left[\frac{2m-1}{2}\pi\frac{w_B}{w_A}\right] \frac{1}{\pi} \left[\frac{1}{\frac{2n-1}{w_B} - \frac{2m-1}{w_A}} + \frac{1}{\frac{2n-1}{w_B} + \frac{2m-1}{w_A}} \right], \tag{C.24}$$

or

$$D_{mn} = k_{xn}^{B} k_{xm}^{A} (1)^{m+1} \cos\left[\frac{2m-1}{2}\pi\frac{w_B}{w_A}\right] \frac{2}{\pi} \frac{\left(\frac{2n-1}{w_B}\right)}{\left(\frac{2n-1}{w_B}\right)^2 - \left(\frac{2m-1}{w_A}\right)^2}. \tag{C.25}$$

The case of $\frac{2n-1}{w_B} = \frac{2m-1}{w_A}$ must be handled separately. When this occurs, $(C.19)$ becomes

$$D_{mn} = k_{xn}^B k_{xm}^A (-1)^{n+m} \int_{\frac{-w_B}{2}}^{\frac{w_B}{2}} \cos^2\left[\frac{2n-1}{w_B}\pi x\right] dx. \tag{C.26}$$

This integral can be evaluated in the manner for C_{mn}, and results in

$$D_{mn} = k_{xn}^B k_{xm}^A (-1)^{n+m} \frac{w_B}{2}. \tag{C.27}$$

Finally, the integral for E_{mn} can be derived in a similar set of steps and given as

$$E_{mn} = \frac{D_{nm}}{Z_n^A}. \tag{C.28}$$

Following similar procedure to that outlined for the reduced-aperture junction integrals, the integrals for the expanded step are derived as follows:

$$L_{mn} = \left(k_{xn}^B\right)^2 \frac{w_B}{2}\delta_{mn} \tag{C.29}$$

$$W_{mn} = \left(k_{xn}^A\right)^2 \frac{w_A}{2Z_n^A}\delta_{mn} \tag{C.30}$$

$$M_{mn} = D_{mn}\Big|_{A\leftrightarrow B} \tag{C.31}$$

$$O_{mn} = \frac{M_{nm}}{Z_n^B}. \tag{C.32}$$

Note to obtain M_{mn} using D_{mn}, all instances of w_A and k_{xn}^A must be changed to w_B and k_{xn}^B, and all instances of w_B and k_{xn}^B must be changed to w_A and k_{xn}^A.

C.2: Reduced Aperture Waveguide for Biaxial Materials

In the calculation of the matrix elements for biaxial material characterization using a reduced aperture waveguide, it is necessary to evaluate the integrals associated with the transverse waveguide fields. These are

$$D_{mn} = \int_{-\frac{a}{2}}^{\frac{a}{2}} e^e_{ym}(x) e^e_{yn}(x) dx, \tag{C.33}$$

$$F_{mn} = \int_{-\frac{w}{2}}^{\frac{w}{2}} e^s_{ym}(x) e^s_{yn}(x) dx, \tag{C.34}$$

$$P_{mn} = Z^s_m \int_{-\frac{w}{2}}^{\frac{w}{2}} h^s_{xm}(x) h^e_{xn}(x) dx, \tag{C.35}$$

$$Q_{mn} = Z^s_m \int_{-\frac{w}{2}}^{\frac{w}{2}} h^s_{xm}(x) h^s_{xn}(x) dx. \tag{C.36}$$

First D_{mn} is expressed as

$$\int_{-\frac{a}{2}}^{\frac{a}{2}} e^e_{ym}(x) e^e_{yn}(x) dx = k^e_{xm} k^e_{xn} \int_{-\frac{a}{2}}^{\frac{a}{2}} \sin\left[k^e_{xm}\left(x - \tfrac{a}{2}\right)\right] \sin\left[k^e_{xn}\left(x - \tfrac{a}{2}\right)\right] dx \tag{C.37}$$

Using the change of variables, where $u = \frac{a}{2} - x$, this becomes

$$D_{mn} = k^e_{xm} k^e_{xn} \int_0^a \sin\left(k^e_{xm} u\right) \sin\left(k^e_{xn} u\right) du. \tag{C.38}$$

From (2.3.2), it is shown that $k^e_{xn} = n\pi/a$ and similarly $k^e_{xm} = m\pi/a$. Therefore

$$D_{mn} = \frac{mn\pi^2}{a^2} \int_0^a \sin\left(\frac{m\pi}{a} u\right) \sin\left(\frac{n\pi}{a} u\right) du. \tag{C.39}$$

Because the integrand is even about x, this integral can be expressed as

$$D_{mn} = \frac{mn\pi^2}{2a^2} \int_{-a}^a \sin\left(\frac{m\pi}{a} u\right) \sin\left(\frac{n\pi}{a} u\right) du \tag{C.40}$$

If $m = n$, then the identity

$$\int \sin^2(ax)\,dx = \frac{x}{2} - \frac{1}{4a}\sin 2ax \tag{C.41}$$

can be used. If $m \neq n$ then $D_{mn} = 0$. Therefore

$$D_{mn} = \begin{cases} \frac{n^2\pi^2}{2a}, & m = n \\ 0, & m \neq n \end{cases} \tag{C.42}$$

or

$$D_{mn} = \frac{n^2\pi^2}{2a}\delta_{mn}. \tag{C.43}$$

The integral for Q_{mn} can be evaluated similarly and is given by

$$Q_{mn} = \frac{n^2\pi^2}{2wZ_n^s}\delta_{mn}. \tag{C.44}$$

Next, the integral for F_{mn} is expressed as

$$F_{mn} = k_{xm}^e k_{cn}^s \int_{-\frac{w}{2}}^{\frac{w}{2}} \sin\left[k_{cm}^e\left(x - \frac{a}{2}\right)\right] \sin\left[k_{cn}^s\left(x - \frac{w}{2}\right)\right] dx. \tag{C.45}$$

This integral will be derived generally, since integrals of similar form will be needed for Chapter 6. Therefore, F_{mn} is written as

$$F_{mn} = k_{xm}^e k_{cn}^s \Phi_{mn}^B, \tag{C.46}$$

where

$$\Phi_{mn}^B = \int_{\nu_1}^{\nu_2} \sin\left[\alpha_m(x - \kappa)\right] \sin\left[\gamma_n(x - \nu_1)\right] dx. \tag{C.47}$$

Here $\alpha_m = k^e_{cm}$, $\gamma_n = k^s_{cn}$, $\nu_2 = w/2$, $\nu_1 = -w/2$, and $\kappa = -a/2$. Expanding the arguments of the sine functions gives

$$\Phi^B_{mn} = \int_{\nu_1}^{\nu_2} \sin(\alpha_m x - \alpha_m \kappa) \sin(\gamma_n x - \gamma_n \nu_1) dx. \tag{C.48}$$

This definite integral now can make use of the expression [62]

$$\int_{\alpha_1}^{\alpha_2} \sin(Ax + B) \sin(Cx + D) dx = \tag{C.49}$$

$$\frac{\sin[(A-C)x + (B-D)]}{2(A-C)} - \frac{\sin[(A+C)x + (B+D)]}{2(A+C)}\Bigg|_{\alpha_1}^{\alpha_2}. \tag{C.50}$$

Therefore Φ^B_{mn} can be expressed as

$$\Phi^B_{mn} = \frac{\sin[(\alpha_m - \gamma_n)x - (\alpha_m\kappa - \gamma_n\nu_1)]}{2(\alpha_m - \gamma_n)} - \frac{\sin[(\alpha_m + \gamma_n)x - (\alpha_m\kappa + \gamma\nu_1)]}{2(\alpha_m + \gamma_n)}\Bigg|_{\nu_1}^{\nu_2} \tag{C.51}$$

Expanding this further gives

$$\Phi^B_{mn} = \frac{\sin(\alpha_m\delta_2 - \gamma_n\Delta) - \sin(\alpha_m\delta_1)}{2(\alpha_m - \gamma_n)} - \frac{\sin(\alpha_m\delta_2 + \gamma_n\Delta) - \sin(\alpha_m\delta_1)}{2(\alpha_m + \gamma_n)}, \tag{C.52}$$

where $\Delta = \nu_2 - \nu_1$, $\delta_1 = \nu_1 - \kappa$, and $\delta_2 = \nu_2 - \kappa$. Multiplying through by $(\alpha_m - \gamma_n)(\alpha_m + \gamma_n)$ to get a common denominator and combining like elements gives

$$\Phi^B_{mn} = \frac{1}{2\left(\alpha_m^2 - \gamma_n^2\right)} \{\alpha_m [\sin(\alpha_m\delta_2 - \gamma_n\Delta) - \sin(\alpha_m\delta_2 + \gamma_n\Delta)] \tag{C.53}$$

$$+\gamma_n [\sin(\alpha_m\delta_2 - \gamma_n\Delta) - \sin(\alpha_m\delta_2 + \gamma_n\Delta)] + 2\gamma_n \sin(\gamma_m\delta_1)\}. \tag{C.54}$$

Using the trigonometric identies

$$\sin u + \sin v = 2\sin\left(\frac{u+v}{2}\right)\cos\left(\frac{u-v}{2}\right) \tag{C.55}$$

$$\sin u - \sin v = 2\cos\left(\frac{u+v}{2}\right)\sin\left(\frac{u-v}{2}\right), \tag{C.56}$$

simplifies Φ^B_{mn} further to

$$\Phi^B_{mn} = \frac{-\alpha_m \cos(\alpha_m\delta_2)\sin(\gamma_n\Delta) + \gamma_n \sin(\alpha_m\delta_2)\cos(\gamma_n\Delta) - \gamma_n \sin(\alpha_m\delta_1)}{\alpha_m^2 - \gamma_n^2}, \tag{C.57}$$

or

$$\Phi^B_{mn} = \frac{\gamma_n\left[\sin(\alpha_m\delta_2)\cos(\gamma_n\Delta) - \sin(\alpha_m\delta_1)\right] - \alpha_m\cos(\alpha_m\delta_2)\sin(\gamma_n\Delta)}{\alpha_m^2 - \gamma_n^2}. \tag{C.58}$$

A special case exists when $\alpha_m = \gamma_n = 0$. This results in $\Phi^B_{mn} = 0$. Therefore,

$$\Phi^B_{mn} = \begin{cases} 0, & \alpha_m = \gamma_n = 0 \\ \dfrac{\gamma_n[\sin(\alpha_m\delta_2)\cos(\gamma_n\Delta) - \sin(\alpha_m\delta_1)] - \alpha_m\cos(\alpha_m\delta_2)\sin(\gamma_n\Delta)}{\alpha_m^2 - \gamma_n^2}, & \text{otherwise} \end{cases} \tag{C.59}$$

Finally the integral for P_{mn} can be evaluated in the manner done for F_{mn} and is given by

$$P_{mn} = \frac{F_{nm}}{Z_n^s}. \tag{C.60}$$

C.3: Gyromagnetic Material Filled Waveguide Cross-section

Closed-form expressions for integrals associated with the transverse waveguide functions used in Section 5.2.1.2 are derived in this appendix. The integrals associated with (5.21)

and (5.25) are

$$\int_0^a \sin\left(k_{xm}^e x\right) \sin\left(k_{xn}^e x\right) dx \tag{C.61}$$

$$\int_0^a \sin\left(k_{xm}^e x\right) \sin\left(k_{cn}^s x\right) dx, \tag{C.62}$$

while the integrals associated with (5.23) and (5.27) are

$$\int_0^a \sin\left(k_{cm}^s x\right) \sin\left(k_{cn}^e x\right) dx \tag{C.63}$$

$$\int_0^a \sin\left(k_{cm}^s x\right) \sin\left(k_{cn}^s x\right) dx \tag{C.64}$$

$$\int_0^a \sin\left(k_{cm}^e x\right) \cos\left(k_{cn}^s x\right) dx. \tag{C.65}$$

First, it is known that $k_{xm}^e = m\pi/a$ and $k_{cn}^s = n\pi/a$. Thus (C.61) - (C.64) become

$$\int_0^a \sin\left(\frac{m\pi}{a}x\right) \sin\left(\frac{n\pi}{a}x\right) dx, \tag{C.66}$$

while (C.65) is given by

$$\int_0^a \sin\left(\frac{m\pi}{a}x\right) \cos\left(\frac{n\pi}{a}x\right) dx. \tag{C.67}$$

Now, since sine is an odd function and the multiplication of two odd functions is an even function, (C.66) can be expressed as

$$\int_0^a \sin\left(\frac{m\pi}{a}x\right) \sin\left(\frac{n\pi}{a}x\right) dx = \frac{1}{2}\int_{-a}^a \sin\left(\frac{m\pi}{a}x\right) \sin\left(\frac{n\pi}{a}x\right) dx. \tag{C.68}$$

If $m = n$, then the identity from (C.41) can be used. If $m \neq n$ then this integral is equal to

zero. Therefore,

$$\int_0^a \sin\left(\frac{m\pi}{a}x\right)\sin\left(\frac{n\pi}{a}x\right)dx = \begin{cases} \frac{a}{2}, & m = n \\ 0, & m \neq n \end{cases} \tag{C.69}$$

or

$$\int_0^a \sin\left(\frac{m\pi}{a}x\right)\sin\left(\frac{n\pi}{a}x\right)dx = \frac{a}{2}\delta_{mn}. \tag{C.70}$$

Next, using a substitution of variables, where $u = \pi/ax$, $(C.67)$ becomes

$$\int_0^a \sin\left(\frac{m\pi}{a}x\right)\cos\left(\frac{n\pi}{a}x\right)dx = \frac{a}{\pi}\int_0^\pi \sin(mu)\cos(nu)\,du. \tag{C.71}$$

The trigonometric identity

$$\sin(x)\cos(y) = \frac{1}{2}\left[\sin(x+y) + \sin(x-y)\right] \tag{C.72}$$

is employed, yielding

$$\int_0^a \sin\left(\frac{m\pi}{a}x\right)\cos\left(\frac{n\pi}{a}x\right)dx = \frac{a}{2\pi}\int_0^\pi \sin\left[(m+n)\,u\right] + \sin\left[(m-n)\,u\right]du. \tag{C.73}$$

If $m = n$, then

$$\int_0^a \sin\left(\frac{m\pi}{a}x\right)\cos\left(\frac{n\pi}{a}x\right)dx = \frac{a}{2\pi}\int_0^\pi \sin(2mu)\,du, \tag{C.74}$$

which when evaluated is equal to zero. If $m \neq n$ then

$$\int_0^a \sin\left(\frac{m\pi}{a}x\right)\cos\left(\frac{n\pi}{a}x\right)dx = \frac{a}{2\pi}\left\{-\frac{\cos\left[(m+n)u\right]}{m+n} - \frac{\cos\left[(m-n)u\right]}{m-n}\right\}\Bigg|_0^\pi. \tag{C.75}$$

Now if $m-n$ is even then

$$\int_0^a \sin\left(\frac{m\pi}{a}x\right)\cos\left(\frac{n\pi}{a}x\right)dx = 0, \tag{C.76}$$

and if $m-n$ is odd

$$\int_0^a \sin\left(\frac{m\pi}{a}x\right)\cos\left(\frac{n\pi}{a}x\right)dx = \frac{a}{2\pi}\left[\frac{1}{m+n}+\frac{1}{m-n}\right]. \tag{C.77}$$

Thus

$$\int_0^a \sin\left(\frac{m\pi}{a}x\right)\cos\left(\frac{n\pi}{a}x\right)dx = \frac{a}{2}\Delta_{mn}, \tag{C.78}$$

where

$$\Delta_{mn} = \begin{cases} 0, & m-n \text{ is even} \\ \frac{4}{\pi}\frac{m}{m^2-n^2}, & m-n \text{ is odd.} \end{cases} \tag{C.79}$$

C.4: Reduced Aperture Waveguide for Gyromagnetic Materials

Closed-form expressions for the matrix entries in (5.55) are derived in this section. The entries are

$$G_{mn} = k^e_{xn} \int_{-\frac{a}{2}}^{\frac{a}{2}} \sin\left[k^e_{xm}\left(x-\frac{a}{2}\right)\right] \sin\left[k^e_{xn}\left(x-\frac{a}{2}\right)\right] dx \tag{C.80}$$

$$J_{mn} = k^s_{cn}\left(1-\frac{\kappa^2}{\mu_g^2}\right) \int_{-\frac{w}{2}}^{\frac{w}{2}} \sin\left[k^e_{xm}\left(x-\frac{a}{2}\right)\right] \sin\left[k^s_{cn}\left(x-\frac{w}{2}\right)\right] dx \tag{C.81}$$

$$K_{mn} = \frac{k^e_{xn}}{Z^e_n} \int_{-\frac{w}{2}}^{\frac{w}{2}} \sin\left[k^s_{cm}\left(x-\frac{w}{2}\right)\right] \sin\left[k^e_{xn}\left(x-\frac{a}{2}\right)\right] dx \tag{C.82}$$

$$L^{\pm}_{mn} = \frac{k^s_{cn}}{Z^s_n} \int_{-\frac{w}{2}}^{\frac{w}{2}} \sin\left[k^s_{cm}\left(x-\frac{w}{2}\right)\right] \left\{\sin\left[k^s_{cn}\left(x-\frac{w}{2}\right)\right] \pm \frac{\kappa k^s_{cn}}{\mu_g \beta^s_n} \cos\left[k^s_{cn}\left(x-\frac{w}{2}\right)\right]\right\} dx. \tag{C.83}$$

First, G_{mn} is extracted in a similar procedure as the entry D_{mn} from Appendix C.2. Thus, G_{mn} is expressed as

$$G_{mn} = k^e_{xn}\frac{a}{2}\delta_{mn}. \tag{C.84}$$

Next, the integral for J_{mn} is extracted similarly as was done for F_{mn} in Appendix C.2, and results in

$$J_{mn} = \begin{cases} 0, & \alpha_m = \gamma_n = 0 \\ Q\dfrac{\gamma_n[\sin(\alpha_m\delta_2)\cos(\gamma_n\Delta) - \sin(\alpha_m\delta_1)] - \alpha_m\cos(\alpha_m\delta_2)\sin(\gamma_n\Delta)}{\alpha_m^2 - \gamma_n^2} & \text{otherwise,} \end{cases} \tag{C.85}$$

where $\alpha_m = k^e_{cm}$, $\gamma_n = k^s_{cn}$, $\delta_1 = -w/2 + a/2$, $\delta_2 = w/2 + a/2$, $\Delta = w$, and $Q = k^s_{cn}\left(1-\kappa^2/\mu_g^2\right)$.

Now, the integral for K_{mn} can be evaluated by once again following the steps done for F_{mn} in Appendix C.2, and is evaluated as

$$K_{mn} = \frac{k^e_{xn} J_{nm}}{Q Z^e_n}. \tag{C.86}$$

Finally, the integral for L_{mn} is evaluated in steps. The first part of the integral examined is

$$\frac{k^s_{cn}}{Z^s_n} \int_{-\frac{w}{2}}^{\frac{w}{2}} \sin\left[k^s_{cm}\left(x - \frac{w}{2}\right)\right] \sin\left[k^s_{cn}\left(x - \frac{w}{2}\right)\right] dx. \tag{C.87}$$

This is a similar integral evaluated to obtain the entry Q_{mn} from Appendix C.2, and may be expressed as

$$\frac{k^s_{cn}}{Z^s_n} \int_{-\frac{w}{2}}^{\frac{w}{2}} \sin\left[k^s_{cm}\left(x - \frac{w}{2}\right)\right] \sin\left[k^s_{cn}\left(x - \frac{w}{2}\right)\right] dx = \frac{w k^s_{cn}}{2 Z^s_n} \delta_{mn}. \tag{C.88}$$

The second part of the integral is expressed as

$$\pm \frac{k^s_{cn}}{Z^s_n} \frac{\kappa k^s_{cn}}{\mu_g \beta^s_n} \int_{-\frac{w}{2}}^{\frac{w}{2}} \sin\left[k^s_{cm}\left(x - \frac{w}{2}\right)\right] \cos\left[k^s_{cn}\left(x - \frac{w}{2}\right)\right] dx. \tag{C.89}$$

Using the substitution of variables $u = \frac{\pi}{w}\left(\frac{w}{2} - x\right)$

$$\pm \frac{k^s_{cn}}{Z^s_n} \frac{\kappa k^s_{cn}}{\mu_g \beta^s_n} \int_{-\frac{w}{2}}^{\frac{w}{2}} \sin\left[k^s_{cm}\left(x - \frac{w}{2}\right)\right] \cos\left[k^s_{cn}\left(x - \frac{w}{2}\right)\right] dx = \mp \frac{k^s_{cn}}{Z^s_n} \frac{\kappa k^s_{cn}}{\mu_g \beta^s_n} \int_0^{\pi} \sin(mu) \cos(nu)\, du. \tag{C.90}$$

Then performing similar steps as was done to evaluate the integral in $(C.71)$, $(C.90)$ becomes

$$\pm\frac{k_{cn}^s}{Z_n^s}\frac{\kappa k_{cn}^s}{\mu g\beta_n^s}\int_{-\frac{w}{2}}^{\frac{w}{2}}\sin\left[k_{cm}^s\left(x-\frac{w}{2}\right)\right]\cos\left[k_{cn}^s\left(x-\frac{w}{2}\right)\right]dx = \mp\frac{k_{cn}^s}{Z_n^s}\frac{\kappa k_{cn}^s}{\mu g\beta_n^s}\frac{w}{2}\Delta_{mn}, \tag{C.91}$$

where

$$\Delta_{mn}=\begin{cases}0, & m-n \text{ is even}\\ \frac{4}{\pi}\frac{m}{m^2-n^2}, & m-n \text{ is odd.}\end{cases} \tag{C.92}$$

Therefore the entry $L_{mn}^{\pm}$ is expressed as

$$L_{mn}^{\pm}=\frac{k_{cn}^s}{Z_n^s}\left(\frac{w}{2}\delta_{mn}\mp\frac{\kappa k_{cn}^s}{\mu g\beta_n^s}\frac{w}{2}\Delta_{mn}\right). \tag{C.93}$$

Additionally, the vectors g and k are given by

$$g_m = G_{m1}k_m = K_{m1}. \tag{C.94}$$

C.5: Waveguide Standard Integrals

Closed-form expressions for the matrix entries in (6.27) are derived in this appendix. The entries are

$$G_{mn} = \int_0^b \int_0^a \vec{e}_m^f(\vec{\rho}) \cdot \vec{e}_n^f(\vec{\rho}) dxdy, \tag{C.95}$$

$$J_{mn}^{\ell,r} = \int_{y_1^{\ell,r}}^{y_2^{\ell,r}} \int_0^a \vec{e}_m^f(\vec{\rho}) \cdot \vec{e}_n^{\ell,r}(\vec{\rho}) dxdy, \tag{C.96}$$

$$K_{mn}^{\ell,r} = \int_{y_1^{\ell,r}}^{y_2^{\ell,r}} \int_0^a \vec{h}_m^{\ell,r}(\vec{\rho}) \cdot \vec{h}_n^f(\vec{\rho}) dxdy, \tag{C.97}$$

$$L_{mn}^{\ell,r} = \int_{y_1^{\ell,r}}^{y_2^{\ell,r}} \int_0^a \vec{h}_m^{\ell,r}(\vec{\rho}) \cdot \vec{h}_n^{\ell,r}(\vec{\rho}) dxdy. \tag{C.98}$$

To simply the derivations, only the integrals for the left aperture are derived in this appendix. This means to get the entries J^r, K^r, and L^r, use the equations for J^l, K^l, and L^l, and change all instances of ℓ to r. The entries depend on whether modes m and n are TE or TM, and are thus split into the following four cases:

Case 1: TE_m, TE_n

First G_{mn} is expressed as

$$\begin{aligned}\int_0^b \int_0^a \vec{e}_m^f(\vec{\rho}) \cdot \vec{e}_n^f(\vec{\rho}) dxdy = \int_0^b \int_0^a \Big[&\hat{x} k_{ym}^f \cos\left(\frac{\pi x}{a}\right) \sin\left(k_{ym}^f y\right) - \\ &\hat{y} \frac{\pi}{a} \sin\left(\frac{\pi x}{a}\right) \cos\left(k_{ym}^f y\right)\Big] \cdot \Big[\hat{x} k_{yn}^f \cos\left(\frac{\pi x}{a}\right) \sin\left(k_{yn}^f y\right) - \\ &\hat{y} \frac{\pi}{a} \sin\left(\frac{\pi x}{a}\right) \cos\left(k_{yn}^f y\right)\Big] dxdy.\end{aligned} \tag{C.99}$$

Expanding the dot product, this becomes

$$G_{mn} = \int_0^a k_{ym}^f k_{yn}^f \cos^2\left(\frac{\pi x}{a}\right) dx \int_0^b \sin\left(k_{ym}^f y\right) \sin\left(k_{yn}^f y\right) dy + \int_0^a \left(\frac{\pi}{a}\right)^2 \sin^2\left(\frac{\pi x}{a}\right) dx \int_0^b \cos\left(k_{ym}^f y\right) \cos\left(k_{yn}^f y\right) dy. \tag{C.100}$$

Using the integral identities

$$\cos^2(Ax)\, dx = \left[\frac{x}{2} + \frac{\sin(2Ax)}{4A}\right] \tag{C.101}$$

$$\sin^2(Ax)\, dx = \left[\frac{x}{2} - \frac{\sin(2Ax)}{4A}\right], \tag{C.102}$$

it can be shown that the integrals over x both become $a/2$. Thus

$$G_{mn} = k_{ym}^f k_{yn}^f \frac{a}{2} \int_0^b \sin\left(k_{ym}^f y\right) \sin\left(k_{yn}^f y\right) dy + \frac{\pi^2}{2a} \int_0^b \cos\left(k_{ym}^f y\right) \cos\left(k_{yn}^f y\right) dy. \tag{C.103}$$

If $m = n$, then the identities in $(C.101)$ and $(C.102)$ can be used again. If $m \neq n$ then $G_{mn} = 0$. Therefore

$$G_{mn} = \begin{cases} \left(k_{cn}^f\right)^2 \frac{ab}{4}, & m = n \\ 0, & m \neq n \end{cases} \tag{C.104}$$

or

$$G_{mn} = \left(k_{cn}^f\right)^2 \frac{ab}{4} \delta_{mn}. \tag{C.105}$$

A special case does exist when $m = n = 1$, which means $k_{y1}^f = 0$. When this occurs

$$G_{mn} = \left(k_{cn}^f\right)^2 \frac{ab}{2} \delta_{mn}. \tag{C.106}$$

Therefore a general expression is given by

$$G_{mn} = \left(k_{cn}^{f}\right)^{2} \frac{ab}{\xi}\delta_{mn}, \tag{C.107}$$

where $\xi = 2$ for $k_{ym}^{f} = k_{yn}^{f} = 0$, and otherwise $\xi = 4$.

The integral for L_{mn}^{ℓ} can be derived in a similar set of steps and is evaluated as

$$L_{mn}^{\ell} = \left(\frac{k_{cn}^{\ell}}{Z_{n}^{\ell}}\right)^{2} \frac{aw^{\ell}}{\zeta}\delta_{mn}, \tag{C.108}$$

where $\zeta = 2$ for $k_{ym}^{\ell} = k_{yn}^{\ell} = 0$, and otherwise $\zeta = 4$.

Next, the integral for J_{mn}^{ℓ} is expressed as

$$J_{mn}^{\ell} = \int_{y_1^{\ell}}^{y_2^{\ell}} \int_{0}^{a} \left[\hat{x}k_{ym}^{f} \cos\left(\frac{\pi x}{a}\right) \sin\left(k_{ym}^{f} y\right) - \hat{y}\frac{\pi}{a} \sin\left(\frac{\pi x}{a}\right) \cos\left(k_{ym}^{f} y\right)\right] \cdot \left[\hat{x}k_{yn}^{\ell} \cos\left(\frac{\pi x}{a}\right) \sin\left(k_{yn}^{\ell}(y - y_1^{\ell})\right) - \hat{y}\frac{\pi}{a} \sin\left(\frac{\pi x}{a}\right) \cos\left(k_{yn}^{\ell}(y - y_1^{\ell})\right)\right] dxdy. \tag{C.109}$$

Expanding the dot product gives

$$J_{mn} = \int_{0}^{a} k_{ym}^{f} k_{yn}^{\ell} \cos^{2}\left(\frac{\pi x}{a}\right) dx \int_{y_1^{\ell}}^{y_2^{\ell}} \sin\left(k_{ym}^{f} y\right) \sin\left(k_{yn}^{\ell}(y - y_1^{\ell})\right) dy + \int_{0}^{a} \left(\frac{\pi}{a}\right)^{2} \sin^{2}\left(\frac{\pi x}{a}\right) dx \int_{y_1^{\ell}}^{y_2^{\ell}} \cos\left(k_{ym}^{f} y\right) \cos\left(k_{yn}^{\ell}(y - y_1^{\ell})\right) dy. \tag{C.110}$$

Once again using $(C.101)$ and $(C.102)$ results in

$$J_{mn} = k_{ym}^{f} k_{yn}^{\ell} \frac{a}{2} \int_{y_1^{\ell}}^{y_2^{\ell}} \sin\left(k_{ym}^{f} y\right) \sin\left(k_{yn}^{\ell}(y - y_1^{\ell})\right) dy + \frac{\pi^{2}}{2a} \int_{y_1^{\ell}}^{y_2^{\ell}} \cos\left(k_{ym}^{f} y\right) \cos\left(k_{yn}^{\ell}(y - y_1^{\ell})\right) dy. \tag{C.111}$$

The general expression for Φ^B_{mn} given in Appendix B.2 can now be used, where

$$\Phi^B_{mn} = \int_{\nu_1}^{\nu 2} \sin\left[\alpha_m\left(x-\kappa\right)\right]\sin\left[\gamma_n\left(x-\nu_1\right)\right]dx. \tag{C.112}$$

It was shown that

$$\Phi^B_{mn} = \begin{cases} 0, & \alpha_m = \gamma_n = 0 \\ \frac{\gamma_n[\sin(\alpha_m\delta_2)\cos(\gamma_n\Delta)-\sin(\alpha_m\delta_1)]-\alpha_m\cos(\alpha_m\delta_2)\sin(\gamma_n\Delta)}{\alpha_m^2-\gamma_n^2} & \text{otherwise.} \end{cases} \tag{C.113}$$

Following the same steps outlined in Section B.2, a similar general integral for

$$\Phi^A_{mn} = \int_{\nu_1}^{\nu 2} \cos\left[\alpha_m\left(x-\kappa\right)\right]\cos\left[\gamma_n\left(x-\nu_1\right)\right]dx, \tag{C.114}$$

can be derived. The result is

$$\Phi^A_{mn} = \begin{cases} \Delta, & \alpha_m = \gamma_n = 0 \\ \frac{\alpha_m[\sin(\alpha_m\delta_2)\cos(\gamma_n\Delta)-\sin(\alpha_m\delta_1)]-\gamma_n\cos(\alpha_m\delta_2)\sin(\gamma_n\Delta)}{\alpha_m^2-\gamma_n^2} & \text{otherwise.} \end{cases} \tag{C.115}$$

Using $(C.113)$ and $(C.115)$, J^ℓ_{mn} reduces to

$$J^\ell_{mn} \;=\; \alpha_m\gamma_n\frac{a}{2}\Phi^B_{mn} + \frac{\pi^2}{2a}\Phi^A_{mn}, \tag{C.116}$$

where $\alpha_m = k^f_{ym}$, $\gamma_n = k^\ell_{yn}$, $\Delta = \Delta^\ell$, $\delta_2 = y^\ell_2$, and $\delta_1 = y^\ell_1$.

The integral for K^ℓ_{mn} can be derived in a similar set of steps and is evaluated as

$$K^\ell_{mn} \;=\; \frac{J^\ell_{nm}}{Z^\ell_m Z^f_n}. \tag{C.117}$$

Following steps similar to those used for Case 1, the rest of the integrals are derived, and given below.

Case 2: $\mathrm{TM}_m, \mathrm{TM}_n$

$$G_{mn} = \left(k_{cn}^f\right)^2 \frac{ab}{\xi}\delta_{mn} \tag{C.118}$$

$$L_{mn}^{\ell} = \left(\frac{k_{cn}^{\ell}}{Z_n^{\ell}}\right)^2 \frac{aw^{\ell}}{\zeta}\delta_{mn} \tag{C.119}$$

$$J_{mn}^{\ell} = \alpha_m\gamma_n\frac{a}{2}\Phi_{mn}^A + \frac{\pi^2}{2a}\Phi_{mn}^B \tag{C.120}$$

$$K_{mn}^{\ell} = \frac{J_{nm}^{\ell}}{Z_m^{\ell}Z_n^f} \tag{C.121}$$

$$\tag{C.122}$$

Case 3:$\mathrm{TE}_m, \mathrm{TM}_n$

$$G_{mn} = 0 \tag{C.123}$$

$$L_{mn}^{\ell} = 0 \tag{C.124}$$

$$J_{mn}^{\ell} = \gamma_n\frac{\pi}{2}\Phi_{mn}^A - \alpha_m\frac{\pi}{2}\Phi_{mn}^B \tag{C.125}$$

$$K_{mn}^{\ell} = \frac{1}{Z_m^{\ell}Z_n^f}\left[\alpha_n\frac{\pi}{2}\Phi_{nm}^A - \gamma_m\frac{\pi}{2}\Phi_{nm}^B\right] \tag{C.126}$$

Case 4: $\mathrm{TM}_m, \mathrm{TE}_n$

$$G_{mn} = 0 \tag{C.127}$$

$$L_{mn}^{\ell} = 0 \tag{C.128}$$

$$J_{mn}^{\ell} = -\gamma_n\frac{\pi}{2}\Phi_{mn}^B + \alpha_m\frac{\pi}{2}\Phi_{mn}^A \tag{C.129}$$

$$K_{mn}^{\ell} = \frac{1}{Z_m^{\ell}Z_n^f}\left[-\alpha_n\frac{\pi}{2}\Phi_{nm}^B + \gamma_m\frac{\pi}{2}\Phi_{nm}^A\right] \tag{C.130}$$

Appendix D: Analysis of NRW Method

Consider an isotropic, lossless, symmetric 2-port network with S-parameters S_{11}, S_{12}, S_{21} and S_{22}. The goal of this appendix is to establish the conditions under which values of μ and ϵ extracted from the S-parameters using the NRW equations will be real.

The S-parameters of a lossless 2-port network satisfy the unitary condition $[S]^T[S^*] = [U]$ or

$$\begin{bmatrix} S_{11} & S_{21} \\ S_{12} & S_{22} \end{bmatrix} \begin{bmatrix} S_{11}^* & S_{12}^* \\ S_{21}^* & S_{22}^* \end{bmatrix} = \begin{bmatrix} 1 & 0 \\ 0 & 1 \end{bmatrix}. \tag{D.1}$$

Writing out the matrix product gives the four equations

$$|S_{11}|^2 + |S_{21}|^2 = 1, \tag{D.2}$$

$$S_{11}S_{12}^* + S_{21}S_{22}^* = 0, \tag{D.3}$$

$$S_{12}S_{11}^* + S_{22}S_{21}^* = 0, \tag{D.4}$$

$$|S_{12}|^2 + |S_{22}|^2 = 1. \tag{D.5}$$

If the network is reciprocal, $S_{12} = S_{21}$. Making this substitution and taking the complex conjugate of (D.4) results in both $(D.3)$ and $(D.4)$ becoming

$$S_{11}S_{21}^* + S_{21}S_{22}^* = 0. \tag{D.6}$$

If the network is also symmetric, such that $S_{11} = S_{22}$, then the allowed values of the S-parameters are subject to two restrictions. The first restriction results from $(D.2)$ and $(D.5)$ both becoming

$$|S_{11}|^2 + |S_{21}|^2 \;\; = \;\; 1. \tag{D.7}$$

The next restriction is derived by first substituting S_{11} for S_{22} in $(D.6)$ yielding

$$S_{11}S_{21}^* + S_{21}S_{11}^* = 0. \tag{D.8}$$

This can be rewritten as

$$\left(S_{11}S_{21}^*\right) + \left(S_{11}S_{21}^*\right)^* = 0, \tag{D.9}$$

or

$$A + A^* = 0, \tag{D.10}$$

where $A = S_{11}S_{21}^*$. The addition of a complex variable with its complex conjugate is just twice the real part of the variable. Thus $(D.9)$ becomes,

$$\mathrm{Re}\left\{S_{11}S_{21}^*\right\} = 0, \tag{D.11}$$

or, by splitting the S-parameters into the real and imaginary parts,

$$\mathrm{Re}\left\{\left(S_{11r} + jS_{11i}\right)\left(S_{21r} + jS_{21i}\right)^*\right\} = 0. \tag{D.12}$$

This restriction on the allowed values of the S-parameters reduces to

$$S_{21r}S_{11r} + S_{21i}S_{11i} \;\; = \;\; 0. \tag{D.13}$$

Examining these restrictions further revels a relationship between S_{11} and S_{21}. From

$(D.13)$, it can be shown that

$$S_{21r} = -S_{21i}\frac{S_{11i}}{S_{11r}} \tag{D.14}$$

and

$$S_{21i} = -S_{21r}\frac{S_{11r}}{S_{11i}}. \tag{D.15}$$

Rearranging $(D.7)$ yields

$$|S_{21}|^2 = 1 - |S_{11}|^2, \tag{D.16}$$

or

$$1 - |S_{11}|^2 = S_{21r}^2 + S_{21i}^2. \tag{D.17}$$

Then substituting $(D.15)$ results in

$$1 - |S_{11}|^2 = S_{21r}^2 + S_{21r}^2\frac{S_{11r}^2}{S_{11i}^2}. \tag{D.18}$$

Factoring out S_{21r}^2 and simplifying gives

$$1 - |S_{11}|^2 = S_{21r}^2\left(\frac{S_{11i}^2 + S_{11r}^2}{S_{11i}^2}\right), \tag{D.19}$$

or

$$1 - |S_{11}|^2 = S_{21r}^2\left(\frac{|S_{11}|^2}{S_{11i}^2}\right). \tag{D.20}$$

Solving for S_{21r} yields

$$S_{21r} = \pm S_{11i} Q, \tag{D.21}$$

where

$$Q = \sqrt{\frac{1 - |S_{11}|^2}{|S_{11}|^2}}. \tag{D.22}$$

A similar process of substituting $(D.14)$ into $(D.17)$, gives an expression for S_{21i}:

$$S_{21i} = \pm S_{11r} Q. \tag{D.23}$$

Using $(D.21)$ and $(D.23)$, it is easily seen that

$$S_{21} = \pm jQS_{11} \tag{D.24}$$

or

$$S_{21} = \pm jQS_{11}^*. \tag{D.25}$$

Two possible values of S_{21} result since the signs on $(D.21)$ and $(D.23)$ do not have to be the same. However, $(D.7)$ and $(D.13)$ must still hold true. By substituting either $(D.24)$ or $(D.25)$ into $(D.7)$ will result in the expressions equaling 1. $(D.13)$ holds true when substituting $(D.24)$, however, substituting $(D.25)$ will not work. Therefore only $(D.24)$ is a valid relationship between S_{11} and S_{21}.

Substituting this relationship into the NRW equations, (3.46) and (3.47), gives

$$V_1 = S_{11}(1 \pm jQ) \tag{D.26}$$

$$V_2 = S_{11}(-1 \pm jQ), \tag{D.27}$$

which satisfy $|V_1| = |V_2| = 1$. From (3.55),

$$\Gamma = X \pm \sqrt{X^2 - 1}, \tag{D.28}$$

where

$$X = \frac{1 - V_1 V_2}{V_1 - V_2}. \tag{D.29}$$

Substituting $(D.26)$ and $(D.27)$ into $(D.29)$ yields

$$X = \frac{1 - S_{11}^2 \left[1 \pm jQ\right] \left[-1 \pm jQ\right]}{2S_{11}}, \tag{D.30}$$

or

$$X = \frac{1 + S_{11}^2 \left[1 + Q^2\right]}{2S_{11}}. \tag{D.31}$$

Using $(D.22)$ gives

$$X = \frac{1 + S_{11}^2 \left[1 + \frac{1 - |S_{11}|^2}{|S_{11}|^2}\right]}{2S_{11}}, \tag{D.32}$$

or

$$X = \frac{1 + \frac{S_{11}^2}{|S_{11}|^2}}{2S_{11}}. \tag{D.33}$$

Multiplying both sides of the equation by $|S_{11}|^2$ produces

$$|S_{11}|^2 X = \frac{|S_{11}|^2 + S_{11}^2}{2S_{11}}, \tag{D.34}$$

and S_{11} can now be split into real and imaginary parts yielding

$$|S_{11}|^2 X = \frac{S_{11r}^2 + S_{11i}^2 + S_{11r}^2 - S_{11i}^2 + 2jS_{11r}S_{11i}}{2S_{11}}. \tag{D.35}$$

This can be simplified to

$$|S_{11}|^2 X = \frac{S_{11r}^2 + jS_{11r}S_{11i}}{S_{11}}. \tag{D.36}$$

Then by factoring S_{11r} gives

$$|S_{11}|^2 X = S_{11r}\frac{S_{11r} + jS_{11i}}{S_{11}}, \tag{D.37}$$

or

$$|S_{11}|^2 X = S_{11r}. \tag{D.38}$$

Thus it is found

$$X = \frac{S_{11r}}{|S_{11}|^2}, \tag{D.39}$$

regardless of the sign chosen in (D.24) and it can be seen that X is real. Evaluating Γ from $(D.28)$ then leads to two possible cases:

Case 1: $X^2 > 1$.

In this case Γ is real. Examining (3.50) and splitting V_1 into real and imaginary parts yields

$$P = \frac{V_{1r} + jV_{1i} - \Gamma}{1 - \Gamma\left(V_{1r} + jV_{1i}\right)}. \tag{D.40}$$

The magnitude of P is expressed as

$$|P| = \frac{(V_{1r} - \Gamma)^2 + V_{1i}^2}{(1 - \Gamma V_{1r})^2 + \Gamma^2 V_{1i}^2}, \tag{D.41}$$

or

$$|P| = \frac{V_{1r}^2 + \Gamma^2 - 2\Gamma V_{1r} + V_{1i}^2}{1 + \Gamma^2 V_{1r}^2 - 2\Gamma V_{1r} + \Gamma^2 V_{1i}^2}. \tag{D.42}$$

Now substituting (3.46) gives

$$|P| = \frac{(S_{21r} + S_{11r})^2 + \Gamma^2 - 2\Gamma\left(S_{21r} + S_{11r}\right) + \left(S_{21i} + S_{11i}\right)^2}{1 + \Gamma^2\left(S_{21r} + S_{11r}\right)^2 - 2\Gamma\left(S_{21r} + S_{11r}\right) + \Gamma^2\left(S_{21i} + S_{11i}\right)^2}. \tag{D.43}$$

By expanding the products and using $(D.13)$ gives

$$|P| = \frac{|S_{21}|^2 + |S_{11}|^2 + \Gamma^2 - 2\Gamma\left(S_{21r} + S_{11r}\right)}{1 + \Gamma^2\left(|S_{21}|^2 + |S_{11}|^2\right) - 2\Gamma\left(S_{21r} + S_{11r}\right)}. \tag{D.44}$$

With the knowledge of $(D.7)$, the magnitude of the propagation factor is determined to be

$$|P| = 1 \tag{D.45}$$

Thus P can be expressed as

$$P = 1\mathrm{e}^{j\phi}, \tag{D.46}$$

and from (3.56), it is determined that

$$\beta_1^s = -\frac{\phi - 2n\pi}{d}, \tag{D.47}$$

which is a real value. Finally, with the knowledge that Γ and β_1^s are both real and from

(3.59) and (3.62) it is found that both μ and ϵ are real.

Case 2: $X^2 \leq 1$.

In this case $\Gamma = A \pm jB$, where $B = \sqrt{1 - A^2}$. This yields $|\Gamma| = 1$, which would represent total reflection in an actual material measurement scenario. Thus, this condition should be avoided when designing a material surrogate. Regardless, there might still exist a special case where ϵ and μ are real. In (3.59), Γ occurs in the ratio

$$\Gamma_R = \frac{1 + \Gamma}{1 - \Gamma}. \tag{D.48}$$

Therefore, start by substituting $\Gamma = A \pm jB$ into $(D.48)$. This results in

$$\Gamma_R = \frac{(1 + A) \pm jB}{(1 - A) \mp jB}. \tag{D.49}$$

Next, multiplying the top and bottom by the complex conjugate of the denominator results in

$$\Gamma_R = \frac{[(1 + A) \pm jB]\,[(1 - A) \pm jB]}{(1 - A)^2 + B^2} \tag{D.50}$$

or

$$\Gamma_R = \frac{\left(1 - A^2\right) \pm jB\,(1 - A + 1 + A) - B}{2\,(1 - A)}. \tag{D.51}$$

This simplifies to

$$\Gamma_R = \pm j\sqrt{\frac{B}{1 - A}} \tag{D.52}$$

or

$$\Gamma_R = \pm j\sqrt{\frac{1 + A}{1 - A}} \tag{D.53}$$

and is thus imaginary. Now as was done in Case 1, when examine the propagation factor,

(3.50) and Γ are split in real and imaginary parts. This results in

$$P = \frac{V_{1r} + jV_{1i} - \left(\Gamma_r + j\Gamma_i\right)}{1 - \left(\Gamma_r + j\Gamma_i\right)\left(V_{1r} + jV_{1i}\right)}. \tag{D.54}$$

or

$$P = \frac{V_{1r} - \Gamma_r + j\left(V_{1i} - \Gamma_i\right)}{1 - \Gamma_r V_{1r} + \Gamma_i V_{1i} - j\left(\Gamma_i V_{1r} + \Gamma_r V_{1i}\right)}. \tag{D.55}$$

Now multiplying the top and bottom by the complex conjugate of the denominator results in

$$P = \frac{\left[V_{1r} - \Gamma_r + j\left(V_{1i} - \Gamma_i\right)\right]\left[1 - \Gamma_r V_{1r} + \Gamma_i V_{1i} + j\left(\Gamma_i V_{1r} + \Gamma_r V_{1i}\right)\right]}{\left(1 - \Gamma_r V_{1r} + \Gamma_i V_{1i}\right)^2 + \left(\Gamma_i V_{1r} + \Gamma_r V_{1i}\right)^2}, \tag{D.56}$$

or

$$P = \frac{\left[V_{1r} - \Gamma_r + j\left(V_{1i} - \Gamma_i\right)\right]\left[1 - \Gamma_r V_{1r} + \Gamma_i V_{1i} + j\left(\Gamma_i V_{1r} + \Gamma_r V_{1i}\right)\right]}{D}, \tag{D.57}$$

where

$$D = \left(1 - \Gamma_r V_{1r} + \Gamma_i V_{1i}\right)^2 + \left(\Gamma_i V_{1r} + \Gamma_r V_{1i}\right)^2. \tag{D.58}$$

Writing $P = P_r + jP_i$, the imaginary part of P is examined. Multiplying both sides of the $(D.58)$ by D and analyzing the imaginary part yields

$$DP_i = \left(V_{1i} - \Gamma_i\right)\left(1 - \Gamma_r V_{1r} + \Gamma_i V_{1i}\right) + \left(V_{1r} - \Gamma_r\right)\left(\Gamma_i V_{1r} + \Gamma_r V_{1i}\right). \tag{D.59}$$

Expanding and simplifying the expression results in

$$DP_i = V_{1i}\left[1 - |\Gamma|^2\right] + \Gamma_i\left[|V_1|^2 - 1\right]. \tag{D.60}$$

Using $|\Gamma| = 1$ and $|V_1| = 1$, this expression reduces to

$$DP_i = 0, \tag{D.61}$$

which proves that P is a real quantity. Now, examining the real part of P shows

$$DP_r = (V_{1r} - \Gamma_r)\left(1 - \Gamma_r V_{1r} + \Gamma_i V_{1i}\right) + \left(V_{1i} - \Gamma_i\right)\left(\Gamma_i V_{1r} + \Gamma_r V_{1i}\right), \tag{D.62}$$

and through similar simplification process that was done for the imaginary part of P, it is determined that

$$DP_r = 2\left(V_{1r} - \Gamma_r\right). \tag{D.63}$$

Expanding the products in D and canceling like terms results in

$$D = 2\left(1 - \Gamma_r V_{1r} + \Gamma_i V_{1i}\right). \tag{D.64}$$

Finally, the propagation constant for Case 1 can be expressed as

$$P = \frac{V_{1r} - \Gamma_r}{1 - \Gamma_r V_{1r} + \Gamma_i V_{1i}}, \tag{D.65}$$

or

$$P = \frac{\Re\{V_1 - \Gamma\}}{\Re\{1 - \Gamma V_1\}}. \tag{D.66}$$

Case 2 can now be split into 2 cases:

Case A: $P > 0$

In this case

$$P = |P| \mathrm{e}^{j0} \tag{D.67}$$

and thus

$$\ln P = \ln |P|, \tag{D.68}$$

which is real. So (3.56) then becomes

$$\beta_1^s = \frac{\ln |P| \pm j2n\pi}{-jd}, \tag{D.69}$$

which is complex unless $n = 0$. In this case β_1^s is imaginary. In (D.53) it is shown that Γ_R is imaginary, thus when β_1^s is complex, which occurs for all values of n except $n = 0$, μ will be complex. If μ is complex, then from (3.62), it can be deduced that ϵ will be complex. Now when $n = 0$, β_1^s is imaginary and Γ_R is imaginary, thus μ will be real. If μ is real, then from (3.62), it can be deduced that ϵ will be real.

Case B: $P < 0$

In this case

$$P = |P|\mathrm{e}^{\pm j\pi} \tag{D.70}$$

and thus

$$\ln P = \ln |P| \pm j\pi. \tag{D.71}$$

Then from (3.56),

$$\beta_1^s = \frac{\ln |P| \pm j\pi \pm j2n\pi}{-jd}, \tag{D.72}$$

and is complex, since $\pm j\pi$ can never cancel with $\pm j2n\pi$. Thus if β_1^s is complex both μ and ϵ will be complex.

So, in summary if the 2-port network being analyzed is lossless and symmetric then

$X = S_{11r}/|S_{11}|^2$ and two cases exist to determine if μ and ϵ are real or complex. First it was determined if $X^2 \geq 1$ then μ and ϵ are real. Next, if $X^2 < 1$ then

$$\frac{1+\Gamma}{1-\Gamma} = \pm j\sqrt{\frac{1+A}{1-A}} \tag{D.73}$$

and is thus imaginary. Then with some effort it was shown that

$$P = \frac{\Re\{V_1 - \Gamma\}}{\Re\{1 - \Gamma V_1\}} \tag{D.74}$$

and is thus real. So, if P is positive and $n = 0$ is chosen in (3.56), β_1^s will be imaginary and again μ and ϵ will be real. However, if P is negative, β will in general be complex and μ and ϵ will in general be complex.

BIBLIOGRAPHY

[1] A. von Hippel, ed., *Dielectric Materials and Applications*, MIT Press, Cambridge, Massachusetts, 1961.

[2] P. F. Wilson, J. W. Adams, and M. T. Ma, "Measurements of the electromagnetic shielding capabilities of materials," *Proceeding of the IEEE*, vol. 74, no.1, pp. 112-115, Jan. 1986.

[3] A. Deutsch, R. S. Krabbenhoft, K. L. Melde, C. W. Surovic, G. A. Katopis, G. V. Kopcsay, Z. Zhou, Z. Chen, Y. H. Kwark, T. M. Winkel, X Gu, and T. E. Standaert, "Application of the short-pulse propagation technique for broadband characterization of PCB and other interconnect technologies," *IEEE Trans. on Electro. Compatibility*, vol. 52, no. 2, May 2010.

[4] A. Dimiev, W. Lu, K. Zeller, B. Crowgey, L. C. Kempel, and J. M. Tour, "Low-loss, high-permittivity composites made from graphene nanoribbons," *Applied Materials & Interfaces*, no. 3, pp. 4657–4661, 2011.

[5] Y. Shirakata, N. Hidaka, M. Ishitsuka, A. Teramoto, and T. Ohmi, "High permeability and low loss Ni-Fe composite material for high-frequency applications," *IEEE Trans. Magn.*, vol. 44, no. 9, pp. 2100–2106, Sept. 2008.

[6] A. Verma, A. K. Saxena, D. C. Dube, "Microwave permittivity and permeability of ferrite-polymer thick films," *Journal of Magn. Magn. Mater.*, no. 263, pp 228–234, 2003.

[7] F. C. Smith, "Effective permittivity of dielectric honeycombs," *IEE Proc. Micro. Antennas Propag.*, vol. 146, no. 1, pp. 55–59, Feb. 1999.

[8] F. C. Smith, F. Scarpa, and B. Chambers, "The electromagnetic properties of re-entrant dielectric honeycombs," *IEEE Microw. Guided Wave Lett.*, vol. 10, no. 11, pp. 451–453, Nov. 2000.

[9] B. Wu, W. Wang, J. Pacheco, X. Chen, J. Lu, T. Grzegorczyk, J. A. Kong, P. Kao, P. A. Theophelakes, and M. J. Hogan, "Anisotropic metamaterials as antenna substrate to enhance directivity," *Micro. Opt. Technol. Lett.*, vol. 48, no. 4, pp. 680–683, Apr. 2006.

[10] L. Kempel, B. Crowgey, and J. Xiao, "Radiation by conformal patch antennas on a magneto-dielectric, low-density material," 3rd *Euro. Conf. on Antennas Propag.*, EuCAP, pp. 2974-2976, 2009.

[11] J. .A. Kong, *Theory of Electromagnetic Waves*, Wiley, New York, 1975.

[12] O. Hashimoto and Y. Shimizu, "Reflecting characteristics of anisotropic rubber sheets and measurement of complex permittivity tensor," *IEEE Trans. Microwave Theory Tech.*, vol. mtt-34, no. 11, pp. 1202–1207, Nov. 1986.

[13] Y. Hong-Cheng, Z. Chao, and Y. Xu, "A new fee-space method for measurement of electromagnetic parameters of biaxial materials at microwave frequencies," *Microwave and Optics Technology Letters*, vol. 46, no. 1, pp. 72–78, 2005.

[14] L. Chen, C. K. Ong, and B. T. G. Tan, "Cavity perturbation technique for the measurement of permittivity tensor of uniaxially anisotropic dielectrics," *IEEE Trans. Instrum. Meas.*, vol. 48, no. 6, pp. 1023–1030, Dec. 1999.

[15] P. I. Dankov, "Two-resonator method for measurements of dielectric anisotropy in multilayer samples," *IEEE Trans. Microwave Theory Tech.*, vol. 54, no. 4, pp. 1534–1544, April 2006.

[16] G. Morin, M. Nachman, "A New Method for Measuring Anisotropy at Microwave Frequencies," *IEEE Trans. Instrum. Meas.*, vol. 28 , no. 3, pp. 198–204, Sept. 1979.

[17] G. Mumcu, K. Sertel, and J. L. Volakis, "A measurement process to characterize natural and engineered low-loss uniaxial dielectric materials at microwave frequencies," *IEEE Trans. Microwave Theory Tech.*, vol. 56, no. 1, pp. 217–223, Jan. 2008.

[18] C. W. Chang, K. M. Chen, and J. Qian, "Nondestructive measurements of complex tensor permittivity of anisotropic materials using a waveguide probe system," *IEEE Trans. Microwave Theory Tech.*, vol. 44, no. 7, pp. 1081–1090, July 1996.

[19] C. W. Chang, K. M. Chen, and J. Qian, "Nondestructive determination of electromagnetic parameters of dielectric materials at X-band frequencies using a waveguide probe system," *IEEE Trans. Instrum. Meas.*, vol 46, no. 5, pp. 1084–1092, Oct. 1997.

[20] N. J. Damaskos, R. B. Mack, A. L. Maffett, W. Parmon, and P. L. Uslenghi, "The inverse problem for biaxial materials," *IEEE Trans. Microwave Theory Tech.*, vol. 32, no. 4, pp. 400–405, Apr. 1984.

[21] M. J. Akhtar, L. E. Feher, and M. Thumm, "A waveguide-based two-step approach for measuring complex permittivity tensor of uniaxial composite materials," *IEEE Trans. Microwave Theory Tech.*, vol. 54, no. 5, pp. 2011–2022, May 2006.

[22] P. Queffelec, M. Le Floc'h, and P. Gelin, "Non-reciprocal cell for the broad-band measurement of tensorial permeability of magnetized ferrites: Direct problem," *IEEE Trans. Microwave Theory Tech.*, vol. 47, no. 4, pp. 390–397, Apr. 1999.

[23] A. M. Nicolson and G. F. Ross, "Measurement of the intrinsic properties of materials by time-domain techniques," *IEEE Trans. Instrum. Meas.*, vol. 19, no. 4, pp. 377–382, Nov. 1970.

[24] W. B. Weir, "Automatic measurement of complex dielectric constant and permeability at microwave frequencies," *Proc. IEEE*, vol. 62, no. 1, pp. 33–36, Jan. 1974.

[25] A. H. Boughriet, C. Legrand, and A. Chapoton, "Noniterative stable transmission/reflection method for low-loss material complex permittivity eetermination," *IEEE Trans. Microw. Theory Tech.*, vol. 45, no. 1, pp. 52–57, Jan. 1997.

[26] N. Belhadj-Tahar, A. Fourrier-Lamer, and H. de Chanterac, "Broadband simultaneous measurement of complex permittivity and permeability using a coaxial discontinuity," *IEEE Trans. Microw. Theory Tech.*, vol. 38, no. 1, pp. 1–7, Jan. 1990.

[27] J. Baker-Jarvis, E. J. Vanzura, and W. A. Kissick, "Improved technique for determining complex permittivity with the transmission/reflection method," *IEEE Trans Microw. Theory Tech.*, vol. 38, no. 8, Aug. 1990.

[28] D. K. Ghodgaonkar, V. V. Varadan, and V. K. Varadan, "Free-space measurement of complex permittivity and complex permeability of magnetic materials at microwave frequencies," *IEEE Trans. Instrum. Meas.*, vol. 39, no. 2, pp. 387–394, Apr. 1990.

[29] W. Barry, "A broad-band, automated, stripline technique for the simultaneous measurement of complex permittivity and permeability," *IEEE Trans. Microw. Theory Tech.*, vol. MTT-34, no. 1, pp. 80–84, Jan. 1986.

[30] M. J. Havrilla and D. P. Nyquist, "Electromagnetic characterization of layered materials via direct and de-embed methods," *IEEE Trans. Instrum. Meas.*, vol. 55, no. 1, pp. 158–163, Feb. 2006.

[31] E. Kilic, U. Siart, and T. F. Eibert, "Regularized 1-D dielectric profile inversion in a uniform metallic waveguide by measurement and simulation," *IEEE Trans. Microwave Theory Tech.*, vol. 60, no. 5, May 2012.

[32] A. Ihamouten, K. Chahine, V. Baltazart, G. Villain, and X. Derobert, "On variants of the frequency power law for the electromagnetic characterization of hydraulic concrete," *IEEE Trans. Instrum. Meas.*, vol. 60, no. 11, pp. 3658–3668, Nov. 2011.

[33] K. M. Fidanboylu, S. M. Riad, and A. Elshabini-Riad, "An enhanced time-domain approach for dielectric characterization using stripline geometry," *IEEE Trans. Instrum. Meas.*, vol. 41, no. 1, pp. 132–136, Feb. 1992.

[34] S. P. Dorey, M. J. Havrilla, L. L. Frasch, C. Choi, and E. J. Rothwell, "Stepped-waveguide material-characterization technique," *IEEE Antennas Propag. Mag.*, vol. 46, no. 1, pp. 170–175, Feb. 2004.

[35] A. Bogle, M. Havrilla, D. Nyquis, L. Kempel, and E. Rothwell, "Electromagnetic material characterization using a partially-filled rectangular waveguide," *J. Electromagnetic Waves and Appl.*, vol. 19, no. 10, pp. 1291–1306, 2005.

[36] R. A. Fenner, E. J. Rothwell, and L. L. Frasch, "A comprehensive analysis of free-space and guided-wave techniques for extracting the permeability and permittivity of materials using reflection-only measurements," *Radio Science*, vol. 47, pp. 1004–1016, Jan. 2012.

[37] C. P. Neo, V. V. Vardan, V. K. Vardan, L. F. Chen, and C. K. Ong, *Microwave Electronics,* John Wiley & Sons Ltd., West Sussex, England, 2004.

[38] A. A. Kalachev, S. M. Matitsin, L. N. Novogrudskiy, K. N. Rozanov, A. K. Sarychev, A. V. Seleznev, and I. V. Kukolev, "The methods of investigation of complex dielectric permittivity of layer polymers containing conductive inclusions," *Opt. and Elec.l Prop. of Polymers, Mats. Research Society Symposia Proceedings*, vol. 214, pp. 119–124, 1991.

[39] N. Maode, S. Yong, U. Jinkui, F. Chenpeng, and X. Deming, "An improved open-ended waveguide measurement technique on parameters ϵ_r and μ_r? of high-loss materials," *IEEE Trans. Instrum. Meas.*, vol. 47, no. 2, Apr. 1999.

[40] G. D. Dester, E. J. Rothwell, and M. J. Havrilla, "Two-iris method for the electromagnetic characterization of conductor-backed absorbing materials using an open-ended waveguide probe," *IEEE Trans. Instrum. Meas.*, vol. 61, no. 4, Apr. 2012.

[41] A. Bogle, "Electromagnetic material characterization of a PEC backed lossy simple media using a rectangular waveguide resonant slot technique," Ph.D. Dissertation, Michigan State University, East Lansing, MI, 2007.

[42] M. M. Scott, and D. L. Faircloth, "Microwave permittivity determination for materials with out-of-plane and off-diagonal dielectric anisotropy," *IEEE Trans. Microw. Theory Tech.*, vol. 61, no. 6, pp. 2471–2480, Jun. 2013.

[43] J. Helszajn, *The Stripline Circulator*, John Wiley & Sons, Canada, 2008.

[44] P. Queffelec, M. Le Floc'h, and P. Gelin, "New method for determining the permeability tensor of magnetized ferrites in a wide frequency range," *IEEE Trans. Microw. Theory Tech.*, vol. 48, no. 8, pp. 1344–1351, Aug. 2000.

[45] R. E. Collin, *Foundations for Microwave Engineering*, McGraw-Hill, Inc., New York, 1992.

[46] G. Dester, "Electromagnetic material characterization of a conductor-backed material," Ph.D. Dissertation, Michigan State University, East Lansing, MI, 2008.

[47] J. Tanton, *Encyclopedia of Mathematics*, Facts on File, Inc., New York, NY, 2005.

[48] M. D. Janezic and J. A. Jargon, "Complex permittivity determination from propagation constant measurements," *IEEE Microw. and Guided Wave Lett.*, vol. 9, no. 2, pp 76–78, Feb. 1999.

[49] B. R. Crowgey, O. Tuncer, J. Tang, E. J. Rothwell, B. Shanker, L. C. Kempel, and M. J. Havrilla, "Characterization of biaxial anisotropic material using a reduced aperture waveguide," *IEEE Trans. Instrum. Meas.*, vol. 62, no. 10, pp. 2739–2750, Oct. 2013.

[50] G. D. Dester, E. J. Rothwell, and M. J. Havrilla, "An extrapolation method for improving the accuracy of material characterization using waveguide probes," *IEEE Microwave Wireless Compon. Lett.*, vol. 20, no. 5, pp. 298–300, May 2010.

[51] R. A. Fenner, "Error analysis of reflection-only material characterization methods," Ph.D. Dissertation, Michigan State University, 2011.

[52] R. E. Collin, "A Simple Artificial Anisotropic Dielectric Medium," *IRE Trans. Microw. Theory Tech.*, pp. 206 - 209, April 1958.

[53] D. S. Killips, L. Kempel, D. Nyquist, and E. Rothwell, "Analysis of layering dielectrics on effective permittivity using wave matrices," IEEE Antennas and Propag. Society International Symposium, Washington, D.C., July 3-8, 2005, vol. 3A, pp. 212-215.

[54] J. C. Rautio, " Measurement of uniaxial anisotropy in Roger RO3010 substrate material," *COMCAS*, 2009.

[55] D. M. Pozar, *Microwave Engineering: Third Edition*, John Wiley & Sons Inc., Hoboken, NJ, 2005.

[56] W. H. Press, W. T. Vetterling, S. A. Teukolsky, and B. P. Flannery, *Numerical Recipes in Fortran; The Art of Scientific Computing: Second Edition*, Cambridge University Press, New York, NY, 1986.

[57] E. J. Rothwell, A. Temme, B. Crowgey, "Pulse reflection from a dielectric discontinuity in a rectangular waveguide," *Prog. In Electro. Research*, vol. 97, pp. 11–25, 2009.

[58] K. M. Lamber, C. L. Kory, "Notch filter insert for rectangular waveguide as a reference standard for material characterization," *NASA Tech Briefs: LEW-18137-1*, Glenn Research Center, Cleveland, OH, Jun. 2006.

[59] R. E. Collin, *Field Theory of Guided Waves*, McGraw-Hill, Hoboken, NJ, 1960.

[60] E. J. Rothwell and M. J. Cloud, *Electromagnetics: Second Edition*, CRC Press, Boca Raton, FL, 2008.

[61] R. F. Harrington, *Time-Harmonic Electromagnetic Fields*, John Wiley & Sons, Inc., New York, 2001.

[62] I. S. Gradshteyn, and I. M. Ryzhik, *Table of Integrals, Series, and Products*, Academic Press, San Diego, 2000.